

PROCEEDINGS OF THE SYMPOSIUM ON
ELECTRON AND ION BEAM
SCIENCE AND TECHNOLOGY
EIGHTH INTERNATIONAL CONFERENCE

Edited by

Robert Bakish

Bakish Materials Corporation
Englewood, New Jersey

and

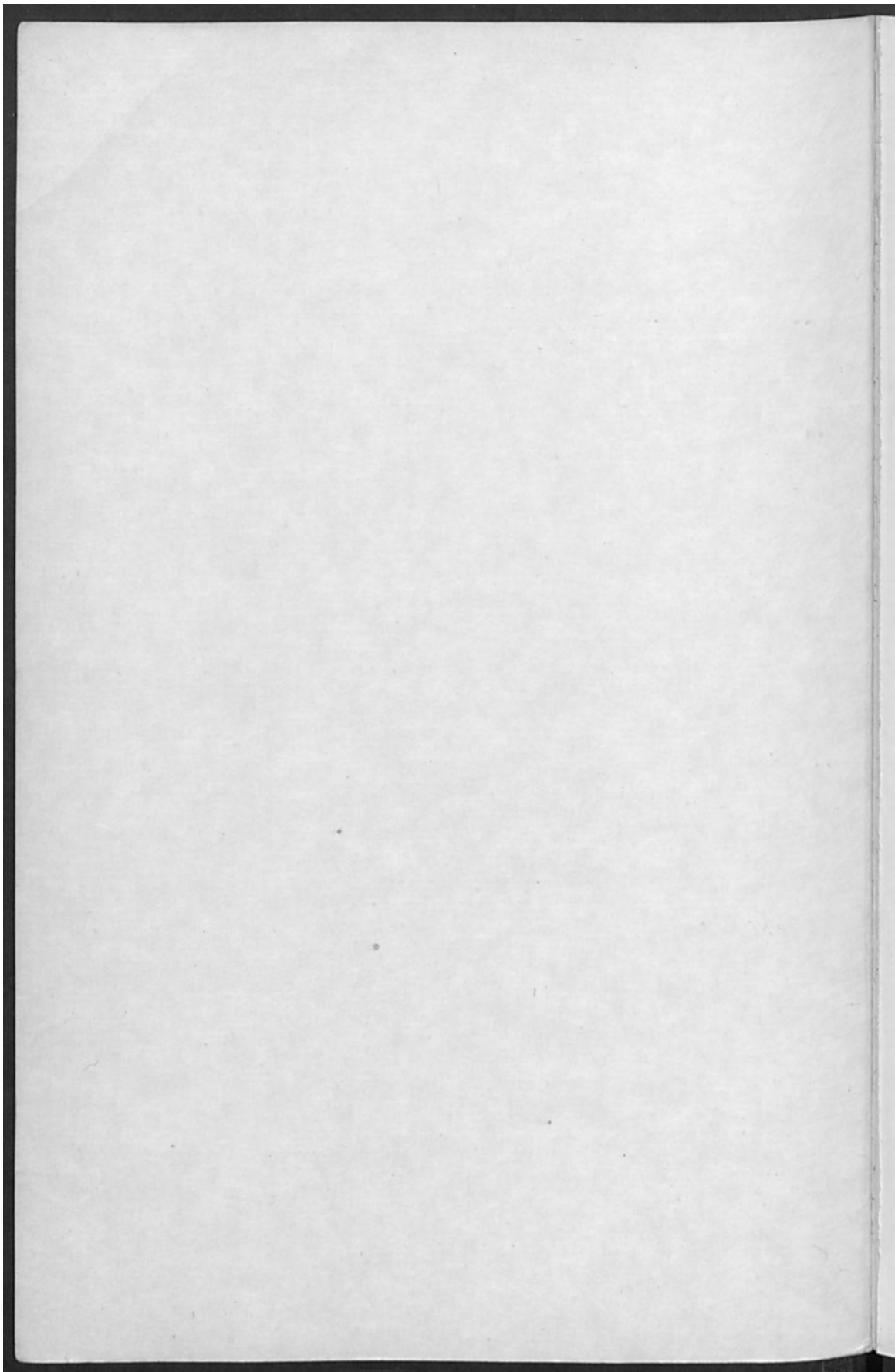
Fairleigh Dickinson University
Teaneck, New Jersey



ELECTRONICS AND ELECTROTHERMICS AND METALLURGY DIVISIONS

Proceedings Volume 78-5

THE ELECTROCHEMICAL SOCIETY, INC., Post Office Box 2071, Princeton, N.J. 08540



R. Bakish
personal copy

PROCEEDINGS OF THE SYMPOSIUM ON
**ELECTRON AND ION BEAM
SCIENCE AND TECHNOLOGY**
EIGHTH INTERNATIONAL CONFERENCE

Edited by

Robert Bakish

Bakish Materials Corporation
Englewood, New Jersey

and

Fairleigh Dickinson University
Teaneck, New Jersey



ELECTRONICS AND ELECTROTHERMICS AND METALLURGY DIVISIONS

Proceedings Volume 78-5

THE ELECTROCHEMICAL SOCIETY, INC., Post Office Box 2071, Princeton, N.J. 08540

The third section considers one of the very critical and "manufacturing rate limiting" of IC's with these systems, i.e., the electron resists which slow down production. Much work has been done here and progress has been made, but it seems that additional improvement will be most welcome.

Section four deals with proximity effects. This section follows the section on resists as these effects play an important role in the ultimate manufacturing objectives. It is the first of our conferences where this topic has sufficient work in progress to devote a session to it.

The fifth section includes the papers dealing with x-ray lithography and related topics. X-ray lithography together with electron lithography are on the way to becoming an inseparable part of the complex IC technology which is still evolving. The editor has also placed three papers dealing with electron beam recording here. While it was hoped that contributions dealing with electron beam recording would have been more numerous, this was not the case even though it appears that much growth is in progress.

The sixth section presents papers dealing with ion implantation and ion etching. Ion implantation is steadily making inroads in device production at the cost of diffusion processes, and much exciting growth lies ahead. The other papers, those dealing with etching and in general gaseous etching techniques, are also making major strides in attempting to become part of the complex IC advanced manufacturing developments. While aqueous etching processes still command a major position, virtues of ion etching processes certainly indicate that we will be seeing a greater fraction of the etching problem being resolved by gaseous etch processes. Many problems here remain to be solved.

The last section in fact is a section with a drastically different common denominator from the preceding six sections. The previous papers had low energy beams as their common denominator. By contrast, papers in this section are dealing with high power beams or thermal beams. After the review paper of K. H. Steigerwald, which considers the whole scope of thermal beams, we have several welding-related papers. Regretfully the response to our call for papers here was also less than satisfactory. The papers submitted for this session by no means indicate the profusion of activities and the tremendous growth that continues to take place here. Electron beam melting, refining, welding, and evaporation have become an inseparable part of today's materials processing technology.

R. Bakish
Englewood, New Jersey
August 30, 1978

INTRODUCTORY REMARKS

Ladies and Gentlemen,

It gives me great pleasure to welcome you here in the city of Seattle, the gem of the U.S. Pacific Northwest, on the occasion of the Eighth International Conference on Electron and Ion Beam Science and Technology. This, as most of you know, is the longest sequential conference held under the sponsorship of The Electrochemical Society. The electron and ion beam science and technology, in which we are all interested, is more vigorous today than in 1964 when I started this conference, and the over 70 papers to be presented here in Seattle are a strong testimonial to this fact. I hope that in the sixteen years since the Toronto event you too have been able to build many friendships with the scientists and engineers who make up this community.

As one who has been responsible for the planning of the event since its inception and who is¹ also the party to edit the manuscript, I have a few comments to make.

I know that you will find the oral presentations throughout the week worthwhile and that your attendance at the Eighth International Conference on Electron and Ion Beam Science and Technology will be both profitable and pleasant. I now present Mr. Steigerwald, our first invited speaker, who will share with us twenty years of progress in electron beams.

R. Bakish
Seattle, Washington
May 22, 1978

¹*Publication Editor's Note:* At this point Dr. Bakish provided some procedural details for submission of papers scheduled for presentation and for inclusion in this volume.

ACKNOWLEDGMENT

The speakers whose presentations are contained in these proceedings, members of the conference committee, and session chairmen and co-chairmen whose names are given below have contributed to the success of this meeting. Their contribution is gratefully acknowledged. M. Allais, W. Barwicz, E. Bas, F. Benesowski, M. Boston, T. H. P. Chang, M. Coutts, L. A. Fontijn, L. Habraken, M. Hatzakis, C. Hayashi, A. E. Jenkins, J. Kelly, G. Molenstedt, S. Namba, W. C. Nixon, N. A. Olshanski, F. S. Ozdemir, B. Paton, H. C. Pfeiffer, K. Pickar, P. Reader, P. Rose, G. Slodzian, W. W. Smeltzer, H. I. Smith, H. D. Steffens, J. B. Thaxter, C. H. Ting, P. A. Turner, M. van Ardenne, A. Wittkower.

Special thanks are given to my wife, Ellen, who patiently puts up with the never ending projects with which I get involved.

TABLE OF CONTENTS

Preface	iii
Introductory Remarks	v
Acknowledgments	vi
<u>SECTION 1 - FUNDAMENTALS OF SYSTEM COMPONENTS</u>	
A High Brightness High Current Field Emission Electron Probe H. P. Kuo and B. Siegel.....	3
Application of Field Emission in High Current Electron Beam Lithography Optics L. Veneklasen, N. Yew, and J. Wiesner.....	11
Developments in Electron Beam Microprojection: The Electromagnetic Zoom Lens of Hybrid Type and Divergent Mask Irradiation A. Oelmann, W. Munchmeyer, and M. Sturm.....	17
Optimization Parameters of Combined Magnetic Lenses and Deflection System for Electron Beam Microlithography E. De Chambost.....	23
Optics of a Variable Shaped Electron Beam Column W. Stickel and H. C. Pfeiffer.....	32
Distortion Correction in Scanning Electron Beam Systems R. Viswanathan, T. H. P. Chang, and D. Coffey.....	44
Development of a UHV 150 kV Microfocus Rod Anode X-Ray System L. A. Fontijn.....	57
Auto-Registration Technique for an Electron Beam Exposure System Using a New Sheet Structured Detector for Back- Scattered Electrons Y. Furukawa, N. Nakayama, Y. Goto, S. Igaki, and T. Inagaki.....	63
Analysis of Straightedge-, Wire- and Double-Wire Probe Data for Determining Electron or Ion Beam Profile S. Ugniewski.....	71

SECTION 2 - ELECTRON BEAM LITHOGRAPHY SYSTEMS

Electron Beam and X-Ray Lithography for Very Large Scale Integration Devices	
T. Hayashi.....	85
The Philips Electron Beam Pattern Generator	
J. P. Beasley, D. B. Spencer, and R. A. Beelaard.....	98
Electron Projection Lithography	
C. E. Fuller, P. A. Gould, and D. J. Vinton.....	108
Electron Lithography System with Variable-Shaped Electron Beam	
G. Cogswell, S. Miyauchi, K. Tanaka, and N. Goto.....	117
Design of Variable Shaped Beam Systems	
E. Goto, T. Soma, M. Idesawa, and T. Sasaki.....	135
Advanced Beam Shaping Techniques for Electron Lithography	
H. C. Pfeiffer and G. O. Langner.....	149
Investigations about High Performance Electron-Microprojection Systems	
B. Lischke, K. Anger, W. Munchmeyer, A. Oelmann, J. Frosien, R. Schmitt, and M. Sturm.....	160
A Study on the Operation Conditions for (1:4) Electron Projection Systems	
B. Lischke, K. Anger, J. Frosien, G. Gorges, and W. Munchmeyer.....	170
Electron Beam Microfabrication Using a Long Working Distance Lens with Post-Lens Deflection	
J. Reeds, K. Amboss, R. Fralick, E. Wolf, and B. Wallman.....	179
A Data Processing System for Electron-Beam Lithography	
N. Sugiyama, N. Aizaki, A. Kawaji, and Y. Tarui.....	184
A Comparison of Pattern Stitching by Subfield Registration and Laser Interferometer Servo Control	
A. D. Wilson, T. W. Studwell, G. Folchi, A. Kern, and H. Voelker.....	198
Use of Simulation to Optimize Projection Printing Profiles	
A. R. Neureuther, M. O'Toole, W. G. Oldham, and S. N. Nandgaonkar.....	206
Electron Beam Microfabrication of GaAs Integrated Circuits	
F. S. Ozdemir, L. H. Hackett, P. T. Greiling, C. F. Krumm, O. W. Otto, and R. F. Lohr.....	216

High Density RAM Cells Fabricated by E-Beam Lithography P. K. Chatterjee, H-S. Fu, R. L. Easley, A. F. Tasch, Jr., and T. C. Holloway.....	222
--	-----

Electrodeposition Process for Fabrication of the Conductor First, SLM, 2 μ m Bubble Memory M. C. Blakeslee, L. T. Romankiw, R. E. Acosta, S. Krongelb, and B. Stoeber.....	232
---	-----

SECTION 3 - ELECTRON RESISTS

Investigations of Electron Beam-Resist Interactions in Electron Lithography M. S. C. Chung and K. L. Tai.....	242
---	-----

Experimental Determination of the Effect of Backscattered Electrons on the Dissolution Rate of PMMA F. Jones and M. Hatzakis.....	256
---	-----

Electron Beam Resist Line Edge Profile Modeling A. R. Neureuther, D. F. Kyser, K. Murata, and C. H. Ting..	265
---	-----

An Exposure Wedge for Electron Beam Lithography Development Control and for the Determination of Resist Development and Proximity Effect Parameters (1) W. D. Grobman and A. J. Speth.....	276
---	-----

Diazo-Type Photoresist Systems under Electron Beam Exposure M. Hatzakis and J. M. Shaw.....	285
--	-----

New Photoresists Containing Thirane Groups J. C. Dubois, A. Eranian, and E. Datamanti.....	303
---	-----

AZ2400 as a Deep-UV Photoresist B. J. Lin.....	320
---	-----

Poly(Methyl Methacrylate-Co-Acrylonitrile) - A Sensitive Positive Resist Y. Hatano, H. Shiraishi, Y. Taniguchi, S. Horigome, S. Nonogaki, and K. Naraoka.....	332
--	-----

Preliminary Investigations of Azide Containing Negative Resists: Poly(Vinylbenzyl Azide) C. W. Wilkins, Jr., E. D. Feit, and M. E. Wurtz.....	341
---	-----

SECTION 4 - PROXIMITY EFFECTS

Computer Control of Proximity and Size Effects in Electron Lithography H. I. Ralph and H. Sewell.....	354
---	-----

Proximity Effect Correction in Electron-Beam Lithography N. D. Wittels and C. I. Youngman.....	361
Proximity Function Approximations for Electron Beam Lithography M. Parikh and D. F. Kyser.....	371
Proximity Effect Corrections in Electron Beam Lithography M. Parikh.....	382
Proximity Effect in FET Fabrication with Electron Beam Lithography H. Nakata, T. Kato, K. Murata, and K. Nagami.....	393
Electron Beam Step and Repeat Proximity Printing H. Bohlen, J. Greschner, W. Kulcke, and P. Nehmiz.....	406
Silicon Supported EB Proximity Masks H. Bohlen, J. Greschner, and P. Nehmiz.....	420

SECTION 5 - X-RAY LITHOGRAPHY

High Speed X-Ray Lithography with Radiation from Laser- Produced Plasmas M. C. Peckerar, J. R. Greig, D. J. Nagel, R. E. Pechacek, and R. R. Whitlock.....	432
Profiles of Structures in PMMA by X-Ray Lithography P. Tischer and E. Hundt.....	444
X-Ray Lithography with Aluminum Radiation and SiC Mask R. K. Watts, K. E. Bean, and T. L. Brewer.....	453
X-Ray Exposure and Development Characteristics of Polyglycidal Methacrylate-Ethyl Acrylate W. D. Buckley and J. A. Dalle Ave.....	458
Fabrication of Optical Devices by X-Ray Lithography by Using Synchrotron Radiation H. Aritome, S. Matsui, K. Moriwaki, S. Hasegawa, and S. Namba.....	468
Magnetic Bubble Device Fabrication Using X-Ray Lithography B. F. Stein and M. J. Casey.....	480
An Electron Gun for Videodisc Recording G. H. N. Riddle, R. R. Demers, and J. Valachovic.....	490

Electron Beam Recording of Masters for the Videodisc J. H. Reisner, G. H. N. Riddle, S. M. Zollers, L. H. Lin, E. D. Simshauser, W. P. Morewood, R. R. Demers, and J. Guarracini.....	500
--	-----

Optical Process Control of Video Recording in Resist Films L. H. Lin.....	517
--	-----

SECTION 6 - ION IMPLANTATION

Ion Implantation Yesterday, Today and Tomorrow P. H. Rose.....	534
---	-----

High Current Ion Implanter Using Microwave Ion Source N. Sakudo, K. Tokiguchi, H. Koike, and I. Kanomata.....	543
--	-----

An Automated Test System for Measuring and Displaying the Doping Uniformity of Ion-Implanted Silicon Wafers F. E. Wahl and D. S. Perloff.....	556
---	-----

Ion Implantation for Large Scale Automated Production of Solar Electric Cells A. R. Kirkpatrick and G. Ryding.....	571
--	-----

Damage Caused by AR Ion Beam Etching H. Yano, H. Hashimoto, and Y. Toyama.....	582
---	-----

SECTION 7 - HIGH POWER BEAMS

History, Present State and Future of the Use of Electron Beams as Thermic Tool H. K. Steigerwald.....	594
---	-----

Possibilities and Future of High Power EBW in the Heavy Industries G. Sayegh and R. Roudier.....	604
--	-----

Temperature Distribution in Solids during Electron Beam Welding G. Basile and A. Moisan.....	618
--	-----

On the Effects of Gas/Vapor and Plasma on High Power Electron Beam Generation and Guidance S. Schiller, G. Jasch, and A. von Ardenne.....	627
---	-----

Electron Beam Machining in the Field of Hybrid Technique S. Schiller, S. Panzer, and J. Henneberger.....	645
---	-----

Tests of Fourth-Order Difference Equations for Laplace's Equation in Cylindrical Coordinates C. E. Kuyatt and A. Galejs.....	655
Subject Index.....	659

A HIGH BRIGHTNESS HIGH CURRENT FIELD EMISSION ELECTRON SOURCE

H. F. Yao* and M. Siegel

School of Applied and Engineering Physics

Cornell University

Ithaca, N.Y. 14853

A high brightness electron probe fusion system can be designed with a field emitter and a pre-accelerator lens with low aberration coefficients and can be operated to minimize the aberrations introduced by the accelerator. Such a system using an electrostatic lens was proposed and designed by Venekian and Siegel (1). A significant improvement in performance can be achieved by using the electrostatic lens with a magnetic lens that has low aberration coefficients.

FUNDAMENTALS OF SYSTEM COMPONENTS

An "optimized" magnetic lens suitable for this application was designed by determining the lowest possible aberration coefficients which are compatible with low lens power consumption and ease of operation of the field emitter. The lens used has lens diameters of 1cm and 2.5cm and a gap of 0.5cm. The axial magnetic field is plotted in Figure 1. The peak axial field was obtained from the following expression:

$$B_z = 0.213 \frac{NI}{10^4}$$

with NI in ampere-turns, B_z in gauss/cm and N in turns. At normal operating conditions, $NI = 500$ ampere-turns, $B_z = 0.1065$ kilogauss. The calculated critical properties of the lens are shown in Figures 2 and 3.

*Now at Hewlett Packard, Palo Alto, Calif.

Table of Contents

1. Introduction	1
2. System Components	10
3. System Architecture	20
4. System Implementation	30
5. System Evaluation	40
6. Conclusion	50

SYSTEM COMPONENTS

Section 1

A HIGH BRIGHTNESS HIGH CURRENT FIELD EMISSION ELECTRON PROBE

H. P. Kuo* and B. Siegel

School of Applied and Engineering Physics

Cornell University

Ithaca, N.Y. 14853

A high brightness electron probe forming system can be designed with a field emitter and a pre-accelerator lens with low aberration coefficients and can be operated to minimize the aberrations introduced by the accelerator. Such a system using an electrostatic einzel lens was proposed and designed by Veneklasen and Siegel (1). A significant improvement in performance can be achieved by replacing the electrostatic lens with a magnetic lens that has much lower aberration coefficients.

An "optimized" magnetic lens suitable for this application was obtained by determining the lowest possible aberration coefficients which are compatible with low lens power consumption and ease of operation of the field emitter. The lens used has bore diameters of 7mm and 2.5mm and a gap of 1mm. The axial magnetic field is plotted in Figure 1. The peak axial field can be obtained from the following expression

$$B_o = 0.315 \frac{4\pi NI}{10S}$$

with NI in ampere turns, S in centimeters and B_o in Gauss. At normal operating conditions, NI = 800 ampere-turns, $B_o = 3.16$ Kilogauss. The calculated optical properties of the lens are shown in Figures 2 and 3.

*Now at Hewlett Packard, Palo Alto, Calif.

Figure 2 shows the focal length, f_o , the object focal point, F_o (measured from the second pole face), the spherical aberration coefficient at infinite magnification, $C_s^{(\infty)}$, and the chromatic aberration coefficient at infinite magnification, $C_c^{(\infty)}$, as functions of lens excitation. The image position, z_i , lens magnification, M_m , spherical aberration coefficient, $C_s(M)$, and chromatic aberration coefficient, $C_c(M)$ (for given magnifications, M_m), are plotted in Figure 3 as functions of lens excitation for a field emitter position of 2.8mm in front of the second pole face.

The physical structure of the lens and field emitter assembly is shown in the cross-sectional schematic, Figure 4. A nitrogen or oxygen processed $<100>$ emitter (2,3) operated at 900°C and a total emission current of $10\mu\text{a}$ was used. The measured angular emissivity was $130\mu\text{a/sr}$ at this emission current.

When the system is operated so that a magnified image of the "source" is formed at the nodal point of the accelerator, as proposed by Veneklasen and Siegel (1), the virtual cross-over size of the beam is determined only by the quality of the pre-accelerator lens. The theoretical virtual cross-over radius can be calculated by quadratic addition of the intrinsic source radius, the source size due to diffraction, and the aberration figures produced by spherical aberration and chromatic aberration. The intrinsic source size was taken to be 60 \AA . The calculated "effective" source size at the emitter (2kV) is shown in Figure 5 as a solid line. The source size was measured at 20kV and extrapolated to 2kV, and these values are also shown in Figure 5 for several acceptance angles.

The source size was measured by using two magnetic lenses after the accelerator to produce a magnified image of the source. This image was swept across orthogonally placed razor edges and the beam diameter was

determined from the maximum slope of the current response, measured as the beam swept across the razor edges. The effective source radius at the tip (2kV) was then calculated using the known magnifications of the lenses in the optical system. The angular aperture of the beam was set by the acceptance angle of physical aperture in the field emission electrode and was measured by observing the geometrical projection of the beam with the lenses off. When a magnetic pre-accelerator lens is used, as in this system, a correction must be made for the beam convergence caused by the fringing magnetic field that extends into the region of the field emitting tip. The details of these methods and measurements have been described elsewhere (2).

As shown in Figure 5, at an acceptance semi-angle of 12.5 mr, the measured radius was 150 Å while the calculated radius was 70 Å. This discrepancy between theoretical and measured source size can be attributed, most probably, to misalignment and astigmatism of the electron optical system or to a larger chromatic aberration figure than assumed in the theoretical model. At larger beam acceptance angles the source size becomes spherical aberration limited and good agreement between theoretical and measured spot sizes was observed. The "effective" brightness of the system can be expressed by,

$$\beta = \frac{J_{\Omega}}{\pi\rho^2} \cdot \frac{V_1}{V_0}$$

where J_{Ω} is the angular emissivity, measured to be 130 μa/sr for a W<100> processed (or built-up) emitter operated at 10 μa total emission current and ρ is the spot radius. For a beam voltage of 20KV the measured

brightness at an acceptance semi-angle of 2×10^{-2} rad. was $\sim 5 \times 10^7$ amps/sr/cm². A similar system with a completely electrostatic gun gave $\beta \sim 6 \times 10^6$ amp/cm²/sr. under the same operating conditions (2).

In practice where high current, high resolution probes are desired, the spot size will be determined by the aberrations of both the first (pre-accelerator) lens and final (projector) lens. For a completely spherical aberration limited system, the final spot size will be

$$\rho = \frac{1}{4} (MC_{s1} \alpha_o^2 + C_{s2} \alpha_i^2)$$

where α_o is the source semi-angle and α_i is the image semi-angle, given by

$$\alpha_i = \frac{1}{M} \frac{V_o}{V_i} = \frac{1}{Mr}$$

If the spot magnification is optimized for the smallest spot at a given current, the following relation is obtained

$$I_{\max} = \frac{6.6r^{\frac{1}{2}} J \Omega}{C_{s1}^{\frac{1}{2}} C_{s2}^{\frac{1}{6}}} \rho^{\frac{2}{3}}$$

Similarly an optimized probe with a thermionic source of brightness β_1 gives the relation,

$$I_{\max} = \frac{10 r \beta_1}{C_{s2}^{\frac{2}{3}}} \rho^{\frac{8}{3}}$$

The probe current as a function of probe radius is plotted in Figure 6 for the field emission and thermionic systems. In comparison, the

field emission system has better performance than the LaB_6 system for probe radii $\leq 1000 \text{ \AA}$. The dashed curve in Figure 6 shows the projected performance of the field emission system with a magnetic pre-accelerator lens and a total emission current of $100 \mu\text{a}$, assuming chromatic aberration effects do not dominate the performance at this higher emission current.

When these sources and systems are used for electron beam lithography the deflection aberrations introduced by the final projector lens and deflector systems are of crucial importance. If a magnetic projector lens is used there are eleven aberrations associated with this system but only the two distortion aberrations are independent of the angular divergence of the electron beam. Therefore the reduction in angular divergence that can be realized with the higher brightness field emission systems provide significant potential in the gain in resolution and/or field size that can be realized. As an example, we have calculated the beam semi-angle on the target assuming the measured data for the field emission system and the reported data on a LaB_6 system. The values obtained are plotted as functions of beam current in Figure 7 for a spot diameter of $0.1 \mu\text{m}$ using a non-limiting projector lens. For currents smaller than 800 na the field emission system gives a rapidly decreasing angular divergence.

Munro has calculated the values of the aberrations at the corners of a $5 \times 5 \text{ mm}$ field for several different configurations of deflector systems using a "good" projector lens with a divergence angle of $5 \times 10^{-3} \text{ rad.}$ and a beam voltage ripple of $1:10^4$ (5). From Figure 7 it can be seen that using the field emission system with an angular aperture of only $2 \times 10^{-3} \text{ rad.}$ provides a focussed probe with substantially greater beam current than a

LaB₆ thermionic source with a 5×10^{-3} rad. angular aperture. Choosing the optimum deflection system from Munro's data (5) in which two in-lens deflector yokes are used, we have calculated that an effective spot size of 0.12 μ m could be realized using dynamic correction of distortion and field curvature. Our data indicates that a beam current of ~70na with 10 μ a total emission could be achieved while the LaB₆ source would give only 1.2na under the same operating conditions. These projections indicate the potential of field emission systems for high resolution and high probe current that can, but are not yet realized for application in electron beam lithography.

REFERENCES

1. L.E. Veneklasen and B.M. Siegel, J. Appl. Phys. 43, 4898, 1972.
2. H.P. Kuo, Thesis, Cornell University, 1976.
3. L.E. Veneklasen and B.M. Siegel, J. Appl. Phys. 43, 1600, 1972.
4. P. Grivet, "Electron Optics", 2nd Edition, Pergamon, New York (1972) p. 775.
5. E. Munro, Proc. 13th Symposium on Electron, Ion, and Photon Beam Technology, 1975, p. 1146.

This work was supported by N.I.H. Grant GM 12873 and N.S.F. Grant BMS 75-21709

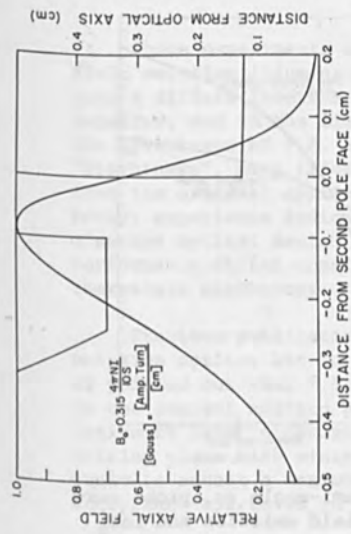


Fig. 1. Axial magnetic field distribution. Straight outlines indicated the shape of the magnetic pole pieces.

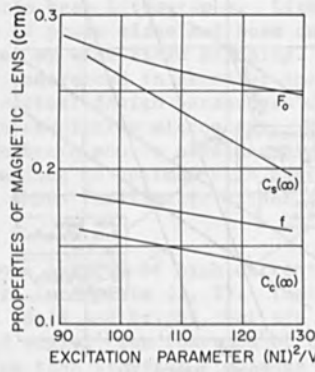


Fig. 2. Optical properties of the magnetic pre-accelerator lens.

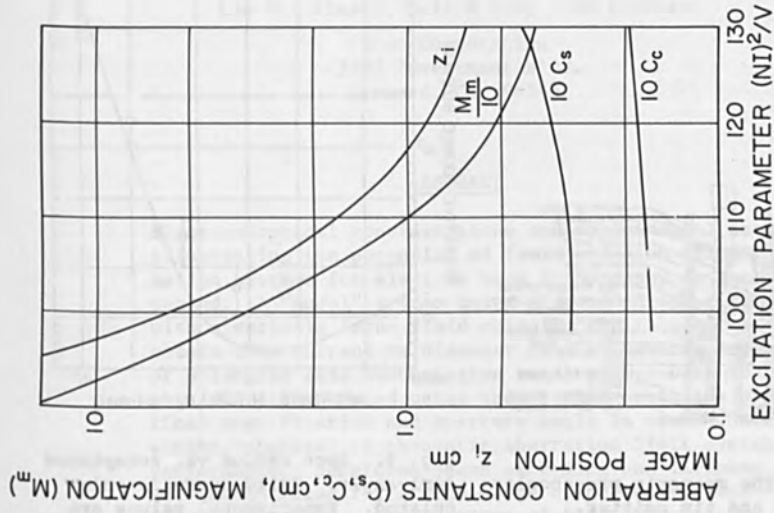


Fig. 3. Electron optical properties of the magnetic lens with a field emitter 2.8 mm from the second pole face.

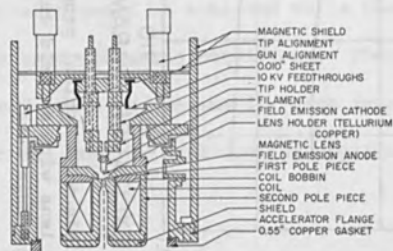


Fig. 4. The magnetic pre-accelerator lens and tip emitter.

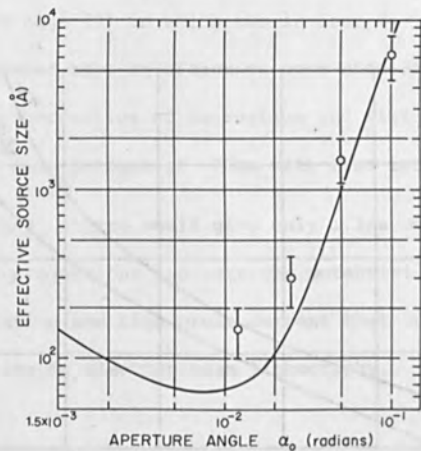


Fig. 5. Spot radius vs. acceptance semi-angle. Solid curve is calculated. Experimental values are shown with estimated error bars.

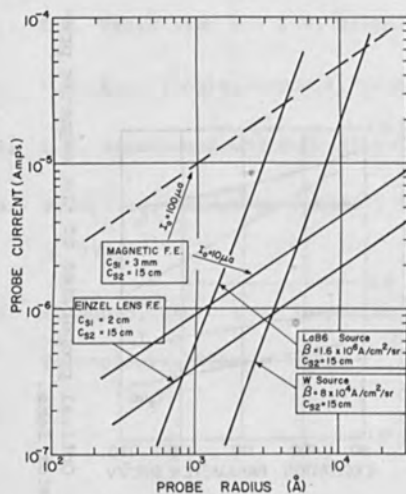


Fig. 6. Probe current vs. probe size for various probe forming systems.

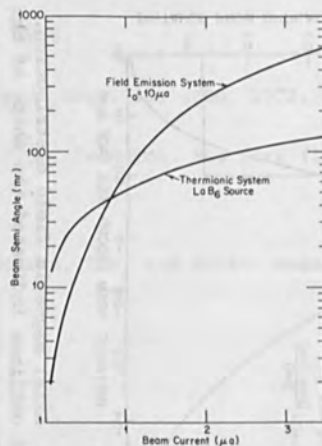


Fig. 7. Semi-angle vs. probe current for field emission and LaB₆ system.

APPLICATION OF FIELD EMISSION IN
HIGH CURRENT ELECTRON BEAM LITHOGRAPHY OPTICS

Lee Veneklasen, Nelson Yew, John Wiesner

Etec Corporation
3392 Investment Blvd.
Hayward, CA 94545

ABSTRACT

Electron optical considerations and experimental data illustrating the potential of field emission illumination systems for electron beam lithography is presented. A "model" system using a standard SEM fitted with a variable focus field emission gun is used to obtain beam current vs diameter data at several sets of objective lens and emission conditions. Data is partially interpreted using theory that optimizes optical magnification and aperture angle in cases where either spherical or chromatic aberration limit system performance. Submicron beams exceeding one microamp are demonstrated for a wide range of objective lens conditions. Broad implications of F.E. illumination upon writing speed and strategies, as well as other system tradeoffs, are isolated for further investigation.

These experiments were designed to investigate the potential of field emission illumination in electron beam lithography. Lithography optics differs from SEM in the range of probe sizes and beam currents required, and in the limitations posed by wide field scanning. While the advantages of F.E. are generally understood in terms of increased "brightness", most literature and practical design parameters derive from its original application in high resolution microscopy. More recent experience indicates that both basic source considerations and electron optical design strategies leading to optimum high current performance differ considerably from those familiar to either F.E. or thermionic microscopy.

Previous publications discuss some aspects of high current field emission optics, but in retrospect are incomplete (1, 2). There, it is pointed out that F.E. sources are small and bright, but are limited in the current emitted per unit solid angle. The function of the optics is less to demagnify the source than transfer its image to the writing plane with minimum degradation. To obtain high currents one wants to accept a maximum angular aperture at the source, however acceptance apertures in the gun are limited by gun aberrations.

Similarly, objective lens apertures are limited by axial aberrations, and even more important, by off-axis aberrations associated with the large scan fields desirable in lithography. Thus an essential aspect of high current field emission optics is to provide for independent optimization of beam radius or aperture angle in a gun and final lens. In practice, this means optimization of the system's total magnification and beam limiting aperture. Given a reliable source with high emission per solid angle and high quality lenses, determination of optimum magnifications, apertures and emission conditions, and the relative importance of various aberrations becomes the goal of this work.

Based on the general principles above, the field emission gun and optical system, shown schematically in Figure 1, were designed. With the exception of the electron gun, the model system is a standard Autoscan SEM whose beam aperture is variable and whose objective lens spherical and chromatic aberration may be varied by choice of working distance. Although the system is hardly suited for lithography, its ability to vary objective lens geometry to model various objective lens design tradeoffs provides valuable insight.

The electron gun uses a <100> built-up (oxygen processed) cathode chosen for reliable and predictable performance at high angular emissivity (3). The gun lens is a tetrode configuration which is an accelerating lens with a control electrode to vary its focal length. The electrode shape and configuration were chosen to minimize aberrations, but final optimization remains subject to the interpretation of the results of this experiment.

The function of the gun lens is to collimate the beam entering the objective lens, providing a variable ratio of gun to objective aperture. For a fixed objective aperture, the more collimated the beam, the larger the angle subtended by the gun lens and the larger the beam current. In other words, the gun lens varies the system magnification.

Figure 2 shows the results of a series of experiments that plot beam current vs probe diameter. The probe diameter criteria is 15 to 85% width of a line scan of secondary emission current as the probe was scanned across sharp edges on a gold plated copper grid. If the probe were Gaussian, the diameter so defined would contain somewhat less than 50% of the total beam. Since the probe current density distribution is clearly a more complicated convolution of aberration figures, this criteria is somewhat pessimistic.

In Figure 2, probe current vs diameter is plotted for several aperture angles as gun collimation (system magnification) was varied. The set of best data points represents a condition where both aperture diameter and magnification were roughly optimum for a particular probe diameter. To indicate the dependence of the system upon source

emission current and objective lens aberrations, the experiments were repeated at two different emission currents and working distances.

Several results seem to bear emphasis. Using a fairly high quality objective lens, probe currents exceeding $1\mu\text{A}$ were obtained in probes of $0.1\text{-}0.5\mu\text{m}$ of interest to advanced lithography. With both objective lens configurations, field emission outperforms tungsten cathodes by factors ranging from 200 to 500X. The crossover point where thermionic cathodes (W or LaB₆) become superior seems to lie in the area of $1\text{-}4\mu\text{m}$ ($5\text{-}10\mu\text{A}$). Insofar as this crossover point has considerable bearing on design decisions, it seems appropriate to point out that the movement of this point to higher currents is due to evolution in F.E. design rather than error in original estimates.

To place these results within a theoretical framework, Figure 3 extends the optimization procedures in reference 1 to include cases where chromatic aberration limits acceptance apertures in the system. To match the data, it is necessary to make some semi-empirical assumptions about the source characteristics; in particular its energy spread at various emission currents. Figure 4 compares the data with optimized current vs probe diameter curves in the ranges where chromatic and spherical aberrations dominate. To match the data, it is necessary to assume increasing energy spread with emission current, suggesting that an optimum emission current exists. The deviation from the theory in the low current, high resolution regions can be explained either by space charge broadening of the virtual source, or more likely by the fact that smaller apertures were not used in the original experiment. Lacking an independent determination of source parameters, the interpretation of the lower current data is inconclusive.

Nevertheless, the prognosis for field emission in the areas of high resolution lithography, now limited by resist sensitivity or exposure time, seems excellent. Subject to parallel evolution of other technologies involved, the implication of Figure 2 is that either (or both) faster exposure of slow, high resolution resists or smaller geometries with present exposure rates become possible.

Perhaps more subtle is the impact upon writing strategies. At any given current and probe diameter, the maximum radius of the beam as it traverses the objective lens and deflection system is characteristically smaller using field emission. One implication is that the field inhomogeneities inherent in lenses and deflection fields have a smaller effect upon the probe diameter as it is scanned off axis, and larger (electromagnetically) scanned fields become possible. In turn, the optical, electronic and mechanical tradeoffs involved in e.g. continuous raster scan stage motion vs quasi-stationary stage vector scan, and shaped or variable shaped beam vs source imaging optics, take on new aspects. The implications of the new gun technology seem to warrant investigation from a broad, operations-oriented viewpoint.

REFERENCES

1. L. H. Veneklasen, Optik 36, 410 (1972).
2. Physical Aspects of Electron Microscopy and Microanalysis, ed. by B. Siegel and D. Beaman. Wiley & Sons, N.Y. (1975).
3. L. H. Veneklasen and B. M. Siegel, J. Appl. Phys. 43, 1600 (1972).

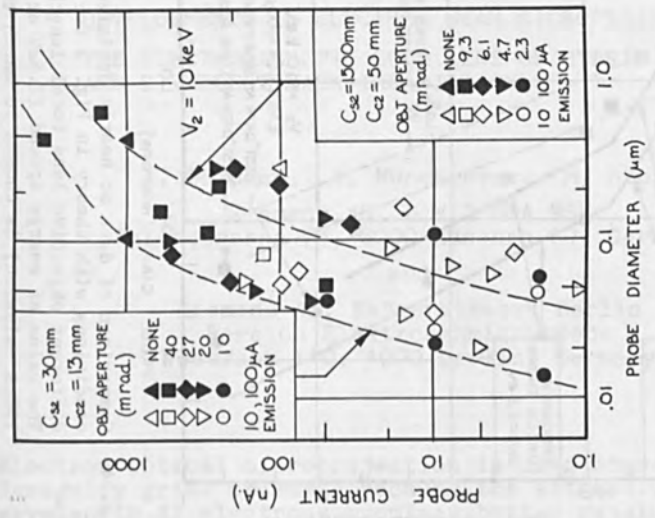


Fig. 2. Results of current vs probe diameter measurements.

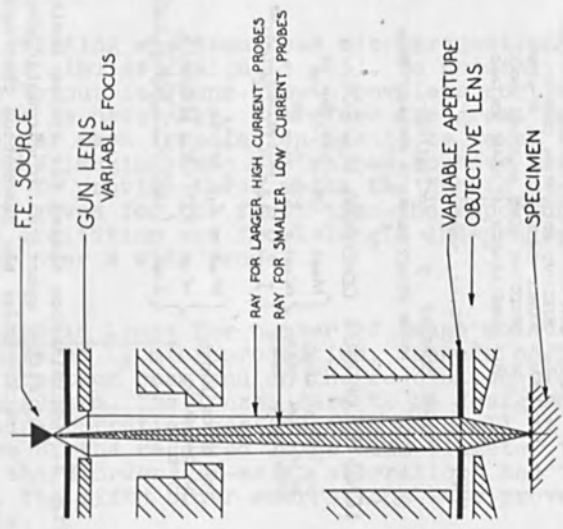


Fig. 1. Schematic diagram of high current F.E. gun optics showing typical ray paths for high and low current operation.

BASIC EQUATION FOR PROBE DIAMETER:

$$\delta^2 = M^2 \delta_s^2 + (C_{s1}^2 M^3 r^3 + C_{s2}^2) \alpha^2 / 4 + (C_{c1}^2 M^2 r + C_{c2}^2 / r^2) (\Delta V / V)^2 \alpha^2 + \lambda_z^2 / 4$$

WHERE M = SYSTEM MAGNIFICATION
 δ_s = SOURCE DIAMETER AT $dI/d\Omega$
 $r = V_z / V_1$ = RATIO OF BEAM TIP VOLTAGE
 C_{s1}, C_{s2} = GUN CHROMATIC / SPHERICAL ABERRATION
 C_{c1}, C_{c2} = OBJECTIVE ABERRATION COEFFS.
 ΔV = SOURCE ENERGY SPREAD AT $dI/d\Omega$
 α = OBJECTIVE LENS APERTURE ANGLE
 λ_z = WAVE LENGTH AT BEAM VOLTAGE

AND: GUN APERTURE $\alpha_0 = M/r \alpha$
 BEAM CURRENT $I = \pi r \alpha_0^2 (dI/d\Omega)$
 WHERE $dI/d\Omega = \text{AMPS/SR. AVAILABLE FROM F.E. DIODE}$

LEADS TO OPTIMUM CONDITIONS M, α FOR:

FOR OPTICS LIMITED BY SPHERICAL ABERRATION (OPTIC 36-410)(PZ2)

$$\begin{cases} M_{\text{opt}} = 1.15 C_{s2}^{1/4} / r^{3/8} C_{s1}^{1/4} \\ \alpha_{\text{opt}} = \delta^{1/3} / C_{s2}^{1/3} \\ I_{\text{opt}} = [4.2 r^{1/4} / C_{s1}^{1/2} C_{s2}^{1/6}] [dI/d\Omega] \delta^{2/3} \end{cases}$$

FOR OPTICS LIMITED BY CHROMATIC EFFECTS

$$\begin{cases} M_{\text{opt}} = C_{c2}^{1/2} / r^{3/4} C_{c1}^{1/2} \\ \alpha_{\text{opt}} = [0.71 r / C_{c2}] [V_1 / \Delta V] \delta \\ I_{\text{opt}} = [1.6 r^{3/2} / C_{c2}] [V_1 / \Delta V] [dI/d\Omega] \delta^2 \end{cases}$$

Fig. 3. Optimization theory for system limited by either spherical or chromatic aberration under the assumption that source size and diffraction are negligible in the higher current ranges.

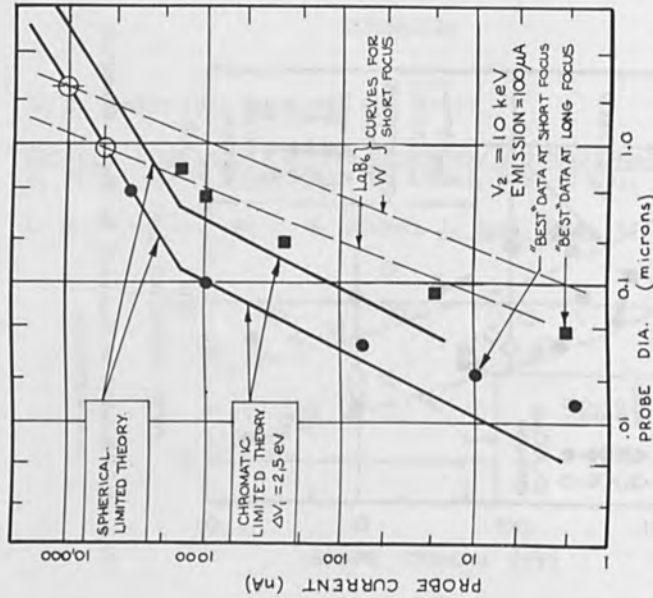


Fig. 4. Comparison of data at nearly optimized conditions with theory in Fig. 3 for two different objective lens focal lengths. The value of energy spread (2.5 eV at 100 μA emission) is chosen to match the experimental data.

DEVELOPMENTS IN ELECTRON BEAM MICROPROJECTION:

THE ELECTROMAGNETIC ZOOM LENS OF HYBRID TYPE
AND DIVERGENT MASK IRRADIATION

A. Oelmann, W. Münchmeyer, M. Sturm

Siemens AG, B WIS GTA MSE
Balanstrasse 73, 8000 München 80, Germany

and

Siemens AG, Meßgerätewerk Berlin
Bereich Elektronenmikroskope
Postfach 140, 1000 Berlin, Germany

Electron optical microprojection is used since 1959 to demagnify grids or masks because the extremely short wavelength of electrons promises better resolution than is obtainable with light. But due to large aberrations of electron optical lenses the improvement is not as large as would be related to the decrease in wavelength.

The existing electron beam microprojection systems are all of similar design (1 - 3). So possibly the best system layout is found. Now a complete control of all parameters is necessary. Therefore the great influence of non parallel mask irradiation has to be taken into account and the imaging lens system has to have means for adjustment. To provide these means the Hybrid Lens was designed which gives for the first time the opportunity to vary lens excitation and focal length independent from each other over a wide range.

The Hybrid Lens: The number of image points, which can be transferred by microprojection, depends on the diameter of the electron beam and on the resolution of the imaging lens system. The lenses have to be designed carefully to obtain aberration coefficients as small as possible. Because of the required large beam diameter the axial and the third order off-axial aberrations had to be calculated. The fifth order aberrations were proved to be negligible.

Different theoretical lens fields $B(z)$ (fig. 1), all having the same focal length $f = 400$ mm, were used to investigate the influence of lens excitation ξ and the maximal slope-steepness B'_{\max} on the aberration coefficients. The optimum lens field was found to have the highest possible excitation - which means a low field maximum B_{\max} - and a small slope-steepness B'_{\max} as shows field no. 4c in fig. 1.

The great influence of B'_{\max} on spherical aberration is shown in fig. 2 and the influence of ξ in fig. 3. Similar behaviour show all isotropic aberrations but not the anisotropic ones. Chromatic aberration on the whole does not depend on said parameters and has to be minimized by using the telecentric beam configuration (1).

The optimum lens field which has low values of B_{\max} and B'_{\max} is given by a design where diameter and length of coils determine the middle part of the field. Only the slopes and field ends are shaped by iron pole pieces (fig. 4). This hybrid design gives the opportunity to vary lens excitation and focal length independently from each other by alternating the coil currents I_1 , I_2 and I_3 , if the coil is divided into three parts (fig. 4).

Because the lens excitation ξ is given by $\xi \sim \int B(z) dz$ and the focal length f is determined approximately by $\frac{1}{f} \sim \int B^2(z) dz$, it is possible to vary f at constant ξ by a variation of the field shape (fig. 5). This variation of the field is done by decreasing the currents I_2 and I_3 and increasing I_1 . Thereby the excitation $\xi = \xi_1 + \xi_2 + \xi_3$ remains constant but the field is shortened and increased - hence f decreased. As well it is possible to vary ξ at constant f .

The variation of f at constant ξ may be used to adjust the imaging lens doublet, its demagnification and to obtain vanishing radial chromatic aberration. The variation of ξ at constant f can be used to obtain vanishing rotational chromatic aberration and may be used for adjustment of the image onto the wafer by rotating it.

The Hybrid Lens is designed for a variation of the field-shape and a shift of the field which are the characteristics of a zoom lens. Such a lens is part of the imaging system of a microprojector, which is discussed elsewhere (4, 5).

Divergent mask irradiation: Even if the aberration coefficients of all lenses and those of the lens systems are minimized the aberration discs still depend on the distance from the optical axis R , the irradiation aperture α and the irradiation angle β . The parameter β is of special importance (6). At parallel mask irradiation ($\beta = 0$) the distortion vanishes. But parallel irradiation is not obtainable because of spherical aberration C_8 of the condenser lens which causes a convergent irradiation $\beta(\text{sph}) \sim -R^3$. On the other hand the number of resolved lines per field is increased, if instead of parallel irradiation an optimum divergent irradiation angle $\beta(\text{opt})$ is used: $\beta(\text{opt}) = f_3 \cdot f_2^{-2} \cdot R$, (f_2, f_3 are the focal length of the imaging lenses). By a defocus Δz_1 of the condenser, the convergent irradiation $\beta(\text{sph})$ and hence the distortion are eliminated at a special R (2): $\Delta z_1 = C_8 \cdot f_1^{-2} \cdot R^2$ (f_1 is the focal length of the condenser).

The optimum divergent irradiation $\beta(\text{opt})$ for high resolution is obtained at a special R if the defocus Δz_2 of the condenser is used: $\Delta z_2 = f_2^2 \cdot f_3 \cdot f_2^{-2} + C_8 \cdot f_1^{-2} \cdot R^2$

As the irradiation angle β influences the distortion and the distortion causes a shift of the pattern, this angle has to be controlled very accurate.

The authors wish to thank Dr. B. Lischke for helpful discussions.

This work was done at Siemens AG, Meßgerätewerk Berlin, Bereich Elektronenmikroskope, and has been supported by the technological program of the Federal Department of Research and Technology of the Federal Republic of Germany. The authors alone are responsible for the contents.

References:

- (1) K. Anger, B. Lischke, W. Münchmeyer, A. Oelmann
patent DT 2515549 C2 (1975)
- (2) M.B. Heritage:
J. Vac. Sci. Technol., Vol. 12, No. 6 (1975), 1135
- (3) H. Koops and W. Bernhard, J. Vac. Sci. Technol.,
Vol. 12, No. 6 (1975), 1141
- (4) B. Lischke, K. Anger, J. Frosien, A. Oelmann
R. Schmitt, M. Sturm, W. Münchmeyer, this issue
- (5) J. Frosien, K. Anger, B. Lischke, G. Gorges,
W. Münchmeyer, this issue
- (6) B. Lischke, K. Anger, A. Oelmann, W. Münchmeyer,
Proc. of the Int. Conf. on Microlithography, p. 167
Paris (1977)

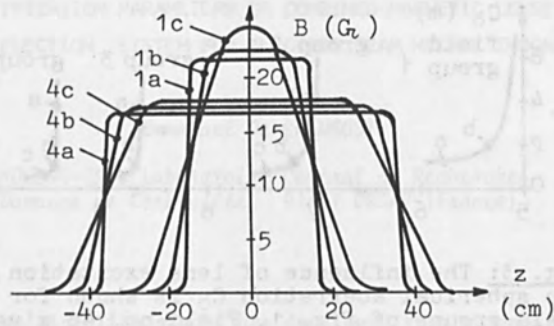


Fig. 1: Theoretical lens fields, all having the same focal length $f = 400$ mm. Field maximum B_{max} and slope-steep-ness B'_{max} are varied.

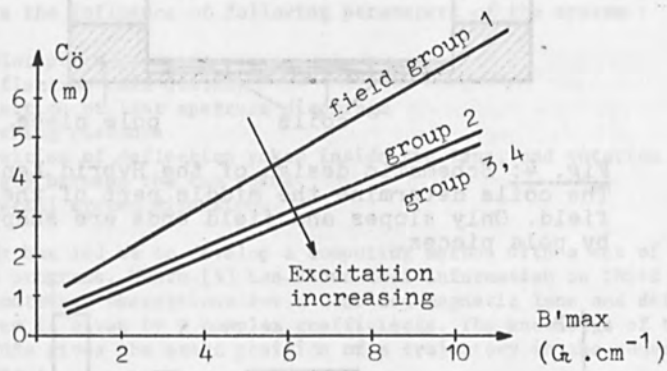


Fig. 2: The influence of B'_{max} on spherical aberration for the field groups of fig. 1 is shown. The field no. 4c gives best results. (Magnification = ∞)

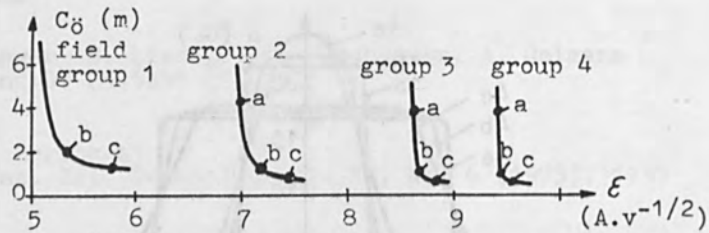


Fig. 3: The influence of lens excitation ϵ on the spherical aberration C_δ is shown for the field groups of fig. 1. Field no. 4c gives best results.

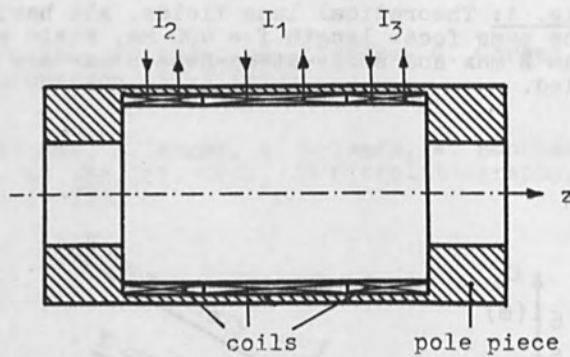


Fig. 4: Schematic design of the Hybrid Lens. The coils determine the middle part of the field. Only slopes and field ends are shaped by pole pieces.

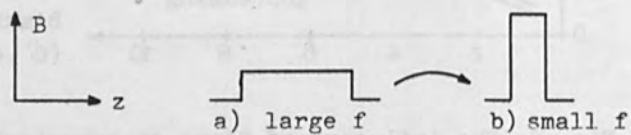


Fig. 5: Schematic for decreasing of f at same field integral and same excitation respectively.

OPTIMIZATION PARAMETERS OF COMBINED MAGNETIC LENSES
AND DEFLECTION SYSTEM FOR ELECTRON BEAM MICROLITHOGRAPHY

Emmanuel De CHAMBOST

THOMSON-CSF, Laboratoire Central de Recherches
Domaine de Corbeville 91401 ORSAY (France)

Electron beam microlithography has developed from scanning electron microscopy [1]. During this development, specific problems have appeared in the field of electron optics for microlithography :

- the speed of the writing beam
- distortion and aberrations on a large scanned field.

This last problem concerns in particular the beam focus and deflection system. Numerous investigations have already been published by some authors : Owen and Nixon [2] have proposed a post deflection system ; Amboss [3] has discussed the design of deflection yokes and Munro [4] has compared different typical solutions. The object of this paper is to discuss the influence of following parameters of the system :

- polar piece geometry
- deflection coil quality
- position of last aperture diaphragm
- working distance
- position of deflection yokes inside the lens, and rotation angle between the two yokes
- overall system dimensions.

This study has led us to develop a computing method with a set of appropriate programs. Munro [5] has shown that information on third order geometrical aberrations for a combined magnetic lens and deflection system is given by 9 complex coefficients. The knowledge of these coefficients gives the exact position of a trajectory in the gaussian image plane :

$$w_i + K_1 w_i^2 \bar{w}_i + K_2 \bar{w}_i^3 + K_3 w_i \bar{w}_i s_i + K_4 w_i^2 \bar{s}_i + K_5 \bar{w}_i^2 s_i \\ + K_6 w_i s_i \bar{s}_i + K_7 \bar{w}_i s_i^2 + K_8 \bar{w}_i \bar{s}_i^2 + K_9 s_i^2 \bar{s}_i$$

Where $w_i = d I$ and $s_i = m s_0$

I is the deflector current

s_0 is the slope of the trajectory before deflection

d deflection constant and m magnification of the lens are the first order complex coefficients of the system.

Calculation of these 9 aberrations coefficients requires knowledge of the lens magnetic field (on axis) and deflection block magnetic field (on axis). The lens magnetic field is computed by a finite element method. We prefer to measure deflection magnetic field on a real deflection block to avoid having to solve a three-dimensional magnetic problem. Another program computes geometric and chromatic aberrations. The data of this program (fig. 1) include both the lens and deflection magnetic fields and some other information such as excitation of the lens coil, position of deflection yokes inside the lens, rotation angle between the yokes and position of last aperture diaphragm.

A test column with its peripheral electronic controls has been set up especially for aberration measurements. The principle of these measurements is the visualisation in the scanning mode of a calibrated pattern fabricated with laser interferometry on an EPG 102 Electron Beam Mask maker. Typically, the measurement method is the following :

- Distortion : Visualisation of the calibrated pattern makes it possible to deflect the beam an exact, known distance. Deflection current is measured.
- Astigmatism and Field Curvature : At a deflected point, focus current increment following both saggital directions is measured. The difference and the mean of both values respectively give Astigmatism and Field Curvature.
- Spherical aberration : Beam diameter is measured by scanning the beam on a Gold on Chromium bench-mark and by analysing the backscattered electron signal.
- Coma : When Field Curvature and astigmatism are experimentally corrected, beam diameter is measured at a deflected point.

The method does not include specific measurements for fourfold aberration (K_2 , K_5 , K_8).

1. Polar Piece Geometry

For a given lens type, small variations in polar piece geometry are not critical for the set of aberrations. For example, in the case of a conventionnal double deflection system, influence of variation of inner diameter of lower polar piece is shown in fig. 3.

Different types of lenses cannot be compared without taking into account the position of the deflection block. Results on spherical aberration only are shown in fig. 4.

2. Deflection winding

The intrinsic geometry of a deflection yoke principally effects fourfold coefficients K_2 , K_3 and K_8 which have to be compared respectively with distortion (K_1), astigmatism (K_4) and coma (K_6). These fourfold coefficients can theoretically be cancelled by designing the winding as shown in fig. 5 with $\theta = 120^\circ$ [3,4].

In practical cases, magnetic shields perturb this theoretical condition and in any case winding 20 or 30 turns following an exact design remains a problem; nevertheless, approaching the condition of $\theta = 120^\circ$ makes it possible to lower fourfold coefficients enough to be negligible with regard to K_1 , K_4 and K_5 respectively.

Another problem is to appreciate the importance of unavoidable defects in winding symmetry which theoretically lead to second order aberrations. Experience has shown that a simple, hand-wound deflector (fig. 6) centered in the column without special adjustment does not show perceptible symmetry aberrations so that the use of obviously more precise printed circuit deflectors is not indispensable.

3. Position of last aperture diaphragm

The position of the last aperture is an important parameter if the diaphragm is located below the deflector. Diaphragm position is critical especially in the case of single deflection in a conventional scanning microscope lens.

As shown in fig. 7, if the diaphragm is located 12 mm above the lower polar piece, aberrations of the system can be favourably compared with a conventional double deflection system (fig. 8).

In this solution, the beam must remain homogeneous far from its central axis in the plane of the aperture diaphragm so that this solution cannot be used for example, in a shaped beam system.

4. Position of the deflector in the lens

In the following discussion, the assumption is made that the last aperture is located above the deflection and lens system.

A single deflection system has been studied by Pfeiffer [6]. It consists of a high spherical aberration symmetrical lens which makes it possible to put the deflector at the symmetry center of the system (fig. 9).

Another case is a single deflector immersed inside a low spherical aberration lens which gives less freedom for the position of the deflector.

In such a system, the deflector cannot be placed too close ($Z < 3\text{cm}$) to the lower polar piece in order to avoid the deflection magnetic field from being strongly distorted by the polar piece. However, in the range $5\text{ cm} > Z > 3\text{ cm}$, such a system may be of interest.

It has already been published that a rotation between the two deflection yokes dramatically lowers aberrations [4,7]. Figure 11 shows variations in different aberration coefficients with rotation angle θ .

Experimental points have been measured on a 2 mm scanned field. Differences between the computed curve and experimental points are thought to be due to measurement unaccuracy, but it has been found that at the values of θ where computed coefficients reach dramatic maxima, measured aberrations do not follow a third-order law. Actually, an examination of trajectories shows that, at these values, trajectories pass near polar pieces in part of the space where the third order approximation of the magnetic field is not valid (fig.12).

5. Working distance and overall system dimensions

Working distance is the last parameter the designer may vary to optimize a system. When working distance increases, aberration coefficients vary typically as follows :

- Spherical aberration and coma increase
- Field curvature and distortion decrease

In a conventional double deflection system, if aperture semi-angle is fixed, for each scanned field, there is an optimum working distance where the number of resolvable points N is maximum. But, for quasi telecentric systems such as optimized twisted yokes system (fig. 13), for each scanned field, the maximum number of points is reached when working distance Z_i is minimum.

At this optimum point, keeping constant the number of points while increasing scanned field is always possible by suitably scaling by k overall system. Therefore the knowledge of system dimensions is needed to compare two different systems.

CONCLUSION

It is not the object of this paper to propose the best solution for the deflection and lens block. In fact, optimization of the block depends on following data which are known if general purposes of the microli-thography system and the philosophy of the design are defined :

- Scan field area
- Number of resolvable points (including distortion)
- Aperture semi angle.

This paper has given some elements which make it possible to optimize the block. Generally there are several possible solutions. One can choose the best solution by taking into account other problems to be solved like eddy current or self inductance of deflection coils.

REFERENCES

- [1]. *Cahen, Sigelle, Trotel*
Proc. 5th International Conference on Electron and Ion Beam
Science and Technology (1972)
- [2]. *Owen, Nixon*
J. Vac. Sci. and Technology 10, p. 983 (1973)
- [3]. *Amboss*
J. Vac. Sci. and Technology 12, p. 1152 (1975)
- [4]. *Munro*
J. Vac. Sci. and Technology 12, n°6 (1975)
- [5]. *Munro*
Optik 39, p. 450 (1974)
- [6]. *Pfeiffer*
J. Vac. Sci. and Technology 12, p. 1170 (1975)
- [7]. *Ohiwa, Goto, Ono*
Electronics and Communication in Japan, vol. 54-B, n°12 (1971)

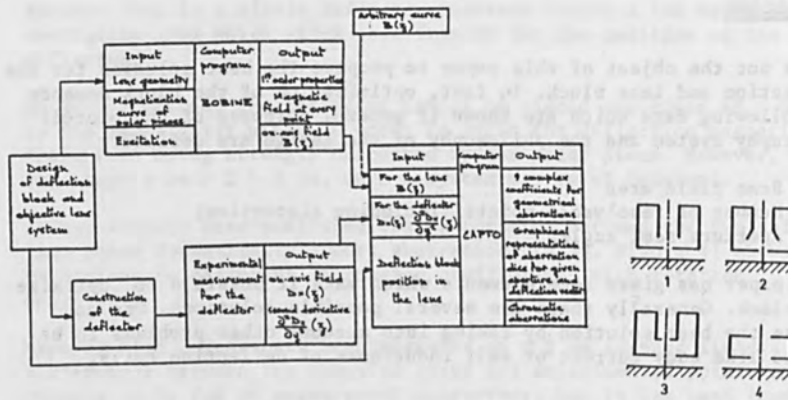


Fig. 1 - Deflection block and lens system analysis

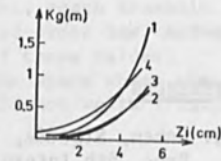
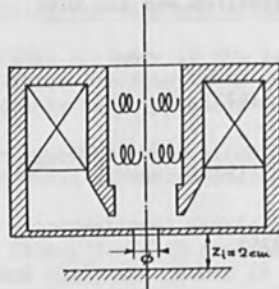


Fig. 4 - Influence of polar piece geometry on spherical aberrations



ϕ	Distortion K_1 (m^{-2})	Field curvature K_2 (m^{-1})	Coma K_3	Spherical aberration K_4 (m)
3	925	158	4.5	0.145
8	925	158.5	4.2	0.145

Fig. 3 - Influence of pole piece inner diameter for conventional pre-lens double deflection



Fig. 5 - Form of deflection coil windings

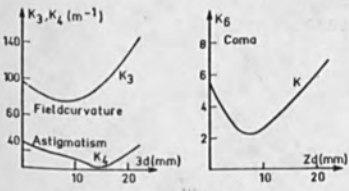
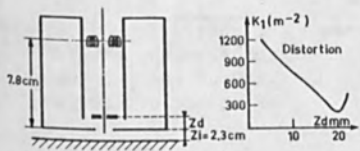


Fig. 7 - Positional influence of the last aperture on geometrical aberrations

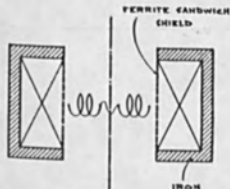


Fig. 9 - Pfeiffer's ferrite sandwich shield solution

	Distorsion K_1 (m^{-2})	Fieldcurvature K_3 (m^{-1})	Coma
Single deflection $Z_d = 10 \text{ cm}$	165 000	2 800	12
Single deflection $Z_d = 1.2 \text{ cm}$	700	100	2
Conventiounal double deflection $Z_d = 10 \text{ cm}$	900	164	4

Fig. 8

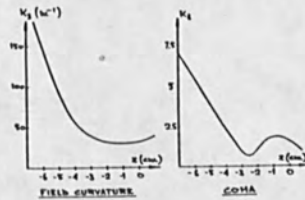
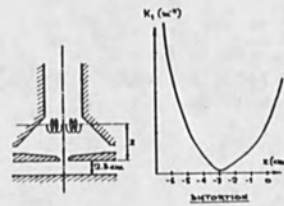


Fig. 10 - Positional influence of single deflection on aberration coefficients

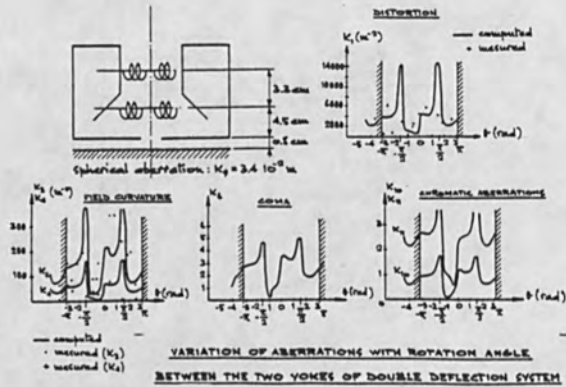


Fig. 11 - Variation of aberrations with rotation angle between the two yokes of double deflection system

Fig. 12 - Principal trajectories in the lens for different values of the rotation

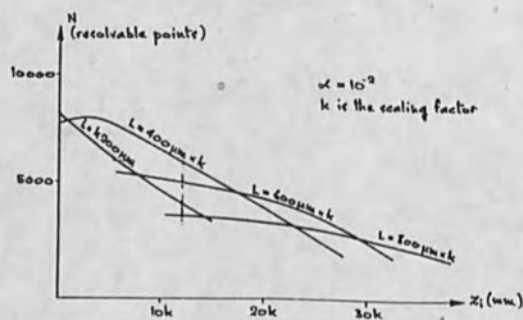
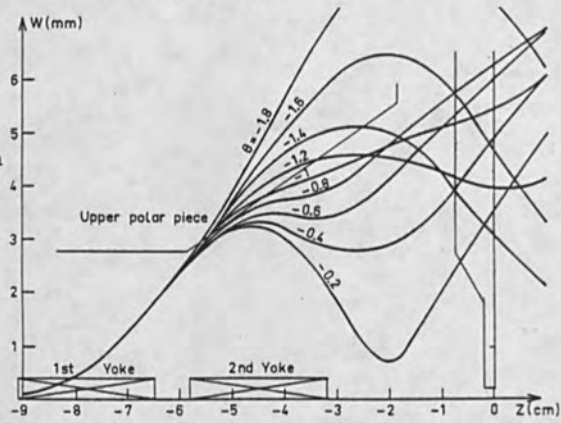


Fig. 13 - Number of resolvable points N on a scanned field L versus working distance Z_i for a twisted yokes system

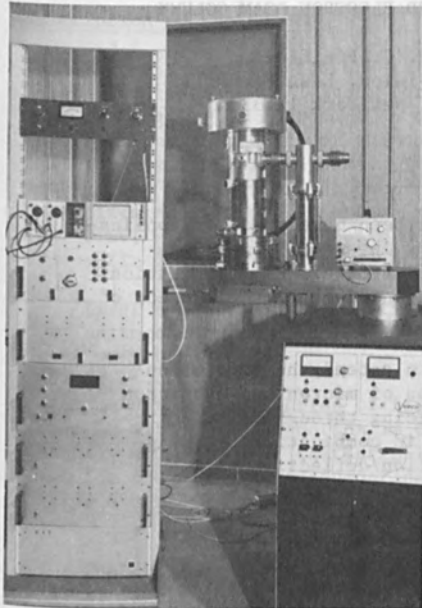


Fig. 2 - Test column

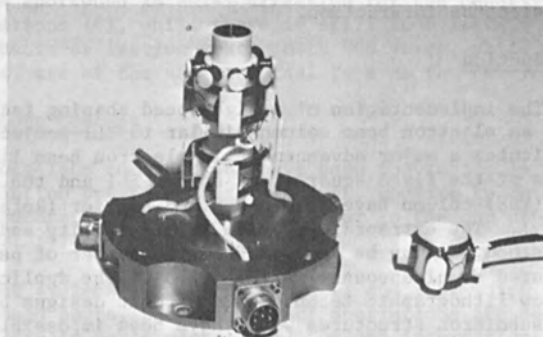


Fig. 6 - Measured deflector

OPTICS OF A VARIABLE SHAPED ELECTRON BEAM COLUMN

W. Stickel and H. C. Pfeiffer
IBM System Products Division, East Fishkill
Hopewell Junction, New York 12533

ABSTRACT

An electron beam column has been developed for application to semiconductor lithography intended to meet the aggressive requirements of future VLSI circuit fabrication. Its function is based on, but extended over, the concept of IBM's square spot forming system ELL.

The primary objective was to extend the resolution capability of ELL into the region of micron and submicron pattern features without sacrificing throughput. The variable spot shaping technique in combination with significant advances in the projection/deflection optics provided the means to achieve the above objectives.

The improvement in resolution of more than 100%, exceeding 4000 fabricated lines/field at 50 Acm^{-2} , was achieved by introducing a second toroidal deflection yoke into the "Inside Lens Deflection" concept and further compacting the lens-assembly. These measures reduced on-axis as well as off-axis aberrations, in particular axial and transverse chromatic aberrations, coma, and electron-electron interaction.

Introduction

The implementation of a high-speed shaping facility of the spot, which an electron beam column similar to ELL projects onto the target, constitutes a major advancement in electron beam lithography. The optics of the fixed square spot system ELL and the new variable shaped spot (VSS) column have been described earlier (Refs. 1 and 2, respectively). The extraordinary gain in flexibility and throughput is well understood, as may be derived from the number of pertinent papers presented simultaneously in 1977 (2,3). The application, however, of the new lithographic technique to circuit designs based on micron or even submicron structures would have been impossible without comparable advancement in the most critical region of the electron optics, the projection-deflection section of the column.

This paper focuses on description and explanation of the improvements made in this area. Experimental results are presented and discussed, evaluating the performance of the new design in comparison to ELL.

Description of the Column

Figure 1 compares the VSS-column with ELL in a simplified schematic way. (See Refs. 1 and 2 for details of the optical concept and beam tracing.) The introduction of the shaping section obviously increases the complexity of the column, imposing higher demands on the stabilization of the beam. The new requirements were met supplementing the ELL closed loop (servo) system (4) with a third lateral beam alignment servo of the same kind as the gun alignment servo of ELL, i.e., with magnetic double deflection yokes to minimize virtual source (image) movement during alignment.

First and second alignment servo (Fig. 1) are electronically coupled together for a similar double-deflection operation to reduce mutual disturbance.

The dynamic correction of field curvature and astigmatism in synchronism with the beam motion is carried out with a control system only slightly modified over that of ELL (4); it was found to be sufficient even for the new projection-deflection design within 7 mm. For larger fields a correction scheme of increased sophistication is in preparation.

The projection-deflection section is shown in more detail in Fig. 2. While the design principle of the section is essentially common to both ELL and VSS and based on the "Deflection Yoke Inside Lens" concept (5), two major changes are noticeable.

The VSS lens is shortened in axial direction for the benefit of reduced axial aberrations (6), while there is still room left to incorporate a second magnetic deflection yoke. Both VSS yokes, while different in dimensions, are of the same toroidal type as the ELL yoke.

Double Yoke Inside Lens Concept

A variety of yoke-lens combinations have been theoretically analyzed (7,8). The solution presented here, however, appears to be the first hardware implementation of a concept similar to the one proposed by Ohiwa et al., 1971 (9).

In probe-forming systems, represented by ELL and VSS, which carry high currents in shaped spots, three groups of aberrations are dominant and determine the ultimate performance: (1) Coulomb interactions between beam electrons lead to space charge broadening and 3-dimensional Boersch effect; (2) chromatic aberrations, aggravated by the axial Boersch effect (energy spread broadening) are separable into axial and transverse (or deflection) aberrations. With the use of magnetic lenses the latter acquires two components, the radial or isotropic and the azimuthal or anisotropic transverse chromatic aberration. (3) Coma dominates the remaining aberrations.

Coulomb interaction, axial chromatic and most third-order aberrations benefit from an object-image distance as short as possible (6) and consequently favor the placement of the deflection yoke inside the lens over any post- or pre-lens deflection configuration (5-7). Any lens at any position with respect to the yoke reduces the transverse chromatic aberration due to their opposed energy dispersion. Optimization of the compensation, however, invariably leads to the yoke inside lens configuration again. The yoke, however, can only be designed to compensate the radial dispersion component of the lens, thus reducing or eliminating the isotropic transverse chromatic aberration. The azimuthal component of the magnetic lens dispersion requires a second yoke for compensation, which is rotated with respect to the first one.

The relations are illustrated in Fig. 3:

A single, isolated yoke (Fig. 3a) responds to electrons of different energy by dispersing them radially so that electrons of higher energy impinge on the target closer to the axis than those of lower energy. When the yoke is placed inside the lens (Fig. 3b), not only the effective deflection direction is rotated, but also the effective sensitivity of the yoke is reduced due to the focussing power of the lens. Electrons of high energy, however, are focussed farther away from the axis than the slower ones, thus reversing the separation caused by the yoke.

The desire to minimize the sum of lens and yoke dispersions $\bar{R}_{\text{lens}} + \bar{R}_{\text{yoke}}$ led to the configuration realized in ELL (5), where the radial component is virtually eliminated, as will be shown, but the azimuthal component solely due to the lens is unaffected.

Figure 3c depicts the more complex situation with two yokes, the deflection direction of the lower yoke being rotated by 90° opposite to the lens rotation. Here the task of minimizing the sum of dispersions does not result in the elimination of one component, but a partial compensation of both components simultaneously, as indicated by the equation in Fig. 3b,c.

The reduction of the transverse chromatic aberration has to be traded off to the relatively more important coma in the new concept; the trade-off leads to the selection of an optimum beam cone angle at a given target current density, therefore given brightness and energy spread.

Experimental Apparatus, Methods, Definitions

The experiments carried out to evaluate the column performance consisted mainly in measuring the edge slopes of spots. This parameter is defined in Fig. 4, which shows the spot current distribution in one lateral dimension. The spot profile is obtained by scanning the beam across a straight wire with constant velocity and differentiating the

signal generated by a detector proportional to the integral of the transmitted beam current.

To achieve accurate measurements of the edge slope, many scan signals were sampled, digitized and accumulated before display. The signal plotted in Fig. 4 is the sum of 128 scans and represents one of the two cross sections through a $2 \mu\text{m}$ square spot, the size of which measured at the 50% intensity level was calibrated against the wire diameter (see e.g., Ref. 2). The profile shown can be interpreted as the convolution of the rectangular intensity distribution of an ideal square spot with the Gaussian profile of the aberration disc belonging to each square spot element. Thus, the resolution, defined as the full width at half height of the aberration disc, corresponds to the width of the spot edge slope measured between the 12 and 88% intensity points.

For convenience of measuring the resolution at many points in the magnetic deflection field a grid of several crossed wires was used as test target.

While the edge slope of a typical spot profile, as represented in Fig. 4, reflects the superimposed impact of many, if not all electron-optical aberrations, a few experimental methods exist to separate or even directly measure individual aberrations.

Spherical aberration E_S is directly measureable as the residual edge slope in the field center for a beam current and current density so drastically reduced that interaction and axial chromatic aberrations become negligible. Thereby it is assumed that the beam cone angle is small enough to render lens coma negligible as well, and that astigmatism is compensated. The equipment used, however, did not permit reduction of current density far enough for an accurate direct measurement.

Therefore, the spherical aberration was determined by extrapolation of a series of measurements with varied current densities.

Axial chromatic aberration E_C was determined directly from edge slope vs. current density measurements. The aberration constant C of the system was derived from the change of spot edge slope in the field center, when the acceleration voltage was changed by a known amount.

Transverse chromatic aberration E_{TC} , not directly accessible, was derived from the measurement of the aberration constants (isotropic C_{TI} and anisotropic C_{TA}) and estimating the actual energy spread $\Delta E = E_C/C$ from axial chromatic aberration measurements, using the calibrated value for the constant as described above. C_{TI} and C_{TA} followed from spot movement, observed on two oscilloscopes, in the corners of the field due to a known change of the acceleration voltage. The accuracy of this measurement is rather limited due to the simultaneous defocussing of the spot (corresponding to the axial chromatic aberration).

Coulomb aberrations (space charge broadening E_{SC} and individual interaction E_I) were derived by interpolation of edge slope measurements at different spot sizes at constant current density, a procedure conveniently carried out with the VSS column, rather elaborately, however, with ELL. Since it was the objective of this investigation to evaluate primarily the VSS-column, variable spot measurements were not carried out with ELL.

Experimental Results

Total and Deflection Aberrations of ELL and VSS Column

Figure 5 summarizes and compares the results for the two columns obtained for the total aberrations in the corners of different deflection fields. The experimental points represented averages over slope measurements of leading and trailing spot edges (Fig. 4) and over corresponding cross sections for all four corners. The edge slopes in X-direction on the positive diagonal $+Y = +X$ correspond to those for Y on the negative diagonal $+Y = +X$. Averaging the data in this manner implies the assumption that individual differences are not intricate to the system or result from mechanical imperfections, but are (as verified) a consequence of the impact, which imperfect beam alignment has on the resolution symmetry.

While the beam aperture angle was adjusted for each column to give minimum aberrations, the brightness, and therefore, the energy spread were the same for both systems, since identical spot sizes and current densities were chosen.

With one quarter of the minimum line width as a requirement sufficient for acceptable line edge definition, it follows from Fig. 5 that, on the average, ELL maintains this resolution for 2000 lines of 2 or 2.5 μm width over a 4 or, respectively, a 5 mm square field. The VSS-column, however, by the same standards, covers a 4 mm field with 4000 lines of 1 μm width, or an 8 mm field with even more than 5000 lines 1.5 μm wide.

Figure 5 also shows the reduction of the lens dependent aberration at field center of about 25%, as expected, just about proportional to the shortening of the object-image distance.

Subtraction of the field center portion E_0 from the total aberrations E yields the deflection dependent aberrations E_D . Assuming validity of Gauss' law of quadratic superposition of independent individual aberrations, $E^2 = E_0 + E_D^2$, the results for E_D show proportionality to the deflection distance, as plotted in Fig. 6. This dependence is to be expected, if transverse chromatic aberration E_{TC} and coma are the dominating deflection aberrations. To estimate the proportion due to uncompensated E_{TC} and due to residual aberrations E_R , the chromatic constants C_T were measured as described, in field corners and at edge midpoints in

X and Y direction. $E_{TC} = C_T \Delta E$ then was calculated assuming an energy spread of $\Delta E = 7.5$ eV in accordance with prior experience. Table 1 summarizes the results obtained for all corners and edge midpoints, normalized to the +X/+Y corner of a 6 mm field:

Table 1. Total and individual deflection aberrations of EL1 and VSS column in +X/+Y corner of 6 mm field (in μm).

	$\Delta E=7.5\text{eV}$								Mean Values				
	E_X	E_Y	E_{DX}	E_{DY}	E_{TCS}	E_{TCY}	E_{RX}	E_{RY}	E	E_0	E_D	E_{TC}	E_R
EL1	0.62	0.75	0.54	0.70	0.39	0.62	0.38	0.33	0.68	0.28	0.62	0.50	0.35
VSS	0.25	0.34	0.12	0.27	0.05	0.21	0.11	0.17	0.30	0.22	0.20	0.13	0.14

While the data in Table 1 are relevant for practical considerations, Table 2 shows the aberrations separated into isotropic and anisotropic components:

Table 2: Isotropic (I) and anisotropic (A) aberration components for EL1 and VSS column in corner of 6 mm field (in μm , unless stated otherwise).

	E_{DI}	E_{DA}	E_{TCI}	E_{TCA}	E_{RI}	E_{RA}	$\frac{C_{TI}}{C_{TA}}$ ($\mu\text{m}/\text{mmV}$)	
EL1	0.12	0.88	0.16	0.71	(.00)	0.51	-0.0051	-0.0223
VSS	0.10	0.28	0.11	0.18	(.00)	0.21	-0.0034	-0.0058

Figure 6 right shows vectorial representations of E_D and E_{TC} for visual rather than practical purposes.

With quadratic superposition applicable also for transverse chromatic aberration and coma, the isotropic component E_{RI} of the residual aberration has to be assumed to be nonexistent. The difference between E_{TCI} and E_{DI} , the former being bigger, obviously must be due to experimental error. The remaining anisotropic residual aberration is comparable in magnitude to the respective transverse chromatic aberrations. The improvement from EL1 to VSS column, therefore, implicated also a sizeable reduction of coma and possibly other residual contributors to the total deflection aberration, in addition to that of the chromatic constituent. While a radial component of the transverse chromatic aberration was measured with both columns, in the case of EL1, its size is insignificant compared to the azimuthal component. Although even smaller in the case of the VSS column, the radial aberration here is relatively more important (leading to a rotation of the aberration vectors in Fig. 6, comparing EL1 with VSS).

Chromatic and Coulomb Aberrations of VSS Column

The following measurements were made in the field center. Figure 7, where the edge slope of the spot is plotted against spot size and, accordingly, current, shows first of all--in gross approximation--a linear deterioration of the edge definition with the total target current (at constant current density). Important to note is that only a fraction, though major, can be attributed to the space charge influence E_{SC} of the beam considered as a continuous fluid. This portion can be compensated by refocussing the spot. The remaining fraction is interpreted as due to individual stochastic electron-electron interactions, leading to anisotropic trajectory displacements and consequently incompensable aberration E_I .

In Fig. 8 an attempt is made to explain the difference between the two effects. If the electron beam can be replaced by a continuous charge, then the forces acting on the electrons #1 and #2 are proportional to their respective distances from the axis, as indicated by the dashed lines. This follows from the model of the charged sphere. Both electrons, therefore, still seem to have emerged from a common, although displaced point, as without space charge, consequently they converge at a common point, also shifted. It is obvious that such a displacement can be compensated with refocussing. If, however, the mean distance of the electrons is large enough to take their corpuscular nature into account, then the forces of the immediate neighbors are dominating. A reference electron traveling on the axis repels the approaching electron #1 more effectively than #2, since #1 remains closer to the reference electron for a longer period of time. After the crossover, the reference electron separates from #1 and #2 so that only part of the initial trajectory displacement is reversed. In Fig. 8, this is drawn as a parallel shift for the sake of simplicity. Electrons from the general electron, fill the cone between corresponding solid and dashed lines and are not focussed simultaneously at the target plane as sketched. Changing the lens power would not restore the original condition.

Closer scrutiny of the interaction dependency $E_I = f(I_T)$ of Fig. 7 leads, after subtraction of the extrapolated value for the "zero-current" aberration $E_0 = 0.175 \mu\text{m}$, to a fairly good approximation by a function $E_I \sim I_T^{2/3}$. At this point there exists no theory which would explain the exponent. Loeffler's theory (10), which predicts a power law, with an exponent of 0.86 rather than 0.67, may not, however, apply directly to the conditions under which the system was operated here.

Some results about the axial chromatic aberration E_C were derived from the measurement of edge slope vs. current density at constant spot size. From Fig. 9, top, a "zero-current density" aberration of $0.067 \mu\text{m}$ is extrapolated, which is essentially identical to the spherical aberration E_S of the lens. Using the data for E_I from Fig. 7, and subtracting

them as well as E_S from the current density curve, the points for E_C are calculated, shown in Fig. 9, bottom, solid line. They are in reasonable agreement with the trend found for the energy spread under similar conditions prior to this investigation (11). In a separate experiment the axial chromatic aberration constant C was determined as described, yielding $C = 0.018 \mu\text{m}/\text{V} \pm 20\%$. From Fig. 9, bottom follows with $E_C = 0.155 \mu\text{m}$ at 50 Acm^{-2} an energy spread of $\Delta E = 8.4 \text{ eV}$, which appears rather high but not unreasonable in view of the accuracy of C .

Going back to Fig. 7, E_0 , which is comprised of spherical as well as chromatic aberration, compares to the result obtained from Fig. 9 fairly well:

$$E_0 \text{ (Fig. 9)} = (E_S^2 + E_C^2)^{1/2} = 0.17 \mu\text{m}, E_0 \text{ (Fig. 7)} = 0.175 \mu\text{m}$$

Additional Experiments

In order to study the significance of the two yokes' mutual orientation, the rotation angle between them was varied from 50 to 110° and the total aberrations measured in the corners of a 6 mm field. While the edge slope increases only slightly towards smaller angles, e.g., from 0.30 at 90° to 0.32 at 70°, it could be traded off to a sensitivity gain of more than 20%. Towards larger angles, however, the edge slope deteriorates far more rapidly. Measurement of the transverse chromatic aberration, which showed a decrease with increasing angle, indicates that coma is mainly responsible for the edge slope at larger angles and transverse chromatic aberration at smaller angles, which corresponds to the results obtained for EL1, where E_{TC} is also dominant.

Summary

It has been demonstrated that by introducing a second deflection yoke, rotated by 90° with respect to the main yoke, and reduction of the object-image distance, the performance of the electron beam column designed for micro-lithography can be improved by more than 100%, making it suitable to meet the requirements of future LSI-circuit technology. This was possible due to the reduction of electron-optical aberrations, which are dominant in high current systems designed for high throughput: Axial and transverse chromatic aberrations, electron-electron interaction, and coma.

It has been also shown that the major portion of edge slope change with variable spot shape at constant exposure density is compensable space charge broadening, but that still a significant uncorrectable fraction remains, the interaction aberration.

Acknowledgement

We gratefully acknowledge the assistance we received from R. J. Quickle and D. Cullum, who helped with the experiments and with the maintenance of the equipment.

References

1. J. L. Mauer, H. C. Pfeiffer, and W. Stickel, Tech. Digest, IEDM, Washington, D.C., 1976, p. 434.
2. H. C. Pfeiffer, 14th Symp. on Electron, Ion and Photon Beam Technol., Plao Alto, 1977 (to be published in J. Vac. Sci. Technol.).
3. E. Gote, T. Soma, and M. Idesawa, 14th EIP Beam Symp., May 1977. M. G. R. Thompson, R. J. Collier, and D. R. Herriott, *ibid*, 1977.
4. S. Doran, M. Perkins, and W. Stickel, J. Vac. Sci. Technol. 12, 1174 (1975).
5. H. C. Pfeiffer, J. Vac. Sci. Technol. 12, 1170 (1975).
6. J. L. Mauer, H. C. Pfeiffer, and W. Stickel, IBM J. Res. Dev. 21, 514, (1977).
7. E. Munro, J. Vac. Sci. Technol. 12, 1146 (1975).
8. E. Goto and T. Soma, *Optik* 48, p. 255, 1977.
9. H. Ohiwa, E. Goto, and A. Ono, *Trans. IECE, Japan*, 54-B, p. 730, 1971 (in Japanese). Also in *Electronics and Communications in Japan*, 54-B, 12, p. 44, 1971.
10. K. H. Loeffler and R. H. Hudgin, *Proc. 7th Int. Conf. El. Microscopy*, Grenoble, 1970, p. 67.
11. H. C. Pfeiffer, unpublished.

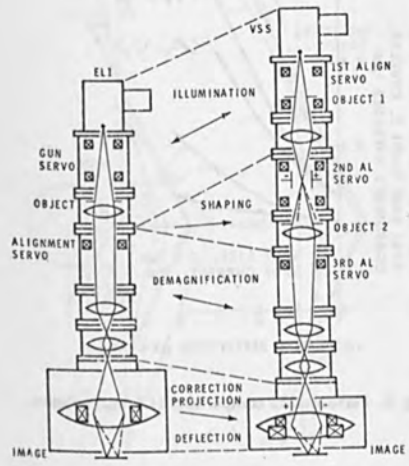


Fig. 1. Comparison of EL1 and VSS column.

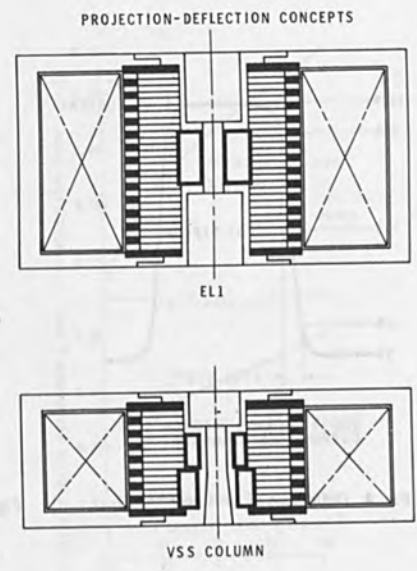


Fig. 2. Projection-deflection concepts.

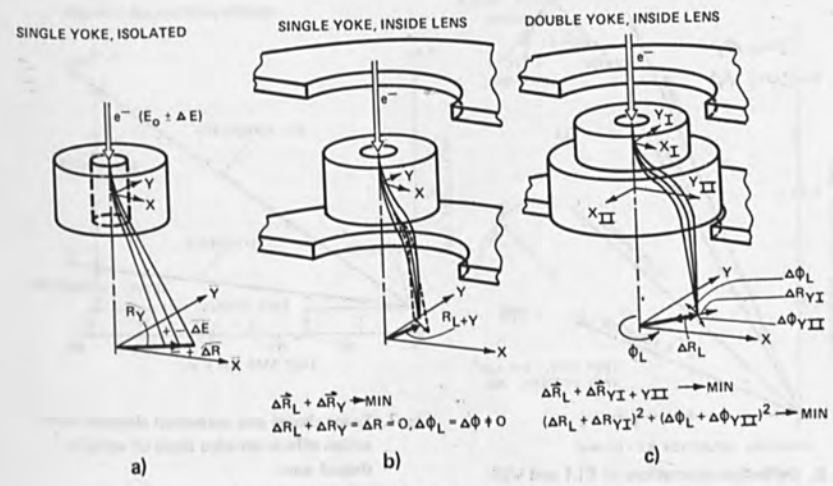


Fig. 3. Compensation of (transverse) chromatic deflection aberration.

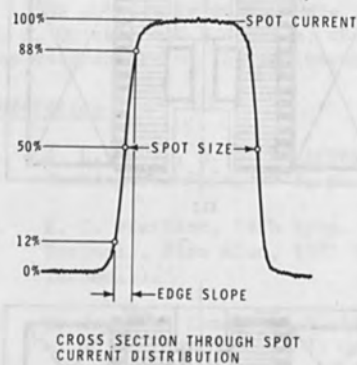


Fig. 4. Definition of spot parameters.

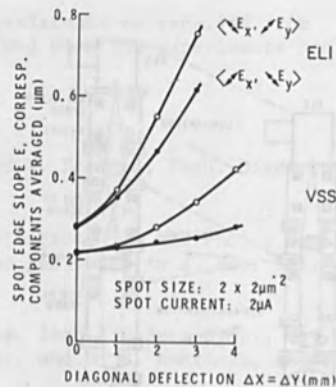


Fig. 5. Performance comparison EL1-VSS column.

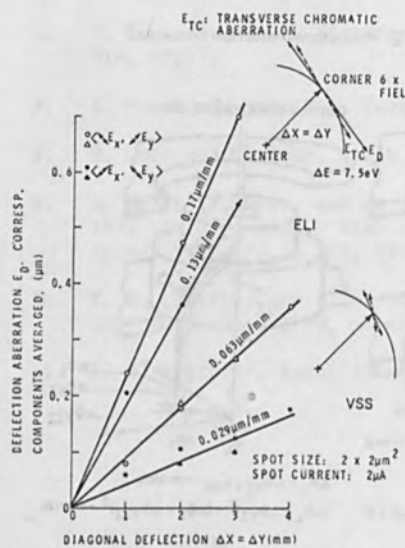


Fig. 6. Deflection aberrations of EL1 and VSS columns.

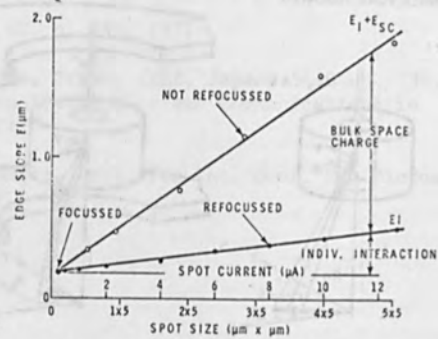


Fig. 7. Space charge and individual electron interaction effects on edge slope of variable shaped spot.

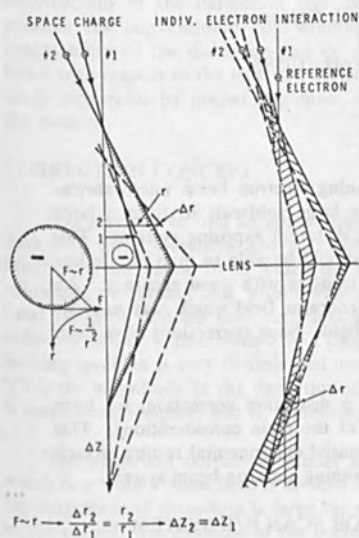


Fig. 8. Explanation of space charge and individual electron interaction effects.

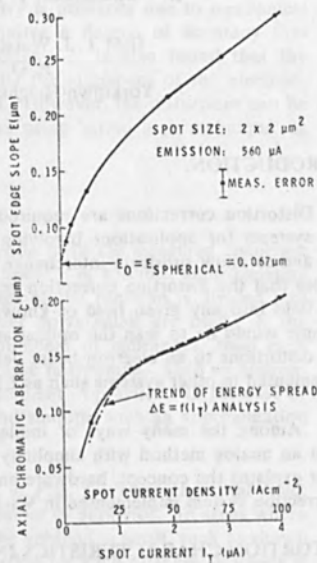


Fig. 9. Edge slope and axial chromatic aberration for variable spot current density at constant emission.

DISTORTION CORRECTION IN SCANNING ELECTRON BEAM SYSTEMS

R. Viswanathan, T. H. P. Chang, D. Coffey

IBM T. J. Watson Research Center
P. O. Box 218
Yorktown Heights, New York 10598

INTRODUCTION

Distortion corrections are required in scanning electron beam microfabrication systems for applications involving stitching large subfields to form a large chip and to allow substrate interchange between different exposing systems. This implies that the distortion correction generator should be able to map the deflection field into any given field of known characteristics with good accuracy. An example would be to map the optical artwork generator field which may have its own distortions to an electron beam deflection field. Such corrections have been implemented in other systems such as ELI⁽¹⁾

Among the many ways of implementing a distortion correction, we have taken an analog method with simplicity as one of the main considerations. This paper explains the concept, hardware and some initial experimental results of such a correction system implemented in VS-I,⁽²⁾ a scanning electron beam system.

DISTORTION CHARACTERISTICS IN VECTOR SCAN E/B SYSTEM

The distortions in the scanning system have to be measured and characterized before a suitable correction scheme can be developed. A method known as 'Stripe Scan Method'⁽³⁾ has been developed for this purpose.

Fig. 1 shows the basic principle of the 'Stripe Scan Method.' In this method, a precise calibration grid of gold lines on a silicon substrate is used as the standard. The electron beam scans the grid lines in a narrow stripe, i.e. the scan amplitude of one axis is considerably smaller than along the other ($\Delta Y \ll X$ as shown in Fig. 4). Backscattered electron signals are detected and the grid line is displayed on a CRT using the standard SEM technique. Because of the inequality of the X and Y scans on the grid, a considerably larger magnification of the narrower scan (ΔY) will be achieved on the CRT, thereby allowing any small dimensional changes in that direction (Y) to be greatly magnified. If any distortion should be present in the deflection, this will show up, in a mirror form, as a distortion in the CRT image of the calibration grid. By adding a d.c. offset to the beam deflection, grid lines positioned anywhere in the field can be addressed and distortion along these lines can also be measured. By interchanging the X and Y scan signals, distortions in the perpendicular direction can be measured in the same way. A typical operating condition in the VS-I system is to use the long scan to cover a distance of 5mm and the narrow scan to cover only a few micrometers so that a measurement accuracy of $<0.1\text{mm}$ can be readily achieved. This technique allows real-time measurement of distortion along any grid lines with rapid switching to any other grid line readily available. One important feature of this technique is that by scanning over an entire grid line, any irregular variation of its width can be detected and accounted for. The measurement accuracy that can be obtained by this method is relative to the calibration grid. These measurements on VS-I indicate that the magnitude of the distortion is approximately 3μ

over a 5mm x 5mm field, and the shape of the distortion is smooth with no discontinuities. The shape of the distortion is basically a pincushion type of distortion, with some asymmetry. The asymmetry is primarily due to mechanical construction of the deflection coil, which requires a degree of accuracy that exceeds the conventional coil winding techniques. It is also found that the repeatability of the distortion can be affected by the alignment of the electron-beam with respect to the lens and deflection coil. However, the distortions can be made repeatable by proper alignment techniques using 'stripe scan technique' as the monitor.

CORRECTION CONCEPT

It is essential to find an approximating function to fit the measured distortion data with good closeness and sufficient smoothness. A suitable approximating function is the spline fit in which the total range of the function is divided into subranges or subsections, within which low order polynomials are used. If the total range is divided into sufficiently large numbers of subranges, then each subrange can be approximated by a simple piecewise polynomial. Such an approximating function is very flexible and easy to implement in practice. In the case of VS-I, the magnitude of the distortion is small and smooth, such an approximation is considered adequate and is, therefore, adapted.

The distortion correction model is shown in Fig. 2. Here the total field, which is a 5mm x 5mm field is divided into a number of subfields. In areas where the magnitude of distortion is large the size of the subfield is small, such as shown in the corner. An example of the correction needed for each of these subfields is illustrated in the upper right hand corner of Fig. 2. The dotted quadrilateral represents the distorted field and the solid box represents the ideal field. The correction scheme involves the following steps. The left side and bottom side are adjusted first, until they are parallel with the solid box, and such a correction is called slope correction denoted by coefficients e and g. The top side and right side are adjusted, which is called trapezoidal correction denoted by coefficients d and h. The field is translated until the bottom right hand side coincides with that of the ideal field. This correction is called offset correction denoted by coefficients a and e. Finally the magnification of the distorted field is adjusted until it overlaps on to the ideal field and such a correction is called gain correction denoted by coefficients b and f. The distortion correction that is required within that subfield is given by the set of equations:

$$X_{d(i,j)} = a_{ij} + b_{ij}x + c_{ij}y + d_{ij}xy$$

$$Y_{d(i,j)} = e_{ij} + f_{ij}y + g_{ij}x + h_{ij}xy$$

Here i, j is the index referred to the X and Y axes and x, y are the variables normalized to the subfield origin in the X and the Y axis respectively. The subfield origin is on the bottom left side of the subfield. A total number of 64 subfields have been chosen for this particular experiment.

CORRECTION HARDWARE

The deflection system in VS-I consists of a dual channel D/A unit, a high accuracy 15 bit positioning D/A converter, and a 10 bit high speed pattern writing D/A converter for each axis, a field size control unit, the distortion correction unit, and a deflection amplifier. As shown in Fig. 3, the distortion unit

is placed in between the field size control unit and the deflection amplifier. Such a scheme allows proper distortion correction to be generated with a full range of field size settings.

Details of the distortion correction unit are shown in Fig. 3. This unit consists of three sections. (1) Subfield detector and encoder. (2) A memory to store the piecewise coefficients for the various subfields and finally (3) an analog processing unit to generate the distortion correction signal.

The subfield detector is an analog to digital convertor, which is given a convert command each time the beam is positioned to a new pattern cell location. (i.e. during the time the pattern generator addresses the positioning D/A converters). The ADC generates digital output codes, which are encoded in a subfield encoder to determine the subfield index (i, j). This index is used as an address in the coefficient memory, which in turn generates the piecewise constants relevant to that zone. These digital data are fed to the analog processor (which consists of DAC, and MDACs) along with the normalized analog input wave form. The appropriate correction signals required within that subfield are generated by the analog processor. As new coefficients are needed only during subfield changes, this approach eliminates the need for large and high speed memory.

The memory size is about 2 K bytes for all the coefficients in both axes; and only 500 bytes are being used in this correction.

CORRECTION PROCEDURE

Several methods are available for setting up distortion correction coefficients. They include collecting positional information using an array of calibration marks in the same way as in the standard registration operation and computing the errors of each mark for compensation⁽⁴⁾. In this work, the distortion corrections were determined using the 'Stripe Scan Method': as described earlier.

As stated previously, the deflection field is divided into a number of small subfields and each side of the subfield is a part the stripe scan line.

As shown in Fig 5, one can display any one of these segments on the CRT and change the slope and offset coefficients to make that segment straight. The coefficients that cause such a change are recorded in the memory. In this way one can correct all the segments of any stripe to match the calibration grid. The advantage of such a scheme is that one is not limited to a few data points to approximate the correction function, but that an entire line is available for curve fitting in an insitu manner. One can achieve better than 0.1 micron correction by this technique. The first distortion corrected line becomes the reference for all other lines, and one can monitor this reference line periodically to reduce errors due to any system drift.

The gain and trapezoidal coefficients are generated by computing the gradients of the stripe lines that form the subfields.

CORRECTION WAVE FORMS

Figs. 6 and 7 illustrate some results using this correction technique. The distortions measured by the 'Stripe Scan Method' of different stripe lines along

the X axis are shown on the left side of Fig. 6, and the correction signals are shown on the right side. As expected, good agreement between these wave forms was observed.

Fig. 7 illustrates the same for the Y axis. However, one can see a periodical jump of the order of 0.3μ in the stripe scan wave form. This is due to the fact that the calibration grid was made using an optical artwork generator. On this artwork generator a long line was generated by butting small line segments and the discrete jumps are due to a small but constant error that occurred during the butting. It is interesting to note that such an error has been reproduced faithfully in the distortion wave form. In order to obtain an accurate deflection field, the effect of errors in the calibration grid could be accounted for by first measuring their magnitudes and then subtracting them from the stripe scan measurements. However, in order to match two different exposing systems, it is only necessary to write a grid using one system and correct the second system using that grid.

CROSSOVER PROBLEMS

Piecewise approximating functions do not have continuous first derivatives and could lead to discontinuities at the boundary between two adjacent subfields. The significance of this problem has been evaluated, and the results are shown in Fig. 8. In Fig. 8 (a), (A) and (B) represent bands of subfields in the upper part of the deflection field and the boundary between them is shown as a heavy line. (C) and (D) represent corresponding bands of fields in the lower part of the deflection field.

Fig. 8(b) shows a correction signal generated for a line in the (A) region, 50μ away from the boundary. Scope trace (A) represents the correction wave form using piecewise constants that reside in (A) band of subfields. Scope trace (B) represents the same line corrected using correction coefficients that reside in the (B) band of subfields. Similar traces are shown for the (C) and (D) subfields in Fig 8(c). The magnitude of the differential error for a 50μ crossover is in the vicinity of 0.15μ for lines A and B. Traces (C) and (D) have negligible differential error. Similar results are displayed in Fig. 8(d) and 8(e) for 100μ crossover. In the VS-I system the pattern length is much less than 20μ and the errors are negligible.

RESULTS

The accuracy of the distortion correction unit was evaluated by using the electron beam system to expose a special grid pattern consisting of a box pattern (the size of the box pattern is $10\mu \times 10\mu$, separated by 160μ from center to center. Such a pattern was written over a $5\text{mm} \times 5\text{mm}$ field. This grid pattern was then measured using an X, Y laser measurement table,⁽⁵⁾ with an accuracy of better than 0.05μ .

Fig. 9 shows the results when no distortion corrections were applied. In this plot, the difference between the actual field position and the corresponding ideal field position, has been plotted with considerable magnification. (magnification = 150).

Fig. 10 shows the same measurement with the distortion correction applied. A significant improvement in the deflection field can be observed. The magnitude

of the residual error over the 5mm field is about 0.2μ representing a linearity of 40ppm.

This error can further be reduced by a second iteration of correction. It is also interesting to note the small periodic kinks in the X lines which are the results of the butting errors of the calibration grid. The faithfulness by which these irregularities can be reproduced in the corrected pattern also serve to demonstrate the accuracy of the correction unit.

SUMMARY

A simple analog distortion correction unit has been developed using a piecewise approximating model for a vector scan electron beam system. Experimental results show that deflection linearity in the order of 40ppm over 5mm field can be achieved.

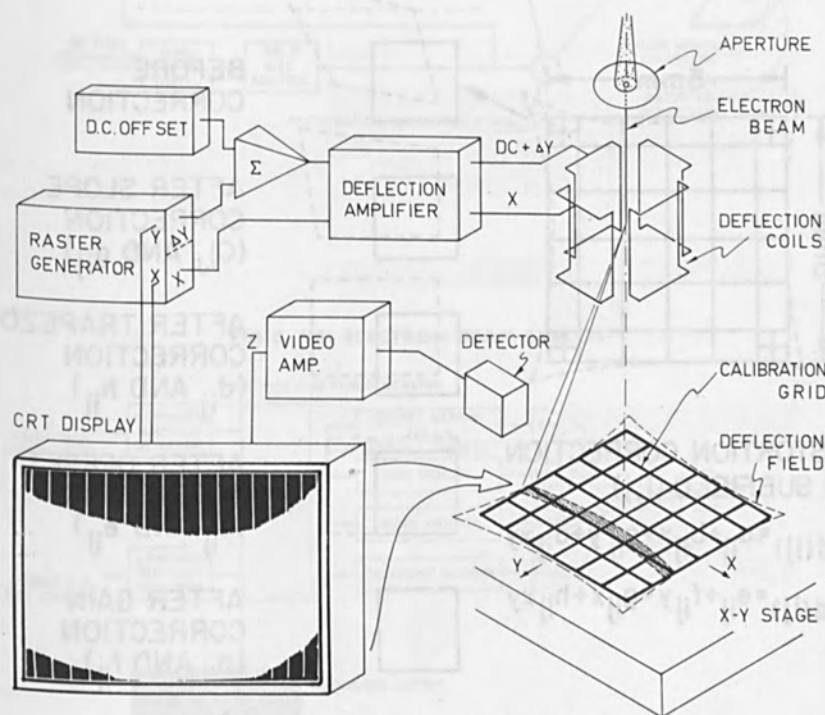
Finally, this unit can be readily extended to provide dynamic corrections for field curvature and astigmatism. Such dynamic corrections can be applied on a similar subfield basis following the same concept as the distortion correction.

ACKNOWLEDGMENT

The authors wish to thank H. Luhn and H. Voelker for their technical contributions in the construction of electrical test units and in sample preparation. The laser interferometer measurements were performed with assistance from P. Coffey, G.S.T., Burlington. Helpful discussion with A. N. Broers, W. Grobman, M. Hatzakis, A. Kern, G. Owen A. J. Speth, A. D. Wilson, and other members of the Electron & Photon Optics Department of IBM Research Center, Yorktown Heights, N. Y. are also appreciated.

REFERENCE

1. * J. F. Loughran, M. S. Michail, P. M. Ryan, and H. Engeik at the International Electron Devices Meeting 1976, Washington, D. C. (pp. 437)
2. T. H. P. Chang, A. J. Speth, C. H. Ting, R. Viswanathan, M. Parikh, and E. Munro, Proc. of Seventh International Conference on Electron and Ion Beam Science and Technology, edited by R. BAKish (Electrochemical Society, Princeton, N.J. 1976, (p 377)
3. T. H. P. Chang, and R. Viswanathan, 'Deflection Distortion in Scanning Electron Beam Systems,' Proceeding of the 14th Symposium on Electron, Ion and Photon BEam Technology, Palo Al, CA, May 1977.
4. A. D. Wilson, T. H. P. Chang, and A. Kern, J. Vacuum Sciencet Technology 12, 240 (1975).
5. An IBM Internal X-Y Coordinate Measuring Machine at GST, Burlington, VT.



STRIPE SCAN METHOD
DEFLECTION DISTORTION MEASUREMENT

FIG 1.

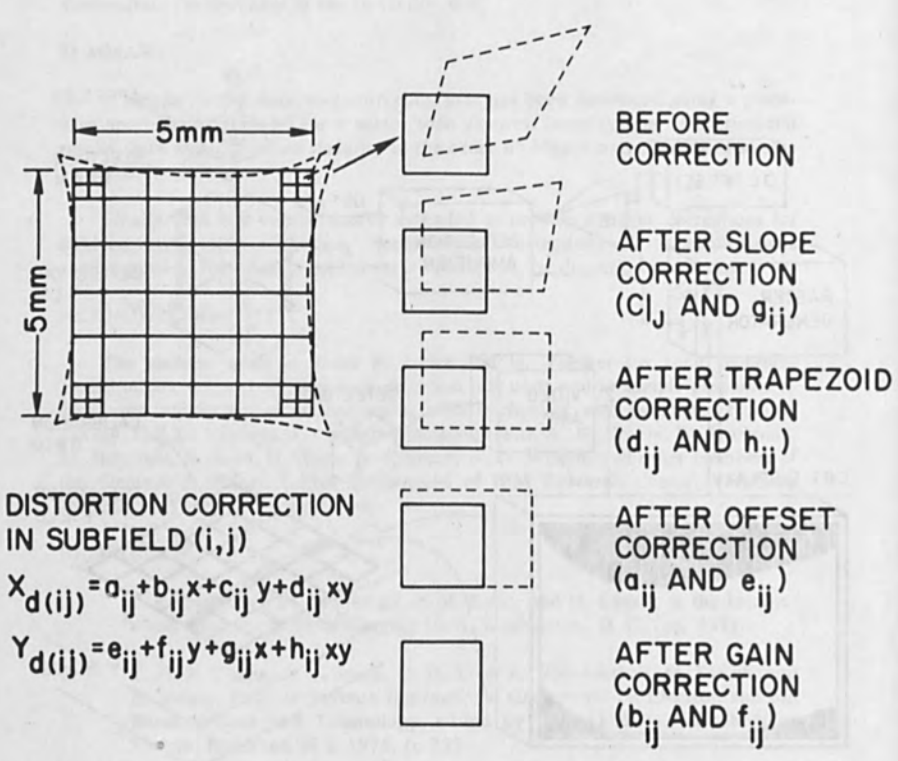


FIG 2. DISTORTION CORRECTION MODEL

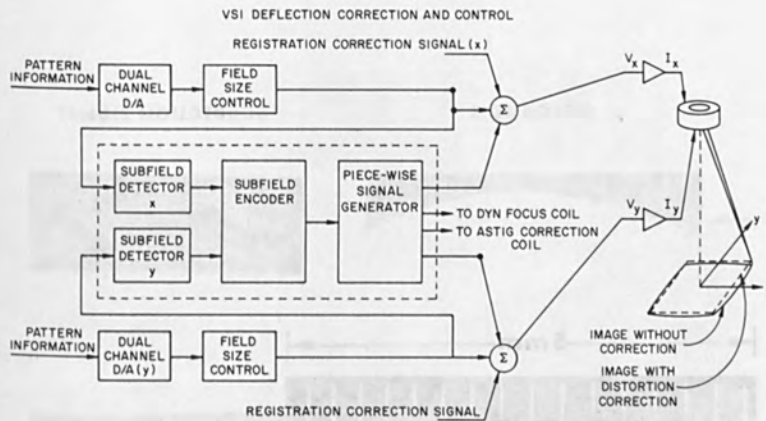


FIG 3. VSI ELECTRON BEAM SYSTEM

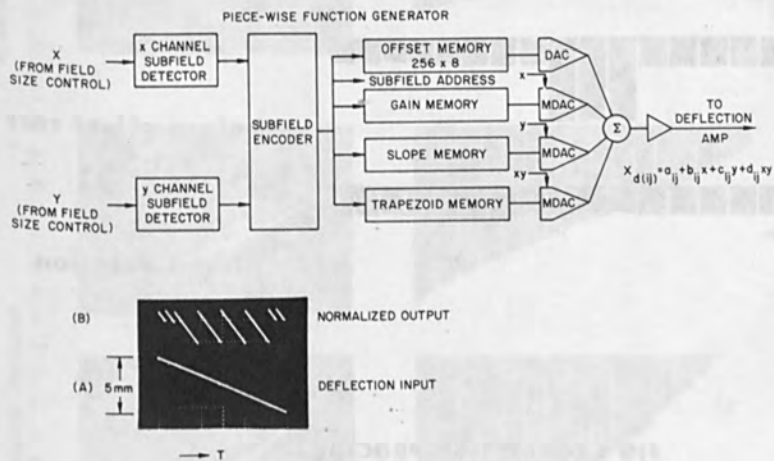


FIG 4. DISTORTION CORRECTION GENERATOR

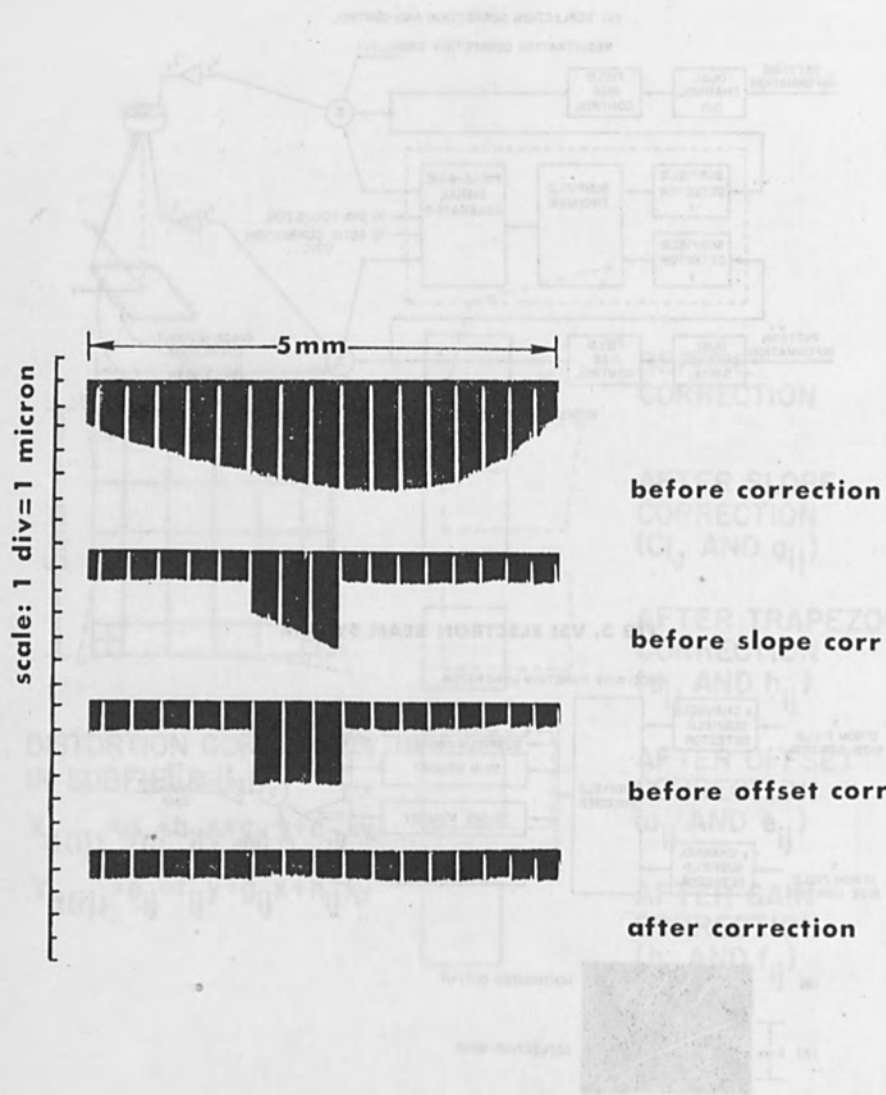


FIG 5. CORRECTION PROCEDURE

FIG 2. DISTORTION CORRECTION MODEL

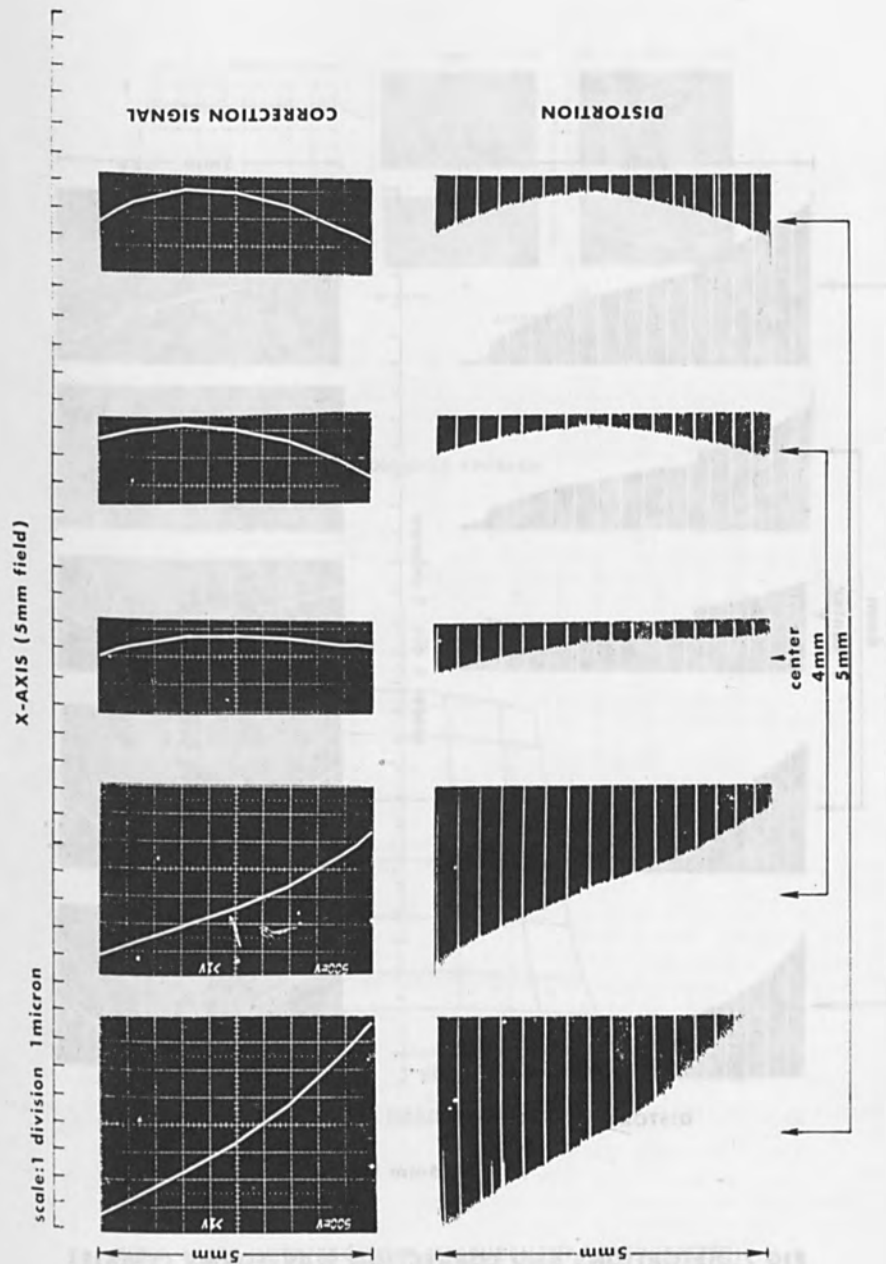


FIG 6. DISTORTIONS AND CORRECTION WAVEFORMS (X-AXIS)

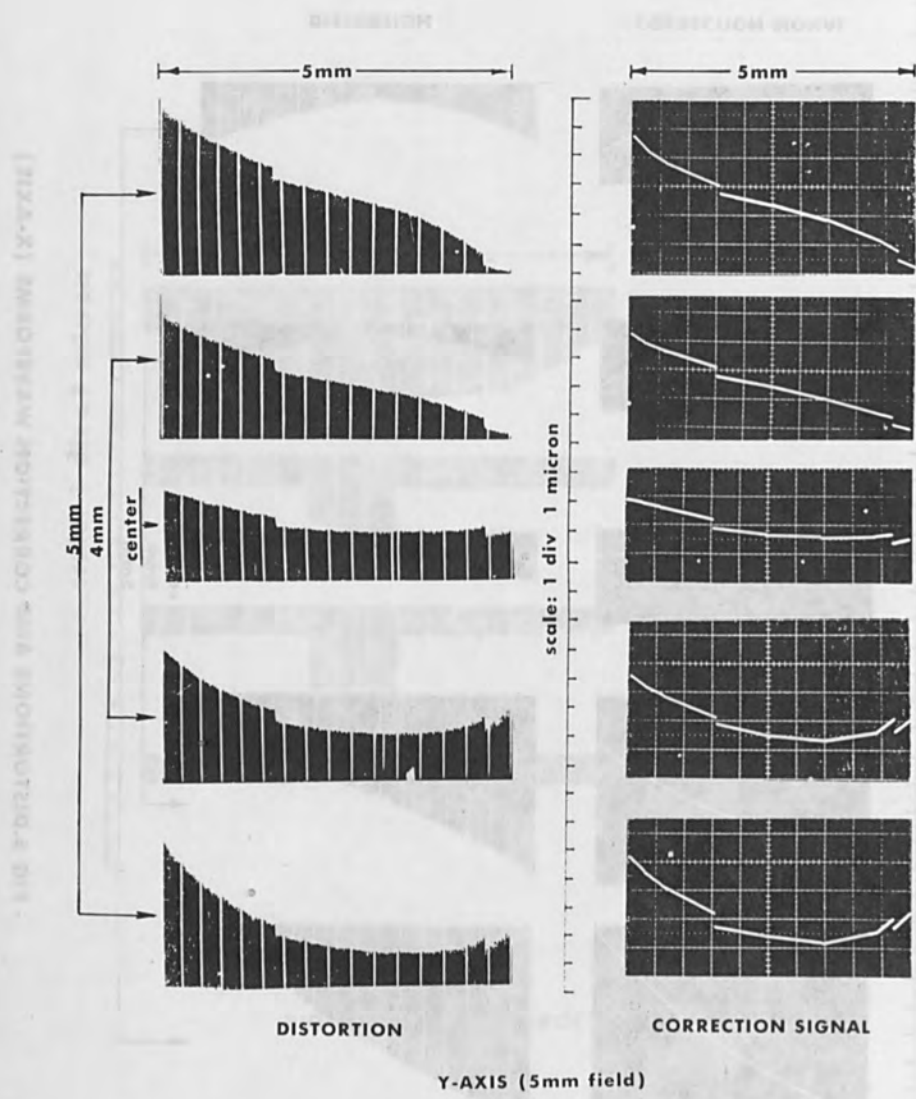


FIG 7. DISTORTIONS AND CORRECTION WAVEFORMS (Y-AXIS)

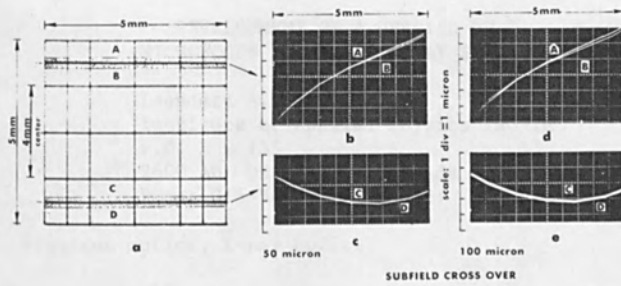
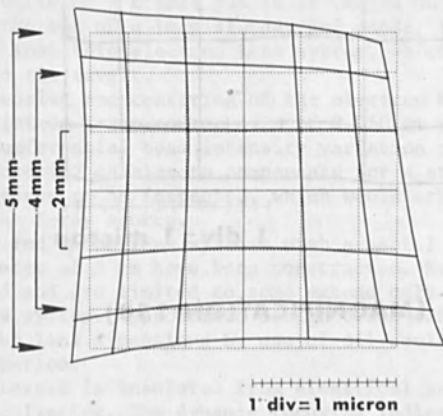
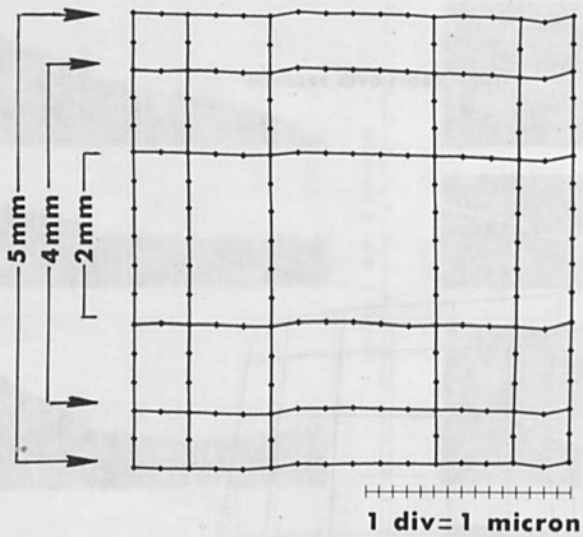


FIG 8. CROSS-OVER PROBLEM



DISTORTION MAP (MAGNIFICATION-150)

FIG 9. LASER INTERFEROMETER MEASUREMENT (UNCORRECTED)



(MAGNIFICATION=150)

FIG 10. LASER INTERFEROMETER MEASUREMENT (CORRECTED)

DEVELOPMENT OF A UHV 150 kV
MICROFOCUS ROD ANODE X-RAY SYSTEM

Leendert A. Fontijn
Institute of Applied Physics TNO-TH
P.O. Box 155
2600 AD DELFT, Netherlands
Phone 015-569300 ext. 321

Topic electron optics, X-ray optics

Abstract

The design features and initial experimental results of an ultra high vacuum version of the 150 kV microfocus rod anode X-ray system are outlined. The laboratory prototype is a demountable metal sealed system for access to the LaB₆ electron gun, the mini-magnetic lens with X-ray target holder and is provided with a 30 l/s getter ion pump.

The effective X-ray source size is less than 0.050 mm.

The X-ray source is positioned at the end of the lens holder with a useful length of 450 mm and a diameter of 9 mm, so permitting orthogonal panoramic inspections for various NDT applications.

Introduction

Microfocus rod anode X-ray techniques (1) call for the small, intense electron source of a triode gun to be imaged on a small tungsten target at the end of a long slender rod anode. This rod anode is actually a long thin electron lens system, which images the electron source onto the target.

Dynamic focusing and centering of the electron beam is provided to assure a minimum X-ray source size of 0.050 mm with good centering for a circumferential beam intensity variation of less than 10%.

Dynamic centering enables to compensate for a stray magnetic field from the object to be inspected, which would otherwise tend to decenter the X-ray source.

Microfocus rod anode lens systems with a useful length of 1 m and an outer diameter of 9 mm have been constructed. Even longer lengths are anticipated and are limited to some extent only by a mechanical droop of the lens system. Appropriate design trade-offs have been made to minimize the lens dimensions by use of oil cooling to meet the lens heat dissipation.

The X-ray target is insulated from electrical ground and is used as a current collector. The dynamic focusing indication is obtained by monitoring the target current signal with an oscilloscope while scanning the beam across the X-ray target. This method is relatively simple and allows dynamic X-ray beam centering and electron beam focusing while the rod anode is in place and ready for an actual exposure. Depending upon the choice of the X-ray target the X-ray beam pattern is panoramic with forward, reverse as well as true radial beam throw.

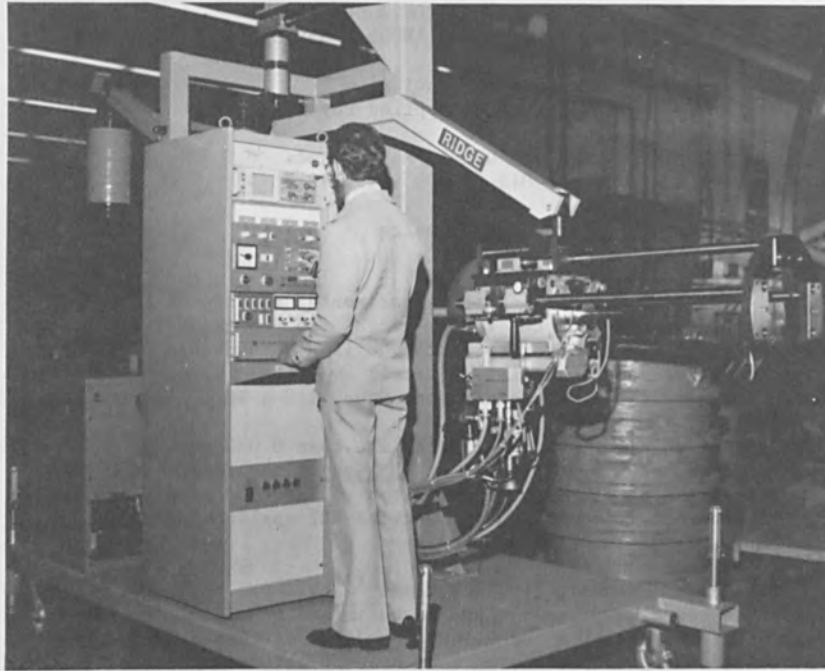


Figure 1

Figure 1 shows the 150 kV cp microfocus rod anode X-ray apparatus at the customer site. Clearly visible on the platform of the "Ridge" positioner are in front of the operator the 19" control cabinet and at the right hand side, mounted in a guidance system the 150 kV microfocus X-ray tube part. This system contains the high tension cable, the oil diffusion pump and the cooling water, oil, power and signal lines. Hardly visible, just under the 2 almost coincidental guiding rods, is the mini-magnetic lens system with target holder (removed lead protection).

Directional beam throw is obtained by using a canted target.

Compared with small-size radio active sources; such as ^{60}Co , ^{192}Ir and ^{170}Tm ; the microfocus X-ray source gives a better radiograph because of:

1. its improvement sharpness, due to the by more than about a factor 10 times smaller radiation source size
2. its improved image contrast, by the wider energy distribution of X-rays.

An additional advantage is the higher radiation output of the microfocus X-ray source, which results in considerable shorter exposure times.

A comparative radiographic sensitivity study of microfocus X-ray and isotopic techniques for boreside radiography of tube-to-tube sheet weldments has been reported by B.E. Foster and R.W. McClung⁽²⁾.

The microfocus rod anode X-ray system has been successfully applied to steam generator and heat exchanger tube-to-tube sheet weldments in both Europe and the USA. Other application areas include marine and aircraft jet engine inspection and numerous other applications where high reliability requirements indicate the use of an ultra-sensitive radiographic technique. This practical high resolution technique allows close monitoring of welding parameters, therefore resulting in an optimized welding process with a lower defect rate and an improved reliability for the weld.

A 150 kV microfocus rod anode X-ray apparatus at the customer site is shown in figure 1.

This is one of four units as delivered in 1977 to Ridge Instruments Co. Inc. (Tucker, Georgia USA) to meet the production X-ray inspection requirements of the tube-to-tube sheet weldments in the sodium to steam heat exchangers of the LMFBR (liquid metal fast breeder reactor) program.

Description of the UHV concept

The same technological advantages of the metal-ceramic X-ray tube construction are of interest in the UHV concept of the 150 kV microfocus X-ray equipment. These are the combination of mechanical strength, small size and low weight of the metal-ceramic X-ray tube construction.

A cross-section drawing of the laboratory prototype, a demountable metal sealed system, is shown in figure 2. Indicated are:

1. the metal ceramic component of the Philips MCN 161 X-ray tube
2. the connection to the 30 l/s getter ion pump
3. the electron gun part of the Philips EM 300/400 electron microscope
4. the anode
5. the mini-magnetic lens system with an effective length of 450 mm and an outer diameter of 9 mm
6. the X-ray target holder with a cone shaped tungsten target. The target is insulated for current measurement.

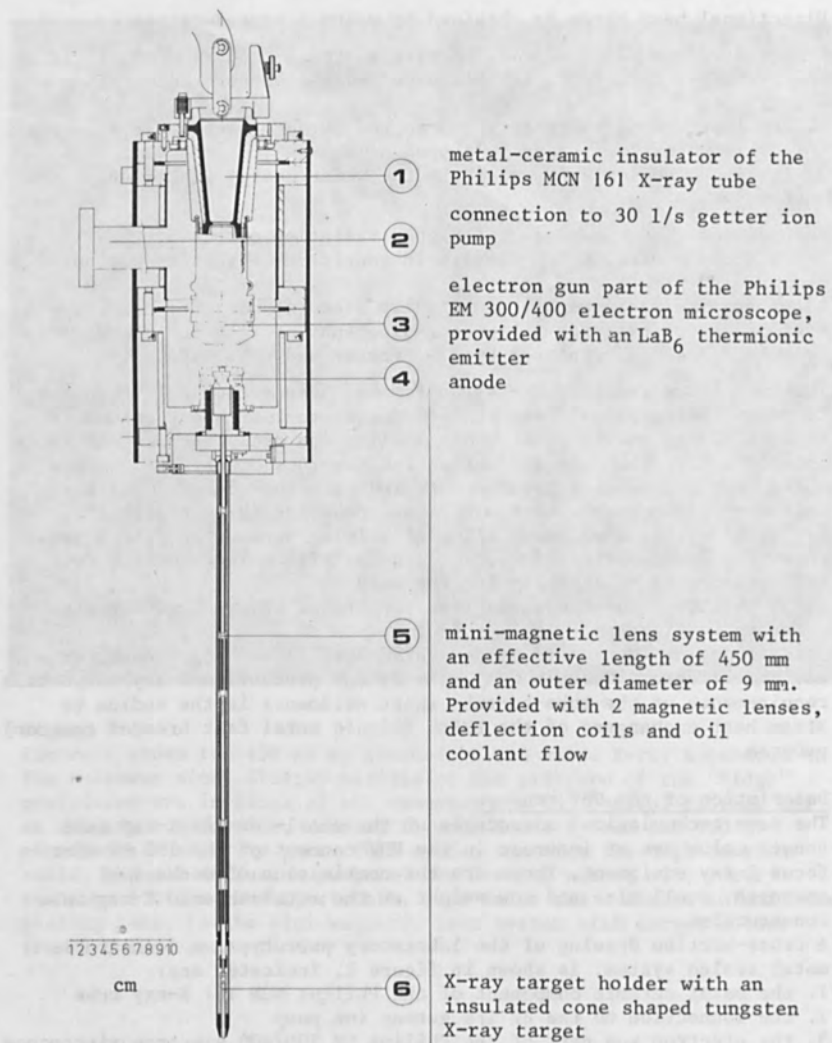


Figure 2

Cross-sectional drawing of the laboratory prototype of a UHV 150 kV microfocus X-ray tube

Although the laboratory prototype is a demountable system for access to the electron gun, lens and target parts, still a high reliability of operation is required for the UHV concept in total. This in view of the fact that an X-ray tube is a replacement part requiring a favourable ratio of effective operation time versus cost of the tube. The most critical part is the heating filament. In the UHV concept of the 150 kV microfocus X-ray tube a LaB_6 thermionic emitter is used. This is a commercially available LaB_6 thermionic emitter with a 100 orientation. The emitting surface is in the shape of a cone. The high brightness capability of the LaB_6 emitter results in a small, round virtual electron source size. A long life time of the heating filament is anticipated of at least 500 hrs initially, but preferably considerably more. Another interesting aspect is the X-ray target construction, which is insulated for current measurement as an aid in electron beam focusing and centering control and for reproducibility of the exposure conditions. In the X-ray target holder a metal-ceramic combination is used as well. The mini-magnetic lens holder is suited for the UHV environment by its welded parts on a stainless steel inner tubing.

Initial experimental results

The following aspects on the laboratory prototype of the UHV 150 kV microfocus X-ray tube have been considered:

1. the vacuum condition and high tension stability
 2. the LaB_6 thermionic emitter
 3. the target construction.
- ad 1. By means of a turbo molecular pump the initial pressure of 10^{-3} Pa to start the getter ion pump is obtained. Ultrasonic cleaning of the vacuum parts is performed. So far a bake-out procedure has not been followed, only a warming up of the gun chamber up to temperatures of about 70°C , which gives some improvement in the vacuum condition to be reached. The usual vacuum then becomes in 10^{-6} to 10^{-5} Pa range. After starting up of this laboratory prototype a high tension conditioning is performed to obtain a microdischarge free operation up to 150 kV at a vacuum pressure, measured in the getter ion pump, of better than 10^{-4} Pa. So far any microdischarges are related to the vacuum condition and not to the high tension generator with the belonging cable and connectors.
- ad 2. The small and round spot on the X-ray target by focusing with the mini-magnetic lens system of the virtual electron source size, as obtained by the LaB_6 thermionic emitter, has been noticed. Still a point of concern is the life-time of the heating filament of this LaB_6 emitter, but an improved version is under development ⁽³⁾.
- ad 3. The target construction is based on a standard UHV feed through with a small outer diameter. It turned out in the experiments that a reliable mechanical connection between the various

components, such as tungsten, stainless steel and aluminum could not be made. A solution has been found in a redesign with vacuum brazed connections, allowing an operating temperature of about 500°C. This is expected to give no problems for operation up to a beam load of 15 W (150 kV, 100 μA beam current).

Conclusion

A metal sealed UHV version of the 150 kV microfocus X-ray tube has been made in a laboratory prototype version. Proper bake-out and handling procedures can lead to a further reduction in size and weight. This will require the know-how and technical capabilities of the metal-ceramic X-ray tube manufacturing process.

REFERENCES

- (1) L.A. Fontijn NDT Conference April, 1978 Mainz,
 Fed. Rep. of Germany
 Paper to be published.
- (2) B.E. Foster Materials Evaluation/July 1977
 R.W. McClung pp.43-46 and p. 51
- (3) L.W. Swanson Private communication.

AUTO-REGISTRATION TECHNIQUE FOR AN ELECTRON BEAM
EXPOSURE SYSTEM USING A NEW SHEET STRUCTURED
DETECTOR FOR BACK-SCATTERED ELECTRONS

Y. Furukawa, N. Nakayama, Y. Goto, S. Igaki and
T. Inagaki
FUJITSU LABORATORIES LTD.
1015 Kamikodanaka, Nakaharaku, Kawasaki, 211, Japan

ABSTRACT

Auto-registration technique for the electron beam exposure using a special detector for detection of back-scattered electrons in a post-lens deflection system has been developed.

The detector is composed of thin optically transparent sheet coated with plastic scintillator. It has the features of large detection area adequate to the detection of back-scattered electrons, good signal-to-noise ratio and fast response in comparison with a solid state detector.

From these points this detector is very useful especially in the post-lens deflection optical system. The detector has been applied to the auto-registration of the electron beam exposure, and the registration accuracy of $\pm 0.2 \mu\text{m}$ (2σ) for 1 mm field size has been achieved within 0.4 second.

I. INTRODUCTION

An auto-registration technique for an electron beam exposure system is indispensable for direct exposure (1). In the auto-registration technique, an electron detector is required to accurately detect a mark signal which indicates the position of the alignment mark on a wafer.

The desirable features of an electron detector for the auto-registration are as follows. The first is that the detector should be one for back-scattered electrons. There are two methods of obtaining a mark signal, i.e. the detection of secondary electrons and back-scattered electrons. Because of its low energy the former has disadvantages that an obtained signal is asymmetrical according to the position of the detector in spite of the symmetrical mark on a wafer and also the signal level changes due to stage movement. On the other hand because of its high energy nearly equal to incident primary electrons, the latter can avoid these disadvantages (2). The second is that a detector should have high sensitivity and fast response. The most

commonly used back-scattered electron detector is of the solid state type (3, 4). It, however, has the difficulty that the large junction capacitance results in a down grading of the frequency characteristics as the detection area increases in order to capture as many electrons as possible. The third is that the detector should be thin, especially for a post-lens deflection optical system which has a narrow space between the electron beam deflector and a wafer. In addition to the above points it should be low in cost, easy to handle and have a long life.

For these requirements, the detector using a high speed plastic scintillator is most practical. The conventional detector using scintillator, however, has too large light guide to the photo-detector to be inserted in the narrow space of the post-lens deflection optical system for the detection of back-scattered electrons efficiently (5). To overcome this problem, a new detector which has a thin sheet structure and can be inserted into the narrow space has been devised and developed. In this paper the structure, the characteristics and the application to the auto-registration technique of this detector are described. This detector was found to have good performances as the detector for back-scattered electrons for the auto-registration technique.

II. NEW SHEET STRUCTURED DETECTOR FOR BACK-SCATTERED ELECTRONS

In Fig.1 the structure of this new detector is shown. The primary electron beam is incident to the specimen through the small hole in the detector. The back-scattered electrons from the specimen impinge on the plastic scintillator film and light is emitted into the sheet. This light is efficiently propagated along the plane of the sheet to a photo-multiplier. At the upper surface of the sheet gratings which have slope to reflect and propagate the light along the sheet plane is formed. The pitch of the gratings is 150 μm . Because the thickness of the plastic scintillator film is required to be more than the penetration depth of electrons to emit light efficiently, a thickness of 20 μm at a primary beam accelerating voltage of 20 to 30 KV was chosen. The surface of the detector is covered by a metal film, which provides a leakage path to prevent build-up of electrons in the plastic scintillator and also efficiently reflects light toward the photo-multiplier. The metal film should have high conductivity, good light reflecting property and low energy loss when the back-scattered electrons pass through the metal to the plastic scintillator. Aluminum film with the thickness 1500 \AA was coated by evaporation. The advantages of this detector are

the thin structure and the fine gratings which change the direction of light propagation.

Fig.2 shows the propagation efficiency versus incident position of light in the detector. To demonstrate the superiority of the gratings for changing the direction of light propagation, the case of the thin prism type with a diffusing surface is also shown. A He-Ne laser 6328 Å light is incident in the propagation plane, glass with a 3 mm thickness, through the diffuser to make the similar scattering as electron does on the scintillator. The output power of the light at the edge of the propagation plane was measured. In the prism type the propagation efficiency of the light decreases as the incident position of the light approaches the output side of the plane. The variation due to the incident position is $\pm 22\%$. In the grating type the propagation efficiency is three times as high as the prism type, and hardly dependent on the incident position. Due to this good uniformity of the propagation efficiency, the detection area of the detector can be enlarged.

Fig.3 shows the sensitivity and linearity of the detector. The accelerating voltage of the primary electron beam is 30 KV. Electrons are back-scattered from the SiO_2 -Si wafer covered with a PMMA resist 5000 Å in thickness. The detector area is 4 cm^2 , and the space between the surface of the scintillator and specimen is 2 mm. Good linearity of output current versus primary beam current is obtained with this detector, and a sensitivity 10 to 100 times higher than a conventional solid state detector can be obtained by choosing an appropriate photo-multiplier anode voltage.

It was confirmed that the decay time between 10 to 90 % of the pre-amplifier output signal is at least less than 140 nano seconds, which includes beam blanking time and response time of the plastic scintillator, photo-multiplier and pre-amplifier. In comparison with a conventional solid state detector, the response of the new detector is 80 times faster for the same detection area in spite of including the decay time of beam blanking (6).

Fig.4 shows a detected mark signal. The mark is chemically etched on a Si wafer and has a width of $3 \mu\text{m}$ and depth of $1.5 \mu\text{m}$. The wafer is covered by a PMMA resist 5000 Å in thickness. The signal-to-noise ratio of the mark signal is about 10, and a symmetrical signal which is necessary for the auto-registration is obtained.

III. APPLICATION TO THE AUTO-REGISTRATION SYSTEM

The new detector has been used in an auto-registration system for the electron beam exposure. Fig.5 shows the block diagram of the auto-registration system. Four alignment marks were previously formed at the corners of the field on a Si wafer. The electron beam scans each mark in the X and Y axis directions, and the back-scattered electrons from the mark are received by the detector. The mark signals are digitalized by the position detector circuits and the position data are led to a computer. Generally speaking, relative errors exist between the mark position and the electron beam deflection field, i.e. shift, field size, rotation and orthogonality errors. The computer calculates these errors, and calculated adjustment values are led to each digital/analog convertor, which adjusts the electron beam deflection system accordingly.

The alignment accuracies of 25 positions in a field were measured after the registration. Fig.6 shows the alignment errors in the field. The dotted line shows the mark field on a wafer and solid line shows the deflection field after the registration. From this result, it was found that the alignment accuracy was within $\pm 0.2 \mu\text{m}$ at 2σ (without correction for pedestal distortion). The registration time was within 0.4 second per a field.

IV. CONCLUSIONS

The sheet structured detector which transforms the direction of the light propagation emitted from plastic scintillator by the gratings has been devised and developed as the back-scattered electron detector for the auto-registration technique. As this detector is very thin, it is very effective especially for the post-lens deflection optical system which has a narrow space between the deflector and a specimen. In this detector the propagation efficiency of the light hardly depended on the incident position of electrons, so the detection area can be extended without the decrease of the response speed. It was also confirmed that this detector has the high sensitivity and good linearity for the current of incident primary electrons. This detector was applied to the auto-registration in the electron beam exposure.

In this paper a photo-multiplier was used as a detector for the light emitted from scintillator. The solid state photo-detector can be also coupled with to insert more than one detector into the electron optical system.

ACKNOWLEDGMENT

The authors express their appreciation to Mr. A. Ihaya for his helpful guidance.

REFERENCES

- (1) A.D.Wilson, T.H.P.Chang and A.Kern, J. Vac. Sci. Technol. Vol. 12, No. 6, Nov/Dec, 1240 (1975)
- (2) T.H.P.Chang, Eighth International Congress on Electron Microscopy, Canberra, Vol. I, 650 (1974)
- (3) E.D.Wolf, P.J.Coane and F.S.Ozdemir, J. Vac. Sci. Technol., Vol. 12, No. 6, Nov/Dec, 1266 (1975)
- (4) D.Stephani and E.Froschile, Fourteenth Symposium on Electron, Ion and Photon Beam Technology, Palo Alto (1977)
- (5) J.P.Beasley and D.G.Squire, IEEE Trans. on Electron Devices, Vol. ED-22, No. 7, 376 (1975)
- (6) Ortec Technical Data, " Silicon Surface-Barrier and Ion-Implanted Detectors for Charged Particles " March (1976)

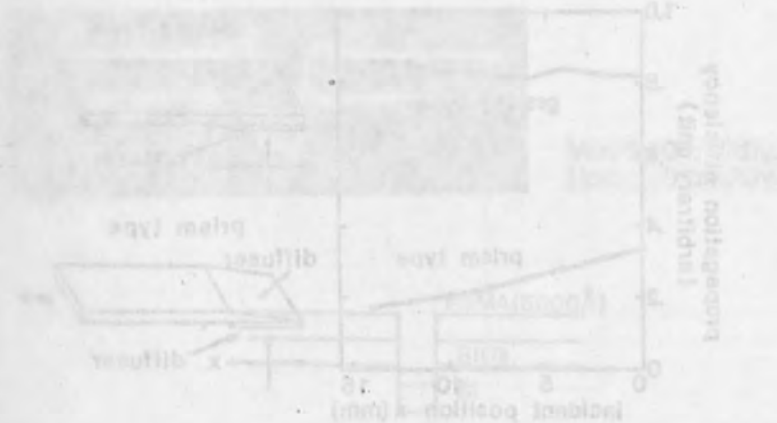


Fig. 2. Stimulation of light propagation
Fig. 4. Mark signal

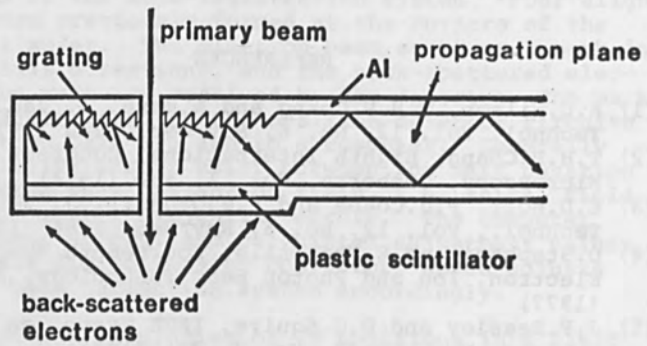


Fig.1 Structure of the new detector

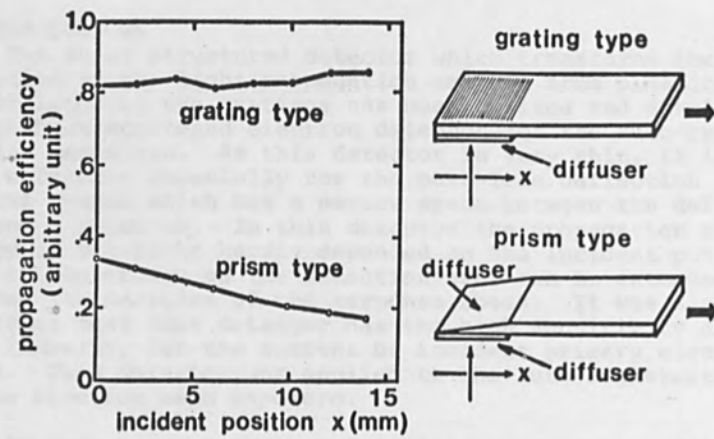


Fig.2 Simulation of light propagation

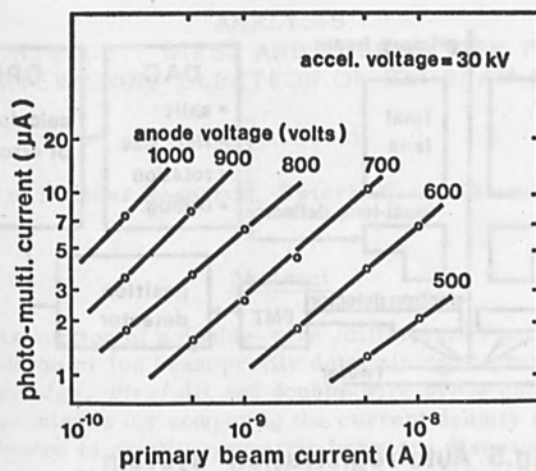
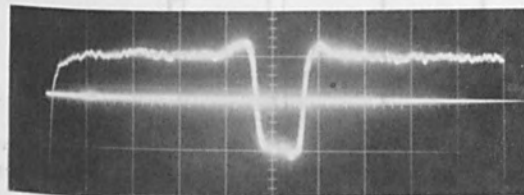


Fig.3 Characteristics of the electron detector



Ver. 500 mV/div.
Hor. 5 $\mu\text{m}/\text{div}.$

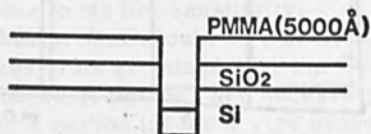


Fig.4 Mark signal

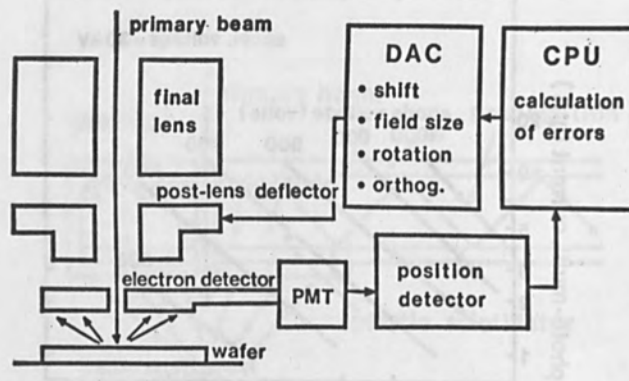


Fig.5 Auto-registration system

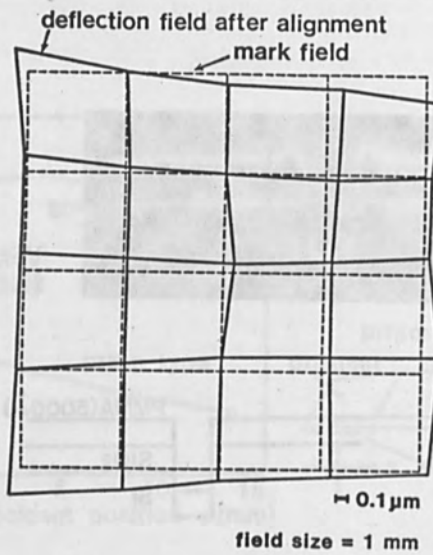


Fig.6 Result of alignment

ANALYSIS
OF STRAIGHTEDGE-, WIRE- AND DOUBLE-WIRE PROBE DATA
FOR DETERMINING ELECTRON OR ION BEAM PROFILE

S. Ugniewski

Institute of Nuclear Research, Swierk 05-400 Otwock, Poland

Abstract

Construction of a double-wire /differential/ probe for an electron or ion beam profile determining is proposed. Straightedge, wire/slit and double-wire probe data reducing techniques for computing the current density radial distribution in axially symmetric beam are discussed. Techniques are based upon 1^o data interpolation, and 2^o data least-squares approximation using orthogonal polynomials. Abel integral equation is used directly to reduce wire probe data, and after modification, to reduce data of two other probes. Techniques are tested by the reconstruction of a Gaussian beam profile.

1. Introduction

Knowledge of current density distribution across charged particle beam is important in applications such as electron beam welding, kinescope and accelerator construction, ion implantation, etc.

Point-probe /pinhole camera/, narrow-slit or fine-wire probe, and wide-slit or straightedge probe have been developed for this aim.

Direct measurements of a beam profile by means of a point-probe are performed rarely due to its low sensitivity.

Readings of two other probes should be transformed mathematically. The integral transforms are simple for the Gaussian-type beam profile only (1, 2). Numerical methods are necessary for beam profiles of any type. Harker's method (3) for a wire probe /interpolation over equidistant in x^2 data points/ and its generalisation by Tatsuno and Makishima (4) increase accuracy in the peripheral part at the cost of a more interesting central part of a beam cross-section.

Nestor and Olsen (5) improved the Harker method by using equidistant in x interpolation for a line /wire/ and surface /straightedge/ probe data reduction. Sioe Yao Kan (6) analysed straightedge probe

data assuming a step equidistant in r interpolation of a beam current density distribution.

Various interpolation methods for surface and line probe data reduction were gathered and compared in papers (7, 8). Differential probe known in optical interferometry but not used in beam profile measurements has also been dealt with there.

Analytic solution based on the least-squares data approximation using orthogonal polynomials was presented for a line probe in paper (9) and for all three a/m kinds of probes in paper (10).

The aim of this paper is:

- 1° to propose a construction of a double-wire probe for beam profile measurements (11),
- 2° to verify the applicability of various numerical methods of surface-, line-, and differential-probe data reducing for beam profile determination.

2. Integral equations

Diagrams of probes are assembled in Fig. 1, where a beam symmetry axis is normal to the paper sheet, x is the direction of scanning, R is the over-all diameter of a beam cross-section, t is the narrow-slit width or the wire effective diameter, and w is the distance between two wires of the double-wire probe. Each wire of the double-wire probe is connected to one input of a differential amplifier of an oscillograph.

Currents of a straightedge-probe $I^S(x)$, a wire-probe $I^L(x)$, and a double-wire probe $I^D(x)$ are mutually related by equations

$$I^L(x) = -t \frac{dI^S(x)}{dx}, \quad I^D(x) = -w \frac{dI^L(x)}{dx} \quad /1/$$

Algebraic signs in these relations are arbitrary. Minus is considered as more convenient in geometrical interpretation and computing.

Integral equations /Volterra equations of the first kind/ connecting the data functions /current $I(x)$ / of each probe with the function to be determined /current density $j(r)$ /, are assembled in Table I /specification for the beam profile measurements of respective equations from papers (7, 8) /.

Table I. Integral equations of probes

Probe	Direct integral equation	Inverted integral equation
Straight-edge	$I^S(x) = 2 \int_x^R j(r)r \arccos \frac{x}{r} dr$	$j(r) = \frac{1}{\pi} \int_r^R \frac{d^2 I^S(x)}{dx^2} \frac{dx}{(x^2 - r^2)^{1/2}}$
Wire	$I^L(x) = 2t \int_x^R \frac{j(r)r dr}{(r^2 - x^2)^{1/2}}$	$j(r) = \frac{-1}{\pi t} \int_r^R \frac{dI^L(x)}{dx} \frac{dx}{(x^2 - r^2)^{1/2}}$
Double wire	$I^D(x) = -2xwt \int_x^R \frac{dj(r)}{dr} \frac{dr}{(r^2 - x^2)^{1/2}}$	$j(r) = \frac{1}{\pi wt} \int_r^R \frac{d^2 I^D(x)}{dx^2} \frac{dx}{(x^2 - r^2)^{1/2}}$

It can be seen from equations in Table I, that a straightedge probe needs no calibration. On the contrary, the knowledge of t in a wire-probe and, additionally, of w in a double-wire probe is necessary.

3. Interpolation methods

Direct integral equation of a wire-probe /Abel integral equation/ is computed by dividing the beam cross-section into $N = R/w, /N$ is arbitrary except for a double-wire probe/, concentric zones and assuming a specific variation of current density in each zone /A-type methods/. Inverted integral equation is computed by dividing the scanning distance R into N intervals and assuming the specific variation of a probe current in each interval /B-type methods/. The use is not made of integral equations for the two other probes.

3.1. A-type methods

Algebraic equations that replace direct integral equations from Table I are presented in Table II. $I_i^S, I_i^L,$ and $I_i^D /i=0, 1, 2, \dots, N-1/$ are sets of N equidistant readings of straightedge-, wire-, and double-wire probe, respectively, j_k is the set of N corresponding current density values to be determined. Matrix $\{a\}$ elements for a line- /wire-/ probe /Abel matrix elements $a_{i,k}^L /$ have been presented for various types of interpolation, in a number of papers (12-15),

and assembled, in unified notation, in paper (16). Matrix $\{a\}$ elements formulas for straightedge-, and double-wire probe are derived /as in (7, 8)/, after approximating Eqs. 1 by

$$I_i^L = \frac{t}{w} (I_i^S - I_{i+1}^S), \quad I_i^D = I_i^L - I_{i+1}^L. \quad /2/$$

Table II. A-type methods

Probe	Algebraic equation	$a_{i,k}$
Straight -edge	$I_i^S = w \sum_{k=i}^{N-1} a_{i,k}^S j_k$	$a_{i,k}^S = a_{i,k}^L + a_{i+1,k}^S (1 - \delta_{i,k})$
Wire	$I_i^L = wt \sum_{k=i}^{N-1} a_{i,k}^L j_k$	$a_{i,k}^L$ - Abel $\{a\}$ matrix
Double wire	$I_i^D = wt \sum_{k=i}^{N-1} a_{i,k}^D j_k$	$a_{i,k}^D = a_{i,k}^L - a_{i+1,k}^L (1 - \delta_{i,k})$

$\delta_{i,k}$ designates the Kronecker symbol / $\delta_{i,k} = 1$, for $k=i$, $\delta_{i,k} = 0$, for $k \neq i$ /.

3.2. B-type methods

Algebraic equations that replace inverted integral equations from Table I are presented in Table III. Matrix $\{b\}$ elements for a wire probe /Abel matrix $b_{i,k}^L$ elements/ are taken from papers (17, 16, 5) and assembled, in unified notation, with their numerical values in paper (16). Matrix $\{b\}$ elements formulas for straightedge-, and double-wire probe are derived using Eq. 2.

Table III. B-type methods

Probe	Algebraic equation	$a_{i,k}$
Straight-edge	$j_i = \frac{1}{w} \sum_{k=i}^{N-1} b_{i,k}^S I_k^S$	$b_{i,k}^S = b_{i,k}^L - b_{i,k-1}^L (1 - \delta_{i,k})$
Wire	$j_i = \frac{1}{wt} \sum_{k=i}^{N-1} b_{i,k}^L I_k^L$	$b_{i,k}^L$ - Abel $\{b\}$ matrix
Double wire	$j_i = \frac{1}{wt} \sum_{k=i}^{N-1} b_{i,k}^D I_k^D$	$b_{i,k}^D = b_{i,k}^L + b_{i,k-1}^D (1 - \delta_{i,k})$

Matrices $b_{i,k}^D$ and $b_{i,k}^L$ in Table III can be presented in an alternative form /see papers (7, 8)/, as $b_{i,k}^D$ - known matrix elements, and $b_{i,k}^L = b_{i,k}^D - b_{i,k-1}^D (1 - \delta_{i,k})$.

Equivalent set of algebraic equations derived using a more exact approximation of the derivatives in Eq. 1 /as in paper (5)/

$$I_i^L = \frac{t}{2w} (I_{i-1}^S - I_{i+1}^S), \quad I_i^D = \frac{1}{2} (I_{i-1}^L - I_{i+1}^L) \quad /3/$$

is presented in Table IV.

Table IV. B-type methods /variant/

Probe	Algebraic equation	$b_{i,k}$
Straight-edge	$j_i = \frac{1}{w} \sum_{k=i-1}^{N-1} b_{i,k}^S I_k^S$	$b_{i,k}^S = \frac{1}{2} b_{i,k+1}^L, k=i-1, k=i$ $\frac{1}{2} (b_{i,k+1}^L - b_{i,k-1}^L), k > i$
Wire	$j_i = \frac{1}{wt} \sum_{k=i}^N b_{i,k}^L I_k^L$	$b_{i,k}^L$ - Abel $\{b\}$ matrix
Double wire	$j_i = \frac{1}{wt} \sum_{k=i+1}^{N+1} b_{i,k}^D I_k^D$	$b_{i,k+1}^D = 2b_{i,k}^L, k=i, k=i+1$ $2b_{i,k}^L + b_{i,k-1}^D, k > i+1$

4. Least-squares data approximation using orthogonal polynomials

According to results of paper (9), the data function in the inverted integral equation for a wire probe can be approximated by the even polynomial

$$I^L(x) = t \sum_{j=0}^m b_{2j}^L x^{2j} \quad /4/$$

The solution of that integral equation is

$$j(r) = \sum_{j=1}^m b_{2j}^L G_{2j}(R, r),$$

where

$$G_{2j}(R, r) = -\frac{2j}{\pi} \sum_{h=0}^{j-1} \binom{j-1}{h} r^{2(j-1-h)} \frac{(R^2 - r^2)^{h+1/2}}{2h+1}$$

is this solution for the monomial $I^L(x) = t x^{2j}$.

According to results of paper (10), analogous relations can be derived for straightedge and double-wire probe after approximating their data functions by odd polynomials and analytic differentiating the first one or integrating the second in Eq. 1. Relations obtained are assembled in Table V. Only $I^S(x) - I^S(0)$ /and not $I^S(x)$ / can be approximated by a function continuous in the center of the coordinate system. This translation is permitted because

$$\frac{d^2}{dx^2} I^S(x) = \frac{d^2}{dx^2} [I^S(x) - I^S(0)] \text{ in the respective equation of Table 1.}$$

Table V. Approximation method

Probe	Approximation polynomial	Algebraic equation
Straight-edge	$I^S(x) - I^S(0) = \sum_{j=0}^m b_{2j+1}^S x^{2j+1}$	$j(r) = - \sum_{j=1}^m (2j+1) b_{2j+1}^S G_{2j}(R, r)$
Wire	$I^L(x) = t \sum_{j=0}^m b_{2j}^L x^{2j}$	$j(r) = \sum_{j=1}^m b_{2j}^L G_{2j}(R, r)$
Double wire	$I^D(x) = wt \sum_{j=1}^m b_{2j-1}^D x^{2j-1}$	$j(r) = - \sum_{j=1}^m \frac{b_{2j-1}^D}{2j} G_{2j}(R, r)$

Data functions are approximated by the least-squares method using polynomials orthogonal over the set of data points, generated by the Forsythe procedure (18, 19). Wire-probe data are previously symmetrised around their axis of symmetry by supplementing the "mirror points" in respect to the experimental data points. Thus, only even polynomials in Eq. 4 are generated. On the contrary, straightedge-, and double-wire probe data are previously supplemented by the anti-symmetric points. Thus, only odd polynomials in respective equations of Table V are generated.

5. Testing

To verify the applicability of various numerical methods, the set of test-functions

$$I^S(x) = \int_x^{\infty} \exp(-v^2) dx = \frac{\sqrt{\pi}}{2} \operatorname{erfc} x,$$

$$I^L(x)/t = \exp(-x^2),$$

$$I^D(x)/wt = 2x \exp(-x^2)$$

is used. For each of these data functions, the Gaussian-type current density distribution

$$j(r) = \frac{1}{\sqrt{\pi}} \exp(-r^2)$$

is envisaged. This test-function is preferred because the deviation of a beam profile from the Gaussian-type is often an object of interest in constructors' and experimentators' practice.

5.1. Accuracy

To examine the accuracy of the interpolation methods, all the algebraic equations from Tables II, III and IV have been computed for various types of interpolation / $N=20$, $R=2$, $I^S(R) \cong 0$, $I^L(R) \cong 0$, $I^D(R) \cong 0$ /. In all the calculations, exact values of data functions /full accuracy of the computer/ have been used. Resultant values of j_i are presented in the left, middle and right column of Fig. 2, respectively.

Four different A-methods /Table II/ are applied for obtaining the left-column plots. The first one is based on step interpolation in r of the resultant function /Mach of Maecker (12)/. The second is based on step/surface interpolation in r by Pearce (13). The third method is based on linear in r interpolation /van Voorhis (14)/, and the fourth one, on linear in r^2 interpolation /Frie (15)/. Elements $a_{i,k}^S$ derived from Pearce's $a_{i,k}^L$ values are identical to those of Sioe Yao Kan method (6). Elements $a_{i,k}^D$ have been previously derived from elements $a_{i,k}^L$ in paper (20) for step interpolation /Mach, Maecker/, and linear interpolation /van Voorhis/.

Two different B-type methods /Table III/ and their variants /Table IV/ are applied for obtaining the middle-column and right-column plots in Fig. 2, respectively. The first method is based on linear in x interpolation of a line /wire/ probe data function /Gorenflo method (17) modified in paper (16) /, and the second is based on linear in x^2 interpolation of the same function /Nestor and Olsen (5) /. Using the latter type interpolation, the elements $b_{i,k}^D$ have been previously derived in paper (20) by means of equation analogous to /2/ and elements $b_{i,k}^S$ have been derived in paper (5) by means of equation analogous to /3/.

Approximation method is not examined here because its accuracy is considerably greater, according to the results of paper (10).

5.2. Errors due to rounding data values

Some calculations are repeated for the same data functions values rounded to two digits to the right of the decimal point, because errors of at least 1% cannot be avoided in real oscillogram readings. Two best interpolation methods are chosen after examination of plots in Fig. 2. The first one /step variation of $j(r)$ / is identical to Sioe Yao Kan method (6) for a surface /straightedge/ probe and to the Pearce (13) for a line /wire/ probe. The second one /linear in x^2 variation of $I(x)$ / is identical to the Nestor and Olsen method (5) for surface and line probe. Results of calculations are presented in Fig. 3.

The same calculations are performed by means of the approximation method using orthogonal polynomials. For a straightedge probe, $I^S(x) - I^S(0) = -\frac{\sqrt{\pi}}{2} \operatorname{erf} x$ is taken as the test-function instead of $I^S(x)$ from Section 5. The results of calculations for $m=4$ are presented also in Fig. 3.

6. Discussion

Remarks below concern mainly data reducing of a straightedge- and double-wire probe because the properties of numerical methods for wire-probe data reducing have been discussed previously (16, 21).

1° Examination of plots in Fig. 2 permits us to conclude that the majority of interpolation methods applied to data reducing of a straightedge probe leads to overestimating the Gaussian-type current density distribution in the central part of a beam cross-section. On the contrary, current density obtained by means of a double-wire probe is underestimated in this region. Only the variant of B-type methods /Table IV/ and the Sioe Yao Kan method are rather free from this inaccuracy. Straightedge-probe data are falsely interpreted by all the interpolation methods near the beam perimeter. Results obtained using high-order interpolation /f.e. linear in r^2 or linear in x^2 / are more exact than using low order interpolation. Results of data reducing of both a/m probes are less exact than those of a wire-probe because the Abel integral equation is chosen to be transformed into algebraic form.

2° Examination of plots in Fig. 3 enables us to conclude that the oscillogram readings of a straightedge probe cannot be reduced by any interpolation method owing to enormous errors due to rounding the data values. Superiority of the approximation methods over all the interpolation methods considered is evident especially for this probe.

7. Conclusions

Systematic search of beam-profile probes and of the numerical methods for data reducing is concluded by results as follows:

- 1° double-wire probe, insensitive to rounding data errors for all the techniques of data interpretation, is proposed;
- 2° numerical method that enables straightedge-probe data reducing, has been proposed and tested.

REFERENCES

1. E.B. Bas, *Optik* 12, 377 /1955/
2. R.B. Fair, *J. Phys. E*, 4, 35 /1971/
3. K.J. Harker, *J. Appl. Phys.* 28, 1354 /1957/
4. G. Tatsuno, H. Makishima, *Electronics a. Communic. Jap.* 55-B, 45 /1972/
5. O.H. Nestor, N.H. Olsen, *S.I.A.M. Rev.* 2, 200 /1960/
6. Sioe Yao Kan, IKE-3-50, Stuttgart 1974
7. S. Ugniewski, INR 1714/XXIV/PP/B, Warsaw 1977 /in Polish/
8. S. Ugniewski, *Computer Phys. Communic.* /1978/, in press
9. S. Ugniewski, *Proc. 13th Int. Conf. Phen. Ionised Gases*, Berlin 1977, p. 205
10. S. Ugniewski, INR 1715/XXIV/PP/B, Warsaw 1977 /in Polish/
11. S. Ugniewski, Patent appl. Inst. Nucl. Res. SW4/22-78/715/78
12. L. Mach, *Wien Akad. Ber. Math. Phys. Klasse* 105, 605 /1896/
H. Maecker, *Z. Phys.* 136, 119 /1953/
13. W.J. Pearce, *Conf. Extr. High Temp.*, Boston 1958, H. Fisher, L.C. Mansur, Eds, J. Wiley N. York 1958, p. 123
14. R. Ladenburg, J. Winckler, C.C. van Voorhis, *Phys. Rev.* 73, 1359 /1948/
15. W. Frie, *Ann. Phys. /Leipzig/* 10, 332 /1963/
16. S. Ugniewski, *Applic. Mathematicae* 17, 901 /1977/
17. R. Gorenflo, IPP/6/19, Garching 1964
18. G.E. Forsythe, *Journ. S.I.A.M.* 5, 74 /1957/
19. Subroutine FLSQFY, *Math. Sc. Library*, p. 5-167, Control Data Corp. 1971
20. M. Sadowski, S. Ugniewski, *J. Techn. Phys.* 17, 365 /1976/
21. S. Ugniewski, *Dissertation /in Polish/*

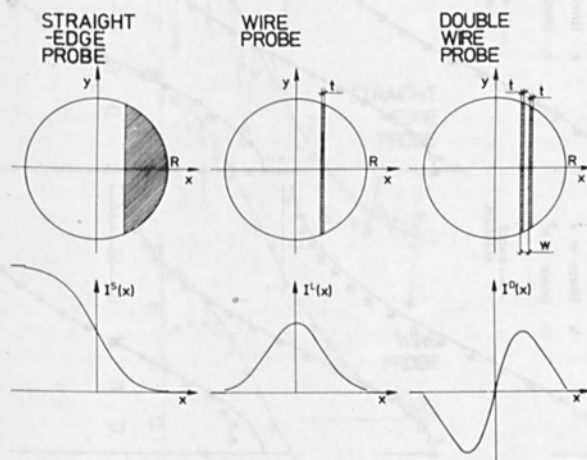


Fig. 1
Diagrams of three probes and their exemplary data functions

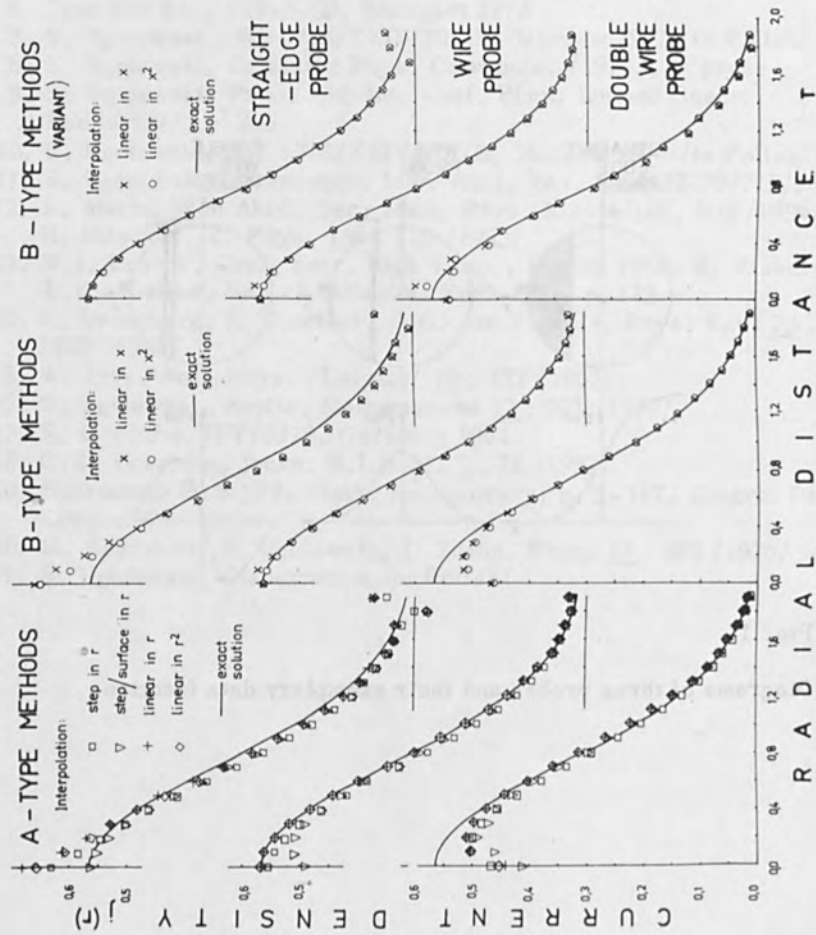


Fig. 2

Reconstruction of a Gaussian-type beam profile by various interpolation methods applied to exact values of data functions.

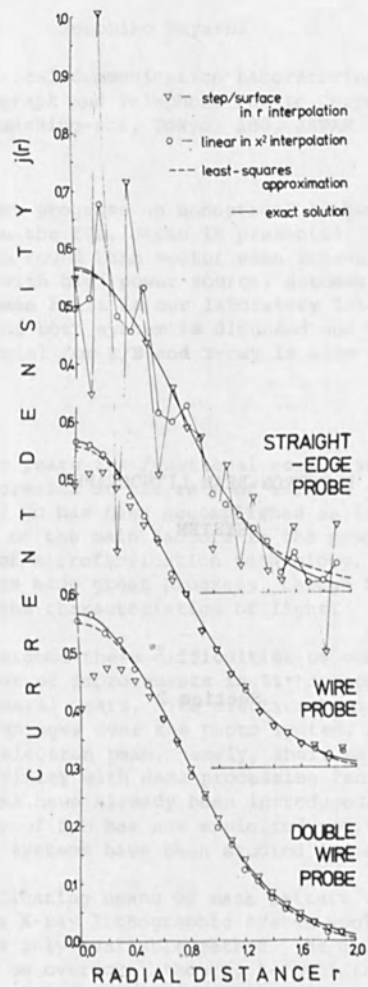
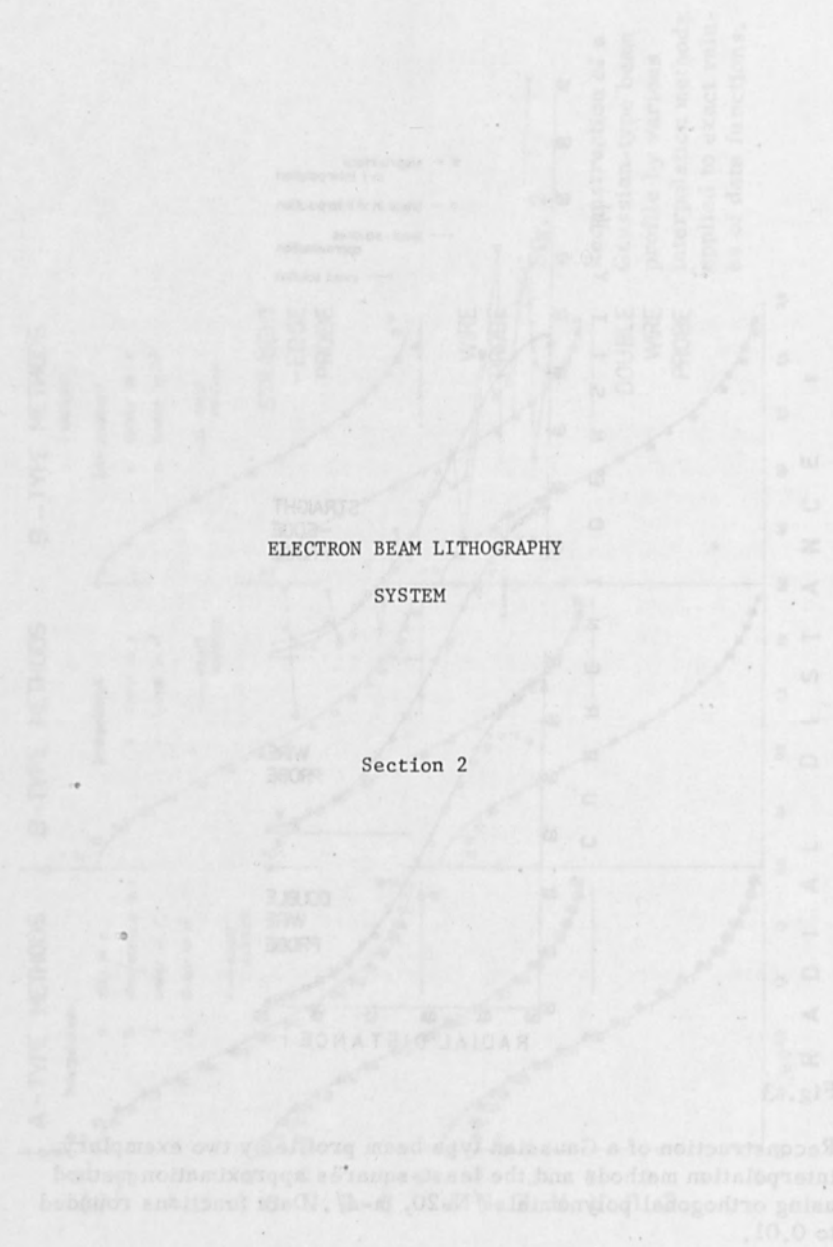


Fig. 3
 Reconstruction of a Gaussian type beam profile by two exemplary interpolation methods and the least-squares approximation method using orthogonal polynomials $/N=20, m=4/$. Data functions rounded to 0.01.

ELECTRON BEAM LITHOGRAPHY
SYSTEM

Section 2



ELECTRON BEAM AND X-RAY LITHOGRAPHY FOR
VERY LARGE SCALE INTEGRATION DEVICES

Tomohiko Hayashi

Electrical Communication Laboratories
Nippon Telegraph and Telephone Public Corporation
Musashino-shi, Tokyo, 180, JAPAN

ABSTRACT: Recent progress on nonoptical lithography, E/B and X-ray system in the ECL, Japan is presented. An experimental E/B system with round beam vector scan scheme and an X-ray exposure system with high power source, automatic aligning mechanism have been built in our laboratory lately. The design consideration of both system is discussed and the improvement of resist material for E/B and X-ray is also described.

Introduction

During the past years the functional complexity of integrated circuit has been increased at the rate of twice a year. Recently, the minimum line width $2\ \mu\text{m}$ has been accomplished as 64 kbit MOS random access memory. One of the main factors in the progress of LSI devices is the improvement of microfabrication technology. The technique of photo-lithography has made great progress, though it has the essential restriction due to the characteristics of light.

In order to overcome these difficulties of conventional photo-lithography, a number of improvements in lithographic techniques have been studied for several years. The electron beam (E/B) lithographic system has many advantages over the photo system, originating from the characteristics of electron beam, namely, short wave length, good controllability and affinity with data processing facility. Several practical E/B systems have already been introduced to production line, but the potentiality of E/B has not exploited yet, thus, various kinds of E/B lithographic systems have been studied in many places.

As for the replicating means of mask pattern with minimum line width near $1\ \mu\text{m}$, the X-ray lithographic system would be the most promising and almost the only available method. As it has many technological problems to be overcome, though, X-ray lithographic system has now been confined in laboratory.

Various kinds of new lithographic technology have been studied enthusiastically all over the world including Japan. The recent progress on E/B and X-ray lithographic systems and resist materials in the Electrical Communication Laboratory, Nippon Telegraph and Telephone Public Corporation is presented here.

Electron Beam Lithographic System

The E/B lithographic system has several advantages over conventional photo lithography, such as: (a) Fine pattern which has the minimum line width close to or less than $1 \mu\text{m}$ can be delineated because the electron beam wave length is by far shorter than that of ultraviolet light. (b) Shorter turn around time (TAT) can be achieved because the intricate process in optical mask fabrication can be drastically simplified. (c) As the case may be, direct pattern drawing onto the wafer without a mask is possible eliminating the time required for mask making and pattern replication. In the early stage of the study of E/B lithographic system, the first forte (a) was emphasized but recently the other fortes (b) and (c) are utilized and several E/B systems have been introduced in the LSI production substituting the photo lithographic system.

Various kinds of E/B lithographic system have been studied throughout the world and each system has its own features as shown in Fig.1.(1)-(5) There will be no single machine which is almighty for all kinds of purposes. So we should select the configuration principle considering the requested specification and circumstances under which it is to be used.

Generally speaking, it may be said that shaped beam method will be suitable for high speed generation, on the other hand the round beam method will be suitable for writing very fine pattern.^(3,4) Comparing the raster scan scheme and the vector scan scheme, it will be impossible to determine which is better unless all conditions are settled.^(1,2) Under some conditions, vector scan scheme is favorable than raster scan in writing fine pattern because of its facility of correction for proximity effect.

A new E/B lithographic system (temporarily named EB-52) has been built recently in the Electrical Communication Laboratory (ECL) as the result of tentative construction and testing of some experimental E/B machines. The main design objectives of our new system are: (a) versatility for device developmental use in the laboratory, (b) ability of drawing very fine pattern necessary to develop very large scale integration devices. Thus, round beam, vector scan method is employed.⁽⁵⁾

The electron optical column of this machine adopts orthodox construction philosophy using post-lens magnetic deflection. At the design of the deflection system, deflection aberration was analyzed by a CAD program which was also developed in the ECL. This program can analyze generally a focusing and deflecting system in which electromagnetic and electrostatic focusing lens field and deflection field are superimposed. Using this program, it is found that overall beam spot size at the corner of 2 mm field is $0.25 \mu\text{m}$ and optimum convergence angle is 3 milli-radian. The electron-optical design specifications are shown in Fig.2.

A LaB₆ single crystal cathode is used as the electron beam source, by which beam current 10 nA is achieved at the beam spot diameter 0.25 μm . A simple XY stage has been developed, employing nonmagnetic ball guide and stepping mechanism driven by pulse motor. The motion of the stage is measured continuously by laser-interferometers and the position signal is fed back to deflection control system in order to compensate the deviation of beam spot position.

Vector scan method has several advantages in comparison with raster scan method such as: (a) Vector scan method takes less futile time than raster scan method, should the pattern coverage ratio be less than a certain value. (b) In case of direct exposure on wafer, frequent position control of electron beam is necessary corresponding to the wafer deformation suffered from heat cycle. Round beam vector scan method can easily execute the beam position control with high accuracy. (c) Vector scan method is capable of correcting proximity effect in drawing very fine pattern including minimum line width close to 1 μm .

Analog scan method is employed in this system, as a result of comparing with digital scan method. In order to draw a very fine pattern accurately in high speed, it is necessary for digital scan method to use a very high speed 16 bit digital to analog converter (DAC). As an example, let's assume the scanning velocity is 2 m/sec and the equivalent minimum address is 0.125 μm , then 16 MHz clock frequency should be needed for DAC. Such high speed 16 bit DAC, however, is not commercially available yet.

On the other hand, in the analog scan method, starting point and ending point of a scanning line are determined by DAC, then a ramp signal generated from line generator connects the two points. Therefore, the performance required to DAC is not severe compared with the digital scan method. The block diagram of DAC used in this system is illustrated in Fig.3.

Fig.4 shows our new system (EB-52), Fig.5 is the specifications of it. A mask pattern for 64 kbit MOS memory drawn by this system is shown in Fig.6. This EB-52 system has been extensively tested for many months to evaluate the performance and reliability, it will be used as a powerful tool for developing new integrated devices in near future.

X-Ray Lithographic system

X-ray lithography is a very promising method for fine pattern replication in LSI production.⁽⁶⁾ Conventional photo lithography is capable of replicating fine pattern less than 2 μm width, but it is considered to be very difficult to replicate fine pattern including minimum line width close to 1 μm with reasonable yield. X-ray lithography has several advantages over photo lithography.

(a) High resolution less than $1\ \mu\text{m}$ can be expected because the interruptions due to diffraction, interference and reflection are almost negligible. (b) High resolution can be achieved with proximity replication, thus the life of mask can be prolonged. (c) Relatively thick resist layer can be used which results in the decrease of defecting spots.

On the other hand, X-ray lithography has several difficulties to be overcome in order to be employed as a practical tool for LSI production, such as high power X-ray source, precision aligning apparatus and durable transparent mask, etc. Recently, an experimental X-ray lithographic system which contains full automatic aligner, high power X-ray source has been developed in the ECL.

In the X-ray exposure system, penumbral blur, a , and run out, b , are produced by diffused X-ray beam and mask to wafer gap, as shown in Fig.7.⁽⁷⁾ In order to make these geometrical distortions as small as possible, it is necessary to decrease X-ray source radius, r , and to enlarge target to mask distance, D . On the contrary, the exposure time is, generally, proportional to D^2/r . Therefore, in the system design, the smaller the geometrical distortion, the more increases the exposure time. The relation between blur, run out and exposure time have to be decided after careful consideration.⁽⁸⁾ Fig.8 shows the conditions by which exposure time can be minimized at a and $b \leq 0.1\ \mu\text{m}$. If the mask to wafer gap deviation can be limited within $4\ \mu\text{m}$, then 4 to $5\ \text{mm}$ will be the optimum radius for X-ray source and the distance D will be about $700\ \text{mm}$.

In the X-ray system, X-ray wave length should be chosen considering how to reduce exposure time. Generally, X-ray transmission loss and resist sensitivity are respectively directly and inversely proportional to the third power of wavelength. Thus, the optimum wavelength is varied with the transmission loss as shown in Fig.9. If the transmission loss parameter, L , becomes considerably small, Si-K α and Al-K α lines are profitable. Such sufficiently small parameter is realized by the use of 2 to $5\ \mu\text{m}$ thick Si mask and $20\ \mu\text{m}$ thick Be window.

Increasing X-ray power, Si is suitable as a target material, because the melting point of Si is higher than that of Al. Accordingly, a water cooled Si rotary target has been newly designed which enables input power as high as $20\ \text{kW}$. The target of $100\ \text{mm}$ diameter is rotated at $6000\ \text{rpm}$. The surface of target is covered by Si film which is deposited on thin Cu base plate by plasma deposition method. By the adoption of Si target structure, durability to heat is improved in addition to increase in input power.

Principle of the aligning method of mask and wafer is shown in Fig. 10. Mask is transparent to visible light and reflective marks are formed on the wafer. Reflected light from mask mark and wafer mark are oscillated by a vibrator, and the detecting light beams are projected to optical sensor through stationaly slit. By measuring the fundamental

component of detected signal, mask mark and wafer mark are aligned to each stationaly slit, thereby assuring the relative positioning of mask and wafer.

As the positioning mechanism, electrodynamic transducers and elastically supported stage with no mechanical backlash or friction are designed and applied to fine positioning along the three axes and inclination.⁽⁹⁾ Electrostrictive transducer driven stage is used for fine positioning of rotary direction. This stage can move at a minimum step of $0.003 \mu\text{m}$ in the stroke range of ± 5 to $\pm 20 \mu\text{m}$, and has resonant frequency of over 140 Hz.

Regarding the X-ray mask membrane, boron doped silicon mask has been used in the laboratory, but the silicon mask substrate is opaque to visible light and the aligning operation has been difficult.⁽¹⁰⁾ Therefore, transparent mask fabrication technique has been studied. Fig.11 shows two kinds of mask fabrication process in which Si_3N_4 film is a main component. Although the layered structure mask of $\text{Si}_3\text{N}_4/\text{Si}(\text{P}^+)$ has visible light transparency of 30%, the mask strength is 1 Kg/cm^2 which is almost the same as that of $3 \mu\text{m}$ thick Si mask. The other one, $\text{Si}_3\text{N}_4/\text{SiO}_2/\text{Si}_3\text{N}_4$ structure mask has high transparency of about 80% and a strength higher than 0.5 kg/cm^2 . This structure enables the formation of 8 mm square window.

Fig.12 shows the X-ray system developed in the ECL recently, and Fig.13 is the outline of specifications. The system performance has been evaluated by examining the replicated pattern accuracy. Fig.14 shows an example of the experiment in which positioning accuracy of $\pm 0.2 \mu\text{m}$ is achieved at the interlock pattern. Exposure time is about 10 min. using highly sensitive resist (e.g. $\sim 100 \text{ J/cm}^2$) on 3 inch diameter wafer.

Resist Materials

Poly methyl methacrylate (PMMA) has been widely used as a micro-fabrication resist because of its high resolution and good machinability, but its sensitivity is not sufficient.⁽¹¹⁾ On the assumption that the introduction of fluorine atoms to the ester chain of PMMA will cause decrease in the binding force of main chain resulting an improvement in sensitivity, fluorine-containing poly methacrylates have been thoroughly studied.⁽¹²⁾ All these materials have 10 to 50 times higher sensitivity than PMMA, c.f. Fig.15.

Among them, hexafluorobutyl methacrylate (FBM) has the highest sensitivity ($0.4 \mu\text{C/cm}^2$) and high γ value (4.5). As for FBM, the great enhancement in sensitivity is expected by the addition of very small quantity of strong solvent to the developer. In case when FBM is applied to thermal process such as post baking, lift off and so on, careful handling would be necessary as the glass transition temperature

is 50°C.

Poly tetrafluoropropyl methacrylate (FPM) which has nearly the same glass transition temperature (101°C) as PMMA was found to be free from the problem of machinability with FBM. By this resist, 0.2 μ m line width pattern can be formed. Of these resists, FBM will be suitable for Cr mask fabrication, and FPM for direct wafer exposure.

Summary

The state of the art of the research in the ECL on microfabrication technology such as E/B and X-ray lithographic systems which has been expected as the key technology for the development of very large scale integration devices is described. As the E/B technology has an enormous potentiality, it will make remarkable progress in near future and many kinds of systems as shown in Fig.1 will be used in various fields. This system, EB-52, has just been accomplished lately and the study on applying it in the actual LSI process will be done hereafter.

The X-ray lithography has been considered as a future technology up to the present, however, it might be applied to practical use earlier than was expected if only some technological difficulties would be overcome. Reliable resist material with high sensitivity and good machinability is indispensable in micro-fabrication process and more improvement would be necessary for the characteristics of resist in future.

References

- 1) D.R.Herriot, et al, IEEE Trns. ED-22, p.385, (1975)
- 2) A.D.Wilson, et al, Proc. 7th Int'l Conf. Electron & Ion Beam Sci.& Tech. p.361 (1976)
- 3) H.S.Yourke, et al, IEDM Washington D.C. Dec. (1976)
- 4) H.C.Pfeiffer, 14th Symp. Electron, Ion & Photon Beam Tech. Palo Alto (1977)
- 5) A.Iwata, et al, Spring meeting of the Inst. Electronics and Communication Engineers of Japan, March (1978)
- 6) D.L.Spears, et al, Electronics Letters, 8, 4, p.102 (1972)
- 7) P.A.Sullivan, et al, J.Vac.Sci.Tech. 12, 6, p.1325 (1975)
- 8) J.H.McCoy, et al, Proc. 6th Int'l Conf. Electron & Ion Beam Sci.& Tech. p.3 (1974)
- 9) S.Yamazaki, et al, 14th Symp. Electron, Ion & Photon Beam Tech. Palo Alto (1977)
- 10) H.I.Smith, et al, J. Vac. Sci. Tech. 10, 6, p.913 (1973)
- 11) I.Haller, et al, I.B.M.J. Res. & Dev. 12, p.251 (1968)
- 12) K.Murase, et al, Int'l Conf. Microlithography, Paris (1977)

Beam shape	Gaussian spot		Shaped		
Scanning system	Vector		Raster	Fixed size / Variable size	
	Digital	Analog		Vector/Raster	
Features	High precision	High speed	Simple deflection system	High speed	
Problems	Complex deflection system		Speed (overhead) time	Proximity effect correction	
	High speed D/A	Analog circuit stability		Fixed minimum feature size	Complex column and control system

Fig.1 Electron beam systems

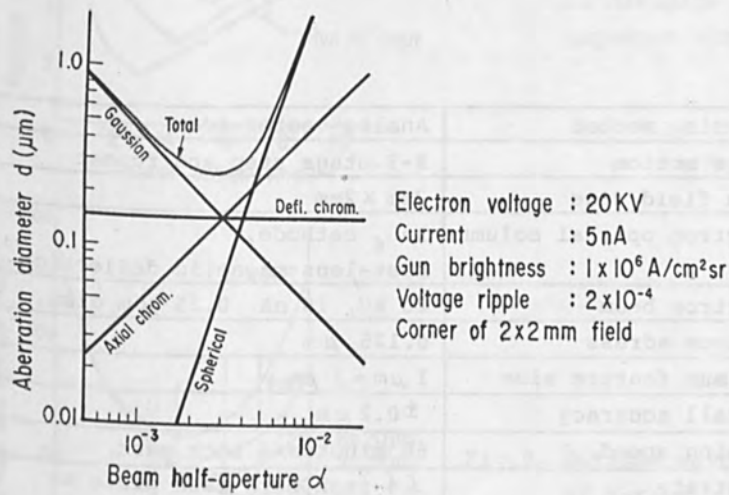


Fig.2 EB-52 electron-optical design by CAD program

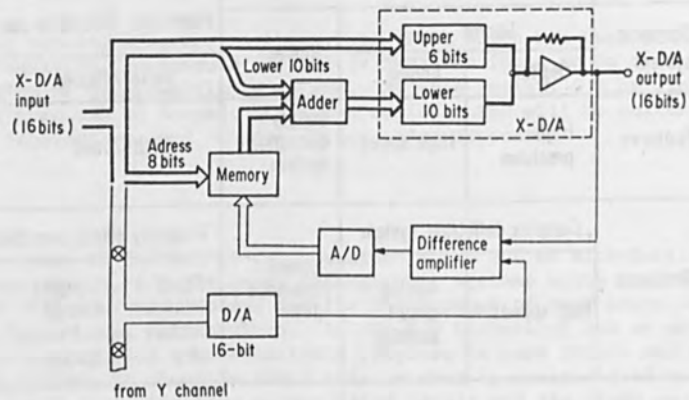
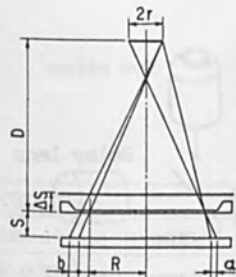


Fig.3 EB-52 16 bit D/A converter

Scanning method	Analog vector scan
Stage motion	X-Y stage step and repeat
Scan field size	2mm X 2mm
Electron optical column	LaB ₆ cathode, Post-lens magnetic deflection
Electron beam	20 kV, 10 nA 0.25 μm diam.
Minimum address	0.125 μm
Minimum feature size	1 μm x 1 μm
Overall accuracy	±0.2 μm
Drawing speed	60 minutes/4 inch mask
Substrate	≤ 4 inch hard mask plate or ≤ 3 inch wafer
Input MT	Standard PG format or EB format

Fig.5 EB-52' specifications



Blur $a = \frac{2r}{D} S$

Run out $b = \frac{\Delta S}{D} (R+r)$

Exposure time $\propto D^2/r$

Fig.7 Geometrical relation in X-ray lithography

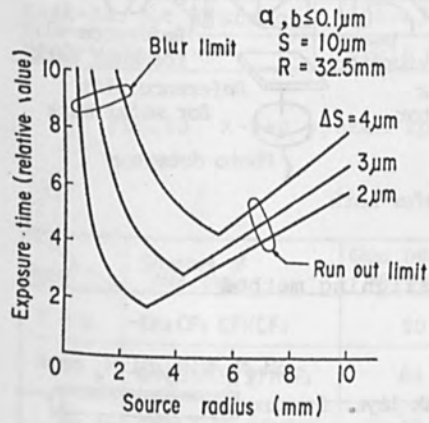


Fig.8 Optimum condition to minimize exposure time

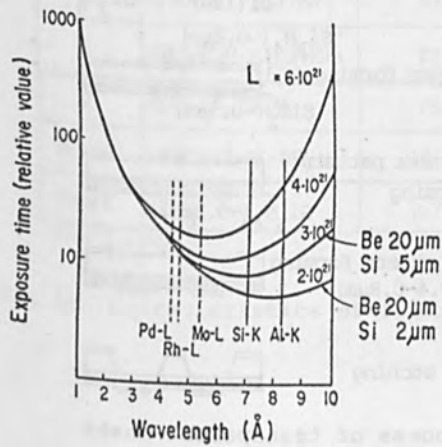


Fig.9 Optimum wavelength of X-rays

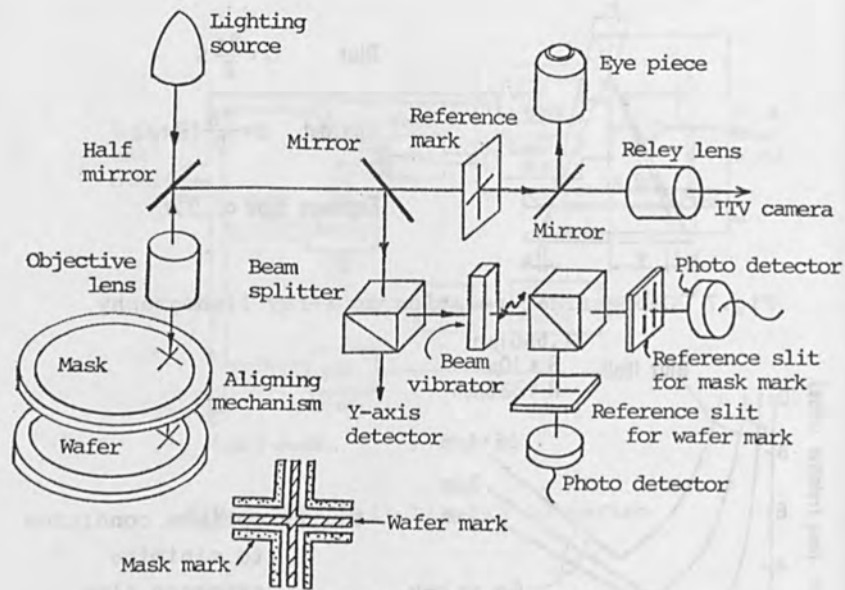


Fig.10 Principle of aligning method

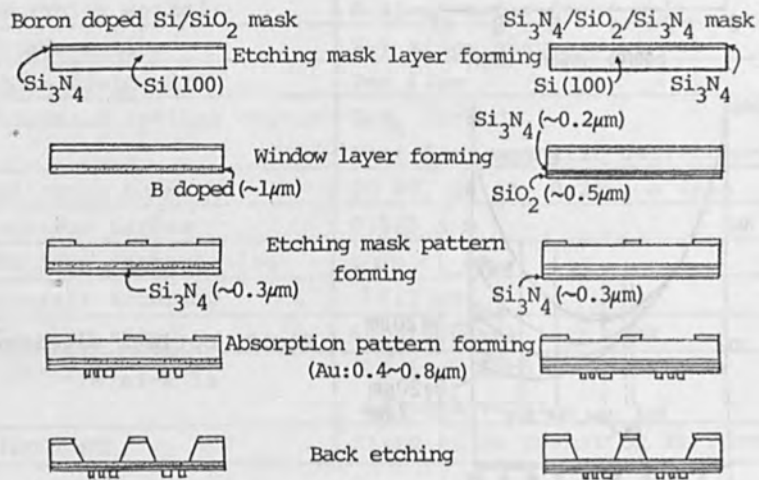


Fig.11 Fabrication process of transparent masks

Resolution	1 μm
Alignment accuracy	0.1 μm
Exposure area	65 mm diam.
X-ray source	7.1 \AA (Si- k_{α}), >20 kW input
Mask-target distance	400~700 mm
Mask-wafer gap	5~10 μm (tolerance $\pm 1 \mu\text{m}$)

Fig.13 X-ray system specifications

Resist	Structure of side chain	Glass transition temperature	EB sensitivity (20KV)	γ value
F B M	-CH ₂ CF ₂ CFHCF ₃	50 °C	0.4 $\mu\text{C}/\text{cm}^2$	4.5
A	-CH(CH ₃)CF ₂ CFHCF ₃	64	6	5
B	-C(CH ₃) ₂ CF ₂ CFHCF ₃	83	1.5	3
C	-C(CH ₃)(C ₂ H ₅)CF ₂ CFHCF ₃	73	1	>3
D	-CH ₂ CF ₂ CF ₂ H	75	1	>3
F P M	-C(CH ₃) ₂ CF ₂ CF ₂ H	101	1.5	4
PMMA	-CH ₃	107	50	3

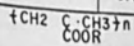


Fig.15 Characteristics of fluorinated polymethacrylates

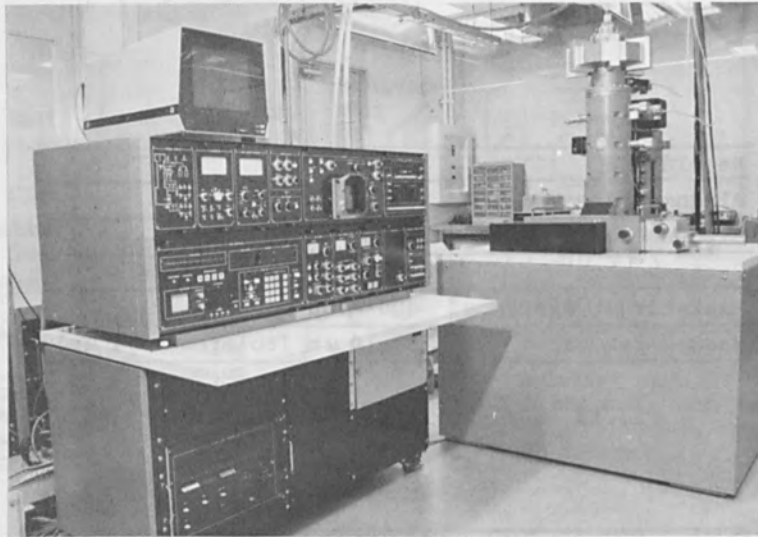


Fig.4 EB-52 system

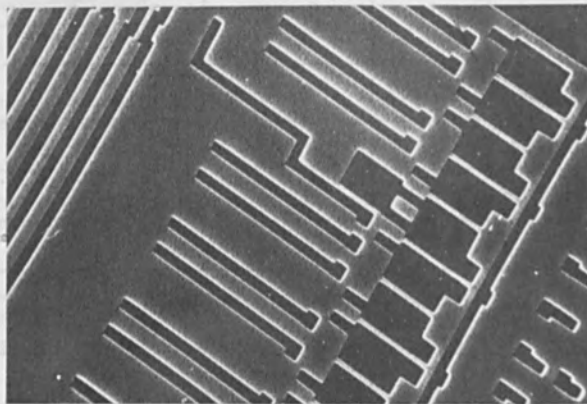


Fig.6 Generated patterns by EB-52

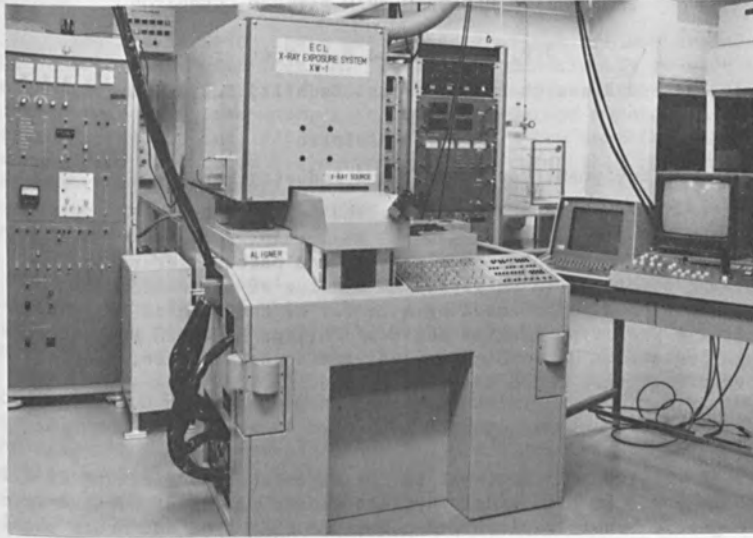
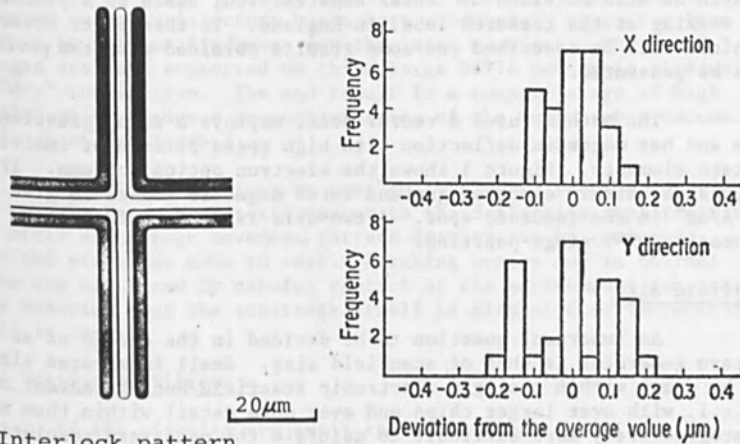


Fig.12 X-ray exposure system



Interlock pattern

Fig.14 Alignment accuracy

THE PHILIPS ELECTRON BEAM PATTERN GENERATOR

J.P. Beasley and D.B. Spencer

Philips Research Laboratories, Redhill, Surrey, England.

R.A. Beelaard

Equipment for Science and Industry Division,
Philips, Eindhoven, The Netherlands.

This paper describes the electron beam pattern generator being developed in Philips. An outline of its design and construction is followed by a review of the results obtained from a prototype machine built at Philips Research Laboratories in England. The machine is designed to be accurate, fast, very versatile and convenient to use.

Introduction

Electron lithography is now an established feature of silicon technology and is also widely applied to the making of surface-wave and magnetic bubble devices. A number of EBES type and other machines are currently in use as maskmakers but, particularly in development, there is an urgent need for a versatile pattern generator, capable not only of high quality mask-making but also of direct writing on substrates at high resolution and with reasonable speed. Within Philips a batch of such machines is under construction, based on a prototype now working at the research labs. in England. In this paper these machines will be described and some results obtained with the prototype will be presented.

The machine uses a vector scan, employs a round gaussian beam and has magnetic deflection with high speed fill-in of individual pattern elements. Figure 1 shows the electron optical column. It uses a tungsten hairpin electron gun and three magnetic lenses to give 100 A/cm^2 in the focussed spot. A two-axis laser interferometer becomes the X-Y stage position.

Scanfield Size

An important question to be decided in the design of an e.b. pattern generator is that of scanfield size. Small integrated circuits can be drawn within a single electronic scanfield but the advent of v.l.s.i. with ever larger chips and ever more detail within them makes it progressively more difficult to maintain the necessary resolution and accuracy within one field. Though much has been done to reduce deflection aberrations. It is our view that sooner or later it will be necessary to build up large chip patterns by patching a number of scanfields together. A rather moderate scanfield size of $1.6 \times 1.6 \text{ mm}$

Maskmaking

The way in which these setting up routines are used depends on the substrate being written on. It is very undesirable to have to put markers on mask substrates because the necessary extra processing introduces defects in the mask, so a reference marker mounted on the substrate holder is used, adjacent to the mask. The beam focus and current and the deflection field are first set up on this reference marker and then patterns are drawn on the mask until it is thought necessary to come back to the marker to check the settings. This may be every few minutes or so depending on machine stability.

Patching and focus errors will occur if the substrate height is different from that of the reference marker, either because the substrate is not flat or because it is not supported horizontally. In our machine, for example, even a $5\ \mu\text{m}$ variation in substrate height very roughly doubles the size of a $0.1\ \mu\text{m}$ beam and changes the scanfield size by $0.2\ \mu\text{m}$ - this is hardly acceptable. The height of the substrate under the column is therefore measured after each movement of the stage, to an accuracy of about $1\ \mu\text{m}$, and the beam focus and deflection amplifier gains are adjusted to compensate for the errors introduced by the change in substrate height.

Another error is introduced by yaw in the mechanical stage which will give rise to skew errors where the scanfields meet and must be kept down to a few arc seconds or allowed for by rotating the scanfield accordingly. This raises the question of mechanical tables. In the prototype we use a 4" stage supplied by Yosemite Labs. and this has proved quite satisfactory but a more advanced 5" stage has been developed in Philips Eindhoven for the later machines. The X and Y carriages are each supported on three large balls moving in slideways with "dry" lubrication. The end result is a compact stage of high precision which produces no contamination of the workchamber vacuum. This is shown in figure 3.

In all our machines we use "pull-in" DACs feeding position error signals from the interferometer to the deflection amplifiers so that, after each stage movement, pattern drawing can be commenced before the stage has come to rest. Patching errors due to thermal effects are minimized by careful control of the workchamber temperature and by ensuring that the substrate itself is also at this temperature when it is loaded.

Direct Writing on Silicon

If the circuits are small the deflection field is set up using four tantalum markers, one in each corner of the scanfield but for v.l.s.i. the markers must be spaced more widely. In that case the interferometer and height sensor are employed to ensure accurate patching between markers, the spacing of the latter being determined by the expected in-plane distortion of the wafers.

has been adopted and attention has been given to accurately joining these together, using a laser interferometer to define the stepping distance between one scanfield and the next. This rather small scanfield eases the problems of deflection electronics instability and noise, beam instability due to any cause and also makes the requirements on the table yaw easier to meet. The limit on the size of the circuit that can be drawn is then only determined by the size of the substrate itself.

Patching Scanfields

The errors at the boundaries between scanfields have to be reduced to less than, say $0.2 \mu\text{m}$ for $2 \mu\text{m}$ geometry and proportionately smaller for finer geometry. They arise either because the scanfields are the wrong shape or size, because they are placed slightly skewed with respect to one another or because the actual stepping distance along the substrate is incorrect.

Taking the first point, our pattern generator is equipped to detect a square heavy metal marker on a silicon glass or other substrate and to define its position within the scanfield co-ordinate system to rather better than $.05 \mu\text{m}$. The field can, therefore, be mapped out, to this accuracy, with respect to the interferometer co-ordinate system by moving a marker around the field and comparing the two co-ordinate systems. The shape of the scanfield can then be altered by computer-controlled adjustments to gain, rotation and keystone correction circuits associated with the main deflection amplifiers to bring the corners of the field to an exact square or rectangle, as measured by the interferometer. The straightness and linearity of the four scanfield boundaries can then also be checked to ensure accurate patching along their whole length. Figure 2 shows some early measurements of scanfield distortion obtained in this way.

As can be seen there is some distortion and non-linearity amounting to $0.7 \mu\text{m}$. As the errors along one edge are matched by similar errors along the opposite edge the maximum patching error that will occur is about $0.17 \mu\text{m}$.

As a preliminary to setting up the scanfield shape in this way the target current is checked and automatically adjusted to within a few per cent by changing the condenser lens excitation. This is necessary because at micron resolution a change in exposure of ten, or even five per cent is sufficient to significantly alter pattern linewidth. The beam is then automatically focussed in a routine in which it is scanned across two marker edges and the risetime of the back-scattered electron signal minimized (to indicate the smallest beam at the target).

Drawing the Patterns

The pattern generator employs an orthodox double magnetic deflection system situated before the objective lens but to speed up the drawing process all patterns are divided up into trapezium elements. These are four-sided figures with two parallel sides. Of course, in the most usual case these are rectangular. They are filled in by a separate deflection system with its own DACs, amplifiers and coils. This constitutes an autonomous hardware system which is provided with dimensional data by the computer. The trapezium generator coils are placed within the main scan coils and are closely similar to them, though they have lower inductance. This ensures that the two scanning systems "match" exactly throughout the main field. Trapezia are drawn point by point at a maximum stepping rate of 10 MHz corresponding to a coverage of $0.1 \text{ mm}^2/\text{second}$ with $0.1 \mu\text{m}$ resolution - suitable for fine patterns. For patterns of coarser geometry the machine can be run much faster by taking double or 5-fold steps in the trapezium generator. This gives a coverage 4 or 25 times faster. For example, patterns can be drawn with a $0.5 \mu\text{m}$ beam at $2.5 \text{ mm}^2/\text{second}$ giving a drawing time for a 3" circular array of about 20 minutes.

On the other hand, to enable good quality sub-micron patterns to be drawn by the machine, the scanfield size can be reduced to 0.8×0.8 or $0.4 \times 0.4 \text{ mm}$. This gives very fine discrimination in the patterns - as little as $0.025 \mu\text{m}$ - but of course the machine speed is greatly reduced.

Data input to the machine consists of lists of trapezium co-ordinates and dimensions on magnetic tape prepared by an e.b.m. post-processor attached to a C.A.D. system. Complicated arrays of different circuits can be built up in accordance with a pre-prepared "pattern layout" description.

For pattern details of $2 \mu\text{m}$ and smaller, however, the "proximity effect" becomes significant and can be corrected for by varying the local exposure. Later in this conference Hugh Ralph will describe his program to derive the exposure dose required in each of our pattern elements. This information is fed to the pattern generator as a speed figure for each trapezium. The trapezium generator has a variable computer-controlled clock to enable each trapezium to be drawn at a different speed (and, therefore, with a different exposure) in accordance with this input data. So far Hugh Ralph's program is only implemented for rectangular elements.

Figures 5 and 6 show the prototype and a later version of the machine respectively.

Figures 7, 8 & 9 show that the machines are capable of drawing both patterns of sub-micron resolution and also large patterns built up from a number of scanfields patched together.

Conclusions

It is believed that the Philips pattern generator as just presented will prove to be a very versatile and accurate machine suitable both for commercial maskmaking and for development work on substrates down to sub-micron resolution. It is designed to be reliable and easy to use. Further research is in hand to improve the machine's speed by amongst other things, the use of a shaped beam and also the adaptation of the marker detection system to accommodate topographical markers for direct slice writing.

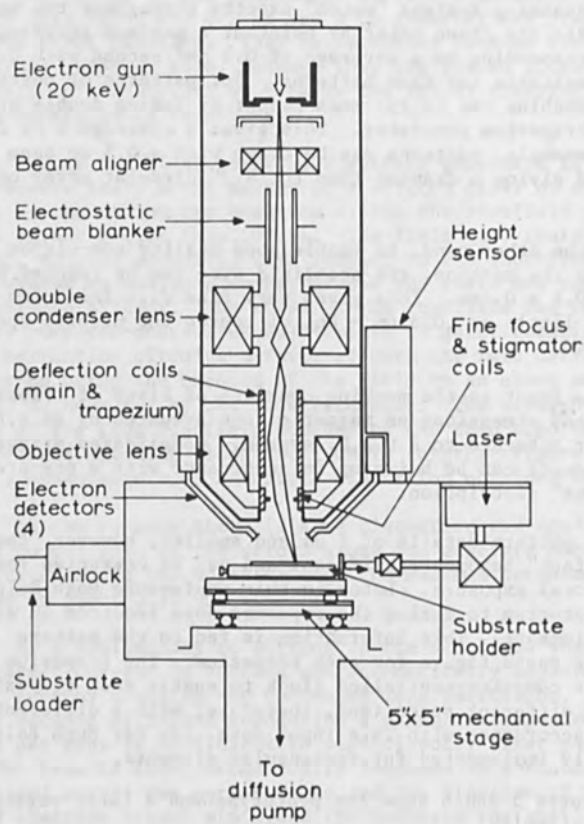


Figure 1: "The Electron Optical Column"

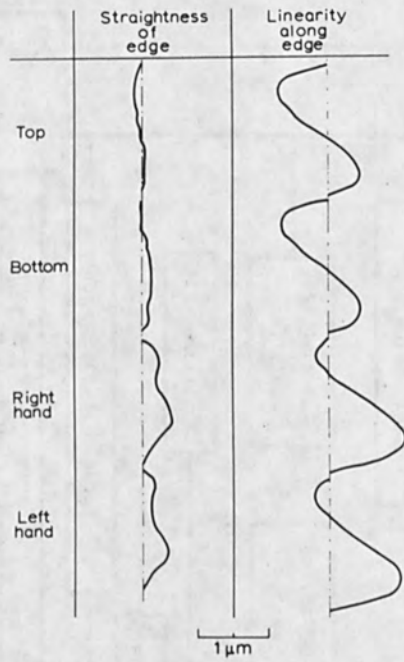


Figure 2: "Scanfield Distortion Measurements" showing maximum distortion of $0.7 \mu\text{m}$ but less than $0.17 \mu\text{m}$ expected patching error.

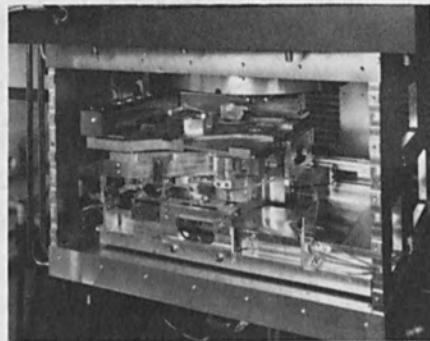


Figure 3: "Precision Mechanical Stage"

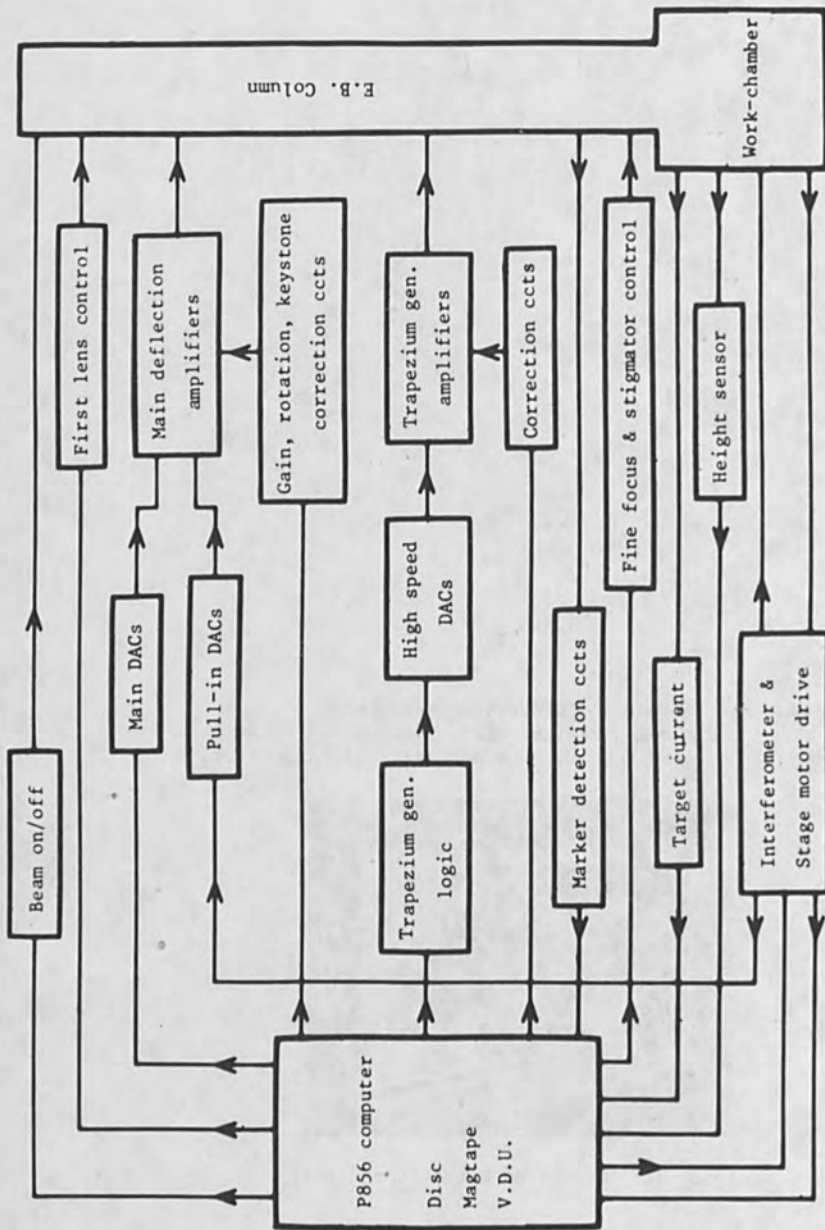


Figure 4: "The Pattern Generator Control System"



Figure 5: "Laboratory Prototype Pattern Generator

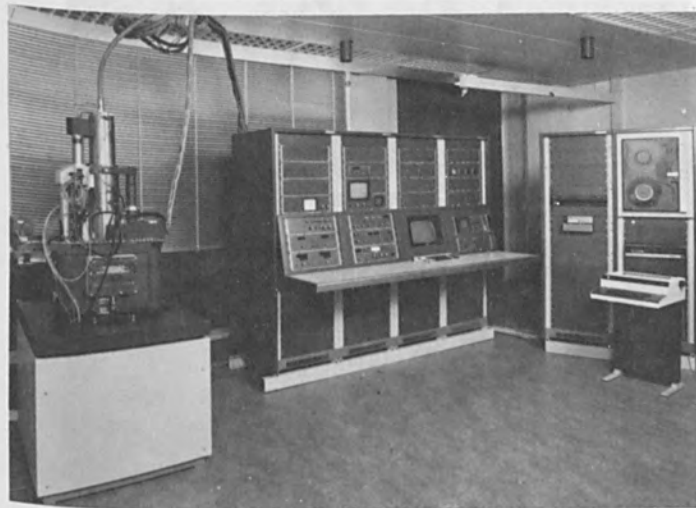


Figure 6: "Later Version of Pattern Generator

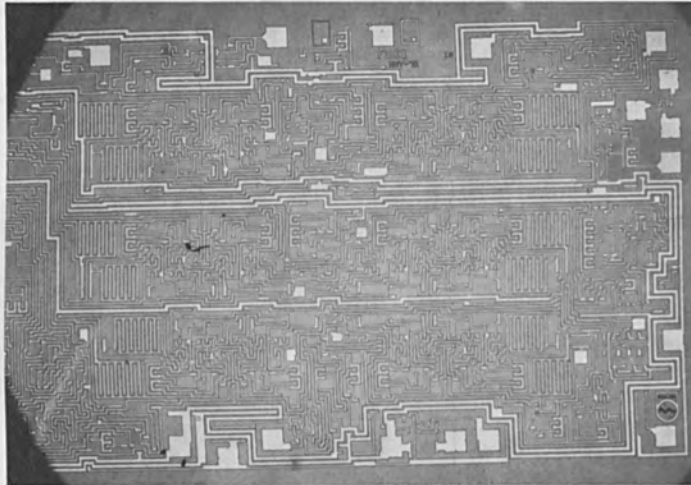


Figure 7: High resolution test pattern in resist.
Linewidths are 0.5, 0.7 and 1.0 μm

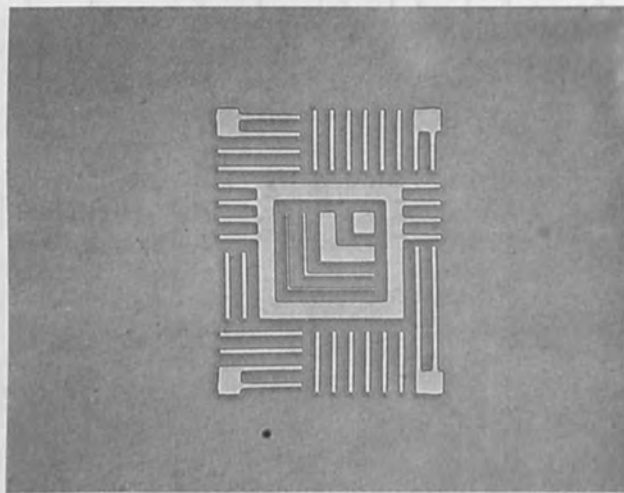


Figure 8: A linear circuit metallization pattern in resist.
Overall pattern size is 4.2 x 2.6 mm.

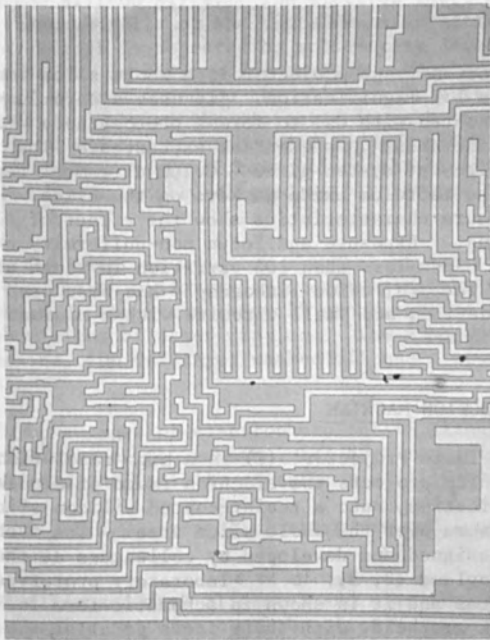


Figure 9: Detail of circuit shown in Figure 8

ELECTRON PROJECTION LITHOGRAPHY

C.E. Fuller, P.A. Gould and D.J. Vinton
Philips Research Laboratories,
Redhill, Surrey, England, RH1 5HA.

Abstract

The electron-image projector is a whole slice imaging system with a 1:1 magnification. It uses a chromium-on-silica mask coated with CsI to form a photocathode which can be used for about 40 sequential exposures. The automatic alignment system gives $\pm 0.1\mu\text{m}$ alignment repeatability at the tantalum oxide markers on the slice. The machine exposure characteristics show the effect of electron backscattering. Exposure and focus non-uniformity over a 2 inch slice cause less than 10% variation in width of a $1\mu\text{m}$ line. The projection lithography has been used to process I²L devices and small circuits with a minimum window size of $2\mu\text{m}$ square.

THE ELECTRON PROJECTION MACHINE

The 'Electron Image Projector' (1) is a high resolution pattern-copying machine which projects the electron image of a mask pattern, with unity magnification, onto a resist-coated silicon slice, to give simultaneous exposure over the whole slice area. The machine used in our work was designed and developed by colleagues at the Philips Laboratories in England (2, 3). It is a laboratory prototype machine, taking 2 inch slices and it is shown in schematic form in Figure 1. The slice and mask are held, with their faces parallel, about $1\frac{1}{2}$ cm apart in the imaging vacuum chamber.

The mask pattern is written in an electron beam pattern generator and etched into a layer of chromium covering a polished silica substrate. The mask is coated on the pattern side with a 80\AA layer of caesium iodide before starting the slice exposures.

During exposure, the mask is illuminated from behind by ultra violet light. The chromium pattern blocks off part of the CsI layer from the light so that electrons are emitted from the CsI photocathode area between the areas of chrome pattern. These electrons are accelerated towards the silicon slice by a 20kv potential and the electron image of the clear areas of the mask pattern is focussed onto the slice by a magnetic field to expose the resist layer.

Beam currents are a few μA per square centimetre of exposed area, and with PMMA resist, this means exposure times of about 1 minute.

The cycle time of our laboratory machine is about 3 minutes per slice exposure.

The machine has the facility for automatic alignment utilising X-rays generated by electrons which strike tantalum oxide marker patterns on the silicon slice. The electron image of the same marker pattern on the mask falls on the tantalum oxide pattern on the slice and the X-ray signal is detected by solid-state detectors behind the slice. The signal is maximum for perfect alignment and reduced if the mask image is misaligned on the slice. By suitably processing the detected signal and moving the projected image by auxiliary magnetic fields for the X and Y corrections and by mechanical rotation of the mask holder for the rotational correction, the electron pattern can be accurately and automatically aligned with reference to the slice markers.

The same CsI layer is used for a number of exposures. Figure 2 shows that the resist window width decreases slightly as a sequence of slices is exposed, and after about 35 exposures the resist pattern begins to show signs of deterioration. The mask can then be removed from the machine, the CsI layer washed off and a new layer deposited in the machine.

The main advantages of electron projection lithography are the relative simplicity of the machine, its high resolution, the short exposure time and the facility of automatic alignment.

For device and I.C. processing there are two important aspects to the lithography:

- (1) the slice and mask alignment and also the registration of the device patterns over the slice;
- and (2) the machine exposure characteristics.

MACHINE ALIGNMENT

The accuracy of the automatic alignment is illustrated in Figure 3. The diagrams show the measured registration on the slice of the exposed and developed marker pattern with the tantalum oxide pattern, for a group of 8 slices. The rotational error shown in the bottom diagram is equivalent to the rotational error at the edge of the slice. There are four points on each diagram for each slice. These are measurements for four alignments done at intervals over a period of 5 to 6 weeks to show the repeatability and stability of the alignment system. The measured repeatability of alignment is within about $\pm 0.1\mu\text{m}$ and some part of this is measurement error.

There is an off-set in the alignment: it is noticeable for the X-error where the offset is about $0.2\mu\text{m}$, this offset depends to some extent on the definition of the marker patterns on the slice and on the mask. This is not important. For slice processing, the important factor is the repeatability of the alignment on each slice, over a sequence of exposures. In general, for slice processing we expect machine alignments which are repeatable to within about $\pm 0.1\mu\text{m}$.

PATTERN REGISTRATION

In whole-slice imaging systems there can of course be run-out in the registration of successive patterns, away from the points of accurate alignment. This may be caused by changes in image or slice distortion, and run-out is a critical feature of whole slice imaging systems.

One potential source of pattern misregistration is bowing of the silicon slice during the slice fabrication process. During the exposure of a slice in the projection machine the slice itself is the anode of the electron imaging system. If the slice is bowed the electric field is distorted in the region close to the slice and this causes distortion of the imaged pattern on the slice. A change in slice bow between exposures will cause a misregistration of patterns away from the accurate alignment at the X-ray marker sites. This run-out is illustrated in Figure 4 which shows the misregistration that occurs on each chip site, over a column of chips, for two exposures of the same mask pattern, where the bow on the slice has been changed by $25\mu\text{m}$ by removing a stressed tantalum layer from the front of the slice between the two exposures. The misregistration varies from zero at the X, Y, alignment marker site, to about $2\mu\text{m}$ at the top edge of the slice.

THE ELECTROSTATIC CHUCK

One answer to this cause of misregistration is to hold the slice against a reference flat during each exposure. In the projection machine this can be done by using an electrostatic chuck, (3) here the slice is positioned against a dielectric layer about 1.0mm thick and the accelerating potential is applied between the slice and the metal backing of the dielectric. This gives a pressure of about $1/10$ atmosphere for a potential difference of 20kV .

Figure 5 shows the improved registration obtained over a slice using the chuck. It shows again the measured misregistration for two exposures of the same mask pattern. The bow of the unsupported slice has been changed between exposures by $38\mu\text{m}$. The misregistration varies over the slice up to a value of about $0.3\mu\text{m}$. This is not

entirely due to a failing in flattening the slice, but is mainly a secondary effect caused by the change of compression in the plane of the slice which gives a change in diameter of the slice of about $0.3\mu\text{m}$ over the 50mm slice. In principle, this effect can be automatically compensated by adjusting the magnification of the projected image during the alignment process. The electrostatic chuck is now being introduced into our laboratory device-processing work.

MACHINE CHARACTERISTICS

The machine exposure characteristics for line window widths down to $0.4\mu\text{m}$ are shown in Figure 6. Each curve shows the measured widths of line windows in developed resist patterns for different exposure levels in the projection machine, using PMMA resist.

The dotted line joins the points on the exposure curves where the line width in the developed resist is the same as the width on the mask. The line illustrates how the exposure level needed to give accurate reproduction of mask features varies with the feature dimensions. This effect is well-known and arises because of electrons which are back-scattered from the substrate and re-enter and expose the resist, beyond the area defined by the primary electron beam (4).

In the projection exposure of a mask which contains windows of different sizes, the backscattering accentuates the difference in size. This problem of window size distortion can be largely overcome by modifying the sizes of device windows at the design stage.

EXPOSURE UNIFORMITY

The uniformity of exposure, and of focus, for the machine is quite adequate over a 2 inch slice, for our device geometries. Figure 7 shows the measured uniformity of window size over a 50mm slice for a $1\mu\text{m}$ line window. Part of the non-uniformity arises from variations on the mask and these are shown separately on the upper diagram.

DEVICE AND CIRCUIT PROCESSING

The initial processing technology has been developed using I^2L device technology, using a minimum window size of $2\mu\text{m}$ square. As far as possible the projection lithography has been coupled with established processing techniques of wet-etching for defining the oxide patterns, and thermal diffusions for the impurity structure - the base to epilayer junction depth is $0.8\mu\text{m}$.

Figure 8 shows an 8-gate I^2L bistable circuit element processed

using the projection technology. Here the minimum design window size is the $2\mu\text{m}$ contact window to the surface collector regions. The measured oxide window size is $2.1\mu\text{m}$. This design incorporates allowances in the design geometry (a) for the window-size distortion due to back-scattered electrons, and (b) for the side-etching which occurs during the wet etch of the oxide windows (this latter allowance is $0.3\mu\text{m}$ per window edge). For example the $2\mu\text{m}$ collector contact window is $1.6\mu\text{m}$ on the mask. The aluminium-silicon interconnection has been defined by the familiar lift-off process. The design width of the metallisation leads is $4\mu\text{m}$.

The detail of the registration and the pattern lithography can be seen in the higher magnification optical photograph shown in Figure 9. This circuit is from a chip close to the alignment marks and so has minimum run-out misregistration due to image or slice distortion. Figure 10 shows the same circuit for a chip positioned at the edge of the 2 inch slice and shows that the present state of the projection technology is adequate to meet the $1.0\mu\text{m}$ tolerance of our $2\mu\text{m}$ window device geometries; even though, in this case, the electrostatic chuck was not used.

ELECTRICAL PERFORMANCE

The I^2L devices have low leakage and the electrical characteristics correspond to the calculated performance. Immediately after the metallisation has been completed, the gain of the vertical transistor is low, as shown in Figure 11 but the expected gain is obtained after a standard aluminium anneal treatment at 460°C .

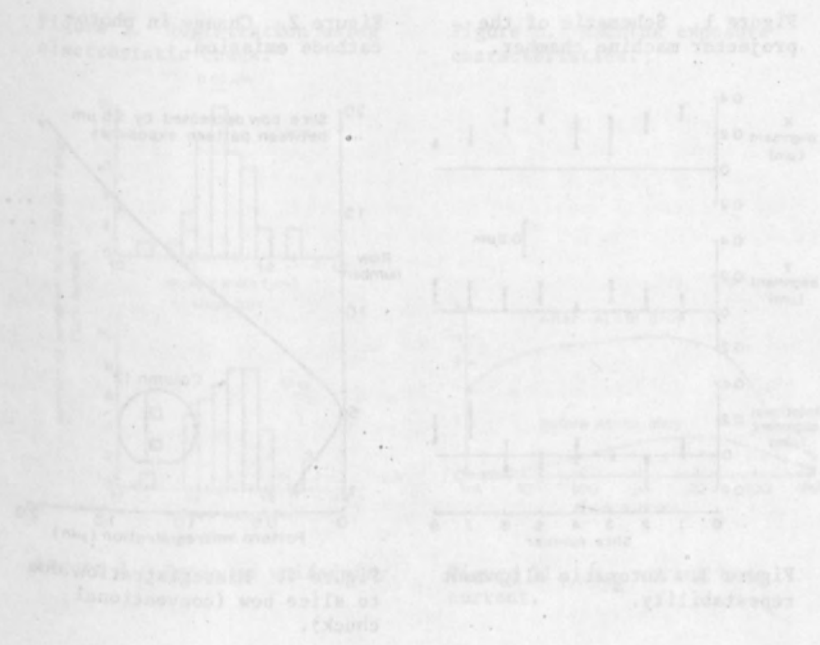
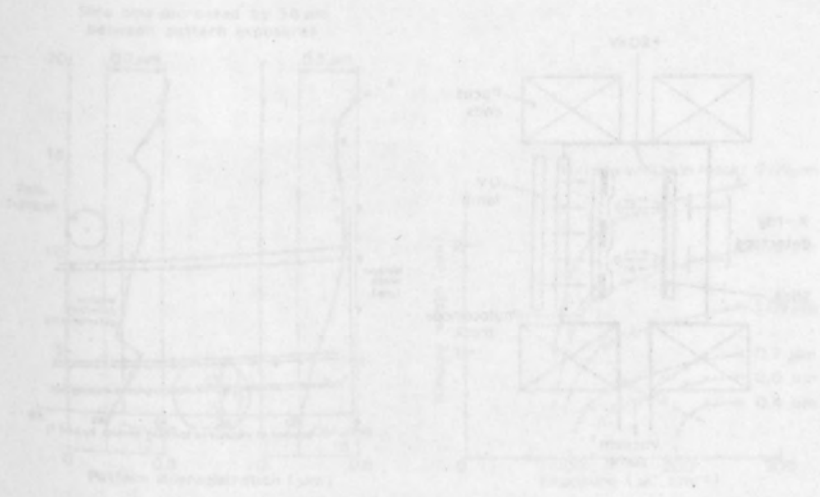
CONCLUSION

Our work on device processing, and the associated work on the detail of the machine exposure characteristics and the lithographic processes, show that electron projection replication offers the basis of a well controlled processing technology with the potential of further development to smaller device geometries.

REFERENCES

- (1) T.W. O'Keefe, J. Vine and R.M. Hardy, Solid State Electronics 12, 841 (1960).
- (2) J.P. Scott, IEEE Trans. Electron Devs., ED-22, 409 (1975).
- (3) J.P. Scott, Solid State Tech., 43 (May 1977).

(4) T.H.F. Chang, J. Vac. Sci. Tech., 12, 1271 (1975).



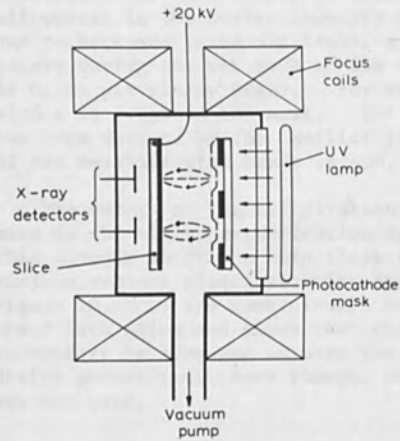


Figure 1. Schematic of the projector machine chamber.

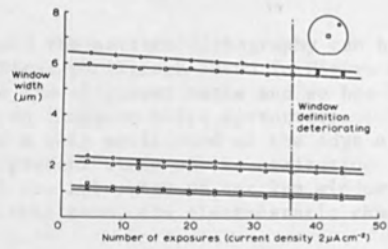


Figure 2. Change in photocathode emission.

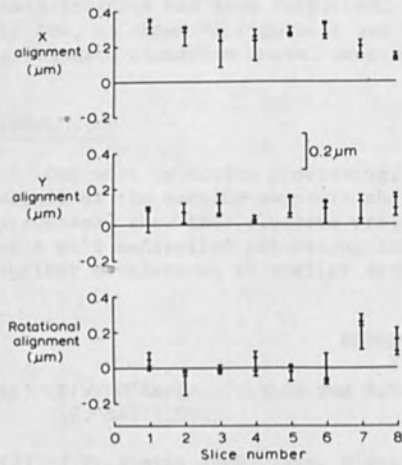


Figure 3. Automatic alignment repeatability.

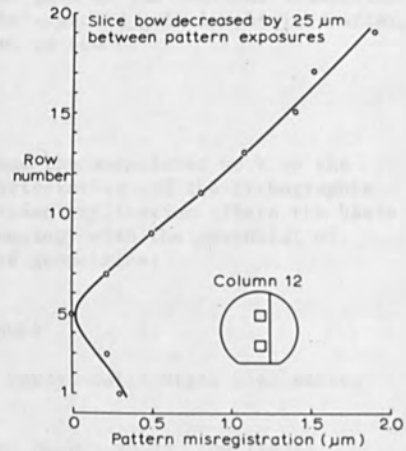


Figure 4. Misregistration due to slice bow (conventional chuck).

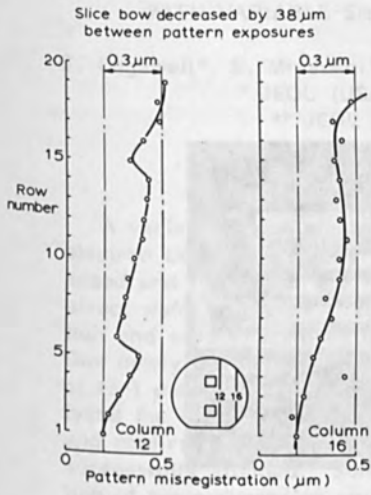


Figure 5. Registration using electrostatic chuck.

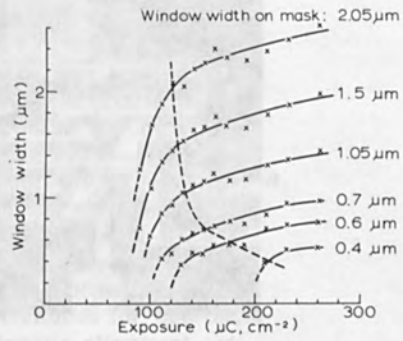


Figure 6. Machine exposure characteristics.

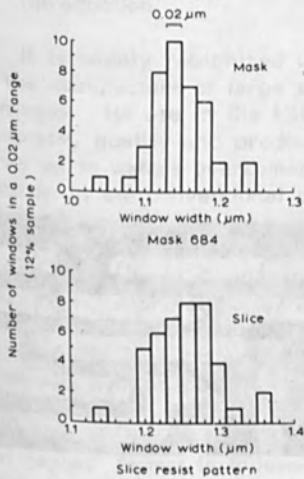


Figure 7. Exposure uniformity.

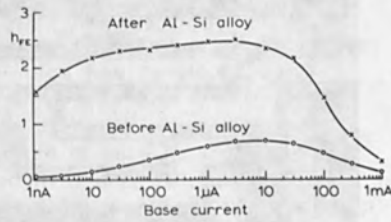


Figure 11. h_{FE} versus base current.

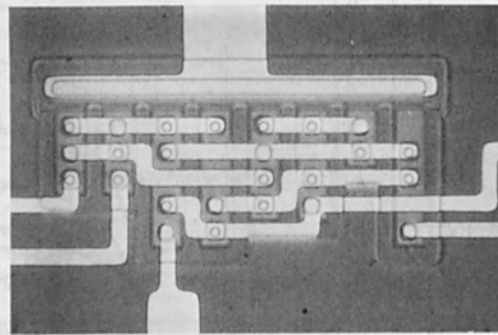


Figure 8. I²L bistable circuit element.

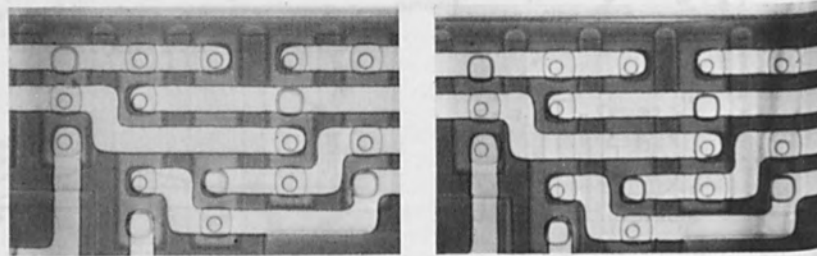


Figure 9. Enlargement of Figure 8 to show registration.

Figure 10. Similar sample to Figure 9 but from near slice edge.

ELECTRON LITHOGRAPHY SYSTEM
WITH VARIABLE-SHAPED ELECTRON BEAM

G. Cogswell*, S. Miyauchi**, K. Tanaka** and N. Goto**

* JEOL (USA) Inc., Boston

** JEOL LTD., Tokyo

Abstract

A variable-shape electron beam was applied to electron beam lithography in order to obtain high speed and high accuracy for IC mask making or direct wafer exposure. The basic system configuration and several features in performance are discussed. Our newly developed EB system has a dynamic range of 25-1 μm square beam in a 0.1 μm step. We analyzed the exposed test patterns and required time, and confirmed that the expected performance was successfully attained. Some techniques for determination of beam dimension and automatic alignment are also discussed.

1. Introduction

It is widely recognized that applying electron beam lithography to the manufacture of large scale integrated devices has many advantages. Its use in the LSI mask production is expected to improve accuracy, quality and productivity, and the direct exposure of patterns on to wafers overcomes the dimensional and procedural obstacles common in the conventional optic methods.

At the present time, two basic types of electron lithography systems have been developed to the level of commercial instrumentation. One, represented by EBES II which was developed by the Bell Telephone Laboratory, scans a small area with a beam unidirectionally in a raster pattern, with the work stage continuously displaced with respect to the beam so as to produce the desired pattern. A few firms have succeeded in commercializing instrumentation on the basis of this concept. In the second type, a "step and repeat" format is followed where the electron beam is randomly scanned over a small field, which is sequentially selected by moving the stage so as to stitch together the desired pattern. This type of system had been commercialized years ago, and recently, an im-

proved EB-50 system by the Nippon Telegraph & Telephone Corp. has proven to be capable of producing 128-K bit chips⁽²⁾. Another system of this category, the EL-1, developed by IBM, achieved a drastic improvement of the exposure efficiency by alternately shifting the position of 2.5mm square beam spot and giving "shot" illumination. At the 14th Symposium on Electron, Ion and Photon Beam Technology, 1977, yet another improvement through rendering the beam size variable was reported.

This report presents an electron lithography system, the JBX-6A, based on a variable-shaped beam exposure system devised by Dr. E. Goto of the Institute of Physical & Chemical Research (Tokyo) and an electron optic system developed by JEOL under the guidance of the VLSI Technology Research Association Cooperative Laboratory (Tokyo). Maximum beam size is 25 μm , and any polygonal pattern with minimum line width 1 μm can be exposed. The maximum cycle of beam "spot" is about 6×10^4 shots/sec. Exposure time for a 4" wafer or mask of normal pattern density is approximately 25 minutes.

2. Electron Optics

Fig. 1 shows a ray diagram for the electron optics of JBX-6A. A 125 μm square aperture (#1) situated below the illumination lens is uniformly illuminated with the beam. A unity-magnification image of the aperture #1 is formed on a second aperture (#2) by the shaping lens. When the beam is deflected by the shaping deflector, the image of aperture #1 is displaced from the aperture #2, and the overlapped area alone is imaged on the work piece through the demagnifying and projection lenses. Hence, the beam cross-section can be turned into a rectangle of any side length by controlling the voltage applied to the shaping deflector. The reduction ratio of aperture image on the work piece is 1/5, and the side of rectangular beam can be varied from zero to 25 μm . In the JBX-6A, the shaping deflector is controlled by an 8-bit D-A converter so as to allow setting dimensions in 0.1- μm steps. Accelerating voltage is fixed at 20 KV so as to secure high accuracy and stability. An image of the electron source is formed on the principal plane of the shaping deflector by the illumination lens, and furthermore, an enlarged image is formed at the center of the projection lens by the action of the shaping and demagnifying lenses. Such an arrangement assures that the current distribution of rectangular beam is not affected by changes in the shaping deflector voltage. The blanking electrode is a device to cut off the beam by shifting the magnified image of the electron source at the center of projection

lens by a few millimeters. Since the diameter of the magnified image is about 400 μm , the beam is effectively cut off by a slit placed in the vicinity of lens center. The rise up/down line of beam is 50 ns. The electron source is required to be characterized not only by high intensity and stability but also by uniform distribution of beam radiation angles. In the JBX-6A, this is realized by establishing a larger emission area and using a cathode lens of shorter focal length in the electron gun.

The sharpness of current distribution at the edge of rectangular beam is an important factor directly affecting the resolution of exposure pattern. As has been reported by several authors⁽⁵⁾, the larger the current is, the more markedly the sharpness is reduced by the "space charge" effect. The latter effect is attributable to change in electron beam energy and shift of trajectory induced by the Coulomb interaction between electrons, and different from the third-order aberration of the electron optic lens. This effect can be reduced by taking into consideration the electron travel distance and the electron density in the path in designing the electron optics. The maximum current density in the JBX-6A is 0.1 A/cm², and 1- μm wide exposures can be obtained on PMMA resist when limiting the maximum rectangle area to 100 μm^2 .

The beam position is controlled by use of an electrostatic deflector of post-lens type located below the projection lens. The stray capacitance of this deflector is 20 pF or so, allowing to provide high speed scanning with negligible hysteresis. Scanning field is 2 x 2 mm, and the intrinsic scan distortion is within 0.3 $\mu\text{m}_{\text{p-p}}$. The scan rotation deviation in the X-Y direction and the scan distortion can be automatically eliminated by the method described below. No variation of resolution within the scan field could be detected. The beam position is controlled by two D-A converters, 16-bit and 12-bit, with minimum steps of 0.05 μm . The electron optics column in JBX-6A contains, besides those components illustrated in Fig. 1, an image rotating lens to set the rectangular beam with respect to the laser reference axis, an alignment coil and a stigmator.

3. System Configuration

A constructional diagram is shown in Fig. 3. At the right, the main body with the electron optics column on the exposure chamber is seen. The work-piece stage can carry a plate or wafer up to 5 inches, and the exposure area is 110 x 120 mm. The

stage is provided with a beam size measuring device and a standard pattern. Above the work-piece, there are a reflected electron detector for auto-pattern registration and a secondary electron scintillator for beam monitor. Pattern data is supplied from a mini-computer, a magnetic tape unit, a magnetic disc memory or a high speed data controller shown at the left, and delivered to the electron optics and the stage controller through a data decoder. Fig. 4 shows an overall view of JBX-6A.

It is particularly important in JBX-6A to control the size and position of the rectangular beam, and to check current density distribution and focusing. The construction and function of the beam measuring device are shown in Fig. 5. A PN-junction for current amplification is provided below crossed tungsten wires slightly thicker than the maximum dimension of beam. The obtained signal is sent to the display monitor and the CPU through a processor which consists of an amplifier, differential circuits, peak detector and digital logic circuits. Examples of actual signal waveform are shown in Fig. 6. All the necessary information, that is, beam dimensions, beam current distribution, focusing, beam orientation, sensitivity of positioning deflector, scan direction deviation and scan distortion are available through this monitor system combined with the laser measurement. In the JBX-6A, the measurement, adjustment and setting of correction factor are incorporated in the maintenance program (MNTE) so that they can be executed automatically before starting exposure or whenever necessary in the course of exposure.

The data processing for pattern exposure and exposure procedures with the JBX-6A are shown in Fig. 7. The data processing, which involves dividing the input data in to beam dimensions and sorting, is covered by an OFF-LINE program (CONV). As the input data, either general PG 3000 FORMAT (DAVID MANN) or PLOTTER FORMAT joining coordinates for corners of polygonal contour is accepted. Dividing process is conducted in three steps; whole data in to 2 x 2 mm scan fields, a scan field into 400 subfields (100 μm), and a subfield into beam spots (maximum side length 25 μm). For instance, in case of using PG 3000 FORMAT, the number of patterns can be approximately doubled by the dividing process. Sorting consists of rearranging shots in the order of increasing length and disposing subfields so as to make zigzag scan within the 2 x 2 mm field. Moreover, 2 x 2 mm fields are laid so that one chip can be exposed as the stage is displaced by 2 mm step. For patterns in a subfield, identical distortion correcting factor is provided by the distortion corrector. The beam position

within a subfield is controlled by a high speed 12-bit D-A converter. The position of subfield within a field is controlled by a 16-bit D-A converter. The data processed by (CONV) are stored in the magnetic disc memory.

The exposure sequence is executed by an ON-LINE program (EXPC). A rectangle in a subfield is realized by alternately repeating to set beam size and position and to give beam shot, while a trapezoid or triangle is exposed by changing the length of major side of rectangular beam in synchronization with the intrafield scanning under the control by the hardware included in the data decoder.

One of the features of the JBX-6A is that the beam dose for each pattern can be varied by shot time modulation or changing trapezoid scan speed. It is very important in a pattern smaller than $2\ \mu\text{m}$ to eliminate dimensional error in small-sized pattern, known as the proximity effect (6). In JBX-6A, this can be fully executed by the dose control. The dose (shot time) modulation factor can be set for each divided pattern, and the decoded signal is sent from the data decoder to the blanking circuit. The program (EXPC) executes the control not only for the intrafield pattern exposure but also for stage movement and for sequential delivery of buffer memory data from the disc. Another important role of (EXPC) is the control of direct exposure of wafers. During direct exposure, the wafer is set in to a holder with a jig, but a small rotational error is inevitable. In case of large-sized wafers, the surface may be badly warped, causing dimensional changes in the exposure pattern. For this reason, the registration marks previously set on the wafer by use of (EXPC) are scanned by the beam immediately before executing the exposure and changes in reflected electron dose are monitored to control the beam positioning with respect to the wafer. For optimum results, marks are set for each field or each chip. Hence, it is possible to eliminate automatically all the errors in the exposure dimension due to warping of wafer and those in the pattern orientation due to rotational deviation. These techniques have already been established by JEOL in such models as JBX-2B and JBX-5A (7). Besides, errors due to incomplete marking or dust can be compensated by program processing, providing highly reliable results. Exposure time consists of stage moving time, shot time, registering time (for wafer only) and time taken by work-piece exchange and automatic beam set-up. When the sensitivity of resist is $10^{-6}\ \text{C}/\text{cm}^2$, the shot time is $10\ \mu\text{s}/\text{shot}$, and with pattern density $200,000\ \text{patterns}/\text{cm}^2$ and exposure area $80 \times 80\ \text{mm}$, the exposure time is about 25 minutes. The speed

of data transfer from the magnetic disk (2 units, 9M Byte each) included in the standard equipment of JBX-6A to the buffer memory (2 sets) is maximum 180 K words/sec. since a rectangular pattern uses 3 words, the exposure rate is 60,000 patterns/sec or so, which is balanced with the shot speed of the electron optics.

4. Basic Performance and Exposure Results

The basic performance of the JBX-6A will be presented by use of a few photographs. Fig. 8 shows a test pattern with a 2 mm field stitched on a ladder pattern. Fig. 9 shows exposure of 1 μm line by use of a beam of 1 μm width and length varying from 1 to 25 μm . The radius of curvature at the tip corner is 0.2 μm or so, providing adequate resolution. Figs. 10 and 11 show parts of test patterns consisting of various-shaped rectangles. In Fig. 11, 1 and 2 are exposed with 2 x 2 μm beam at same shot time 200 μs , emphasizing the importance of the proximity effect. Fig. 12 shows a slanting line exposed in the same way as shown in Fig. 7, and the edge of slanting side is smooth. Fig. 13 shows an example of IC pattern exposure, in which the minimum line width is 2 μm . Fig. 14 shows a test pattern for checking the stitching accuracy at the boundary between 2 mm fields. At the corner joining four fields, 2 μm wide lines are combined at 0.2 μm or better accuracy.

5. Conclusion

It was demonstrated that the JBX-6A system using a variable-shaped electron beam could expose pattern of minimum dimensions 1 μm with practical exposing efficiency for mask exposure and direct exposure of wafer. This system has excellent resolution which characterizes electron beam lithography, allowing realization of exposures of 1 μm or finer patterns. Moreover, it is expected that the exposure time for 4" wafer is shortened by 10 to 20 minutes, so as to meet the requirements for high speed exposure of high density pattern in the future VLSI field.

The authors are grateful to those who cooperated in developing the present system; Mr. S. Takayanagi and Mr. T. Yuasa for the system design, Dr. T. Someya and Mr. M. Isobe for the electron optics, Mr. M. Takeuchi for the program and CPU control, and Mr. H. Okugi, Mr. U. Ohashi and Mr. T. Suzuki for the design.

REFERENCES

1. Herriott, D.R., Collier, R.J., Alles O.S., Stafford, J.W.: EBES, A Practical Electron Lithographic System, IEEE Trans. on Electron Devices, Vol. ED-22, No. 7, p385 (1975).
2. Private report.
3. Yourke, H.S., Weber, E.V.: High Through-put Scanning Electron Beam Lithography System EL-1, IEDM Tech. Digest, p431 (1976).
4. Goto, E., Soma, T., Idesawa, M.: A Design of Variable Aperture Projection and Scanning System for Electron Beam, 14th Symp. on Electron, Ion and Photon Beam Technol. (Palo Alto, 1977).
5. Pfeiffer, H.C.: Basic Limitations of Probe Forming System due to Electron - Electron Interaction, Proc. of 5th SEM Symp. p113 (1972).
6. Chan, T.H.P.: Proximity Effect in Electron-Beam Lithography J. of Vacuum Sci. & Technol. Vol. 12, No. 6, p1271 (1975).
7. Miyauchi, S., Tanaka, T., Russ, J.C.: Automatic Positioning of Scanning Electron Beam Exposure, IEEE Trans. on Electron Devices, Vol. ED-17, No. 6, p450 (1970).

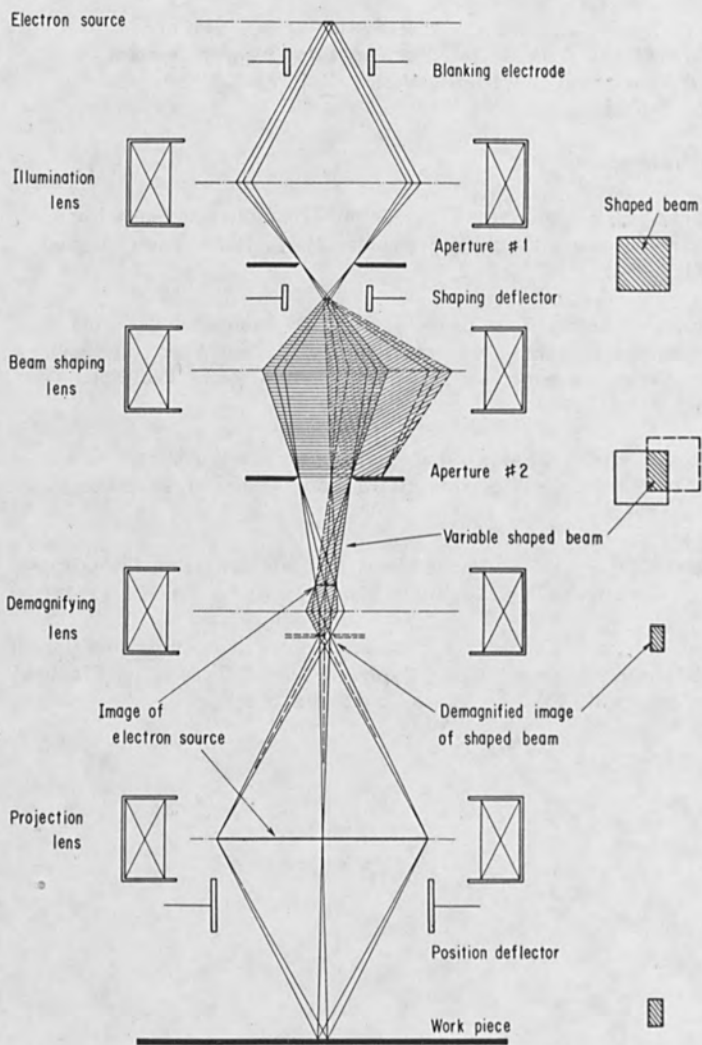


Figure 1

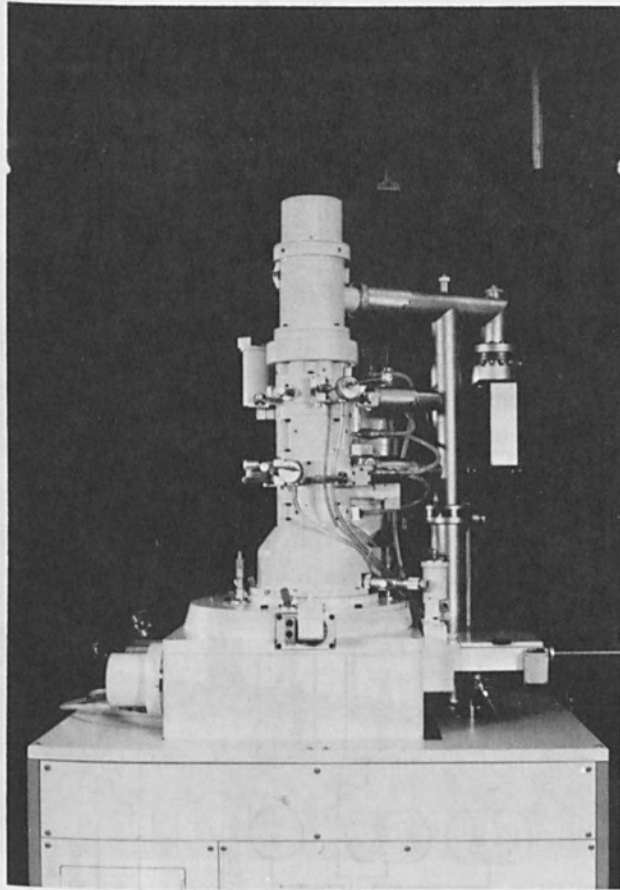


Figure 2

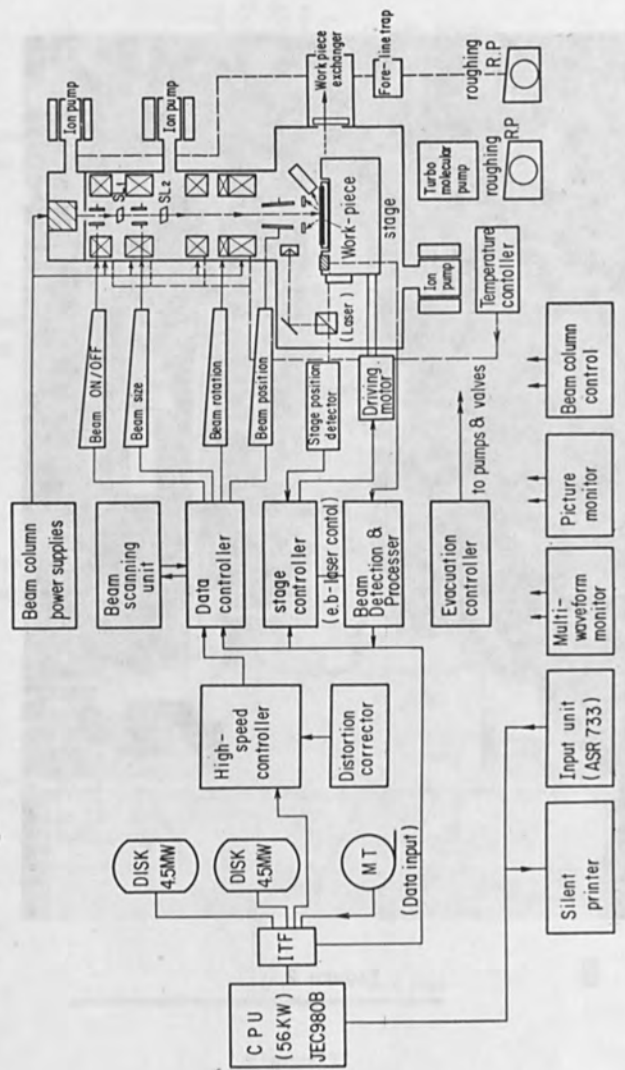


Figure 3

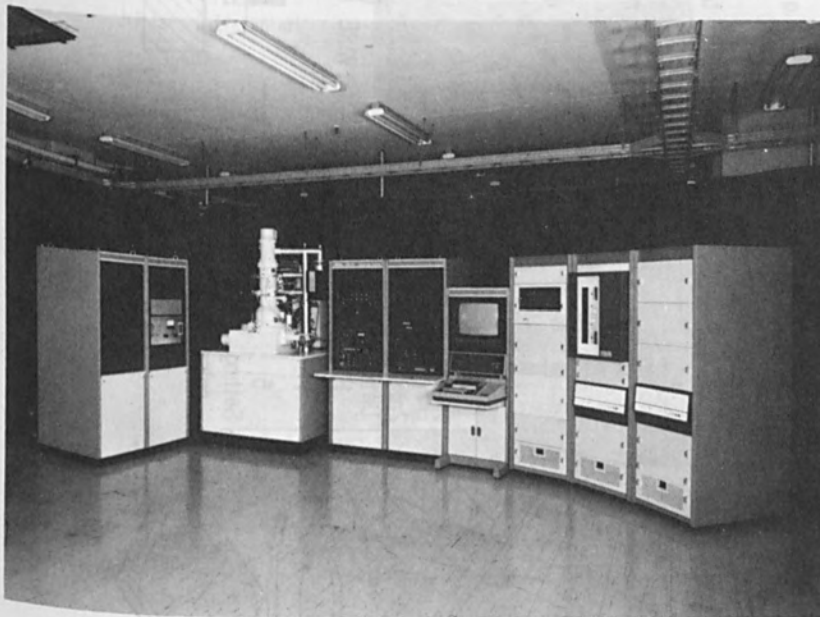
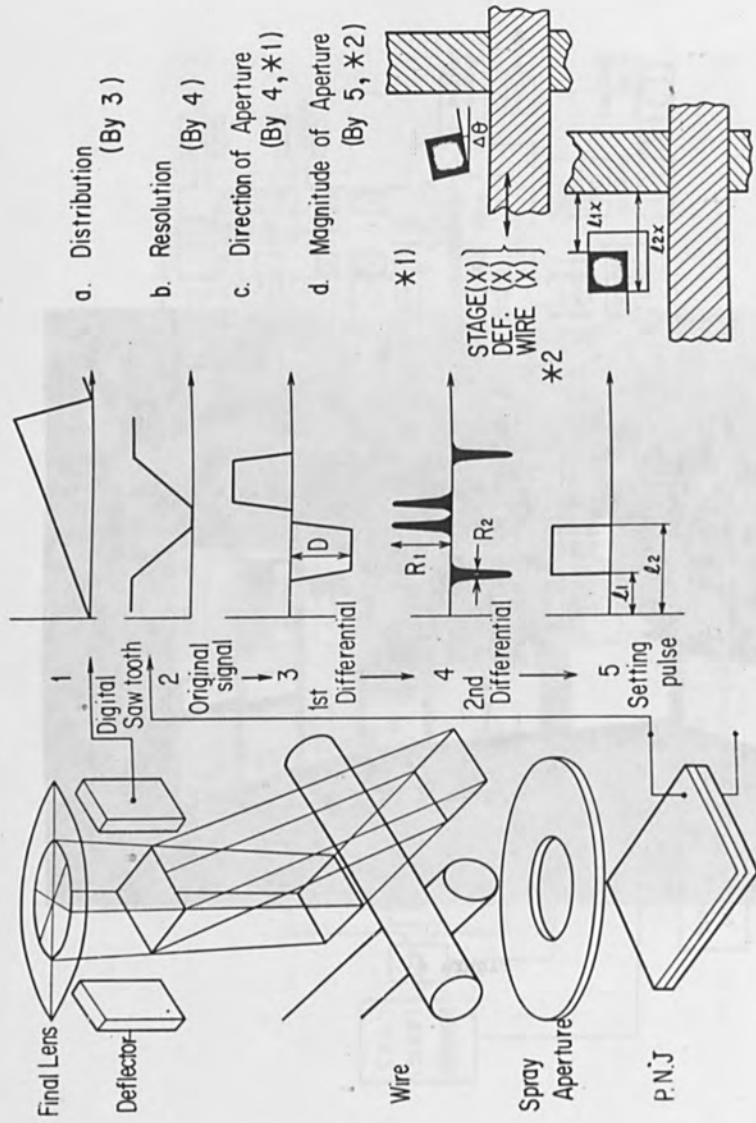


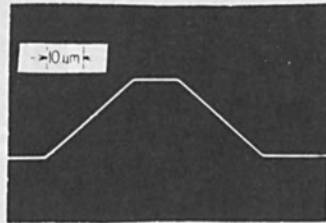
Figure 4



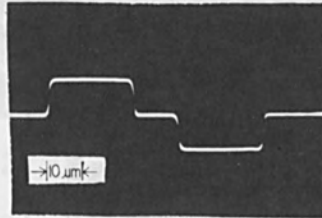
- a. Distribution (By 3)
- b. Resolution (By 4)
- c. Direction of Aperture (By 4, *1)
- d. Magnitude of Aperture (By 5, *2)

Figure 5

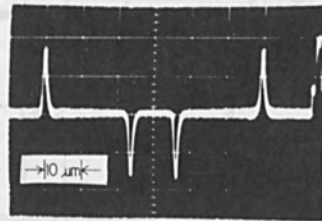
A.
a) Original Signal
(P N J out)



b) 1st. Differential
Signal.



c) 2nd Differential
Signal.



B.
Enlarged signal
of 2nd Differential

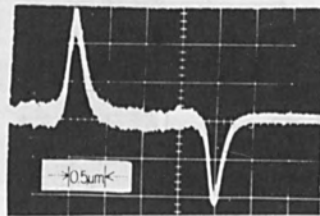


Figure 6

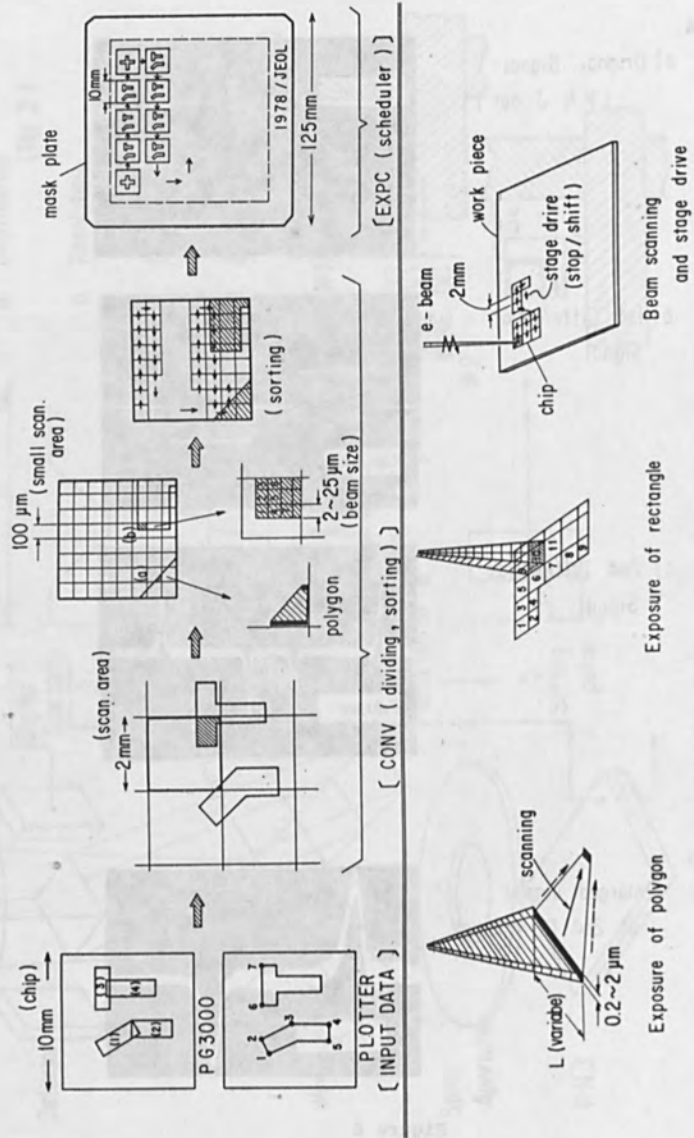


Figure 7

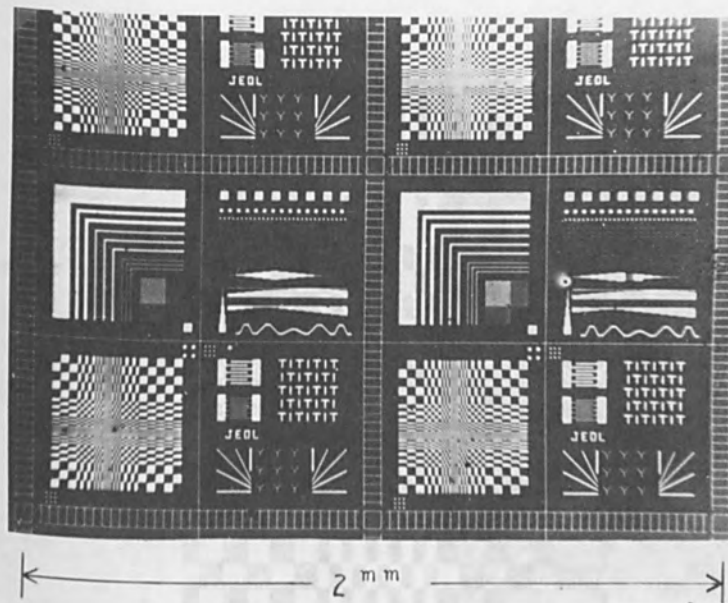


Figure 8

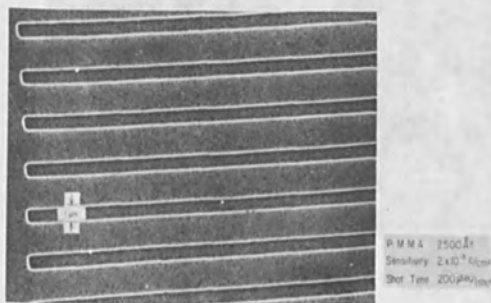


Figure 9

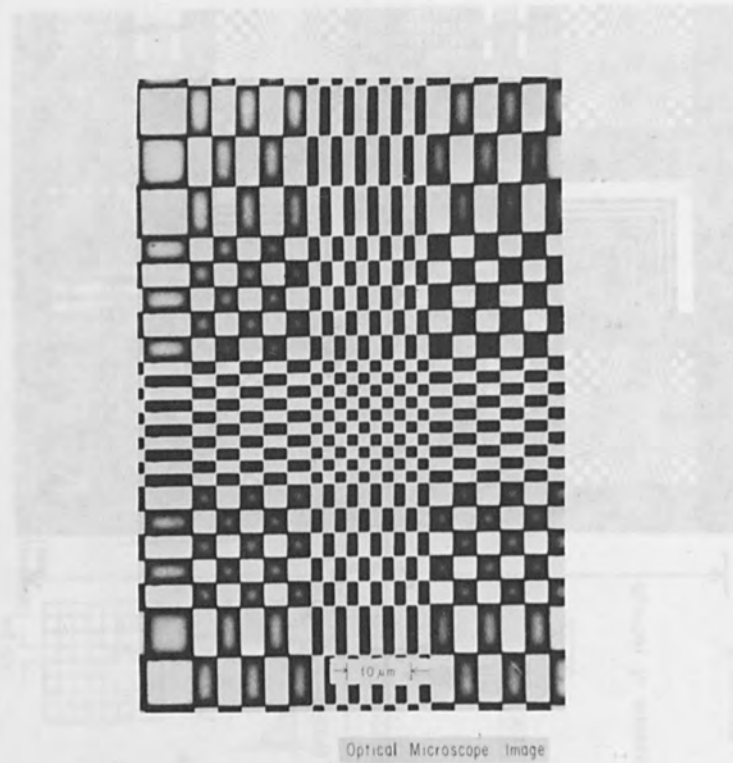


Figure 10

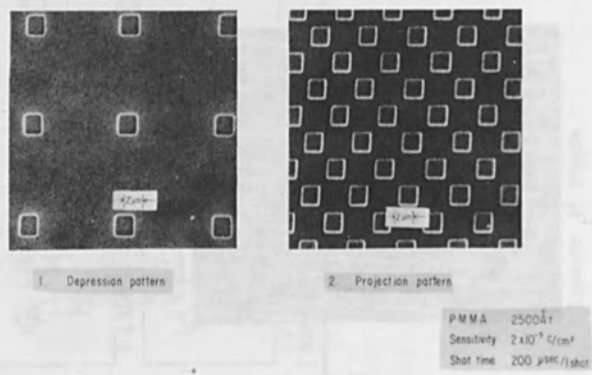


Figure 11

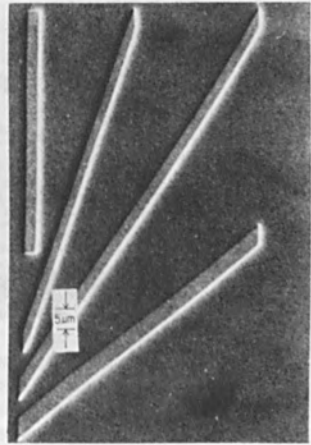
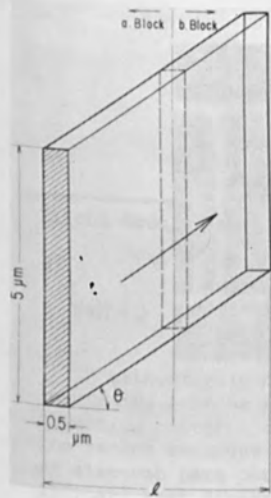
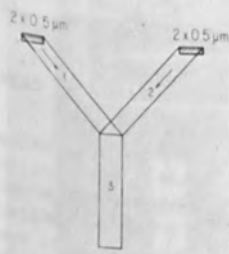


Figure 12



Exposure Method

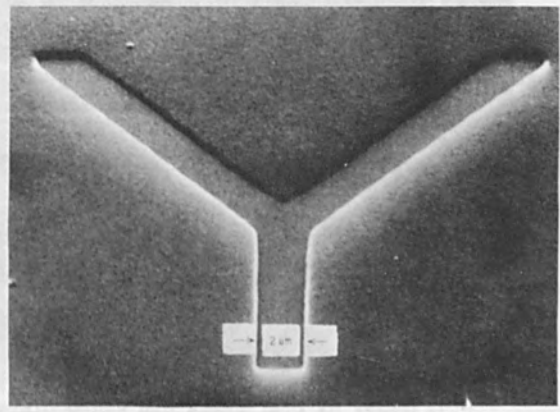
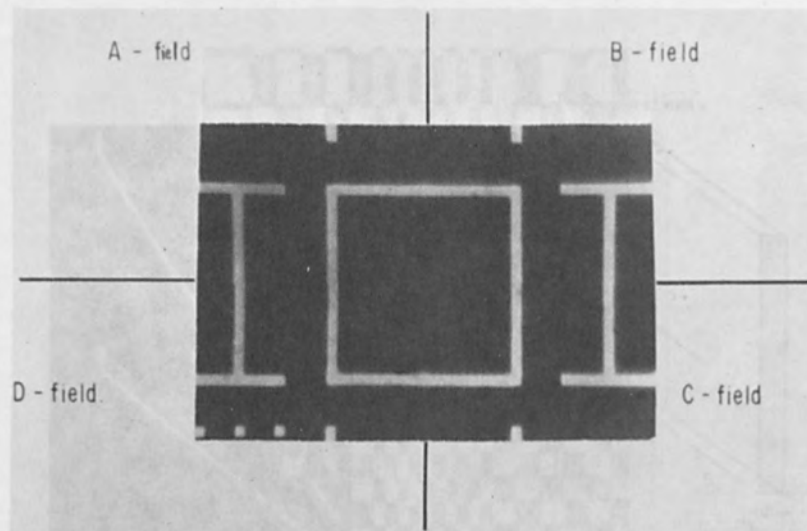


Figure 13



Enlarged SEM image

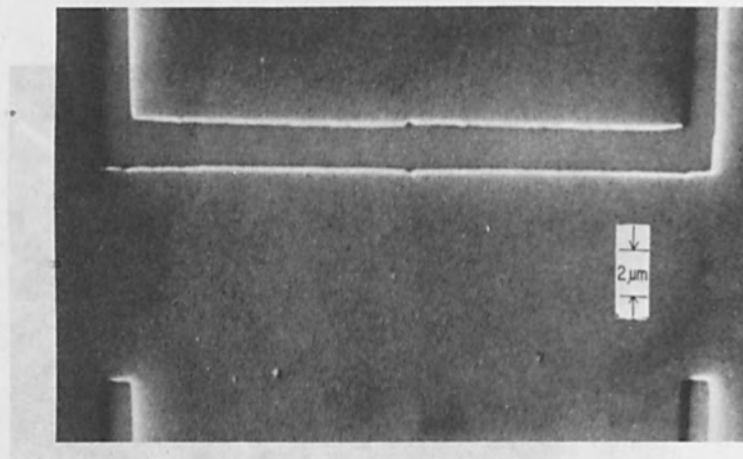


Figure 14

DESIGN OF VARIABLE SHAPED BEAM SYSTEMS

Eiichi Goto, Takashi Soma, Masanori Idesawa and Tateaki Sasaki

The Institute of Physical and Chemical Research
Wako-shi, Saitama 351 Japan

Lithographic methods and direct electron beam pattern generation schemes to be used for advanced LSI fabrication requiring patterns of sub-optical resolution are reviewed. The recent advances in electron optics pertinent to the design of electron beam pattern generators are described, which indicate that direct generation of patterns with 0.1 μm resolution at the speed of $1 \text{ cm}^2/\text{sec}$ would be feasible by using the variable shaped beam scheme.

§1. Introduction

Electron beam pattern generation is indispensable for drawing VLSI patterns with sub-optical and sub-micron dimensions.

The development of practical electron beam pattern generation schemes is reviewed in Section 2. The recent advances in electron optics, i.e., the theoretical foundation of the image-forming processes of electron beams, are reviewed in Section 3 and their implications to the practical systems are discussed in Section 4. Fly's eye optics which may find some use in the future, are discussed in Section 5.

§2. Electron Beam Pattern Generation Schemes

Fig. 1 shows three practical electron beam pattern generation schemes, and their developments are summarized in table 1.

In Fig. 1, "Spot Scanning" means that an electron beam, with a small circular cross-section (spot), typically of 0.1 micron in diameter, is deflected electrically (by applying magnetic deflection field or electrostatic deflection field or both) and the pattern is generated by scanning the beam across the area to be exposed to the beam. In other words, the pattern is generated similarly to the pictures on a television screen, except for much increased resolution. So far as scanning and the resolution are concerned, this scheme is similar to SEM (Scanning Electron Microscope). Actually, SEM's with slight modifications were used in the first models of pattern-generating machines. For example, the first Japanese pattern-generating machine JBX-2A was developed concurrently with the first SEM, JSM-1. Using this spot scanning machine (JBX-2A), Tarui and his collaborators successfully made MOS transistors purely with electron beam pattern generation without using any masks at all in 1968 [L1].

EBES2 and VL-1 (entries 4 and 5, table 1) are also "spot scanning" machines. In EBES2 the electron beam is deflected electrically only in one direction (deflection width 0.128 ~ 0.256 mm) and the target is scanned mechanically in the other direction so as to scan and generate two dimensional patterns. In VL-1 the electron beam is deflected two dimensionally within a square scanning area of 5 mm x 5 mm.

Referring to Fig. 1, "Fixed Shaped Beam" means that the cross-section of the electron beam at the target has a fixed shape, typically a square of 2.5 μm by 2.5 μm . This is achieved by projecting the image of a mask with a square hole on it to the target. The pattern is generated by scanning and/or patching the area to be exposed to the beam. EL-1 is a "fixed shaped beam" machine.

In Fig. 1, "Variable Shaped Beam" means that the shape of the cross-section of the beam at the target is variable, typically a rectangle x by y μm with x and y being varied from 0.1 to 25 μm . This is achieved, for example, by using two masks each having a square hole. The image of the first mask is projected on the second mask and the image of the second mask is further projected on the target. The combined action of the two masks are varied by the beam-shaping deflector placed between the two masks, and the shaped beam is directed to a selected position on the target by means of beam-positioning deflector placed between the second mask and the target. The "variable shaped beam" concept was first reported at the May 1977 EIPBT (Electron, Ion and Photon Beam Technology) Symposium independently by the present authors' group and by three other groups. (entries 6, 7, 8, and 9, table 1).

The authors' variable shaped beam scheme has been implemented by JEOL in their JBX-6A machine. The engineering features and practical lithographic results of JBX-6A are reported at this conference by G. Cogswell et al of JEOL. [L16].

Entry 10 in table 1 shows the result of the design and feasibility studies made by the authors' group on the variable shaped beam scheme.

Before making comparison and evaluation of the various pattern generation schemes we shall review the recent advances in electron optics.

§3. Advances in Electron Optics

The studies on the image-forming processes of electron beams are called electron optics. Similarly to glass (light) optics, the deviations in the actual image from the ideal image are called geometrical aberrations.

The term "geometrical" means that the wave nature of the beam is being neglected. Since the wave nature or quantum mechanical effects can be neglected in the schemes shown in table 1, we shall drop the term "geometrical" hereinafter for simplicity. The aberration theory of the pure (deflection-less) image-forming process of electron beams is well established and we can learn the results from definitive text books on the subject, such as those authored by Glaser [E1] and El-Kareh [E2].

However, when electrical deflection of the beam enters, the theories developed up to the 1960's are all incomplete in that the focusing field and the deflection field are spacially separated. A unified treatment of spacially superimposed focusing and deflecting fields are needed for the full development of the aberration theory and this has been accomplished only very recently.

Electron optics is a rather specialized art full of jargon, of lengthy mathematical formulas and odd terminologies for non-specialists. The authors will try their best to review the advance without using the jargon. Nevertheless, for the sake of clarity, we shall need the definitions, at least, of some quantities.

Figure 2 shows the definitions of three optical parameters α , β and γ . We assume that there is a final electron lens (the objective lens) which projects the beam on the target. The shape of the beam on the target is called the image. The distance (specifically called the working distance in pattern-generating machines) from the objective lens to the target is denoted by L .

The parameter $\alpha = F/2 = a/L$, with a being the aperture radius of the lens, is the half aperture angle at the image. The brightness of an optical lens (say of a camera) is usually measured by using an index F called the F-number. Hence, $\alpha = F/2$ means that α is the index representing the brightness of the electron lens.

The parameter $\beta = b/L$, with b being the size of the image, is an index representing the size of the electronic image relative to the (working) distance L .

The parameter $\gamma = c/L$, with c being the amount (or the length) of deflection on the target, is an index representing the amount of deflection relative to L .

The ratio $\Delta V/V$, with V being the acceleration voltage of the electron, represents the relative spread in electron energy, which may be caused by thermal effects on the cathode, variations in the accelerating voltage itself as well as by the Boersch effect to be discussed later.

The aberration theory has to do with expressing the quantity $\delta w = \delta(x + iy)$, the deviation of the actual beam point incident on the target from the ideal point, as a function of α , β , γ and $\Delta V/V$.

This function is usually expanded into a Taylor series, and each term is given a specific name. For example, the terms including the energy spread index ($\Delta V/V$) are called chromatic aberrations.

The recent advances in the aberration theory and results in the design of electron optical systems which reduced aberrations are summarized in Table 2.

Field	Content(Aberration=Ab.)	Year	Author(s)	References
F* D*				
1 M M	$\exists f, f(\alpha, 0, \gamma) = g(\alpha)$	Ab. Elimination	1971 Ohiwa, Goto, Ono	[E4]
2 M M	$\min f(\alpha, 0, \gamma) $	Ab. Reduction	1973 Owen, Nixon	[E5]
3 M M	$f(\alpha, 0, \gamma, \Delta V/V)$	Ab. Formula	1974 Munro	[E6]
4 M M	$\min f(\alpha, 0, \gamma, \Delta V/V) $	Ab. Reduction	1975 Munro	[E7]
5 M M	$\min f(\alpha, 0, \gamma, \Delta V/V) $	Ab. Reduction	1975 Pfeiffer	[E8]
6 M M	$\exists f, f(\alpha, \beta, \gamma, \Delta V/V) = g(\alpha, \beta, 0, \Delta V/V)$		1977 Goto, Soma	[E9]
7 M M	$\min f(\alpha, \beta, \gamma, \Delta V/V) $	Ab. Reduction	1977 Goto, Soma, Idesawa	[L9]
8 ME ME	$f(\alpha, \beta, \gamma, \Delta V/V)$	Ab. Formula	1977 Soma	[E11]
9 M E	$\min f(\alpha, \beta, \gamma, \Delta V/V) $	Ab. Reduction	197x Soma	[to be published]

F*:Focusing Field, D*:Deflection Field.

M:Magnetic, E:Electro-Static, ME:Combined Magnetic and Electro-Static.

Table 2. Advances in Electron Optics of Deflection Systems.

First, note that the deflection-less ($\gamma = 0$) pure image-forming case has to do with the special case $\delta w = f(\alpha, \beta, 0, \Delta V/V)$, and that for "spot scanning" the point image ($\beta = 0$) function $f(\alpha, 0, \gamma, \Delta V/V)$ would be sufficient but the full function $f(\alpha, \beta, \gamma, \Delta V/V)$ would be needed for "fixed- and variable-shaped" beam schemes.

Ohiwa, Goto and Ono (#1 in Table 2) introduced a MOL (Moving Objective Lens) concept and showed that there exists a system for point image ($\beta = 0$) free of all deflection-induced aberrations, i.e., $f(\alpha, 0, \gamma, 0) = g(\alpha)$. Chromatic aberrations, however, were not included ($\Delta V/V = 0$, was assumed).

Munro (#3) derived the formula for point image case ($\beta = 0$) with chromatic aberrations.

Goto and Soma (#6) derived the formula for the finite image case ($\beta \neq 0$) and also theoretically proved the existence of systems free of all deflection-induced aberrations by making use of the MOL concept.

Soma (#7) derived the most general formula valid for any combination of magnetic and electro-static fields and for electrons running at relativistic speeds. The formula is some 80 pages long and the computerized formula manipulation system REDUCE² [E12] was utilized for the derivation. It is extremely difficult to handle such a long formula without a computer formula manipulation system.

The other entries in table 2 with "min" (for minimization) gave practical results in reducing various aberrations (there are some 20 aberrations.)

We want to emphasize that, in all the aberration reduction calculations made by the authors' group (entries 1, 6, 7, 8 and 9 in table 2), we also required the beam to land vertically on the target. As a result of these studies, all aberrations except for two have been found to be either eliminable or negligibly small in practice. The two are the spherical aberration δ_w_s and the axial chromatic aberration δ_w_a , which have the following forms:

$$\delta_w_s = S\alpha^3, \delta_w_a = A\alpha \cdot \Delta V/V$$

where S and A are the aberration constants. Note that these aberrations exist even in the deflection-less point image case ($\beta = \gamma = 0$), i.e., $f(\alpha, 0, 0, \Delta V/V) = S\alpha^3 + A\alpha(\Delta V/V)$. In spite of a great number of efforts trying to eliminate the spherical aberration, no practicable scheme has been found yet. [E3]

§4. Limits on Current Density and Exposure Speed

Besides geometrical aberrations there is another factor, not having its counter part in light optics, which causes broadening in the shape of electron beams. That is the electron-electron interaction: When the intensity of an electron beam is increased beyond a certain limit the electrons would start to repel each other and collide with others thereby broadening the shape of the beam. The theory of such broadening is not in a fully satisfactory form [B2] at present.

Among others the Boersch effect, named after the first observer of the effect [B1], is a controversial issue. Some experimentalists have even questioned the very existence of the effect itself [B5, B6]. Boersch and some others [B6] observed broadening in electron energy ($\Delta V/V$) which is much larger than the thermal fluctuations to be expected from the cathode temperature, when electrons are passed through a spacial region of high electron density. The Boersch effect would imply an increase of chromatic aberrations. In addition to the Boersch effect, the space charge causes the displacement of electron trajectories. By regarding the electron beam as a continuous and charged fluid, the displacement caused by the average (averaged over all electron trajectories) space charge effect can be easily derived, yielding the following to be called the space charge broadening formula:

$$\delta w_{sc} = KIL/(Vva), \text{ (in CGS units),}$$

where α is the half aperture angle, V the accelerating voltage and L is the path length of the electron. Further, I is the total beam current (not the current density per unit area), v is the electron speed ($v = \sqrt{2eV/m}$), and K is a number of the order of unity, which does not depend critically upon the image size β nor on other

detailed structure of the system.

Besides the average space charge effect, there exists stochastic broadening in electron beam shapes caused by the corpuscular nature of electrons.

There is no satisfactory theory for such broadening yet. Thus, computer simulation of a large number (10V or more) of an electron trajectories (called the Monte Carlo method by some authors) is the only practical method at present.

One of the authors (T. Sasaki) made such simulation studies and his results (to be submitted to Optik for publication) indicate the following: a) The broadening can be decomposed into two parts, the average part which can be compensated by refocusing and the stochastic part which cannot be. (Stickel and Pfeifer gave similar results [L15]. b) The order of magnitude of the both parts is the same as that given by the space charge formula δw_{sc} with $K = 1$.

Thus, we may well use it as a "rule of thumb."

The experiments performed on JBX-6A (table 1) indicate that axial chromatic aberration and chromatic aberrations due to the Boersch effect could hardly affect the projected 0.1 micron resolution and that the observed broadening of the image agrees reasonably well with the space charge formula δw_{sc} . Thus, the spherical aberration δw_s and the space charge broadening δw_{sc} are concluded to be the major limitations imposed on the resolution and on the beam current.

The space charge broadening $\delta w_{sc} = KIL/(Vv\alpha)$ would be reduced by increasing α , the brightness of the objective lens, but this would increase the spherical aberration $\delta w_s = S\alpha^3$. Hence, there is an optimum value of α as a result of compromise. The lithographic process requires the acceleration voltage V to be around 20 K volts. Using the design figures of $L = S = 10$ cm, we arrived at the conclusion that "more than 1 micro ampere beam current would be feasible at 0.1 micro meter resolution" as indicated in table 2.

The following are the implications of a 1 μ A beam current.

1. The lithographic sensitivity of the advanced electron resist is better than 10^{-6} coulombs/cm². Hence, exposure speed of 1 cm²/sec would be achieved (20 sec exposure time for 2 inch wafer).
2. If "spot scanning" with 1 μ A beam current in a 0.1 spot were used, scanning speed of 10^{10} spots/sec (10 Giga-Hz) would be needed, which would be extremely difficult to engineer. For this reason alone, one would have to use "shaped beam" schemes in order to reduce the scanning speed.
3. Moreover, 1 μ A in a 0.1 μ m spot implies 10^4 A/cm² in current density. A very bright cathode (e.g. field emission type) would be needed to realize such high current densities, but this would reduce the engineering freedom in the cathode design. The current density would be greatly reduced in "shaped beam" schemes.
4. From those considerations just given, "shaped beam" schemes are believed to be quite advantageous and even a necessity for attaining high exposure speed. On the other hand, "spot scanning" may be advantageous for lower speed devices because of its structural simplicity.

§5. Fly's Eye Optics for Pure Electrical Large Area Scanning

In all the electron beam pattern generation schemes described in section 2 (cf. table 1), the electrically scanned areas (typically 5×5 mm²) are too small to cover the entire target area of silicon wafers, typically 2 to 5 inches in diameter. Hence, the target is placed on a mechanical scannable stage so as to back up the electrical scanning. The widening of the electrical scanned area is difficult because it would imply an increase in the working distance L resulting in an adverse effect on the space charge aberration $\delta w_{sc} = KIL/(Vv\alpha)$.

Fly's eye optics may provide a method for scanning a large area purely electrically. Fig. 3 shows two fly's eye schemes. The "post deflection" type was invented by Newberry [F1] and the "double deflection" type, by one of the present authors [EG] [F2, F3, F6].

In Fig. 3, FEL (Fly's Eye Lens) is illustrated by a matrix of lenses. In both types, the electron beam is selectively passed through a specific lens in the FEL by the action of the main deflector MD. The beam is further deflected by sub-deflector(s) SD(s), so as to scan a small area. The difference between the two schemes consists in that while a number of small sub-deflectors are placed after the FEL in the "post deflection" scheme, a single sub-deflector placed before the FEL is sufficient in the "double deflection" scheme. Lenses L1 and L2 are inserted in the figure for the explanatory purpose and they may be removed.

The "post deflection" scheme and its modifications are used in electron beam memory schemes, with sub-micron memory cells [F4, F5, F7]. The "double deflection" scheme is used in very high precision cathode ray tubes [F2, F3, F6].

56. Conclusion

Electron beam pattern generators with 0.1 micron resolution running at a speed greater than $1 \text{ cm}^2/\text{sec}$ are believed to be technologically feasible, based on electron optical studies. The "variable shaped beam" scheme will be used in faster machines and the "spot scanning" scheme, in slower machines.

The impacts of such pattern generators on LSI fabrication are rather difficult to foresee precisely because of the conglomerate nature of the LSI technology. We, as specialists in electron optics, firmly believe that electron beam can never be the bottleneck in the development of advanced LSI's with sub-micron and sub-optical patterns.

We would like to acknowledge Messrs. S. Miyauchi, K. Tanaka and T. Someya of JEOL for stimulating discussions.

REFERENCES

Lithography by electron beam

- [L1] Tarui, Y., S. Denda, H. Baba, S. Miyauchi and K. Tanaka, "An electron beam exposure system for integrated circuits," Trans, IECE Japan, 51-C, 2, p. 74, Feb. 1968, (in Japanese).
- [L2] Miyauch, S., K. Tanaka, and J. C. Russ, "IC pattern exposure by scanning electron beam apparatus," Solid State Technol., p. 43, July 1969.
- [L3] Herriott, D.R., D. S. Alles, R.J. Collier, and J. W. Stafford, "EBES: A practical electron lithographic system," IEEE Trans., ED-22, 7, p. 385, July 1975.

- [L4] Alles, D.S., F. R. Ashley, R. J. Collier, E. A. Gere, D. R. Herriott, A. M. Johnson, and M. G. R. Thomson, "A second generation EBES," Suppl. IEDM Tech. Digest, p. 1, Dec. 1975.
- [L5] Speth, A. J., A. D. Wilson, A. Kern, and T. H. P. Chang, "Electron-beam lithography using vector-scan technique," J. Vac. Sci. Technol., 12, p. 1235, 1975.
- [L6] Soma, T., M. Idesawa, and E. Goto, "A new electron beam exposure scheme of scanning type," IEDM Tech. Digest, p. 20, Dec. 1975.
- [L7] Yourke, H.S., and E. V. Weber, "A high-throughput scanning-electron-beam lithography system," IEDM Tech. Digest, p. 431, Dec. 1976.
- [L8] Mauer, J. L., H. C. Pfeiffer, and W. Stickel, "Electron optics of the electron-lithography system, EL-1," *ibid*, p. 434, 1976.
- [L9] Goto, E., T. Soma, and M. Idesawa, "A design of a variable aperture projection and scanning system for electron beam," 14th EIP Beam Symp. May 1977.
- [L10] Pfeiffer, H.C., "Variable spot shaping for electron beam lithography," *ibid*, 1977.
- [L11] Thomson, M.G.R., R. J. Collier, and D. R. Herriott, "A double aperture method of producing variably shaped writing spots for electron lithography," *ibid*, 1977.
- [L12] Trotel, J., "E-beam dynamic shaping," *ibid*, 1977.
- [L13] Scott, J. P., "Recent progress on the electron image projection," *ibid*, 1977.
- [L14] Speidel, R., and M. Mayr, "Electron beam projection system with photocathode," *Optik*, 48, 2, p. 247, 1977.
- [L15] Stickel, W. and H. C. Pfeiffer "Optics of a variable shaped electron beam column" at this conference.
- [L16] Cogswell, G., S. Miyauchi, K. Tanaka and N. Goto "Variable shaped electron beam lithography" at this conference.

Electron optics

- [E1] Glaser, W., "Grundlagen der Elektronenoptik," Springer, Verlag, 1952.
- [E2] El-Kareh, A.B. and J. C. J. El-Kareh, "Electron beam, lens, and optics," vol. 1, 2, Academic Press, 1970.
- [E3] Septier, A., "The struggle to overcome spherical aberration in electron optics," *Adv. in Optical and Electron Microscopy*, Academic Press, 1966.
- [E4] Ohiwa, H., E. Goto, and A. Ono, "Elimination of third-order aberrations in electron-beam scanning systems," *Trans. IECE Japan*, 54-B, p. 730, 1971, (in Japanese). Also in *Electronics and Communications in Japan*, 54-B, 12, p. 44, 1971.

- [E5] Owen, G. and W. C. Nixon, "Aberration correction for increased lines per field in scanning electron beam technology," J. Vac. Sci. Technol. 10, p. 983, 1973.
- [E6] Munro, E., "Calculation of the optical properties of combined magnetic lenses and deflection systems with superimposed fields," Optik, 39, p. 450, 1974.
- [E7] Munro, E., "Design and optimization of magnetic lenses and deflection systems for electron optics," J. Vac. Sci. Technol. 12, p. 1146, 1975.
- [E8] Pfeiffer, H.C., "New imaging and deflection concept for probe-forming microfabrication systems," J. Vac. Sci. Technol., 12, p. 1170, 1975.
- [E9] Goto, E. and T. Soma, "MOL (moving objective lens) Formulation of deflective aberration free system," Optik 48, p. 255, 1977.
- [E10] Hawkes, P.W., "Computer calculation of formulae for electron lens aberration coefficients," Optik 48, p. 29, 1977.
- [E11] Soma, T., "Relativistic aberration formula for combined electric-magnetic focusing-deflection system," Optik 49, p. 255, 1977.

- [E12] Hearn, A. C., "Reduce 2 user's manual," Dept. Computer Science, Univ. Utah, Salt Lake City, Utah, 1974.

Beam broadening

- [B1] Boersch, H., "Experimentelle Bestimmung der Energieverteilung in thermisch ausgeblenden Elektronenstrahlen," Z. Phys, 139, p. 115, 1954.
- [B2] Zimmermann, B., "Broadened energy distribution in electron beams," Adv. Electronics and Electron Phys. 29, p. 251, Academic Press, 1970.
- [B3] Pfeiffer, H. C., "Experimental investigation of energy broadening in electron optical instruments," 11th EIP Beam Symp. 1971.
- [B4] Pfeiffer, H. C., "Basic limitation of probe forming systems due to electron-electron interaction," Proc. 5th SEM Symp. 1972.
- [B5] Ichinokawa, T., "Effect of electron source to energy resolution in electron velocity analysis - Interpretation of Boersch effect," JJAP 8, p. 137, Feb. 1969.
- [B6] Ditchfield, R. W., "Energy broadening of the electron beam in the electron microscope," Optik 48, p. 163, June 1977.

Fly's eye lens optics

- [F1] Newberry, S. P., T. H. Klotz, Jr. and E. C. Buschmann, "Advances in fly's eye electron optics," Proc. Nat'l. Electronics Conf. 23, p. 76, 1967.

- F2 Goto, E., T. Soma, and A. Ono, "Ultra-high precision cathode ray tube," J. Inst. TV Engrs. Japan 26, p. 21, 1972, (in Japanese).
- F3 Shibata, S., T. Soma, E. Goto, and A. Ono, "A new type of cathode ray tube suitable for bubble chamber film measurements," Nucl. Instr. Methods, 123, p. 431, 1975.
- F4 Hughes, W.C., C. Q. Lemmong, H. G. Parks, G. W. Ellis, G. E. Possin, and R. H. Wilson, "BEAMOS - A new electronic digital memory," AFIPS Conf. Proc. 44, p. 541, 1975.
- F5 Speliotis, D. E., "Bridging the memory access gap," AFIPS Conf. Proc. 44, p. 501, 1975.
- F6 Ono, A., M. Fukawa, H. Kichimi, H. Kodama, T. Murakami, R. Sugahara, A. Suzuki, and K. Takahashi, "An automatic film scanner (KAMA) utilizing a new type CRT with double deflection scheme," Nucl. Instr. Methods, 141, p. 193, March 1977.
- F7 Parks, H. G., "Matrix lens electron beam recovery systems," 14th EIP Beam Symp. May 1977.

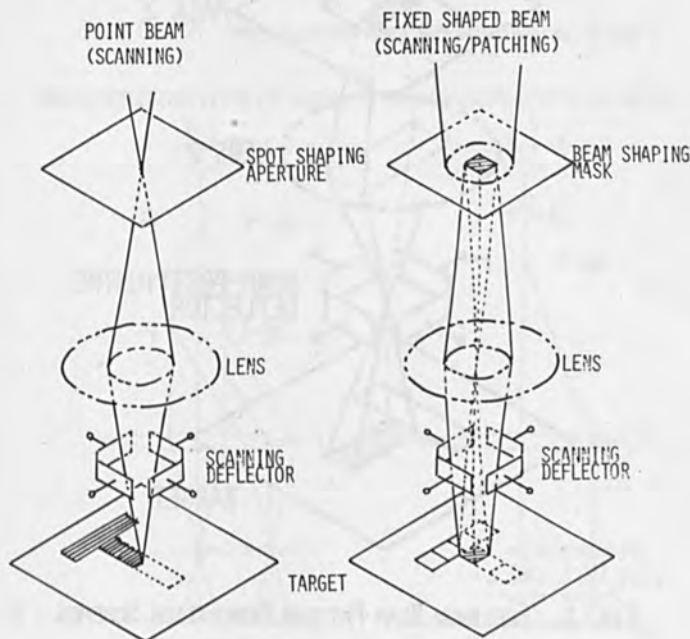


FIG. 1. ELECTRON BEAM PATTERN GENERATION SCHEMES - 1

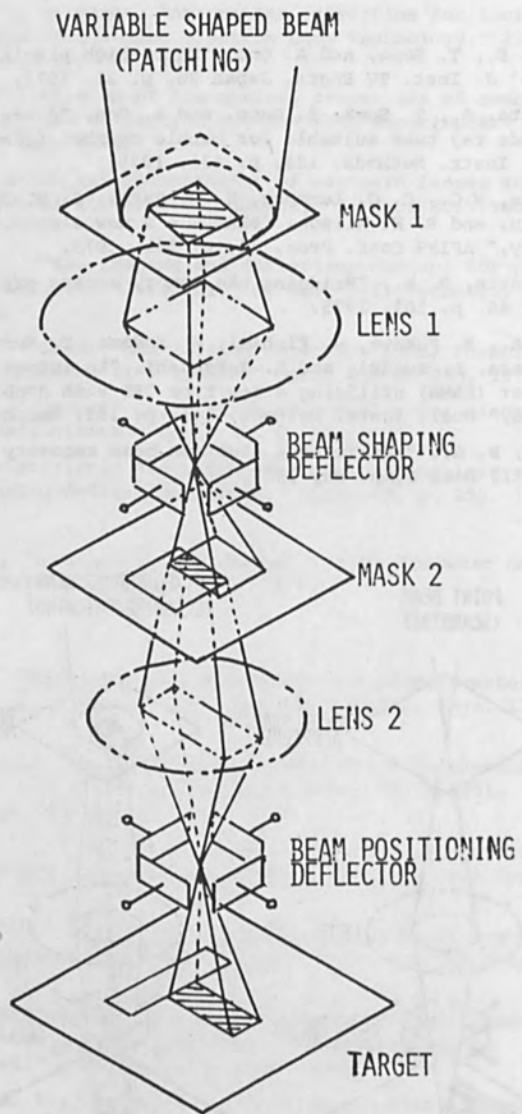


FIG. 1. ELECTRON BEAM PATTERN GENERATION SCHEMES - 2

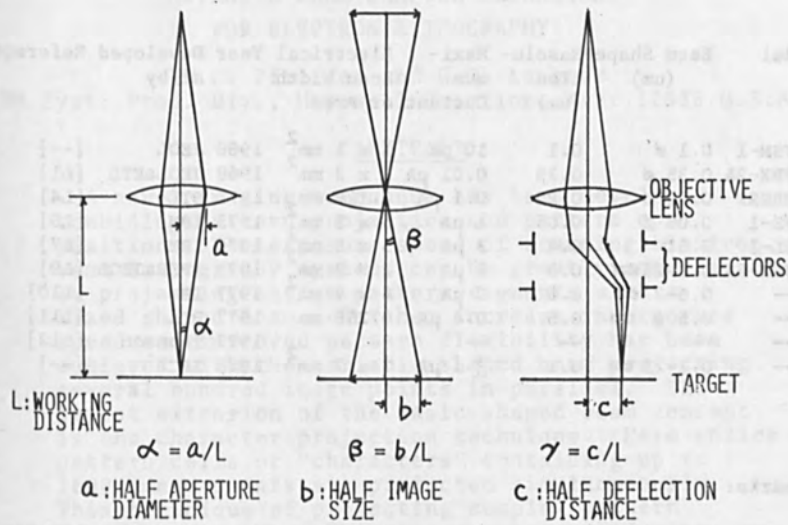


FIG. 2. THREE ELECTRON OPTICAL PARAMETERS: α , β AND γ

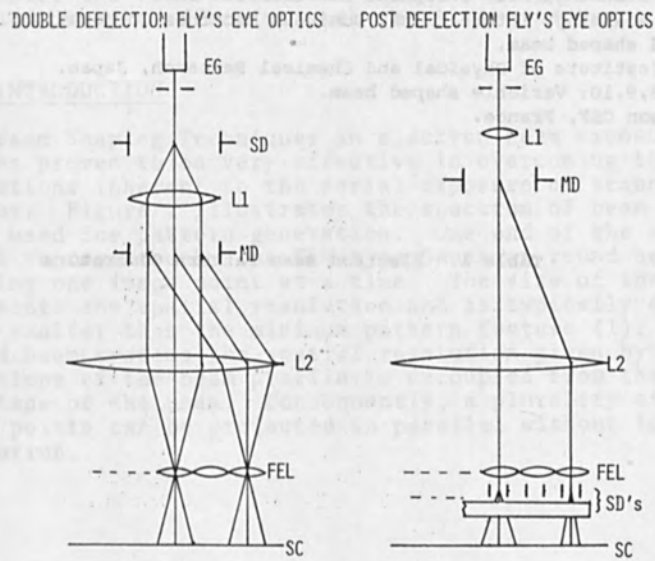


FIG. 3. FLY'S EYE OPTICAL SCHEMES

Model	Beam Shape (μm)	Resolu- tion (μm)	Maxi- mum Current	Electrical Scan Width or Area	Year Developed	Reference at/by
1 JSM-1	0.1 ϕ	0.1	10 pA	1 x 1 mm ²	1966	JEOL [--]
2 JBX-2A	0.35 ϕ	0.35	0.01 μA	2 x 2 mm ²	1968	JEOL&ETL [L1]
3 EBES2	0.25 ϕ	0.25	0.1 μA	0.128 mm ²	1975	BTL [L4]
4 VS-1	0.05 ϕ	0.05	1 μA	5 x 5 mm ²	1975	IBM [L5]
5 EL-1	2.5 \square	0.4	3 μA	5 x 5 mm ²	1976	IBM [L7]
6 JBX-6A	0.5-25 \square	0.5	1 μA	2 x 2 mm ²	1977	IPCR&JEOL [L9]
7 --	0.6-2 \square	0.6	2 μA	4 x 4 mm ²	1977	IBM [L10]
8 --	0.5 \square	0.5	0.4 μA	0.256 mm ²	1977	BTL [L11]
9 --	--	--	--	--	1977	Thomson [L12]
10 --	0.1-25 \square	0.1	≥ 1 μA	7 x 7 mm ²	1978	IPCR [--]

Remarks:

1. SEM (Scanning Electron Microscope), Japan Electron Optics Laboratory Co., Ltd.
2. Spot scanning, Electro Technical Laboratory, Japan.
3. Spot scanning, Bell Telephone Laboratories Inc.
4. Spot scanning, International Business Machines Corporation.
5. Fixed shaped beam.
6. The Institute of Physical and Chemical Research, Japan.
- 6,7,8,9,10: Variable shaped beam.
9. Thomson CSF, France.

Table 1. Electron Beam Pattern Generators

ADVANCED BEAM SHAPING TECHNIQUES
FOR ELECTRON LITHOGRAPHY

H.C. Pfeiffer and G.O. Langner
IBM Syst. Prod. Div., Hopewell Junction, N.Y. 12533 U.S.A.

ABSTRACT

A novel imaging technique has been developed combining pattern projection and pattern composition. The exposure speed of scanning electron beam lithography systems can be greatly enhanced by projecting entire pattern segments with a fixed shaped beam. Further increase in exposure speed and improved pattern flexibility has been achieved with the variable-shaped beam projecting several hundred image points in parallel. The latest extension of the basic shaped beam concept is the character projection technique. Here entire pattern cells or "characters" containing up to 1600 image points are projected simultaneously. This technique of projecting complex pattern features provides ultimate exposure speed without excessive deflection speed and at a drastically reduced data rate. The technique also overcomes the restrictions to rectilinear geometries and is most effective with repetitive patterns.

1. INTRODUCTION

Beam Shaping Techniques in electron beam exposure systems proved to be very effective in overcoming thruput limitations inherent to the serial exposure of scanning systems. Figure 1 illustrates the spectrum of beam profiles used for pattern generation. One end of the spectrum is represented by the SEM-type Gaussian round beam exposing one image point at a time. The size of the spot represents the spatial resolution and is typically 4 to 5 times smaller than the minimum pattern feature (1). For shaped beam systems the spatial resolution given by the edge slope of the beam profile is decoupled from the size and shape of the beam. Consequently, a plurality of image points can be projected in parallel without loss of resolution.

In the case of the fixed shape beam, a square aperture is projected to fit the minimum pattern feature containing 25 image points (2). The variable shaped beam is generated projecting 2 square apertures superimposed (3,4). The compound image formed by both apertures can be varied in size and shape to produce the various pattern elements containing up to a hundred or even more image points.

The primary subject of this paper is shown at the other end of the beam shaping spectrum: the "Character Projection". This technique represents the most advanced combination of pattern projection utilizing its potential for high exposure rate and pattern composition with exposure flexibility. In the illustrated application, complex pattern cells containing up to 1600 image points (of which e.g. 450 are exposed) are addressed in parallel. This technique of projecting entire pattern features provides ultimate exposure speed without excessive deflection speed and at a drastically reduced data rate. The technique also overcomes the restriction to rectangular geometries. It is most effective with repetitive patterns but all integrated circuit patterns are more or less repetitive.

2. BEAM SHAPING TECHNIQUES

2.1 The Variable-Shaped Spot (VSS) System.

The character projection system is an extension of the variable-shaped system (3). Figure 2 illustrates the basic VSS shaping method. Two square apertures shape the beam spot. The electron source illuminates the first square aperture placed between the source and the first condenser. The first condenser performs the two functions of imaging this first square aperture onto the second square aperture and projecting the image of the source into the center of the spot shaping deflector. The image of the first square aperture can be shifted laterally with respect to the second aperture. A particular fraction of the total beam, which depends on the signal applied to the electrostatic shaping deflectors, passes through both apertures. The compound image formed by both apertures is subsequently demagnified and projected on the target.

2.2 Character Projection

Using an aperture plate with a multitude of patterns - "characters" - instead of a single square aperture, as shown in Fig. 3, permits the generation of complex patterns requiring only one single exposure flash. Not only whole characters can be selected but any section of any shape in the aperture plate can be chosen to compose images. Non-rectilinear and curved patterns can easily be included.

3. ELECTRON OPTICS

3.1 Electron Beam Column

Figure 4 shows schematically the arrangement and the image formation of the electron optical column. It is a 5-lens system designed as an electron-optical bench of modular components.

The electron source illuminates the first square aperture which acts as one object for demagnification and projection. The second object is the pattern aperture which contains the array of "character" shapes. Variably illuminated with the image of the first aperture, however, many times the size of its square shape (25X). Koehler's illumination principle is used to separate the source image from the object images. The first condenser performs the dual function of imaging the first square aperture into the plane of the pattern aperture and projects the image of the source into the center of the spot shaping deflector. The spot shaping deflector permits placement of the first aperture image at any character or portion of any character shape at the apertures and is subsequently demagnified by demagnification lenses and projected onto the target. The second condenser controls the illumination projecting the source image into the entrance pupil of the two-stage demagnification and the projection section. The placement of the composite image at the target is performed by a main magnetic deflection yoke located inside the projection lens (2), and an electrostatic deflection unit (not shown in Fig. 4) to compensate for pattern offset.

Alignment servos maintain the illumination at the first and third aperture (in the plane of the entrance pupil of the 2nd demagnification lens) and correct for any drift between first and second aperture (5). All apertures are heated to prevent contamination. The first and second aperture as well as the shaping deflectors, the deflection yoke, and the electrostatic deflection unit can be mechanically adjusted from the outside to compensate for image rotation.

The adjustment of pattern composition is performed with the aid of a 2-stage electron optical magnification below the target which magnifies the target images and projects them onto a phosphor screen (6) which is displayed on closed-circuit-TV. In addition, scanning techniques are employed to display pattern stitching.

3.2 Spherical Aberration Correction

Large pattern plates with a multitude of patterns require a relatively large deflection angle of the shaping deflection and consequently a relatively large angle of incidence into the 2nd condenser lens (see Fig. 5) causing spherical aberration. The result of this spherical aberration is movement of the image of the source (crossover), as indicated in Fig. 5a. This movement, if uncorrected, would be responsible for changes in illumination and increased aberrations in the projector-deflector system. Blur in the source image due to condenser aberrations can be neglected because the beam semiangle is small compared to the deflection angle. The spherical aberration of the 2nd condenser has been corrected in the reported system, removing the obstacle of utilizing large area character plates and a great variety of shapes. The correction has been accomplished by using two shaping deflectors in series (Fig. 5b).

The radial movement of the source image due to 3rd-order spherical aberration (see Fig. 5a) amounts to:

$$\delta = C_s' f^3 \quad \text{-- (1)}$$

Where C_s' is related to the spherical aberration constant C_s as defined for trajectories entering the lens parallel to the axis by:

$$C'_s = \left(\frac{a}{f_0}\right)^4 M C_s \quad \dots(2)$$

In Eq. (2) M denotes the magnification, f_0 the Gaussian focal length, and a the distance of the source image from the principal plane of the lens.

The motion of the source image is prevented when the deflection angle γ'_1 , in the main shaping deflector (see Fig. 5b) is given by:

$$\gamma'_1 = K_1 r (1 + K_2 r^2) \quad \dots(3)$$

and the deflection angle γ'_2 in the auxiliary correction shaping deflector as:

$$\gamma'_2 = K_3 r^3 \quad \dots(4)$$

The constants K_1 , K_2 , and K_3 are related to C'_s (Eq. (2)), a , and the distance d between the deflection centers of the main and the correction shaping deflectors by:

$$K_1 = \frac{1}{a} \quad \dots(5)$$

$$K_2 = \frac{C'_s}{a^2} \left(\frac{1}{d} - \frac{1}{a}\right) \quad \dots(6)$$

$$K_3 = \frac{C'_s}{a^3 d} \quad \dots(7)$$

For small deflections it is sufficient when the deflection of the auxiliary deflector is an adjustable constant fraction of the main deflection. Correct compensation using drivers which provide signals in accordance with Eqs. (3) and (4) permits the utilization of a matrix at least 5x5 images of the first square aperture.

4. PATTERN COMPOSITION

Pattern cells are defined by a reference grid in the target plane. The main deflection positions the center of the aperture plate into the center of each pattern cell (Fig. 6). Figure 6 shows an example of an aperture plate actually used. The composition of a pattern using three shapes from the aperture plate is indicated. The position of any selected shape projected on the wafer with respect to the cell center is dictated by

its position on the aperture plate. This is indicated by the open shapes (1), (2), (3) in Fig. 6. In order to move these shapes into their nominal position (shown solid in Fig. 6) the position offset must be corrected by an auxiliary (electrostatic) deflection superimposed on the main deflection. The exposure of each shape within a given cell is defined by a set of data describing the shaping in X-and Y-direction, the position offset correction in X-and Y-direction, and if necessary, the exposure time to correct for proximity effects.

In the design of the aperture plates two points have been considered in particular. Firstly, enough area had to be provided around each character to avoid interference with an adjacent character when any desired portion of the character is selected, and secondly stitching of patterns on the target was confined to non-critical areas avoiding placement errors to impact circuit functions, e.g. stitching is avoided in gaps of magnetic-bubble patterns as demonstrated in Fig. 7 which shows a "short" "race track" of T -and -I-bars. This pattern requires 17 exposures in 14 cells. Using the VSS (see Fig. 2), 33 exposures would be needed in the minimum. Character projection reduces the total amount of data required to write a pattern. Maintaining the data-rate and deflection speed, the throughput can be increased by reducing the time to expose a field, or maintaining the throughput, the data-rate, deflection speed, and beam current can be reduced resulting in higher resolution and/or less costly data-processing equipment. Apertures have also been designed for non-rectilinear and for curved shapes. This greatly extends the flexibility of shaped-beam lithography.

5. EXPERIMENTAL RESULTS

Figure 8 shows micrographs of a 4mm x 4mm chip filled with 16000 "short racetrack" patterns discussed in sect. 4, Fig. 7. There is no difference in image quality between the center and the corners of the field. The total number of exposure flashes is 3×10^4 and requires a few tenths of a second. The pattern is equivalent to 4000 fabricated lines per field or more than 16,000 resolved lines per field. Using suitably prepared garnet wafers and the usual permalloy-plating techniques, magnetic bubbles were successfully propagated on all locations of the chips.

6. CONCLUSION

The combination of pattern projection and pattern composition has been achieved with a shaped beam electron lithography system. The projection of entire pattern cells and the composition of highly complex pattern features has been experimentally demonstrated. The electron optics has been improved over previous beam shaping systems. A large variety of different shapes can be stored on one aperture plate and projected by correction of the spherical aberration. The character projection technique eliminates the restrictions to rectangular geometries and enhances the exposure rate of the basic variable shaped beam concept without excessive deflection speed and at a drastically reduced data rate.

ACKNOWLEDGEMENTS

We gratefully acknowledge the dedicated effort by Mr. T. Spohr in fabricating aperture plates of excellent quality. We are indebted to M. Hatzakis and J. V. Powers for the preparation and processing of the garnet wafers, and to L. Allman, all of IBM-Thomas Watson Research Lab, for performing the measurements on the magnetic bubble propagation.

References

1. A. D. Wilson, T.H.P. Chang, A.J. Speth, and A. Kern, Scanning Electron Microscopy Symp., Toronto, Canada, 1, 660, (1976).
2. H. C. Pfeiffer, J. Vac. Sci. Technol. 12, 1170 (1977).
3. H. C. Pfeiffer, Intern. Conf. on Microlithography, Paris, 145, (1977).
4. H. C. Pfeiffer, 14th EIP Beam Symp., Palo Alto, Calif., May 1977.
E. Goto, T. Soma, and M. Idesawa, *ibid.*
M.G.R. Thomson, R.J. Collier, and D.R. Herriott, *ibid.*
J. Trotel, *ibid.*
5. S. Doran, M. Perkins, and W. Stickel, J. Vac. Sci. Technol. 12, 1174, (1975).
6. H.C. Pfeiffer, and K.H. Loeffler, Septieme Congres International de Microscopie Electronique, Grenoble, 1970, p.63.

PATTERN GENERATION AND BEAM PROFILES

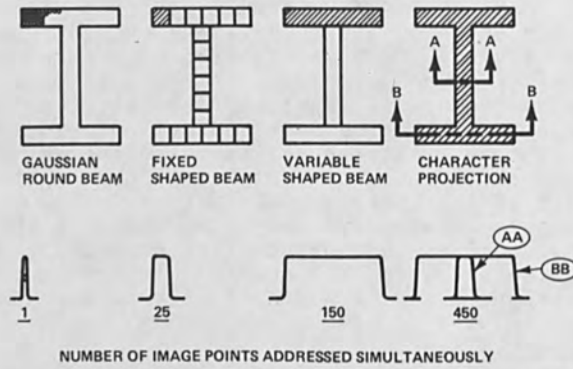


Fig. 1. Spectrum of electron-beam lithography concepts from SEM-type Gaussian round beam via shaped square beam and variable-shaped rectangular beam to characters.

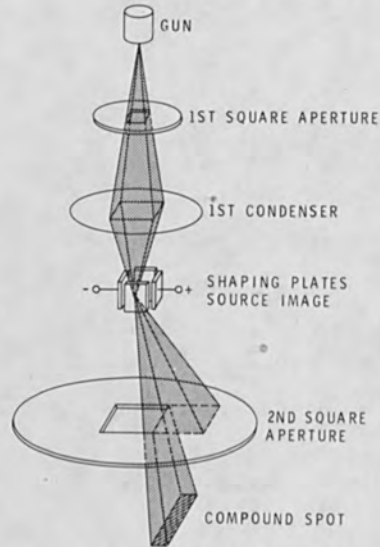


Fig. 2. Principle of the variable-shaped spot (VSS).

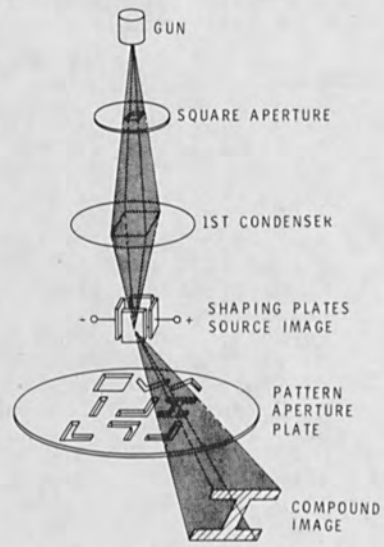


Fig. 3. Principle of "character-projection".

Fig. 4. Schematic of the electron beam exposure column for character writing. Characters are selected by variable illumination. The compound image of the square aperture and the character plate is demagnified in two stages and projected onto the wafer. The convergence points of the electron beam are the images of the source which control illumination and therefore must not move regardless of the pattern selected on the pattern aperture. Shaping is performed electrostatically, placement of the compound image is achieved by dual channel deflection with a magnetic deflection yoke and an electrostatic offset deflector.

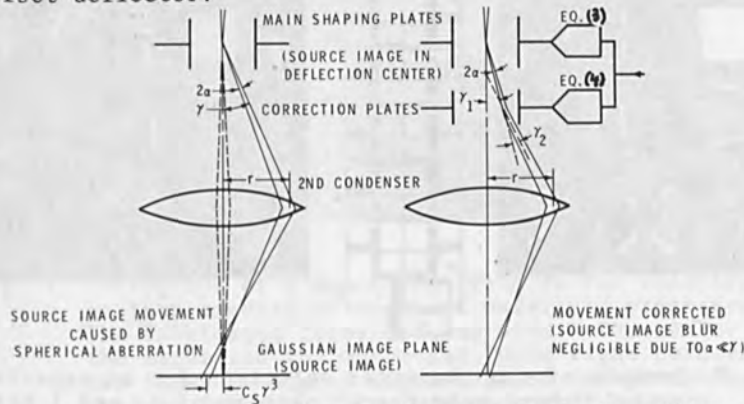
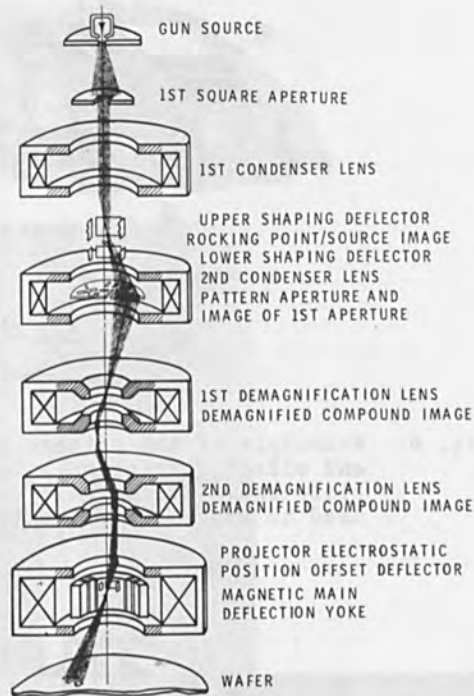


Fig. 5. Correction principle for spherical aberration of the 2nd condenser lens.
 (a) Uncorrected (b) Corrected

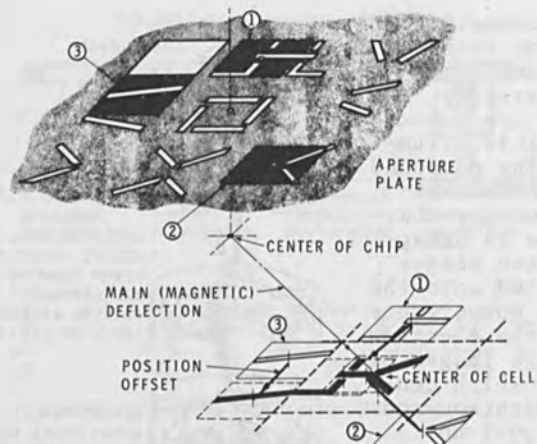


Fig. 6. Principle of the pattern selection, projection, and offset correction. The pattern aperture plate shown has actually been fabricated and used to expose experimental bubble devices.

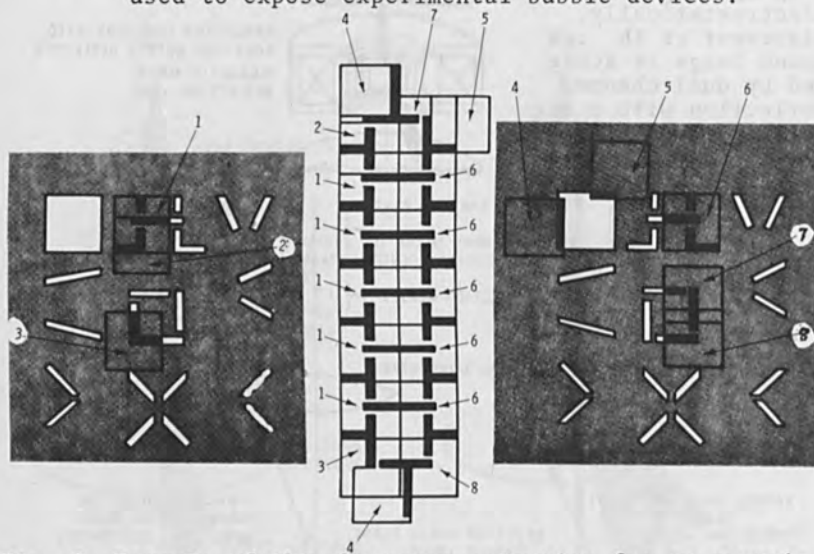


Fig. 7. Example of the character selection for an experimental "short race-track" pattern of T- and I-bars. Each race-track requires 17 exposure instructions consisting of shaping, offset correction, deflection, and unblinking duration.

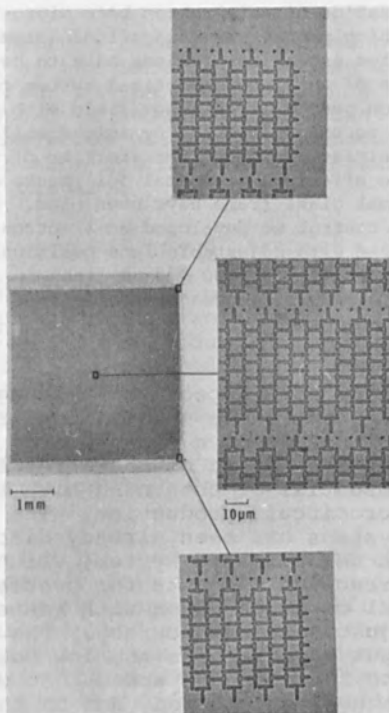


Fig. 8. Micrograph of a 4mm x 4mm field of the race-track pattern exposed on a garnet wafer and processed. The fabricated lines are 1µm wide. The center of the wafer and the upper and lower right corners are shown at higher magnification demonstrating uniform image quality independent of beam deflection.

INVESTIGATIONS ABOUT HIGH PERFORMANCE
ELECTRON-MICROPROJECTION SYSTEMS

B. Lischke, K. Anger, W. Münchmeyer, A. Oelmann,
J. Frosien, R. Schmitt, M. Sturm
Siemens AG, Meßgerätewerk Berlin
Bereich Elektronenmikroskope
Postfach 140, 1000 Berlin 13, Germany

For the realization of an electron beam micro-fabrication system which projects a demagnified image of a mask onto a wafer two essential problems have to be solved: (i) the design of an electron-optical system capable of high resolution over a large image field with an extreme magnification accuracy (ii) the dynamic stability of the masks. To minimize the dynamic distortion of the mask due to heating effects, thin metal foil masks stretched in an isothermal glass frame have been used. For exact magnification control we developed an electron-optical zoom lens system with adjustable lens position. This system is capable of printing $0.3 \mu\text{m}$ lines in an image field of 1 cm at fourfold demagnification.

Introduction

We investigated some aspects of a demagnifying electron-projection system, where a foil mask is illuminated by electrons and imaged onto a wafer coated with a resist. It is obvious that the design of the large field projection optics is essential of obtaining high resolution lithography for microcircuit production. The theoretical limits of such systems has been already discussed;^{1,2} we now realized such an optimized system, which was equipped with suitable correction elements for precise pattern generation. Special care was taken with respect to the demagnification adjustment and accuracy. The requirements for high throughput capabilities and low costs are closely related to the exposure speed. So we discuss this problem in the first section, and in the following the imaging concept of the projection system is described.

Limitations of the exposure speed

For a rough estimate it is sufficient to discuss a schematic of a scanning system, which is compared with a microprojection system (fig. 1). We take into account only the limitations by the brightness of the electron source and the resist sensitivity and assume no limitations by the electronic components. The source of a scanning system, consisting of a square aperture for example,

is imaged onto the wafer. For very coarse structures with no restrictions concerning the resolution the total beam current of the source i_{\max} can be used for irradiating the resist. The exposure speed

$$\tau \left[\frac{\text{cm}^2}{\text{s}} \right] = i\sigma = i_{\max}\sigma = \text{const} \quad (1)$$

is high and independent of the structure size d . (i - probe current, σ - resist sensitivity cm^2/As , i_{\max} - source current).

If the structure size is decreased by shortening the focal length f of the lens, and keeping the aperture constant, the current in the electron probe decreases too and the exposure speed is reduced significantly. This can be deduced from the probe current, expressed by the brightness of the electron gun B and the aperture of the lens α (fig. 1, upper diagram)

$$\tau = \pi \cdot B\alpha^2 \cdot \sigma \cdot d^2 = \text{const} \cdot d^2 < i_{\max} \cdot \sigma \quad (2)$$

In a shaped beam system the probe diameter d equals the minimum structure size. The edge slope or aberration disk δ respectively should be about 20 % of d . In a first approximation this is ensured because of

$$\delta \approx 2C_F^A \cdot \alpha \cdot \frac{\Delta E}{E} \approx 2f \cdot \alpha \cdot \frac{\Delta E}{E} \leq 0,2d \quad (3)$$

(C_F^A - axial achromatic aberration). With decreased focal length the aberration disk decreases too at constant aperture.

In the projection system the total current is projected with a condenser lens on the mask and without any loss on the wafer. By an increased demagnification the same current is available and consequently the exposure speed becomes independent of the structure size, so that equation (1) holds in the whole region. The demagnifying electron projection is superior to scanning systems in its exposure speed of pattern below $2 \mu\text{m}$.

Actually the exposure speed of a projection system should be as large as that of a scanning system for coarse structures. The difference however is produced by the influence of the mask. Due to the beam current the mask is heated and a dynamic distortion occurs, which limits the tolerable current and the maximum exposure speed to about $1 \text{ cm}^2/\text{s}$ in the mask plane.

The mask consists of a thin metal foil some 50 mm in size and about $1 \mu\text{m}$ thick, which is stretched in an isothermal glass-frame. The fabrication technique was described in ³(see fig. 2).

Due to heating by the electron beam the mask is sagging but without changing its position at the center. Because of the isothermal glass frame the distortion is zero for several positions and low between them even for large beam currents. Consequently the overall lateral distortion is small. A current density of 10^{-6} A/cm^2 in the mask plane causes a temperature rise of about 10°C connected with a sag of about $350 \mu\text{m}$, but causes a lateral distortion of only $0.5 \mu\text{m}$ which can be read from the lower plot. This seems to be a tolerable value for the generation of $1 \mu\text{m}$ pattern using a 1 : 4 projection system.

Experimental set-up: The achromatic zoom lens system

The large diameter of the mask requires a novel electron-optical system capable of high resolution over a large field with low distortion.

A schematic of the electron projector is shown in fig. 3. This system was proposed independently in 1975 by several authors.⁴⁻⁶ Essentially it consists of a condenser system illuminating the mask and two imaging lenses. The mask is located in the front focal plane of the first imaging lens while the wafer is situated in the back focal plane of the second lens. To keep the chromatic error of rotation small, the excitation of both lenses should be equal but of opposite sign. Then the focal lengths of both lenses are fixed. Since the demagnification is determined by the ratio of the focal lengths, a suitable adjustment of the demagnification requires a change of the focal length without changing the lens excitation.

The chromatic error of magnification becomes small, if the distance of both imaging lenses is equal to the sum of their focal lengths. This requires a shift of one magnetic lens to its exact position without changing the focal length. We solved these two problems, a focal change at constant excitation and a lens shift at constant focal length, by developing a zooming lens system.

In the lower part of fig. 4 a schematic of the achromatic imaging system is illustrated. It shows the two lenses with their main excitation coils, which are surrounded by the iron circuit. These main coils are excited with an identical but opposite directed current

yielding a magnetic field distribution which is plotted in the upper solid line of fig. 4. One of the lenses is equipped with additional coils. The outer coils are assigned for a suitable adjustment of the focal length at constant excitation. The field strength is lowered in the center and increased at the side yielding a changed focal length. Because the sum of the ampere turns in the three coils is zero, the excitation of the lens remains unchanged.

The inner two coils are supplied with a current of opposite sign, lowering the magnetic field at one end and increasing it at the other end, effecting a field shift along the optical axis, which is indicated in the dotted upper curve. This procedure operates like a displacement of the whole lens.

Fig. 5 shows the field distribution of the zooming lens as it has been constructed by our group. The lens center is variable over 20 mm in both directions, which is represented in the diagram on the right. A small lens shift can be performed without any significant effect on the lens aberrations, although the field distribution becomes slightly asymmetrical.

The field distribution below corresponds to a focal change of 12 mm, so that the demagnification can be adjusted within 6 % without any change of the lens excitation. So the lenses are equipped with suitable correction elements necessary for a precise pattern generation.

Results and discussion

The realization of the electron optical zoom lens system is represented in fig. 6. After suitable collimation by a two lens condenser system the mask is illuminated by 10 keV electrons from a conventional tungsten electron gun. The mask contains openings in a matrix appropriate to the circuit pattern. The mask openings are then imaged by the magnetic zoom lens system onto the wafer with a 4 fold reduction in size to give a 1 cm chip.

On the right a grid mask containing $1\ \mu\text{m}$ grating lines is demagnified producing about $0.3\ \mu\text{m}$ lines in the resist. The micrographs taken from the center and from the side at a distance of 5 mm demonstrate, that the $0.3\ \mu\text{m}$ lines are clearly resolved over the whole image field of 10 mm in diameter.

For test purposes we used small grid masks. Electron beam microfabrication systems however require a more complicated pattern and the "stencil problem" occurs when a desired image requires an electron-opaque area which is completely surrounded by an electron transparent area. A solution to the mask stencil problem has been carried out by the four step exposure technique with the multi-beam-mask, as it was already described.^{3,7} With this type of mask fixed in an isothermal glass-frame it is possible to generate pattern with arbitrary size and shape.

The mask must not contain the whole pattern, but it can be composed of sub-elements, as is shown schematically in fig. 7. Only one part of the mask is illuminated forming an electron probe of the desired shape. This method is quite similar an advanced variable shaped beam technique. With this type of instrument it is possible to combine the high exposure speed of the electron projector with the flexibility of a scanning system.

In summary we obtained the following results: The demagnifying electron-projection is superior to other microfabrication systems in its exposure speed of micron and of submicron pattern. The limiting factor is the mask and its distortion due to heating effects. With the isothermal glass-frame mask an exposure speed of 1 cm²/s should be obtainable.

For high resolution over a large image field we developed a zooming lens system with vanishing chromatic aberrations. The lenses are equipped with suitable correction elements for a precise pattern generation. This system is capable of printing 0.3 μm lines in an image field of 1 cm. The distortion and the alignment problems are discussed in more detail elsewhere.³

ACKNOWLEDGMENTS

The authors gratefully acknowledge the work of Dr. Schuster-Woldan, Dr. Weingand, Dr. Politycki and Dr. Meyer in fabricating the masks used in this work.

This work has been supported under the technological program of the Federal Department of Research and Technology of the FRG. The authors alone are responsible for the contents.

REFERENCES

1. B. Lischke, K. Anger, A. Oelmann, W. Münchmeyer:
Int. conf. on microlithography, p. 167 (1977) Paris
2. B. Lischke, W. Münchmeyer, Optik (1978), to be publ.
3. B. Lischke, K. Anger, J. Frosien, A. Oelmann,
H. Schuster-Woldan: Int. conf. on microlithographie
p. 163 (1977) Paris
4. K. Anger, B. Lischke, W. Münchmeyer, A. Oelmann
Patentschrift DT 2515549 C 2 (1975)
5. M.B. Heritage, J. Vac. Sci. Technol. 12 (1975) 1135
6. H. Koops, W. Bernhard, J. Vac. Sci. Technol. 12 (1975)
411
7. M.B. Heritage, P.E. Stuckert, V. DiMilia, Proc. of the
Symp. on Electron and Ion Beam Science and Technology
348 (1976) Washington, USA
8. B. Lischke, K. Anger, J. Frosien, G. Gorges,
W. Münchmeyer: this issue

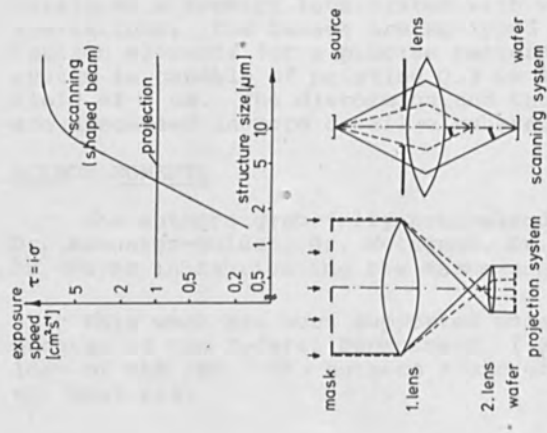


Fig. 1

Limitations of the exposure speed due to brightness and resist sensitivity. While the exposure speed in an electron projection system is independent of the structure size, it decreases significantly in a scanning system, where the source current is reduced to the probe current by the lens aperture.

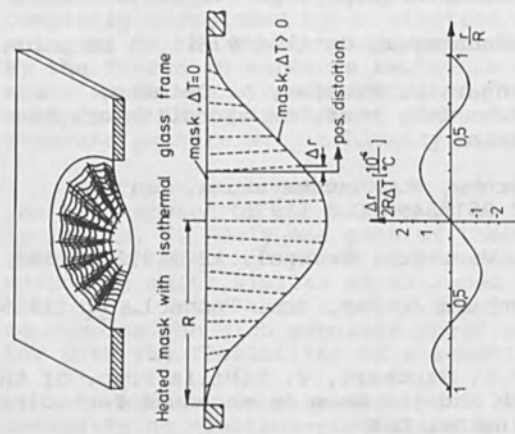


Fig. 2

Mask sag and lateral distortion due to mask heating. The isothermal glass-frame limits the dynamic distortion in radial direction to tolerable values. The distortion in azimuthal direction is negligible.

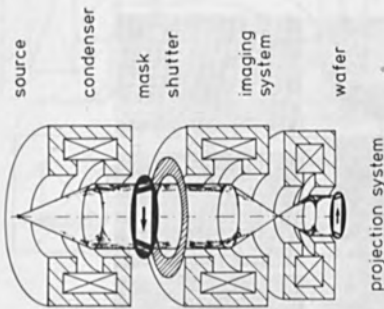
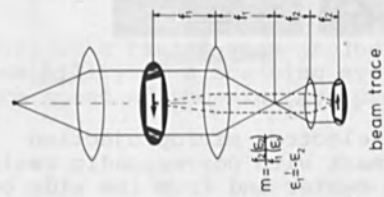


Fig. 3

The electron microprojector operates in a telecentric beam trace. The condenser consists of a hybrid lens with small aberrations, and the projection system is free of chromatic aberrations.

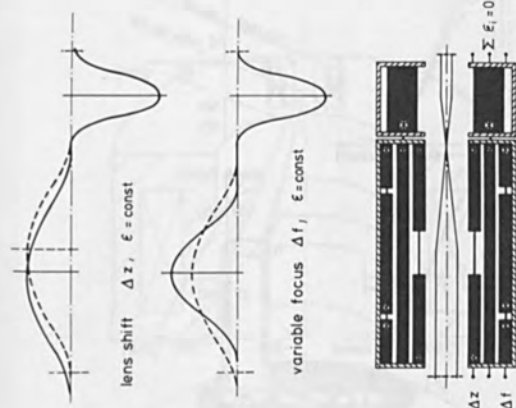


Fig. 4

Principle of a zooming lens system with suitable correction elements for a lens shift and a variable focal length at constant lens excitation.

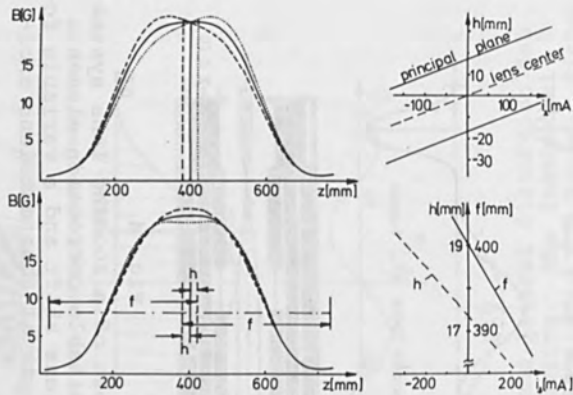


Fig. 5

Zooming lens for variable lens position (upper diagram) and variable focal length (lower diagram) at constant excitation.

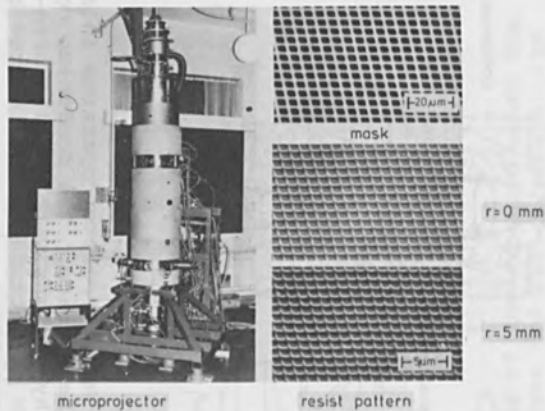


Fig. 6

High performance electron microprojection system and test mask with correspondig resist pattern from the center and from the side of the image field.

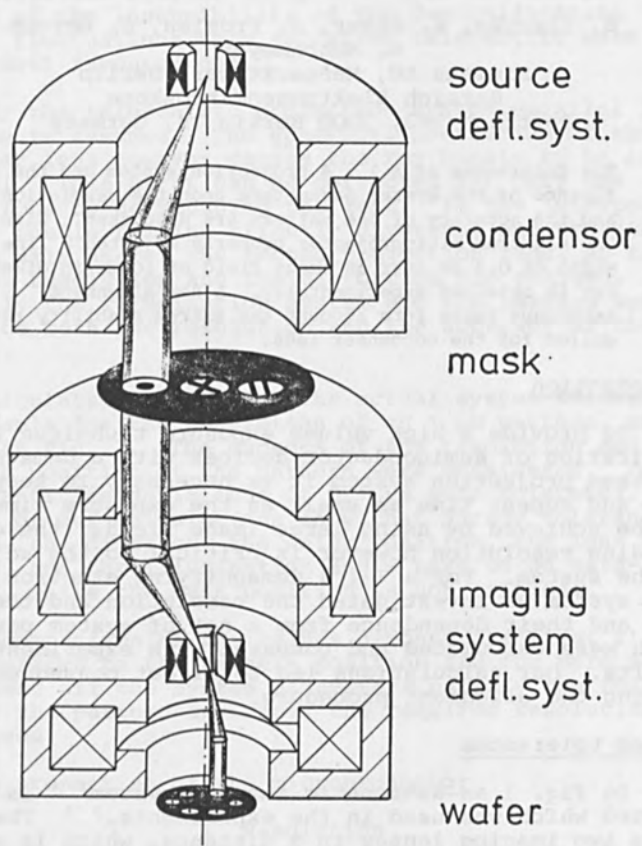


Fig. 7

Schematic of a raster-scan-projector, which combines the flexibility of a scanning system with the high exposure speed of the electron projector.

A STUDY ON THE OPERATION CONDITIONS FOR (1 : 4)
ELECTRON PROJECTION SYSTEMS

B. Lischke, K. Anger, J. Frosien, G. Gorges
W. Münchmeyer
Siemens AG, Meßgerätewerk Berlin
Bereich Elektronenmikroskope
Postfach 140, 1000 Berlin 13, Germany

The tolerances of a 1 : 4 projection system and the influence of the system parameters upon the resolution and the accuracy of the pattern are discussed. With the electron microprojector properly adjusted a line width of 0.4 μm over an image field of 10 mm in diameter is obtained experimentally. A new alignment technique takes into account the extreme stability required for the condenser lens.

Introduction

To provide a high volume exposure technique for the fabrication of semiconductor devices with a demagnifying electron projection system it is necessary to keep the step and repeat time as small as the exposure time.¹ This can be achieved by using large image fields, the corresponding resolution however is critical to the adjustment of the system. For a 1 : 4 demagnifying electron projection system we investigated the resolution and the distortion and their dependence from a set of system parameters, which were calculated and compared with experimental results. Our calculations led to direct consequences concerning the alignment procedure.

System tolerances

In fig. 1 an achromatic imaging system²⁻⁴ is illustrated which was used in the experiments.⁵⁻⁶ The figure shows two imaging lenses in a distance, which is equal to the sum of their focal lengths. A mask is located in the front focal plane of the first imaging lens, while the wafer is situated in the back focal plane of the second lens. Every deviation from this ideal beam trace leads to a resolution loss and a less accurate pattern. A change in the demagnification for example is equivalent to a wrong edge position of the generated pattern.

If the lens distance differs from the sum of the focal lengths by the amount Δz_m , the demagnification V depends on the mask position Δz_o . Getting a slightly different position after a replacement of the mask the de-

magnification is altered and the accuracy of the pattern is reduced. Only for the exact lens position $\Delta z_m = 0$ the demagnification becomes independent of the mask position. Because of the insensibility of the demagnification against fluctuations this so called telecentric beam trace is the most favoured one.

For the telecentric projection system parallel illumination is assumed. The spherical aberration of the condenser lens however causes the ray bundle to be non-parallel. This error can be corrected for only one radial zone by defocussing the lens. In the interpace the ray bundle remains slightly divergent and crosses the optical axis nearer the second projection lens, so that both the resolution and the distortion are changed. Consequently the illumination system and the imaging system influence both the resolution and the accuracy of the pattern.

Calculated results for the actual system tolerances permissible for the generation of an $1 \mu\text{m}$ pattern, are listed in fig. 2. The aspects of the resolution and of the edge position of the pattern were considered. For both quantities deviations of $0.1 \mu\text{m}$ were tolerated. The results of our calculations show that narrow tolerances for the lens distance, the wafer position, the lens excitations, and the illumination angle have to be established, while the mask position is not critical.

A comparison of the values demonstrate (fig. 2), that those related to the pattern position are the more important ones. If the system parameters satisfy the tolerances for the pattern accuracy, the required resolution is guaranteed.

Imaging properties of the microprojector

1. Resolution

Using third order aberration theory the resolution for a proper adjusted 1 : 4 projector was calculated. In an ideal electron projector a slit in the mask plane is scaled down without any loss of resolution and contrast. The "transfer-function" for a perfect system is represented as a straight line in fig. 3. The upper diagram relates the pattern size in the image to the pattern size in the mask. For an ideal 1 : 4 system the image size is exactly a quarter of the object size (see fig. 3).

The real projector however produces an enlarged slit image due to the diffraction at the mask and the aberrations of the projection system. The actual magnitude of such structures depends on its distance R from the optical axis. For the practical application it is reasonable to use masks, whose finest details are larger than the value corresponding to the minimum of the curves. At the optical axis ($R = 0$), mask details down to 40 nm are demagnified to 10 nm without any significant resolution loss. Smaller mask structures yield an image pattern, whose size is increased due to the aberrations and the contrast is lowered. For a mask with a radius of 20 mm for instance, the limit for a reasonable mask structure has an amount of 1 μm corresponding to an image structure of about 0.4 μm in size. The number of resolved lines per field is plotted below. For smallest details of 1 μm in the mask a suitable mask diameter would be about 40 mm. It should be noted, that these results are calculated for the Gaussian image plane. In an optimum image plane (plane of least confusion) they are slightly improved.

The experimental results concerning a test mask and its resist pattern are shown in fig. 4. The mask contains a periodic structure of 4 μm . The 1 μm lines obtained in the resist have a good quality in the centre as well as at the side of the image field in a radial distance of 5 mm. Even smaller structures down to 0.4 μm are well resolved. The results demonstrate that the resolution is very close to the theoretical predictions. The corresponding depth of focus has an amount of 100 μm .

2. Distortion

In the case of parallel illumination the calculated distortion is approximately zero.⁷⁻⁸ Because of the spherical aberration of the condenser lens the illumination angle depends on the distance from the axis and is different from zero. With a suitable defocusing of the condenser parallel illumination is achieved for one definite radial zone in the mask plane at $R = 40$ mm for example. In the corresponding image zone the distortion equals zero, as shown in fig. 5, where the distortion as a function of the chip radius is presented in the upper part. Two systems are compared with scaling factors of 1 : 10 and 1 : 4 respectively. For increasing chip radius the illumination is no longer parallel and the distortion increases drastically. If divergent illumination is applied, the distortion is enlarged at all radii. The results from fig. 5 demonstrate for the 1 : 4 system, that the distortion is about 0.3 % in the best case and

depends critically on the illumination conditions.

Fig. 6 presents a grid mask and its demagnified resist pattern, which was used for distortion measurements of the imaging system. The grating lines in the mask have a width of $22\ \mu\text{m}$, corresponding to a spacing of about $5\ \mu\text{m}$ in the resist pattern. The actual distortion is smaller 0.5 % at each point of the image, which agrees with the theoretical predictions. In these measurements the error of 0.3 % was largest in the center.

Alignment procedure

For the overlaying pattern generation a procedure for the alignment of the projection mask with respect to the wafer is necessary. From fig. 2 one can notice, that the illumination system requires an even higher accuracy than the imaging system itself. The illumination angle is the most important parameter of the whole system. Because of the high requirements on the stability of the illumination system any change of the condenser lens excitation for the purpose of an alignment³ is not practicable.

In fig. 7 is illustrated how an alignment can be realized without any change of the lens excitation. During the alignment mode the mask pattern is covered by a segment shutter, located below the projection mask. Only small slits surrounding the pattern are imaged onto the wafer, forming slit shaped electron probes. With these shaped beams registration marks on the wafer are scanned. The procedure yield alignment signals, which can be processed in the conventional manner, so that a determination of the wafer position can be performed. If the alignment is accomplished the segment shutter will be withdrawn and the exposure can be carried out, as is shown in the right of fig. 7. With this procedure an alignment method is available, which is compatible with the requirement of an extreme condenser lens stability.

Results

For an electron projection system with a demagnification of 1 : 4 the tolerances for the operation parameters have been investigated. Having the imaging system properly adjusted a minimum line width of $0.4\ \mu\text{m}$ over an image field of 10 mm in diameter was achieved. The distortion obtained is less than 1 % and the depth of focus has an amount of $100\ \mu\text{m}$. The extreme stability required for the condenser lens leads to a new alignment technique suitable for the application in the projector.

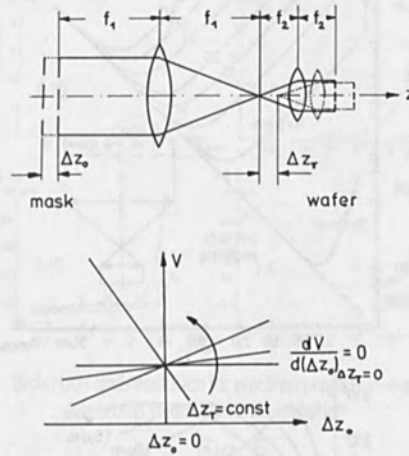
ACKNOWLEDGMENTS

The authors gratefully acknowledge the work of Dr. Schuster-Woldan, Dr. Weingand, Dr. Politycki and Dr. Meyer in fabricating the masks used in this work. We also acknowledge the contributions of G. Friedrich, R. Schmitt and M. Sturm in establishing this system.

This work has been supported under the technological program of the Federal Department of Research and Technology of the FRG. The authors alone are responsible for the contents.

REFERENCES

1. A. Oelmann, B. Lischke, E. Kutzer, Int. conf. on microlithography, p. 171 (1977) Paris
2. K. Anger, B. Lischke, W. Münchmeyer, A. Oelmann Patentschrift DT 2515549 C 2 (1975)
3. M.B. Heritage, J. Vac. Sci. Technol. 12 (1975) 1135
4. H. Koops, W. Bernhard, J. Vac. Sci. Technol. 12 (1975) 411
5. B. Lischke, K. Anger, A. Oelmann, R. Schmitt, M. Sturm, W. Münchmeyer: this issue
6. J. Frosien, K. Anger, B. Lischke, A. Oelmann, W. Münchmeyer, R. Schmitt, Proc. of the conf. on microcircuit engineering (1978), Cambridge, G.B.
7. B. Lischke, K. Anger, A. Oelmann, W. Münchmeyer: Int. conf. on microlithography, p. 167 (1977) Paris
8. B. Lischke, W. Münchmeyer, Optik (1978), to be publ.



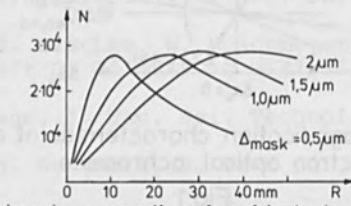
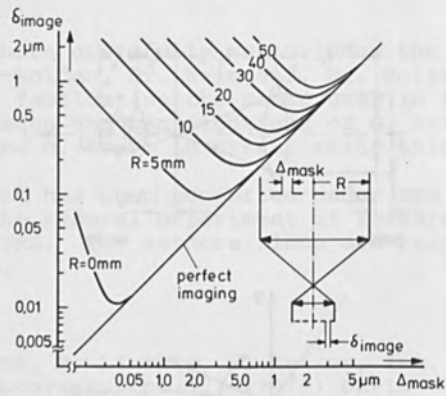
Demagnification characteristic of an electron optical achromate

Fig.1

deviations	edge shift of 0,1 μm		resolution loss of 0,1 μm	
	theor.	exp.	theor.	exp.
<u>imaging system</u>				
object plane Δz_0 [mm]	3,2	—	20	—
lens distance Δz_1 [mm]	1	—	3,8	—
image plane Δz_1 [mm]	0,1	—	1,2	1
lens excitation $\Delta t/t$	$3 \cdot 10^{-3}$	$1,3 \cdot 10^{-3}$	$2,5 \cdot 10^{-2}$	$1 \cdot 10^{-2}$
<u>illumination system</u>				
illumination angle $\Delta \beta$ [rad]	$1,2 \cdot 10^{-5}$	$1,5 \cdot 10^{-5}$	$5 \cdot 10^{-3}$	—
lens excitation $\Delta t/t$	$2,5 \cdot 10^{-4}$	$2 \cdot 10^{-4}$	10^{-1}	—

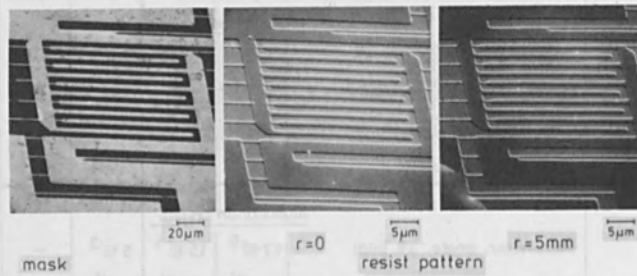
Tolerances in a 1:4 electron projection system

Fig.2



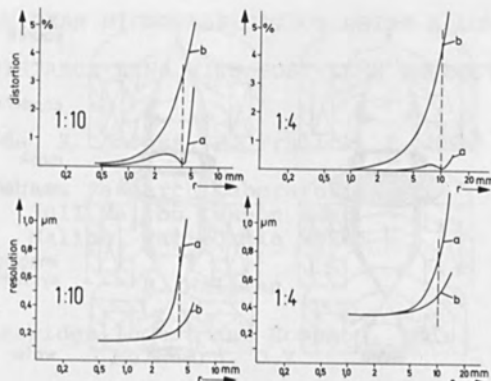
Imaging properties of an 1:4 electron proj. system (parallel illumination)

Fig. 3



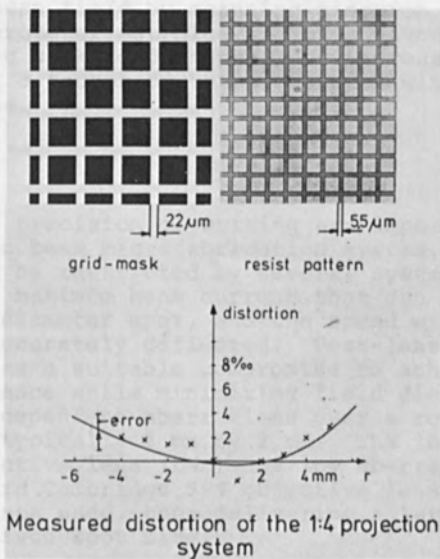
Large area pattern generation of submicron structures

Fig. 4



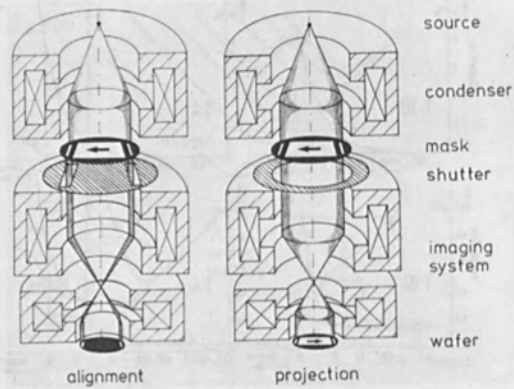
Distortion and resolution for electron projection-systems
(a)parallel (b)divergent illumination

Fig. 5



Measured distortion of the 1:4 projection system

Fig. 6



Alignment and projection mode in the electron microprojector

Fig. 7

ELECTRON BEAM MICROFABRICATION USING A LONG
WORKING DISTANCE LENS WITH POST-LENS DEFLECTION

J. Reeds, K. Amboss, R. Fralick, E. Wolf

Hughes Research Laboratories
3011 Malibu Canyon Road
Malibu, California 90265

B. Wallman

Cambridge Instrument Company, Ltd.
Melbourn, U.K.

ABSTRACT

An electron-beam microfabrication system has been modified by the addition of a special long working distance objective lens, in conjunction with a post-lens deflection coil. Field distortion of less than 1 micron has been verified over a 2 mm scan field by scanning electron microscopy/laser interferometer metrology. For a given beam diameter, the long working distance lens increases beam current by about a factor of three compared with a standard objective lens.

INTRODUCTION

The speed and precision of writing are important parameters of an electron beam microfabrication system. Maximum writing speed may be restricted by several system limitations, including the maximum beam current that can be focused into a given diameter spot, and the speed with which the beam can be accurately deflected. Post-lens deflection was selected as a suitable compromise to achieve high-speed performance while minimizing field distortion and the aperture dependent aberrations over a relatively large field, typically 2 mm by 2 mm. The long working distance objective lens (LWD) has low aberrations compared to the standard Cambridge S-4 objective lens at the 5 cm working distance used, thus delivering a larger beam current into a given spot size.

THE MICROFABRICATION SYSTEM

The microfabrication system (Figure 1) is based on a Cambridge S4-10 scanning electron microscope, incorporates a pneumatic suspension system for vibration isolation, a lanthanum hexaboride gun for higher brightness, electrostatic beam blanking, and a laser interferometer controlled x-y stage¹, in addition to the LWD objective lens and the post-lens deflection coil. The electron-optical parameters of the post-lens deflection coil have been previously reported². A precision ceramic mandrel has been used for winding the coil to provide accurate and stable geometry. The LWD objective lens was designed by Cambridge Instrument Company as a replacement for the standard S4-10 objective lens. Figure 2 shows the post-lens deflection coil mounted on the LWD objective lens. Relatively large ceramic flanges are provided on the deflection coil in order to minimize eddy current induced distortions by keeping conductive material as remote as possible. The coil is mounted to the lens with a rotary mount to allow it to be precisely orientated.

Field distortion of the post-lens deflection coil (including the effects of the deflection amplifiers and pattern generator) was measured by writing a uniformly spaced grid pattern on a PMMA coated silicon wafer. The pattern was developed, evaporated with gold, and a gold lift-off performed, leaving a grid of gold lines. The silicon wafer was then remounted in the microfabrication system which has a precision laser interferometer controlled stage. Using the stage as a scanning electron microscope, the intersections of the grid were imaged at high magnification and precisely centered on the display screen by moving the x-y stage. The x and y coordinate locations of each intersection were then read from the laser interferometer displays. Periodically during the measurements, the starting location was rechecked to minimize electron beam drift errors (which are of the order of 0.5 microns/30 minutes). The results of the field distortion measurements are shown in Figure 3. The field distortion of a nominal 2 mm by 2 mm field was a maximum of 0.8 microns at one corner of the field. This value corresponds closely to the predicted maximum distortion. The skew between the x and y deflections was measured to be 0.07. This may be easily corrected with dynamic skew correction. Deflection over a 2 mm field causes spot diameter growth of approximately 0.2 microns (depending on final aperture size) due to field curvature. This can be corrected by means of a two-turn dynamic focus coil which is located inside the bore of the final lens.

The LWD lens was originally characterized by Cambridge Instrument Company. At the 5 cm working distance used, its spherical aberration coefficient (C_s) was found to be about 64 cm compared to about 360 cm for the standard Cambridge S4-10 objective lens at the same working distance. The LWD lens performance was subsequently verified by additional testing after it was installed on the microfabrication system. On-axis spot diameter was measured by a method similar to that described by Joy³. The focused beam was scanned over a very small tungsten wire (~ 1 micron) and the beam passing the wire was collected in a Faraday cup and analyzed. This arrangement allows both the beam diameter and the beam current to be simultaneously determined. Performance of the LWD lens is shown in Figure 4. Compared to a standard S-4 objective lens, the LWD lens increases beam current by about a factor of three for a given beam diameter. To obtain the increased beam current, a larger limiting aperture was used which reduces depth of focus slightly. Optimum aperture semi-angle for a given beam diameter is shown in Figure 4.

SUMMARY

Increased exposure speed over a 2 mm field was accomplished by the incorporation of the LWD lens and post-lens deflection coil in an electron beam microfabrication system. The system is presently in daily use providing direct wafer exposures of patterns with submicron dimensions.

REFERENCES

1. Pasiecznik, J., J. Reeds, J. Vac. Sci. Technol., 1978.
2. Amboss, K., J. Vac. Sci. Technol., 12, (1152) 1975.
3. Joy, D. C., Scanning Electron Microscopy, 1974 (Part I), Pg. 327.

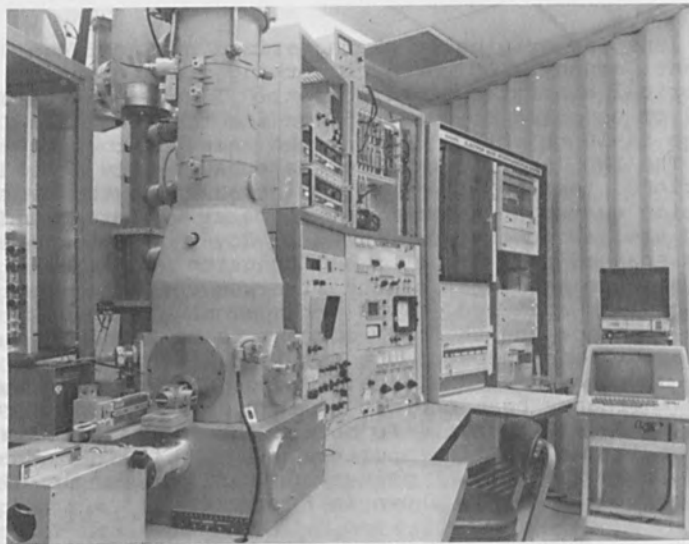


Figure 1. Microfabrication System With Long Working Distance Objective Lens.



Figure 2. LWD Lens With Post-Lens Deflection Coil In Rotary Mount.

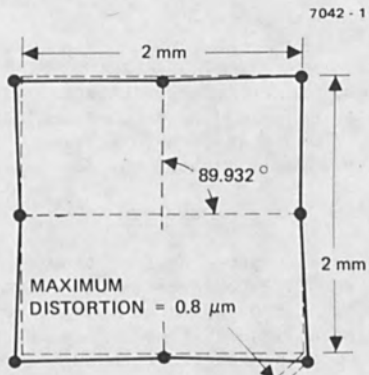


FIGURE 3. FIELD DISTORTION

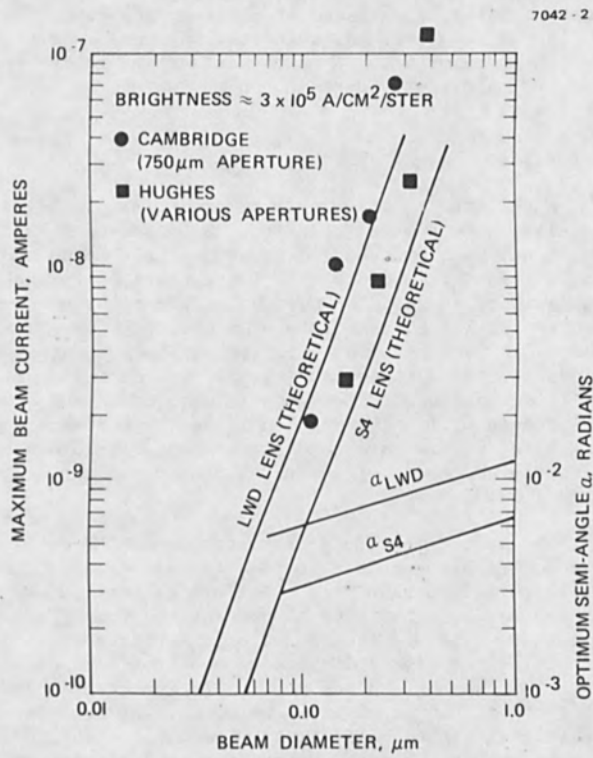


FIGURE 4. LWD LENS PERFORMANCE

A DATA PROCESSING SYSTEM FOR ELECTRON-BEAM LITHOGRAPHY
Naoshi Sugiyama, Naoaki Aizaki, Akira Kawaji, Yasuo Tarui
VLSI Technology Research Association
Cooperative Laboratories
4-1-1, Miyazaki, Takatsu-ku, Kawasaki, 213, Japan

ABSTRACT

A data processing system AMDES (Automatic Masking-Data generation for Electron-beam exposure System) for delineating submicron patterns using electron-beam exposing equipment is described. This system offers a faster method to handle finer scale information necessary to delineate integrated circuit submicron patterns. Advanced computing techniques are presented, correcting field distortion, proximity effect, generating positive/negative polarity data and eliminating unnecessary overlapped exposure. By using this system, submitting to the 1 μm design rule, a highly integrated resist pattern was produced by directly exposing on the wafer.

I. Introduction

Manufacturing of very large scale integrated circuit chips requires fine pattern handling. Electron-beam hardware development has been progressing towards higher speed and higher precision. However, in order to utilize these equipments to a maximum extent, adequate support by utilization techniques (i.e., software) is indispensable. Software systems developed and reported in publications up to now all seem to have several limitations in regard to processing speed, accuracy or flexibility. [1] Successful performances in high speed and high accuracy pattern will only be accomplished by software whose efficient large volume data handling method, flexible pattern data structure and their efficient allocation in the computer memory are fully devised.

This paper introduces new software AMDES developed by the authors. Electron-beam exposure data are generated based on the mask pattern design data. Pattern distortion due to electron-beam deflection is to be compensated for by analyzing inverse mapping of distortion function. Furthermore, a method of compensating for distortion due to the proximity effect is proposed. This method applies a multiple integral around the ϵ -neighborhood of the representative point, which gives the exposure intensity threshold value. Computing algorithms have also been proposed to handle arbitrary shaped pattern data to

remove overlapping, which causes multiple exposure, to invert mask pattern polarity that produces negative exposure patterns, and to partition patterns into subfields whose domains are limited by the electron-beam equipment scanning angle.

2. Distortion Correction Algorithm

Let the input signal coordinate be $x = (x,y)$ and the coordinate of the point actually exposed be $X = (X,Y)$. Then, the relation between x and X is expressed as $X = G(x)$. $G(x)$ is called the mapping function, including trapezoidal, pinclusion and gain distortions. In order to expose required point X , it is necessary to input the signal to expose point \bar{x} , which is expressed as

$$\bar{x} = G^{-1}(X)$$

Inverse mapping function $G^{-1}(X)$ is calculated by the Newton-Raphson iteration method:

$$x_{k+1} = x_k - H^{-1} (G(x_k) - \bar{x})$$

where

$$H = \frac{\partial G(x_k)}{\partial x_k}$$

and where initial point x_0 may be conveniently chosen as target point \bar{x} . Only two or three Newton-Raphson iterations were necessary to converge to the resultant coordinate with adequate accuracy. A sample distortion distribution calculation is shown in Fig. 1. Detailed analysis shows that, when maximum distortion is 5 points (i.e., maximum distortion in 1.5 $\mu\text{m}/5\text{mm}$ scan field), correction by linear inverse interpolation will give sufficient accuracy.

3. Proximity Effect Correction

3.1 Summary

The contour of patterns exposed with an electron-beam has a swelling out tendency, due to the electron back-scattered effect inside the wafer material. This proximity effect phenomenon causes deterioration in fine patterns resolvability especially when they are closely located. For a pattern correction required to counteract the proximity effect,

the following two fundamental processes will be required:

- (a) Calculate deformed shape of the arbitrarily given design pattern when exposed on the wafer.
- (b) Correct pattern shape and exposure dose, using information gained from the former analysis.

For analyzing (a), least square fitting of the exposure intensity distribution (EID) function $F(r)$ against experimental measurement is made. Efficient calculation of double integral around given point X , as shown in Fig. 2, i.e.,

$$\iint_A F(\|x - y\|) d^2y$$

enables obtaining exposure dose at X . It is not productive to obtain (b), or correction evaluation, by evaluating exposure dose for all the sides in each pattern. Instead, a representative point is chosen, where maximum exposure dose is expected and the superimposition principle [2] is applied only to that point.

3.2 EID Function

The EID function can be evaluated by either analytical or experimental means. The former method usually consists of the Monte Carlo method or other simulation techniques. Though these methods are of interest in themselves, they are not completely suitable for the present purposes. Instead, the experimentally obtained EID curve is approximated by some appropriate function. Following Chang [2], it is assumed that $F(r)$ is in the form

$$F(r) = C_1 \exp\{- (r/\sigma_1)^2\} + C_2 \exp\{- (r/\sigma_2)^2\}$$

where two Gaussian distributions are assumed to represent the incident beam and backscattered electrons. To determine parameters C_1 , C_2 , σ_1 and σ_2 , $F(r)$ is fitted to the experimental setup by the weighted least square method.

These parameters depend on several physical factors, such as beam accelerating voltage, resist material and thickness, substrate material, the chemical development process used, etc.

Table 1 shows several examples including the results obtained by other researchers. Comparing these results, several interesting observations will be made. As the beam accelerating

voltage becomes higher, probability of the internal scattering is decreased and therefore values C_0 , C_1 , C_2 , C_0/C_2 , C_1/C_2 , σ_0 , σ_1 and σ_2 become smaller. As is well known the developer sensitivity depends on the ratio of MIBK/IPA and the sensitivity becomes higher when MIBK/IPA is large. This effect is represented by the fact that C_2/C_1 is larger as MIBK/IPA becomes large.

3.3 Proximity Effect Compensation

To compensate for the proximity effect produced by the electron-beam distributed over arbitrary patterns, exposure intensity should be varied with pattern geometry. Formally, the problem can be stated as follows. Find the electron-beam intensity incident on any point X such that exposure intensity $E(X)$ at point X satisfies the condition

$$l(x) \leq E(X) \leq u(x)$$

where $l(x)$ and $u(x)$ are given lower and upper values respectively, for E at X . This paper describes one realistic solution of the above problem. Let

$$I_0 > I_1 > I_2 \dots\dots$$

be the possible incident beam intensities sequence. Let a set of exposed connected patterns be $A_1, A_2 \dots\dots A_n$. Denote the fact that beam intensity to pattern A_i is I_j by

$$l(i) = j$$

First, set $l(i) = 0$ for $i = 1, \dots\dots n$ and repeat the following procedures for $i = 1, \dots\dots n$.

1. Pick out pattern A_i
2. Determine all patterns $A_{i_1}, \dots\dots, A_{i_m}$ which are adjacent to A_i .
3. Repeat the following steps for $k = 1, \dots\dots m$.
 - 3-1 Determine a sample point between A_i and A_{i_k} and calculate the amount of exposure intensity at that point.
 - 3-2 If exposure at the sample point exceeds the threshold value, add one to the smaller of $l(i)$ or $l(i_k)$. If exposure is less than the threshold, repeat this action until the condition is satisfied.

When the above procedures are expected for $i = 1, \dots, n$ every pattern is assigned an appropriate incident beam intensity. The following describes somewhat detailed technique for executing the above procedures. For the sake of brevity, all patterns A_i , $i = 1, \dots, n$ are assumed to be isolated convex polytopes. Modification to a more general case can be accomplished by the direct forward, but cumbersome way.

In the above described procedure to compensate for the proximity effect, all patterns which are adjacent to a given convex polytope A_i should be formed. A practical method for this purpose is shown below.

Let ϵ be a "characteristic length" determined by the shape of the EID function. Namely, ϵ is an upper limit of r at which $F(r)$ cannot be regarded to approximate zero. Define A_i^ϵ , which is an "extended" A_i pattern, as shown in Fig. 3. Next, we obtain intersections of A_i^ϵ and other patterns and find A_{ik} , $k = 1, \dots, m$ for which

$$A_i^\epsilon \cap A_k \neq \emptyset$$

These patterns are the desired ones which are adjacent to A_i .

To avoid computing exposure intensities at a large number of points and to decrease computation time to a feasible level, special sampling points were chosen and exposure intensity was determined only at these points. Assume that

$$A_1^\epsilon \cap A_2 \neq \emptyset$$

Then the sample point used to compensate for the proximity effect between A_1 and A_2 is determined as shown in Fig. 4.

4. Multiple Exposure Elimination

In order to check figure overlapping, the following mathematical techniques were used.

- (a) Indexes representing the reference coordinate are applied to each pattern. Particularly, when the patterns contain angle lines, indexes obtained by rotating coordinates shown in Fig. 5, $\min (1/2 (X_i + Y_i))$ and $\max (1/2 (-X_i + Y_i))$ are recommended.

- (b) Furthermore, in order to minimize the number of pattern indexes comparison derived by (a), the number of patterns to be handled in a batch should be approximately twice the number of patterns which cross the boundary of the subdivided field.

The fact is shown by the formula.

$$R = K \times \frac{n^2}{2} + \frac{n_L^2}{2}$$

$$n_L = N - n - (n-r)(k-1) + r$$

and

N : total number of patterns

n : number of patterns to be handled in a batch

r : number of patterns which cross the boundary.

5. Pattern Data Processing Algorithm

Let us explain the pattern data processing algorithm according to Fig. 6. The main pattern processing purpose for positive lithography is multiple exposure elimination. Assume patterns P_1 , P_2 and P_3 are given patterns. First, take P_1 and eliminate overlapped portions from P_2 and P_3 . In order to do this, make new patterns $P_4 = P_2 - P_1$ and $P_5 = P_3 - P_1$. Next, take P_4 and eliminate overlapped portions with P_5 , i.e., make a new pattern $P_6 = P_5 - P_4$, the thus broken down elements are further subdivided into trapezoidal pattern elements, compatible to the EB.

Negative processing is carried out by subtracting each input pattern from a rectangular area representing the whole region. For practical use, complement area \bar{P}_1 to P_1 is subdivided into two areas, $\bar{P}_{1,1}$ and $\bar{P}_{1,2}$, by the boundary lines determined by two points which have maximum and minimum y-coordinates. Then, P_3 is subtracted from complemented patterns. Again, trapezoid subdivisions are made to produce EB patterns. As a fundamental tool to carry out the above procedures, algorithms have been proposed to obtain the intersection of two patterns and the difference between two patterns.

6. Sample Results

This section discusses some results obtained from the AMDES. Figure 7 shows input patterns that include overlapping of two or more patterns. Figure 8 shows negative configuration of the input patterns with overlapped part removed, followed by trapezoid partition processing. Exposed patterns are derived by reducing the size of all patterns to 1/5 of those produced while submitting to the conventional 5 μm design rule. Part is then enlarged and shown in photo.1. Minimum line width is 1 μm . This system utilizes the ACOS-6 computer and two electron-beam exposure equipments. One is the JEOL-5AR, manufactured by JEOL Ltd. The other is the EBMF 2, manufactured by Cambridge Instruments. Both are operated in vector scan mode.

7. Conclusion

A data processing system for exposing fine patterns in integrated circuit printing has been described. Software is mainly discussed along with computing techniques adopted here. Although, in an actual implementation of this system to various applications, detailed construction might suffer some modifications, the computing technique discussed here will remain a fundamental principle for electron beam utilization in fine pattern lithography. A considerable amount of processing time has been necessary because VLSI chip design pattern count is of the 10^6 order. Reducing computing time by fully utilizing various computing techniques, such as efficient pattern data buffering, using high-speed arithmetic algorithms and so on, will be important subjects to be resolved in the future.

ACKNOWLEDGEMENTS

The authors would like to express their appreciation to H. Shiraki and K. Saitoh in VLSI Research Association, and to K. Ono, H. Yamashita and K. Kurihara, Ono Systems, Inc., for many helpful discussions.

REFERENCES

- [1] M. Fujinami, H. Oshiba, A. Kondo and K. Komatsu, Nat. Conv. Rec. IECE, Japan, S3-1, P2-260, 1977
- [2] T.H.P. Chang, "Proximity effect in electron beam lithography", J. Vac. Sci. Technol. Vol. 12, No. 6, 1975, PP1271-1275.

[3] K. Komatsu, Y. Sakakibara, The 25th, Spring Meeting, JSAP, Tokyo, 1978, PP257

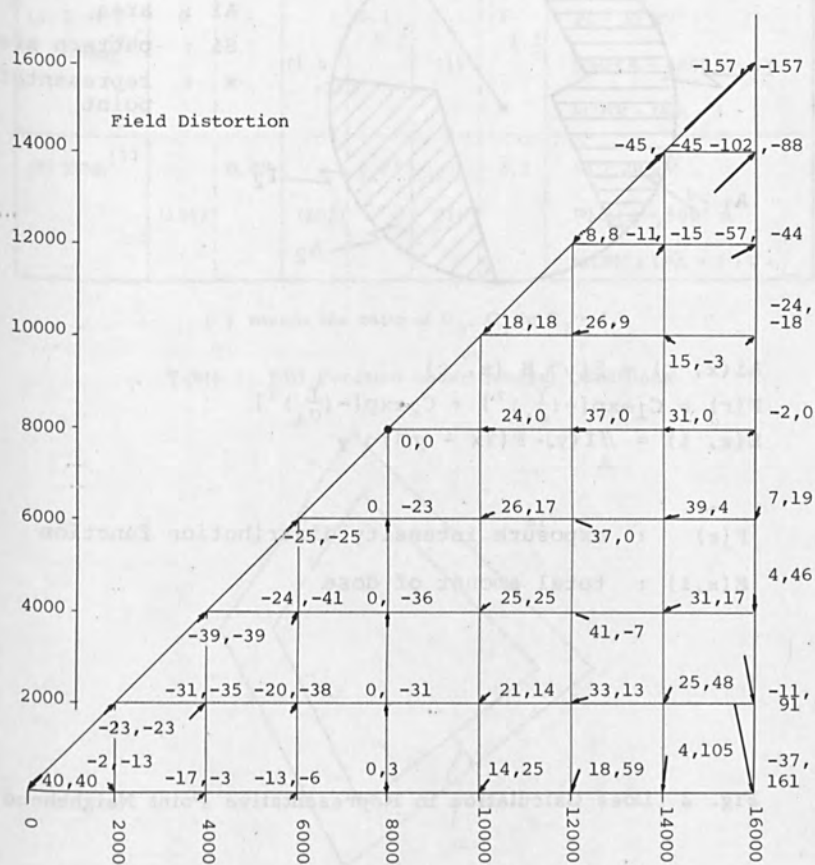
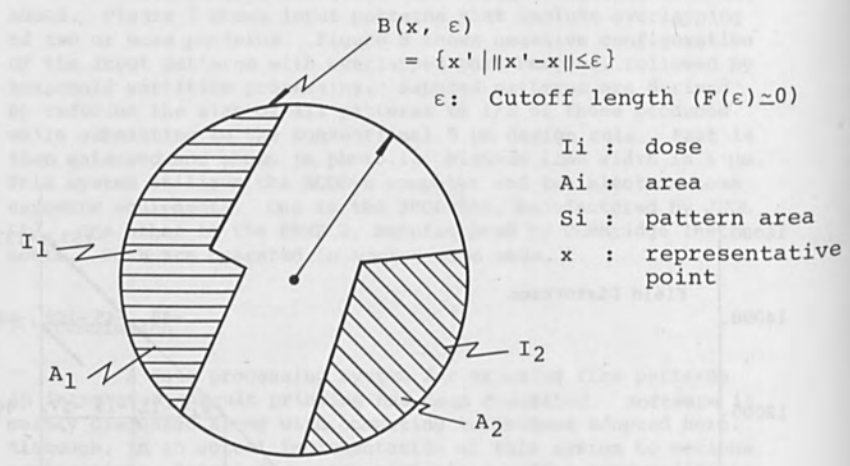


Fig. 1 Sample Distortion Distribution Analysis



$$A_i(x, \epsilon) = S_i \cap B(x, \epsilon)$$

$$F(r) = C_1 \exp[-(\frac{r}{\sigma_1})^2] + C_2 \exp[-(\frac{r}{\sigma_2})^2]$$

$$E(x, i) = \iint_A I(y) \cdot F(\|x - y\|) d^2y$$

$F(r)$: exposure intensity distribution function
 $E(x, i)$: total amount of dose

Fig. 2 Does Calculation in Representative Point Neighborhood

$$F(r) = C_0 \exp\left(-\frac{\gamma^2}{\sigma_0^2}\right) + C_1 \exp\left(-\frac{\gamma^2}{\sigma_1^2}\right) + C_2 \exp\left(-\frac{\gamma^2}{\sigma_2^2}\right)$$

Examples	C_0	σ_0	C_1	σ_1	C_2	σ_2	Conditions
(1) Authors	0	-	26.4 (87)	0.3	0.305 (1)	1.6	$V_i = 20 \text{ kV}$ PMMA = 5000 Å MIBK : IPA = 1 : 1
(2) T. H. P. Chang ^[2]	0	-	(1.5 -3)	0.1- 0.2	(1)	1- 1.2	$V_i = 25 \text{ kV}$ PMMA = 6000 Å MIBK : IPA = 1 : 1
(3) ECL ^[3]	(194)	0.09	(202)	0.21	(1)	2.2	$V_i = 20 \text{ kV}$ PMMA = 5000 Å MIBK : IPA = 1 : 2

() means the ratio of C_0 , C_1 to $C_2 = 1$.

Table 1 EID Function under Several Conditions

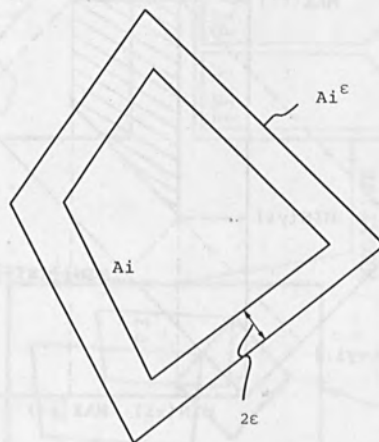
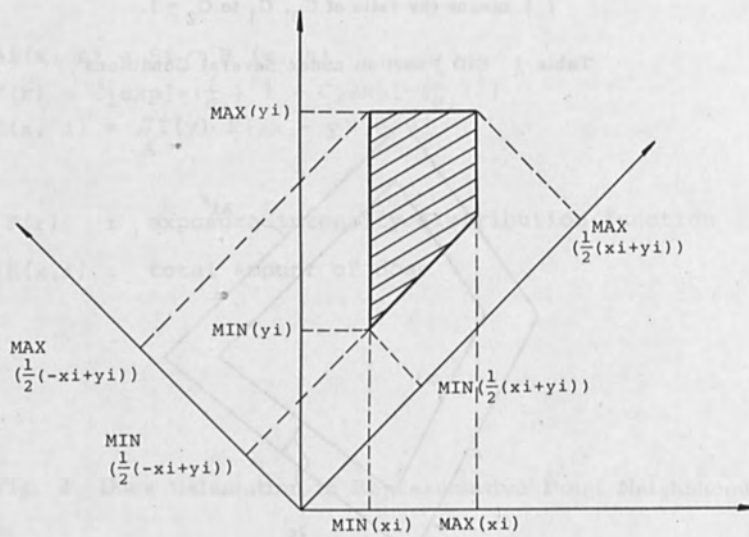
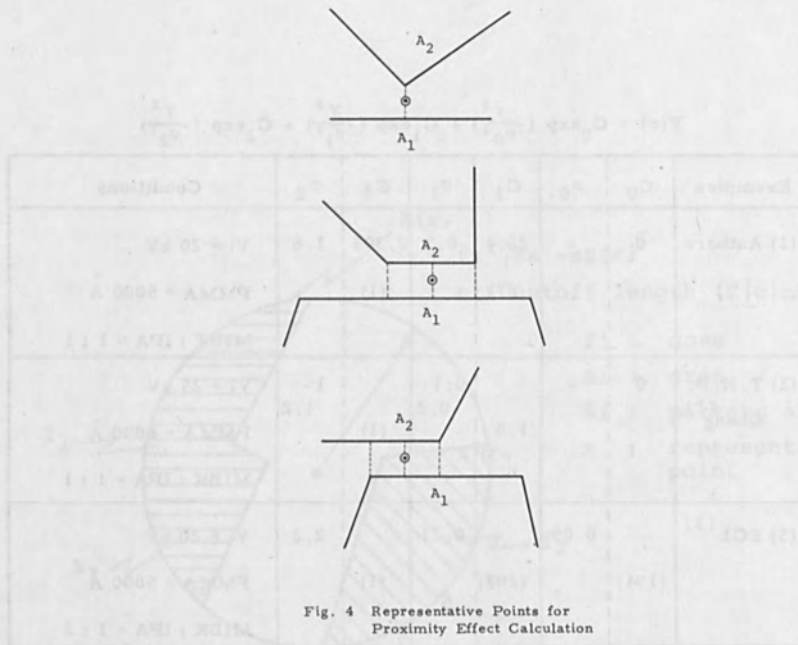


Fig. 3 Extended Ai Pattern



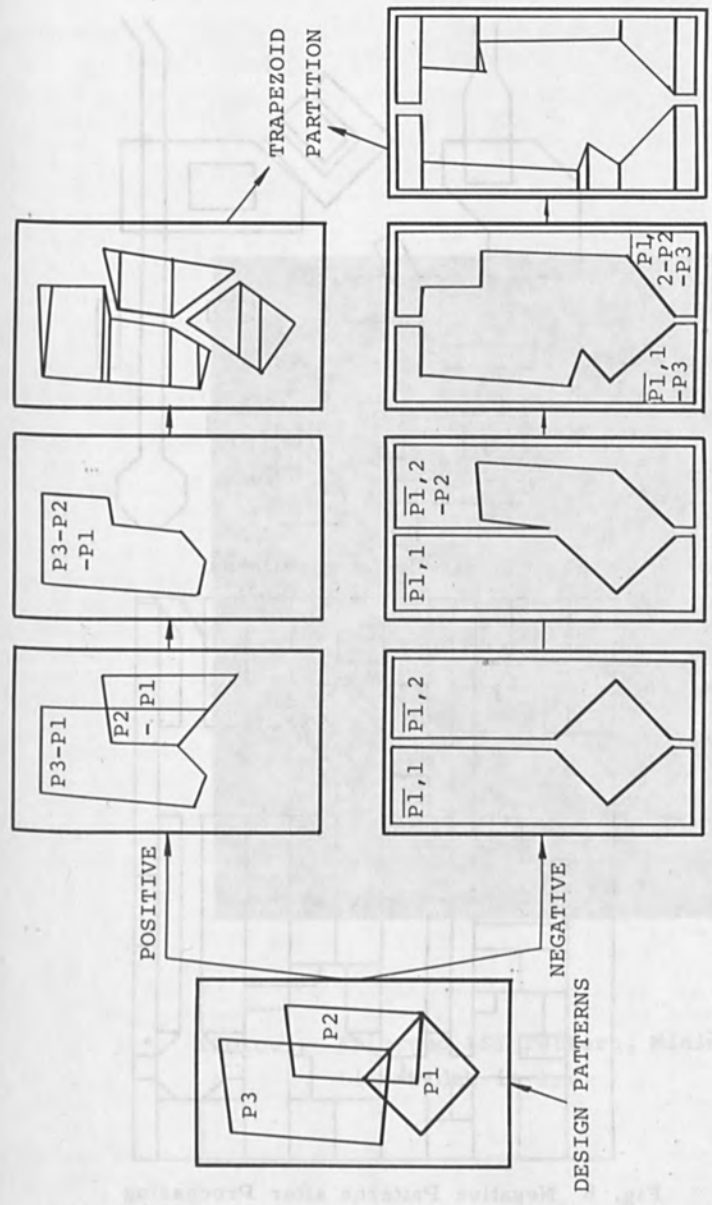


Fig. 6 Algorithm for Removing Overlapped Patterns

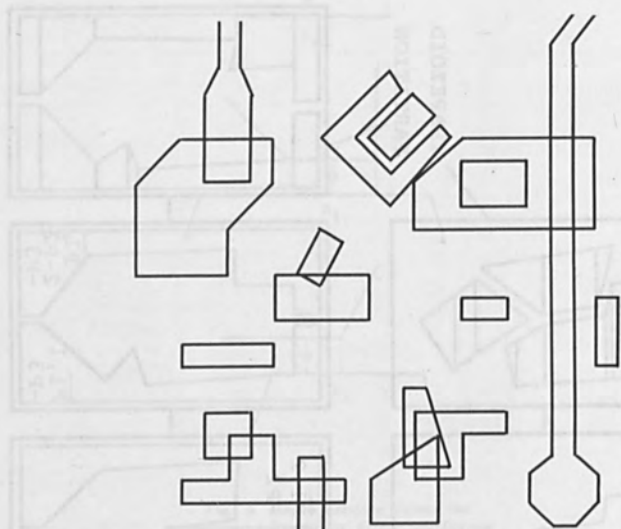


Fig. 7 Sample Input Patterns

The figure displays several distinct geometric shapes and patterns. On the left, there is a complex, multi-sided polygon. In the center, there are several smaller, simpler shapes including rectangles and a small trapezoid. On the right, there is a vertical structure consisting of a long stem with a circular base and a rectangular top section. The patterns are drawn with thin black lines on a white background.

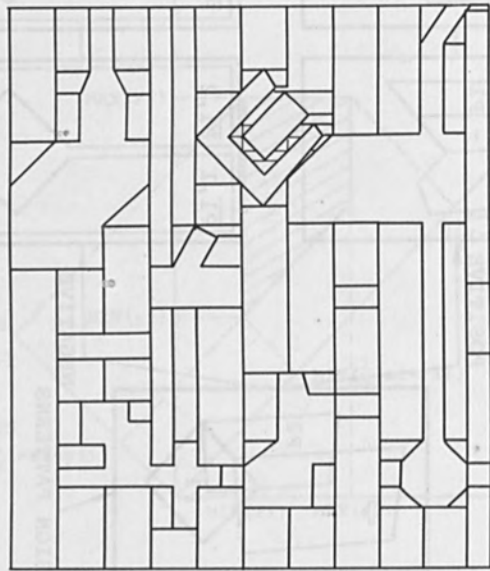


Fig. 8 Negative Patterns after Processing Trapezoid Partition

The figure shows a large rectangular area filled with a dense, complex pattern of lines. The pattern consists of numerous vertical and horizontal segments of varying lengths, creating a grid-like structure with many small, irregular openings. The overall appearance is that of a highly detailed, partitioned space.

INTRODUCTION
AN ADAPTATION OF THE LITHOGRAPHY BY A BEAM OF ELECTRONS

The development of a technology for the fabrication of integrated circuits with a minimum line width of 1 μ m is essential for the realization of high-speed, high-capacity digital systems. The use of electron beams for lithography offers several advantages over conventional optical lithography, such as the ability to focus the beam to a very small spot size and the absence of diffraction orders. This method allows the production of patterns with a minimum line width of 1 μ m, which is necessary for the realization of high-speed, high-capacity digital systems.

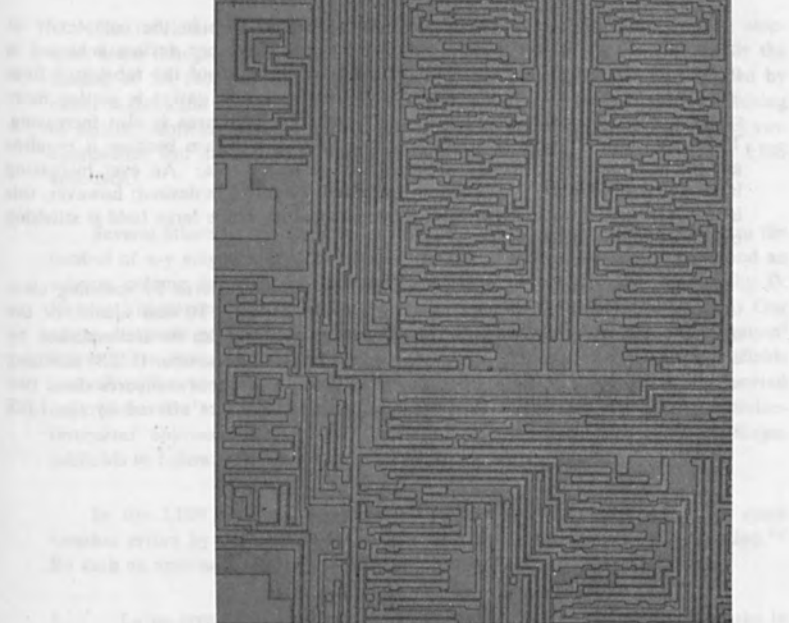


Photo.1. Enlarged LSI Pattern. Minimum Line Width is 1 μ m.

**A COMPARISON OF PATTERN STITCHING BY SUBFIELD REGISTRATION
AND LASER INTERFEROMETER SERVO CONTROL**

A. D. Wilson, T. W. Studwell, G. Folchi, A. Kern, H. Voelker
IBM T. J. Watson Research Center
P. O. Box 218
Yorktown Heights, New York 10598

ABSTRACT

In recent years there has been a continual increase in the complexity of integrated circuit devices, exotic memory devices, and other devices achieved in part by clever design and also by a reduction in the size of the fabricated lines and primitive elements of a device. However, while the device is getting more complex and with finer lines, the size of the total chip area is also increasing. These effects place greater strain on the lithography system because it requires greater resolution and overlay accuracy over a larger area. An ever increasing large size deflecting field with nearly unlimited resolution is desired; however, this is difficult to practically achieve. An alternative to a single large field is stitching by registration or laser table.

The fabrication of micron and submicron circuit patterns by scanning electron beam lithography over extensive areas, for example 10 mm square, or the making of 5X reduction mask reticles over larger areas, can be accomplished by either registration stitching¹ or laser interferometer servo system (LISS) stitching of smaller subfields into the desired size pattern. This paper compares these two approaches and attempts to show the potential advantages offered by the LISS approach.



Fig. 1. Schematic Diagram of Laser Interferometer Servo System (LISS) Stitching

INTRODUCTION

In recent years there has been a continual increase in the complexity of integrated circuit devices, exotic memory devices, and other devices achieved in part by clever design and also by a reduction in the size of the fabricated lines and primitive elements of a device. However, while the device is getting more complex and with finer lines, the size of the total chip area is also increasing. These effects place greater strain on the lithography system because it requires greater resolution and overlay accuracy over a larger area. An ever increasing large size deflecting field with nearly unlimited resolution is desired; however, this is difficult to practically achieve. An alternative to a single large field is stitching by registration or laser table.

The fabrication of micron and submicron circuit patterns by scanning electron beam lithography over extensive areas, for example 10 mm square, or the making of 5X reduction mask reticles over larger areas, can be accomplished by either registration stitching¹ or laser interferometer servo system (LISS) stitching of smaller subfields into the desired size pattern. This paper compares these two approaches and attempts to show the potential advantages offered by the LISS approach.

Several others in the lithography field have applied laser interferometry to the control of x-y stages: O. Cahen and J. Trotel² implemented a laser stage and an e-beam column (published 1970) and the Bell Laboratory group headed by D. Herriott³ implemented a continuous stage and column combination (EBES). Our paper discusses some stitching experiments conducted on an IBM VSI System⁴ where there exists the capability of accurate stitching of high resolution fields several millimeters in size using registration mask technique¹. The reported experiments are examples of stitching 0.5 mm square fields using the laser interferometer approach with results on stitching by interferometry using larger subfields to follow at a later date.

In the LISS approach, a laser interferometer is used to correct for stage location errors by deflecting the electron beam to the intended stage location.^{2,3} By such an approach, several enhancements to e-beam lithography occur:

1. Large area chips or patterns can be written without registration marks in the interior chip area,
2. A large portion of the stage move-time can occur during pattern write-time and thus the stage move-time does not significantly influence the system thruput, and
3. The deflection system can be simplified.

Figure 1 illustrates the LISS principle and figure 2 shows some additional details of the system used in this study. If a scanning e-beam system has an interferometrically controlled x-y stage then a number of other attractive system options are possible as illustrated in Figure 3.

REGISTRATION vs LASER STITCHED PATTERNS

Large area chips as illustrated in figure 4, fabricated by the stitching of subfields to a number of registration marks produces highly accurate overlays and if marks can be located within the interior of the chip, the chip size is unlimited; however, in some cases, registration marks cannot be located in the chip interior region because of device reasons and thus the final chip linear size is limited to twice the stitched field size, typically 2 to 4 mm for 1 micron lines. We are assuming that 3 marks are required for each written field. Because system thruput is influenced by the xy-stage move and settle times and the registration cycle time, elimination of these can improve overall system performance.

The sequence followed in stitching patterns is to first locate on the substrate a reference mark and register to it and calibrate the registration and/or interferometer systems. If stitching is being done by registration, the stage is moved to the first subfield chip site, allowed to settle and then a registration is performed and the pattern is written. A move is executed to the next subfield site and the process continues until the chip has been completed. If stitching is being done by LISS, the stage is moved to the intended first subfield and as soon as the LISS is tracking the stage, the pattern writing is initiated. This may be sometime before the mechanical stage reaches the actual subfield site. When the pattern is finished, the stage is moved to the next subfield location and pattern writing again occurs as soon as tracking is attained, etc.

Figure 5 illustrates these two sequences and includes some typical times for stage move, settle, registration and writing. To compare the system performance achieved using either of these two approaches a thruput example is contained in Figure 6. When stitching is done by registration, the registration and stage move-times in this example comprise about 60% of the pattern write time and they significantly influence the system thruput. On the other hand, when stitching is done by LISS, the pattern can be divided into many additional subfields such that the stage can be tracked during the step from one subfield to another. The pattern writing is initiated during these short stage jumps from one subfield to another. If the pattern write time is equal to or greater than the stage step time, then no stage overhead is encountered in the system thruput.

Using small subfields stitched together to construct a large dense pattern can alter significantly the emphasis of development in deflection schemes for scanning electron-beam lithography machines. It is difficult to achieve a deflection system capable of fabrication of high contrast 1 micron lines over a 10 mm square area and with minor field distortions. The small-field stitched approach significantly simplifies the deflection hardware requirements because in some systems distortion corrections may be required for fields of 1 mm or greater.

STITCHING ACCURACY

The stitching accuracy attainable by registration and LISS are comparable for non-distorted substrates. In registration, the ultimate accuracy is on the order of one least significant bit of deflection and this typically can be 0.06 to 0.12 micron for 2 mm fields. Using LISS and a suitable flat travel, low roll, pitch and yaw stage typical stitching errors at the corners of joined fields are on the order of 0.09 micron. The various contributing factors to this error are laser stability, interferometer resolution, stage roll, yaw pitch, etc. In this example, the laser stability is 0.5 ppm and interferometer resolution error is $0.01 \mu (\lambda/32)$. For roll,

pitch, yaw, etc., errors we allow 3 arcs secs. per axis distributed over 10 cm and assume pivot lengths of 2 cm which yields errors on the order of 0.025 micron. Assuming we are using a 14 bit D/A converter, one LSB equals 0.079 micron for a dynamic range of ± 648 microns which is necessary for stitching 500 micron fields with a minimum of stage overheads. For thermal substrate errors we allow a temperature variation during the whole operation of 0.1°C , a sample length of 3 cm, and expansion coefficient of $6.3 \text{ ppm}/^{\circ}\text{C}$, which yields an error of 0.02 micron. The root sum square error for LISS is thus on the order of 0.09 micron.

MAGNETIC INTERACTION EFFECTS

As the beam of electrons travels from the final lens to the substrate any interaction with a stray magnetic field that is changed by motion of the stage will introduce an unwanted shift of beam motion. These stray fields could be that of the final lens or generated by some magnetic material associated with the x-y stage. Any magnetic or paramagnetic material located on the moving stage and in close proximity to the substrate has been found to cause beam shift during stage motion. Use of aluminum in place of these materials has eliminated the unwanted effects. To determine the extent of the beam shifts and the effectiveness of abatement techniques a wire grid was rigidly mounted directly onto the final lens slightly above the plane of the substrate. The beam was focused at high magnification on this grid and then with the vector scan system⁴ in SEM mode the stage was moved throughout its entire travel area 10cm x 10cm. Any beam motion was easily observed and photographically recorded. Prior to reduction of the effects a 7 micron beam shift was observed with certain types of substrate holders on the stage. After locating and removing sources of the beam shift, for example, use of stainless steel where it should not have been, shielding slightly magnetized lead screws, degaussing fastening screws, bearings, etc., the beam shift was reduced to 0.3 micron for a full 10 cm at stage travel. Further reduction is possible by more attention to degaussing of stage component parts during assembly.

EXAMPLE

An example of a laser interferometer stitched pattern written on an IBM VSI⁴ system is shown in Figure 7. This pattern was fabricated by stitching in a 40 by 40 array of 500 micron square fields creating a two centimeter square chip, (a 20,000 line field with 1 micron lines). The test pattern is a T and I bar cell structure which permits an easy assessment of the stitching errors. The lines and gaps are each 1 micron wide and written in PMMA on silicon. The typical stitching errors are on the order of 0.1 micron. Figure 8 illustrates a vernier test pattern stitched again in the same manner. The vernier sensitivity is 0.1 micron per bar. The vernier bar spacing is 1 micron. Figure 9 shows 1/2 micron T-I bar test patterns stitched over a 1 cm square field, or a 20,000 line field. The stitching errors are on the order of 0.06 micron which indicate the accuracy of stitching to limited, at this level, not by the laser interferometer resolution, but by the resolution of beam incrementing accuracy.

SUMMARY

Key points of comparison between registration and LISS stitched patterns are highlighted in Figure 10. Using the LISS approach to field stitching, we find that many fewer registration marks are required on the substrate and the chip area is fully useable, the overall system thruput is higher, the chip size is unlimited for undistorted wafers, the individually written field size can be significantly smaller

than the desired chip size easing the deflection system requirements of dynamic distortion and focus corrections, and stitching accuracy can be on the order of 0.1 micron.

A vector scan type system with an accurate stage error servo to the electron beam can be used in a "write on the fly" mode and this can minimize the stage step and repeat time without introducing any deleterious effects on the pattern quality.

REFERENCES

1. A. D. Wilson, *et. al*, *J. Vac. Sci. Tech.*, vol. 12, 1975, pp. (1240-1245).
2. O. Cahen, J. Trotel, 4th *Electron, Ion & Beam Science & Technology*, R. Bakish, Editor, 1970, p. (581).
3. D. R. Herriott, *et. al.*, *IEEE Transactions on E.D.* Vol. ED-22, 1975, pp. (385-392).
4. T. H. P. Chang, *et.al.*, *Electron and Ion Beam Science and Technology, Seventh International Conference*, R. Bakis, Editor, 1976, pp. (377-391).

T. H. P. Chang, *Ibid*, pp. (392-410).

A. D. Wilson, *Ibid*, pp. (361-376).

ACKNOWLEDGEMENTS

The authors wish to thank T.H.P. Chang and Alec Broers for their encouragement during this project, W. Blair for assistance in the magnetic interaction study, and Hans Luhn for the fine SEM analysis and photography of the stitched patterns.

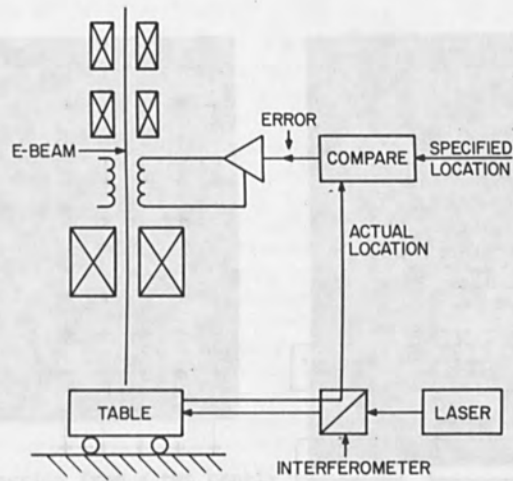


Fig. 1. Laser Interferometer Servo System (LISS) Principle

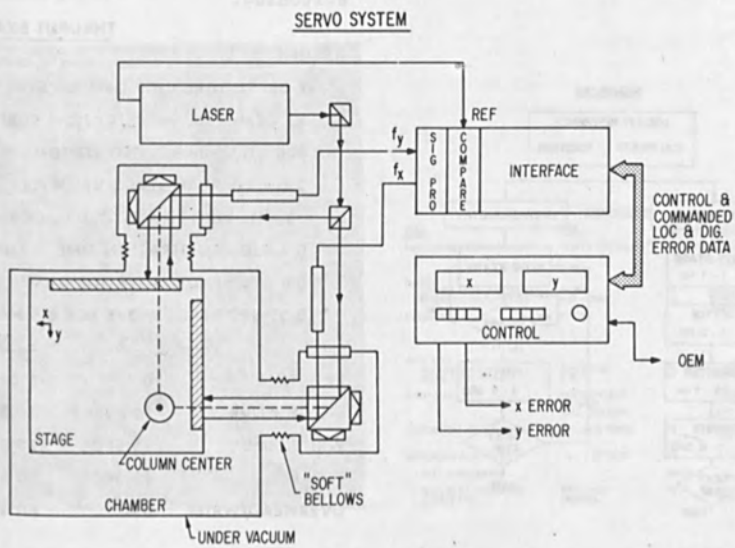


Fig. 2. LISS Functional Organization

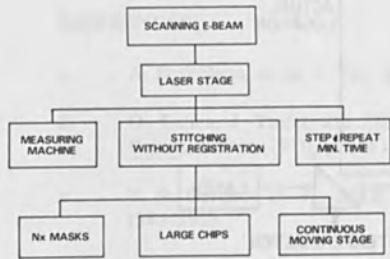


Fig. 3. New Options for Scanning Electron Beam Lithography

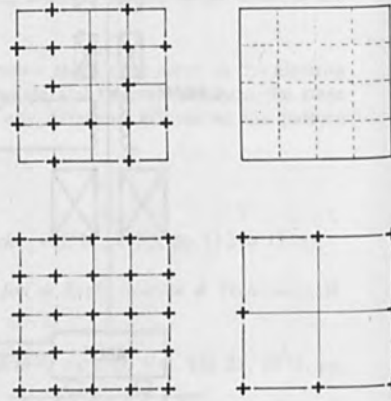


Fig. 4. Fabrication of large patterns from a group of small sub-fields by registration and LISS stitching.

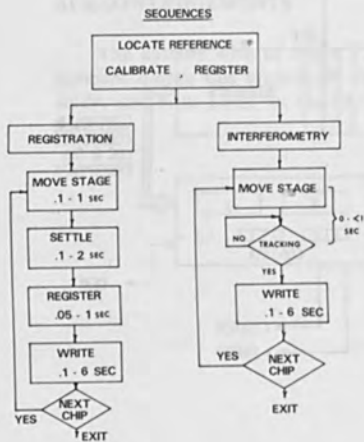


Fig. 5. System Sequences in Pattern Stitching by Registration and LISS.

THRUPUT EXAMPLE

ASSUME

- 1 CM SQUARE CHIP OF 1 MICRON LINES
- 25 - 2mm SQ. REGISTRATION SUBFIELDS
- 400 - 0.5 mm SQ. INTERFEROMETRY SUBFIELDS
- 2 cm sec PEAK STAGE VELOCITY
- 20 MHz WRITE RATE AT 30% COVERAGE
- 0.2 SEC REGISTRATION TIME FIELD
- 0.4 SEC STAGE MOVE FOR 2 mm
- 0.05 SEC STAGE MOVE FOR 0.5 MM

	LISS	REGISTRATION
REG. TIME	0	5 SEC
STAGE MOVE	(20 SEC)	10 SEC
WRITE TIME	25 SEC	25 SEC
TOTAL	25 SEC	40 SEC
OVERHEAD/WRITE	0%	60%

Fig. 6. Thruput with Stitching, An Example

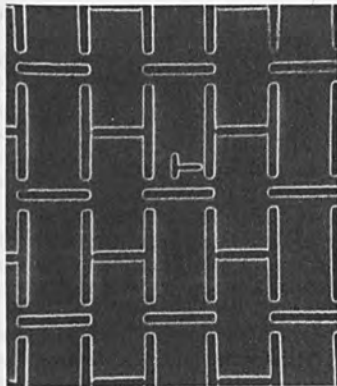


Fig. 7. Section from a two centimeter square laser stitched chip made from 40 by 40 array of 0.05 cm square subfields, 1 micron lines/gaps.

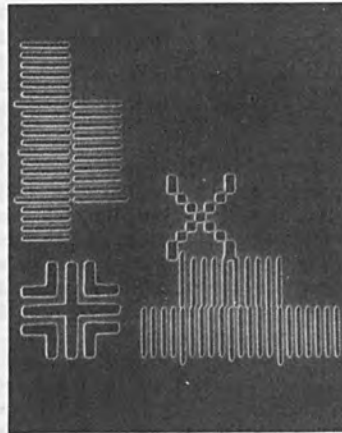


Fig. 8. Vernier test pattern, 0.1 micron sensitivity.

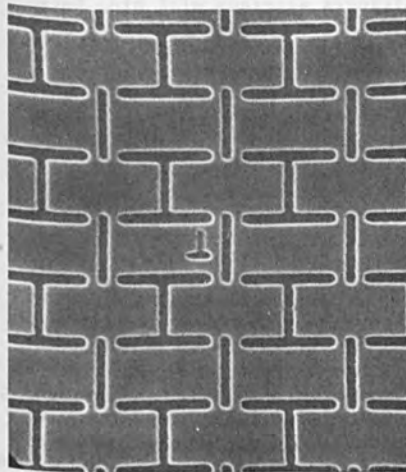


Fig. 9. Section from a one centimeter square laser stitched chip, 1/2 micron lines/gaps.

ITEM	COMPARISONS		REGISTRATION
	LISS	VS	
SUBSTRATE PREPARATION	FEWER MARKS, 0.1°C		REGISTRATION MARKS NO SPECIAL TEMPERATURE
MARKS	NONE	VS	FULL COVERAGE
SINGLE LEVEL PATTERNS	REF. MARK	VS	FULL COVERAGE
OVERLAID MULTILEVELS			
THRUPUT	BETTER		
CHIP SIZE	UNLIMITED	VS	2X SINGLE FIELD SIZE
NO INTERIOR MARKS	0%	VS	0.05
MARK OCCUPANCY			
FIELD SIZE	INDEPENDENT OF CHIP AND SMALLER		USUALLY 1/3, 1/2, ETC OF CHIP
DISTORTION CORRECTION	USUALLY NONE	VS	AMOUNT DEPENDING ON FIELD SIZE
STITCHING ACCURACY	-0.1 - TYPICAL	VS	0.05 to .12 - TYPICAL
FLAT SUBSTRATES		EQUAL	
NON-FLAT, DISTORTED SUBSTRATES	KEYSTONE ERRORS	VS	LOWER 2nd ORDER ERRORS

Fig. 10. A comparison of stitching by registration and LISS.

USE OF SIMULATION TO OPTIMIZE PROJECTION PRINTING PROFILES

A. R. Neureuther, M. O'Toole, W. G. Oldham and S. N. Nandgaonkar
Department of Electrical Engineering and Computer Sciences
and the Electronics Research Laboratory
University of California, Berkeley, California 94720

ABSTRACT

A user oriented computer program for the "Simulation and Modeling of Photolithography and Etching" (SAMPLE) is used to explore some of the important parameters in projection printing. The photolithography portion of program SAMPLE is based on an exposure-bleaching development-etching model for positive photoresist. Studies of resist-oxide thickness variations show that typically the critical exposure can change by $\pm 16\%$ for resist alone and by $\pm 29\%$ for resist and oxide. Mask linewidth compensation is shown to be feasible but less important than controlling resist and oxide thickness. Defocus shows resist profile degradation even at one Rayleigh defocus unit. Underfilling the entrance pupil is treated approximately and shows a significant improvement in the resist edge slope and line edge ripple. Parameters for single wavelength exposure at 4358A with a numerical aperture of 0.28 are used.

I. INTRODUCTION

As linewidth is reduced in photolithography the shape of the resist line edge profile becomes increasingly important. Computer simulation can be used to study resist profiles in developing technology for high resolution lithography. A user oriented computer program for the purpose of "Simulation and Modeling of Photolithography and Etching" (SAMPLE) is being developed at the University of California at Berkeley. In this paper SAMPLE is used to explore some of the important parameters in projection printing. The structure and operation of the program is summarized only briefly as the details are being made available elsewhere (1).

Four basic considerations are explored from the point of view of their impact on the resist line edge profile. The first is the impact of standing waves in the oxide and resist layers. They primarily affect the required exposure and also influence the resist linewidth at the oxide interface. The second area is the possibility of correcting mask linewidth to compensate for degradation of the intensity pattern which occurs during imaging. These effects are pattern dependent and are most pronounced for opening narrow lines in the resist. The change of the resist profile as a function of wafer displacement from the focal plane is the third aspect. It indicates the critical importance of wafer flatness. Finally, the improvement in resist edge quality possible through the underfilling of the entrance pupil of the lens is considered.

II. PROGRAM SAMPLE

The approach used in the lithography portions of program SAMPLE is similar to the earlier work (2-9). A new organizational scheme and a new development algorithm are the most noteworthy features. SAMPLE is built around a machine concept in that the profile being processed is viewed as a wafer moving from machine to machine. The machines are operated by a controller which is interfaced to the user through an input interpreter. All parameters have default values so that only modified values need be input specified.

The first machine of the simulator calculates the horizontal intensity profile for one of three possible mask patterns: an isolated line, an isolated space, or a pattern of periodic lines and spaces. The method of optical transfer functions is used in which the amplitude of the spatial frequencies of the mask are weighted by the modulation transfer function (mtf) of the lens. The mtf of the projection optical system can be inputted directly or calculated from various parameters and conditions. Examples are the numerical aperture (NA) and defocus distance in Rayleigh quarter-wave units ($\delta = (\lambda_0)/(2(NA)^2)$). Partial coherence or underfilling the entrance pupil is treated in an approximate manner in the framework of the mtf approach.

The second machine treats multiple reflection or standing wave effects which occur in the vertical direction. These constructive and destructive interference effects result in large intensity variations vertically throughout the resist and oxide layers. A multi-layer thin film analysis algorithm is used (10). In the analysis the resist layer itself is typically divided into 50 sublayers. The optical absorption of each sublayer is allowed to change in accordance with the accumulated absorbed energy throughout the exposure. This allows bleaching to occur during the exposure process.

The horizontal and vertical intensity effects are combined in the third machine. This combination is only approximate in that it assumes all rays are vertical in the resist. Actual rays which make up the projected image are nearly vertical and upon entering the resist they bend further toward the vertical. Although this assumption is not absolutely necessary, it greatly reduces the computation time required compared to that for a rigorous solution of the time-varying electromagnetic boundary value problem.

The resist development in the fourth machine is based on a string development algorithm (11) which models the resist developer interface as a moving string of line segments. The output contours are the nodes on the string. Segments shorter than $.03\mu\text{m}$ are typically required.

Many physical parameters are required in the simulation. The work here is for a single wavelength exposure at 4358\AA . The resist parameters for AZ1350J reported by Shaw and Hatzakis (12) for this wavelength are $A = .551$, $B = .058$, $C = .010$. The development parameters for AZ 1:1 developer at 20°C are $E1 = 5.63$, $E2 = 7.43$ and $E3 = -12.6$.

The refractive indices of the oxide, silicon and resist are 1.47, 4.73-j.14 and 1.68-j ($\lambda(M+B)/(4000\pi)$) respectively. Here M is the inhibitor concentration (2).

An example of a simulated output profile is shown in Figure 1. Here 0.94 μm of resist over 0.068 μm of oxide has been exposed in an optical system with a numerical aperture of 0.28 and a partial coherence factor of $\sigma = 0.7$. The mask was an equal line and space with a 3.0 μm pitch. The development contours are for 15 sec intervals. The standing wave fingers are at the half wavelength spacings in the resist (.13 μm). The fingers are due to destructive interference nulls which produce little exposure and a low etch rate.

The parameters for Figure 1 were chosen to represent the experimental conditions under which the SEM in Figure 2 was produced. The simulated profile shows the same basic features and kinds of effects. However certain experimental parameters (dose and resist prebake conditions) were not carefully determined and a detailed quantitative comparison is not possible. The slope and position of the ripples are in good agreement between simulation and experiment. However, the size of the edge ripple is apparently exaggerated in the simulation, as is the sharpness of the fringes.

III. APPLICATION STUDIES

To choose a nominal exposure and development condition for the investigation a procedure similar to that used in the laboratory was conducted. A sequence of exposures were made to determine a critical exposure dose such that large areas open in 30 sec of development. The critical dose thus determined is called D₃₀. In practice we might typically develop for twice as long, 60 sec, in order to be reasonably assured of clearing small spaces.

The critical dose D₃₀ is a strong function of resist and oxide thickness. This sensitivity stems from two phenomena: (1) the impedance matching properties of the resist/oxide layers depend sensitively on the total optical thickness of the films (as well as average index) and (2) the position and number of standing waves in the resist depend sensitively on the optical thickness of the layers under the resist. A minimum of intensity occurs at the silicon interface and repeats periodically at $\lambda/2$ intervals. At intervening positions shifted by $\lambda/4$ a maximum occurs. Thus for any position in the resist maximum or minimum intensity occurs when the effective optical thickness of the underlying material is $((N\lambda/2) + (\lambda/4))$ or $(N\lambda/2)$ respectively.

The extrema of the variations of D₃₀ tend to occur when a maximum or minimum of the standing wave occurs at the air or oxide interface. This is primarily because the resist and oxide layers tend to provide impedance matching for the highly reflective silicon surface. The matching is best for a total resist and oxide optical thickness of $(N\lambda/2 + \lambda/4)$ or a maximum at the air interface. Very little impedance

matching occurs when the total optical thickness is $N\lambda/2$ or a minimum occurs at the air interface. For example, for zero oxide thickness Figure 3 shows that in going from a minimum condition of $0.7778\mu\text{m}$ of resist to a maximum $0.8427\mu\text{m}$, D_{30} decreases from 125 mJ/cm^2 to 90 mJ/cm^2 .

The introduction of an oxide layer which has a slightly lower refractive index can result in an even larger variation in the critical dose D_{30} . The special case of replacing $\lambda/2$ of resist ($.1293\mu\text{m}$) with $\lambda/2$ of oxide ($.1479\mu\text{m}$) which produces a minimum at the oxide interface should have little effect from an impedance matching point of view. The result in the second column show that this is indeed the case. For both total optical thickness cases D_{30} decreases only slightly. The slightly decrease is primarily due to the fact that the resist thickness has been reduced. These two cases will be referred to as MAX-MIN and MIN-MIN where the first and second parts of the label indicate the intensity of the standing wave at the air and resist interface respectively.

Replacing $\lambda/4$ of the resist ($.645\mu\text{m}$) with $\lambda/4$ of oxide ($.0737\mu\text{m}$) produces a maximum at the oxide interface and strongly affects the impedance matching. For a total optical thickness of $(N\lambda/2 + \lambda/4)$, the $\lambda/4$ of the oxide acts as a quarter wave transformer and a maximum occurs both at the air and resist interface (MAX-MAX). Since the refractive index of the oxide (1.47) is smaller compared to $\sqrt{4.73}$ than the refractive index of the resist (1.68), the matching is not as good. As a result D_{30} increases slightly from 90 mJ/cm^2 for no oxide to 95 mJ/cm^2 even though the resist thickness is reduced.

When the total optical thickness is $N\lambda/2$ a minimum and maximum occur at the air and oxide interfaces (MIN-MAX). Quarter wave transform effects occur in both the resist and oxide. The impedance transformation in the resist basically reverses the impedance transformation in the oxide. The ordering of the refractive indices in moving away from the silicon surface is not monotonically decreasing and as a result the opposing quarter wave transform effects introduce an even larger impedance mismatch. This requires a higher D_{30} of 145 mJ/cm^2 . It is interesting to note that the two extreme values of the critical dose (MIN-MAX) and (MAX-MIN) occur for essentially the same resist thickness. This further emphasizes that impedance matching is the dominant factor in resist and oxide thickness effects.

From the critical dose data a single, nominal dose of 120 mJ/cm^2 and development for 60 sec was chosen for studying line edge profile effects. An equal line and space pattern with $3.0\mu\text{m}$ pitch was then exposed and developed for each of the four oxide and resist thickness cases. The profile for the MAX-MIN case is shown in Figure 4. Note that the maximum at the air interface and finite contrast result in some thickness loss at the top in the normally unexposed area. More importantly the intensity minimum at the oxide interface results in a thin finger of resist along this interface. The MIN-MAX profile is given in Figure 5. Less thickness loss occurs, but a rapid undercutting occurs at the oxide interface. Around the

nominal linewidth position (.75 μ m), the lateral etching in the MIN-MAX case is moving more rapidly than in the previous MAX-MIN case. This represents an increased sensitivity to development time and may offset the advantage of the MIN-MAX case in having a low sensitivity to small oxide thickness variations (13).

The dose sensitivity of the four oxide and resist thickness cases is considered in Figure 6. Here the half-linewidth at the oxide-resist interface is plotted as a function of dose. Generally, considerable over etching occurs indicating that the procedure which was chosen to open small spaces produces thinning of small lines. The cases where an intensity maximum occurs at the oxide interface tends to have a steeper slope and is more sensitive to the dose. The spread in linewidth between the various thickness conditions is rather large. Actual profiles would probably not have such a large variation since the experimental finger length is shorter than the simulated finger length.

The resist opening linewidth at the oxide interface is not in general the same as the original mask linewidth. For example the slight over exposure and development which was chosen to clear small spaces would likely produce a constant offset between resist and mask linewidth. More importantly for small linewidths the limitations of the optical system reduce edge slope and contrast of the projected intensity profile. The proximity of nearby patterns also modifies the intensity profile. Resist and mask linewidth data which reflect these effects are shown in Figure 7. Here the resist linewidth is defined as the width of the resist opening at the oxide interface. The interconnected data points are for equal lines and spaces. The individual points are for isolated lines. For a given resist and oxide thickness the deviation from the equal resist and mask linewidth line is fairly constant. At 1.5 μ m, isolated lines are slightly narrower than equal line and space patterns due to a higher background intensity. This effect is however less significant than the linewidth variations introduced by resist and oxide thickness effects.

Depth of focus becomes a critical problem as the resolution is improved. This is because the depth of focus decreases as the square of the improvement in resolution. For example, for a NA of .28 at 4358 \AA , the 60% mtf of a diffraction limited lens occurs at an equal line and space pattern of $L = .78 (\lambda_0)/(NA) = 1.2\mu\text{m}$. The corresponding Rayleigh quarter wave criterion for depth of focus is $\delta = (\lambda_0)/(2(NA)^2) = 2.8\mu\text{m}$. Wafer flatness can easily be on the order of the depth of focus unit and it is important to consider how the line edge profile degrades with wafer height variations. In Figure 8 the effect of wafer locations of 0, 1.5 and 3.0 μ m from the focal plane are shown. While the case chosen is the most sensitive one, it is clear that degradation of resist profiles can be substantial at one Rayleigh defocus unit.

The very strong decrease of the depth of field with numerical aperture raises the question of optimization of numerical aperture for maximum useful resolution on non-flat wafer. Figure 9 shows how

an equal line and space pattern with $5\mu\text{m}$ pitch degrades with wafer height for an optical system with NA of .28. The corresponding profiles for NA = .167 are shown in Figure 10. The profiles of Figure 10 while not as vertical behave more uniformly with large wafer height variations. Thus it appears better to adjust the minimum F/number in accordance with wafer flatness than to attempt to always operate a high resolution lens at its minimum F/number.

It is well-known that underfilling the entrance pupil which is often referred to as partial coherence can be used to improve optical system performance. This will no doubt affect the resist line edge profile. An approximate approach was used to estimate the significance of partial coherence effects on resist profiles. The approach makes the approximation that an effective mtf can be used where the mtf is constructed from overlapping two circles of unequal radii. The ratio of the radii is referred to as the degree of partial coherence σ (14).

Results of the approximate simulation of partial coherence are shown in Figure 11. Reducing σ from 1 to .7 tends to increase resist edge slope and reduce the ripple. These improvements are primarily due to the increased edge slope of the image intensity. The approximate model indicates that partial coherence effects may be quite significant. A more rigorous model of partial coherence is presently under development.

IV. CONCLUSION

Application studies using "Simulation and Modeling of Photolithography and Etching" (SAMPLE) indicate that for single wavelength exposure at 4358\AA resist-oxide thickness variations can change the critical exposure by $\pm 16\%$ for resist alone and by $\pm 29\%$ for resist and oxide. The greatest sensitivity to resist thickness occurs for about 700\AA or a quarter wave of oxide. Rapid underetching is also associated with this oxide thickness. Mask linewidth compensation to obtain the correct linewidth is feasible but not as important as controlling resist and oxide thickness. Defocus effects can significantly degrade the resist profile at one Rayleigh defocus unit. It appears best to stop down the lens such that wafer height variations remain within one Rayleigh defocus unit and sacrifice infocus resolution. The underfilling of the entrance pupil of the lens, may significantly effect resist edge slope and line edge ripple. It may also affect focus tolerance in a positive sense.

V. ACKNOWLEDGEMENT

Research sponsored by the National Science Foundation Grant ENG77-14660 and by an industrial Grant from Hughes Aircraft, Signetics (U.S. Phillips) and Intel Corporations.

- (1) W. Oldham, S. Nandgaonkar, A. Neureuther, M. O'Toole, "A General Simulator for VLSI Lithography and Etching Processes. Part I-Applications to Projection Lithography," to be submitted to IEEE Transactions on Electron Devices, VLSI issue.

- (2) F. H. Dill, "Optical Lithography," IEEE Trans. Elec. Dev., ED-22, No. 7, pp. 440-444, July 1975.
- (3) F. H. Dill, W. P. Hornberger, P. S. Hauge, and J. M. Shaw, "Characterization of Positive Photoresist," IEEE Trans. on Electron Devices, Vol. ED-22, No. 7, pp. 445-452, July 1975.
- (4) F. H. Dill, A. R. Neureuther, T. A. Tuttle, and E. J. Walker, "Modeling Projection Printing of Positive Photoresist," IEEE Trans. Electron Devices, Vol. ED-22, No. 7, pp. 456-464, July 1975.
- (5) M. A. Narasimhan, "Simulation of Projection Printed Images in Positive Photoresist," Proceedings of the Winter Symposium '75 on Micro-Photofabrication," SPSE, February 1975.
- (6) M. A. Narasimham, "Projection Printed Images in Positive Photoresists Under Partially Coherent Optics," SPSE Conference on Image Analysis and Evaluation, July 1976, Toronto, Canada.
- (7) M. A. Narasimham and F. H. Dill, "Projection Printed Photolithographic Images in Positive Photoresists Under Polychromatic Exposures," SPSE 30th Annual Conference, May 1977, North Hollywood, California.
- (8) M. A. Narasimham and J. H. Carter, Jr., "Effects on Defocus on Photolithographic Images Made with Projection Printing Systems," SPIE Proceedings Semiconductor Microlithography III, 1978, to be published.
- (9) A. Brochet, G. Dubroeuq, "Modeling of positive resists - application to the projection of thin structures on silicon," Proceedings of the International Conference on Microlithography, Paris, France, June 1977.
- (10) P. H. Berning, "Theory and Calculations of Optical Thin Films," Physics of Thin Films, Vol. 1, Academic Press, New York, 1963.
- (11) R. E. Jewett, P. I. Hagouel, A. R. Neureuther, and T. Van Duzer, "Line-Profile Resist Development Simulation Techniques," Polymer Engineering and Science, Vol. 14, No. 6, pp. 381-384, June 1977.
- (12) J. M. Shaw and M. Hatzakis, "Performance Characteristics of Diazo-Type Photoresists Under e-Beam and Optical Exposure," Trans. of IEEE on Electron Devices, ED-25, No. 4, pp. 425-430, April 1978.
- (13) J. B. Cuthbert, "Optical Projection Printing," Solid State Technology, pp. 59-69, August 1977.
- (14) M. Hugues, M. Babolst and P. Tigrest, "Lenses for Microelectronics", and "Use in a Photodemagnifier," Proceedings of the International Conference on Microlithography, Paris, France, June, 1977.

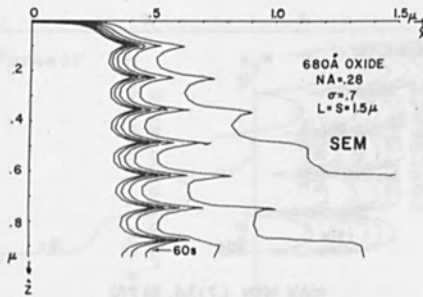


Figure 1. Simulated resist profile with 15 sec development contours.

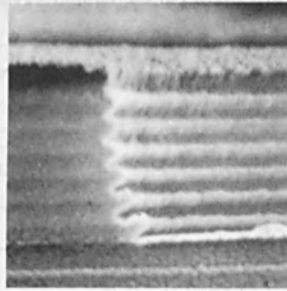


Figure 2. SEM of projection printed resist profile in AZ1350J.

		OPTICAL THICKNESS OF OXIDE		
		NONE	MIN	MAX
		0	1/2	1/3
TOTAL	MIN	$r_0(\mu)$.7778	.6485
OPTICAL		$r_0(\mu)$	—	.3478
THICKNESS		$D_{30}(\text{mJ/cm}^2)$	125	145
OF				
RESIST	MAX	$r_0(\mu)$.9427	.7134
AND		$r_0(\mu)$	—	.3478
OXIDE		$D_{30}(\text{mJ/cm}^2)$	90	95

D_{30} = DOSE TO CLEAR LARGE AREA IN 30 SEC. OF DEVELOPMENT.

Figure 3. Critical dose required to open large spaces in 30 sec development for various oxide and total resist and oxide optical thicknesses.

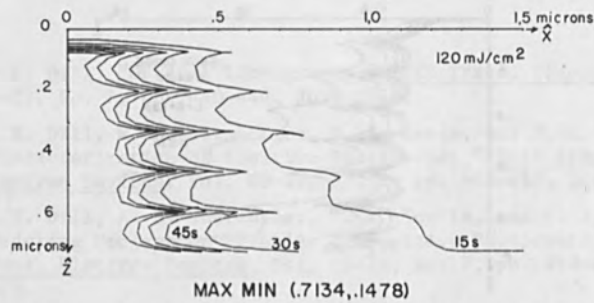


Figure 4. Resist profile for a maximum and minimum intensity at the air and oxide interfaces respectively.

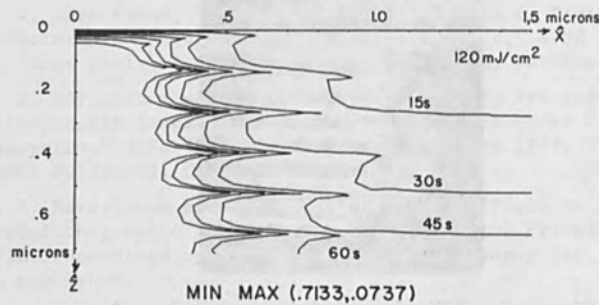


Figure 5. Resist profile for a minimum and a maximum intensity at the air and oxide interfaces respectively.

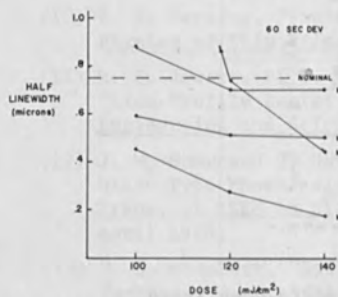


Figure 6. Dose sensitivity for the four oxide and resist thickness of Figure 3.

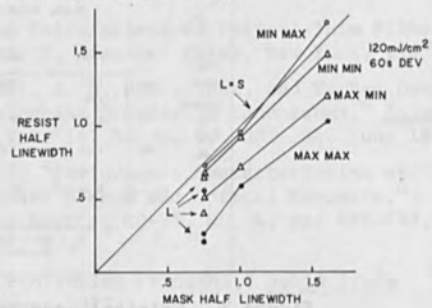


Figure 7. Resist half linewidth as a function of mask half linewidth. units are μm .

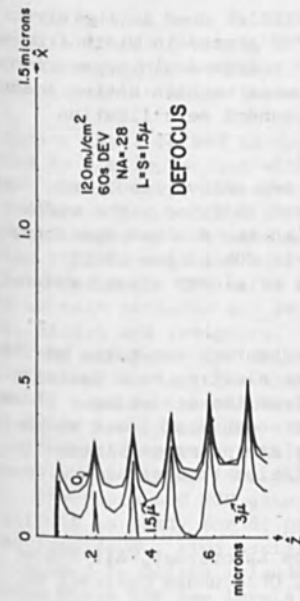


Figure 8. Resist profiles for a 3.0µm equal line plus space with defocusing at NA = 0.28.

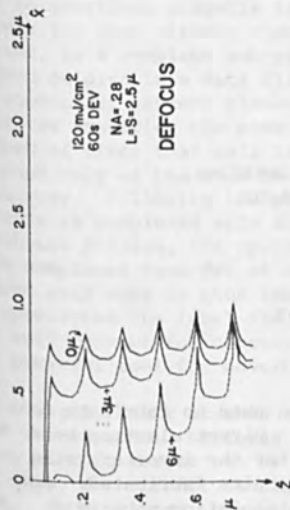


Figure 9. Resist profiles for a 5.0µm equal line plus space with defocusing at NA = 0.28.

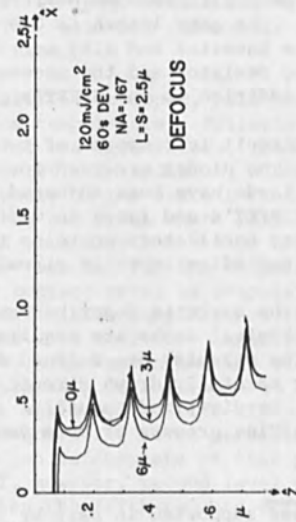


Figure 10. Resist profiles for 5.0µm equal plus space with defocusing at NA = 0.167.

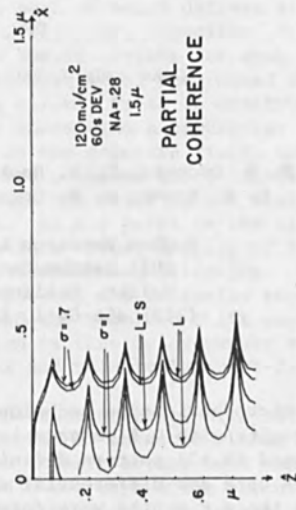


Figure 11. Resist profiles for a 3.0µm equal line plus space with partial coherence.

ELECTRON BEAM MICROFABRICATION

OF

GaAs INTEGRATED CIRCUITS*

F. S. Ozdemir, L. H. Hackett, P. T. Greiling,
C. F. Krumm, O. W. Otto and R. F. Lohr

Hughes Research Laboratories
3011 Malibu Canyon Road
Malibu, California 90265
(213) 456-6411, Extension 303

Electron beam microfabrication techniques have been used to fabricate GaAs integrated circuits with 0.5 μm gate length SBFET. Direct electron beam exposure was used in all pattern definition steps for the inverter, ring oscillator, NOR gate and differential amplifier circuits fabricated. Active layers for these circuits were formed in semi-insulating substrate by ion implantation.

The Schottky barrier field effect transistors (SBFET's) used in the circuits operate as depletion mode devices. The SBFET's vary in width from 10 to 50 μm 's. The gate length is 0.5 μm and the source-drain separation is 3.0 μm . The inverter and ring oscillator circuits contain active loads, diodes, probing resistor and the necessary interconnect metallization structures in addition to the SBFET's.

The inverter circuit is composed of two SBFET's, two active loads and three diodes. The diodes are used for output level shifting. The width of the active loads have been adjusted to establish the desired operating points in the SBFET's and range in width from 50 to 80% of the SBFET width. The ring oscillators contains three, five or eleven stages and are formed by cascading inverter circuits.

In developing the circuits described here, full advantage was taken of the fact that no physical masks are required in direct electron beam pattern definition. The circuits are defined digitally from the beginning. There is no need for carefully drawn circuit layouts for each mask level which must, in turn, be digitized manually. Thus there are no errors introduced by a drafting process or by a manual translation to digital.

* This work was supported in part by the Avionics Laboratory, Air Force Systems Command, Wright-Patterson Air Force Base, Ohio under Contract No. F33615-76-C-1214, Lutz Micheel, Contract Monitor.

A special computer program was employed at an interactive graphics terminal to construct circuits from "cells", each of which defines all mask levels for each circuit element, be it a resistor, capacitor, diode, transistor, or a complete sub-circuit. The specifications for each cell are stored on disc in a data file, with each mask level determined by a set of elementary pattern elements. When a circuit is to be constructed, the operator specifies the name of the file containing a particular cell, the number of times that cell is to appear in the exposure field, the location of each copy of the cell in the field, and a unique label identifying each copy. Following the placement of all the cells in the field, the circuit is completed with interconnects. At any point in the circuit synthesis process, the operator may obtain a visual display of the circuit completed thus far at any desired level of magnification. A misplaced cell copy is thus immediately apparent, and is easily repositioned by specifying the label for that copy and the required shift coordinates. The cell concept for circuit construction is thus an extremely efficient and powerful tool for developing complex and relatively error-free designs.

The overall result of this approach to pattern generation is extremely fast turn-around. Patterns can be corrected or enhanced within one day. A new circuit layout can be verified (at 1X with actual test exposures) and ready for circuit fabrication two to three days after circuit definition. We have used this approach to pattern generation extensively in the work reported in this paper.

The circuits that were fabricated utilize six mask levels. They are: a) mesa, b) ohmic contact, c) gate, d) first level metallization, e) insulation, f) second level metallization. The following summarizes the fabrication process in which these masks are used.

The active layer formed is specially qualified Cr doped, bulk-grown substrates by ion implanting with Si at room temperature. Following an implant anneal step, the mesa patterns for the transistors, loads, diodes, and resistors are exposed in electron resist. In addition, a set of alignment marks are defined at the periphery of the circuit field. A wet etching step removes the active layer from all areas where patterns have not been defined. The wafer is recoated with electron resist and the ohmic contact patterns are registered and exposed for the transistors, loads, diodes and resistors. The ohmic contact metal is evaporated, lifted off and alloyed. The third pattern definition step defines the 0.5 μm gate patterns for all the transistors and load devices. Lift-off metallization is used for these structures also. The fourth masking step is composed of low resolution structures such as 5 μm interconnect lines and (50 μm)² contact pads. Metallization is again by the lift-off process. In cases where circuit design does not require two level metallization (e.g., inverters and NOR gates) fabrication is complete at this point and the circuit is ready for dc probing. If, however, second level metallization is required (e.g., ring oscillators), then the fifth pattern definition step is used to define islands of deposited SiO₂ by the lift-off process in areas where the two levels of metallization meet each other. The sixth

and final masking step defines, again by lift-off metallization, the second level metallization consisting of low resolution structures similar to the first level metallization patterns. At this point the circuit is ready for dc probing. Circuits selected for RF measurements are cut out of the wafer and mounted on a co-planar waveguide board. Thermo-compression wire bonding with 0.7 mil Au wire establishes the necessary electrical connection between the circuit chip and the waveguide board.

In addition to the circuits, a series of test structure patterns were incorporated into the processing. These structures were designed to provide dc electrical feedback from the changes made in the semiconductor processing. The test structures occupy three pattern or circuit fields and contain the following devices and structures:

- a) Variable length and variable gap ohmic contact;
- b) Interconnect metallization series resistance;
- c) Gate series resistance;
- d) Variable length resistors;
- e) Variable area interdigitated diodes;
- f) Hall pattern;
- g) Variable width individual transistors;
- h) Sections of the inverter circuit with variable width devices and provisions to individually probe all circuit elements within the inverter.

DC electrical measurements made on the test structures were used to establish and maintain the desired semiconductor processing baseline and to provide input to the circuit modeling and design efforts.

Figure 1 shows four 2-input NOR gates fabricated in a $(1 \text{ mm})^2$ scanfield. All FET's and diodes are $50 \mu\text{m}$ wide and the two load transistors are 25 and $40 \mu\text{m}$ wide. Figure 2 shows a magnified view of one of the NOR gates. All gate lengths are $0.5 \mu\text{m}$.

Figure 3 shows a five stage ring oscillator circuit. The sequence of inverter stages have been folded around in the design to minimize the signal path length. In addition to the five stages, an additional inverter stage was included to buffer the ring oscillator from the probing resistor used to measure the oscillation frequency. Figure 4 shows a detail of the central portion of the ring oscillator. Signal propagation is from left-to-right in the top half and from right to left in the bottom half of the figure.

Figure 5 is a scanning electron microscope photomicrograph of the channel area of one of the FET's fabricated by direct electron beam microfabrication. The figure shows the $0.5 \mu\text{m}$ length gate structure on the FET mesa and its transition off of the mesa to the interconnect metallization. The source and drain can be seen in their alloyed form on both sides of the gate.

Large signal switching characteristics of the inverter were measured. DC characterization has shown an output swing of 0 to -2 volts for a corresponding -2 to 0 volt input swing. High frequency measurements of the large signal switching characteristics of the inverter showed no degradation in the frequency out to 5 GHz.

Three stage ring oscillators were also measured. The oscillation frequency for the three stages was 7.4 GHz which translates to a propagation delay per stage of 45 picoseconds. The associated power dissipation per stage was 78 milliwatts. Thus the speed-power product is approximately 3.5 picojoules.

In conclusion, electron beam microfabrication techniques have been applied to ion implanted GaAs substrates to realize the fastest room temperature digital switching circuits that have been reported to date.

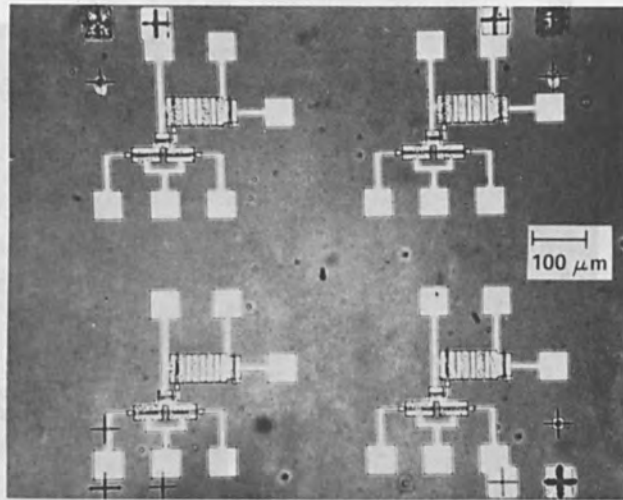


Fig. 1. Four 2-Input NOR Gates Fabricated in a $(1 \text{ mm})^2$ Scanfield.

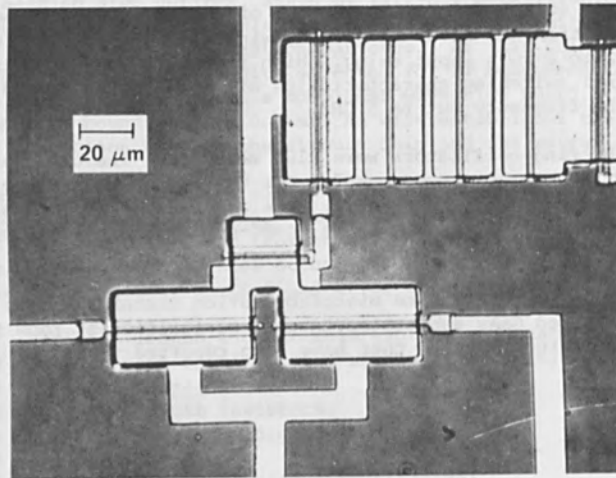


Fig. 2. Detail of Four NOR Gate Pattern Showing One of NOR Gates.

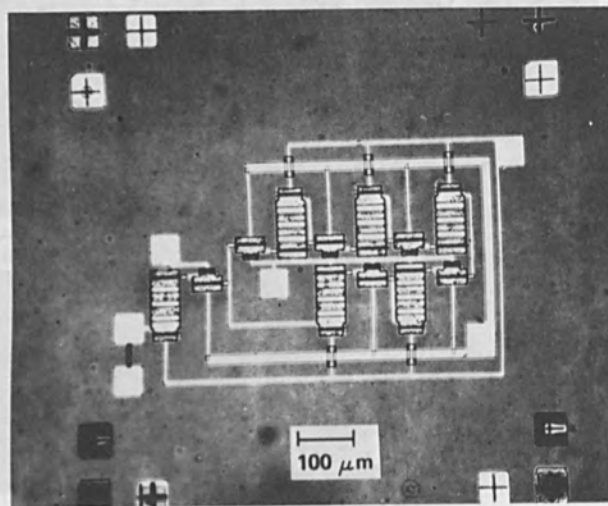


Fig. 3. Five-Stage Ring Oscillator Circuit With Output Stage and Probing Resistor.

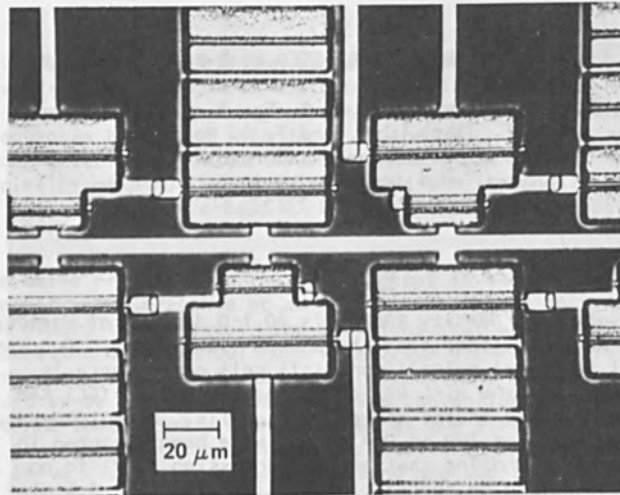


Fig. 4. Detail of Five-Stage Ring Oscillator Circuit.

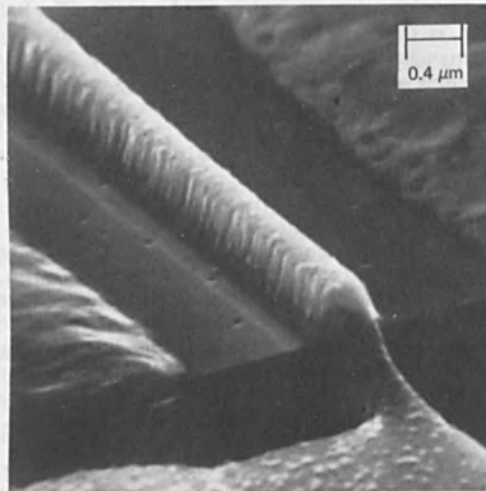


Fig. 5. Scanning Electron Photomicrograph Showing The 0.5 μ m Gate, Source/Drain Boundary and Mesa Edge of One of the FETs in the Five-Stage Ring Oscillator Circuit.

HIGH DENSITY RAM CELLS FABRICATED BY E-BEAM LITHOGRAPHY

Pallab K. Chatterjee, H-S. Fu, R. L. Easley,
A. F. Tasch, Jr., and T. C. Holloway
Central Research Laboratories
Texas Instruments Inc.
Dallas, TX 75222

ABSTRACT

Very high density RAM cells ($0.1-0.3 \text{ mil}^2$) of various kinds have been fabricated by e-beam lithography. Conventional two-level polysilicon (I-T) cell performance is compared with the Hi-C RAM cell, charge coupled (CC) RAM cell and merged charge memory (MCM) cells. Room temperature leakage rates as low as 0.4 nA/cm^2 have been measured in these cells, showing that e-beam processing leads to no residual damage or degradation of lifetime. The 0.1 mil^2 cells correspond to packing densities of 10 million bits per square inch.

The MCM cell has a smaller charge capacity and higher leakage at room temperature compared to the CC, HiC and I-T cell, and is more susceptible to read out errors due to word line feed through and bit pattern. It has, however, a small activation rate of leakage because diffusion components of leakage are effectively cut off. The activation rate of leakage of the CC RAM cell is also found to be smaller than the (I-T) cell, because the diffusion components are minimized.

The trend toward lower cost per bit, and higher performance memories has driven various integrated circuit technologies to very high density. The dynamic Random Access Memories (dRAMs) have evolved in the past few years to densities of 16Kbits per chip in routine production today with 65Kbit dRAMs being developed by various semiconductor houses. The evolution of the dynamic RAM has been principally due to two main factors. First, the lithography techniques have been refined continuously to where we may optically print $3-4 \mu\text{m}$ geometries with $\pm 1 \mu\text{m}$ level-to-level registration routinely over 3" diameter silicon wafers. Second, clever memory cell designs have simplified the cell structure thereby increasing the packing density.

In this paper we have compared the performance of various new cell design concepts with the conventional one-transistor-one-capacitor I-T cell used in dRAMs today. Electron beam lithography provides the attractive capability of small geometry patterning and accurate level-to-level registration and has been used to fabricate the 0.1 mil^2 ($65 \mu\text{m}^2$) cells. This demonstrates that advanced dynamic MOS

devices using multilevel silicon gates and metallization may be fabricated in an e-beam compatible process. Since dynamic MOS devices are very sensitive to the damage created by e-beam radiation, proper anneal sequences have been introduced in the process. The excellent leakage characteristics of our dynamics RAMs ($\sim 0.4 \text{ nA/cm}^2$) and the characteristics of n-MOS devices fabricated simultaneously clearly indicate that the use of e-beam lithography will not degrade the performance of these devices.

The basic principle in the dRAM concept is the storage of a charge packet. The presence or absence of the charge packet constitutes the binary information. The functions that are essential to the useful operation of a RAM cell are a) storage element to store charge, b) address element to select the cell, c) read and d) write elements to read in and sense the charge packet. The conventional I-T cell (1) used in dRAMs today uses a MOS capacitor as the storage element, a MOS pass transistor as the address element and a diffused source/drain to serve the dual purpose of reading and sensing the charge packet. The cross-section of a conventional nMOS dRAM cell is shown in Figure 1. In normal operation the storage electrode is held at a positive potential. The transfer gate (or address line) is held at or near ground potential in the store mode. This creates a potential well under the storage gate which may be filled with electrons to serve as a charge packet. The information is written into the cell by holding the bit/sense line high [1] or low [0] and turning the address gate high. To "read" the charge packet the bit line is floated at a high positive potential and the word line is pulsed high. The change in the word line voltage due to the charge packet is detected as the signal.

A charge storage cell of this kind utilizes a non-equilibrium condition under the storage gate. Minority carriers generated in or near the vicinity of the depletion region under the storage electrode are collected as leakage charge in the storage well. Data in the storage well must therefore be periodically refreshed in order to avoid errors.

The two major parameters which determine the quality of a dRAM cell are the size of the charge packet and the leakage rate. Comparison of the performance of various cell structures will be based on these two figures of merit.

Historically, the improvements in packing density have been realized both by shrinking dimensions and invention of cell structures with fewer elements. Recently two different cell structures have been reported which merge two of the three major elements of the I-T cell.

The charge coupled (CC) RAM cell (2) merges the transfer line and the storage gates into a single gate as shown in Figure 2(a).

The storage portion of this cell contains a shallow n-type implant which acts as a positive Q_{SS} and shifts the threshold to depletion mode and deep p-type implant which increases the body effect. The surface potential vs. gate voltage curves of the storage and transfer region are shown in Figure 2(b). When the gate is held at or near ground potential the surface potential in the storage region is higher than that in the transfer region so that charge may be stored. When the gate electrode is pulsed high, the transfer region potential becomes higher than the storage region potential and charge may be read in or out. The charge capacity of this cell under high density scaling conditions has been shown to approach that of the I-T cell (3). Although this structure is conceptionally simple to fabricate compared to the I-T cell, it requires a critical alignment at the edge of the implants which forms the boundary between the storage and transfer gates. It is essential that the edge of the p-type implant be contained inside the n-type implant in order that the cell may operate as described above. The critical registration capability of the e-beam is thus ideally suited for the fabrication of this structure.

The Hi-Capacity (Hi-C) RAM cell structure shown in Figure 3 combines the I-T operation with the CC RAM cell concept to increase the charge storage capacity. The storage area is selectively implanted to increase the substrate doping whereby the depletion capacitance is increased, and adds to the charge storage capacity provided by the oxide capacitance. However, this increased capacity decreases the potential swing at the Si/SiO₂ interface so that the net charge stored is not increased. The potential swing may be restored if a shallow n-type implant is performed to act as a positive Q_{SS} . This cell has the same complexity as the I-T cell, but has twice the charge packet size, so that it may be laid out in a smaller area, thereby improving the packing density.

The merged charge memory (MCM) cell (5) combines the bit store and sense (BSS) functions on a single capacitor electrode as shown in Figure 4. Parallel to every N of these BSS lines is a diffusion stripe which serves as a fill and spill charge injector as shown in Figure 4 whenever one of the transfer gate word lines perpendicular to the BSS lines is turned on. This provides a better storage to cell area ratio and a simpler and very dense structure. However, the charge storage capacity is reduced and the output becomes bit pattern sensitive so that pairs of cells storing complementary data may be required for reliable detection. The operation of this cell has been described in detail in reference (5).

To compare the performance of the various cells at high density we have fabricated all the above structures simultaneously using the Texas Instruments EBMI electron beam lithography system to pattern all nine mask levels. Five levels were patterned using approximately 6000Å layer of PMMA and four using 4000-5000Å of TI309, a high contrast negative resist developed at Texas Instruments. The type of resist

was chosen to ensure minimum e-beam slice writing time and maximum throughput. L-shaped $6\ \mu\text{m}$ deep alignment marks were etched into the silicon at the corners of each field prior to processing. The secondary electron signal from the edges of these marks are used for registration of each field position on the $2''$ wafer. Level-to-level registration accuracy of better than $\pm 1500\text{\AA}$ was obtained. Minimum pattern dimension was $1.5\ \mu\text{m}$. Since registration accuracy depends on the integrity of these alignment marks it is important to protect them through the processing sequences which involve wet or dry etching. A standard self-aligned gate 2 level poly n-MOS process was used.

Since the I-T, CC and HiC cells are identical in operation, they have been fabricated to share the same bit line and read/write circuitry. Figure 5 shows a photomicrograph of a few of the high density cells. Cells with a minimum area of $0.1\ \text{mil}^2$ ($65\ \mu\text{m}^2$) have been fabricated. These correspond to a packing density of ~ 10 million bits/ in^2 . The gate oxide thickness for these devices was 500\AA , and the channel region of the MOSFET was double implanted to avoid short channel threshold lowering and punch through effects (6).

These cells were operated with the substrate grounded and $V_{DD} = 5$ volts. The reduced voltages are required to ensure that the electric field in the oxide region is not increased. In Table I we have listed the charge capacity and leakage rates per unit area of storage for $0.3\ \text{mil}^2$ and $0.1\ \text{mil}^2$ I-T CC HiC, RAM cells and the MCM cell. The charge capacity of the I-T, CC and HiC cells are determined by measuring the current in the precharge node. The CC RAM cell shows about $\sim 80\%$ of the charge capacity of the I-T and CC cells. These results bear out the high density predictions made in references (3) and (4). It is seen that the charge capacity of the $0.3\ \text{mil}^2$ cells per unit area is larger than the $0.1\ \text{mil}^2$ cells under identical structure and operating conditions. This strongly suggests that the storage well size is really dependent on the periphery to area ratio. Since at $0.1\ \text{mil}^2$ cell size the tapered region between the gate and field oxide has a significant dimension, this is not very surprising. The MCM cell has been operated as described in reference (5), but with voltage levels similar to the I-T cell. The charge capacity of the MCM cell is experimentally difficult to determine since the detection involves a displacement current rather than a particle current at the output. The numbers quoted in Table I are based on certain capacitance ratio estimates, which may involve $\pm 20\%$ error, in conjunction with the output voltage swing. The charge capacity of the MCM cell is seen to be much smaller than that of the I-T cell.

Some of the aspects of the operation of these cells at these dimensions and voltages need to be noted. All double level cells are fabricated assuming adequate fringing effects may be relied upon to control the interelectrode surface potential. However, in 2 level polysilicon gate structures, significant interelectrode potential barriers may be introduced due to a combination of gate oxide non-

uniformity and impurity segregation effects in the interelectrode region. These interelectrode barriers are especially significant at lower operating voltages where overdrive margins are reduced, and may cause a significant degradation of charge storage capacity. The operation of the MCM cell suffers from an additional drawback. In order to perform the "read" operation, the word line requires to be pulsed while the storage line is floating in order to perform the fill and spill. However, this causes an interelectrode capacitor feed through on the storage gate which tends to mask the change in potential due to signal charge. The clock rise times are thus extremely critical to the operation of the cell. Since the charge capacity of the cell is low, more sensitive output detection schemes are required. If we designed the CC cell for an equivalent charge storage capacity, and signal detection capability we would have little advantage in packing density in the MCM cell.

The leakage performance of these cells is interesting to compare. The leakage rate is measured by emptying the storage well of the cell and stopping the clocks in a storage mode for a known interval and reading the analog output of the cell due to the leakage charge. It has been shown that leakage charge in dynamic memory structures is generated by two components. The first is generation in the depletion region and the second is the component of leakage generated in the field region which diffuses into the cell. It has been shown (7) that the CC RAM cell structure can effectively cut off the contribution of the field and periphery component, since the storage electrode is held at ground in the store mode, whereas it is held at V_{DD} in the I-T cell. The field contribution is considerable only if the bulk lifetime is very large. We have measured leakage rates in these cells which are as low as 0.4 nA/cm^2 at room temperatures. This demonstrates that the electron beam lithography has not resulted in any residual damage in these devices.

The temperature dependence of the leakage rate provides an estimate of the functional contribution of the generation and diffusion components of leakage. The activation energy corresponding to a pure generation case is $E_g/2$ whereas that corresponding to a pure diffusion is E_g (where E_g is the silicon bandgap). It is seen that the isolated CC RAM cell has a lower activation of the leakage rate than isolated I-T cell (Figure 6). This agrees with the data of reference (7) where the CC RAM structure was shown to be capable of minimizing the field leakage component. The MCM cell shows a higher leakage rate at room temperature than the CC or I-T cell, probably because there are no bit lines in the vicinity of each cell which may attract leakage electrons, as is the case with I-T and CC cells. However, the activation energy corresponds almost exactly to a pure generation condition. This may be because each cell is surrounded by accumulated gates on two edges and storage gates on the other two, so that very little field contribution may be expected.

In summary, we have demonstrated that electron beam lithography may be used to fabricate the various dynamic RAM cell structures which have been proposed as candidates for very high density memories. We have compared I-T, Hi-C, CC and MCM cells fabricated by e-beam lithography. The MCM cell has the highest packing density and lowest charge capacity. The CC RAM cell has about 80% of the charge capacity of the I-T cell but has a higher packing density. It also has the lowest leakage rate at room temperature. The leakage rates measured at room temperature ($\sim 0.4 \text{ nA/cm}^2$) compare with the very best ever reported in the literature, so that e-beam lithography damage to the MOS structures is completely annealed out by the process.

REFERENCES

1. W. E. Engeler, J. J. Tiemann, and R. D. Baertsch, IEEE J. Solid State Circuits, SC-7, p. 330 (1972).
2. A. F. Tasch, Jr., R. C. Frye and H-S. Fu, IEEE Trans. Electron Devices ED-23, p. 126 (1976).
3. A. F. Tasch, Jr., H-S. Fu, T. C. Holloway and R. C. Frye, IEEE J. Solid State Circuits, SC-11, p. 575 (1976).
4. A. F. Tasch, Jr., P. K. Chatterjee, H-S. Fu and T. C. Holloway, IEEE Trans. Electron Devices ED-25, p. 33 (1978).
5. H. S. Lee, IBM J. Res. Develop., p. 402, Sept. (1977).
6. P. P. Wang, IEEE Trans. Electron Dev. ED 24, p. 196 (1977).
7. P. K. Chatterjee, A. F. Tasch, Jr., H-S. Fu and T. C. Holloway, Device Research Conference, Ithaca, June (1977).

Table 1
Comparison of Performance of Various DRAM Cells

Type of Cell	Area mil ² (μm^2)	Charge Capacity e/cm ²	Leakage Rate nA/cm ² at 23°C
I-T	.3 (195)	1.28×10^{12}	1.1
	.11 (71)	1.2×10^{12}	1.3
Hi-C	.3 (195)	2.1×10^{12}	.95
	.11 (71)	1.9×10^{12}	.75
CC	.28 (182)	1.04×10^{12}	.45
	.1 (65)	$.89 \times 10^{12}$.4
MCM	.15 (98)	5.4×10^{11}	8

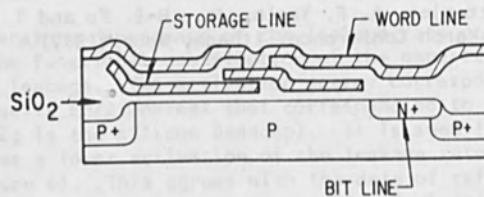


Fig. 1. Cross-section of a conventional (1-T) cell.

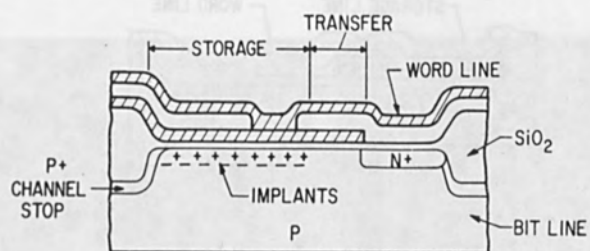


Fig. 2(a). Cross-section of a charge coupled RAM cell.

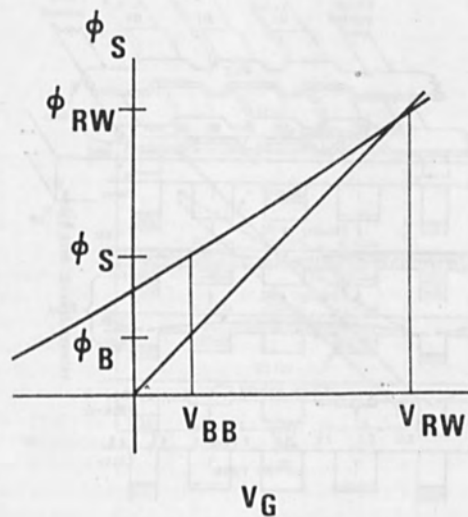


Fig. 2(b). ϕ_S vs. V_G curves for the storage (top curve) and transfer regions, (bottom curve).

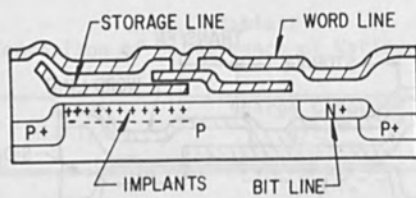


Fig. 3. Cross-section of the Hi-C RAM cell.

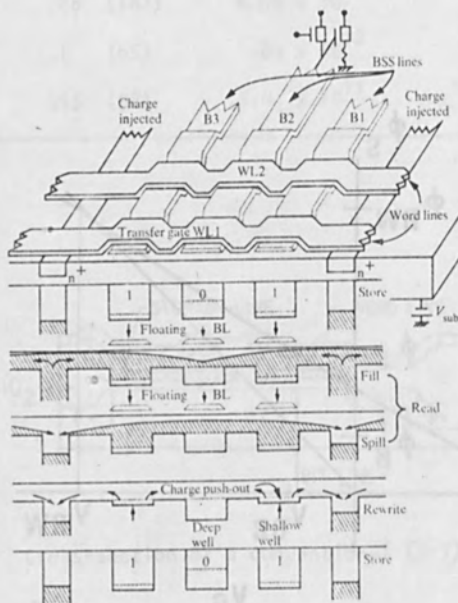


Fig. 4. Structure and operation of the Merged Charge Memory Cell (after Lee (5)).

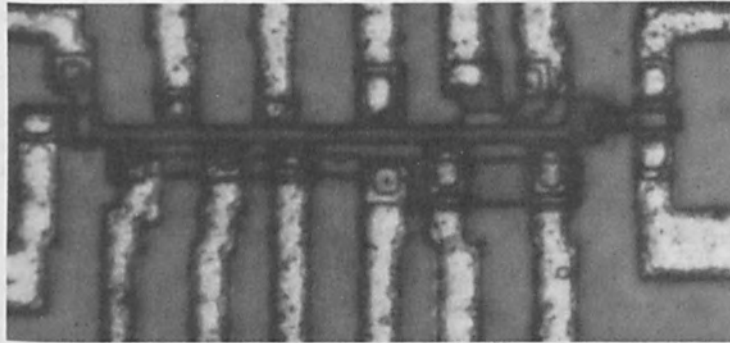


Fig. 5. Photomicrograph of electron beam lithography defined 0.1 mil^2 and 0.3 mil^2 RAM cells.

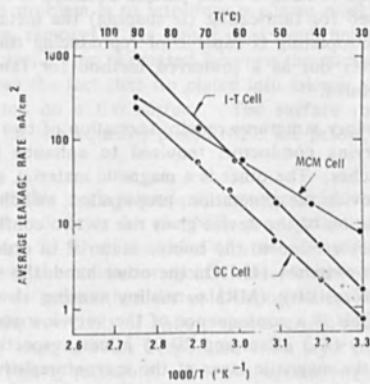


Fig. 6. Temperature dependence of leakage rates of the various DRAM cell.

ELECTRODEPOSITION PROCESS FOR FABRICATION OF THE
CONDUCTOR FIRST, SLM, 2 μ m BUBBLE MEMORY

M.C. Blakeslee, L.T. Romankiw, R.E. Acosta, S. Krongelb, B. Stoeber.
IBM Thomas J. Watson Research Center
Yorktown Heights, New York 10598

ABSTRACT

A simple process has been developed for the fabrication of 2 μ m single level masking bar bubble memory devices. The process is a hybrid of an additive and a subtractive process. It uses electroplated Au for the conductor level, which has been shown to have superior qualities as the substrate upon which to deposit the magnetic layer. In addition, an insulating pedestal is provided under the MR sensor to maximize the bubble detector signal. Reliance on the unique ability of electroplating to faithfully reproduce the minutest details of a stencil produced by lithography makes this process very promising for extendibility to sub-micron dimensions.

INTRODUCTION

The potential capability of magnetic bubble memories for high bit density and large capacity per chip can only be achieved by developing techniques for fabrication of uniform and accurate micropatterns.

As the size of the bubbles in magnetic bubble devices is reduced to the micron and submicron level the requirements for resolution of the linewidth and of the spacing between the lines become very stringent. The developments and improvements in lithography (e-beam, X-ray, deep UV, etc.) all come to naught if the pattern obtained is deteriorated by limitations inherent to the processes used for fabricating (*ie* shaping) the metal structure. It has been demonstrated (1,2) that electroplating is capable of reproducing the minutest details of the lithography, and hence stands out as a preferred method for fabrication of high density magnetic bubble device structures.

Magnetic bubble memory structures require formation of two levels of metallurgy (3). One level is a current-carrying conductor, required to enhance the performance of the current-assisted transfer switches. The other is a magnetic material, such as permalloy, having in-plane magnetization to provide the generation, propagation, switching, and detection of the bubbles. Thus, optimal operation of the device gives rise to two conflicting requirements. It is important to have the conductor close to the bubble material in order to improve the operational margins of the transfer switches (4). On the other hand, the shunting effect of a thick conductor under the magnetoresistive (MR) permalloy sensing element reduces the output signal to a very low level. This is a consequence of the very low resistivity of the conductor compared to that of permalloy (2-3 $\mu\Omega\text{cm}$ and 20-25 $\mu\Omega\text{cm}$, respectively). In order to avoid having the conductor under the magnetic layer of the magnetoresistive sensor, the fabrication of such devices previously required two separate masking operations, and an alignment to close tolerances. In this process a step is created at the point where the magnetic layer crosses over the conductor, which can result in local magnetic instabilities, and which could become a grave problem when scaling down to smaller bubble sizes. To prevent these local instabilities, and to avoid the critical alignment necessary when going to 2 μ m bubbles and below, single level masking (SLM) using only a single, crude, mask alignment has been proposed. Two of these processes were described by Kryder (5) and by Ahn et al (6).

This paper describes a process which relies on e-beam, X-ray, or deep UV lithography, electrodeposition, and sputter etching to form SLM structures for $2\mu\text{m}$ bubble devices with an SiO_2 pedestal to elevate the MR sensor. Because electrodeposition through a mask most faithfully reproduces the mask itself, this process lends itself readily to scaling down to $1\mu\text{m}$, and smaller, bubble devices.

PROCESS CONSIDERATIONS

Our goal was to develop the simplest process which would yield $2\mu\text{m}$ bubble devices of acceptable operational margins and that would be directly extendable to devices for bubbles of smaller dimensions. In doing this we have investigated fabrication schemes of three types: all subtractive, all additive, and a hybrid of the two.

The all-subtractive process requires deposition of the conductor and NiFe in sheet form either by evaporation, electroplating, or by a combination of the two, and subsequent patterning of the device elements by sputter etching. The sputter etch mask can be formed either by electrodepositing or evaporating a slow etching metal such as Ti or Cr through a lithographic mask, or by using an appropriate resist pattern. All these variations suffer from the possible loss of resolution during formation of the sputtering mask, as well as from difficulties in maintaining dimensional control. The latter are due to bevelling and redeposition during etching. These problems may severely limit the extendibility of the subtractive process to the 1 micron and sub-micron size bubble devices.

Additive processes require double level masking so that Au is deposited only where required for the conductor function, and does not interfere with the sensing part of the structure. In this process alignment becomes extremely difficult when working with $2\mu\text{m}$ bubble devices, and may become completely impossible in micron and submicron devices. One way of eliminating this problem is to introduce a coarse masking of the sensor area prior to plating of the conductor, removal of the sensor mask, and then plating of the NiFe through the first mask. In either case, a step is created between the conductor and the MR sensor. The process also suffers from the fact that Au plated into micron and submicron lines tends to be rougher than that plated on a flat surface. The surface roughness adversely affects the magnetic properties of the subsequently plated NiFe, see below, and hence it affects the device operation.

Another facet of this work extensively investigated techniques of conductor deposition which produce the best underlayer for the NiFe propagation elements. Details of that study are reported in Reference 7. From the point of view of minimizing the coercivity, H_c , of the NiFe deposited on top of the conductor, gold electroplated from the Sel-Rex BDT-510* bath consistently yielded better results than did gold deposited by either sputtering or evaporation. It was also found that the coercivity of NiFe plated over Au was lowered, and the shape of the B-H loop improved, by using a 200\AA evaporated NiFe layer as a "seed" layer for the subsequently plated NiFe. This is fortunate, since evaporated NiFe is the plating base of choice with our pedestal process because it does not lower the MR signal of the sensors. Thus, the underlayer of evaporated NiFe serves a dual purpose: it provides a conducting surface for electroplating the MR detector on top of the SiO_2 pedestal, and at the same time it helps to lower the H_c of the electroplated NiFe film.

* Sel-Rex Corp., Nutley, N.J., BDT Series of Au-Plating Processes, Bulletin MP-201.

The process developed in the present study avoids the problems of the all-subtractive processes, as well as those of the all-additive ones, by requiring only a crude alignment to permit positioning of the sensor atop a non-conducting pedestal (at the desired distance from the bubble film), by allowing the Au to be deposited in sheet form (the process which optimizes the magnetic properties of the subsequently plated NiFe (7)), and by utilizing NiFe plated through a mask to define the underlying Au conductor.

An additional advantage of this process is the built-in test for continuity of the MR sensor lines stepping over the non-conducting pedestal: if these lines are not continuous the sensor does not plate. Also, the device can be tested after deposition of the patterned permalloy for preliminary indication of the bubble propagation margins. Thus reworking, or discarding of the specimen, is possible before further processing.

PROCESS DESCRIPTION

Figures 1a through 1e show the steps involved in fabricating the structure. These are: formation of an SiO₂ pedestal, electrodeposition of the conductor in sheet form, patterning of permalloy by electrodeposition through a mask, and subtractive patterning of the conductor by sputter etching.

Formation of the Pedestal in SiO₂

The pedestal is formed in 2,000 to 3,000 Å thick sputter deposited SiO₂ on top of a garnet wafer (with or without a thin protective SiO₂ coating). Photo resist or e-beam resist is exposed without registration and developed to define the sensor pedestal area. The SiO₂ is then etched using 10% buffered HF. A slight overhang is created in the resist during chemical etching. Before removing the resist, a thin adhesion layer and a plating base are deposited by vacuum evaporation over the entire wafer. A standard lift-off technique employed for removal of the resist at this point leaves the pedestal-sensor area, where no conductor is desired, free of plating base, see Figure 1a.

Conductor Electrodeposition

The adhesion layer and plating base consist of 100Å Ti and 400Å of Au deposited by evaporation at R.T.. The wafer is electroplated with 3,000 to 4,000 Å of gold to match, or to slightly exceed, the height of the SiO₂ pedestal (Figure 1b). A Sel-Rex BDT-510* gold bath is used in this step. The advantage of electrodeposition of the gold is that the electroplated gold butts against the SiO₂ and forms a fissure-free structure. This allows for electrical continuity of the subsequently plated NiFe elements at the Au-SiO₂ boundary.

In Figure 2 are SEM photographs of nominal 1 μm wide NiFe sensor lines stepping from gold onto the SiO₂ pedestal. The lines are shown before (a) and after (b) subtractive patterning of the conductor as explained below.

Patterning of Permalloy by Electrodeposition Through a Mask

A 200 Å film of permalloy is now evaporated on the wafer at RT, to form a plating base for the permalloy pattern on top of the pedestal (Figure 1c). Besides its role as plating base, permalloy has a beneficial effect on the magnetic properties of permalloy plated on top of Au (7). Resist is applied, and after non-critical registration of the MR sensor to the pedestal, it is exposed using the IBM vector scan e-beam system, X-rays, or deep UV. The pattern contains all the permalloy features (propagation, generation, and magnetoresistive sensor elements), and all conductor features. Approximately 5,000 Å of permalloy are then plated from a modified Wolf's bath in a paddle type cell (8).

The faithfulness of reproduction of the details in the lithography is shown in Figure 3. The ripples in the edge of the pattern are those produced by the vector scan system in the e-beam resist.

The magnetic properties of permalloy show a strong dependence on composition and film thickness (9). In turn, the thickness and composition of plated NiFe are very sensitive to variations in current density. When plating through a mask this problem is exacerbated due to the non-uniform pattern density and to the various sizes of the elements where plating is taking place. See Figure 4. To minimize variations in the permalloy we use the approach described in Reference 10.

When the composition of the magnetic elements is outside the range that gives minimum coercivity, it becomes necessary to increase the thickness of the permalloy to maintain the same operational margins. Since the permalloy is used as a mask for the subtractive patterning of the conductor (see below), thicker permalloy carries as a penalty a poorer definition of the pattern because of the problems of bevelling and redeposition.

Subtractive Patterning of the Conductor by Sputter Etching

The resist is removed, and the electroplated permalloy pattern obtained is used as a mask for shaping of the conductor by sputter etching (Figure 1e). Since pure Ar plasma etching would result in roughening and removal of an excessive amount of NiFe, the sputter etching of gold is done in a mixture of O₂ and Ar (11). The presence of O₂ slows down the etching rate of permalloy by approximately a factor of five, thus creating an etch rate ratio, Au : Permalloy, of approximately 10:1. Thus only 600 Å permalloy are removed when sputter etching through 200 Å of permalloy, 3,000 Å of Au and 100 Å of Ti. The low etch rate of the permalloy layer in Ar/O₂ plasma minimizes bevelling, redeposition on the edges, and deterioration of the magnetic properties.

CONCLUSIONS

The process described has been used to fabricate 5, 4, 3, and 2 μm bubble T-I and C bar bubble memory devices. The process makes use of electrodeposition in conjunction with e-beam, X-ray, or deep UV conformable lithography. Since electrodeposition very faithfully reproduces the lithography, the dimensional control and extendibility to bubble devices smaller than 2 μm is limited primarily by the lithography. The steps subsequent to the lithography are chosen and optimized to minimize changes in cross-section and magnetic properties of the permalloy pattern.

This process is straightforward, simple, and promising from the point of view of extendibility to 1 μm and to sub-micron bubbles. Using it we have fabricated 2 μm T-I bar and C bar devices with minimum drive fields of 15-20 Oe, and propagation margins of 25 % at 40 Oe in-plane magnetic drive field. The small step in the permalloy at the edge of the SiO₂ pedestal had no detectable influence on the bubble propagation in these devices, and adequate sense signal were obtained from the detectors.

ACKNOWLEDGMENTS

We express our thanks to T. Donahue, W. Grobman, and H. Luhn, for the e-beam lithography work; to R. Feder, E. Spiller, and J. Topalian for the X-ray lithography; to B. Lin for conformable lithography; to L. Allman, M. Cohen, K. Halloway, and M. Kryder for magnetic testing of the devices; to C. D. Cullum, F. Mayadas, and E. Pugh for encouragement; to K.Y. Ahn and A.M. Tuxford for helpful discussions.

REFERENCES

1. L.T. Romankiw, S. Krongelb, E.E. Castellani, J. Powers, A. Pfeiffer, B. Stoerber, "Additive Electroplating Technique for Fabrication of Magnetic Devices", Proc. International Conf. on Magnetism, 1973, Vol. 6, 104-111
2. L.T. Romankiw, M. Hatzakis, and E.E. Castellani, "Additive Electroplating Limits for Gold Conductors Using PMMA Electron Beam Resist", Paper 208, ECS Meeting, Spring 1974.
3. A.H. Bobeck, I. Danylchuk, F.C. Rossol, and W. Strauss, IEEE Trans. on Magnetics, MAG-9, 474 (1973).
4. M.S. Cohen, G.W. Beall, W.J. Hsieh and H. Chang, IEEE Trans. on Magnetics, MAG-13, 1264 (1977).
5. M.H. Kryder, M.S. Cohen, N.J. Mazzeo, and J.V. Powers, IEEE Trans. on Magnetics, MAG-14, 46 (1978).
6. K.Y. Ahn, D.E. Cox, J.V. Powers, and A.M. Tuxford, INTERMAG 1978, Florence, Italy.
7. L.T. Romankiw, M.C. Blakeslee, and R.E. Acosta, INTERMAG 1978, Florence, Italy.
8. L.T. Romankiw, R.E. Acosta, and J.V. Powers, Paper 287, Electrochemical Society Meeting Fall 1977, Atlanta, Ga.
9. L. T. Romankiw and D. A. Thompson "Magnetic Properties of Plated Films" Chapter 23, pp 389-426, Properties of Electrodeposits their Measurement and Significance, edited by R. Sard, H. Leidheiser, Field Grown, The Electrochemical Society, Princeton, NJ. (1975)
10. L.T. Romankiw, S. Krongelb, E.E. Castellani, A.T. Pfeiffer, B. Stoerber, and J.D. Olsen, IEEE Trans. on Magnetics, Vol. MAG-10, 828-31, (1974).
11. S. Krongelb and L.T. Romankiw, IBM Technical Disclosure Bull., 20, (3), 1230 (1977).

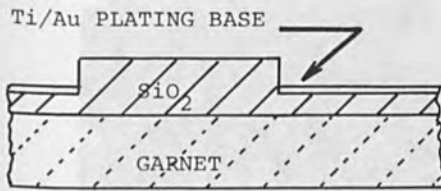


Figure 1(a). Structure after SiO_2 etching and plating base deposition using a lift-off technique.

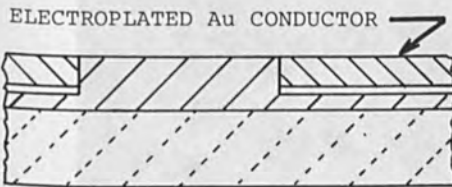


Figure 1(b). Structure after the Au conductor plating to match the pedestal thickness.

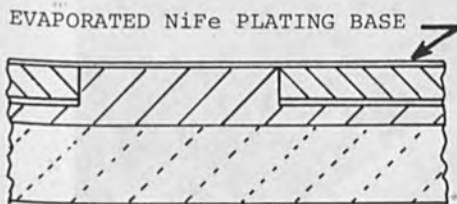


Figure 1(c). Structure after evaporation of the permalloy metallization, the plating base for the subsequent selective electrodeposition of permalloy on the pedestal and on the Au conductor.

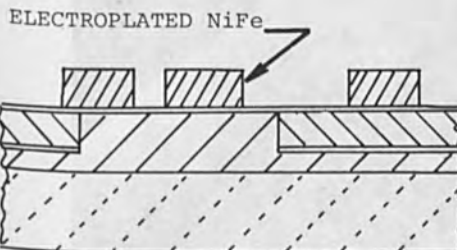


Figure 1(d). Structure after electrodeposition of the permalloy pattern through the e-beam or x-Ray resist mask. Resist has been removed. Electrodeposited permalloy will be subsequently used as a sputter-etch mask.

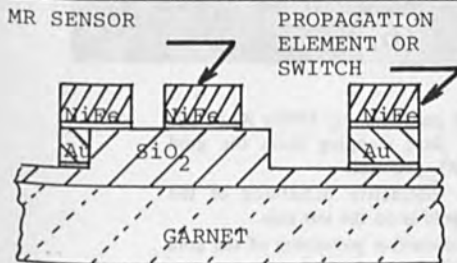


Figure 1(e). Completed structure after sputter etching of Au in O_2/Ar atmosphere. Magnetoresistive sensor is on top of SiO_2 pedestal, propagation elements and switches are on top of the conductors.

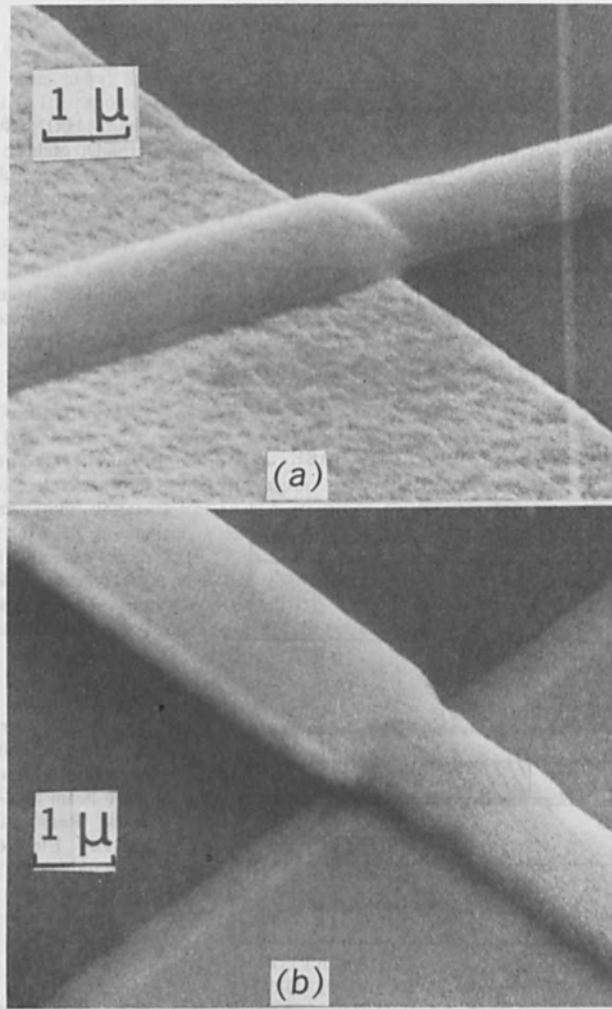


Figure 2. SEM photographs, 10000 X, of Ni-Fe sensor lines stepping from the gold onto the SiO₂ pedestal.
a) Before subtractive patterning of the gold. The gold is on the left side.
b) After subtractive patterning of the gold down to SiO₂ protective coat.

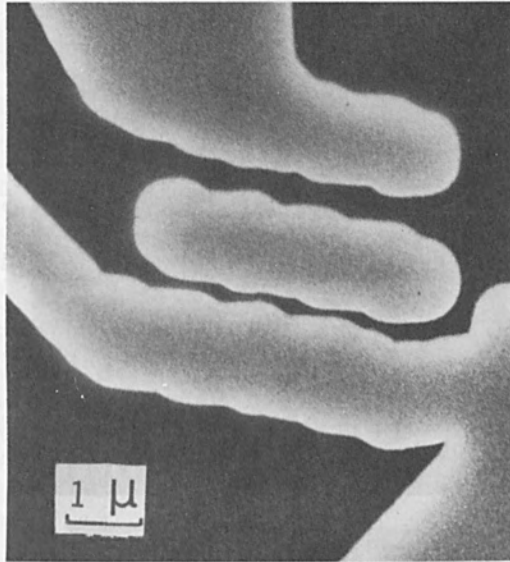


Figure 3. SEM photograph, 10000 X, of NiFe magnetic elements electroplated through an e-beam mask.

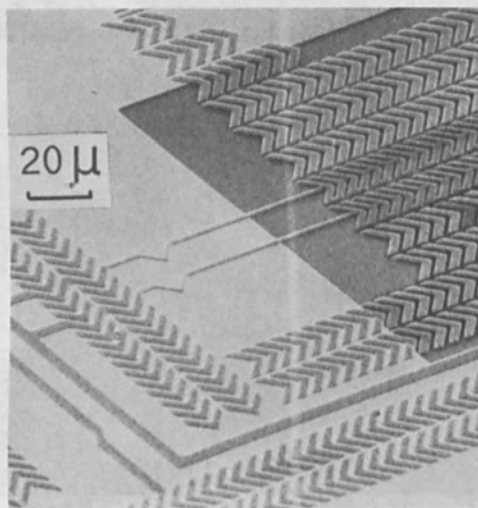
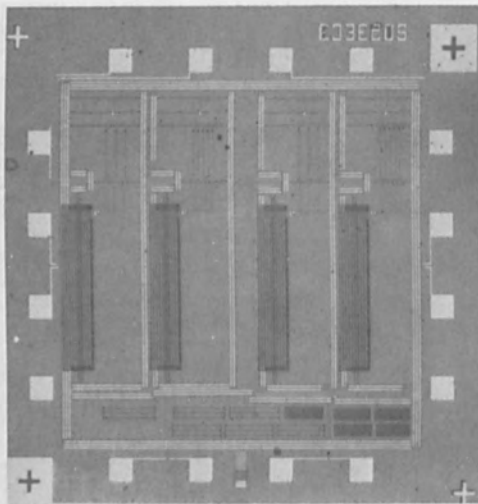


Figure 4. SEM photographs of a magnetic bubble device showing large variations in element size and pattern density.

The interaction of low incident electrons with a polymer resist-coated substrate have been investigated theoretically and experimentally. Monte Carlo calculations have been performed which take into account the scattering of electrons by the polymer chains and the resulting energy loss. The results show that the energy loss is significant and that the electrons are scattered in a random manner. This is in contrast to the case of a metal substrate where the electrons are scattered in a specular manner.

ELECTRON RESISTS

The spatial spreading and energy distribution of electrons incident on a polymer resist-coated substrate are of fundamental importance in electron lithography. We have investigated this problem theoretically and experimentally. Monte Carlo calculations have been performed which take into account the scattering of electrons by the polymer chains and the resulting energy loss. The results show that the energy loss is significant and that the electrons are scattered in a random manner. This is in contrast to the case of a metal substrate where the electrons are scattered in a specular manner.

Section 3

The lateral structure of our Monte Carlo calculations is very similar to that employed in earlier work in this area (1, 2). The straight-ahead potential used with a screened Rutherford potential being used to model the interaction between electrons and the polymer chains. The results show that the energy loss is significant and that the electrons are scattered in a random manner. This is in contrast to the case of a metal substrate where the electrons are scattered in a specular manner.

INVESTIGATIONS OF ELECTRON BEAM-RESIST
INTERACTIONS IN ELECTRON LITHOGRAPHY

M. S. C. Chung and K. L. Tai
Bell Laboratories
Murray Hill, New Jersey 07974

ABSTRACT

The interactions of keV incident electrons with a polymer resist-on-substrate system have been investigated theoretically and experimentally. Monte Carlo calculations have been performed in which both a continuous slowing down approximation and an energy straggling theory due to Landau are used. The theoretical predictions have been compared with the results of some experimental measurements using negative electron resists.

I. INTRODUCTION

The spatial spreading and energy dissipation profiles of kilovolt incident electrons in a polymer resist-on-substrate system are of fundamental importance in electron lithography. We have investigated this problem theoretically and experimentally. The theoretical work consists of Monte Carlo calculations in which both a continuous slowing down approximation (CSDA) and an energy straggling model utilizing the Landau energy loss distribution (1) are used. This approach is significantly different from earlier work in which the CSDA is used exclusively (2),(3). We have tried to ascertain the validities of our calculations by comparing them with experimental results obtained from negative electron resists. Again, this represents a significant departure from previous work in which the well-known positive resist PMMA was used (3).

II. BRIEF DESCRIPTION OF MONTE CARLO CALCULATIONS

The internal structure of our Monte Carlo calculations is very similar to that employed in earlier work in this area (2),(3). The single scattering approach is used with a screened Rutherford potential being used to model the individual target atomic nuclei. The electron step length s is determined by the elastic scattering

mean free path modified to take into account inelastic scattering in the manner of Kulchitsky and Latyshev (4). In between elastic scattering events, the incident electrons are assumed to dissipate energy via inelastic collisions with the target atomic electrons. Two different approaches are used to model the energy loss process. In the first approach, the energy loss ΔE suffered by the incident electron in traversing a step length s is determined within the CSDA via Bethe's mean stopping power formula,

$$\Delta E = \frac{2\pi n e^4 s}{E} \log \left(\frac{1.166E}{J} \right) \quad (1)$$

where n is the density of atomic electrons in the medium in which the incident electron is located, E is the incident electron energy at the beginning of the step, J is the adjusted mean ionization potential of the medium and e is the electronic charge.

In the second approach, the energy loss ΔE is sampled from the Landau energy straggling distribution (1) $f_{LD}(\Delta E, s)$ in the following manner,

$$R = F(\Delta E) = \int_0^{\Delta E} f_{LD}(\Delta E', s) d(\Delta E') \quad (2)$$

where R is a random number uniformly distributed in the interval (0,1). In choosing ΔE according to Eq. (2), account is taken of the statistical fluctuations occurring in the energy loss act. In both Monte Carlo approaches, quantities such as the spatial variations of the energy dissipation density within the polymer layer corresponding to point and line electron sources are calculated. The method of evaluation of these quantities is identical to previous work (2),(3). In addition, the situation corresponding to a free standing resist film has also been investigated. In the next section we present some of the results of our Monte Carlo calculations together with comparisons with relevant experimental data.

III. MONTE CARLO RESULTS AND COMPARISONS WITH EXPERIMENTAL DATA

A. Forward Beam Spreading

We have calculated the radial area probability density of keV incident electrons transmitted through various

thicknesses of a free standing resist film. In Fig. 1 we show the results of a typical calculation for 20 kV electrons incident on an 8000 Å thick free standing film of an experimental resist (copolymer 18DA). The ordinate denotes the probability per unit area of the transmitted electrons while the abscissa represents the radial distance of the transmitted electrons measured from their point of incidence. (We are considering the case of normal incidence only in all our calculations.) The calculated fractional transmission (η_t) and backscattering (η_b) coefficients are as indicated. In Fig. 1, we have also plotted the area probability distribution of the transmitted electrons given by an approximate solution of the Boltzmann Transport Equation first derived by Fermi (5). The parameter λ_{tr} in Fig. 1 represents the electron transport mean free path appearing in Fermi's solution. In Fig. 2, we present the Monte Carlo results for the partially integrated transmission probability versus one of the transverse directions x for an incident Gaussian beam of radius σ_0 equal to 2000 Å transmitted through three thicknesses of the resist considered in Fig. 1. The incident electron energy in Fig. 2 is 10 kV.

We have attempted to measure experimentally the forward spreading of an incident electron beam transmitted through various thicknesses of resist as follows. Thin layers (~ 500 Å) of gold are first deposited onto a silicon wafer. Windows are subsequently etched open in the gold films after direct electron beam exposure using PBS (6) as a mask. After removal of PBS, a layer of the experimental resist (copolymer 18DA) is spin-coated on top of the gold film. The gold film with the overlying resist coating is then floated off the silicon wafer in water and picked up onto grids. The sample is put in an SEM and a focused beam of known Gaussian radius is scanned repeatedly in a line fashion across the resist surface traversing an open window in the supporting gold film. The transmitted current as a function of beam position was measured by a fast current amplifier and recorded in a multi-channel-analyzer. Measurements were made for 10, 20, and 30 kV incident electron energies and for different resist thicknesses. In Fig. 3 we give a schematic representation of the experimental situation. In Figs. 4 to 6 we present the results of our experimental measurements of the forward beam spreading. In these figures the quantity plotted is the distance measured between the 50% and 20% points of the collected transmitted current as a function of resist thickness. The experimental data are compared with the theoretical predictions based on both our present Monte Carlo calculations and Fermi's approximate solution

to the transport equation (5). The agreement in both cases is fair with Fermi's solution in surprisingly better agreement with experiment.

B. Effective Backscattering Coefficient

For a uniform incident dose distribution, the energy dissipation density at any depth z into the resist can be written as

$$\begin{aligned}
 R(z) &= \frac{D_0}{e} \left[\left(\frac{dE}{dz} \right)_{FS} + \left(\frac{dE}{dz} \right)_{BS} \right] \\
 &= \frac{D_0}{e} \left(\frac{dE}{dz} \right)_{FS} [1 + \eta_{eff}]
 \end{aligned}
 \tag{3}$$

where $\left(\frac{dE}{dz} \right)_{FS}$ and $\left(\frac{dE}{dz} \right)_{BS}$ are the energy dissipated per unit distance along z due to the forward scattered electrons and electrons backscattered from the substrate respectively. The parameter η_{eff} is the effective backscattering coefficient and is given by

$$\eta_{eff} = \left(\frac{dE}{dz} \right)_{BS} / \left(\frac{dE}{dz} \right)_{FS}
 \tag{4}$$

We have attempted to measure the interface value of η_{eff} in the following manner. Thin layers of Si_3N_4 ($\sim 1000 \text{ \AA}$) are deposited on both sides of a Si wafer. Windows are opened in the Si_3N_4 on the back side of the wafer using conventional lithographic techniques. The exposed areas in the back surface of the Si wafer are then etched all the way to the front Si_3N_4 layer using a solution of 44% KOH in H_2O at 90°C . The resulting structure consists of thin windows in the Si_3N_4 supported by the unetched bulk Si. A layer of the negative electron resist PGMA-Co-EA (or COP) (7) is then spin coated onto the surface of the Si_3N_4 . A series of pad exposures with varying amounts of uniform incident doses (Coul/cm^2) are then made in the resist in an SEM making sure that each pad lay partially over a window area in the underlying Si_3N_4 layer. After development, the fractional remaining pad thicknesses corresponding to those areas lying over the thin Si_3N_4 windows were measured optically. By comparing the resulting contrast curve with those obtained from the same initial thickness of resist with the same incident electron energy but for different bulk substrates, the interface value of η_{eff} for these substrates can be

estimated as follows. Let the extrapolated value of the critical gel dose corresponding to zero developed resist thickness for the case of the thin Si_3N_4 window be D_g^{io} . Let D_g^i be the corresponding critical gel dose for a particular bulk substrate. Let E_c be the critical energy density for the onset of insoluble gel. Assuming that the electron backscattering from the thin Si_3N_4 window is negligible, we can write

$$E_c = \frac{D_g^{io}}{e} \left(\frac{dE}{dz} \right)_{FS}^I \quad (5)$$

$$= \frac{D_g^i}{e} \left[\left(\frac{dE}{dz} \right)_{FS}^I + \left(\frac{dE}{dz} \right)_{BS}^I \right]$$

where the superscript I denotes the interface value. From Eqs. (4) and (5) one can derive the interface value of η_{eff} for the particular substrate considered as follows

$$\eta_{eff}^I = D_g^{io}/D_g^i - 1 \quad (6)$$

In Fig. 7 we show a sketch of the Si_3N_4 window structure and in Fig. 8 we present the measured contrast curves for 20 kV electrons incident on a 6600 Å layer of COP on three different substrates as indicated. (The backscattering of the 4000 Å Au layer on Si considered in Fig. 8 should be identical to bulk Au for 20 kV electrons. See Ref. (8)). In Figs. 9 and 10 we present the results of Monte Carlo calculations of $\left(\frac{dE}{dz} \right)_{FS}$ and $\left[\left(\frac{dE}{dz} \right)_{FS} + \left(\frac{dE}{dz} \right)_{BS} \right]$ for 20 kV electrons incident on a 6500 Å

layer of COP on an Si and an Au substrate respectively. In both cases, results obtained via both the CSDA and the Landau energy straggling model are presented. In Table 1 the experimental values of η_{eff}^I for the two substrates considered are compared with the Monte Carlo values calculated via the two energy loss models discussed. Both models are in good agreement with the experimental data in Table 1. (The difference in initial resist thickness of 100 Å between theory and experiment should be insignificant at 20 kV.)

C. Probing of the Energy Dissipation Profile

The last situation we shall discuss involves exposure geometries consisting of arrays made up of a large number of overlapping identical Gaussian line scans. In Fig. 11 we show the Monte Carlo results for the energy dissipation density per unit input line dose $H(y,z)$ ($\text{eV}/\text{Coul}\cdot\text{cm}^2$) evaluated at the interface between a 6500 \AA layer of COP and an Si substrate for 20 kV incident electrons. Two sets of theoretical results are shown corresponding to a CSDA approach and one based on Landau's energy straggling theory (LD). Also in Fig. 11 we present the experimentally determined interface values of $H(y,z=t)$. In this figure, y is the lateral distance (transverse to the line scan direction) measured from the edge of the array, a_0 is the center-to-center line spacing and σ_0 is the incident beam's Gaussian radius. The experimental values of $H(y,z=t)$ were determined via the following relation

$$H(y,z=t) = E_c / \ell(y) \quad (7)$$

where $\ell(y)$ denotes the input line dose (Coul/cm) corresponding to a developed lateral extent y of resist measured from the array edge at the interface. By changing the input line dose, $H(y,z=t)$ can be probed experimentally the results of which are shown in Fig. 11 for the particular exposure parameters indicated. The experimental results in Fig. 11 are in satisfactory agreement with the Monte Carlo results from both energy loss models.

IV. DISCUSSION

From the previous sections and the results presented, it appears that our Monte Carlo calculations based on both the CSDA and the Landau energy straggling theory are in good qualitative and in some cases quantitative agreement with experiment. Our experimental results were obtained from a negative resist and are restricted to the resist-substrate interface. These results are hence significantly different from earlier work by previous authors involving the positive resist PMMA (3). The satisfactory overall agreement between theory and experiment obtained in the present work constitutes further evidence for the usefulness of Monte Carlo techniques in modeling electron beam-resist interactions in electron lithography.

V. ACKNOWLEDGEMENTS

We thank R. D. Heidenreich for many stimulating discussions and constant advice and encouragement during the present work. We are also grateful to L. F. Thompson and E. D. Feit for providing the negative resists used in our experiments and for discussions.

REFERENCES

- (1) L. Landau, J. Phys. (U.S.S.R.) 8, 201 (1944).
- (2) D. F. Kyser and K. Murata, Proc. 6th Int. Conf. Elect. and Ion Beam Sci. and Tech., Electrochem. Soc., Princeton, N. J. (1974), p. 205.
- (3) R. J. Hawryluk, A. M. Hawryluk, and H. I. Smith, J. Appl. Phys. 45, 2551 (1974), 46, 2528 (1975).
- (4) L. A. Kulchitsky and G. D. Latyshev, Phys. Rev. 61, 254 (1942).
- (5) B. Rossi and K. Griesen, Rev. Mod. Phys. 13, 240 (1941).
- (6) M. J. Bowden, L. F. Thompson, and J. P. Ballantyne, J. Vac. Sci. Tech. 12, 1294 (1975).
- (7) L. F. Thompson, J. P. Ballantyne, and E. D. Feit, J. Vac. Sci. Tech. 12, 1280 (1975).
- (8) L. Reimer and E. Krefting, in NBS Spec. Publ., No. 460, p. 45 (1976).

Exposure Situation	η_{eff}^I	
	Monte Carlo	Experiment
6600 Å COP/Si	CSDA 1.10	Landau Theory 0.93
		1.0
6600 Å COP/Au	1.82	1.89
		2.0

Table 1. Comparison of experimental and theoretical values for η_{eff}^I for two substrates. Incident electron energy is 20 keV.

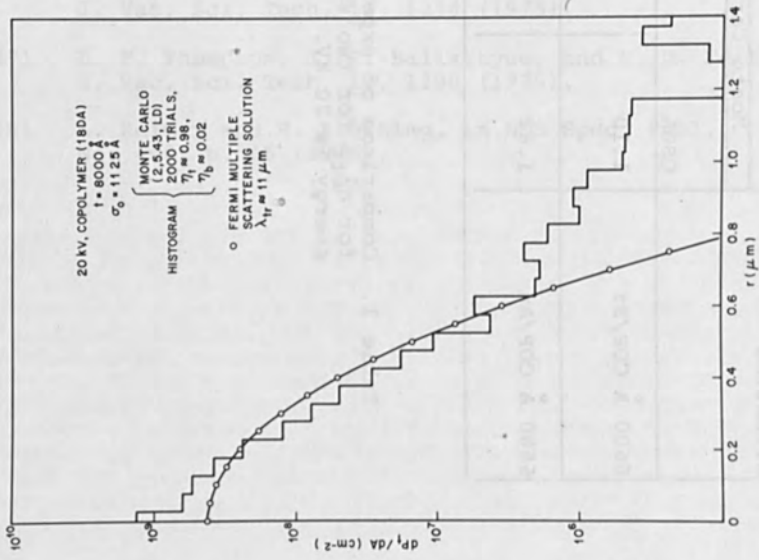


Fig. 1 Theoretical transmission probabilities per unit area versus radial distance, r .

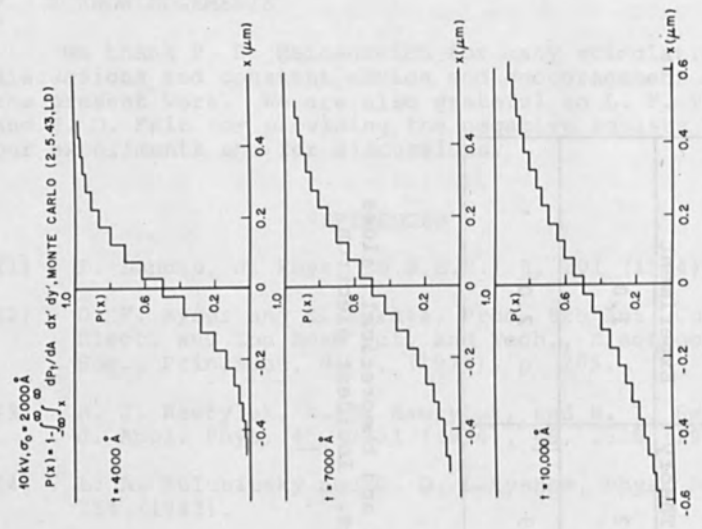


Fig. 2 Partially integrated transmission probabilities versus transverse distance, x .

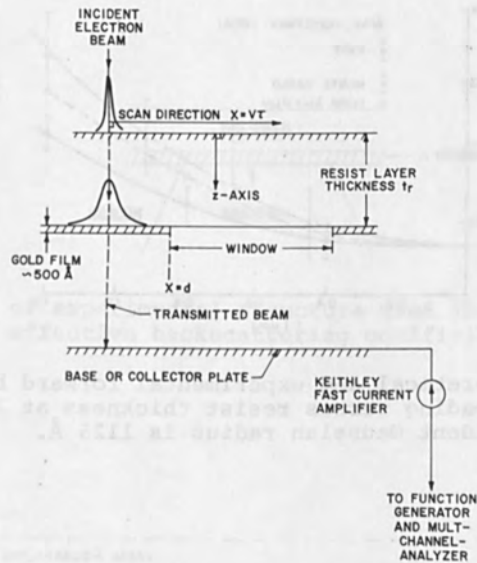


Fig. 3 Sketch of experimental set-up used in measurements of forward beam spreading.

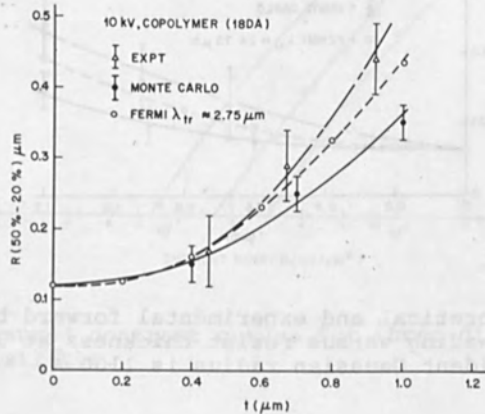


Fig. 4 Theoretical and experimental forward beam spreading versus resist thickness at 10 kV. Incident Gaussian radius is 2000 \AA .

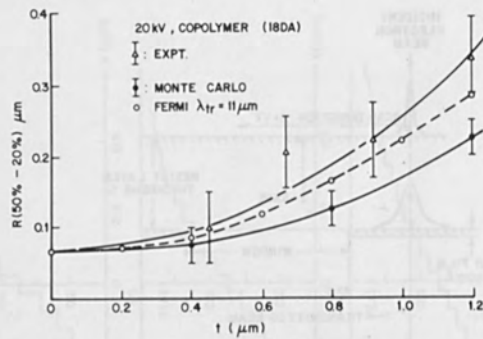


Fig. 5 Theoretical and experimental forward beam spreading versus resist thickness at 20 kV. Incident Gaussian radius is 1125 Å.

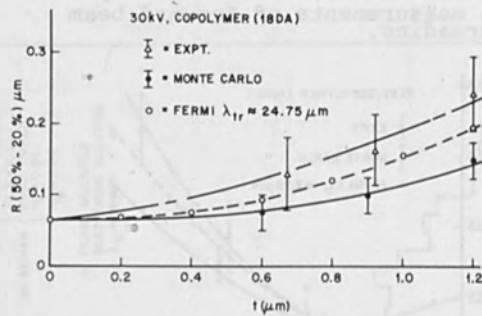


Fig. 6 Theoretical and experimental forward beam spreading versus resist thickness at 30 kV. Incident Gaussian radius is 1100 Å.

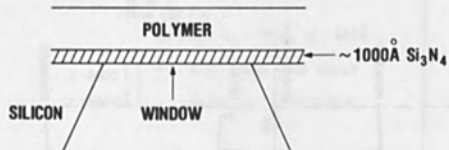


Fig. 7 Sketch of experimental structure used in determining effective backscattering coefficient.

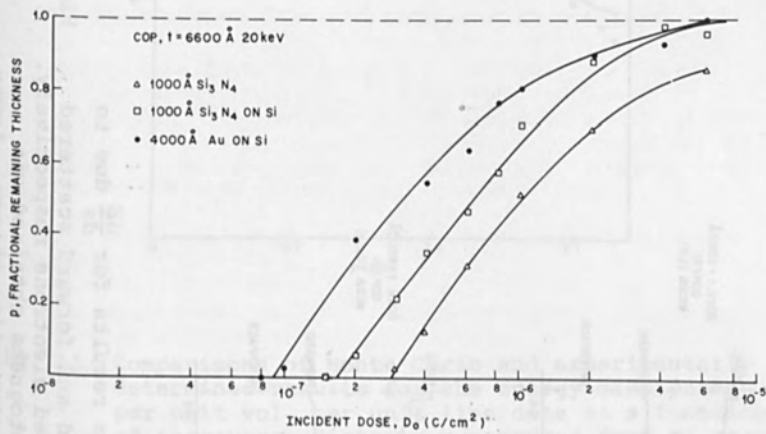


Fig. 8 Measured contrast curves for three different substrates.

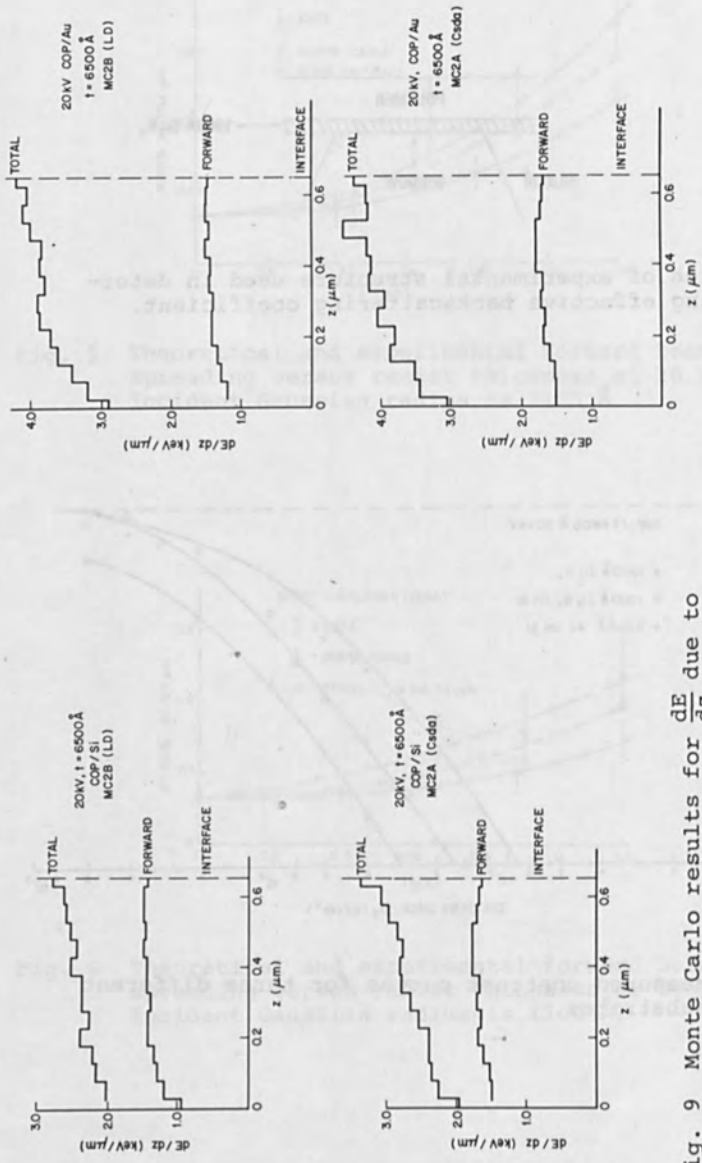


Fig. 9 Monte Carlo results for $\frac{dE}{dz}$ due to forward scattered and forward scattered plus backscattered electrons respectively. Upper set of histograms obtained via Landau's energy straggling theory. Lower histograms obtained via the CSDA. Substrate is silicon.

Fig. 10 Same as Fig. 9 but for a gold substrate.

INTRODUCTION

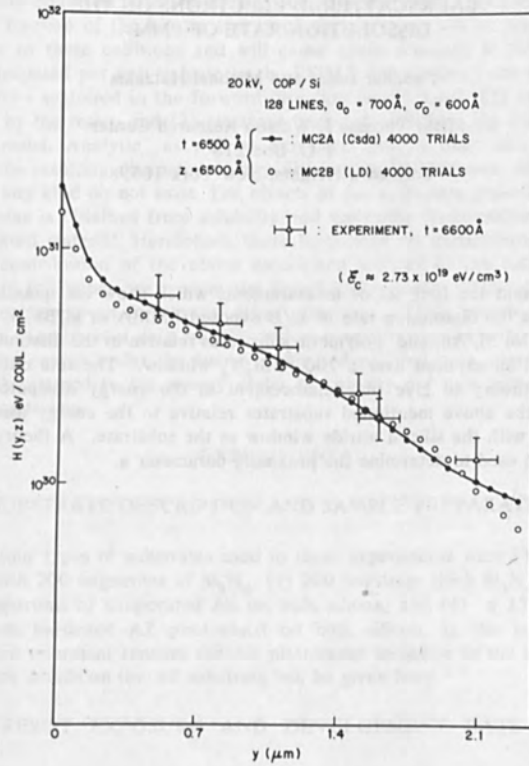


Fig. 11 Comparisons of Monte Carlo and experimentally determined results for the energy dissipated per unit vol. per unit line dose as a function of transverse distance y measured from an array edge. The Monte Carlo results denoted by MC2A are obtained via the CSDA; those denoted by MC2B are obtained via Landau's energy straggling theory.

EXPERIMENTAL DETERMINATION OF THE EFFECT OF
BACKSCATTERED ELECTRONS ON THE
DISSOLUTION RATE OF PMMA

Fletcher Jones and Michael Hatzakis

IBM Thomas J. Watson Research Center
P.O. Box 218
Yorktown Heights, New York 10598

ABSTRACT

We present the first set of measurements which show the quantitative enhancement in the dissolution rate of E/B exposed PMMA in MIBK as a function of substrate for Si, Au, and polymeric substrates relative to the dissolution rate of the PMMA film exposed over a 200 Å Si₃N₄ window. The rate data are combined with theory to give the enhancement in the energy dissipated per unit volume for the above mentioned substrates relative to the energy dissipated per unit volume with the silicon nitride window as the substrate. A theory of Chang and Parikh is used to determine the proximity parameter η .

INTRODUCTION

Electrons passing through a thin layer of PMMA on a silicon substrate will suffer many collisions with the atomic nuclei in the PMMA and the silicon substrate. A fraction of the kinetic energy of the electrons will be dissipated in the resist due to these collisions and will cause chain scissions in the resist. The energy dissipated per unit volume in the PMMA layer arises from three sources: (1) electrons scattered in the forward direction in the resist, (2) electrons backscattered by the resist, and (3) electrons backscattered from the silicon substrate into the resist. Analytic as well as numerical models exist which attempt to describe the resulting dissipated energy distribution.^{1,2} However, direct measurements of any kind do not exist. The effects of the ionization processes caused by the electrons is obtained from solubility and molecular fragmentation analysis of the irradiated material. Heretofore, there have been no experiments which separate the contribution of the above mentioned sources to the solubility of the material. In this paper, we present the experimental results of this decomposition. Results are also given for several other substrates. These results are combined with other experimental data and theoretical considerations in order to obtain the ratio of the energy under the energy dissipated per unit area curve due to electrons backscattered to the energy under the energy per unit area curve due to forward scattering.

EXPERIMENTAL

(a) SUBSTRATE DESCRIPTION AND SAMPLE PREPARATION

The four types of substrates used in these experiments were (1) bulk silicon covered with 200 angstroms of Si_3N_4 , (2) 200 angstrom thick Si_3N_4 window, (3) 10000 angstroms of evaporated Au on bulk silicon, and (4) a 15 micron thick temperature hardened AZ photoresist on bulk silicon. In the latter case the temperature treatment renders the AZ photoresist insoluble in the PMMA developer. More details on the AZ substrate will be given later.

(b) RESIST EXPOSURE AND DEVELOPMENT RATE MEASUREMENTS

The substrate-resist system used to separate the backscatter of silicon from the other two contributions is shown in the lower part of fig.(1) where a 1.2 micron thick PMMA(2041) film baked at a temperature of 160 C covers a substrate consisting of 200 angstroms of Si_3N_4 on bulk silicon. In one region of the substrate, the silicon has been back etched to expose a 0.1 mm square window of silicon nitride. Since the silicon nitride window is only 200 angstroms thick, the number of electrons backscattered into the resist from this region will be negligible. The sample is placed in a scanning electron microscope and squares 100.0 microns on a side are irradiated in the region over the bulk silicon as well as in the region over the silicon nitride window. The energy of the incident electrons is 20.0 keV and the half-width of the Gaussian spot is approximately 300 angstroms. The surface charge density in all that follows is 20.0 microcoulombs per square centimeter. The sample is removed after exposure and developed in concentrated MIBK at room temperature. The development time is noted and a dissolution rate is assigned to each region. The dissolution rate over the nitride window is 445 Å/min., while the dissolution rate over the bulk substrate is 570 Å/minute. The dissolution rate for exposures over large areas of PMMA on gold is 800 Å/min. In the above and all that follows, the error in the rate measurements is ± 10

$\text{\AA}/\text{min}$. The results are shown in table I.

The upper part of fig.(1) shows the substrate-resist system used to separate the forward scattering from the backscattering contributions of the PMMA and the silicon substrate. A long line 0.5 microns in width is written across the two regions of the substrate. The line is developed and the dissolution rate, R , over each region is recorded. In this case the dissolution rates over bulk silicon and over the Si_3N_4 window were equal to $270 \text{\AA}/\text{min}$. For the gold substrate the dissolution rate of the 0.5 micron wide line was found to be $250 \text{\AA}/\text{min}$. The exposure and developer parameters are the same as stated earlier. The results are given in table II.

The contribution of backscattered electrons from a bulk substrate of temperature hardened AZ photoresist to the dissolution rate of PMMA was obtained as follows. The substrate was prepared by spinning a 15.0 micron thick layer of AZ photoresist onto a silicon wafer and baking at a temperature which was high enough to harden the AZ film and render it insoluble in the MIBK developer. A 200.0\AA thick film of aluminum is evaporated over half of the wafer in order to eliminate the effects of charging in that region. The effects of charging can be investigated in the region without the aluminum. Large squares were exposed in a 1.2 micron thick PMMA film over both regions and the dissolution rate, R , for each was recorded. The dissolution rate in the aluminum covered region was $540.0 \text{\AA}/\text{min}$., while the dissolution rate in the region without the aluminum was $545 \text{\AA}/\text{min}$. The $5 \text{\AA}/\text{min}$ difference between them is within the error of the experiment. The result shown in table I is for the aluminum covered half of the AZ polymer substrate.

DISCUSSION OF EXPERIMENTAL RESULTS

The ratio of the dissolution rate for the 100 micron square of resist exposed over bulk silicon to the dissolution rate of the 100 micron square of resist over the Si_3N_4 window is 1.28. Thus the backscatter from the silicon substrate increases the dissolution rate of the large area by 28%. However, the dissolution rate of the 1/2 micron line in 1.2 micron thick resist is $270 \text{\AA}/\text{min}$. over the bulk substrate and over the Si_3N_4 window. This result indicates that the large angle backscatter phenomenon which characterizes scattering from the silicon substrate gives a negligible contribution to the narrow but isolated line. As shown in fig.(2), electrons scattered from the silicon substrate will contribute primarily to regions outside of that illuminated by the incident beam. However, the decrease in the dissolution rate over the Si_3N_4 window indicates that large angle scattering events (e.g. backscattering) in the PMMA do not contribute significantly to the dissolution rate of the PMMA in the illuminated region of the 1/2 micron line and that the same scattering events contribute significantly to the solubility for large area exposures. It is interesting to note here that the 1/2 micron wide line written over the AZ substrate has a dissolution rate of $260 \text{\AA}/\text{min}$., while the dissolution rate of the 1/2 micron wide line written on the gold substrate is $250 \text{\AA}/\text{min}$. The small difference in the rates is not surprising in light of the previous argument. Therefore, in the following we assume that the dissolution rate of $270 \text{\AA}/\text{min}$. is the dissolution rate due to forward scattering alone.

Finally, the exposure of the resist over the AZ polymer substrate shows that backscatter from a thick polymer substrate is not at all negligible. The dissolution rate for a large area of PMMA exposed over the bulk silicon and the AZ substrate

are 570 Å/min and 540 Å/min. respectively. The rate for PMMA over the nitride window is 445 Å/min. Thus, the increase in the dissolution rate due to the backscatter from the polymer substrate is 21%, while the same increase for the PMMA over silicon is 28%.

BACKSCATTER CONTRIBUTION TO ENERGY DISSIPATED PER UNIT VOLUME

It can be shown that the relation between the surface dosage,³ Q_0 , and the dissolution rate of PMMA(2041) in MIBK developer at room temperature is

$$R = R_0 + k(Q_0)^{1.3} \quad (1)$$

where R_0 ($= 42 \text{ Å/min}$) is the background or unexposed dissolution rate of PMMA in MIBK at room temperature. Since the energy dissipated per unit volume E_v scales with Q_0 , we can write the above equation as

$$R = R_0 + a(E_v)^{1.3} \quad (2)$$

where a is a constant. The validity of this expression has been determined from experimental and theoretical considerations that will be presented elsewhere.⁴

Let R_{sub} and R_{wind} equal the dissolution rate of a PMMA film on an arbitrary substrate and on the Si_3N_4 window respectively. Assume that the corresponding energy dissipated per unit volume is E_{sub} and E_{wind} respectively. Using equation (2) we find

$$\frac{R_{\text{sub}} - R_0}{R_{\text{wind}} - R_0} = \left(\frac{E_{\text{sub}}}{E_{\text{wind}}} \right)^{1.3} \quad (3)$$

The above equation can be solved for $E_{\text{sub}}/E_{\text{wind}}$ if R_{sub} and R_{wind} are known. For blanket exposures or exposures over large areas of the substrates described earlier, the left hand side of equation (3) is given in column 3 of table III. The corresponding values of $E_{\text{sub}}/E_{\text{wind}}$ are given in column 4 of table III. The fractional or percent increase in the energy dissipated per unit volume for a given substrate relative to the energy dissipated per unit volume with the window as the substrate is given in column 5 of table III.

CALCULATION OF A PROXIMITY PARAMETER

A recent investigation by Parikh⁵ has shown that the variation in the resist dissolution rates due to proximity effects could be greatly reduced if the dosage given to an image in a scanning E/B system is determined by its position relative to other images in the system. However, in order to determine the dosages a complex arrangement of images should receive, it is necessary to know the way electrons dissipate energy as they move through the resist.

To first order, Chang⁶ has shown that the energy dissipated per unit area by forward scattered electrons or by backscattered electrons can be represented by a gaussian. Following Parikh⁵, we write the sum of these gaussians for PMMA on silicon as

$$f_p(r) = K(\exp(-r^2/\beta_f^2) + \eta(\beta_f^2/\beta_b^2)\exp(-r^2/\beta_b^2)) \quad (4)$$

The only experimental method we have at present for determining the parameters in the above equation is through development of exposed images of various sizes. There is a problem involved with this procedure in that a developer can and will often wash out and distort fine details in an image. Furthermore due to non-linearities in the resist-developer system, gross errors could be introduced by this experimental method. The above equation is already an indication of the omission of details of the actual energy dependence in the resist. It is generally shown by most theoretical considerations that there is a depth dependence to the energy dissipated in the polymer film. This dependence is completely omitted from equation (4). For the sake of simplicity we also omit the depth dependence in what follows. However, we must remember that the actual situation is more complicated than the one represented by equation (4).

It will be shown elsewhere⁴ that a number of polymer systems that undergo chain scission or break down when illuminated with ultraviolet radiation have a dissolution rate which can be expressed as

$$R = R_0 + a(E_v)^p \quad (5)$$

where R_0 is the unexposed dissolution rate and a and p are constants characteristic of the resist-developer system. For the PMMA-MIBK system, R_0 and p are shown in equation (2). Since there is no depth dependence in equation (5) we replace E_v by E_a , the energy per unit area. Thus equation (5) becomes

$$R = R_0 + a'(E_a)^p \quad (6)$$

If only forward scattering were present in the resist system, the total energy, E_f , received by a point, P , in a resist system that was blanket exposed is given by the integral of the first term in equation (4) over the surface area of the resist. Thus,

$$E_f = \int_0^\infty K \exp(-r^2/\beta_f^2) 2\pi r \, dr \quad (7)$$

or

$$E_f = K\pi\beta_f^2 \quad (8)$$

The corresponding dissolution rate is

$$R_F = R_0 + a'(K\pi\beta_f^2)^p \quad (9)$$

When backscatter is included, the total energy, E_T , received by a point is given by integration of equation (4) or

$$E_T = \int_0^\infty f_p 2\pi r \, dr \quad (10)$$

or

$$E_T = K\pi\beta_f^2(1 + \eta) \quad (11)$$

The corresponding dissolution rate is given by

$$R_T = R_0 + a'(K\pi\beta_f^2(1 + \eta))^p \quad (12)$$

Equation (9) and (12) can be combined to give

$$\frac{R_T - R_0}{R_F - R_0} = (1 + \eta)^p \quad (13)$$

For the PMMA-MIBK system equation (12) becomes

$$\frac{R_T - R_0}{R_F - R_0} = (1 + \eta)^{1.3} \quad (14)$$

Hence, if the left hand side of eq.(13) is known, then the proximity parameter, η , can be calculated from the above equation. Assuming that R_F is 270 Å/min. and that R_T is 570 Å/min., we find that η has the value of 0.91. The value of η determined by Parikh by a method described in reference (5) is 0.6. The developer for this system is 1:1 IPA:MIBK. Grobmann and Speth⁷ reported a value of 0.86 for a developer mixture of 2:3 MIBK:IPA at 23 C. For the above experiments, the energy of the electron beam was 25.0 keV. Using a Monte-Carlo program, Kyser and Parikh⁸ found η to be approximately 0.5 over an electron incident energy range of 15 to 25 keV. It is clear that a whole range of η 's can be obtained from the set of experiments described above. The values of η determined by the above authors for silicon are given in table IV. The difference found among the various experimental results could be due to the type of developer used. The low value indicated by the Monte-Carlo calculations could be an indication of the degree of distortion introduced by the resist-developer system. For a thick Au substrate, R_T was found to be 800 Å/min. and the calculated value of η is 1.52.

Before concluding, we want to re-emphasize that the rate R_T is due to contributions from all of the scattering events occurring in the resist. We have used the first term in equation (4) to represent the forward scattering. We have used the second term to represent the very large angle scattering events in the resist and the contributions of electrons backscattered from the substrate. In general the sum of these three contributions cannot be expressed as a sum of two Gaussians. By lumping the two terms together as contributions due to the total

backscatter, it is obvious that the value of η obtained will be larger than that found by considering only backscattered electrons from the substrate.

SUMMARY

We have shown the relative effect of three types of electron scattering on the dissolution rate of PMMA. This was accomplished by selecting several combinations of substrates, exposing resist images of various sizes, and recording the corresponding dissolution rate. The three types of scattering events were (1) forward scattering, (2) backscatter in the PMMA, and (3) backscatter of electrons from the substrate into the PMMA film. A theory giving the relation between dissolution rate and the energy dissipated per unit volume in the resist was used to give the fractional increase in the dissipated energy due to electrons backscattered from various substrates relative to the dissipated energy density with a 200 Å thick film of Si_3N_4 as the substrate. Heretofore this increase had never been determined experimentally. Finally the rate vs energy equation was used with a theory of Chang and Parikh to determine the proximity parameter η for Si and Au.

ACKNOWLEDGEMENTS

We wish to thank D. Kyser and W. Grobman for useful conversations.

REFERENCES

1. R. J. Nosker, *J. Appl. Phys.* 40, 1872 (1969).
2. D. Kyser and K. Murata, *Proc. 6th Int. Conf. on Electron and Ion Beam Science and Technology* (The Electrochemical Society, 1974), P. 205.
3. M. Hatzakis, C. H. Ting, and N. Viswanathan, *Proc. 6th Int. Conf. on Electron and Ion Beam Science and Technology* (The Electrochemical Society, 1974), p. 542.
4. F. Jones and D. Kyser - to be published
5. M. Parikh, *J. Vac. Sci. Technol.* (1978, to be published).
6. T. H. P. Chang, *J. Vac. Sci. Tech.* 12, 1271 (1975).
7. W. Grobman and Speth, *Proc. 8th Int. Conf. on Electron and Ion Beam Science and Technology* (The Electrochemical Society 1978), to be published.
8. M. Parikh and D. Kyser, *Proc. 8th Int. Conf. on Electron and Ion Beam Science and Technology* (The Electrochemical Society 1978), to be published.

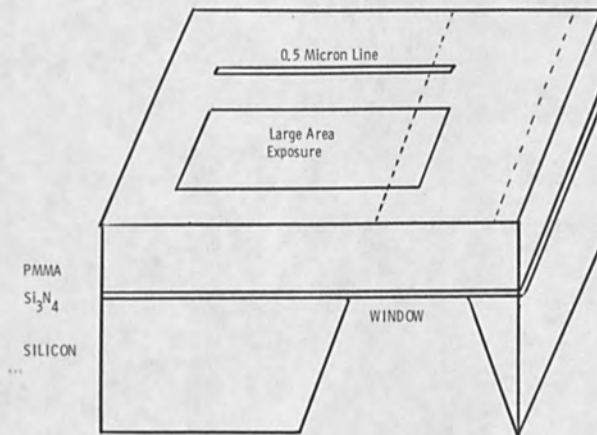


Fig. (1) Resist-substrate system used to expose 1/2 micron lines and large areas. See text for description.

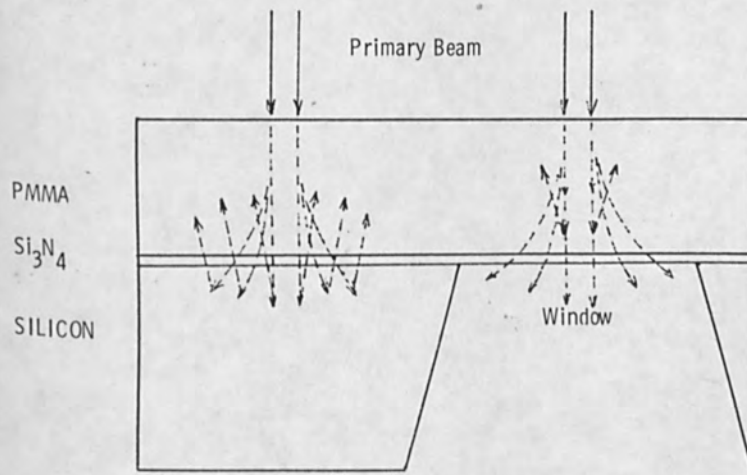


Fig. (2) Illustration of electron scattering events for narrow lines written over silicon and over the 200 Å thick Si_3N_4 window.

TABLE I

SOLUBILITY DATA ON LARGE AREA EXPOSURE
PMMA 1.2 Micron Thick, Exposed at 20 KV, Q=2x10⁻⁵ Coul/cm²

SUBSTRATE	R (A/Min.)	R/R _{wind}
Si ₃ N ₄ window	445	1.00
AZ polymer	540	1.21
SILICON	570	1.28
GOLD	800	1.80

TABLE II

SOLUBILITY DATA ON 0.5 MICRON WIDE ISOLATED LINES
PMMA 1.2 Micron Thick, Exposed at 20 KV, Q=2x10⁻⁵ Coul/cm²

SUBSTRATE	R (A/Min.)	R/R _{wind}
Si ₃ N ₄ window	270	0.60
AZ polymer	260	0.58
SILICON	270	0.60
GOLD	250	0.56

TABLE III

SUBSTRATE CONTRIBUTION IN LARGE AREA EXPOSURES
PMMA 1.2 Micron Thick, Exposed at 20 KV, Q=2x10⁻⁵ Coul/cm²
Unexposed PMMA (2041) Solubility in MIBK R₀=42 A/Min.

SUBSTRATE	R-R ₀ (A/Min.)	$\frac{R_{sub}-R_0}{R_{wind}-R_0}$	$\frac{E_{sub}}{E_{wind}}$	%
Si ₃ N ₄ window	428	1	1	-
AZ polymer	498	1.235	1.176	17.6
SILICON	528	1.31	1.23	23
GOLD	758	1.88	1.63	63

Where: $\frac{R_{sub}-R_0}{R_{wind}-R_0} = (E_{sub}/E_{wind})^{1.3}$

TABLE IV

COMPARISON OF VALUES FOR THE PROXIMITY PARAMETER η
FOR PMMA ON SILICON EXPOSED AT 20 KV

Where: $\frac{R_{sub}-R_0}{R_{wind}-R_0} = (1+\eta)^{1.3}$

1)	η	METHOD	AUTHOR
1)	0.91	EXP- THEOR.	JONES-HATAKIS
2)	0.86	" "	GROBMAN-SPETH
3)	0.60	" "	PARIKH
4)	0.50	MONTE-CARLO	KYSER-PARIKH

ELECTRON BEAM RESIST LINE EDGE PROFILE MODELING

A. R. Neureuther, D. F. Kyser, K. Murata, and C. H. Ting
IBM Research Laboratory, San Jose, California 95193

ABSTRACT

Resist edge profiles of lines produced by electron beam exposure are explored through the use of numerical simulation. The modeling approach uses Monte Carlo simulation of electron scattering and energy dissipation, a simple etch rate versus dose model for the resist, and a string development algorithm. The simulation was made on an IBM 370/158 and primarily considers a multiple-spot Gaussian beam exposure of PMMA resist. An absolute quantitative evaluation of the simulation accuracy is made based on resist exposure-development measurements and a comparison with SEM's of experimental profiles. The comparisons indicate that the present simulation model is of sufficient accuracy to be used as a quantitative processing aid.

INTRODUCTION

Computer simulation of line edge profiles can be used as a processing aid in the electron beam fabrication of devices. This necessitates combining models for all the important factors such as electron scattering in materials, the electron beam exposure tool, the substrate geometry, and the resist solubility characteristics. These factors must be considered in the context of the complete lithography process. This paper describes a complete simulation model and compares the accuracy of the results with SEM profiles on an absolute quantitative basis. The impact of various factors such as the resist model, the exposure beam quality, the substrate atomic number, and proximity effects are explored.

The modeling approach used here is based on combining previously developed energy deposition and surface etching programs with an exposure synthesis program and resist model data. Initially, the spatial distribution of energy deposited in the resist by a δ -function line source is calculated. It is based on simulating a large number of individual electron trajectories for statistical precision [1]. Each trajectory is composed of a series of step lengths between elastic scattering points. Each step length is the energy-dependent mean free path for scattering. The angle of scattering is chosen in a random manner, and continuous energy loss between collisions is assumed. The present version allows for a layer of arbitrary material and thickness on top of the substrate. This typically requires about 20 minutes of CPU time for 50,000 trajectories and only needs to be done once for a given resist thickness and substrate configuration.

By using the δ -function energy deposition result and superposition, the energy density (J/cm^3) in the resist can be calculated for arbitrary beam shapes. This results in a considerable savings of computer time. Individual lines can be specified by a sequence of δ -function exposures or by a sequence of Gaussian line exposures. Internally in the program each Gaussian line exposure is formed by a convolution with the δ -function exposure. The Gaussian lines are then superimposed to form a given written line. Any written line exposure can then be periodically arranged. For the 20 keV - 25 keV exposures used, proximity effects out to a distance of 5 μm were considered.

The least understood, and perhaps most critical submodel, is the resist exposure and development model. The approach taken here is to assume that development is a surface etching phenomena at a local etch rate determined by the dose in the material being removed. For this model the resist can be characterized by an etch rate versus dose curve. Quantitative data has been determined [2] for PMMA DuPont Elvacite 2010* (*Tradename) in concentrated MIBK developer (1:0) and is reproduced in Figure 1. The equation for the curve is:

$$R(D) = R_1 \left(C_m + \frac{D}{D_0} \right)^\alpha \quad (1)$$

where D is the absorbed energy in J/cm^3 . Here R_1 is the background etch rate in $\text{\AA}/\text{sec}$, C_m is a constant inversely proportional to the initial number average molecular weight, D_0 is the reference or knee energy (the intercept of the low dose and high dose asymptotes) in J/cm^3 , and α is the asymptotic slope at very high dose. The results given for 2041* are based on scaling C_m according to the values given in Reference 2. Elvacite 2010* developed in a 1:1 dilution of MIBK with IPA was used in the experimental work reported here. New measurements for this resist and developer and the room temperature conditions used in the present experiment are shown in Figure 1. Parameters for the corresponding algebraic model with a background etch rate of 1 $\text{\AA}/\text{sec}$ are shown in Table 1. An alternative algebraic model for a zero background etch rate is also shown.

The development is simulated by using a string of straight line segments [3] to follow the developer-resist interface as a function of time. During each development time step, each node on the string is advanced at the local etch rate in the direction of the perpendicular bisector of the angle between adjacent segments. Segments are periodically added and deleted on the basis of length, and loops are deleted just prior to profile output times. The algorithm averages about 500 node advances per second, and typically 20 to 40 nodes are advanced 100 times. The convolution, etching, and graphics display require about 10 seconds of CPU time altogether.

COMPARISON OF SIMULATION WITH EXPERIMENT

There was no doubt from the beginning that the present model would show the right kinds of effects with changes in parameters. The main concern was, however, how accurate the simulation would be on a quantitative basis. To make this assessment, an absolute quantitative comparison experiment was planned. The comparison spanned parameter variations in dose, written linewidth, and periodic arraying. The idea was to see how well line edge profiles calculated from a single set of a priori measured model parameters would track the experimental SEM profiles throughout the family and range of experiment conditions.

The nominal conditions for the comparisons were 1.0 μm of PMMA 2010* on silicon exposed at a dose of 80 $\mu\text{C}/\text{cm}^2$ by 20 keV electrons on our Vector-Scan lithography system, VS-1 [4]. The development was in a 1:1 mixture of MIBK and IPA for three minutes at room temperature. The patterns were written at a density of 10 spots per micron in each direction. The simulation assumed 10 Gaussian line sources per micron. Figure 2 shows a comparison for a 0.25 μm line written with three beam spots at doses of 60, 80, and 100 $\mu\text{C}/\text{cm}^2$. The simulated profiles are shown at 20 second intervals so that the ninth profile (next to last) corresponds to the correct (three-minute) development time. According to the plan, all the parameter values used in the comparison were determined a priori on an absolute basis. There is, however, one exception. To match top and bottom rounding and sidewall slope of the profiles, the nominal spot size estimate of 0.1 μm diameter was increased to about .25 μm diameter ($\sigma = .1 \mu\text{m}$). Using the adjusted standard deviation σ of .1 μm , the variation with dose shown in Figure 2 is quite good. Results for 0.5 μm lines written with five spots given in Figure 3 show similar agreement in shape and depth with change in dose. Generally, the larger the lines the better the agreement. The most critical test of simulation is the periodic arraying of small lines and spaces. SEM's for an array of five .25 μm lines are shown in Figure 4. Note that proximity effects make the center line slightly deeper than its outboard neighbors. The simulation of a five-line array is shown in Figure 6. The proximity effect on the relative depth of the lines is reproduced. However, the absolute quantitative comparison is not improved even when a zero background etch rate model is used. The basic problem is that each simulated line tends to be somewhat wider than the actual line. Although the array shows this most clearly, this same effect is also apparent upon close examination of Figure 2 for single 0.25 μ lines.

Achieving more detailed agreement between simulation and experiment involves taking a closer look at the model parameters and implicit model assumptions. One of the important inputs which is relatively unknown is the beam shape during dynamic writing. The results are also sensitive to the resist model, both in terms of quantitative data and in terms of fundamental conceptual assumptions. Further detailed exploration is, of course, needed. However, the

comparison of experimental and simulation profiles is sufficiently good for simulation to be used as a quantitative processing aid.

EXPLORATORY STUDIES

The purpose of the exploratory (i.e., theoretical) studies is to gain insight as to how factors such as dose, beam quality, resist solubility characteristics, and substrate properties affect line edge profiles. The exploratory studies are done in a context typical of writing optical masks in $0.5 \mu\text{m}$ resist on $.08 \mu\text{m}$ Cr on SiO_2 . For high contrast the resist model for PMMA 2041* was used at a nominal dose of $80 \mu\text{C}/\text{cm}^2$ at 25 keV. This operating point produces rather high quality profiles in developed resist with nearly vertical walls.

A typical line edge profile is shown in Figure 6 as a function of development time. The four Gaussian line sources to produce this profile were located at $-.1875$, $-.0625$, $+.0625$, and $+.1875 \mu\text{m}$ and each had a standard deviation of $.05 \mu\text{m}$. Only the right half of the symmetrical line is shown. The correct nominal half-linewidth of $0.25 \mu\text{m}$ is obtained in 80 sec development. Continued development results in a slight overetching but a more vertical profile. The distance between development contours gives some indication of the sensitivity of linewidth to development time.

The effect of the development process and resist solubility characteristics is illustrated in Figure 7. Here three dotted curves indicate constant energy contours for energy levels in J/cm^3 . The constant energy contours tend to be undercut and show etching beyond the nominal linewidth at moderate dose levels. The solid lines are 80 sec development contours for various resist models. The PMMA 2041* model for (1:0) developer shows an overcut profile slope which is due to the additional delay in developer action in reaching the bottom of the line and opening it. PMMA 2010* with 1:0 developer has a higher background rate than PMMA 2041* and shows both increased linewidth and top loss. Results for two hypothetical resists are shown. These resists have zero background rate and high asymptotic etch rate slope. These changes tend to make the profile converge to a constant energy profile of value D_0 . When allowed to converge to constant energy profiles, the profiles are relatively insensitive to overdevelopment and are similar in dose sensitivity to the constant energy contours. However, if these high contrast resists were used in a process which interrupted the development before the profiles converged to constant energy profiles, very high development time and exposure dose sensitivities would be observed.

Beam quality is a very important factor in determining edge profile shape, as illustrated in Figure 8. Here the standard deviation of the Gaussian beam was decreased from $.05 \mu\text{m}$ to $.025 \mu\text{m}$. The resultant 80 sec development profile changed from overcut in Figure 6 to undercut in Figure 8. This indicates that if line edge

slope is to be used to characterize resists, the electron beam spot used as the exposure tool in the study must also be characterized. Unequal weighting of the Gaussian lines forming the written line was also considered. Weighting the outer Gaussians as much as 1.5 times the inner Gaussian gave only a minor improvement in edge slope. However, increasing the weighting factor further resulted in the center of the line opening much later than the edge.

Electron scattering in the resist and substrate also affects profile quality. The energy density distribution broadens with depth, and for an ideal 25 keV δ -function line exposure it has a standard deviation of about .05 μm at the resist-Cr interface. The broadening is reflected in the developed line edge profiles for a δ -function line source shown in Figure 9. This indicates that it would be difficult to produce and control linewidths smaller than .2 μm on Cr masks.

It is interesting to use the model to study line edge profile changes which occur with dose compensation for proximity effects. Figure 10 shows a series of shifted line edge profiles for various linewidths. The parameters were chosen such that at 80 $\mu\text{C}/\text{cm}^2$ the four-spot (.5 μm) line gave the correct linewidth. As linewidth increases, the intra-proximity effect increases the relative dose which, in turn, causes line broadening and shoulder decrease. Figure 11 shows the profiles when the dose is compensated such that each line has the correct edge location regardless of linewidth. The corrected exposure dosages are given in parenthesis for each linewidth. The resulting profiles are almost identical and differ mainly in shoulder height.

Simulation with various substrates was used to explore effects of backscattering from the substrate. Removing the 800 \AA of Cr produced little change, indicating that the Cr thickness is not a critical parameter. Results for Si substrates were also quite similar to the mask substrate results. Using Au substrates produced a very large effect as can be seen in Figure 12. Here a general increase in the effective exposure has opened the line at only 50 sec development time. The slope is also lower, which indicates a decrease in the quality of the line edge profile. Reducing the dose to compensate for early development will only further degrade the line edge slope. The dotted line in Figure 12 indicates the 50 sec developed profile for a periodic array of 0.5 μm lines on 1.0 μm centers. The dashed line is for a dose compensation of the periodic array to produce the correct linewidth at 50 sec. Although the magnitude of the relative dose compensation is similar to that required for mask writing, the additional backscattering has resulted in a lower slope which remains after compensation. Thus, it is expected that dose compensation for proximity effects will be accompanied by inherent profile degradation with high Z substrates.

CONCLUSIONS

A simulation model combining Monte Carlo calculation of energy deposition and resist solubility data was used to study the impact of various processing parameters in the context of the entire electron beam lithography process. Superposition of exposure effects and a surface etching resist model are used to facilitate rapid simulation. Quantitative data for the resist exposure-development behavior is the most important empirical input. Knowledge of the dynamic beam quality of the exposure tool is also important. Comparisons with experimental SEM's on an absolute quantitative basis show that simulation can be used as a quantitative processing aid.

The exploratory studies have yielded a number of results relevant to writing high quality line edge profiles in PMMA on optical mask blanks. While constant energy profiles are usually undercut (such as would be required for liftoff), the delay in etching to the bottom frequently causes developed profiles to be overcut. This effect is reduced by decreasing the background etch rate R_1 and increasing the contrast α . Generally, the profiles for high contrast resists tend to converge to constant energy contours. This convergence tendency reduces sensitivity to development time, and results in a tolerable sensitivity to dose variations.

The beam spot diameter and intensity profile is a critical system parameter. It not only affects linewidth but can also convert overcut profiles to undercut ones. Electron scattering in the resist produces a standard deviation of about $.05 \mu\text{m}$ in the energy distribution from a 25 keV δ -function line source at the resist-Cr interface. The scattering also makes it difficult to open lines smaller than $.2 \mu\text{m}$ on Cr masks. Dose compensation for proximity effects were found to be typically on the order of +8% to -15% for $0.25 \mu\text{m}$ and $2.0 \mu\text{m}$ lines, relative to $0.5 \mu\text{m}$ lines. The line edge profiles after compensation were almost identical. For high Z substrates the background exposure is significantly increased. Dose compensation cannot compensate for the accompanying degradation of the profile slope.

REFERENCES

1. D. F. Kyser and K. Murata, Proc. Sixth Int'l Conf. on Electron and Ion Beam Sci. and Tech. (Electrochemical Society, 1974), pp. 205-223.
2. M. Hatzakis, C. H. Ting, and N. Viswanathan, Ibid., pp. 542-579, 1974.
3. R. E. Jewett, P. I. Hagouel, A. R. Neureuther, and T. Van Duzer, Polymer Eng. Sci. 17(6), pp. 381-384 (June, 1977).
4. T. H. P. Chang, A. D. Wilson, A. J. Speth, and C. H. Ting, Proc. Seventh Int'l Conf. on Electron and Ion Beam Sci. and Tech. (Electrochemical Society, 1976), pp. 392-410.

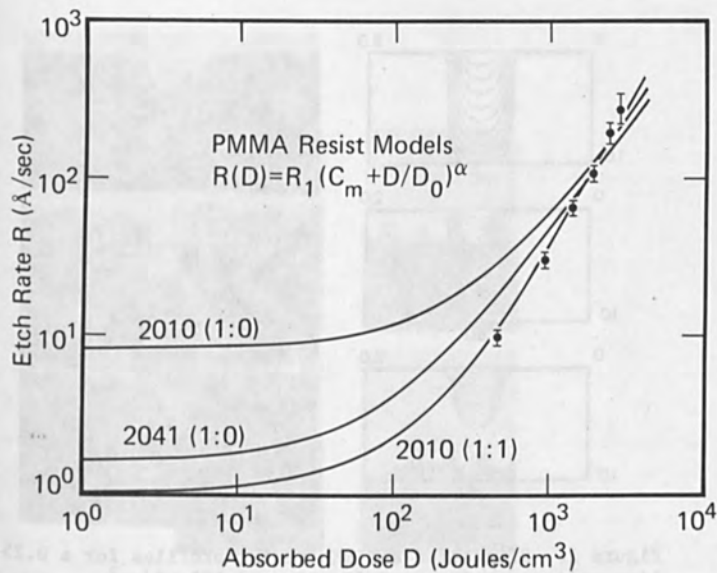


Figure 1. Resist etch rate versus absorbed dose for PMMA Elvacite 2010* and 2041* for development in a mixture of MIBK and IPA.

Table I. Etch rate equation parameters used in Figure 1.

PMMA ETCH RATE MODEL						
PMMA	DEV	R_1	C_m	D_0	a	COMMENT
2010	CONC	8.33	1.0	325	1.404	DATA FIT
2041	CONC	8.33	.309	325	1.404	M_N SCALED
2010	1:1	1.0	1.0	199	2.0	DATA FIT
2010	1:1	1.0	0.0	173	2.0	DATA FIT

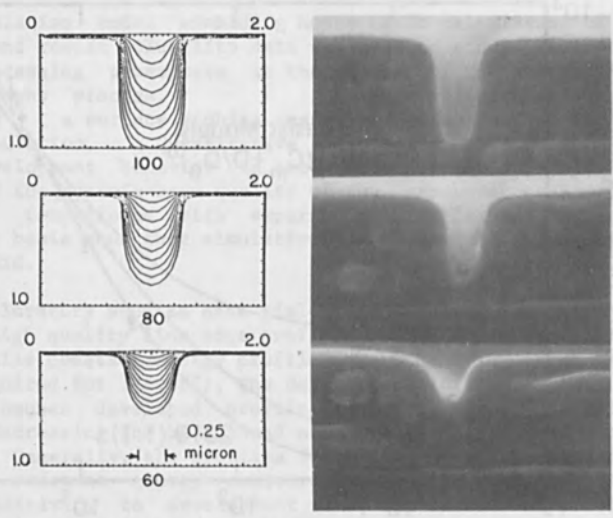


Figure 2. Simulation and SEM resist profiles for a 0.25 μm line written at doses of 60, 80, and 100 $\mu\text{C}/\text{cm}^2$. Contours: 20 sec intervals. Development time: 180 sec.

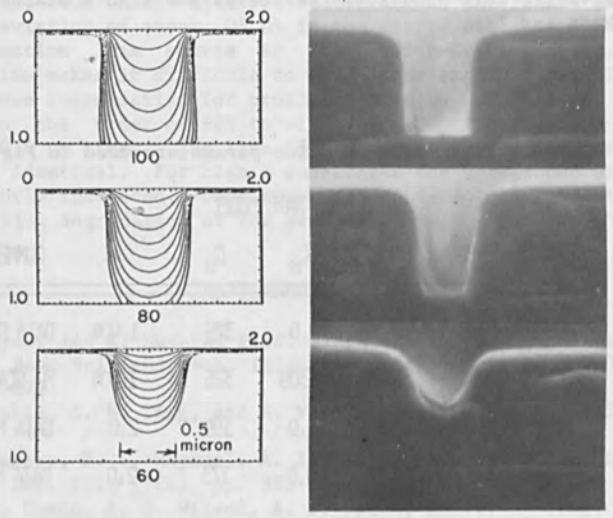


Figure 3. Simulation and SEM resist profiles for a 0.5 μm line at doses of 60, 80, and 100 $\mu\text{C}/\text{cm}^2$.

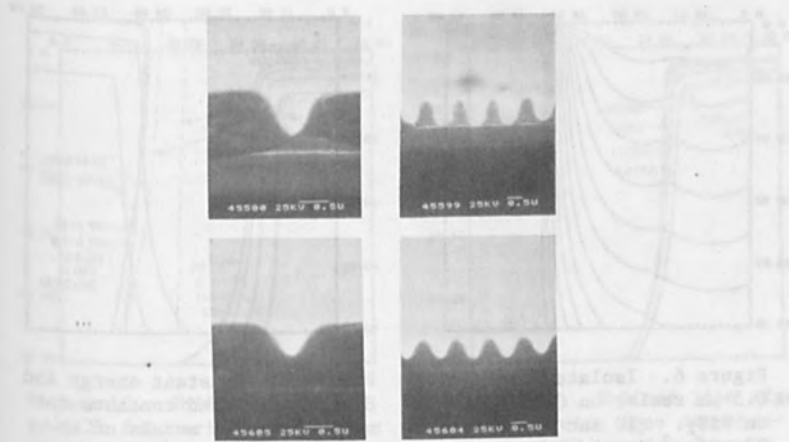


Figure 4. SEM of single and array of five 0.5 μm lines on 1.0 μm centers at doses of 100 $\mu\text{C}/\text{cm}^2$ (top) and 80 $\mu\text{C}/\text{cm}^2$ (bottom).

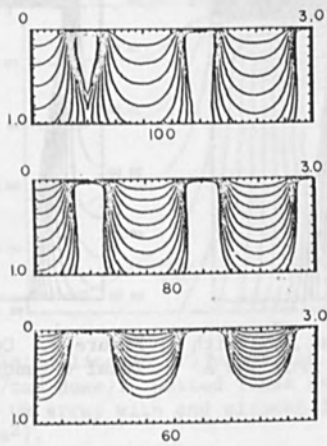


Figure 5. Simulated array of five 0.6 μm lines on 1.2 μm centers at doses of 60, 80, and 100 $\mu\text{C}/\text{cm}^2$.

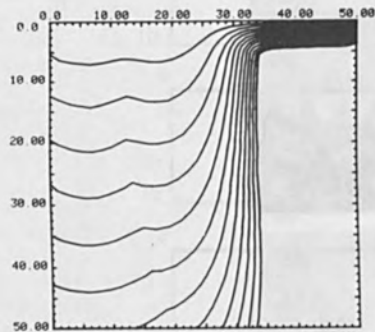


Figure 6. Isolated line in 0.5 μm resist on 0.08 μm Cr on SiO_2 . (10 sec contours, 80 $\mu\text{C}/\text{cm}^2$ dose)

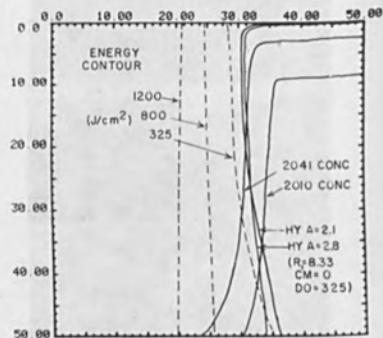


Figure 7. Constant energy and 80 sec developed contours for various resist models of an isolated line.

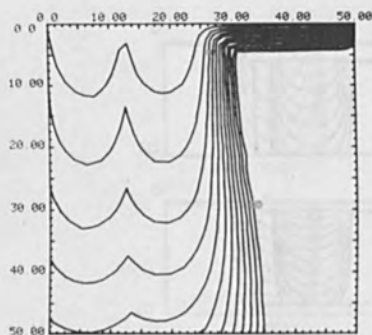


Figure 8. Isolated line with σ of beam reduced from 500 \AA to 250 \AA .

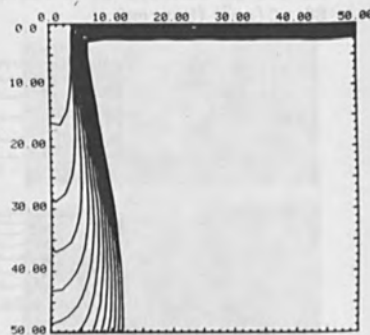


Figure 9. Contours for an ideal δ -function line exposure.

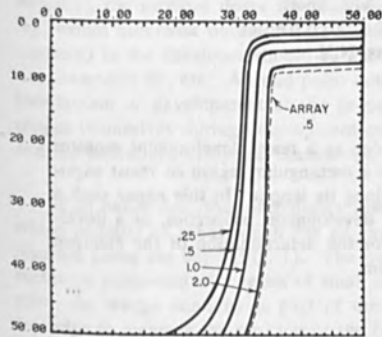


Figure 10. Shifted line edge profile for various linewidths at $80 \mu\text{C}/\text{cm}^2$ and 80 sec development.

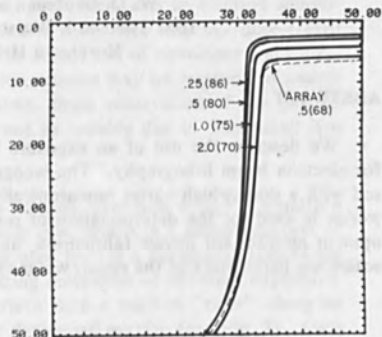


Figure 11. Shifted line edge profiles with dose compensation and 80 sec development.

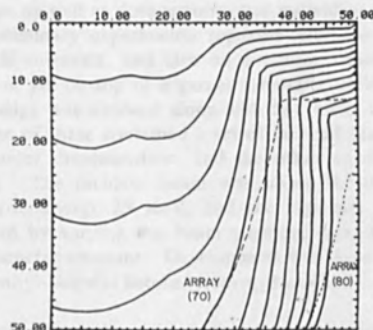


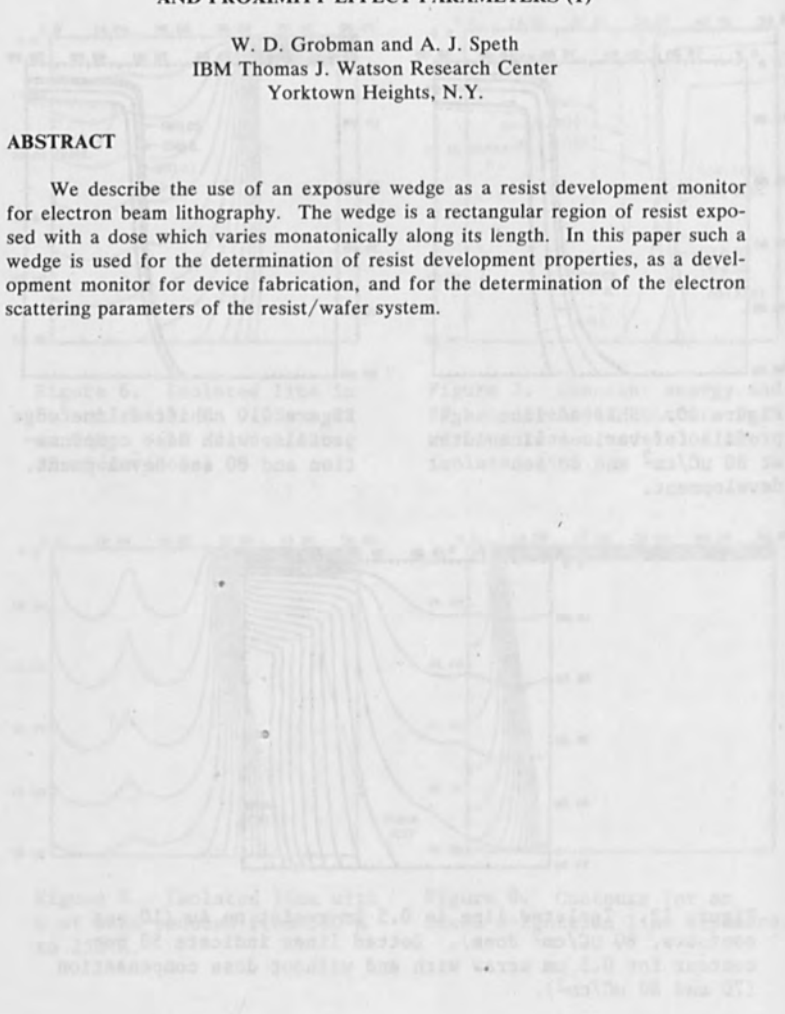
Figure 12. Isolated line in $0.5 \mu\text{m}$ resist on Au (10 sec contours, $80 \mu\text{C}/\text{cm}^2$ dose). Dotted lines indicate 50 sec contour for $0.5 \mu\text{m}$ array with and without dose compensation (70 and $80 \mu\text{C}/\text{cm}^2$).

AN EXPOSURE WEDGE FOR ELECTRON BEAM LITHOGRAPHY
DEVELOPMENT CONTROL AND FOR THE
DETERMINATION OF RESIST DEVELOPMENT
AND PROXIMITY EFFECT PARAMETERS (1)

W. D. Grobman and A. J. Speth
IBM Thomas J. Watson Research Center
Yorktown Heights, N.Y.

ABSTRACT

We describe the use of an exposure wedge as a resist development monitor for electron beam lithography. The wedge is a rectangular region of resist exposed with a dose which varies monotonically along its length. In this paper such a wedge is used for the determination of resist development properties, as a development monitor for device fabrication, and for the determination of the electron scattering parameters of the resist/wafer system.



I. INTRODUCTION

A quantitative understanding of the response of resist to electron exposure is central to the control of resist development during device fabrication. In particular, due to the proximity effect (2,3), typical patterns with a variety of shapes of small dimensions can be properly developed only if three conditions are met: The dose in the resist for different shapes must be understood and controlled by adjusting the incident doses for individual shapes which, due to electron scattering, would otherwise obtain different doses. The resist etch rate vs. dose (resist contrast) in the developer should be known as a function of developer concentration, temperature, etc. An end point detection scheme may be required to enable termination of development at the proper time, since observation of the pattern shapes themselves during development may not be reliable due to their small size and the limitations of optical microscopy.

This paper describes preliminary results with an 'exposure wedge' - a pattern which consists of a bar which has an exposure dose which is a linear function of position along the bar. (Fig. 1). The wedge used here is a horizontal 1mmx4mm rectangle composed of a series of small abutting rectangles of different exposures. Also, the wedge contains as part of the pattern data a built-in "ruler" along its top edge to measure the position of the fully developed portion (see Fig. 2). Such an exposure wedge is used here for proximity function parameter determination, for resist etch rate determination, and for development end point detection. Fig. 2 is a photograph of such an exposure wedge.

The experiments were done in an IBM vector scan electron beam system (4) with shape-by-shape programable exposure doses which enable simple fabrication of an exposure wedge, as well as dosage control of individual shapes for proximity correction. Our preliminary experiments reported here are on 0.6 micrometer thick PMMA on a Si substrate, and also on a sample consisting of 0.6 μm of PMMA on 0.35 μm of Au on top of a garnet substrate, both baked at 160C for 60 minutes. The wedge was exposed along with two other types of patterns on the same wafer. One of these contained a set of isolated lines of various widths for proximity parameter determination, and the other consisted of a series of closely spaced bars. The incident beam was about 0.2-0.35 micrometers in diameter with electron energy 25 KeV, and the exposure dose for individual shapes was controlled by varying the beam stepping rate, keeping the incident beam current and diameter constant. Development was done at a temperature of 23C in 2:3 or 1:1 methyl-isobutyl ketone: isopropyl alcohol.

II. RESIST DEVELOPMENT MEASUREMENT AND MONITORING

First, development rate vs. exposure was measured for PMMA on Si by developing a wedge for five second intervals, followed by drying and microscope inspection to measure the position along the wedge (and thus the dose) at which the 0.6 microns of resist had just disappeared. Two wedges were exposed on one wafer to cover the desired exposure range. In Fig. 3 we plot the development time vs. dose. In this figure we also plot the corresponding resist etch rate vs. dose. It is significant that this entire curve, characterizing the resist contrast vs. dose, was obtained from one sample in about one hour of measurement time, due to the wide range of doses on a wedge and the ease of converting the position of the full development point on the wedge to a dose value.

The position of the edge separating fully developed and partially developed resist in the wedge is quite visible since dark interference fringes appear rapidly in the resist as its thickness increases from zero. Also, due to the range of exposures on a wedge, this edge has an x position which is a rapid function of development time. For these two reasons, the wedge is a very sensitive development guide which is easily used in our laboratory to achieve highly reproducible resist development during device fabrication.

III. PROXIMITY PARAMETER DETERMINATION

For a beam incident at $r=0$ on a resist-coated substrate, we denote by $f(r)d^2r$ the distribution of *effective dose* in the resist at distance r from the evident beam. (We emphasize that $f(r)$ is related to the *effective dose* in the resist, *not* the number of electrons per unit area. Electrons scattering in the resist and substrate achieve a range of energies so that different electrons have different efficiencies for resist exposure. In the present paper we only measure the effects of the electrons on resist development.) We assume that $f(r)$ is normalized ($2\pi \int f(r)rdr=1$) and that $f(r)$ is the sum of two gaussians of the form

$$f(r) = \frac{1}{\pi(1+\eta)} \left[\frac{e^{-r^2/\alpha^2}}{\alpha^2} + \eta \frac{e^{-r^2/\beta^2}}{\beta^2} \right] \quad (1)$$

where the gaussian with range α represents the sum of the incident electron beam, which spreads a small amount in the resist ($\alpha \ll 1 \mu\text{m}$), and the portion of this beam which backscatters directly from the substrate at angles close to 180° . Due to this latter contribution, as well as the fact that we measure effective dose and not true dose, the first gaussian is not simply related to the incident electron dose in coulombs/cm². The second gaussian represents the electrons which multiply scatter at large angles in the resist and substrate and cause a low intensity dose at large distances ($r \geq 1 \mu\text{m}$) from the origin. This analysis contains no dependence on z , the coordinate normal to the wafer, and thus represents the thin resist limit.

We determine respectively, α , β and η (the range of the "incident" and "backscattered" effective doses and the "backscattered ratio") by a technique illustrated in Fig. 4. In this technique a wedge (dimension $\approx 1\text{mm}$) is exposed with a true *incident dose* of $Q_{\text{WEDGE}}(X)$, while a series of small bars of widths $W=W_1, W_2, \dots$ which are of the order of $1 \mu\text{m}$ are exposed by an incident dose Q_0 . The effective dose in the resist at the center ($r=0$) of one of these small shapes, denoted Q_{RESIST} , is Q_0 times the integral of $f(r)$ over the area of the shape. At a point X in the wedge, the effective dose is $Q_{\text{WEDGE}}(X)$ times $f(r)$ integrated over an area so large that the integral is 1 due to the normalization of $f(r)$. A constant relating the effective dose to the incident dose has been ignored in these two cases, since it would cancel out in our analysis.

We develop the resist-covered wafer until a bar of a particular width W_n has its resist in the center just cleared out. The point x in the wedge which has reached the same developed condition is determined, and the resist dose for these two features is equated:

$$Q_0 \int_{\Lambda(W_n)} f(r) d^2r = Q_{\text{WEDGE}}(X)$$

or

$$\frac{Q_{\text{WEDGE}}(X)}{Q_0} = \frac{\int f(r) d^2r}{A(W_n)} \quad (2)$$

Where $A(W_n)$ denotes an area integral over the area of the shape of width W_n . The left hand side of (2) represents the experimental data, which is plotted as a function of W in Fig. 5 for 0.6μ of PMMA on Si or on 0.35μ of Au on garnet. The right hand side of (2) is a function of W which depends on the three parameters α , β and η , which are adjusted for the best fit between the model and experiment. For each sample, two curves are plotted in Fig. 5. One is for isolated bars of width W , and the other is for patterns of such bars separated by unexposed regions of width W . The data points for both geometries are fit by theoretical curves with a single set of parameters. The fits, to 10-12 data points, are very good and make a strong point for the nature of the function $f(r)$ in Eq. (1) and for the values of the parameters obtained here. The effective distribution $f(r)$ is plotted in Fig. 6. The even bars in Fig. 5 show the greater uncertainty in data taken from smaller width test shapes. The fit of the model to the data is much better than this estimated experimental uncertainty. The parameters α , β and η are independent in fitting the model to the data, and β and η are uniquely determined even by the data at large values of W .

The present paper gives preliminary results of the technique. In these preliminary experiments, the beam size and beam stepping distance were a large fraction of $1 \mu\text{m}$, contributing to the large value of α for Au on garnet (see Fig. 5B). A further contribution to α for the case of an Au substrate is suggested in Ref. 5, and is due to large angle elastic backscattering from the high Z material. A future, more detailed paper will give our final results for α , β , and η , based on experiments in which the electron optical conditions are chosen to minimize beam size and beam stepping distance so that α can represent the intrinsic width of the scattering function central peak.

IV. CONCLUSIONS

This paper has shown that a simple technique which uses an exposure wedge can generate the parameters which determine $f(r)$ - a function which is the necessary input for any program which corrects electron beam pattern data for the proximity effect. This determination has been a weak point in proximity correction techniques in the past. Also, once proximity correction is implemented in small geometry ($\leq 1/2 \mu\text{m}$) patterns, an easily visible development guide is required to reproducibly develop patterns too small to monitor accurately using optical microscopy. Our exposure wedge also serves as such a device. Thus it presents an effective and simple tool for use in electron beam microfabrication at dimensions close to the inherent limits of the technology.

ACKNOWLEDGEMENTS

We wish to acknowledge the technical assistance of T. Donohue, and useful conversations with T. H. P. Chang and M. Parikh.

REFERENCES

1. Some of the material presented here has also been presented in the Proceedings of "Microcircuit Engineering '78", Cambridge, England, April 1978.
2. T. H. P. Chang, "Proximity Effect in Electron-beam Lithography", J. Vac. Sci. Technol. 12, 1271 (1975).
3. M. Parikh, "Self-consistent Proximity Effect Correction Technique for Resist Exposure (SPECTRE)", J. Vac. Sci. Technol., January 1978.
4. A. J. Speth, A. D. Wilson, A. Kern and T. H. P. Chang, "Electron-beam Lithography using Vector Scan Techniques", J. Vac. Sci. Technol. 12, 1235 (1975).
5. M. Parikh and D. F. Kyser, "Proximity Function Approximations for Electron Beam Lithography," Proc. of the 8th Int. Conf. on Electron & Ion Beam Science & Technol., R. Bakish, Ed. (Seattle, 1978).

FIGURE CAPTIONS

- Figure 1 Schematic illustrations of exposure wedge. The exposure varies linearly with position. Upon development for some period, the resist at the heavily exposed end of the wedge has zero thickness. At points of weaker exposure, the resist thickness increases monotonically with position.
- Figure 2 The wedge shown is one in which the exposure vs position is a stepwise approximation to the curve in Fig. 1. Bands of different shading, corresponding to resist of different thickness, are readily apparent, as is the position of the boundary between resist of zero and non-zero thickness.
- Figure 3 Development time to zero thickness (t) and corresponding resist development rate (R) measured as a function of Q_0 , the incident dose in units of 10^{-5} coulombs/cm².
- Figure 4 Illustration of the technique for determining the electron scattering function parameters. The effective dose Q_{resist} at the point X on the wedge at which resist thickness is just zero is proportional to the incident dose $Q_{\text{wedge}}(X)$. For incident dose Q_0 on a small shape for which the resist has just thinned to zero thickness at the center, the effective dose is also Q_{resist} and is Q_0 times the integral of the scattering function over the area of the small shape. Equating these two, one obtains the fact that $Q_{\text{wedge}}(X)/Q_0$ (which can be measured) is the integral of $f(r)$ over the area of the small shape.
- Figure 5 Plots of measured values of Q_{wedge}/Q_0 vs width of bar patterns (W) for a pattern of isolated bars(O) and of a series of bars of width W separated by spaces of width $W(X)$. The theoretical fit to the data is represented as dashed lines, and the scattering function parameters which yielded the dashed, theoretical curves are given. Panel (a) is for $\sim 6000 \text{ \AA}$ PMMA on Si, Panel (b) is for $\sim 6000 \text{ \AA}$ PMMA on 3500 \AA Au on a garnet substrate.
- Figure 6 Electron scattering function $f(r)$ (in units of μm^{-2}) for the two resist/substrate systems shown in Fig. 5. $f(r)$ is normalized to unity as described in the text. The function is shown both at the scale shown on the ordinate, and also increased in amplitude by a factor of 100.

E-BEAM EXPOSURE WEDGE
DEVELOPMENT
MONITOR

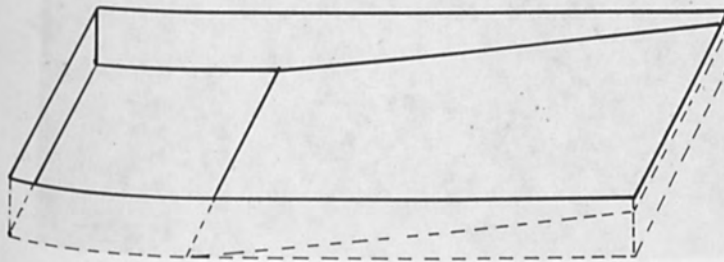
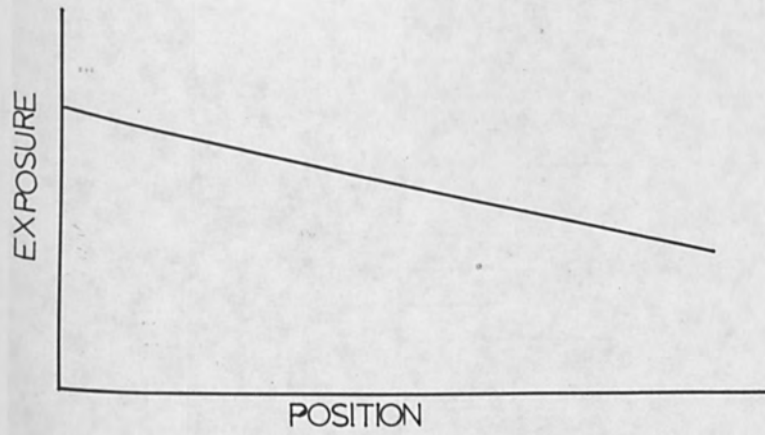


Figure 1

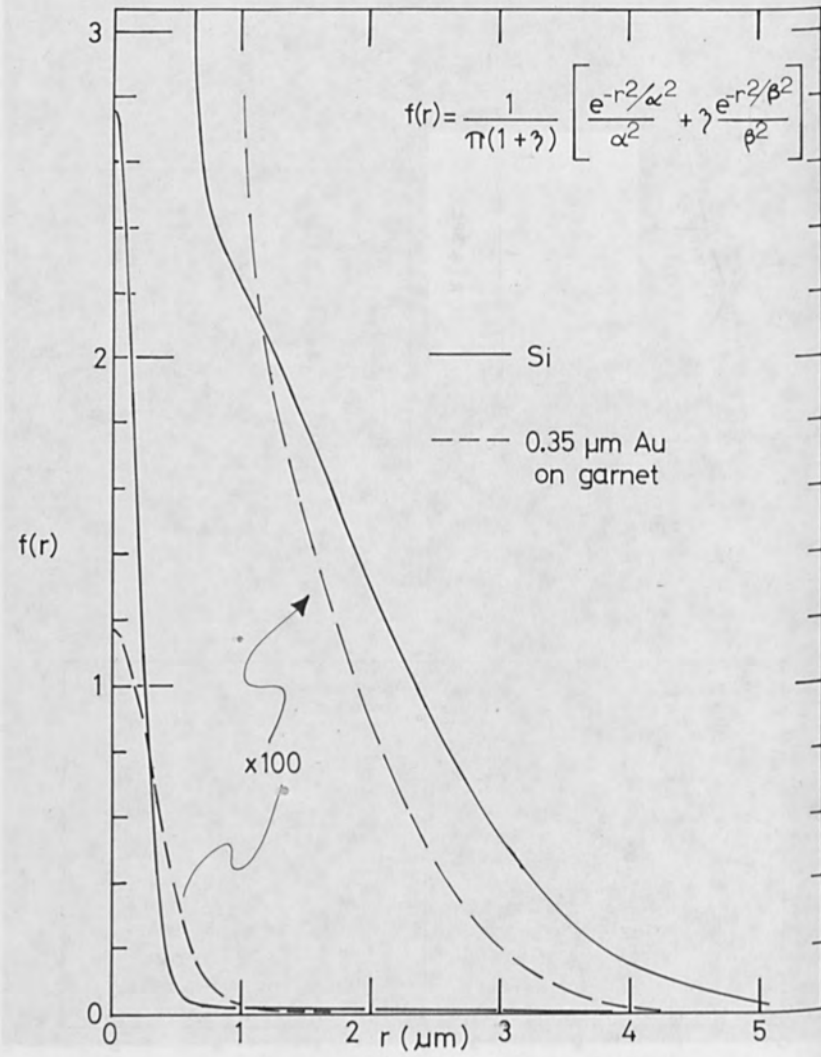


Figure 6

DIAZO-TYPE PHOTORESIST SYSTEMS UNDER ELECTRON BEAM EXPOSURE

M. Hatzakis and J. M. Shaw

IBM Thomas J. Watson Research Center
P. O. Box 218
Yorktown Heights, New York 10598

The electron beam exposure characteristics of several diazo-type positive photoresists such as Shipley AZ 2400 and AZ 1350-J, Kodak #809 and Polychrome PC 129 have been studied with SEM examination of exposed and developed resist profiles.

Resist performance was studied as a function of electron beam exposure density and developer concentration.

These tests indicate that Shipley AZ 2400 resist is superior to all other resists tested requiring an exposure of 2×10^{-5} Coul/cm² for vertical resist profiles, at 20 KV.

I. INTRODUCTION

Electron beam lithography is being increasingly considered as an alternate tool to UV lithography for the fabrication of devices directly on silicon or for photomasks. Although electron beam resists such as PMMA⁽¹⁾, PBS⁽²⁾ and others have been already used with electron beam exposure systems to fabricate both devices⁽³⁾ and masks⁽⁴⁾, the acceptance of these resists in the manufacturing environment has been very slow due to uncertainties and unknowns associated with processing of these materials. In contrast, diazo-type photoresists such as Shipley AZ 1350 and AZ 2400, Kodak #809, Polychrome PC 129 and others have been used for a number of years for the production of both integrated circuits and photomasks with UV lithography. As a result of this, a very high level of confidence exists among manufacturing people over use of these materials. Moreover these resists are more resistant to the plasma etching environment than either PMMA or PBS.

For these reasons, it has been decided to examine diazo-type photoresists as possible candidates for electron beam resists. Initial experiments, directed at measuring the UV and electron beam sensitivity of photoresists, indicated that AZ 2400 exhibits higher contrast than all other materials tested⁽⁵⁾.

In this paper a more detailed study of electron beam sensitivity has been conducted using the optimum developer for each resist.

II. EXPERIMENTAL CONDITIONS

For direct comparison purposes all experiments were conducted on silicon wafers coated by spinning with the resist tested, to a thickness of approximately 1.2 micrometers and baked at 82°C for 20 minutes in air before exposure.

All exposures were carried out in a flying spot scanner-controlled electron beam system, which has already been described elsewhere⁽⁶⁾, at 20 KV beam accelerating potential. A line pattern consisting of one to twenty micrometers wide lines, running along the slow scan direction of the system, was exposed on all wafers at variable beam current and constant exposure time, corresponding to exposures ranging from 5×10^{-6} to 5×10^{-5} coul/cm². The optimum developer for each resist was determined by developing the lowest exposure (5×10^{-6} coul/cm²) in a variety of developers and concentrations and selecting the one which was able to completely develop the pattern in a reasonable time (under 15 min.) and with minimum unexposed resist thickness loss. This is obviously a time consuming process and represents the major part of the experimental work.

Subsequently, the optimum developer solution for each resist was used to develop all exposures to the point where the finest (1 micrometer) lines were cleared-out. Each exposure field was then fractured in a direction perpendicular to the direction of the developed lines by first scribing a line with a tungsten carbide tip on either side of the line pattern and applying pressure on the silicon wafer over a sharp edge. All samples were inserted in a holder, metallized with 500Å of evaporated aluminum and examined in the scanning electron microscope (SEM).

Temperature stability measurements were conducted by exposing several patterns with equal exposures on a silicon wafer, developing the resist and then fracturing each line pattern successively after heating the wafer at various temperatures.

III. RESULTS AND DISCUSSION

Figures 1-6 show the SEM line profiles for the resists tested taken at one micron and four micron pattern linewidths and varying exposure density. For each case a portion of the wafer was also examined in the SEM before development in order to establish the exact resist starting thickness. From these photos a variety of resist sensitivity data can be extracted:

1. The resist profile angle to the surface normal can be measured for each exposure and resist system.
2. From the development time data for each resist and developer solution, the exposed resist solubility can be measured as a function of exposure.
3. The unexposed resist thickness, remaining after development, can be measured and related to the initial resist thickness.

As it can be seen from these photos, Kodak #809 and Polychrome PC 129 exhibit very low contrast in the range of exposures used while Shipley AZ 1350-J and AZ 2400 exhibit high contrast, (vertical resist profiles) and little thickness loss during development. Also note that AZ 1350-J can be developed with two developer solutions, Shipley AZ straight and Shipley 2401, diluted in water to a concentration of one part developer to four parts water. (Figures 3 and 4). The importance of developer concentration is seen in Figures 5 and 6 with AZ 2400 resist. Note that a change in 2401 developer concentration from 1:3.5 (Fig. 5) to 1:2.5 (Fig. 6) reduces the resist contrast (no vertical resist profiles can be obtained even at the higher exposure) and significantly increases the unexposed resist thickness loss.

The optimum developer and concentration for the resists tested are shown in Table I. Note that Polychrome PC 129 cannot be developed with the developer supplied by the manufacturer even at full strength, therefore, an alternative developer solution was chosen.

The data extracted from the resist profile photos of Figures 1-6 were plotted in a series of curves shown in Figures 7-11. Figure 7 compares the resist profile angle to the surface normal at various exposures to that of PMMA resist. Note that in order to obtain vertical resist profiles of one micron wide lines in one micron thick resist at 20 KV with PMMA resist, a dose of 8×10^{-5} coul/cm² is required, while with AZ 2400 similar profiles can be obtained at 2×10^{-5} coul/cm².

In Figure 8, the solubility as a function of exposure is plotted for three of the resists tested. The slope of these curves represent the rate of solubility change as a function of exposure which can be considered as the contrast for a positive resist. Note that the contrast increases with exposure, as expected and that for any exposure it is highest for Shipley AZ 2400.

The third method of comparing sensitivity with positive resists consists of plotting the normalized unexposed resist thickness, remaining on the workpiece after complete development of the exposed resist pattern. This method is equally important because it allows direct determination of unexposed resist thickness loss as a function of exposure. The thickness loss data for the four resists tested is plotted in Figure 9. Note again that Shipley AZ 1350-J and AZ 2400 exhibit the least thickness loss as compared to Kodak and Polychrome. As it can be seen in Figure 9, the point at which 90-95% of the original resist thickness remains corresponds to the exposure at which vertical resist walls in the developed image are obtained. Furthermore, this method of reporting sensitivity allows direct comparison between positive and negative resists. Figure 10 shows plots of resist thickness remaining for two negative⁽⁷⁾ and two positive⁽⁸⁾ electron resists. Note again that the point at which 90% of the resist thickness remains corresponds to the exposure required to obtain vertical walls for the positive resists. For negative resists of the type shown in Figure 10, exposure at the 90% thickness remaining point or at a point obtained by the extrapolation of the linear portion of the curve (as shown by the dotted line), may be impractical because of resolution limitations. Any other exposure point can be selected, however, from the curves.

For these reasons this form of reporting sensitivity for both positive and negative electron and x-ray resists is preferred and is suggested for consideration to other workers in the field.

The sensitivity of Shipley AZ 2400 with the optimum developer and with a more concentrated solution of AZ 2401 developer is shown in Figure 11. Note that due to excessive thickness loss with the stronger developer solution, the apparent sensitivity of the resist is very significantly lower than with the optimum 1:3.5 dilution. Further dilution results in extremely long development times for the lower exposures and eventual loss of resist adhesion to the substrate.

Figure 9 indicates that the sensitivities of AZ 1350-J and AZ 2400 are very similar (both with the optimum developer) although an SEM examination of the developed pattern surface for the two resists, shown in Figure 12, reveals resist thickness variations which result in pattern line width variations with the 1350 J resist. This is the result of radial striations caused by the resist spinning operation and are always present with this resist especially when some unexposed resist thickness loss takes place during development. This effect is totally absent with AZ 2400 resist as it can be seen in Figure 12, therefore this resist is superior to AZ 1350-J as far as resolution and line width control are concerned.

The thermal stability characteristics of AZ 2400 after development are shown in Figure 13. Note that if the temperature of the sample is raised quickly, by insertion in an oven preset at that temperature, resist flow begins at 120°C as shown by the left hand side of the figure. It however the temperature is raised slowly from room temperature in a period

of 10-15 minutes, then resist flow is almost totally absent even up to 140°C. This form of heating in fact is more likely to be encountered during processing such as lift-off metal evaporation of reactive ion etching, which always starts at room temperature with loading of the wafers in to the system. Figure 14 is intended to demonstrate the resolution capabilities of Shipley AZ 2400 resist exposed at 2×10^{-5} coul/cm² and developed in 1:3.5 solution of AZ 2401 developer in water. The pattern shown on top of the figure is an SEM photo of a zone plate fractured after development in such a way that resist profiles can be observed at the edge with linewidths and spacings that decrease towards the edges of the pattern. Various profiles at high magnification are shown below with the narrowest linewidth approximately 3000Å in one micron thick resist with vertical edges. These profiles demonstrate resolution and aspect ratios previously considered possible only with PMMA exposed at 8×10^{-5} coul/cm².

IV. CONCLUSIONS

The exposure and development characteristics of several diazo-type positive photoresists under electron beam exposure were measured. The results indicate that Shipley AZ 2400 is superior to all others tested, with a nominal sensitivity (vertical resist walls in one micron thick resist layer) of 2×10^{-5} coul/cm² at 20 KV. This represents an improvement over standard PMMA of a factor of four while maintaining comparable resolution and higher temperature stability with gradual heating of the developed resist pattern. This resist system is suggested to workers in the field as a useful medium for mask or direct device fabrication with electron beam microfabrication systems.

V. REFERENCES

1. M. Hatzakis, *J. Electrochemical Society*, 116, 1034 (1969).
2. M. J. Bowden, L. F. Thompson, *J. Appl. Polym. Sci.*, 17, 3211 (1973).
3. H. N. Yu, et. al., *J. Vac. Sci. Technol.*, Vol. 12, No. 6, 1297 (1975).
4. R. F. W. Pease et. al. *IEEE Trans. Electron Devices*, ED-22, No. 7, 393 (1975).
5. J. M. Shaw and M. Hatzakis, *IEEE Trans. Electron Devices*, ED-25, No. 4, 425 (1978).
6. R. F. M. Thornley, M. Hatzakis and V. A. Dhaka, *IEEE Trans. Electron Devices*, ED-17, 961 (1970).
7. L. F. Thompson, J. P. Ballantyne, E. D. Feit, *J. Vac. Sci. Technol.*, Vol. 12, No. 6, 1280 (1975).
8. M. Hatzakis, *J. Vac. Sci. Technol.*, Vol. 12, No. 6, 1279 (1975).

VI. FIGURE CAPTIONS

TABLE I: Optimum developer solutions for each of the photoresists tested under e-beam exposure.

1. SEM profiles of Kodak 809 photoresist.
2. SEM profiles of Polychrome PC-129 photoresist.
3. SEM profiles of Shipley AZ 1350-J with AZ developer.
4. SEM profiles of Shipley AZ 1350-J with 2401 developer.
5. SEM profiles of Shipley AZ 2400 with 1:3.5 solution of 2401 developer in water.
6. SEM profiles of Shipley AZ 2400 with 1:2.5 solution of 2401 developer in water.
7. Graph of developed resist profile angle to the surface normal as a function of e-beam exposure for the resists tested, in comparison to PMMA resist.
8. Resist solubility in the optimum developer (see Table I) as a function of e-beam exposure for three of the photoresists tested.
9. Plots of normalized resist thickness remaining after developer as a function of e-beam exposure dose for four of the resists tested with the optimum developer.
10. Plots of normalized resist thickness remaining after development for two positive (right) and two negative (left) resists as a function of e-beam exposure dose.
11. Plots of normalized resist thickness as a function of exposure dose for AZ 2400 and the two developer concentrations used.
12. SEM surface photos of the developed resist image at 10^{-5} Coul./cm² exposure for 8 shipley AZ 2400 and Shipley AZ 1350-J using the optimum developer for each resist.
13. Temperature stability of developed AZ 2400 resist crosssections exposed at 2×10^{-5} Coul./cm². The left hand side shows resist flow under quick heating, the right hand side, no detectable flow under gradual heating.
14. SEM photos of a zone plate pattern (top) and crosssections of Shipley AZ 2400 resist exposed at 2×10^{-5} Coul./cm² and developed in the optimum developer.

OPTIMUM DEVELOPER SOLUTIONS FOR THE RESISTS
 TESTED WITH ELECTRON BEAM EXPOSURE IN THE RANGE
 OF 5×10^{-6} TO 5×10^{-5} Coul/cm², 20 KV.

<u>RESIST</u>	<u>DEV. SOLUTION</u>
AZ 1350-J	AZ STRAIGHT
"	1:4 SHIPLEY 2401 IN WATER
AZ 2400	1:3.5 SHIPLEY 2401 IN WATER
POLYCHROME PC-129	1:6 SHIPLEY 303 IN WATER
KODAK 809	2:1 KODAK DEV. IN WATER

Table I

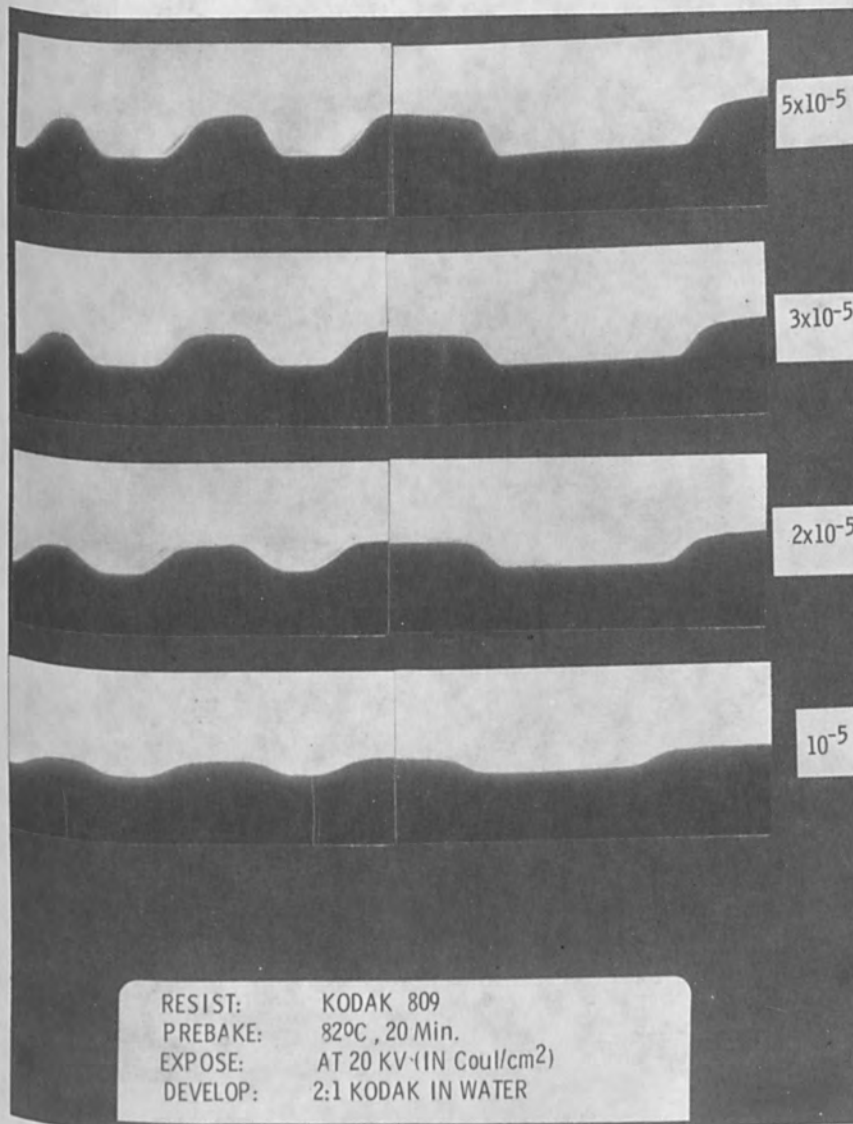


Figure 1

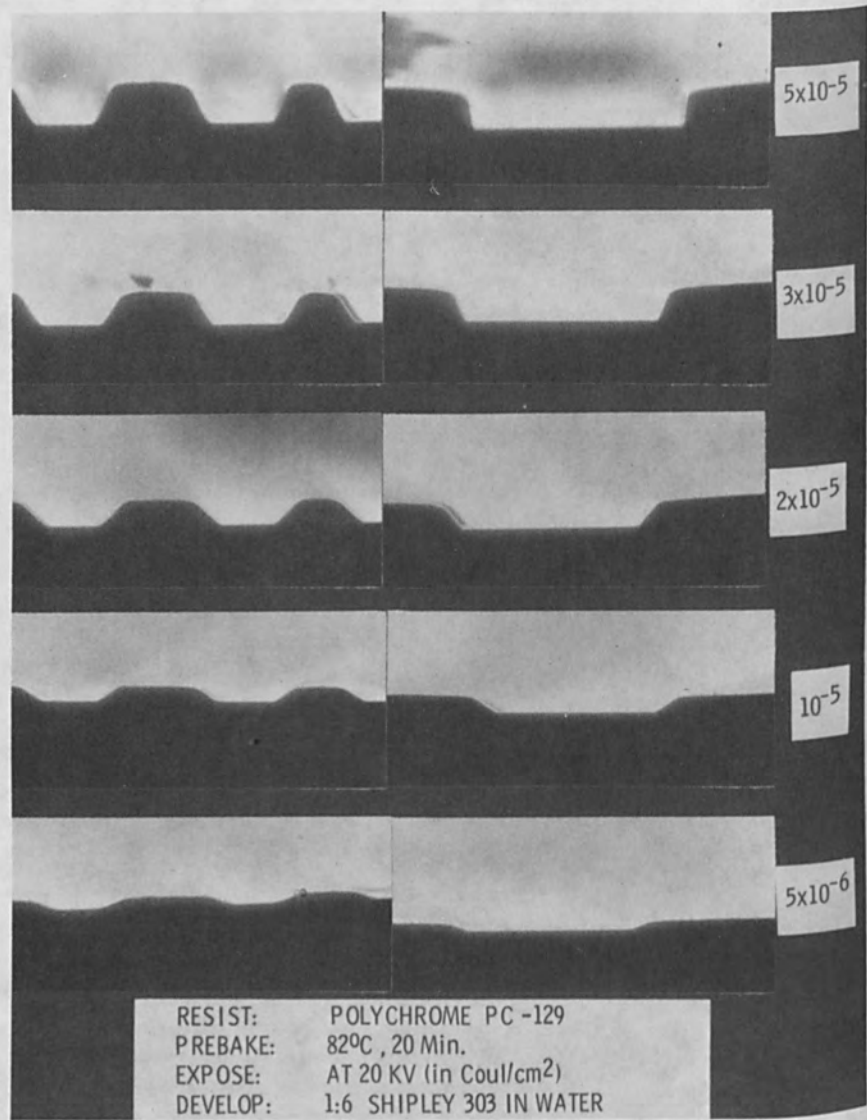


Figure 2

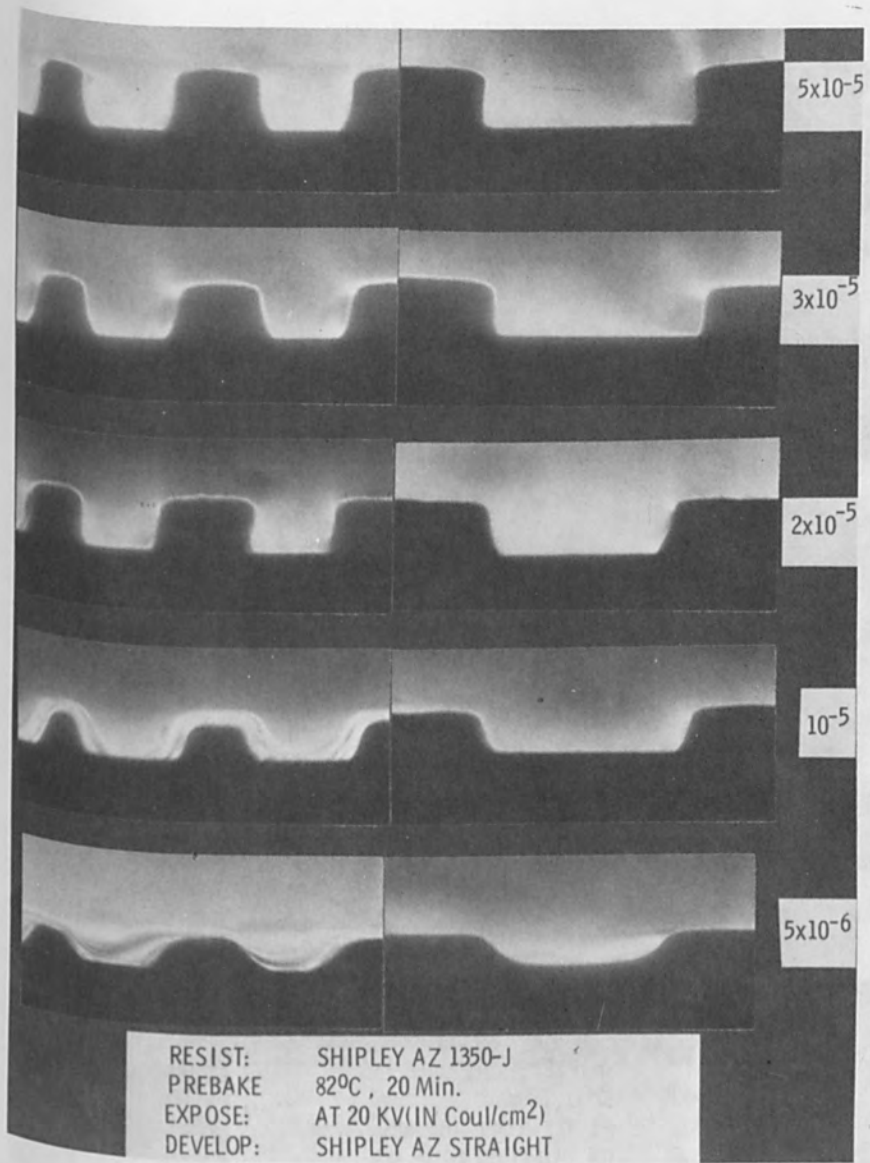


Figure 3

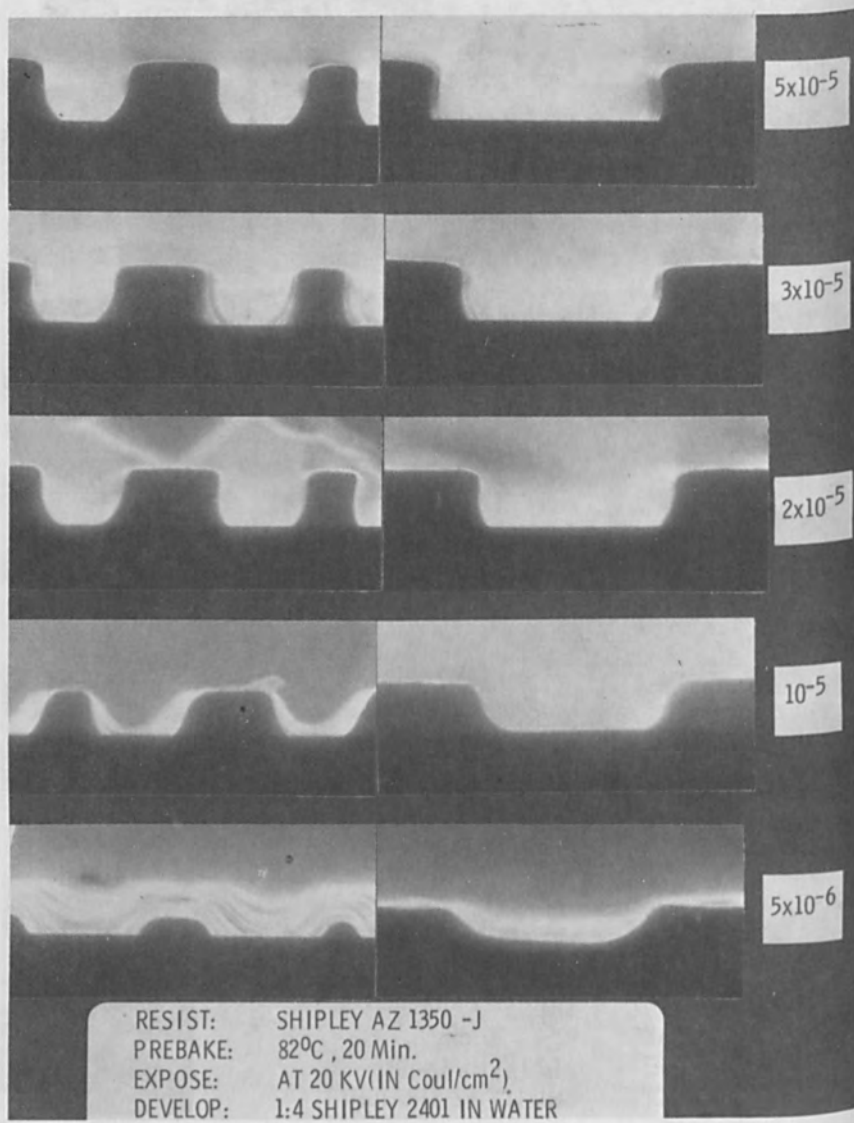


Figure 4

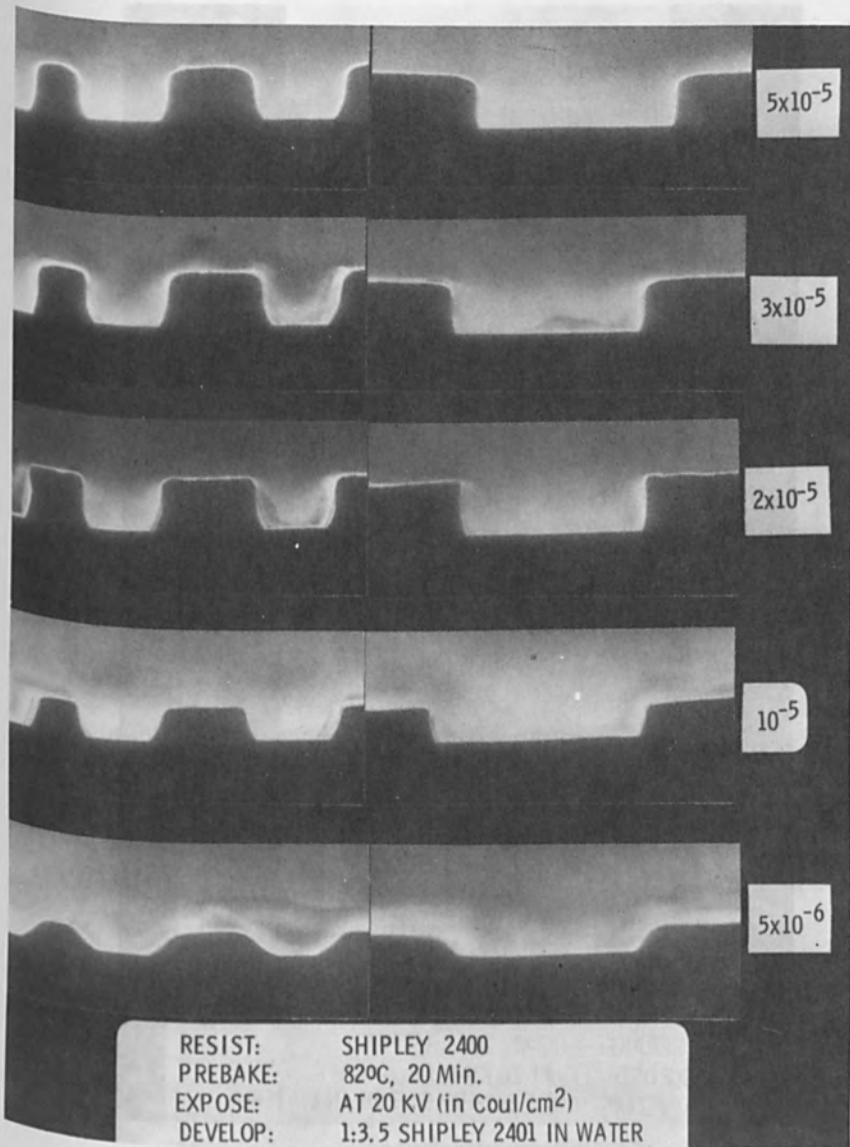


Figure 5

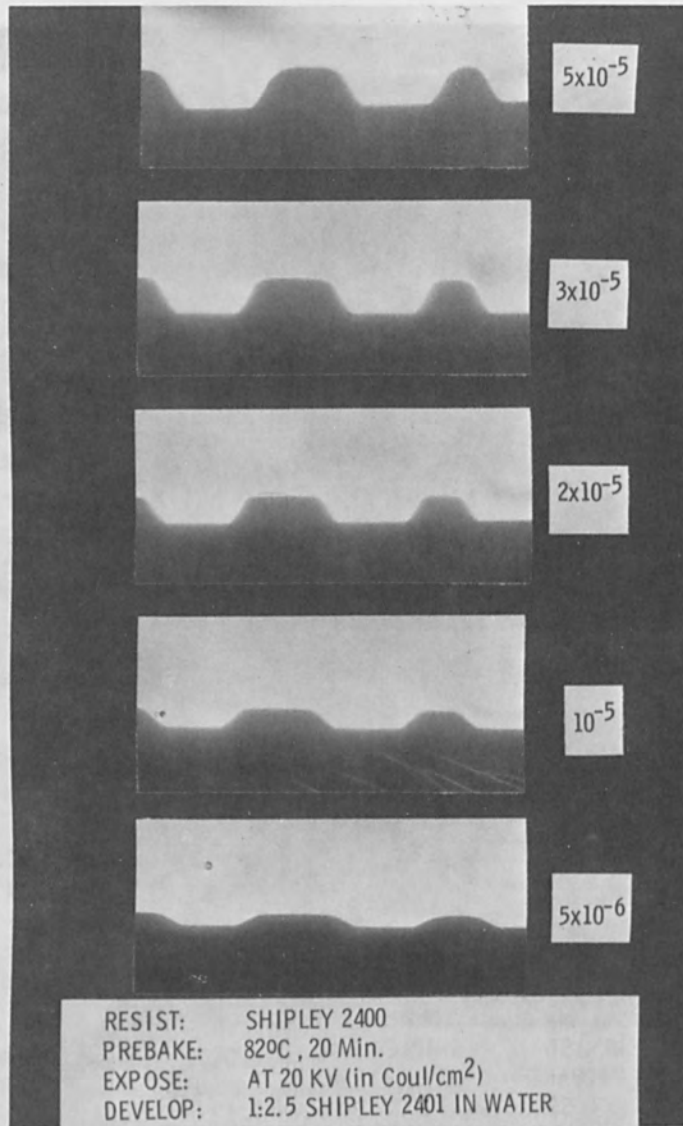


Figure 6

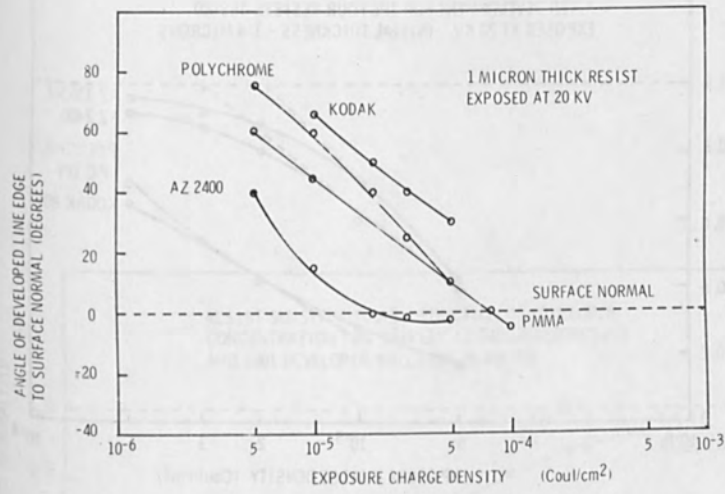


Figure 7

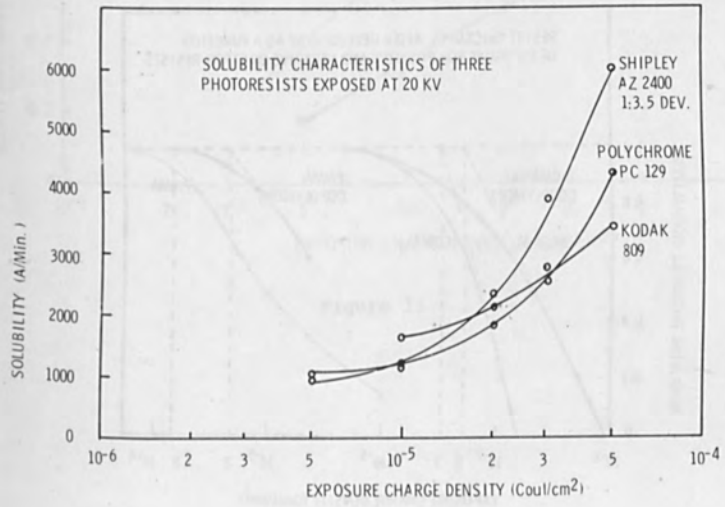


Figure 8

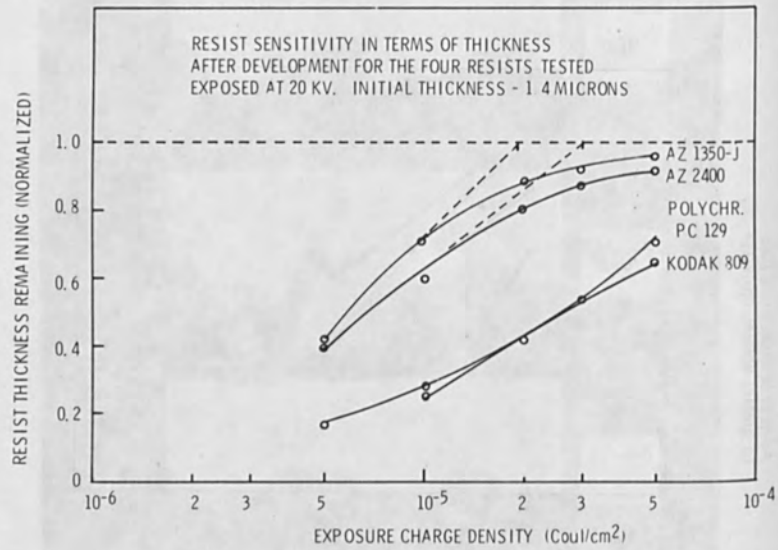


Figure 9

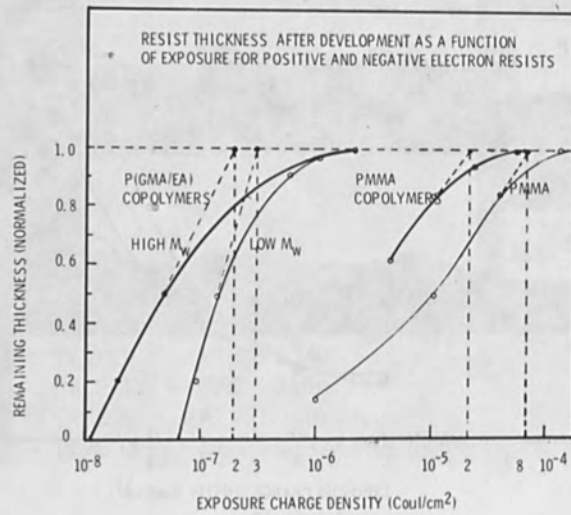


Figure 10

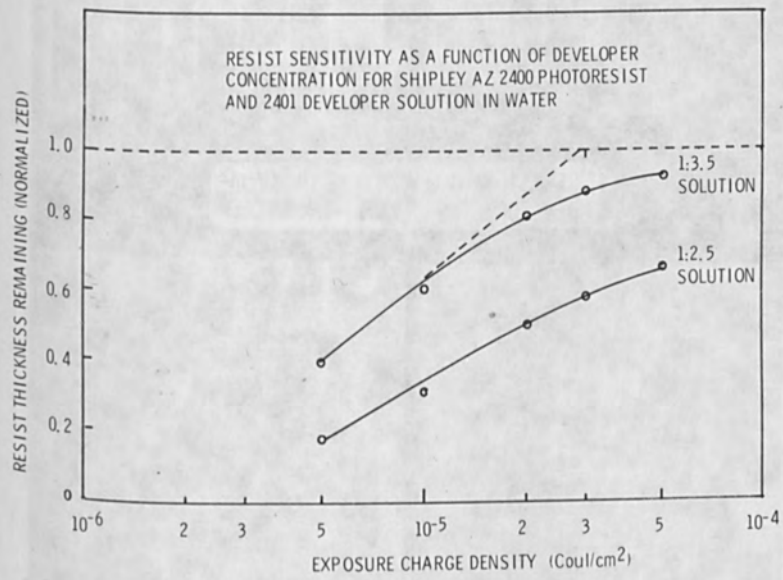


Figure 11

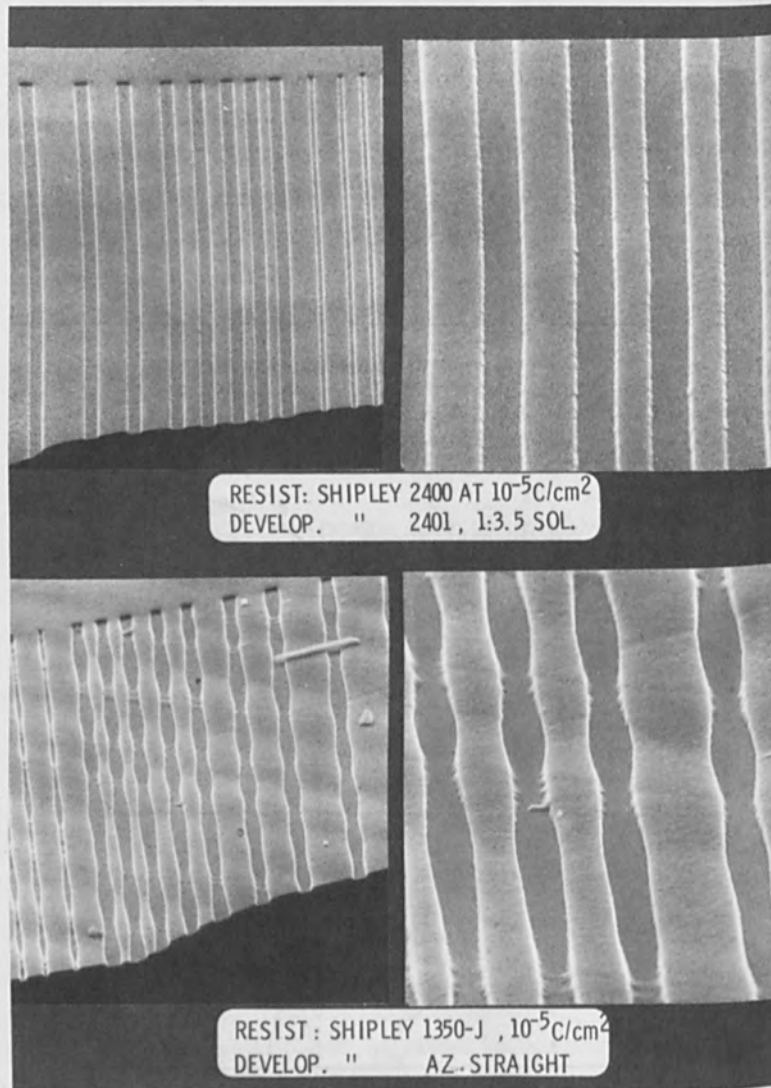


Figure 12

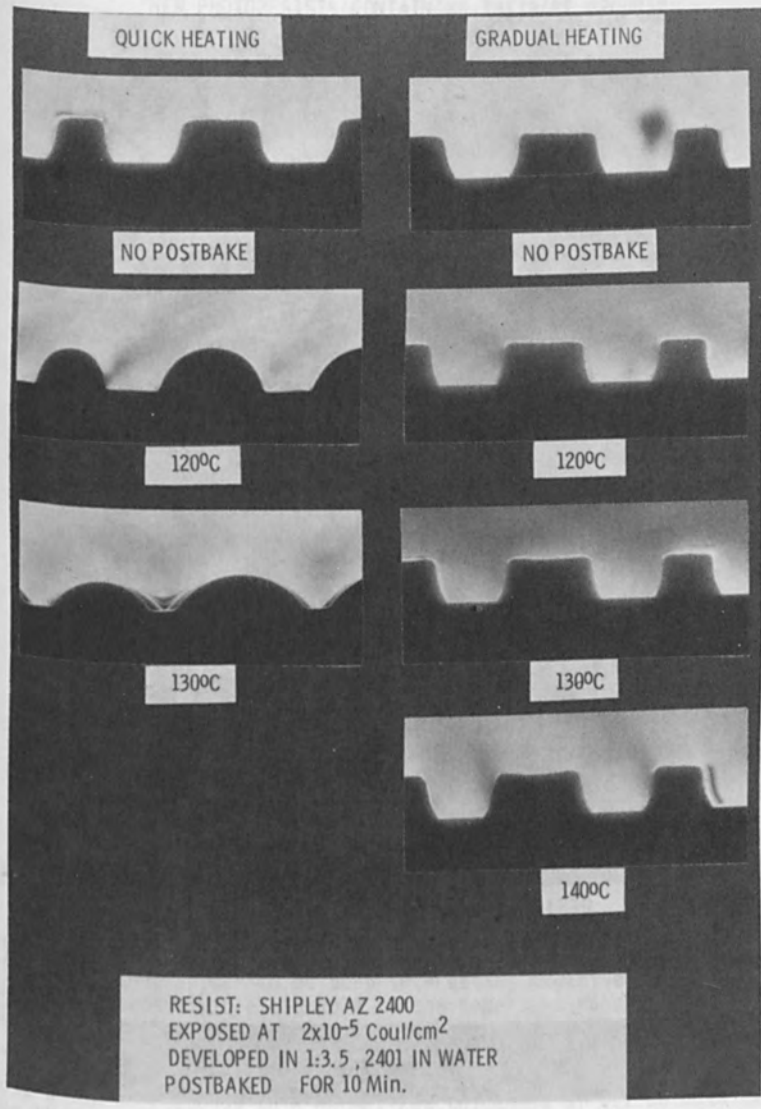


Figure 13

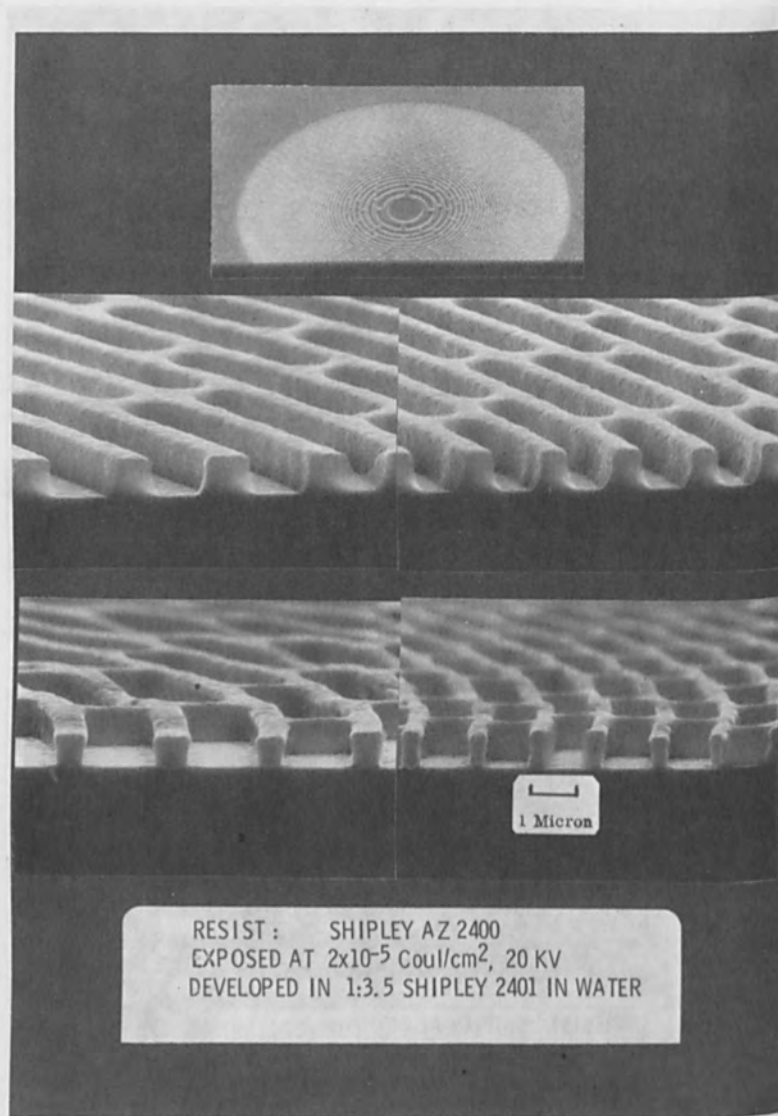


Figure 14

"NEW PHOTORESISTS CONTAINING THIRANE GROUPS"

J.C. Dubois - A. Eranian - E. Datamanti

Thomson-CSF Laboratoire Central de Recherches
Domaine de Corbeville 91401 ORSAY (France)

ABSTRACT

Crosslinking of polymers containing thirane rings $\begin{matrix} \diagup & & \diagdown \\ & C - C & \\ \diagdown & & \diagup \\ & S & \end{matrix}$ has been photosensitized in the near U.V. range by aryl diazonium salts releasing Lewis acids under irradiation.

Photolysis kinetics of two sensitizers of this series has been studied. In both cases, the photodegradation reaction has been found to be governed by the following time dependent law : $\ln \frac{(e^{2.3D_0} - 1)}{(e^{2.3Dt} - 1)} = \alpha t$ where α is a constant

Furthermore, the photolysis rate at two wavelengths has been compared. When corrected by the actual absorbed energy, it appears to be higher at 404.7 nm than at 365 nm for both sensitizers.

As far as photosensitization itself is concerned, the exposure characteristics of such a system have been specified : the sensitivity to U.V. light varying from 2.5 to 1 mJ/cm² depending on the amount of sensitizer, the contrast value being close to unity. Masking patterns with a 2 to 1.5 μ m linewidth have been obtained on Si substrates with SiO₂ surfaces.

INTRODUCTION

Polymers containing thirane groups $\begin{matrix} \diagup & & \diagdown \\ & C - C & \\ \diagdown & & \diagup \\ & S & \end{matrix}$ have been found to be sensitive to electron beam irradiation (1) $\begin{matrix} \diagup & & \diagdown \\ & C - C & \\ \diagdown & & \diagup \\ & S & \end{matrix}$ and to soft X-ray irradiation. They appear to be very interesting negative resists due to their high sensitivity assignable to the important reactivity of the thirane ring.

Assuming the sensitivity for negative resists to be the exposure dose which corresponds to a normalized thickness of 0.7 we obtained for these polymers :

$\sigma = 6 \times 10^{-7}$ C/cm² for an electron beam irradiation (20 keV)

$\sigma = 80$ J/cm³ for a soft X-ray irradiation (8.34 Å).

Containing only thirane groups with no other absorbing chromophores, they are not sensitive by themselves in the near U.V. range. Actually, the thirane ring absorption is characterized by one band in the region of 260 nm (2) which does not fit in with the maximum emission lines of a mercury source.

However, as it has been achieved for epoxy polymers (3), it is possible to photosensitize the thirane polymers in the 360-405 nm range and simultaneously to initiate their crosslinking by means of aryldiazonium salts with complex halide anions.

Figure 1 shows the general structure of such compounds and summarizes the photosensitization mechanism which involves two steps. The first one corresponds to the photolysis of the aryldiazonium salts leading to Lewis acids. The second one consists of the chemical initiation of the thirane polymers crosslinking by the Lewis acids yielded. These initiators are characterized by one free orbital. Therefore, they can accept an electron pair from the thirane ring sulphur atom leading to a coordinate bond and promoting ring opening. Thus, the crosslinking reaction propagates via a cationic mechanism.

It is worth emphasizing that light is necessary only for the first step, the second one being able to occur in the dark.

STRUCTURE AND SYNTHESIS OF THIRANE POLYMERS

Unlike the poly(glycidyl methacrylates)(PGMA), homopolymers obtained from 2,3-epithiopropyl methacrylate(ETMA) were found to be unsuitable for microlithography applications because of their insolubility. Due to the high reactivity of the thirane ring, their structure may result in a complete crosslinked network.

That is why we have prepared copolymers from 2,3-epithiopropyl methacrylate. Methyl methacrylate (MMA) was chosen as the other comonomer due to its properties of good adhesion.

The structure of the synthesized copolymers : P (ETMA-co-MMA) is represented on figure 2 where it is compared to that of the well known P (GMA-co-MMA).

Even in the case of a copolymerization, the thirane monomer initial ratio should not exceed 50 % ; otherwise the resulting copolymer is insoluble. Hence, we considered a monomer initial ratio

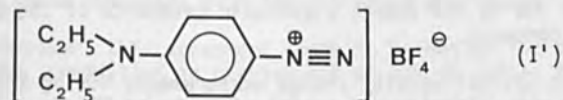
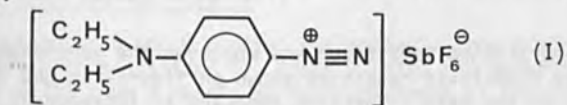
$$\frac{[\text{ETMA}]}{[\text{MMA}]} = \frac{1}{2}$$

The copolymerization has already been described in details earlier (1). It was carried out using α, α' -azobisisobutyronitrile (AIBN) as free radical catalyst. The structure of the copolymers was determined using elementary analysis and infrared spectrometry.

The synthesis of the thiirane monomer : 2,3-epithiopropyl methacrylate was achieved according to Rogers' method (4) from glycidyl methacrylate, as shown on figure 3.

STRUCTURE AND SYNTHESIS OF DIAZONIUM SENSITIZERS

Two aryldiazonium salts with complex halide anions were chosen for the studies. Their structure only differs from the nature of the anion :



Under irradiation, the released Lewis acids are respectively SbF_5 (II) and BF_3 (II').

Compound (I') is commercially available whereas compound (I) was synthesized through precipitation from an aqueous solution of the former by addition of the organic-free complex salt NaSbF_6 .

SPECTROSCOPIC PROPERTIES OF THE DIAZONIUM SENSITIZERS

The absorption spectra of the two diazonium compounds were determined in acetonitrile using a Perkin Elmer 550 double beam spectrophotometer with one cm length quartz cells.

Salt (I) shows (figure 4a) a main band centered at 377.5 nm (with a molar extinction coefficient $\epsilon = 4.44 \times 10^4$ liter.mole⁻¹.cm⁻¹) and a weaker peak near 242.5 nm (with $\epsilon = 3.94 \times 10^3$ liter.mole⁻¹.cm⁻¹).

As expected from the identical structure of the aryldiazonium moiety which is predominantly responsible for the electronic system extension, the absorption maximum of salt (I') is very close to that of salt (I) : $\lambda(\text{max}) = 374$ nm, but the absorption intensity is a little higher ($\epsilon = 6 \times 10^4$ liter.mole⁻¹.cm⁻¹). As shown on figure 7a, the spectrum is also characterized by another band in the U.V. range at 263.5 nm ($\epsilon = 1.24 \times 10^4$ liter.mole⁻¹.cm⁻¹).

The location of the main absorption bands of both diazonium salts (I) and (I') allows to photolyze them by a mercury lamp. Thus, their photolysis was studied at two Hg efficient emission lines : 365 nm and 404.7 nm.

PHOTOLYSIS PROPERTIES OF THE DIAZONIUM SENSITIZERS

A quartz cell containing each diazonium salt solution in acetonitrile (initial optical density D_0 at main peak maximum) was irradiated, over different lengths of time, using a Philips 7023 halogen lamp (100 W) through interference filters Balzers BUV-6 and BA-5 centered at 365 nm ($T_{\max} = 35\%$, $\Delta\lambda (1/2) = 100 \text{ \AA}$) and 404.7 nm ($T_{\max} = 40\%$, $\Delta\lambda (1/2) = 100 \text{ \AA}$) respectively. For each exposure time t , the absorption spectrum was determined and the optical density D_t at the maximum noted.

Whatever the studied sensitizer and whatever the wavelength of irradiation, the photolysis causes, as shown on figures 4b and 7b, both a decrease of the main absorption band and an increase of the secondary band due to the weaker electronic resonance of the photodecomposition compound.

From these optical density change measurements during the irradiation, photolysis kinetics and photolysis rate at 365 nm and 404.7 nm were studied for both sensitizers.

a) Photolysis kinetics :

- Theoretical approach :

The decrease of the optical density D_t ($D_t = \epsilon \times C_t \times \ell$) (ϵ : molar extinction coefficient, C_t : concentration of the photoactive species, ℓ : optical path length) is directly proportional to the absorbed light intensity I_{abs} and thus may be written as :

$$-\left(\frac{dD_t}{dt}\right) = k I_{\text{abs}} \quad \text{where } k \text{ is a constant}$$

According to Beer-Lambert's law,

$$I_{\text{trans}} = I_0 \cdot 10^{-D_t} = I_0 e^{-2.3D_t}$$

where I_0 and I_{trans} are the incident and transmitted light intensities respectively.

Thus, the absorbed light intensity I_{abs} which is given by : $I_{\text{abs}} = I_0 - I_{\text{trans}}$ can be expressed as : $I_{\text{abs}} = I_0 (1 - e^{-2.3D_t})$

Substitution of that expression into the first equation leads to

$$-\frac{dD_t}{(1 - e^{-2.3D_t})} = k I_0 dt$$

Upon integration between $t = 0$ and t , the following photolysis kinetics law is obtained

$$\ln \frac{(e^{2.3D_0} - 1)}{(e^{2.3D_t} - 1)} = 2.3 k I_0 t$$

where D_0 is the initial optical density and D_t the optical density after an irradiation time t .

- Experimental results :

Figures 5 and 8 plotted respectively from experimental data obtained with sensitizer (I) (SbF_6^- salt) and sensitizer (I') (BF_4^- salt) show a nearly perfect agreement of the photolysis kinetics of these compounds with the law found previously.

However, this agreement seems to be better for both sensitizers when irradiation is carried out at 365 nm rather than at 404.7 nm.

b) Comparison of the sensitizers photolysis at 365 nm and 404.7 nm.

- General :

On figures 6 (for sensitizer (I)) and 9 (for sensitizer (I')) are plotted the per cent photolysis rates :

$$100 \times \left(1 - \frac{D_t}{D_0} \right)$$

at main peak maximum versus the irradiation time t for the 365 nm and 404.7 nm centered excitations.

The curves in broken line, obtained from the measured values of the per cent photolysis rate were corrected for the same absorbed energy (100 mW) to give those in solid line. This correction required the determination of the actual energy density absorbed throughout each excitation band (λ_1, λ_2) which is given by the expression :

$$N_{\text{abs}}(\Delta\lambda) = \int_{\lambda_1}^{\lambda_2} \mathcal{N}_{\text{abs}}(\lambda) d\lambda$$

where $\mathcal{N}_{\text{abs}}(\lambda)$, number of absorbed quanta at a wavelength λ is deduced both from absorption probability, i.e. from optical density $D(\lambda)$ and from the number of excitation quanta $\mathcal{N}_{\text{exc}}(\lambda)$ at the same wavelength, as follows :

$$\mathcal{N}_{\text{abs}}(\lambda) = D(\lambda) \times \mathcal{N}_{\text{exc}}(\lambda)$$

$\mathcal{N}_{\text{exc}}(\lambda)$ may be expressed itself as the product of the interference filter transmission coefficient $T(\lambda)$ by the emitted energy density $E(T, \lambda)$ of the halogen source at the corresponding wavelength. Assuming the emission to be that of a black body at the absolute temperature $T = 3300^\circ\text{K}$, $E(T, \lambda)$ may be determined at each wavelength from Planck's formula.

$$\text{Thus, } \mathcal{N}_{\text{exc}}(\lambda) = T(\lambda) \times E(T, \lambda)$$

Substituting $\mathcal{N}_{\text{exc}}(\lambda)$ and $\mathcal{N}_{\text{abs}}(\lambda)$ provides the expression of the actual energy density absorbed in the range (λ_1, λ_2) :

$$N_{\text{abs}}(\Delta\lambda) = \int_{\lambda_1}^{\lambda_2} D(\lambda) \times T(\lambda) \times E(T, \lambda) d\lambda$$

- Results :

On table 1, are presented the absorbed energy values for both sensitizers in the two excitation bands and the corresponding per cent photolysis rates for the same absorbed energy (100 mW). These rates are expressed as the slopes at the origin of the corrected curves plotted on figures 6 and 9.

For both sensitizers, the absolute photolysis rate was found to be higher when excitation was carried out in the 404.7 nm band rather than in the 365 nm band. Furthermore, as far as the structure of the sensitizers was concerned, the photolysis of the SbF_6^- salt (I) appeared to be more efficient than the BF_4^- salt (I') one. Therefore, we used sensitizer (I) for the studies about thirane polymers photosensitization.

PHOTOSENSITIZATION OF THIRANE COPOLYMERS BY ARYLDIAZONIUM SENSITIZERS

Different amounts of sensitizer (I) varying from 2 % to 10 % of the weight of the polymer were added to solutions of P(ETMA(1)-co-MMA(2)) in methylisobutyl ketone (MIBK). Films of these formulations were spin-coated on oxidized silicon wafers (1100 Å thick SiO_2 layers) to obtain 5000 Å thick films.

In a first step, the exposures were carried out without any wavelength selection. Two irradiation devices were used.

For the exposure characteristics determination, the samples were irradiated at a distance of 12 cm using a high pressure mercury lamp

Philips HPR 125 through a range of optical densities (Kodak 1A Photographic set tablet).

The ability to produce patterns in the resist for microlithography applications was tested using a MJB 55 Karl Süss irradiation machine. In this case, the mask used consisted of a 3000 Å thick absorbing layer of Fe₂O₃ deposited on a transparent borosilicate glass which was kept in contact with the sample.

To improve adhesion of the resist to the SiO₂ layer, the samples were baked after exposure and prior to development during 6 minutes at 95°C. As nitrogen is evolved by the aryldiazonium salt photolysis, this post-baking may also allow to let out of the resist layer the nitrogen bubbles produced.

The development was then achieved at room temperature by dipping the sample during 30 seconds into a mixture of methylethyl ketone (MEK)-ethyl alcohol (ratio 5/1.8).

For a 5 % sensitizer (I) amount, the exposure curve of P(ETMA(1)-co-MMA(2)) is shown on figure 10, comparatively to that of P(GMA(2)-co-MMA(1)). As it can be seen, photosensitized thirane copolymers were found to be about 2.5 times more sensitive ($\sigma = 1 \text{ mJ/cm}^2$ corresponding to a normalized thickness of 0.7) than the corresponding epoxy copolymers with a contrast ratio close to theirs ($\gamma = 1.3$ when defined as the slope of the straight line passing through the zero and 0.7 normalized thickness points).

The sensitivity gain obtained with thirane copolymers with respect to the corresponding epoxy copolymers when photosensitization is achieved by aryldiazonium salts is however lower than in the case of electron beam irradiation (gain of about 25 at 20 keV) and soft X-ray irradiation (gain of about 10 at 8.34 Å).

Two hypotheses may be put forward to explain the relative reactivity decrease of the thirane ring compared to that of the epoxy ring. The first one is based upon the involvement of a sensitizing entity which does not belong to the polymer itself. The second one takes into consideration the cationic nature of the crosslinking mechanism which may enhance the relative ability of the epoxy ring to open comparatively to a free radical process occurring in the case of an electron beam or soft X-ray irradiation.

As far as the masking properties of thirane polymers are concerned, figures 11a and 11b reproduce scanning electron microscope pictures of patterns with 2 µm wide lines drawn in a 5000 Å thick film of P(ETMA(1)-co-MMA(2)) + 5 % sensitizer (I). It is to be noticed that the minimum linewidth obtained was 1.5 µm for a 1.5 µm gap corresponding to a resolution of 330 pairs of lines/mm.

When chemical etching is wanted, a baking at 95°C during 30 minutes is necessary to increase adhesion of the resist. The 1100 Å thick SiO₂ layer is then etched during 100 seconds in a buffered hydrofluoric acid solution.

Stripping of thirane polymers can be achieved by using either a sulfochromic mixture at 65°C with mechanical stirring or a 100 W O₂ plasma.

CONCLUSIONS

Thirane copolymers photosensitized by aryldiazonium salts are very interesting resists due to their high sensitivity (1 mJ/cm²) assignable to the important reactivity of the thirane ring. They can be used easily for lithography applications when submicronic linewidths are not required. Furthermore, as they are negative working, they can be used also for industrial coatings.

ACKNOWLEDGMENTS

The authors would like to thank the "Délégation Générale à la Recherche Scientifique et Technique" which sponsored partly this work.

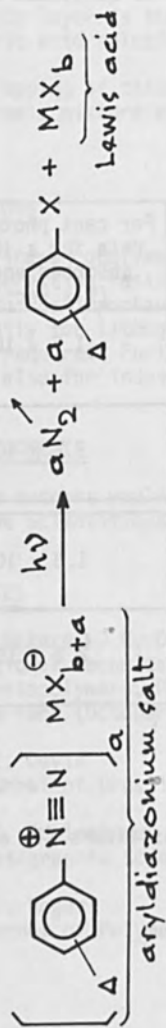
REFERENCES

- (1) M. Gazard, J.C. Dubois, A. Eranian
Regional Technical Conference, Soc. of Plastics Engineers,
"Photopolymers, Principles, Process and Materials", Nevele,
New-York (October 1976).
- (2) R.E. Davis
Journal of Organic Chemistry 23, 216 (1958).
- (3) S.I. Schlesinger
Photographic Science and Engineering 18 (4), 387 (1974).
- (4) F.E. Rogers
Journal of Polymer Science, Part A, 3, 2701 (1965).

Sensitizer	Center of the excitation band (nm)	Absorbed energy (mW)	Per cent photolysis rate for a 100 mW absorbed energy (% x sec ⁻¹)
(I) (SbF ₆ [⊖] salt)	365	120.2	1.7 x 10 ⁻²
	404.7	35.1	3.2 x 10 ⁻²
(I') (BF ₄ [⊖] salt)	365	168.5	1.3 x 10 ⁻²
	404.7	71.5	2.2 x 10 ⁻²

Table 1 : Photolysis rate characteristics of sensitizers (I) and (I') at 365 nm and 404.7 nm.

• Step 1: Photolysis of aryldiazonium sensitizers



Δ : one or several substituents on the aromatic ring

M: Fe, Sn, Sb, Bi, B, P, As

X: F, Cl

• Step 2: Crosslinking chemically initiated by the Lewis acids produced

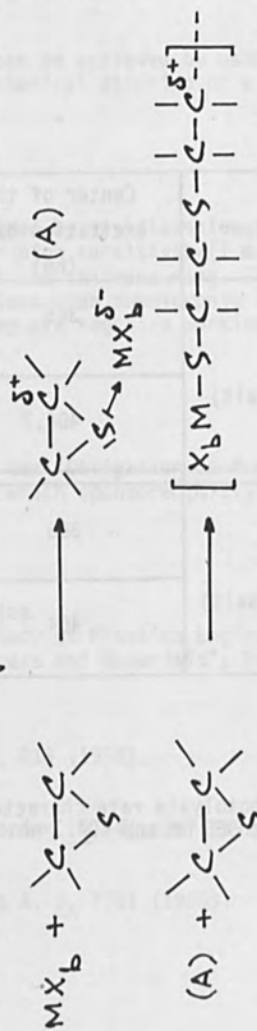
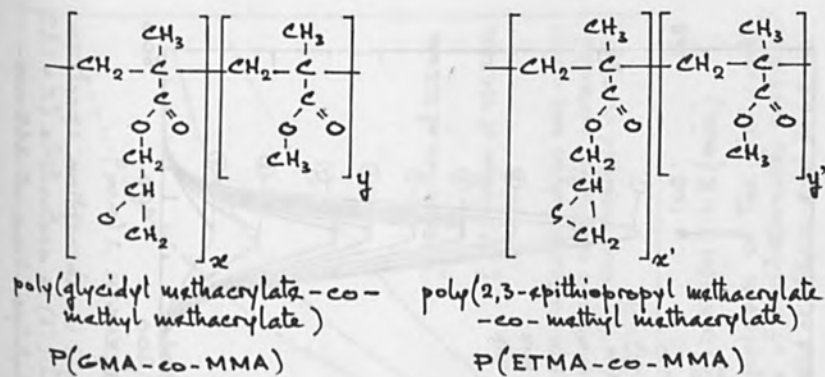


FIG. 1 - Photosensitized crosslinking of polymers containing thiirane rings by aryldiazonium salts



$$\frac{[\text{GMA}]}{[\text{MMA}]} = 2 \quad \text{monomer initial ratio} \quad \frac{[\text{ETMA}]}{[\text{MMA}]} = \frac{1}{2}$$

FIG. 2 - structure of the studied thiirane polymers compared with that of epoxy polymers.

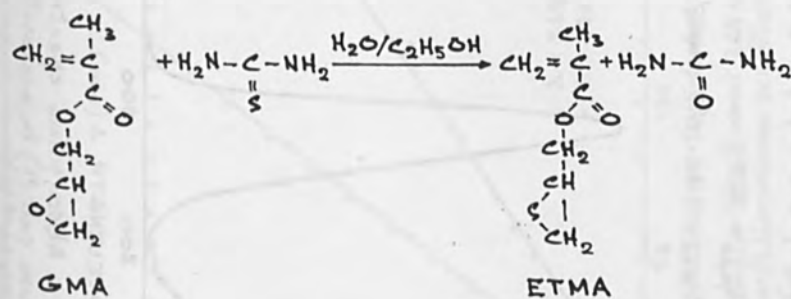


FIG. 3 - synthesis of 2,3-epithiopropyl methacrylate (ETMA) from glycidyl methacrylate (GMA) according to Rogers' method.

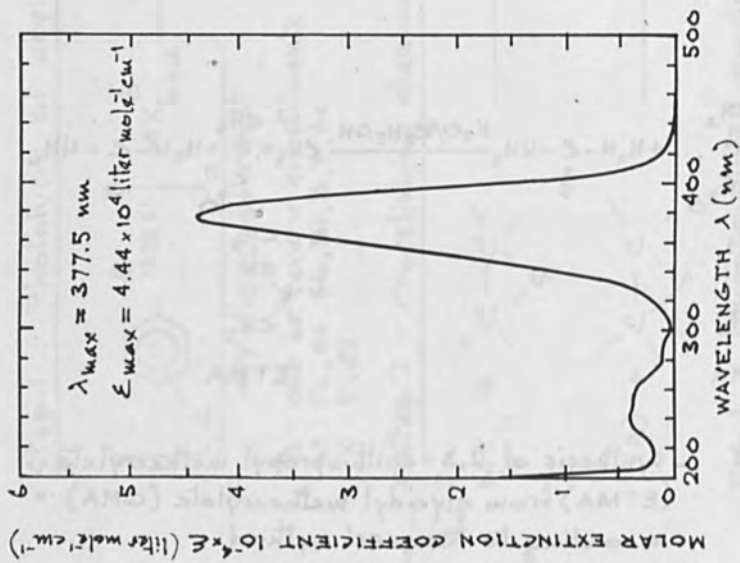


FIG. 4a - Absorption spectrum of diazonium salt (I) in acetonitrile ($c = 1.62 \times 10^{-5} \text{ M}$)

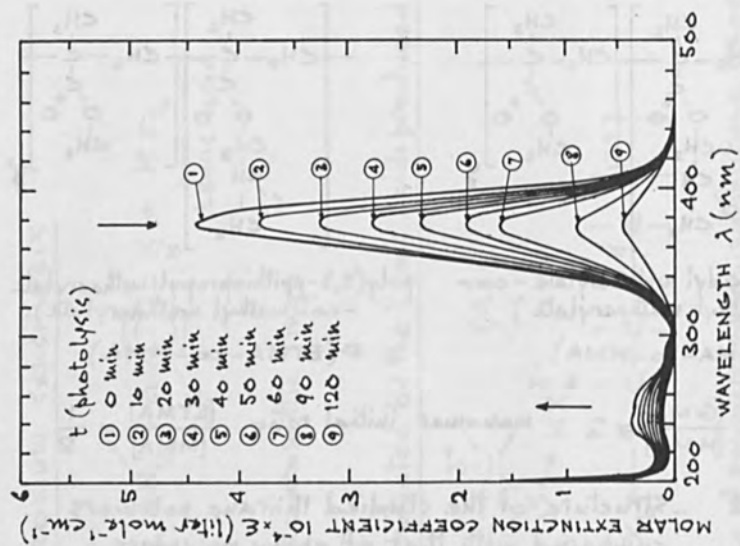


FIG. 4b - Changes in absorption spectrum of diazonium salt (I) in acetonitrile ($c = 1.62 \times 10^{-5} \text{ M}$) with photolysis time at 365 nm

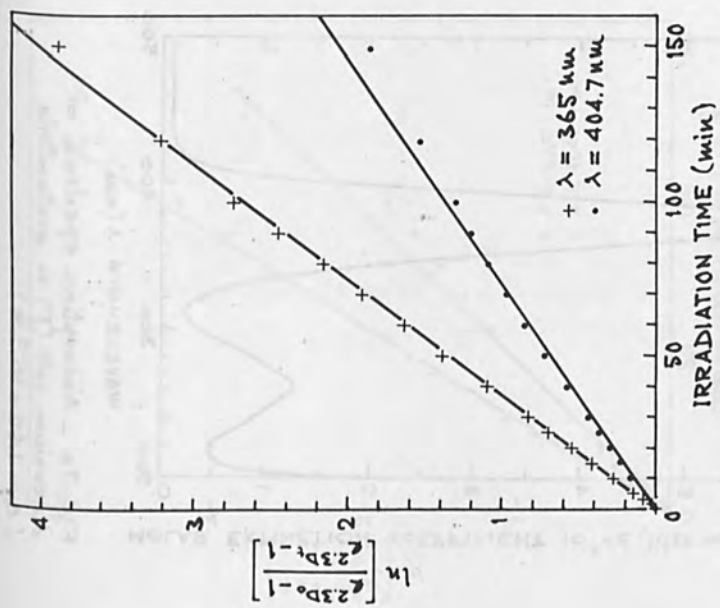


FIG. 5 - Photolysis kinetics at 365 nm and 404.7 nm of aryl diazonium sensitizer (I) in acetonitrile.

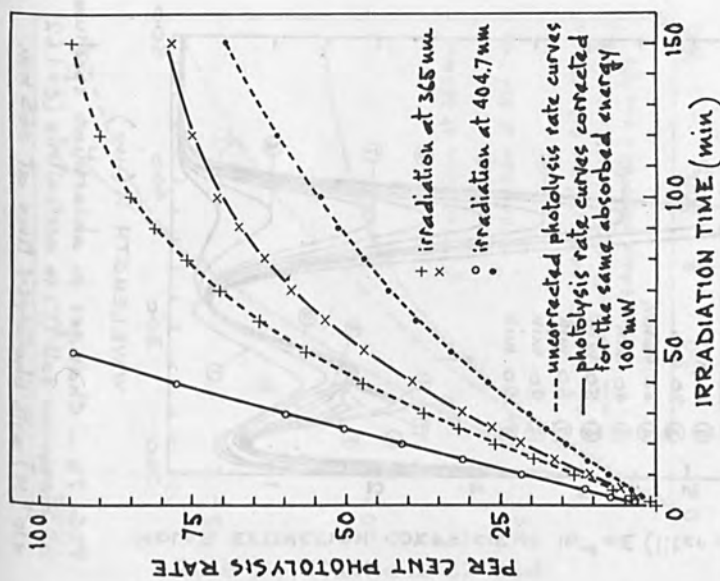


FIG. 6 - Comparison of the per cent photolysis rate of aryl diazonium sensitizer (I) in acetonitrile at 365 nm and 404.7 nm

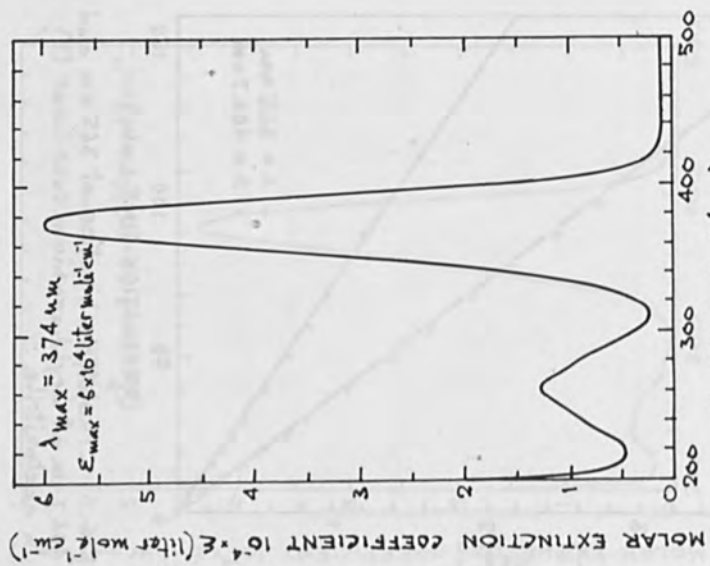


FIG. 7a - Absorption spectrum of diazonium salt (I') in acetonitrile ($c = 1.62 \times 10^{-5} \text{ M}$)

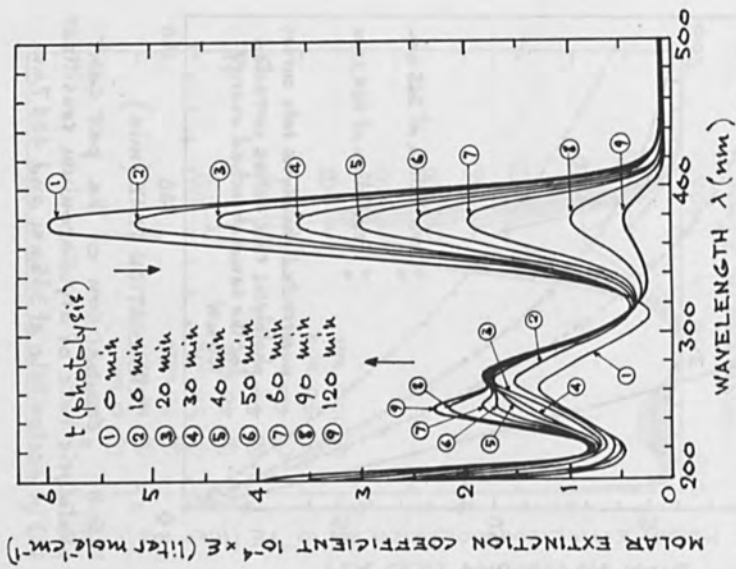


FIG. 7b - Changes in absorption spectrum of diazonium salt (I') in acetonitrile ($c = 1.62 \times 10^{-5} \text{ M}$) with photolysis time at 365 nm

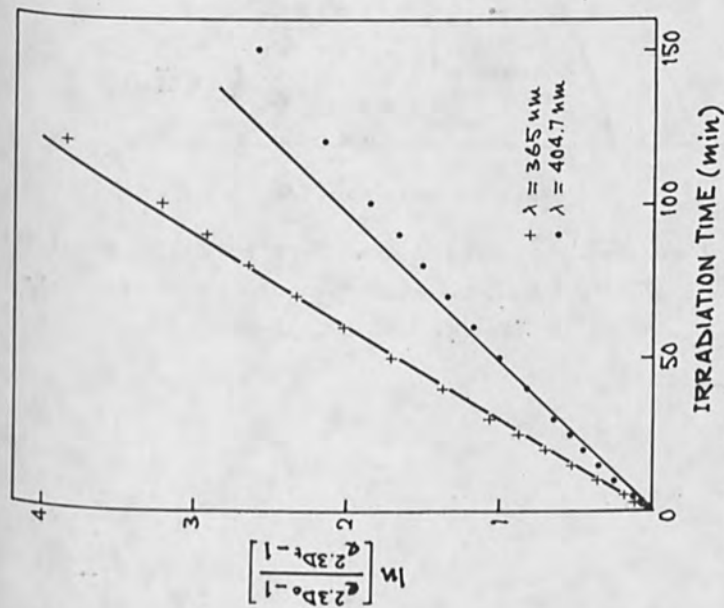


FIG. 8 - Photolysis kinetics at 365 nm and 404.7 nm of aryl diazonium salt (I') in acetonitrile.

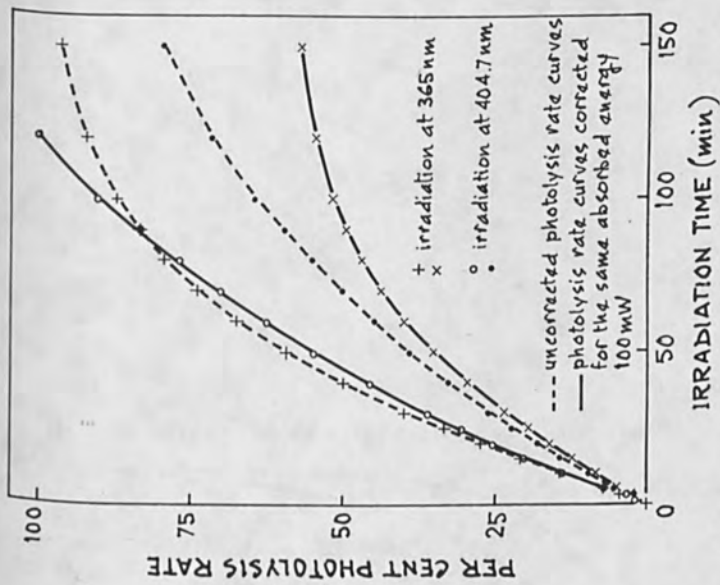


FIG. 9 - Comparison of the per cent photolysis rate of aryl diazonium sensitizer (I') in acetonitrile at 365 nm and 404.7 nm

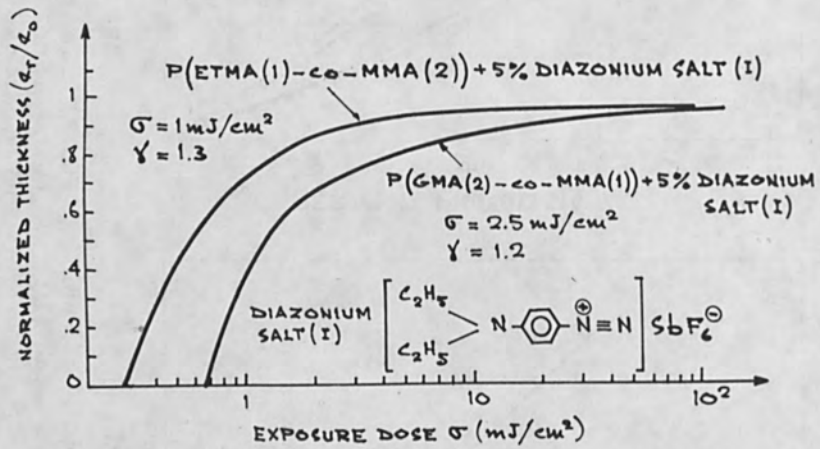
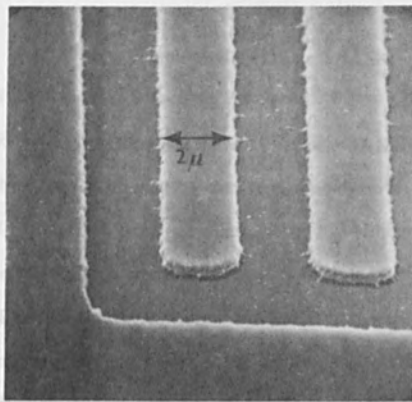
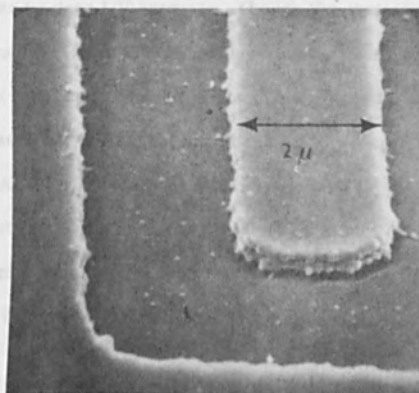


FIG.10 - Comparison of the exposure curves of polymers with thirane and epoxy groups, photosensitized in the U.V. range by aryl diazonium salts.



a) View of a part of the pattern



b) Enlarged view of one pattern line

Figure 11 : Scanning electron microscope pictures of $2 \mu\text{m}$ wide lines drawn in a 5000 \AA thick film of photosensitized thirane copolymers $\text{P}(\text{ETMA}(1)\text{-co-MMA}(2)) + 5\%$ sensitizer (I).

AZ2400 as a Deep-UV Photoresist

B. J. Lin

IBM Thomas J. Watson Research Center

Yorktown Heights, New York 10598

ABSTRACT

The photosensitivity and the method of its evaluation are given for AZ2400 in the deep-UV region. The spectral transmission of AZ2400 as a function of exposure is also given. Experimental results of micrometer-size features delineated in 0.4 and 1.1 μm of resists are shown. The advantages and limitations of AZ2400 as a deep-UV resist and mask material are discussed in comparison to polymethyl methacrylate (PMMA) and AZ1350J respectively.

I. Introduction

Smaller feature sizes and larger height-to-width aspect ratio in photoresist images can be achieved by using 200-260 nm deep-uv light instead of 310-430 nm near-uv and visible light (1). The well known electron-beam resist, polymethyl methacrylate (PMMA), was used as the deep-uv resist. The image in PMMA not only can have smaller dimension and higher aspect ratio but it also has very little undercut because of low optical absorption. It is self-filtering due to absence of photosensitivity above 260 nm. However, exposure level in the order of 500 mJ/cm^2 is required to produce a relative dissolution rate above 100. Using a 5 kW Mercury arc lamp and 10% collection efficiency, an exposure time of 1 minute is required to expose an 83 mm wafer.

Two photoresists of the AZ family, namely AZ2400 and AZ1350J, were found to exhibit changes in dissolution rate by deep-UV exposure. Though the photosensitivities are an order of magnitude higher than that of PMMA, AZ1350J is not very useful as a deep-UV resist because of high optical absorption in the deep-UV region. Instead, after delineation with near-UV light, it is suitable as a deep-UV mask material (2). On the other hand, the deep-UV absorption by AZ2400 is much less than that of AZ1350J. Therefore, AZ2400 is suitable for many deep-UV applications. Mifune (3) used AZ1350J as a deep-UV resist instead of a mask material. Kodate (4) used AZ2400 with an unfiltered deuterium light source, thus exposing the photoresist with a very broad spectrum of light ranging from the visible to deep-UV.

In the following sections, the photosensitivity of AZ2400 and the method of evaluation are given. The spectral transmission as a function of exposure is shown. Then, experimental printing results and suggested applications follow.

II. Evaluation of Spectral Photosensitivity

Two problems are generally encountered in spectral photosensitivity measurement of photoresists in the deep-UV region. The first problem is low light intensity. High intensity mercury or xenon lamps cannot be used because of strong scattered light in the unwanted spectral region. The deuterium lamp is usable because it has an evenly distributed spectrum throughout the sensitive

region of most photoresists as shown in Fig. 1. However, the most intensive deuterium lamp operating at a 180 watt input power can only produce a monochromator output in the order of 0.01 mW/cm^2 . This is when a Bausch & Lomb high intensity grating monochromator equipped with the visible-UV grating is used. The entrance and exit slit openings are set at 3.4 mm and 1.6 mm. An exposure time of 1.4 hour is required for a resist requiring 50 mJ/cm^2 exposure such as AZ2400 and 14 hours for PMMA which has to be exposed to 500 mJ/cm^2 . The second problem is that of obtaining a uniform illumination to make the power density measurement accurate.

In order to overcome these problems, a double exposure technique with concentric masks was developed. The mask and the test sample are rotated during exposure. A typical mask shown in Fig. 2a consists of seven bands of chromium coating which thickness starts from 5 nm and increasing in 5 nm increments. With this mask, seven different exposures of known ratio may be obtained with one single monochromator exposure, avoiding the uncertainty caused by variation of the intensity of the light source, development and other processing conditions, and saving the trouble of exposing seven times separately. Before the band mask is used, the sample is exposed with the ring mask consisting of concentric transparent rings shown in Fig. 2b. The ring images are to be completely developed and the exposed substrate surface to be used as the reference for measurement of thickness of the remaining resist. The orthogonal opaque band is used to trace back the original thickness, using the known unexposed dissolution rate evaluated from a separate test. The two masks and the substrate of the samples are carefully machined to a tight tolerance to fit the holder in order that along the rings, the illumination is uniform.

The power density at the rings is calibrated by rotating and exposing Kodak 649F plates in the sample plane for each wavelength evaluated. The exposure-development of the Kodak emulsion plates was set within a region of a constant γ . A densitometric reading was taken and transformed into relative power density distribution. The total power within a circle of 1 cm^2 area was measured with a calibrated UDC 505UV photodiode. Hence, the absolute power density distribution is computed for each wavelength.

Because of optical absorption in the photoresist, the exposure is an exponential function of the penetration depth z in the photoresist and the dissolution rate also becomes a function of z . Using the experimental values of the 7 resist step heights, development time, the unexposed dissolution rate, and the absorption coefficient, the resist dissolution rate as a function of exposure can be computed in terms of a power series expansion up to the seventh order. The method and result of the computation will be presented elsewhere. Here, the resultant resist step heights are given for the seven exposures with a common development time. This information is directly applicable for practical estimation of required exposure as a function of resist thickness.

A nominal film thickness of $1.1\ \mu\text{m}$ of AZ2400 was spun on 0.25 mm quartz disks. After being exposed through the monochromator, the resist was developed for 4 minutes in a developer consisting of one part AZ2401 developer and 3.5 parts deionized water. The resist step heights were evaluated with a Fizeau-type multiple-beam interferometer and the thickness range estimated with a stylus device. The result is shown in Fig. 3 for the wavelengths of 230, 240, 254, 280, 313, 365, and 405 nm. The 254, 313, 365, and 405 nm curves are reasonably straight as expected from a typical resist dissolution rate curve. Therefore, they are extended into the region of higher dissolution rate for estimation of shorter development times. The exposure required to clear $1.1\ \mu\text{m}$ of resist is between 20 to $200\ \text{mJ}/\text{cm}^2$ for development times between 1 to 4 minutes. The 240 and 280 nm curves are very nonlinear which is possibly caused by the extremely high optical absorption at these wavelengths. At 240 nm the photosensitivity is already very low. At 230 nm, the photoresist did not show response for exposures up to $100\ \text{mJ}/\text{cm}^2$. Though some photosensitivity is exhibited at 240 and 280 nm, the very high optical absorption prevents useful applications at these wavelengths.

III. Spectral Transmission

The spectral transmission from 200 to 450 nm, of $1.1\ \mu\text{m}$ of AZ2400 on a 0.25 mm quartz substrate was evaluated with a Beckman DB GT double-beam spectrophotometer using a blank quartz of identical thickness in the reference beam. In order to understand the photochemistry and investigate the possibility of using AZ2400 as a deep-UV mask material, the spectral transmission

but for $1.1\ \mu\text{m}$, the advantage is reduced to only 2.5. Using a filter to remove the near-UV light further reduces the sensitivity advantage. The $3\ \mu\text{m}$ upper limit of PMMA thickness cannot be achieved with AZ2400 because the overcut patterns will run into each other even if the long exposure time can be tolerated. On the other hand, in situations where in-situ development during exposure is permitted, the speed advantage of AZ2400 is retained. For example, developer immersion can be used for the fabrication of gratings by laser interference. From the resolution point of view, it is also advantageous to do proximity and projection printing with developer immersion.

For processes requiring less than $1.5\ \mu\text{m}$ of resist, the overcut profile of AZ2400 is not much worse than that of most near-UV resists. AZ2400 may be preferred over PMMA for other reasons besides being faster. Using a broad band source such as Xe-Hg arc lamps or deuterium lamps with proper condensers, one universal resist and associated processing system can be maintained for both near-UV and deep-UV. Combined near-UV and deep-UV exposures can be used for less critical steps. Deep-UV exposure can be obtained by simply inserting a suitable filter in the light beam.

AZ2400 contains a photoactive compound and a resin whereas there is only a resin in PMMA. Extra degrees of freedom are possible for resist characteristic and process control. In addition, the aromatic resin in the AZ resist system generally has a slower reactive ion etching rate than the aliphatic resin in PMMA.

AZ2400 is more transparent than AZ1350J, therefore less overcut is exhibited in AZ2400 images. This is desirable for wafer exposures but becomes a disadvantage when AZ2400 is considered as a deep-UV mask material. When both are unexposed, $0.7\ \mu\text{m}$ of AZ2400 is needed to give a contrast of 100 in a Mercury and PMMA system, whereas only $0.2\ \mu\text{m}$ of AZ1350J is sufficient. However, if both resists are allowed to age by exposure, the transmission peak at 252 nm is erased, improving the mask contrast significantly. After aging, AZ2400 can be exposed many times in air without losing its high absorption. Whereas, AZ1350J has to be used in vacuum if a mask life of more than 500 passes is required.

VI. Conclusion

AZ2400 can be used as a deep-UV resist for applications requiring $1.5\ \mu\text{m}$ of resist thickness or less. The high-photosensitivity advantage is significant for a resist thickness below $0.5\ \mu\text{m}$ but only moderate for larger thicknesses. However, because the development and subsequent fabrication processes are independent of the wavelength used, AZ2400 is desirable as a universal resist in a broad band printer which can be switched from a combined near-UV and deep-UV illumination to deep-UV by the insertion of a bandpass filter. A further advantage is the additional degree of freedom in the choice, proportion, and distribution of the photo active compound.

AZ2400 can also be used as a deep-UV mask material if it is aged by exposure after delineation. As a mask material it requires less processing steps, is inexpensive to recycle, and has fewer pinhole defects. While a smaller thickness of AZ1350 can be similarly used, AZ2400 offers better stability for repeated exposure in air.

Acknowledgement

The author is indebted to C. Lapadulat for technical assistance. Support and encouragement from J.S. Wilczynski and A.N. Broers are deeply appreciated.

REFERENCES

1. B.J. Lin, *J. Vac. Sci. Technol.*, Vol. 12, 1317 (1975).
2. B.J. Lin, 31st annual conference, SPSE, May 1978.
3. Y. Nakane and T. Mifune, Sony Corp., report in Japanese.
4. K. Kodate, Record of National Convention of Japan Society of Applied Physics, 28a-G-1 p 200, March 1978.
5. J.M. Shaw and M. Hatzakis, *IEEE Tran. Electron Devices*, vol ED-25, 425 (1978).

FIGURES

1. The deep-UV, near-UV, and visible spectrum of a 180 watt deuterium lamp.
2. (a) The chromium mask which contains seven bands of chromium coating which thickness starts from 5 nm in 5 nm increments. The orthogonal band is 150 nm of chromium and is used as an opaque reference.
(b) Thin ring openings in this opaque chromium mask are used to define constant exposure lines.
3. Developed thickness versus exposure for AZ2400 at seven wavelengths.
4. Spectral transmission of AZ2400 as a function of exposure.
5. (a) 1.3 μm openings spaced 0.7 μm apart, in 0.4 μm of AZ2400, exposed with 252 nm light of 10 nm bandwidth.
(b) 1.2 μm openings in 0.3 μm spacings in 1.1 μm of AZ2400, similarly exposed as in 5a but a factor of 4 longer.
(c) 1.8 μm openings in 1.8 μm of AZ2400, exposed as in 5b.
6. (a) 1.2 μm openings spaced 0.7 μm in 2.2 μm of AZ2400. The entire radiation spectrum of the deuterium lamp was used.
(b) Same as 6a but with 1 mm of pyrex in the beam to filter the deep-UV components. Only 1.6 μm of photoresist was delineated.

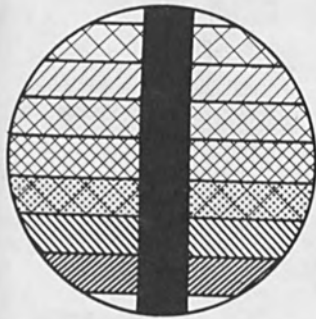
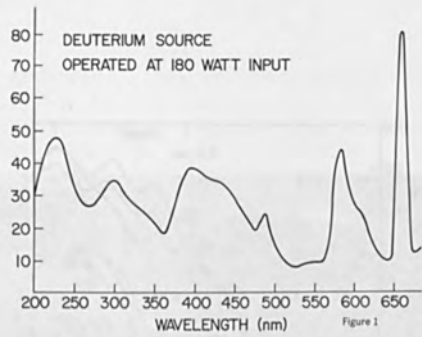


Figure 2a

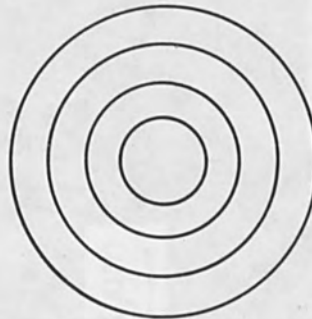


Figure 2b

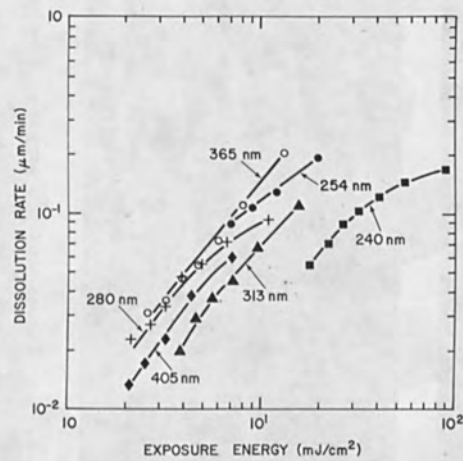


Figure 3

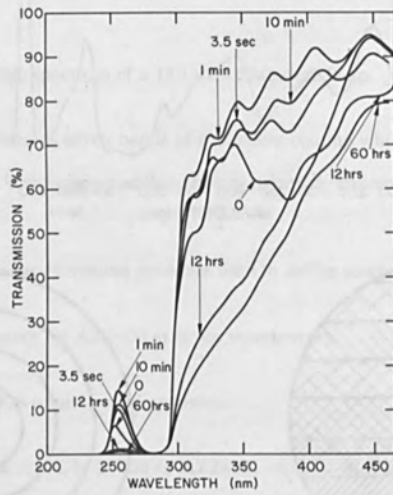


Figure 4

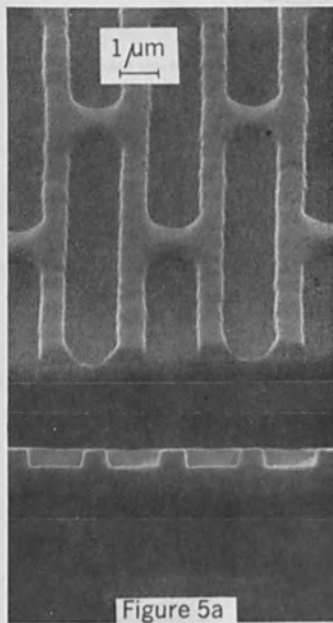


Figure 5a

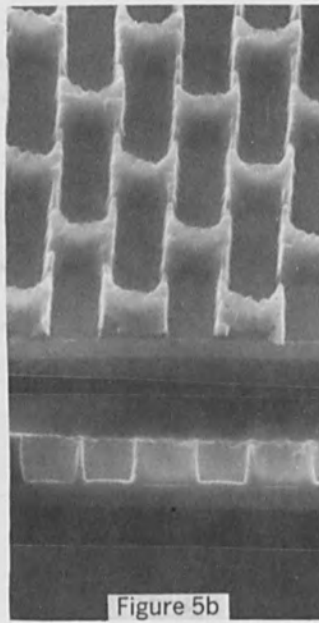


Figure 5b



Figure 5c

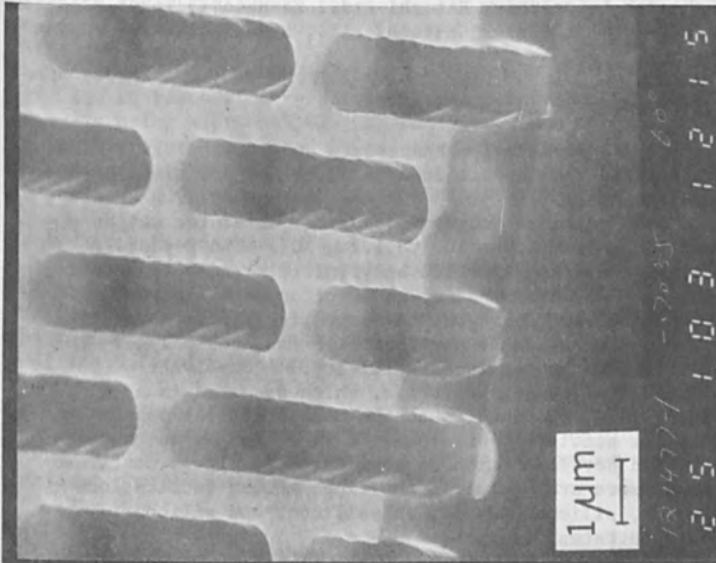


Figure 6b

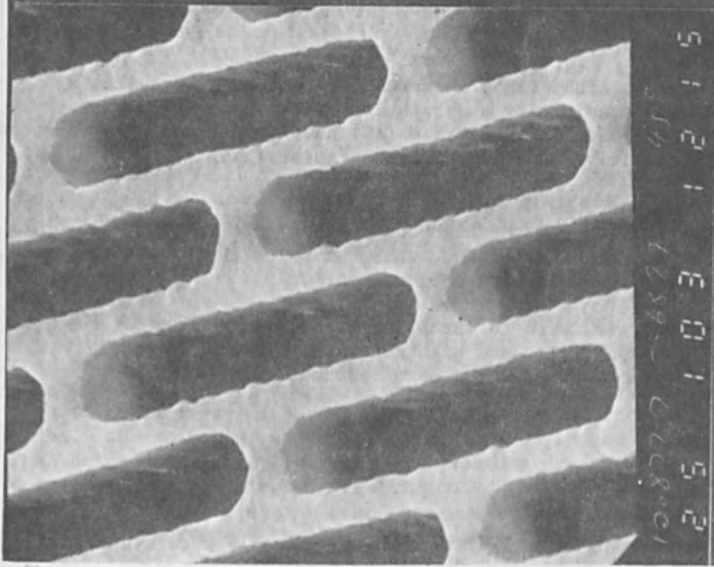


Figure 6a

POLY(METHYL METHACRYLATE-CO-ACRYLONITRILE)-A SENSITIVE POSITIVE RESIST

Y. Hatano, H. Shiraishi, Y. Taniguchi, S. Horigome, S. Nonogaki
and K. Naraoka*
Central Research Laboratory, Hitachi Ltd., Kokubunji, Tokyo, Japan
* Device Development Center, Hitachi Ltd., Kodaira, Tokyo, Japan

ABSTRACT

Copolymers of methyl methacrylate and acrylonitrile are synthesized and investigated as practical positive electron resists.

The most suitable range of copolymer molecular weight is found to be from 6.0×10^5 to 1.2×10^6 . The G-values of a copolymer containing 7 mole% acrylonitrile and poly methyl methacrylate, as determined by an electron beam exposure, are almost the same and equal to about 1.3. It is revealed that the incorporation of acrylonitrile enhances polymer solubility, thus increasing sensitivity. A copolymer containing 11 mole% acrylonitrile, which has a maximum dissolving rate, is found to be the most practical copolymer resist. Its sensitivity reaches 4×10^{-6} C/cm² when exposed at 15 kV and developed with isoamyl acetate. It is confirmed that copolymers are useful in the fine pattern fabrications of chromium, silicon dioxide, polysilicon, and silicon nitride substrates.

INTRODUCTION

Electron beam lithography in submicron technology requires a resist with high sensitivity and high contrast. Copolymers of methyl methacrylate (MMA) and acrylonitrile (AN) have been previously reported to be highly sensitive positive electron resists(1).

One of the purposes of this work was to clarify the reasons for this high sensitivity and the high contrast of copolymers by measuring the molecular weight distribution, chain scission efficiency (G-value), and solubility characteristics to developers.

Other objectives were to establish processing conditions for obtaining high sensitivity and high contrast, as well as to apply copolymers to practical electron beam fabrication of various fine patterns.

EXPERIMENTAL

Polymer Preparation

Copolymers containing 7-16 mole%AN (P(MMA-AN)) were synthesized

by bulk polymerization with 2,2'-azobisisobutyronitrile as a radical initiator in nitrogen atmosphere. Their weight average molecular weights (M_w) ranged from 6.0×10^5 to 1.2×10^6 . Poly(methyl methacrylate) (PMMA) with the molecular weight of 7.0×10^5 was prepared by the same procedure for comparison.

Characterization

The contents of acrylonitrile were determined by elementary analysis using a Hitachi 026 CHN analyzer. The molecular weights of the polymers were measured by gel permeation chromatography performed on a Hitachi 635 instrument. The glass transition temperatures of the polymers were determined by differential thermal analysis.

Sensitivity Measurement

Resist films were spin-coated onto a silicon substrate by using a solution of 4wt% polymer in ethylene glycol monomethyl ether acetate. The films were then prebaked, and exposed to an undeflected, nearly collimated electron beam at the acceleration voltage of 15 kV, on a modified Hitachi electron microscope.

After the exposure, the resist layers were developed in isoamyl acetate. The sensitivity curves were obtained by plotting the thicknesses of the layers measured with an interferometer against the incident charge densities.

Pattern Fabrications

Exposure patterns were defined by an electron beam drafting machine, specially designed by Hitachi Central Research Laboratory. The accelerating voltage was 15 kV.

RESULTS AND DISCUSSION

The exposure characteristics of a copolymer containing 7 mole%AN and that of PMMA are shown in Fig. 1. The processing conditions were selected for the PMMA so as to exhibit a higher sensitivity. Even under these conditions, the sensitivity of the copolymer is higher than that of the PMMA.

The sensitivity is considered to be a function of the G-values and the solubility characteristics of the resist material. The G-value in this case represents the number of scissions of the polymer molecules induced per 100 eV of energy absorbed. This value can be calculated from the efficiency of decomposition caused by electron beam irradiation. The molecular weight distributions of the copolymer and the PMMA before and after electron beam exposure are shown in Fig. 2. Comparison of these two figures indicates that the copolymer and the PMMA decompose by electron beam exposure with almost the same efficiencies. This agreement can be seen more clearly in Fig. 3, where the inverse number average molecular weight (M_n) is plotted against the

charge density. The observed correlations for the copolymer and for the PMMA are almost identical as seen in the figure. The G-values can be obtained from the slope of the straight line in Fig. 3. The same calculation reported by Hatzakis, et al. (2) gives the same G-values (about 1.3) for these two polymers.

Baking conditions and the nature of the developers are important factors in obtaining high sensitivity and high contrast. The significant effect of prebaking in dissolution characteristics is shown in Figs. 4 and 5. If the copolymer film is prebaked adequately and exposed to an electron beam, film thickness decreases linearly with the increase in development time, as shown by curve 1 in Fig. 4. It is observed that there is no difference between the molecular weight distributions of the dissolved and the remaining copolymers, as shown in Fig. 5(a). Therefore, it is considered that prebaked and exposed copolymer dissolves from the film surface gradually without any fractional dissolution. On the other hand, dissolution behavior of non-prebaked copolymer is considerably different, as shown by Curve 2 in Fig. 4. Thus, a significant difference can be observed between the molecular weight distributions of the dissolved and the undissolved copolymers shown in Fig. 5(b). This fractional dissolution may lower sensitivity and therefore must be avoided.

The relationship between development time and copolymer composition under non-fractional development conditions is shown in Fig. 6. Samples were prebaked at 170°C for 30 min. The curves show that a 11 mole%AN copolymer is developed at a minimum development time. The glass transition temperature is plotted against copolymer composition in Fig. 7. The curve is quite similar to those shown in Fig. 6. From these results, it is seen that dissolving rate increases with the decrease in glass transition temperature. These phenomena may be explained in terms of a disordering of the molecular arrangement caused by acrylonitrile incorporation.

As indicated above, the copolymer containing 11 mole%AN is regarded to be most practical, because it can be developed in the shortest time. The sensitivity curve of this copolymer is shown in Fig. 8, together with that of the PMMA. The processing conditions were selected for the copolymer to exhibit a higher sensitivity. Pattern fabrication of various substrates was attempted by using this copolymer. The resist film was prebaked at 170°C for 30 min, exposed at 4×10^{-6} C/cm², developed by immersing in isoamyl acetate for 15 min, and postbaked at 130°C for 30 min. Then, light asher treatment with oxygen gas plasma was employed to eliminate the very thin resist layer which remained in the exposed area. The substrates used were chromium, silicon dioxide, polysilicon and silicon nitride. They were etched with either wet or dry etchants. It was confirmed that fine patterns were successfully etched in these substrates; Examples of patterns thus obtained are shown in Fig. 9.

CONCLUSIONS

Copolymers of methyl methacrylate and acrylonitrile have been shown to be useful positive electron resists. A copolymer containing 11 mole% acrylonitrile has been found to be the most practical resist and to give a high sensitivity of 4×10^{-6} C/cm². The copolymer resist is applied successfully to the fine pattern fabrication of chromium, silicon dioxide, polysilicon, and silicon nitride substrates.

This would seem to open the way for broader application of P(MMA-AN) in fabrication of highly sophisticated fine pattern devices.

REFERENCES

- 1) Y. Hatano, H. Morishita, and S. Nonogaki, "A Modified Methyl Methacrylate Positive Resist", ACS Organic Coatings and Plastics Chemistry, Vol. 35, No. 2, P. 258, 1975.
- 2) M. Hatzakis, C.H. Ting, and N.S. Viswanathan, "Fundamental Aspects of Electron Beam Exposure of Polymeric Resist System", Proc. 6th International Conference, Electron and Ion Beam Science and Technology, pp. 542-579, 1974.

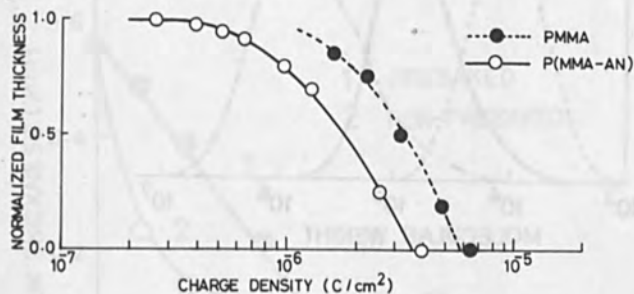


Fig. 1 Exposure characteristics of P(MMA-AN) (7 mole% AN) and PMMA.
Molecular weight (\bar{M}_w): 6.9×10^5 for P(MMA-AN), 7.0×10^5 for PMMA; Film thickness: 0.33 μ m; Prebake: 130°C, 30 min; Development: isoamyl acetate, 25.0°C, 15 min; Acceleration voltage: 15 kV.

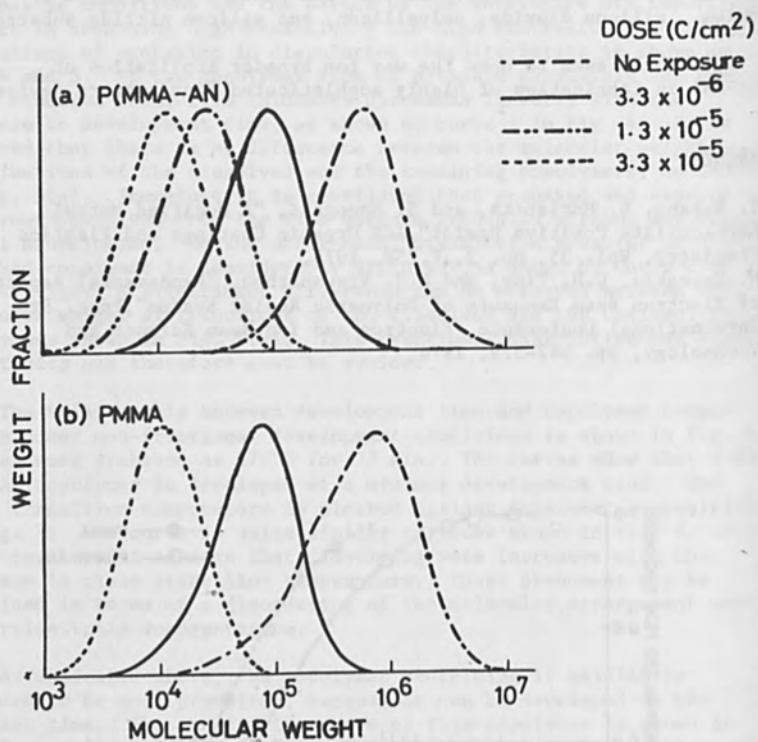


Fig. 2 Changes in molecular weight distributions of P(MMA-AN) (7 mole%AN) and PMMA upon electron beam exposure. Initial molecular weight (\bar{M}_w): 6.9×10^5 for P(MMA-AN), 7.0×10^5 for PMMA; Prebake: 130°C , 30 min; Film thickness: $0.8 \mu\text{m}$; Acceleration voltage: 15 kV.

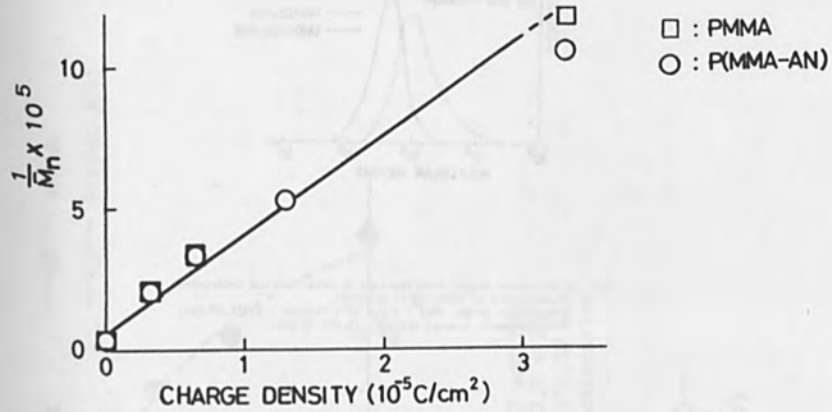


Fig. 3 Inverse number average molecular weights P(MMA-AN) (7 mole%AN) and PMMA as functions of charge density.

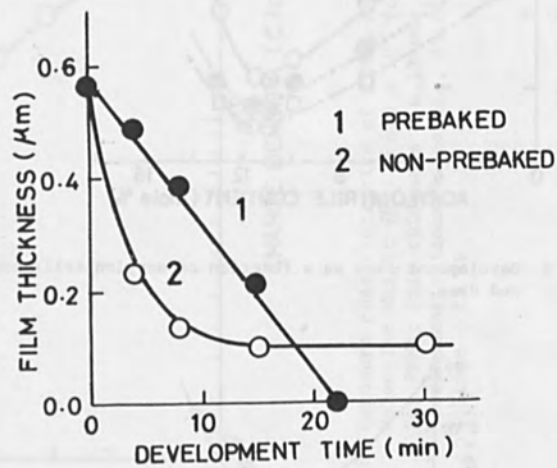


Fig. 4 Solubility characteristics of P(MMA-AN) (7 mole%AN) exposed at $3.3 \times 10^{-6} \text{ C/cm}^2$.
 Molecular weight (\bar{M}_w) : 6.9×10^5 ; Prebake : 130°C , 30 min;
 Development: isoamyl acetate, 25.0°C ; Acceleration voltage : 15 kV.

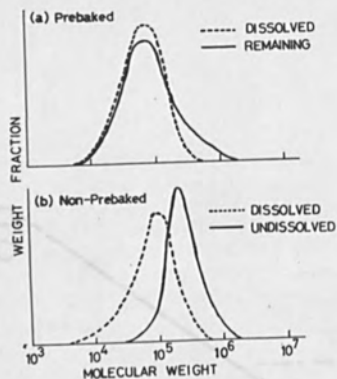


Fig. 5 Molecular weight distributions of dissolved and undissolved components of P(MMA-AN) (7 mole%AN).
Molecular weight (M_w): 6.9×10^5 ; Prebake: 130°C , 30 min;
Development: isoamyl acetate, 25.0°C , 16 min.

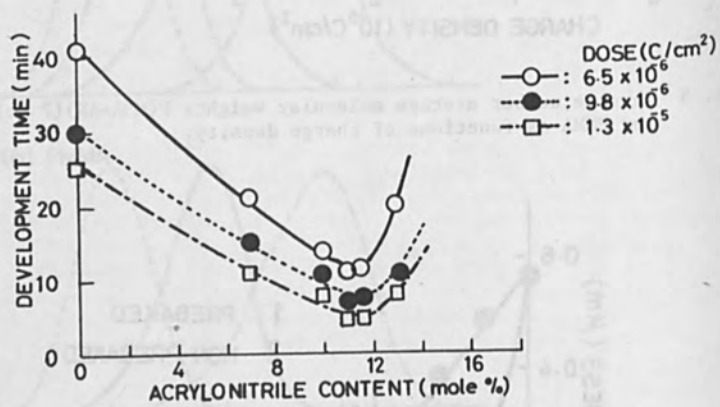


Fig. 6 Development time as a function of acrylonitrile content and dose.

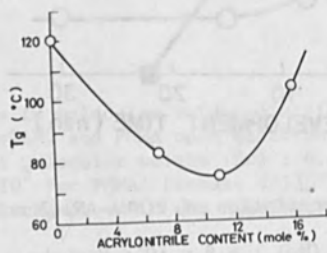


Fig. 7 Glass transition temperature (T_g) as a function of acrylonitrile content.

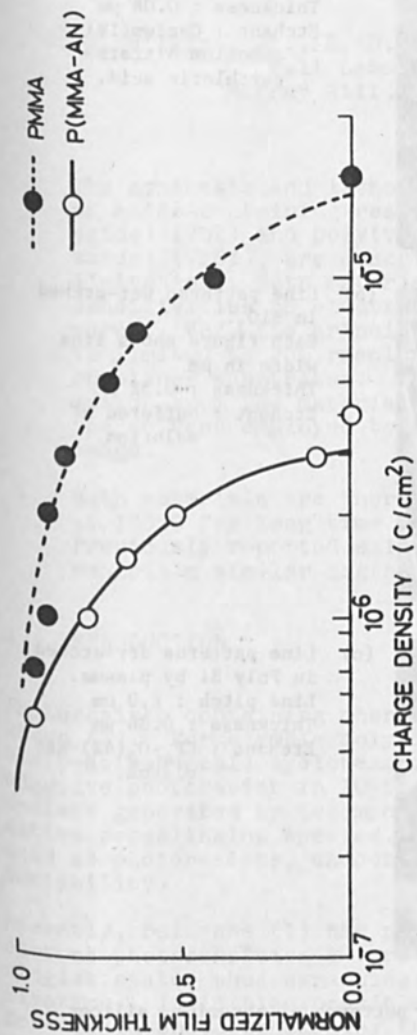
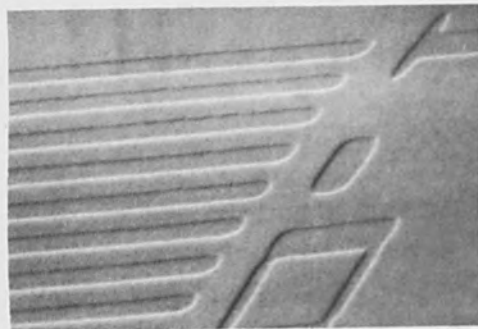


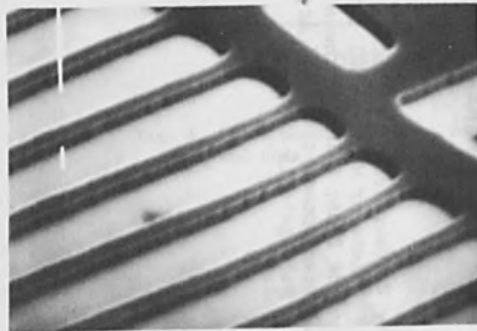
Fig. 8 Exposure characteristics of P(MMA-AN) (11 mole%AN) and PMMA. Molecular Weight (M_w) : 6.0×10^5 for P(MMA-AN), 7.0×10^5 for PMMA; Film thickness : 0.33 μ m; Prebake : 170°C, 30 min; Development : isoamyl acetate, 25.0°C, 15 min; Acceleration voltage : 15 kV.



(a) Line patterns wet-etched in Cr.
Line width : 1 μm
Thickness : 0.08 μm
Etchant : Cerium(IV) ammonium nitrate-perchloric acid.



(b) Line patterns wet-etched in SiO_2 .
Each figure shows line width in μm
Thickness : 0.52 μm
Etchant : buffered HF solution.



(c) Line patterns dry-etched in Poly Si by plasma.
Line pitch : 2.0 μm
Thickness : 0.36 μm
Etchant : $\text{CF}_4\text{-O}_2$ (4%)-gas plasma.

Fig. 9 SEM photomicrographs of etched patterns of chromium, silicon dioxide, and polysilicon.
Resist : P(MMA-AN) (11 mole% AN, $\bar{M}_w = 1.2 \times 10^6$);
Dose : $4.0\text{-}4.5 \times 10^{-6}$ C/cm²; Developer : isoamyl acetate (23.0°C); Development time : 16 min.

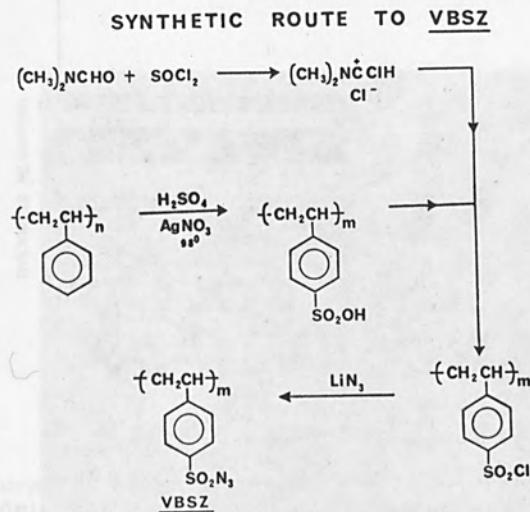


Figure 2. Reaction path for preparation of poly(vinylbenzene sulfonyl azide).

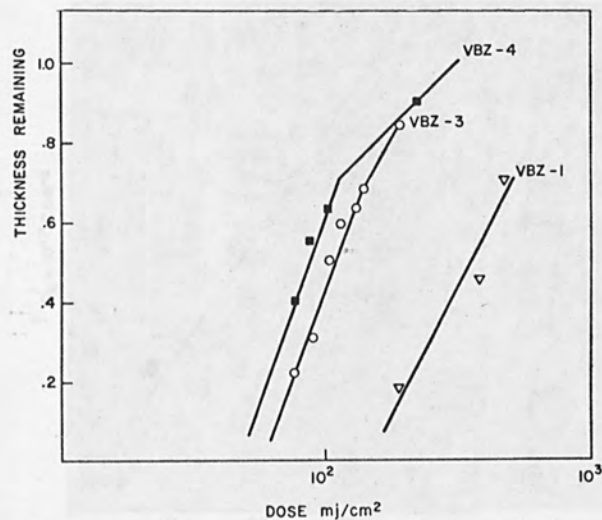


Figure 3. Response curves for poly(vinylbenzyl azide) when used as a photoresist.

This study is a preliminary investigation of the use of benzyl azide and sulfonyl azide polymers as resists. poly(vinylbenzyl azide) and poly(vinylbenzene sulfonylazide) were chosen as representative materials. These polymers were evaluated as photo- and electron-beam resists.

II. EXPERIMENTAL

1. Chemicals

Vinylbenzyl chloride was obtained from Polyscience, Inc. or from Dow Chemical Co. and was distilled before use. Sodium azide was obtained from Eastman Chemical Co. and used as received. Lithium azide was obtained from Eastman Chemical Co. and dried at 76°C in vacuum before use. N,N-Dimethylformamide (DMF) was obtained from Fisher Scientific Co. It was dried over cupric sulfate and molecular sieve and distilled under vacuum immediately before use. Polystyrene was obtained from Pressure Chemical Co.

2. Syntheses

Poly(vinylbenzyl chloride) was polymerized in solution. The monomer was polymerized in refluxing benzene with benzoyl peroxide as initiator. The molecular weight was varied by changing the catalyst concentration. Conversions were kept to less than 50 percent in order to minimize dispersivity.

Poly(vinylbenzyl azide), VBZ, was prepared by adding sodium azide (1.69 g, 0.026 mol) to a solution of poly(vinylbenzyl chloride) [4.0g, 0.026 mol] in DMF (40ml). The suspension was stirred at ambient temperature for 1 hr; the polymer was isolated by filtration and precipitation from methanol. An infrared spectrum of VBZ is given in Fig. 1. Percent conversion was determined as nitrogen incorporation by elemental analysis (Childers Laboratories).

Polystyrene was sulfonated with sulfuric acid by the procedure of Mukherjee and Raha (3) to >0.80-SO₃H groups/phenyl groups. The -SO₃H groups were converted to -SO₂Cl groups with Vilsmeier reagent (two-fold excess of thionyl chloride) by the procedure of Bosshard et al. (4). The -SO₂Cl groups were converted to sulfonyl azide, -SO₂N₃, with lithium azide (three-fold excess relative to thionyl chloride). The polymer is purified by precipitation in

water. Infrared analysis (Fig. 1) shows almost complete conversion of $-SO_3H$ to $-SO_2N_3$. Figure 2 depicts this reaction path for the preparation of poly(vinylbenzene sulfonyl azide) VBSZ.

3. Resist Processing

Resist solutions were prepared by dissolving the polymers in cyclopentanone or cyclohexanone. 9,10-Dimethylantracene (2% by weight of polymer) was added to resist solutions used as photoresists. No sensitizer was added to solutions used as electron resists. A Headway Research spinner was used to apply resist solutions to silicon wafers. The resist coated wafers were prebaked at $80^\circ C$ for 15 min. Photoresists were exposed through a chrome on glass step tablet with a Cobilt contact printer fitted with a high pressure mercury arc lamp. The resolution of this equipment with negative resists is about $1\mu m$. Various resist sensitivities were determined by plotting the thickness of the polymer film remaining after development against exposure dose. Developing was achieved by using methyl ethyl ketone: alcohol mixtures. A Sloan Dektak or a Nomarski Polarization Interferometer were used for thickness measurements.

Electron resists were evaluated by exposing 1-mm square pads at various electron doses with a Cambridge Mark II scanning electron microscope modified for beam writing. Sensitivity curves were obtained by plotting pad thickness after development versus dose. Developed patterns were post-baked for 10 min at $130^\circ C$.

III. RESULTS AND DISCUSSION

1. Photoresists

Results presented in Fig. 3 indicate that VBZ requires 100-500 mJ/cm^2 in a contact printer to maintain 60% of the initial film thickness (0.6-0.8 μm) after development. These materials are slower than the commercial phenyl azide photoresists. There are several possible explanations for this reduced sensitivity. An intramolecular rearrangement to an imine may compete with discrete nitrene formation. Also, azides in commercial resists are very efficiently decomposed without external sensitization; they are the primary light absorber and their absorption spectra match the spectral output of the exposure system. Increasing the sensitizer concentration or the use of a

more efficient sensitizer might increase the speed of VBZ.

Several workers (1,6,7) have suggested that photosensitization of alkyl and aromatic azides by aromatic hydrocarbons, occurs through the singlet state. Delzenne (1) has reported that among the aromatic hydrocarbons anthracene and its substitution products were particularly effective. 9,10-Dimethylantracene was found to be a photosensitizer for VBZ. Exposing VBZ in air in a projection printer decreased the rate of crosslinking. It is unclear at this stage whether oxygen intercepts the intermediate nitrene, as described by Shimizu and Bird, (8) or intercepts the excited states of the azide or the sensitizer. It should be noted that in contact printing, oxygen in the resist is consumed and not replenished from the atmosphere (8).

Inspection of Fig. 3 and Table 1 reveals that sensitivity of VBZ increases in parallel with weight average molecular weight.

Contrast values for VBZ when used as a photoresist are present in Table 1. The values were determined by taking the slope of the linear portion of the curves shown in Fig. 3. The values range between 1.2 and 1.82. It should be pointed out that these polymers contain very high azide incorporation. Samples with lower azide content are being evaluated to determine how this parameter affects the contrast values.

Figures 4 and 5 reveal that VBZ is capable of resolving 2.0 μ m lines and spaces in 0.5 μ m thick films. Advanced state of the art negative photoresists must be able to resolve 1.0 μ m lines and spaces in films 0.7 μ m thick and be capable of exposure in air (5).

VBSZ is very photosensitive even without added sensitizers. Thin films of the material are quickly crosslinked on exposure to white fluorescent lighting. Experiments designed to reduce the azide content and thereby moderate photosensitivity are in progress.

2. Electron Resists

The first systematic use of polymers containing benzyl azides as electron resists is reported here and raises the possibility of using the same resist in a combination of photolithographic and electron lithographic processing. It is interesting to note that the first materials evaluated for use as electron resists were the commercially

available photoresists. These materials had poor electron-beam sensitivity, low contrast and poor resolution. Their sensitivities had been carefully optimized for exposure to high pressure mercury arc lamps. The resolution of these materials was limited in part by flow characteristic of the resins. To date, there is no known correlation between contrast in photon and electron exposures.

The lithographic performance and polymeric parameters of VBZ when used as an electron resist are depicted graphically in Fig. 6 and summarized in Table 2, respectively. Inspection of Table 2 reveals that VBZ meets the sensitivity requirements for direct device fabrication (9). Poly(vinylbenzyl azide) has a $D_g^{0.6}$ of $5.0-28 \times 10^{-7}$ C cm⁻² at 20 kV.

It has been established that the interface gel dose (D_g^i), or the minimum dose necessary to form the first insoluble gel is inversely proportional to polymer molecular weight (10). Interface gel dose is determined by extrapolation of the linear portion of the curves shown in Fig. 3. The relationship between D_g^i and molecular weight for VBZ is shown in Fig. 7.

Contrast values for VBZ range from 0.84 to 1.2. Current thinking on contrast requirements for direct device fabrication indicates that a value of 1.6 or greater will be required (11).

VBZ is capable of resolving 2 μ m lines and spaces in 0.5 μ m of resist using methyl ethyl ketone: methanol mixtures as developers. For direct fabrication the resolution requirement is less than 1.0 μ m in final film thicknesses between 0.6 and 0.9 μ m (9).

The data in Table 2 show that VBSZ is less sensitive to electrons at a given M_w than VBZ. Unfortunately, the preparative sequence that converts polystyrene into VBSZ seriously degrades the molecular weight of the starting polymer, e.g. VBSZ-1 of $M_w \sim 12,000$ was prepared from polystyrene of $M_w = 51,000$. This drastic lowering of the M_w of the starting material probably occurs at the very beginning of the synthesis, i.e. in the sulfonation step. Although VBSZ-2 is 60 times more sensitive than the polystyrene from which it is prepared ($D_g^i \sim 3 \times 10^{-5}$), it is 7 times faster than the sulfonated polystyrene ($D_g^i = 3.5 \times 10^{-6}$).

3. Thermal Stability

The commercial azide based photoresist decomposes with an activation energy of 23 Kcal/mole (8). Takeishi and Okawa (12) have reported that poly(vinyl chloride) containing azide groups decomposes rapidly above 140°C. The kinetic parameters for phenyl azide are $\Delta H^\ddagger = 39$ Kcal mole⁻¹, $\Delta S^\ddagger = 18.7$ eu ($k_{100^\circ\text{C}} = 1.23 \times 10^{-6}$ sec⁻¹) and for benzene sulfonyl azide are $\Delta H^\ddagger = 33$ Kcal mol⁻¹, $\Delta S^\ddagger = 5.2$ eu ($k_{100^\circ\text{C}} = 4.61 \times 10^{-6}$ sec⁻¹) (13). Clearly, none of these azides are particularly stable at temperatures above 100°C. Differential thermal analysis showed that the onset of rapid decomposition of VBZ occurred near 180°C and of VBSZ near 145°C. Both materials were successfully prebaked, however; VBZ for 15 min. at 80°C without fogging. Fogging does occur at higher temperatures. Experiments to determine the long term stability of VBZ are in progress.

IV. CONCLUSIONS

1. Poly(vinylbenzyl azide) has been found to be both a photoresist (contact printing) and an electron resist, that is capable of 2 μm resolution in films 0.5 μm thick.
2. Poly(vinylbenzyl azide) has been found to be thermally stable above 100°C with degradation occurring near 180°C.
3. Poly(vinylbenzyl azide) electron resists meet the sensitivity requirement for direct device fabrication by electron beam. The contrast of the material, however, and the developer system used limit its resolving power to 2 μm .
4. Poly(vinylbenzene sulfonyl azide) is very photo- and electron-sensitive. It is less thermally stable than VBZ. Some of this sensitivity must be reduced before VBSZ can become a workable lithographic material.

V. ACKNOWLEDGMENTS

The authors would like to thank K. Tai, M. Chung and L. F. Thompson for electron resist exposures and L. E. Stillwagon for GPC measurements.

REFERENCES

1. G. A. Delzenne, Ency. of Polym. Sci. and Tech., Suppl. Vol. 1, p. 401 (1976).
2. T. Hirai, Y. Hatano and S. Nonogaki, J. Electrochem. Soc., 118, 669 (1971).
3. A. R. Mukherjee and C. R. Raha, Macromol. Syn., Vol. 3, 140 (1969).
4. H. H. Bosshard, R. Mory, M. Schmid and H. Zollinger, Helv. Chim. Acta, 42, 1653 (1959).
5. J. D. Cuthbert, Solid State Technol., 20, 59 (1977).
6. F. D. Lewis and W. H. Saunders, Jr., J. Am. Chem. Soc., 90, 7034 (1968).
7. R. M. Moriarty and R. C. Reardon, Tetrahedron, 26, 1379 (1970).
8. S. Shimizu and G. R. Bird, J. Electro. Chem. Soc., 124, 1394 (1977); and private communications.
9. L. F. Thompson, L. E. Stillwagon and E. M. Doerries, 14th Symposium on Electron, Ion, and Photon Beam Conference, Palo Alto, CA, May 1977.
10. H. Y. Ku and L. C. Scala, J. Electrochem., 116, 980 (1969).
11. K. L. Tai, Private communication.
12. M. Takeishi and M. Okawara, Polym. Lett., 7, 201 (1969).
13. R. A. Abramovitch and E. P. Kyba, "Decomposition of Organic Azides", in The Chemistry of the Azido Compounds, S. Patai, Ed. Chpt. 5, Interscience, New York, NY, 1971.

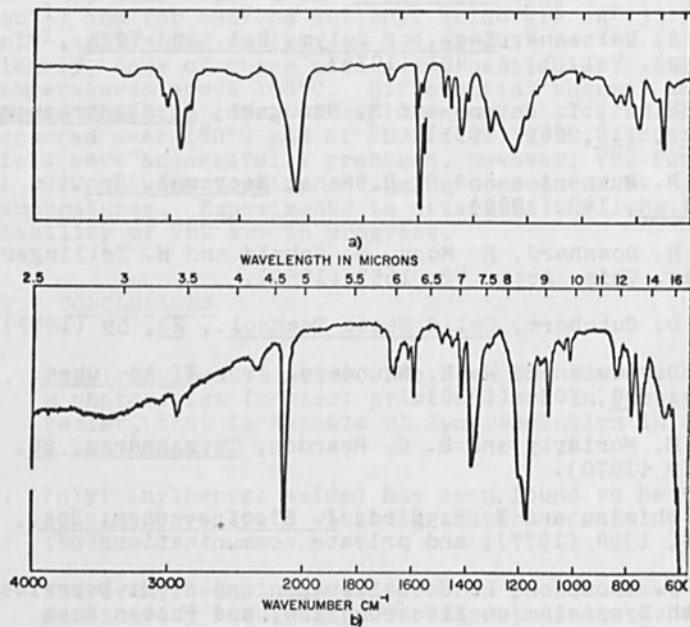


Figure 1. Infrared spectrum a) of poly(vinylbenzyl azide) and b) of poly(vinylbenzene sulfonyl azide).

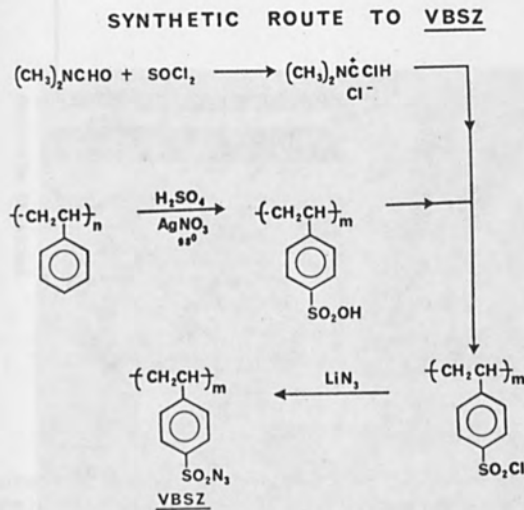


Figure 2. Reaction path for preparation of poly(vinylbenzene sulfonyl azide).

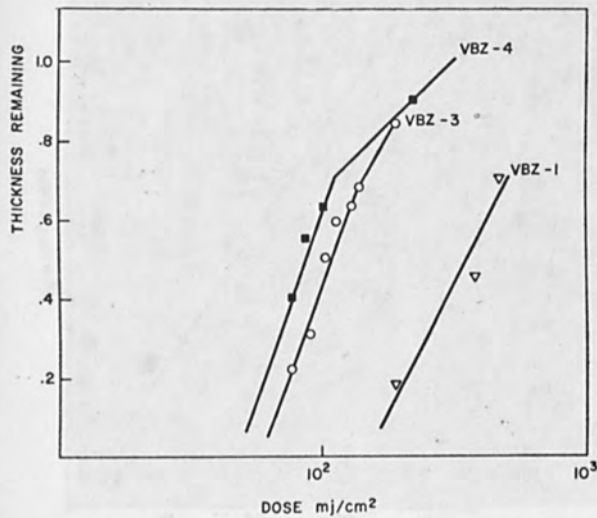


Figure 3. Response curves for poly(vinylbenzyl azide) when used as a photoresist.

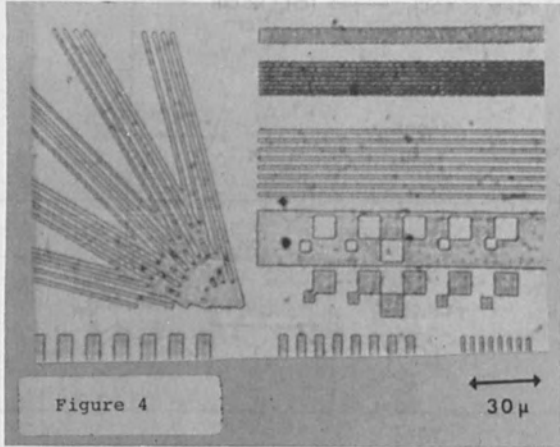


Figure 4. Photomicrographs of VBZ showing lines and spaces.

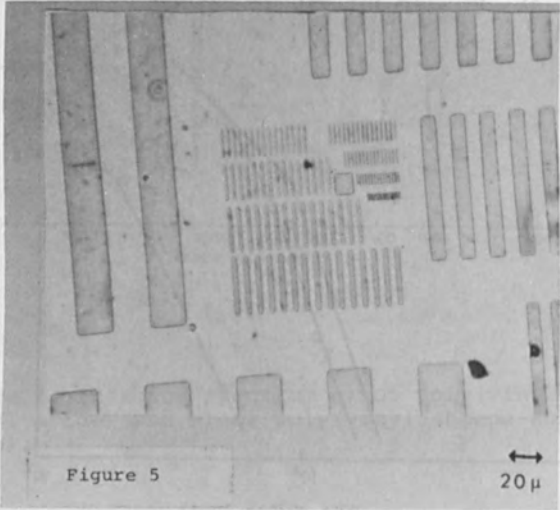


Figure 5. Photomicrographs of VBZ showing lines and spaces.

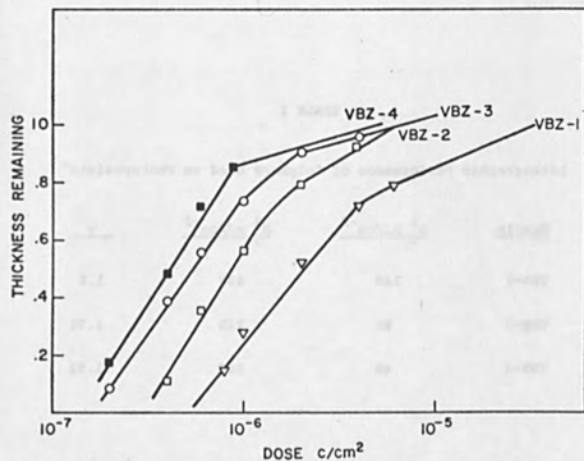


Figure 6. Response curves for poly(vinylbenzyl azide) when used as an electron resist.

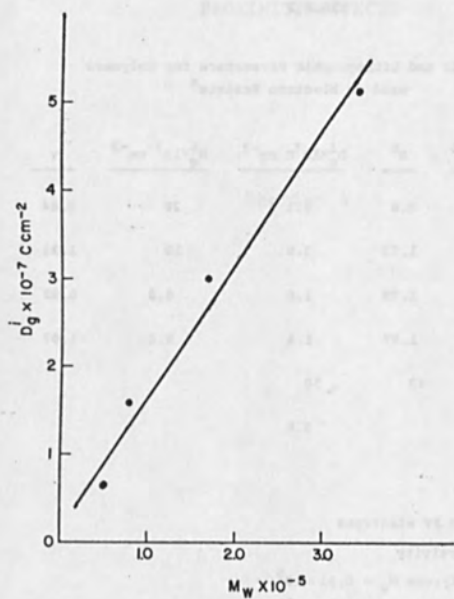


Figure 7. The inverse relationship between D_g^1 and molecular weight for poly(vinylbenzyl azide).

TABLE 1

Lithographic Performance of Polymers used as Photoresists^a

Sample	$D_g^4 \text{ mJ/cm}^{-2}$	$D_g^6 \text{ mJ/cm}^{-2}$	γ
VBZ-1	140	430	1.2
VBZ-3	90	125	1.76
VBZ-4	48	100	1.82

^a Polymers are characterized in Table 2

TABLE 2

Polymeric and Lithographic Parameters for Polymers used as Electron Resists^a

Sample	$M_w \times 10^{-5}$	R^b	$D_g^4 \times 10^7 \text{ cm}^{-2}$	$D_g^6 \times 10^7 \text{ cm}^{-2}$	γ
VBZ-1	0.288	2.6	5.1	28	0.84
VBZ-2	0.809	1.73	3.0	10	1.21
VBZ-3	1.31	1.79	1.6	6.8	0.92
VBZ-4	1.69	1.87	1.4	5.0	1.07
VBSZ-1	0.12 ^c	<2	50		
VBSZ-2	d		5.0		

^a Exposed with 20 kV electrons^b R = poly dispersivity^c Starting polystyrene $M_w = 0.51 \times 10^5$ ^d Starting polystyrene $M_w = 1.6 \times 10^5$

PROXIMITY EFFECTS

The present study was designed to investigate the effects of proximity on the performance of a task. The study was conducted in a laboratory setting and involved a number of participants. The results of the study are presented below.

The study was conducted in a laboratory setting and involved a number of participants. The results of the study are presented below. The study was designed to investigate the effects of proximity on the performance of a task.

PROXIMITY EFFECTS

The present study was designed to investigate the effects of proximity on the performance of a task. The study was conducted in a laboratory setting and involved a number of participants. The results of the study are presented below.

The study was conducted in a laboratory setting and involved a number of participants. The results of the study are presented below. The study was designed to investigate the effects of proximity on the performance of a task.

Section 4

The study was conducted in a laboratory setting and involved a number of participants. The results of the study are presented below. The study was designed to investigate the effects of proximity on the performance of a task.

COMPUTER CONTROL OF PROXIMITY AND SIZE EFFECTS IN ELECTRON
LITHOGRAPHY

H.I. Ralph and H. Sewell

Philips Research Laboratories, Redhill, Surrey RH1 5HA, England.

In the generation of patterns using electron beam lithography, distortions occur in the pattern due to the presence of backscattering electrons. The exposure effects of these backscattered electrons have therefore to be assessed and compensated for in order to produce high fidelity patterns specially when pattern dimensions are less than $3\mu\text{m}$.

This paper assesses the problems, discusses methods of compensation, and demonstrates how with the aid of a computer program patterns can be processed and exposure levels adjusted to give compensation for electron scattering effects. The excellent results of this computer compensation are compared with the non compensated case by studying a test pattern, the minimum dimension of which is $0.5\mu\text{m}$.

Electron lithography is increasingly being used for the fabrication of photomasks for the Electronics Industry. In this process a layer of electron sensitive resist material is applied to a chromium coated glass plate or silicon slice and is irradiated with a beam of high energy electrons, which is continuously deflected so as to describe the desired pattern. The resist is exposed by the electrons from the beam as they travel towards the substrate, spreading out slightly in the resist as they go. As they slow down, however, they suffer large angle scattering events with increasing probability so that a significant number of the electrons travel back through the resist to the vacuum. These electrons expose the resist at a low level several microns from the point where they first entered. Backscattered electrons entering on one side of a narrow figure partially expose it on the other side giving rise to the size effect. Similarly electrons entering near the edge of one figure in a pattern partially expose a closely neighbouring figure giving rise to the proximity effect. The manifestation of the size effect is that small figures irradiated and developed under the same conditions as larger figures come out too small even though the larger figures are correct. The proximity effect is manifest in the over exposure of closely adjacent figures where similar isolated figures are correctly exposed.

These effects can be quantified by the introduction of an "exposure profile". It is found experimentally that there is a fairly well defined critical exposure which marks a boundary between easily soluble and nearly insoluble resist. In any exposed pattern

the value of the exposure at any point is the number by which the dose of the whole pattern must be divided in order for the resist at that point to become just critically exposed.

The exposure profile of any figure can, then, in principle be measured by irradiating the resist in that pattern with different doses over a wide range and recording the dimensions of the developed figure as a function of dose. We have obtained exposure profiles in this way on the electron beam machine at our Laboratories. Figure 1 shows the exposure profile for a number of line widths including the edge of a very wide line (1).

Having obtained the curves of figure 1 we tried to verify the additivity principle which supposes that the exposure profile of a complex pattern can be obtained by summing the profiles of its elementary parts. By using the profiles in figure 1 we have predicted the profiles of long pads of various widths and groups of long windows and compared them to the measured results. The results for long pads are shown in figure 2 where the solid curves represent the predictions and the points represent measurements directly on pads. The results for groups of windows are shown in figures 3 and 4. It is seen from these figures that additivity appears to hold so long as the dimensions of the pattern are not less than 1μ . At 1μ dimensions agreement is not so good but measurements are difficult using optical microscopy and further investigation is necessary.

We have considered various ways of making alterations to the irradiated pattern. We can:

- (i) irradiate the areas in between the windows
- (ii) give different doses to different windows
- (iii) shift the boundaries of the irradiated areas
- (iv) split the windows and give different parts different doses

Of these the first method which is a useful ad hoc method for certain classes of patterns turns out to be not generally useful. The second method can give significant improvements but different edges of a feature may have very different environments so that some compromise value of the dose has to be chosen. The other two methods each give sufficient freedom to make it possible to get the whole of the pattern correct. We have found that method (iv) is superior to method (iii) for use on our electron beam writing machine because it reduces the sensitivity of the developed pattern to errors in the dose and to defocussing of the beam. We find experimentally also that the beam stepping distance, the minimum amount by which we can shift the edge of a figure, is too large to give a sufficiently fine adjustment with method (iii).

The origin of the insensitivity to dose and beam focus can be seen with reference to the exposure profile of a very wide line in figure 1. The dose given is chosen to give critical exposure at the edge of the irradiated area. It can be seen from figure 1 that this point is exactly half way up the curve where the curve is steepest. The sensitivity of the edge position to dose error is thereby minimised. Further this point is the centre of skew symmetry. When the beam becomes defocussed, provided that it remains symmetric the curve of figure 1 will remain skew symmetric and the point at the centre of skew symmetry will remain fixed. Therefore the position where the resist is critically exposed also remains fixed. Strictly speaking these arguments are really valid only for very large windows but it turns out that they apply well to smaller windows above about $\frac{1}{2}\mu$ in size.

We have written a computer simulation program which is able to plot out the developed pattern from input defining an irradiated pattern. Experimenting with this program we found that method (iv) above is able to produce patterns very close to the original. An example of a simulation is shown in figure 5. The required pattern is shown in figure 5a and the result of irradiating the pattern uniformly is shown in 5b. The dose used in 5b is that required to make a very large window come out correctly. To get the pattern correct the irradiated areas have been cut into half micron squares shown in figure 5c and their individual doses carefully chosen. The result of the simulation for this case is shown in figure 5d. It can be seen that, except for rounding of corners the original pattern is very well reproduced.

The only remaining problem is to devise a method of determining the doses required for each square. One method would be to select a point somewhere in each square and calculate the exposure, at that point, in terms of the doses in all the other $\frac{1}{2}\mu$ squares. Writing the exposure of the point in the n-th square as e_n , the dose given to the m-th square as d_m , and the exposure in the n-th square due to a dose of unity in the m-th square as C_{nm} , the additivity assumption gives:

$$e_n = \sum_m C_{nm} d_m$$

The required exposure at the point chosen in each square is known so that if there are N squares, then there are N equations with N doses, d_m , to calculate and a unique solution is ensured.

Unfortunately, for a pattern of any reasonable size, N is of the order of 10^6 and the problem is prohibitively large. We could instead use some sort of iterative method but we find that the doses we calculate vary over a wide range so that an iterative method takes a long time to converge. Lastly we notice that to estimate the effect of all the other square on any particular one we have to

compare all the others to it. For 10^6 squares that means a total of 5×10^{11} comparisons must be made. If each one takes $100\mu\text{s}$ this job will take a year and a half.

Because the effective range of the backscattered electrons is limited ($2-3\mu$ from a 20keV beam) it is not necessary to account for the exposure effect of elements at distances greater than this. Therefore the number of comparisons that have to be made can be reduced by sorting the figures of the whole field into subfields. Suppose the area of the whole pattern is divided into 10^4 subfields each with an average of 100 elementary squares. Now only 5×10^3 comparisons have to be made in each subfield and the amount of work necessary is reduced by four orders of magnitude and becomes about an hour and a half. Further savings in time can be made by dividing the figures into shapes more significant than half micron squares and so reducing the number of comparisons to be made. Also we have been able to reduce the number of iterations to one. The difficulty is that although for each figure of the pattern the positions of neighbouring figures are known the irradiation doses are not. However, the similar information is known for the environment of the neighbouring figures and this information can be used to estimate the final doses of the neighbouring figures.

We have written a computer program to calculate the doses required for any pattern along the lines of the above discussion. The method it uses can be regarded as iterative but satisfactory results are obtained without reiterating. In fact the doses used to get the pattern of figure 5d were obtained using this program. The divisions of the individual figures of a pattern are made according to the requirement of having different doses. Figure 6 shows part of a pattern processed by the program after it has been cut up into different parts. The area in the middle of a figure is given a preset dose not chosen by calculation.

Lastly in figure 7 we show photographs of a developed pattern in PMMA both with a uniform dose everywhere and with doses corrected by our program. In the former case the reproduction is very poor with all the features generally undersized especially the isolated 1μ features which are not exposed out. Corners are rounded and T's tapered. For the corrected case the line dimensions are correct as shown in table I and there is a reduction of corner rounding and taper on the T's.

ACKNOWLEDGEMENT

We should like to express our thanks to all the members of Philips Research Laboratories whose co-operation has made this work possible. We are particularly grateful to Mr. D.R. Stocks for his programming work.

REFERENCES

H. Sewell, 14th Symposium on Electron, Ion and Photon Beam Technology, to be published in J. Vac. Sci. and Tech.

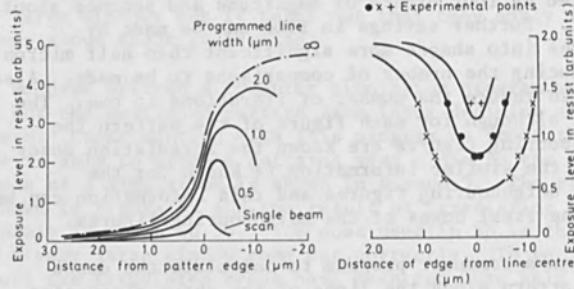


Fig. 1. Exposure profiles of Line Windows.

Fig. 2. Predicted exposure profiles of line pads.

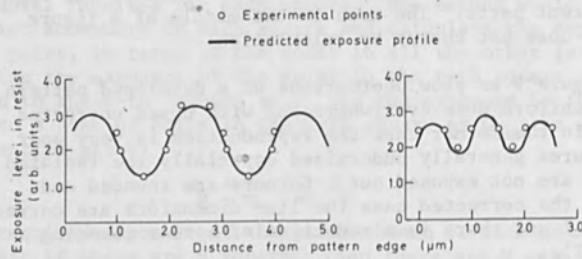


Fig. 3. Exposure profiles of three 1.0 μ m windows spaced by 1 μ m.

Fig. 4. Exposure profile of three 0.5 μ m windows spaced by 0.5 μ m.

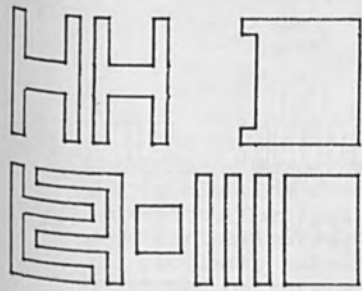


Fig. 5a. Uniformly irradiated pattern.

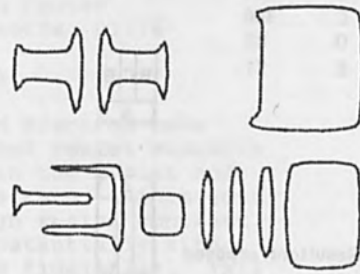


Fig. 5b. Simulation of developed pattern after irradiation in the manner of figure 5a.

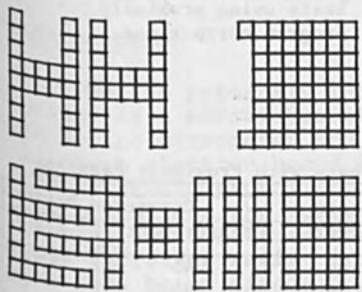


Fig. 5c. Pattern irradiated with doses chosen individually for each square.

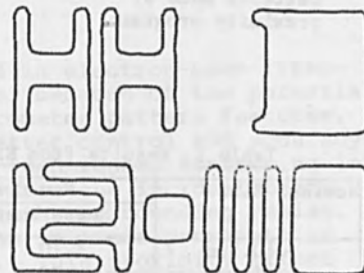


Fig. 5d. Simulation of developed pattern after irradiation in the manner of figure 5c.

Dose code	Dose
A	167
B	125
C	100
D	83
E	71

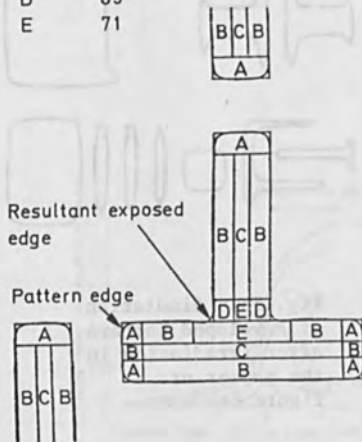


Fig. 6. Division of patterns made by proximity programs.

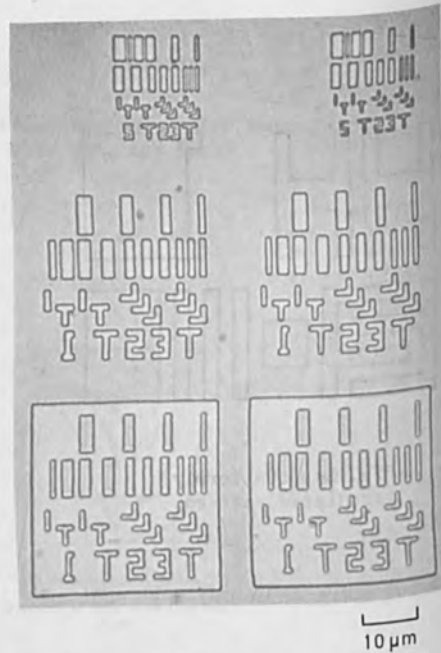


Fig. 7. Exposure tests using proximity program corrections.

Table I. Results from Exposure Tests with Proximity Programs

Nominal Size	Non Correct Pattern		Corrected Pattern	
	Measurement	Error	Measurement	Error
Line Widths	0.5μm	<.10	.45	-.05
	1.0μm	.70	.95	-.05
	1.5μm	1.20	1.43	-.07
	2.0μm	1.76	1.97	-.03
	2.5μm	2.37	2.45	-.05
Line Pad	1.0μm	-	1.05	+.05
	1.5μm	1.29	1.54	+.04
	2.0μm	1.91	1.98	-.02
	2.5μm	2.33	2.55	+.05

Pattern 10% Underdeveloped. PMMA resist 3000Å.

PROXIMITY EFFECT CORRECTION IN ELECTRON-BEAM LITHOGRAPHY

N. D. Wittels and C. I. Youngman
Sperry Research Center
Sudbury, Massachusetts 01776

Abstract

The proximity effect in electron-beam lithography describes enhanced resist exposure due to electron scattering in the resist and backscattering from the substrate. Since good edge definition requires high resist contrast, the proximity effect can substantially alter developed pattern shapes and fidelities. This effect increases as pattern sizes decrease and becomes rather severe for submicrometer geometries. We have explored methods of compensating for the proximity effect in submicrometer patterns exposed on a vector-scan exposure system. In this paper we discuss computation methods for achieving the correction. Average dose equalization and contour fitting are used for adjusting the exposure system's writing instructions to produce optimal patterns in the developed resist. We discuss how to implement these methods and present typical results.

Introduction

We are primarily interested in electron-beam lithography as a microfabrication tool because of the potential to define micrometer and submicrometer pattern features. Although electron beams allow better control and accuracy than standard photolithographic techniques, scattering in the resist and the substrate diverts the incident beam, causing it to diffuse throughout the surrounding resist. This increases resist irradiation in areas proximate to the area being directly exposed. This proximity effect strongly influences both the optimal electron dose and the shape of the developed resist profile. One effect of electron scattering is to produce a nonuniform dose in the resist; underlying regions are generally more heavily exposed than the surface (1). This effect is used in conjunction with development conditions to control the shape and line-edge profiles (undercut vs overcut) (2). These profiles usually have microfabrication processing importance so it is necessary to experimentally determine the exposure/development combination yielding the desired

shape. The resulting pattern, viewed from above, corresponds to the development isocontour. There is an associated critical dose such that in a positive resist the pattern regions receiving electron doses (direct plus scattered electrons) greater than the critical dose will have the resist removed during development, while those with less than the critical dose will have the resist remaining after development.* It is possible to adjust electron-beam exposure parameters so that the development isocontour, the curve along which the dose just equals the critical dose, most closely resembles the desired patterns. In a previous paper (3) we have discussed the overall problem of how to achieve this within the context of vector-scan electron-beam lithography. In this paper, we present the computational methods used.

Vector-Scan Systems

By "vector-scan" we mean an electron-beam lithography system in which an exposure pattern is composed of a sequence of primitive figure exposures. Most lithography systems use rectangles, trapezoids, parallelograms, or triangles as their primitive figures, but in this paper we shall discuss the case of rectangles because it is mathematically the simplest and because it corresponds to the hardware/software pattern generator on the ETEC LEBES exposure system we have used in our experimental work. We shall assume that the desired pattern is specified in terms of figures (closed boundaries with no imbedded surfaces, i.e., no annuli) (3). Associated with each figure in a pattern is a curve specifying the outer boundaries (the figure outline), Fig. 1. In order to generate a figure in a vector-scan system, the figure must be decomposed into primitive figures (see Fig. 2) which can be uniquely specified by a set of geometric descriptors and an exposure value E .

We use exposure to denote the incident electron density produced by the electron beam and dose to denote the total resist irradiation due to incident and back-scattered electrons. Both are expressed in units of $\mu\text{C}/\mu\text{m}^2$. In the case of rectangles, four geometric values suffice: x_1, x_2, y_1, y_2 , see Fig. 3. These five parameters (E, x_1, x_2, y_1, y_2) are the variables that we seek to adjust in order to make the developed resist

* When negative resists are used, those regions receiving doses less than the critical dose will be removed during development.

pattern most closely approximate the specified figure outline.

Electron-Dose Calculation

We have found that the dual gaussian model proposed by Chang (4) predicts the two-dimensional electron scattering with sufficient accuracy for promimity-effect corrections. In this model, the electron dose at a point produced by an electron beam striking the resist at a distance $r(\mu\text{m})$ away is proportional to the quantity

$$\alpha^2 e^{-(\alpha r)^2} + b\beta^2 e^{-(\beta r)^2} \quad (1)$$

where $\alpha(\mu\text{m}^{-1})$ is a function of the electron-beam size and b (dimensionless) and $\beta(\mu\text{m}^{-1})$ characterize the electron scattering within the substrate and the resist. The parameter α is inversely related to the beam diameter for a gaussian-shaped round beam or to the current density profile at the edge of a shaped beam. We assume that these three parameters, which can be empirically determined for a given set of writing conditions, are known (3).

The electron dose at a point (x,y) due to the exposure received by the n th rectangle in a pattern is a function of physical parameters α , β , b , and the five rectangle parameters:

$$f(x, y, \alpha, \beta, b, x_1, x_2, y_1, y_2)$$

Since α , β , b are constant for an entire pattern, we can introduce the notation

$$f_n(x,y) = \frac{1}{\pi} \iint_{A_n} \left[\alpha^2 e^{-(\alpha r)^2} + b\beta^2 e^{-(\beta r)^2} \right] dA_n \quad (2)$$

where r is the distance from (x, y) to the differential area element dA_n in the integration. Using this notation, the dose to point (x,y) is just the sum of f_n over all rectangles:

$$D(x,y) = \sum_n E_n f_n(x,y) \quad (3)$$

Expressions for $f(x,y)$ that are analytic with respect to the geometric parameters can be found for most primitive figures. The function $D(x,y)$ is compared with the critical dose D_c to determine how to adjust the primitive figure parameters. The two strategies we have examined for making this comparison and adjustment are presented in the next sections.

Equal Average Dose

The average electron dose received by the m th rectangle in a pattern is expressed in Eq. (4):

$$D_m = \frac{1}{A_m} \iint_{A_m} \sum_n E_n f_n(x,y) dA_m \quad (4)$$

where A_m represents the area of the m th rectangle. This average dose will have components due to exposure of surrounding rectangles, so one proximity effect strategy is to examine the contributions made to the dose of every rectangle by the incident electrons and backscattered electrons from all rectangles in the pattern. The incident exposures E_n are then adjusted to equalize the average box doses:

$$D_m = D_{av} \quad (5)$$

This approach is mathematically attractive in that exactly one rectangle parameter, the exposure, is used to fit one parameter per rectangle, the average dose. Because the equations for D_m , Eq. (5), are linear with respect to the exposures and $f_n(x,y)$ is analytic, the integration in Eq. (4) is easy to perform; correction involves the solution of N simultaneous linear equations, where N is the total number of rectangles, a fast straightforward task (5).

One difficulty with this approach is that it does not directly suggest what the average rectangle dose D_{av} ought to be. Figure 4 shows a computer simulation of development isocontours for a simple figure. The curves represent different ratios of the average rectangle dose to the critical dose. The correct average rectangle dose can only be determined experimentally; the value will change when the exposure and development parameters are changed. Nevertheless, we have found the equal average dose strategy useful as a first-order strategy to correct for the most obvious proximity effect: large pattern features

generally develop before small ones. After correction the central portions of figures generally receive the same dose, but specifying equal average doses for rectangles still allows the actual dose within the rectangle to vary considerably from point to point. In particular, slight dose variations along the figure perimeter can result in unacceptably large developed-edge displacements, due to the high contrast of electron-sensitive resists. It is fairly common practice in electron-beam lithography to make figures slightly oversized or undersized to correct for this aspect of the proximity effect. A method we have found useful for doing this in a systematic way is presented in the next section.

Contour Fitting

The goal of lithography is to make the development isocontour, the curve along which the equation

$$D(x,y) = D_c \quad (6)$$

applies, conform to the figure specification. Thus, it is worth the effort to find the solution to Eq. (6), which is a complicated, nonlinear analytic equation. The solutions of this equation are those depicted in our diagrams of development isocontours. Ideally, we would like to find the set of rectangle parameters such that the solution of Eq. (6) exactly coincides with the figure specification. In general, no such solution exists so we find an optimal solution by fitting the development isocontour to the specification, in the least-squares sense. The figure specification is expressed as a sequence of sample points whose weights and spacing along the figure perimeter are chosen to accentuate areas where pattern accuracy is most important, see Fig. 5. The rectangle parameters are then chosen (6) to minimize ϵ in the following equation:

$$\epsilon = \sum_i \omega_i [D(x_i, y_i) - D_c] \quad (7)$$

where (x_i, y_i) are the coordinates of the i th sample point and ω_i is its weight. Alternatively, instead of the difference between the sample point dose and the critical dose, the perpendicular distance between (x_i, y_i) and the development isocontour curve, can be used in the minimization procedure. In general, we find that the best fit often results in changing a figure's overall shape and size and in introducing gaps or overlaps between rectangles inside a figure (see Fig. 6).

In many figures, particularly those that are made of many primitive figures, the minimization problem, Eq. (7), is not well conditioned: a range of rectangle parameter values may result in almost equally good fits. This situation, which most least-squares minimization programs find confusing, can be ameliorated by solving for a subset of the total 5N parameters. If necessary, the minimization can be performed several times, in sequence, until all of the parameters have been optimized. Also, we have found it useful to choose at least three times as many sample points as there are variable parameters. That is, when solving for ten rectangle parameters it is desirable to choose a minimum of thirty sample points.

Conclusions

On the basis of our experience we have found an effective proximity-effect correction algorithm that consists of the following steps:

(1) Adjust rectangle parameters to equalize the average rectangle doses to a value which places the development isocontour near the specified pattern outline.

(2) Use contour fitting to adjust rectangle dimensions that form the outside of the figures (scale the figure to be larger or smaller).

(3) Use contour fitting to adjust rectangle dimensions that abut each other (introduce gaps or rectangle overlaps inside the figure).

Steps (2) and (3) can be performed interactively, if necessary.

We have applied this approach to a variety of lithography problems. As an example, consider the microfabrication of the half-disc magnetic bubble propagator shown in Figure. 1. The best-fit development isocontour fits everywhere to within $0.1 \mu\text{m}$ of the specification, see Fig. 7. When this device was exposed in PMMA resist with a 1.0 nA , $0.3 \mu\text{m}$ diameter beam of 20 kV electrons, the developed pattern fit within $0.2 \mu\text{m}$ of the specification (3).

The methods we have presented are applicable to other exposure systems, substrates, and resists than we have used. Although we have only experimentally verified proximity-effect corrections in the case where patterns are composed of rectangles, effective correction seems to

be achievable with other primitive figures as well.

Acknowledgements

We gratefully acknowledge the important contributions other people have made to this work. We received encouragement and helpful suggestions from F. A. Sewell, Jr. and J. A. Donahue; S. L. Teeter and W. S. Willman wrote the computer graphics programs; G. T. Scott and A. R. Roberts helped with the preparation of this manuscript.

References

- (1) M. Hatzakis, Appl. Phys. Letters 18, 7-15 (1971).
- (2) M. Hatzakis, C. H. Ting and N. Viswanathan, Proc. 6th Intn'l. Conf. Electron and Ion Beam Sci. and Tech., San Francisco, May 12-17, 1974, 542-579.
- (3) C. I. Youngman and N. D. Wittels, Proc. S.P.I.E. Conference on Semiconductor Microlithography III, vol. 135, 1978 (in press).
- (4) T. H. P. Chang, J. Vac. Sci. Technology 12, 1271-1275 (1975).
- (5) M. Parikh, 14th Symp. on Electron Ion and Photon-Beam Tech., Palo Alto, May 25-27, 1977.
- (6) R. Fletcher and M. J. D. Powell, Computer J. 6, 163-168 (1963).



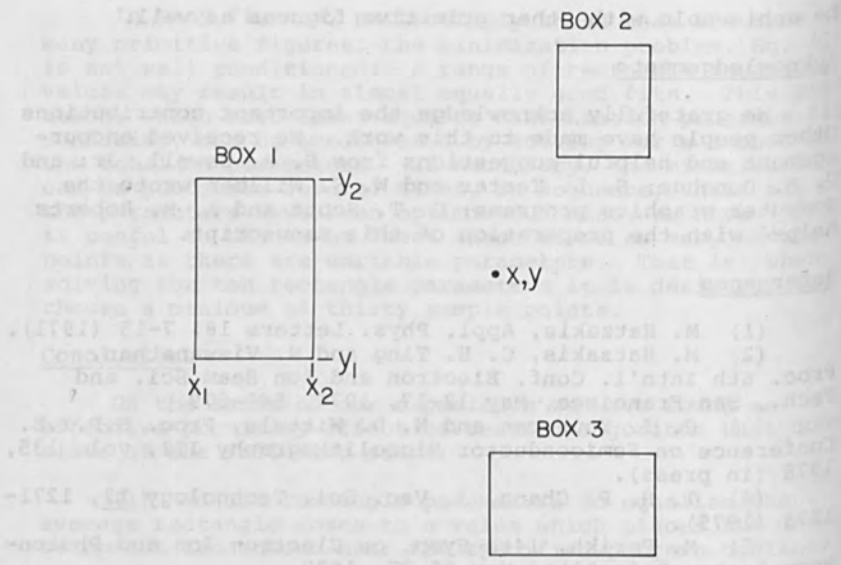


FIG. 3 Definition of the four geometric rectangle parameters, the minimum and maximum x and y dimensions. These plus the rectangle exposure are used to calculate the dose at any point x,y.

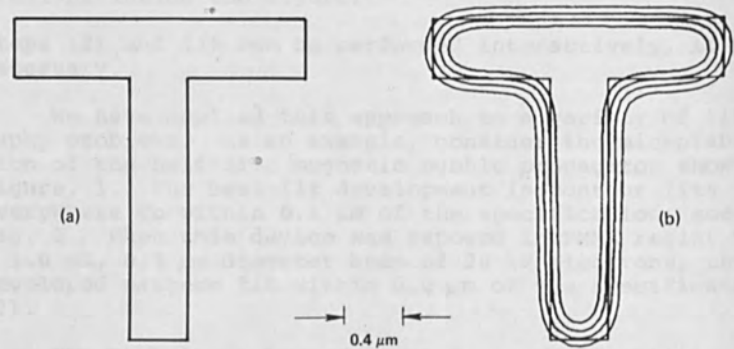
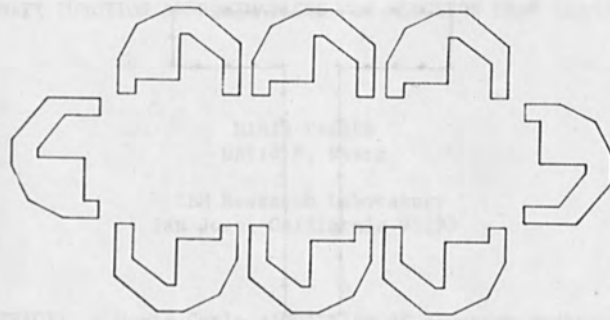


FIG. 4 (a) A T-bar magnetic bubble propagator with $0.4 \mu\text{m}$ wide lines; (b) Computer model of the figure written with a $0.3 \mu\text{m}$ electron beam. The curved lines, starting at the inside, represent development iso-contours for average doses 1.1, 1.3, 1.8, and 2.7 times the critical dose, respectively.



(a)

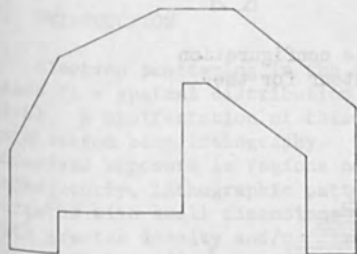


(b)

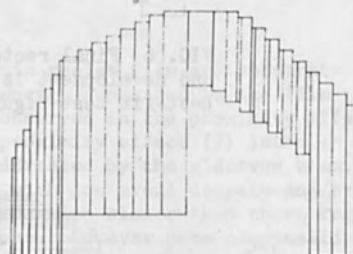


(c)

FIG. 1 A pattern (a); a figure (b); and a primitive figure (c).



(a)



(b)

FIG. 2 A half-disc magnetic bubble propagation element. (a) Outline of the specified figure; (b) Decomposition into primitive figures: in this case, rectangles.

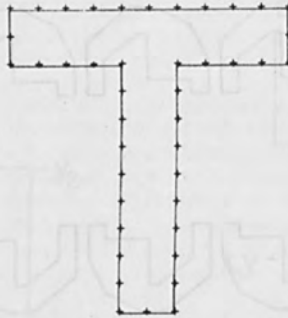


FIG. 5 A typical selection of sample points for the simple test figure shown in Fig. 4.

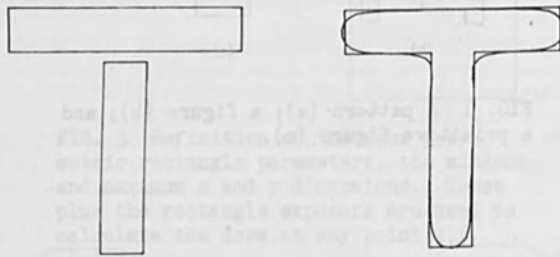


FIG. 6 Final rectangle configuration and development isocontour for the best-fit test figure.

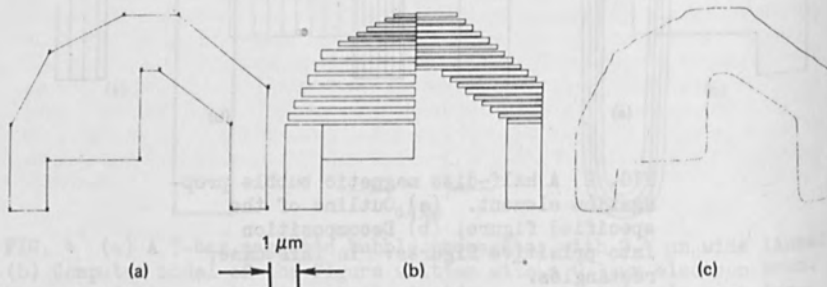


FIG. 7 A magnetic bubble propagator. (a) Figure specification; (b) Decomposition into rectangles; (c) Development isocontour plot.

PROXIMITY FUNCTION APPROXIMATIONS FOR ELECTRON BEAM LITHOGRAPHY

Mihir Parikh
David F. Kyser

IBM Research Laboratory
San Jose, California 95193

ABSTRACT: A Monte Carlo simulation of electron scattering in the resist and substrate of a target in electron lithography was used to obtain the spatial distribution of energy deposition in the resist. Analytical approximations were subsequently obtained by a least squares fit of Gaussian functions to the forward and backward scattered components of these distributions. The parameters in the analytical functions were deduced and a compendium of values are tabulated for a variety of resist thicknesses and incident electron energies. The parameters were found to be in reasonable agreement with available experimental data. These approximations and parameters provide quantitative guidelines for understanding and compensating for electron scattering and proximity effects in electron beam lithography.

I. INTRODUCTION

Electron scattering in the organic resist film and substrate leads to a spatial distribution of energy deposited in the film (1-6). A manifestation of this is observed in the proximity effect in electron beam lithography. The proximity effect (7) leads to undesired exposure in regions not addressed by the electron beam. Consequently, lithographic patterns with low areal density and/or patterns with small dimensions will develop slower than those regions with greater density and/or dimensions. However some compensation for proximity effects can be achieved via appropriate adjustments to incident electron exposure (8) or to changes in pattern dimension (9). A quantitative description of electron scattering and electron deposition in the resist and substrate can be obtained via theoretical simulation (4-6) of electron scattering or via experiment (10). However, the results from the theoretical calculations are available only as complicated analytical formulae or in a numerical form; thus they cannot be used easily.

In this paper, we will describe a technique for fitting the results from a theoretical simulation with simple analytical

functions and provide a compendium for cases relevant to practical electron beam lithography. In particular, we have considered silicon substrates, beam voltages from 10 to 40 keV, and PMMA film thicknesses from 0.5 to 1.5 μm . Thus a comprehensive range of parameters has been considered and interpolation or extrapolation from our results is possible. In all of this work, we make the implicit assumption that the energy deposition can be directly related to the developed image in the resist film. Thus we assume that the cumulative effect of electron scattering, energy deposition, molecular fragmentation and the development process can be approximated by the energy deposition alone.

II. MONTE CARLO SIMULATION

The model used for the Monte Carlo (MC) simulation of electron scattering and energy deposition in the resist and substrate has been described in detail elsewhere (11,12). Here only a brief outline will be presented. The first electron scattering event, assumed to be at the surface, involves statistical changes in the angles θ and ϕ . These are calculated from random numbers and the differential cross section for elastic scattering as given by the screened Rutherford formula. The mean-free path between elastic scattering events λ is determined by the total elastic scattering cross section. Thus the direction of an electron after elastic scattering and the distance to the next scattering position is uniquely determined by θ , ϕ and λ . The energy loss between scattering points is calculated by the continuous-slowing-down-approximation (CSDA). Thus the energy loss in an elemental volume in the target is given by the Bethe expression for energy loss times the path length of the electron in that volume element. The calculation is repeated to yield new positions in the target from a new set of random numbers until the energy of the electron falls below a predefined value.

In order to simulate the effect of a real electron beam, a large number of incident electrons is utilized. We have chosen to simulate an ideal point source (i.e., a delta function) of electrons. The distributions obtained from such a source are applicable to arbitrary sources via a mathematical convolution. For each electron, a new set of random numbers are used, thereby ensuring that no two trajectories are identical. Statistical accuracy of the calculation increases with increasing number of incident electrons n and is proportional to $n^{-1/2}$. The present calculations were performed on an IBM System 360/195 with typically 10,000 to 50,000 trajectories for a particular simulation.

The total deposition of energy density ΔE at any point in the resist due to an electron moving at an angle θ with respect to the z axis is separated into two components. These are: (1) the energy

deposited ΔE_f due to forward scattered electrons, i.e., those following trajectories with $0 \leq \theta \leq \frac{\pi}{2}$ and (2) the energy deposited ΔE_b due to backward scattered electrons, i.e., those with $\pi/2 < \theta \leq \pi$. The energy loss is calculated in a donut-shaped volume with an inner radius r and an outer radius $r + \Delta r$ with a thickness Δz at a depth z from the resist surface. Typically Δr and Δz are chosen to be $\sim 250-1000 \text{ \AA}$. The radial distribution of ΔE_f and ΔE_b can then be plotted as a histogram with spatial resolution Δr . An example of such a distribution is shown in Fig. 1. Hereafter, we shall call these radial distributions of energy deposition density ΔE_i , for each component i , the energy deposition functions (EDF).

III. ANALYTICAL APPROXIMATIONS TO THE EDF

The approximation of the EDF by an analytical function serves two purposes: (1) It provides a simple formula which can be subsequently used in applications (8,13) relating to electron lithography, and (2) it can provide macroscopic parameters that are physically meaningful, thereby making possible a comparison with other electron scattering parameters. A simple analytical function, which has been used previously (7,8), is a Gaussian for each component of the EDF. Thus we have chosen to approximate the EDF with:

$$f(r) = c_f \exp(-r^2/\beta_f^2) + c_b \exp(-r^2/\beta_b^2) \quad (1)$$

where β_f and β_b are the "characteristic widths" of the forward and backward scattered distributions and c_f and c_b are weighting constants for these distributions, respectively. While β_f and β_b are physically meaningful, the parameters c_f and c_b lack any physical interpretation. However, the ratio of the integrated distributions for the two components is meaningful. In particular, if we define:

$$I_i \equiv c_i \int_0^\infty \int_0^{2\pi} \exp(-r^2/\beta_i^2) d\theta 2\pi r dr, \quad (2)$$

then the quantity:

$$\eta_E \equiv I_b/I_f = c_b \beta_b^2 / c_f \beta_f^2 \quad (3)$$

can be defined, which has a physical interpretation. Thus Eq. (1) can be rewritten as:

$$f(r) = k[\exp(-r^2/\beta_f^2) + \eta_E \beta_f^2/\beta_b^2 \exp(-r^2/\beta_b^2)] \quad (4)$$

where k is a normalization constant; explicitly it is equal to c_f .

Since the EDF are obtained for a mathematical point (i.e., delta function) source of incident electrons, the $f(r)$ obtained from (4)

are only applicable to point sources. However, the extension to real electron beams with finite diameters is trivial. In particular, if a real electron beam can be represented by a Gaussian function with a "characteristic width" β^* , then $f(r)$ for a real source is obtained by adding β_f or β_b in quadrature with β^* to form β_f^* and β_b^* . These new values are then used in Eq. (4), and η_E is unchanged for a real electron beam.

The approximation of the EDF by an analytical formula [Eq. (4)] involves, in principle, a nonlinear least squares fit of the EDF data with the parameters in the formula as variables. However, the nonlinear least squares fit of the EDF data can be avoided by two simplifications: (1) The EDF data can be separated into two components as described earlier. (2) The EDF data can be plotted in the form $\ln(\Delta E)$ vs r^2 (for each component), thereby yielding a straight line for a pure Gaussian distribution. In such a case, a linear least squares fit can be achieved. The statistical accuracy of the data in an EDF is taken into account during the least squares fitting by assuming that the standard deviation of each data point is inversely proportional to the square root of the energy deposited ΔE_i , for each component i .

IV. RESULTS AND DISCUSSION

A. Silicon Substrate

Figures 2a and 2b show a typical result of linear least squares fit of EDF data for the forward scattered electrons and the backward scattered electrons. The quality of fit for the backward scattered distribution is considerably better than that for the forward scattered distribution. However, the fit is constrained such that the integral of the forward scattered EDF is equal to the integral of the first term in $f(r)$ obtained after the fit. The use of this constraint leads to an overestimate of β_f ; however, this is to be expected since the forward scattered distribution has been predicted (15) to decrease with radius r even faster than a Gaussian. While the quality of fit for the forward scattered distribution is relatively poor, the results shown for β_f are still applicable under the following condition: when the characteristic width β^* of the incident beam is comparable to or larger than β_f , the result of the convolution is dominated by β^* . Thus errors in β_f become relatively insignificant in such a case. However, in those cases when β^* is smaller than β_f , the errors in β_f^* are due to the overestimation.

Table I shows a compendium of the three parameters that define $f(r)$. The parameter β_f shows the following trends with incident electron energy and resist thickness: (1) It increases with increasing depth in the resist for a given electron energy. Figure 3 shows this graphically; note that film thickness is not an important

parameter. For example β_f for a 0.5 μm film at 0.5 μm depth is the same as that for a 1.5 μm film at 0.5 μm depth for a given incident electron energy. The values for β_f below 0.05 μm are beyond the limits of the resolution in our MC simulation and thus have been extrapolated to zero. (2) For a given film thickness, β_f decreases with increasing electron energy, as expected (Fig. 4).

The behavior of β_b with incident electron energy is also shown in Fig. 4 for a film thickness of 1.0 μm . Notice the monotonic increase in β_b with increasing electron energy. In order to see the dependence of β_b on electron range in the substrate we show in Table I the MC range R of electrons in pure silicon and the ratio β_b/R . The MC range R is calculated from our MC calculations to be the total distance travelled by an electron within a bare substrate for an electron incident with energy E_0 . The quantity β_b/R depends weakly on incident electron energy. Thus estimates of β_b can be made for other electron energies. Finally, the dependence of β_b with depth in the resist and with film thickness is very weak for a given electron energy (Table I).

The parameter η_E (Table I) depends weakly on electron energy and resist thickness; the reason for this behavior is discussed elsewhere (16). An alternative parameter in $f(r)$ that can be used instead of η_E is the quantity c_b/c_f . This parameter has the disadvantage of not being easily interpreted physically. In addition it also suffers from large variations in magnitude for typical cases encountered in practical electron beam lithography. For example, while η_E is approximately constant (~ 0.5), one has for c_b/c_f :

t	E_0	β_f^*	β_b^*	c_b/c_f
0.5	10	0.30	0.68	0.097
0.5	25	0.21	2.61	0.003

Here we have used β_f^* and β_b^* with the assumption of $\beta^* \sim 0.2$. The units used above are the same as those used in Table I.

B. Copper and Gold Substrates

For copper and gold substrates, a behavior that is different than that for silicon substrates is observed for the backward scattered component of the EDF. An example of this is shown in Fig. 5, for the case of 0.5 μm film on a copper substrate. Notice that even on a $\log(\Delta E_b)$ vs r^2 plot, the distribution is nonlinear. However, the distribution is such that the backward scattered EDF can be separated into two components and thus be approximated by two overlapping Gaussians. As before, the forward scattered EDF has been approximated by just one Gaussian. Due to a lack of space, the results obtained for these substrates cannot be given fully. A more detailed analysis of these results can be found in ref. (16).

C. Comparison with Experimental Results

Comparison of our calculated values (of the parameters in the analytical approximation to the EDF) with the experimental data is difficult. This is because of the limited availability of detailed experimental work that can be directly correlated with the EDF or the parameters in its analytical approximation. There are a few experiments which have reported the parameters in Eq. (4). Table II shows a comparison for the parameters β_f , η_E , β_b between our theoretical values (for a point source) and the available experimental results (8,10).

The parameters obtained from a proximity correction technique (8) are in general agreement with our calculated values. However these experimental values (17) are not unique but merely an operationally correct set. Note that the discrepancy in the value β_b is probably due to the insensitivity of the proximity effect correction technique and hence the deduction of these parameters. Also note that only a few combinations of these parameters in $f(r)$ were used in the attempts (17) to correct for the proximity effect.

The experiments reported in Ref. 10 provide a set of parameters based on exposure and development of patterns consisting of a collection of rectangles with a variety of lines and spacings. The parameters β_b deduced from these measurements is in good agreement with our calculations. Note however that the large experimental value of β_f is due to the incident beam size β^* (reported to be $0.2 \mu\text{m}$). Thus when this β^* is convolved with our calculated value of β_f ($0.06 \mu\text{m}$), the agreement with experiment is quite good. However, the discrepancy in η_E is unresolved. It is possible that our results for energy deposition only cannot be directly compared to the experimental data, which has been obtained from chemically developed resists.

The experiments reported in ref. (18) provide, after an Abel inversion of the line width data, the electron dose q required to develop a hole in PMMA with radius r . After replotting the data in the form of $\log(q)$ versus r^2 and fitting a straight line to it (for the high dose region only), we deduced a value for β_b of $2.5 \mu\text{m}$ at $E_0=20 \text{ keV}$. This value agrees quite well with our theoretical prediction. Due to the nature of the experimental data, we were unable to consider the low dose region and deduce a value for β_f or η_E .

Lastly, some results have been reported for the radius r developed in a very thin ($0.1 \mu\text{m}$) PMMA film on silicon due to exposure by only backscattered electrons from a point source beam (19). By defining the radius R_b as the value of r where the integrated distribution $F(r)=0.9$, they obtained $R_b=0.75, 2.5, \text{ and } 5.4 \mu\text{m}$ at

$E_0=10, 20, \text{ and } 30 \text{ keV}$, respectively. These values are comparable to those shown in Table I for β_b , after interpolation.

V. CONCLUSIONS

In summary, we can delineate our work into the following parts:

- (1) MC simulation of electron scattering and energy deposition was used to calculate the two components (the forward scattered and the backward scattered) of the EDF for a point source of electrons incident on a resist-substrate system. (2) Analytical approximation to the EDF was made with the assumption of a Gaussian function for each component. A least squares fit to the EDF was obtained for each of the components. (3) Parameters for these analytical functions were obtained for a variety of resist thicknesses and incident electron energies. For copper and gold substrates, the approximation to the backward scattered component of the EDF required two Gaussians, compared to only one Gaussian required for silicon.
- (4) Fairly good agreement with available experimental data was found. However there is a need for more systematic experimental studies.
- (5) The analytical approximation to the EDF and the parameters which we have obtained here provide quantitative guidelines for understanding and correcting the complex processes due to electron scattering in electron lithography.

REFERENCES

1. M. Hatzakis, *Appl. Phys. Lett.* 18, 7 (1971).
2. E. D. Wolf, F. S. Ozdemir, W. E. Perkins, and P. J. Coane, *Rec. 11th Symp. on Electron, Ion, and Laser Beam Technology* (San Francisco Press, 1971), p. 331.
3. R. F. Herzog, J. S. Greeneich, and T. E. Everhart, *IEEE Trans. Electron Devices* ED-19, 624 (1972).
4. J. S. Greeneich and T. Van Duzer, *IEEE Trans. Electron Devices* ED-21, 286 (1974).
5. R. Hawryluk, A. Hawryluk, and H. Smith, *J. Appl. Phys.* 45, 2551 (1974).
6. D. F. Kyser and K. Murata, *Proc. 6th Int. Conf. on Electron and Ion Beam Science and Technology* (The Electrochemical Society, 1974), p. 205.
7. T. H. P. Chang, *J. Vac. Sci. Tech.* 12, 1271 (1975).
8. M. Parikh, *J. Vac. Sci. Tech.* (1978), to be published. Also available as IBM Research Report No. RC-6666 (August 1977).
9. H. Sewell, *J. Vac. Sci. Tech.* (1978), to be published.
10. W. D. Grobman and A. J. Speth, *Proc. 8th Int. Conf. on Electron and Ion Beam Science and Technology* (The Electrochemical Society, 1978), to be published.
11. K. Murata, T. Matsukawa, and R. Shimizu, *Jap. J. Appl. Phys.* 10, 678 (1971).
12. K. Murata, T. Matsukawa, and R. Shimizu, *Proc. 6th Int. Conf. on X-Ray Optics and Microanalysis* (Univ. of Tokyo Press, 1972), p. 105.
13. D. F. Kyser and N. S. Viswanathan, *J. Vac. Sci. Tech.* 12, 1305 (1975).
14. IBM Corp., *System/360 Subroutine Library-Mathematics Users Guide* (1974), p. 362.
15. G. Molière, *Z. Phys.* 156, 318 (1959).
16. M. Parikh and D. F. Kyser, "Energy Deposition Functions in Electron Resist Films on Substrates," submitted for publication (1978).

17. M. Parikh, "Corrections to Proximity Effects in Electron Beam Lithography: III-Experiments," submitted for publication (1978).
18. R. Hawryluk, H. Smith, A. Soares, and A. Hawryluk, J. Appl. Phys. 46, 2528 (1975).
19. K. Murata, M. Kotera, and K. Nagami, "Surface Distribution of Backscattered Electrons in the SEM and EPMA," Proc. 8th Int. Conf. on X-Ray Optics and Microanalysis, (Boston, 1977), to be published.

TABLE I. Compendium of Gaussian parameters for Eq. (4). The parameter R is total Monte Carlo path length, and the substrate is Si.

E_0 (keV)	t (μm)	β_f (μm)	η_E	β_b (μm)	R(μm)	β_b/R
10	0.5	0.22	0.51	0.65	1.58	0.41
15	0.5	0.13	0.51	1.14		
15	1.0	0.44	0.52	1.41	3.12	0.45
25	0.5	0.06	0.51	2.6		
25	1.0	0.22	0.49	2.9	7.36	0.39
25	1.5	0.43	0.52	2.9		
40	0.5	0.04	0.42	6.0		
40	1.0	0.11	0.45	6.0	16.22	0.37
40	1.5	0.22	0.44	6.2		

Note: All parameters are evaluated at $z = t$.
For parameter β_f , see text for limits of applicability.

Table 2. Comparison of experimental data with theory for silicon substrates.

Source	β_f (μm)	η_E	β_b (μm)
Ref 8 [1,3]	0.1	0.6	1.0
Ref 10 [1]	0.25	0.86	2.35
This work [2]	0.06	0.51	2.6

- Notes:
- [1] t (PMMA) = 6000Å, $E_0 = 25$ keV
 - [2] t (PMMA) = 5000Å, $E_0 = 25$ keV; calculated parameters are for a point source.
 - [3] Deduced from proximity corrected patterns; parameters not unique.

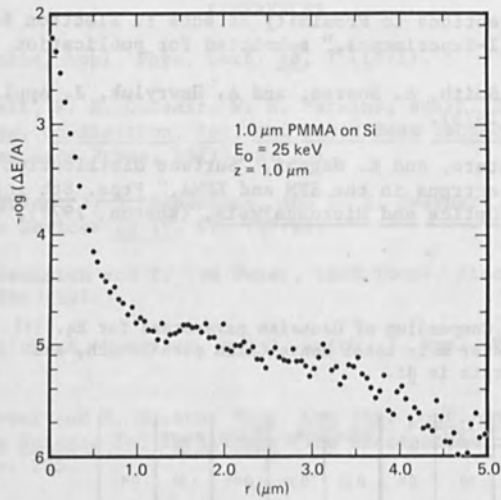


Figure 1. Radial distribution of the total energy density calculated with Monte Carlo method. The constant $A = (8/\pi) \times 10^{18} \text{ eV/cm}^3/\text{electron}$.

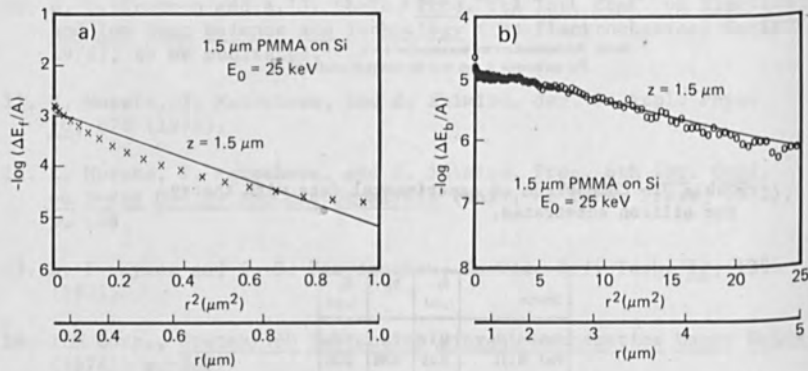


Figure 2. Radial distribution of the energy deposited by (a) forward scattered and (b) backward scattered electrons. The symbols denote Monte Carlo calculations and the straight lines are a least-squares approximation. Note the two radial scales (r and r^2); the constant $A = (8/\pi) \times 10^{18} \text{ eV/cm}^3/\text{electron}$.

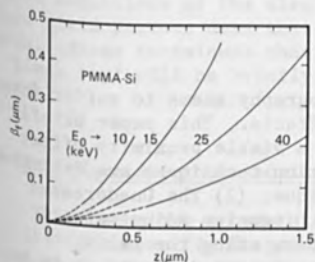


Figure 3. Variation of β_f with depth z for different incident electron energies E_0 .

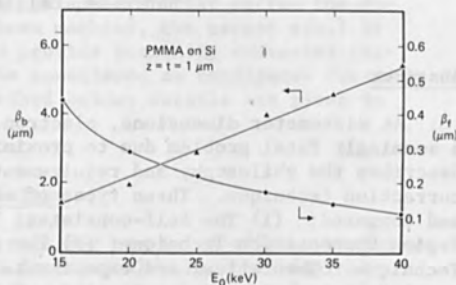


Figure 4. Dependence of β_b and β_f on incident electron energy E_0 for the depth $z = t$.

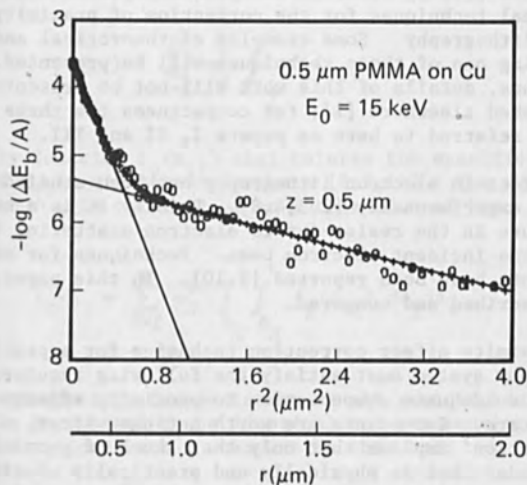


Figure 5. Radial distribution of the energy deposited by backward scattered electrons for PMMA on a Cu substrate. The symbols denote the Monte Carlo calculation and the two straight lines are the two components required for an approximation. Note the two radial scales (r and r^2); the constant $A = (64/\pi) \times 10^{18}$ eV/cm³/electron.

PROXIMITY EFFECT CORRECTIONS IN
ELECTRON BEAM LITHOGRAPHY

Mihir Parikh
IBM Research Laboratory
San Jose, California 95193

Abstract

At micrometer dimensions, electron lithography seems to suffer from a seemingly fatal problem due to proximity effects. This paper briefly describes the philosophy and requirements of a viable proximity effect correction technique. Three types of correction techniques are described and compared: (1) The Self-consistent Technique; (2) The Unaddressed Region Compensation Technique; (3) The Shape Dimension Adjustment Technique. Theoretical and experimental results using the self-consistent technique are presented. Such a technique is found to be both adequate and practical for sub-micron lithography.

1. Introduction

This paper will briefly describe the philosophy, the requirements and the mathematical techniques for the correction of proximity effects in electron beam lithography. Some examples of theoretical and experimental results using one of these techniques will be presented. Owing to space limitations, details of this work will not be presented here but will be published elsewhere [1]; for compactness the three papers in Ref. 1 will be referred to here as papers I, II and III.

Proximity effect* in electron lithography has been studied theoretically [5,6,7] and experimentally [2,3,4,8]. Briefly it is a name given to unwanted exposure in the resist due to electron scattering in regions not addressed by the incident electron beam. Techniques for corrections to proximity effects have been reported [9,10]. In this paper, several techniques are described and compared.

A viable proximity effect correction technique for a practical electron lithography system must satisfy the following requirements: (a) It must provide adequate compensation to proximity effects for all shapes in the pattern. Two points are worth noting: First, the phrase 'adequate compensation' implies that only that level of proximity compensation is demanded that is physically and practically meaningful in comparison with the resolution of the lithographic system. Second, all shapes in a complex pattern need to be corrected, i.e., those that lie within an array as well as those that lie on the periphery of an array or are 'isolated'. (b) It must be implementable to large, practical electron lithographic patterns, with only reasonable requirements on computation time and storage. (c) It must require minimal human intervention or interpretation of pattern. Computationally, the corrections

obtained must be mathematically unique and have no ambiguity based on methods of computation.

In short, an aim of the lithographer might be to possess a computational 'black box' that would accept as its' input, arbitrary pattern data and for a given set of physical parameters (that define the exposure conditions of the electron beam machine, the target etc.) it would yield pattern data that would provide proximity corrected patterns. Three techniques that can be considered as candidates for such a 'black box' will be briefly described below; details are given in paper I.

2. Self-Consistent Correction Technique

This technique attempts to correct for proximity effects by imposing that the specific fragmentation (or equivalently, the resultant exposure due to both incident electrons as well as scattered electrons) in all regions addressed by the electron beam be on the average equal. Thus incident electron exposures in each of the addressed regions that would make this possible are computed. Figure 1 shows as an example the exposure of three shapes by an electron beam machine. The specific fragmentation per unit area $\epsilon(r_i)$ at the point r_i in the region I due to n_j^0 incident electrons per unit area is:

$$\epsilon(r_i) = \sum_{J=1}^m n_J^0 \int_{A_J} f_p(r_{ij}) dA_J \quad (1)$$

The proximity function $f_p(r_{ij})$ that relates the specific fragmentation at the point r_{ij} is discussed elsewhere [8,9,11]. The average specific fragmentation $\bar{\epsilon}_I$ is obtained by an integration of Eqn. (1) over dA_i . Thus:

$$\bar{\epsilon}_I \cdot A_I = \sum_{J=1}^m n_J^0 \int_{A_I} \int_{A_J} f_p(r_{ij}) dA_J dA_i \quad (2)$$

If the average specific fragmentation in all regions addressed by the electron beam is imposed to be identical and set equal to say ϵ_0 , a system of m equations with m unknowns is obtained:

$$\left\{ \bar{\epsilon}_0 = \sum_{J=1}^m n_J^0 \int_{A_I} \int_{A_J} f_p(r_{ij}) dA_J dA_i / A_I \right\}_m \quad (3)$$

These system of m equations can be solved to yield a unique solution (paper II). In addition the solution is unambiguously defined by the pattern data and parameters to the proximity function.

A variation of the above solution can be obtained if instead of defining the averaging of $\epsilon(r_i)$ by $\bar{\epsilon}_I$, the $\epsilon(r_i)$ is monitored at 'sample points' in the pattern. Figure 2 shows one definition of sample points (five per shape). Here one obtains a system of $n \times m$ equations with m unknowns (n_I^0) for the case of n sample points per shape:

$$\left\{ \epsilon(r_i) = \sum_{J=1}^m n_J^0 \int_{A_J} f_p(r_{ij}) dA_J \right\}_{n \times m} \quad (4)$$

Notice that while only a two-dimensional integration over one area is involved here, the number of equations far exceeds the number of unknowns. Such an over-determined system of equations can yield only an approximate least squares solution. In addition, such a solution is unique only for a given number and location of the sample points; as such the solution ambiguously depends on a subjective definition of sample points. Note that if as the number of sample points increases, the values for n_I^0 obtained from Eqn. (4) approach those computed from Eqn. (3). Finally, computation time is significantly greater for a least squares solution of the over-determined system of equations in Eqn. (4) as compared to that for the fully determined system of equations in Eqn. (3).

3. Un-addressed Region Compensation Technique

Here the specific fragmentation in regions not addressed by the electron beam is considered. Figure 3 shows a collection of arbitrary shapes as well as "unaddressed" regions surrounding these shapes. These latter regions need to be arbitrarily and subjectively defined in terms of their location and size around each shape in the pattern. If $\epsilon(r_i)$ and $\delta(r_i)$ are respectively defined to be the specific fragmentation that are received at points within the shapes and the unaddressed regions, then in analogy with Eqn. (2), $\bar{\epsilon}_I$ and $\bar{\delta}_I$ can be defined. If for all I , $\bar{\epsilon}_I \rightarrow \bar{\epsilon}_0$ and $\bar{\delta}_I \rightarrow \bar{\delta}_0$, then one can impose $\bar{\delta}_0 \ll \bar{\epsilon}_0$. A system of over-determined equations (Sec. IV, paper I) are obtained with m unknowns (n_I^0) and $(m+l)$ equations corresponding to m shapes and l un-addressed regions. An approximate solution is obtained in such a case. Such a solution has the severe shortcoming of being dependent on the magnitude of $\bar{\delta}_0/\bar{\epsilon}_0$, and of being dependent on the sub-division of the pattern into the number and location of the un-addressed regions. In addition, computation time is increased over that in the self-consistent technique.

4. Shape Dimension Adjustment Technique

Unlike the techniques discussed above this technique (Fig. 4) attempts to compensate for proximity effect by computing changes in the dimension of the addressed regions instead of computing changes in the incident electron exposures. The mathematical formulations (Sec. IV, paper I) of such a technique leads to a highly under-determined system of

equations i.e., there are more unknowns (number of dimensions/shape times number of shapes) than there are equations (number of shapes). Solution to such a system of equations does not exist. If however only one dimension is varied per shape, e.g., the magnification of the shape about its designed centroid, then a fully determined system of equations are obtained. However, the equations are non-linear because the unknown quantities are embedded in the limits of the convolution integrals. Solution to such a system of equation is possible for special cases, but in general for an arbitrarily large pattern, the solution of such equations is expected to be highly impractical.

5. Comparison of Techniques

The self-consistent technique has the advantage of being unambiguously defined and mathematically unique. If instead of insisting on an equal average specific fragmentation $\bar{\epsilon}_0$, sample points are defined, the technique becomes subject to definitions of these points and its' solution is approximate in the least squares sense. The computation time also increases. If unaddressed regions outside the defined shapes are considered, the solution is again dependent on the subjectively defined location and size of the unaddressed regions as well as on the parameters $\bar{\delta}_0$ and $\bar{\epsilon}_0$. In general, such a solution is unreliable for arbitrary patterns. The adjustment of shape dimensions rather than incident electron exposures may simplify the operation of an electron beam machine. However, in general the changes in pattern dimensions for an arbitrarily large pattern cannot be computed; for special cases such changes can be approximately calculated.

6. SPECTRE

A proximity effect correction program package called SPECTRE [9] (for Self-consistent Proximity Effect Correction Technique for Resist Exposure) has been developed; it uses the self-consistent technique as described earlier. Figure 5 shows the overall structure of the program. Details of the algorithms and the organization of the program are given in papers II and III. Note that as shown in Fig. 4, after an initial input of parameters regarding the pattern, the electron beam machine and the target, the data for the entire pattern is sequentially tagged, sorted and corrected without any human intervention or interpretation. Thus as far as the electron lithographer is concerned a 'black box' for proximity corrections has been created. The storage requirements for SPECTRE are defined primarily by the storage necessary for the solution of linear equations; the computation speed is determined by both the evaluation of the integrals and by the solution of the linear equations. In the case of a pattern with an arbitrary arrangement of 10^4 rectangular shapes, SPECTRE requires a storage of less than 256 K bytes and computes corrections for all 10^4 shapes in 10^2 secs. of CPU time on the IBM Model 370/168.

7. Theoretical Results

The quality of corrections that can be realized through the use of SPECTRE can be monitored by a graphics program called RESPECT (for Resultant Exposure Study of Proximity Effect Correction Techniques). The specific fragmentation or resultant exposure $\epsilon(r_i)$ in Eqn. (1) can be computed and contours corresponding to equal ϵ can be plotted; thus contour lines will define developed patterns in the resist. Figure 6 shows an example of such a plot for a pattern consisting of an array of $1/2\mu\text{m}$ lines with $1/4\mu\text{m}$ gaps. Notice that all edges of the designed lines in the corrected pattern (Fig. 6b) are defined by the $\epsilon = 0.7$ contour line, while in the uncorrected pattern (Fig. 6a) this is not the case, especially for the line at the edge of the array. While it is not shown in Fig. 6, both the uncorrected and the corrected patterns with large ($> 2\mu\text{m}$) geometries are delineated by the $\epsilon = 0.7$ contour and thus develop simultaneously.

8. Experimental Results

The experimental technique and the results using SPECTRE are described in detail in paper III. Here, one example (Fig. 7) is shown. The uncorrected pattern in Fig. 7a shows adequate development in the interior regions of the array of densely packed 'Chevrons'; the edges of the array suffer from insufficient development due to the lack of proximity effect. Also the relatively sparse 'T-I Bar' pattern suffers from a similar under-development. The corrected pattern (Fig. 7b) yields all shapes at the same level of development. Note that over-development of the uncorrected pattern would lead to more complete development of the under-exposed regions, but only at the expense of significant decrease in gaps between the 'Chevrons'. Thus over-development cannot compensate for the proximity effect.

9. Conclusion

This paper has briefly described the philosophy and requirements of a practically feasible proximity effect correction technique. In that light, three types of correction techniques are discussed and compared. Results, both theoretical and experimental, using the self-consistent technique are presented. In our experience, such a technique has been found to be quite adequate for sub-micron lithography and computationally practical for automatic corrections of large electron lithographic patterns.

Acknowledgements

I am thankful to each and every member of the team that created the Vector Scan Machines at IBM for discussions and support, thereby making this work possible.

REFERENCES

1. (a) M. Parikh, "Corrections to Proximity Effects in Electron Beam Lithography: I-Theory", submitted for publication, available as IBM Report RJ2252.
- (b) M. Parikh, "Corrections to Proximity Effects in Electron Beam Lithography: II-Implementation", submitted for publication, available as IBM Report RJ2253.
- (c) M. Parikh, "Corrections to Proximity Effects in Electron Beam Lithography: III-Experiments", submitted for publication, available as IBM Report RJ2254.
2. M. Hatzakis, Appl. Phys. Lett. 18,7 (1971).
3. E. Wolf, F. S. Ozdemir, W. Perkins and P. Coane, in Record of the Eleventh Symposium on Electron, Ion and Laser Beam Technology, Boulder, Colorado, ed. R. F. M. Thornley (San Francisco Press, 1971).
4. R. F. Herzog, J. S. Greeneich, T. E. Everhart and T. van Duzer, IEEE Trans. on Electron Devices ED-19, 624 (1972).
5. J. Greeneich and T. van Duzer, IEEE Trans. on Electron Devices ED-21, 286 (1974).
6. R. Hawryluk, A. Hawryluk and H. Smith, J. Appl. Phys. 45, 2551 (1974).
7. D. F. Kyser and K. Murata, Proc. of the 6th Int. Conf. on Electron and Ion Beam Sci. and Tech. ed., R. Bakish (1974).
8. T. H. P. Chang, J. Vac. Sci. and Tech. 12, 1271 (1975).
9. M. Parikh, 14th Symp. on Electron, Ion and Photon-Beam Tech., Palo Alto, Calif. (May 1977); to be published in J. Vac. Sci. and Tech. (1978).
10. M. Sewell, 14th Symp. on Electron, Ion and Photon-Beam Tech., Palo Alto, Calif. (May 1977); to be published in J. Vac. Sci. and Tech. (1978).
11. M. Parikh and D. F. Kyser, "Proximity Function Approximations in Electron Beam Lithography", this proceedings.

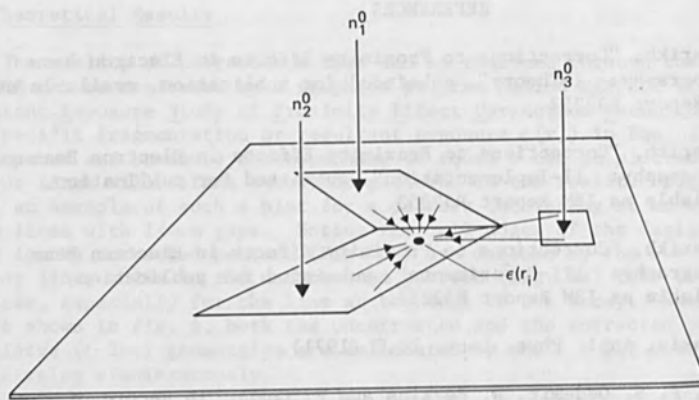


Figure 1. Schematic showing the principle of the "Self-consistent Technique." The specific fragmentation $\epsilon(r_1)$ at point r_1 is due to electron scattered from the three regions addressed by the electron beam, each with n_I^0 electrons per unit area.

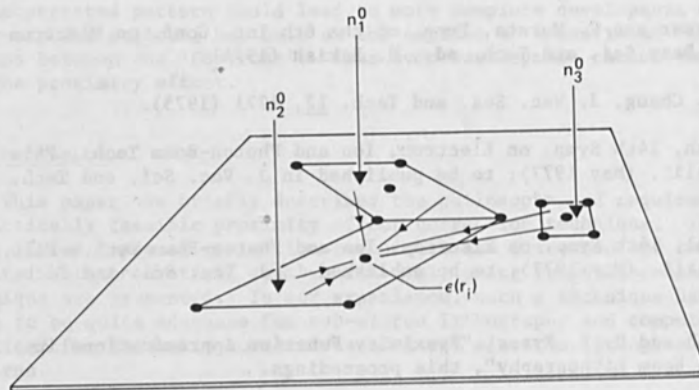


Figure 2. Schematic showing the definition of sample points. Note five points per shape are used in this example.

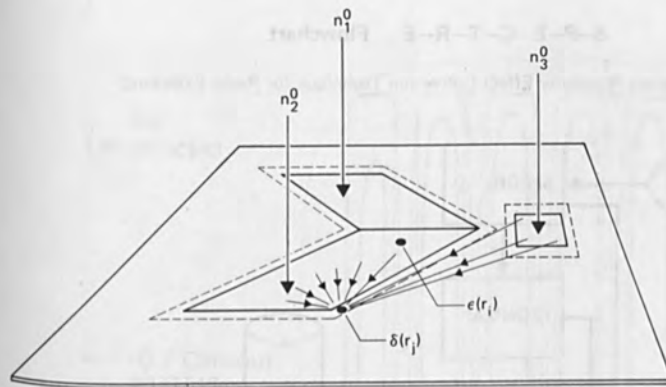


Figure 3. Schematic showing the principle of the "Unaddressed Region Compensation" technique. The specific fragmentation $\epsilon(r_i)$ and $\delta(r_i)$ at points r_i and r_i in region 2 due to electrons scattered from the regions addressed by the electron beam each with n_1^0 and n_j^0 electrons per unit area.

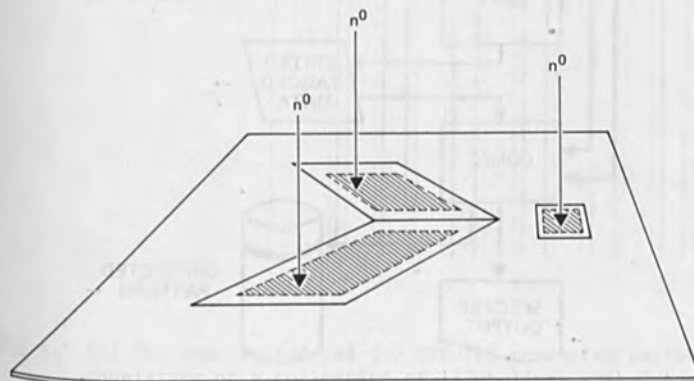


Figure 4. Schematic showing the principle of the "Shape Dimension Adjustment" technique. The regions exposed by the electron beam are shown by the shaded areas; the designed regions to be obtained after development are defined by the area enclosed within the solid lines.

S-P-E-C-T-R-E Flowchart

(Self-consistent Proximity Effect Correction Technique for Resist Exposure)

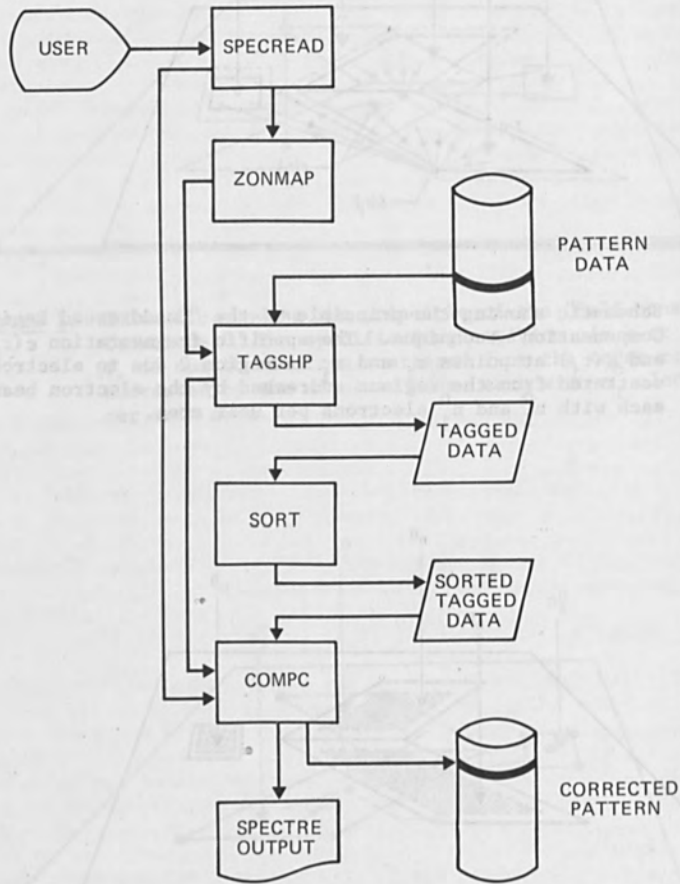


Figure 5. Flow chart to 'SPECTRE'

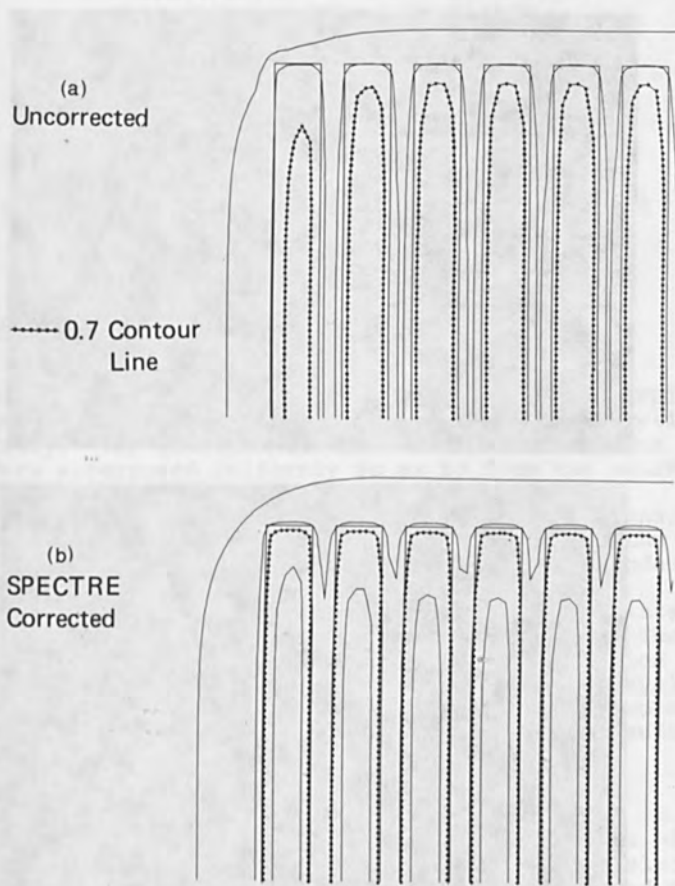
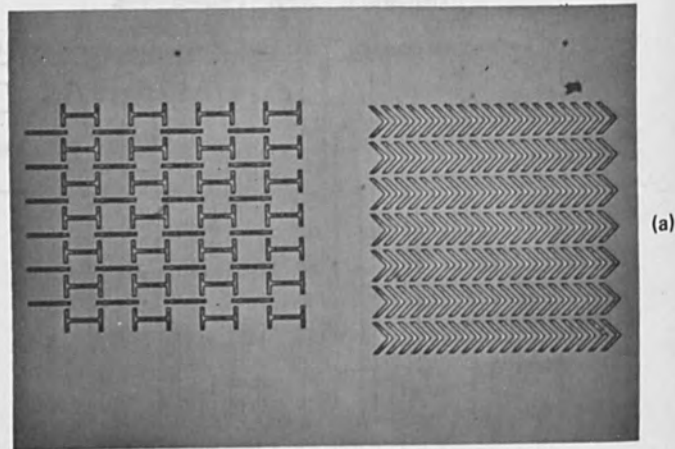
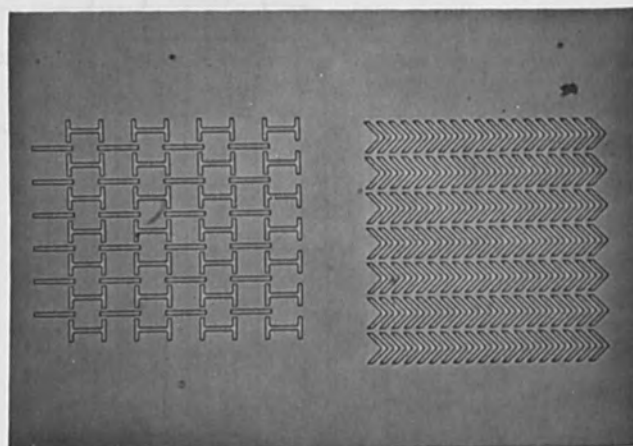


Figure 6. (a) The uncorrected and (b) SPECTRE corrected patterns consisting of a collection of $1/2\mu\text{m}$ lines with $1/4\mu\text{m}$ gaps. The four contours correspond to $\epsilon = 0.1, 0.4, 0.7$ and 1.0 ; note that $\epsilon = 0.7$ is delineated as (\dashrightarrow).



(a)



(b)

Figure 7. Optical micrograph showing (a) the uncorrected pattern consisting of 'Chevrons' and 'T-I Bars'. Line widths are $\sim 1\mu\text{m}$.

PROXIMITY EFFECT IN FET FABRICATION
WITH ELECTRON BEAM LITHOGRAPHY

Hidefumi Nakata and Takaaki Kato
LSI Development Laboratory
Mitsubishi Electric Corporation
Itami, Hyogo, Japan

Kenji Murata and Koichi Nagami
Electronics Department, College of Engineering
University of Osaka Prefecture
Sakai, Osaka, Japan

ABSTRACT

The interproximity effect in electron beam microfabrication of a source/drain pattern of FET has been investigated experimentally and theoretically. The Gaussian-distributed electron probes were superposed uniformly so as to form the source-drain pattern. From this calculation three-dimensional spatial contours of equi-energy density were obtained, which are directly related to the experimental resist profiles according to a model of the critical absorbed energy density for a development process. Comparison of the calculated contours is made with experimental profiles. The experimental result shows that the determination of the optimum dose to obtain a designed interval between the source and the drain patterns is more difficult than predicted by the calculated result.

I. INTRODUCTION

The technology of electron beam lithography is of great importance in the submicron fabrication of electron devices. However, before this technology is raised to the practicable stage, there are a lot of problems to be solved in the electron beam exposure system itself, and in the electron resist materials, etc. As for the system, some efforts are made to shorten the exposure time with a system which forms a rectangular beam shape of a variable size corresponding to an exposure pattern. Also many investigations to find electron resist materials with both a high sensitivity and a practically sufficient resolution have been performed. Another important problem in submicron fabrication is the proximity effect which is caused by electron backscattering from the substrate. Even though we performed some exposure experiment under

the same conditions of dose and development, we have different profiles of the developed electron resist depending on the substrate material or structure, the exposed pattern size, whether the pattern is isolated or not, etc. The absorbed energy density distribution necessary to analyze this effect has been investigated both by analytical scattering theories[1-5] and Monte Carlo calculations[5-8]. In a recent paper on the proximity effect correction method by Parikh[9] the experimental result which was obtained by Chang[10] is used. Although the Monte Carlo method requires much computational time compared with the analytical method, it seems to be more accurate and can be applied more generally. The spatial distribution of the absorbed energy density in electron resist films under electron irradiation is calculated by the Monte Carlo calculation. We can predict a developed profile by combining this spatial distribution with a solubility characteristic model of the resist. There are several reports on this subject such as the time evolution of the developed profile[11,13] and the quantitative analysis of the proximity effect among the paralleled spaced lines[4,12]. Once we have a theoretical means to predict the developed profile correctly, a proximity effect correction may be carried out in a further step.

In the present study we take up the source/drain pattern in the FET fabrication as the example of the proximity effect among patterns(so-called interproximity effect) as shown in Fig.1 and discuss the effect in a comparison between the Monte Carlo result and experimental profiles.

II. CALCULATION PROCEDURE

1. Radial distribution of the absorbed energy density for a point source electron beam

First the radial distribution of the absorbed energy density for a point source electron beam was calculated using the Monte Carlo model proposed by Kyser and Murata[7]. The model is based on the single scattering theory, where the following three basic equations are utilized.

$$\rho \Lambda = (N_A \sum c_i \sigma_i / A_i)^{-1}, \quad (1)$$

$$\frac{d\sigma_i}{d\Omega} = \frac{Z_i(Z_i + 1)e^4}{4E^2(1 - \cos \theta + 2\beta_i)^2}, \quad (2)$$

$$\frac{dE}{ds} = - \frac{2 \pi e^4 \rho N_A}{E} \sum_i \frac{C_i Z_i}{A_i} \ln\left(\frac{1.166E}{J_i}\right). \quad (3)$$

The first equation represents the mean free path, the second the screened Rutherford scattering cross section and the third the Bethe energy loss law. A simple explanation of the model is the following. An electron trajectory is divided into many small steps. The step length at each stage is taken equal to the mean free path. A scattering angle is determined from a generated uniform random number using eq.(2). The energy loss is calculated by eq.(3). The trajectory is followed until the electron energy slows down to 200eV. Thus an energy that all electrons dissipated can be obtained as a function of position. Actually a resist film of 4000Å thickness was divided into four layers. Moreover the layer was divided into concentric donut-shaped volumes. The radial distribution of the absorbed energy is obtained as a histogram. The number of calculated trajectories is typically 5000.

2. Convolution with electron probe size

We assume the following Gaussian form for an incident electron intensity distribution as shown in Fig.2.

$$g(r) = \frac{1}{2\pi\sigma^2} \exp\left(-\frac{r^2}{2\sigma^2}\right), \quad (4)$$

where σ is the standard deviation. The electron probe radius is defined as $R=1.35$, within which 80% of the total intensity is included. To convolve the radial distribution for a point source electron beam with the Gaussian beam, the following calculation is carried out. The sample surface was divided into small sections, specified by an index (i, j) as shown in Fig.3. The Gaussian beam is incident at the origin. Then, the number of incident electrons in the shaded part can be obtained by the following equation.

$$f_{i,j} = n_0 \cdot \int_{\theta_{j-1}}^{\theta_j} \int_{r_{i-1}}^{r_i} g(r) r dr d\theta \quad (5)$$

$$= \frac{\Delta\theta}{2\pi} \left[\exp\left(-\frac{r_{i-1}^2}{2\sigma^2}\right) - \exp\left(-\frac{r_i^2}{2\sigma^2}\right) \right],$$

where $\Delta\theta = \theta_j - \theta_{j-1}$, n_0 is the total number of incident electrons. Under the conditions of the incident beam current I , the scanning frequency f and the electronic charge e , a value of n_0 is calculated by

$$n_0 = I/e \cdot f \quad (6)$$

The absorbed energy at the position P which is at a distance of L from the origin is given by

$$F_{i,j}(s) = f_{i,j} \cdot h(s), \quad (7)$$

where $h(s)$ is the radial energy intensity distribution at a certain depth calculated in the previous section and s is the distance between P and Q ($r=(r_i+r_{i-1})/2$, $\theta=(\theta_j+\theta_{j-1})/2$). By summing up $F_{i,j}(s)$ over the whole sample surface the absorbed energy $E(L)$, can be obtained at the point P which is at the distance of L when the Gaussian-distributed electron probe is incident at the origin.

$$E(L) = \sum_{i,j} F_{i,j}(s), \quad (8)$$

where $s = (r^2 + L^2 - 2rL \cos \theta)^{1/2}$.

It should be noted here that the absorbed energy distribution $E(L)$ is also a function of depth.

3. Superposition of the Gaussian-distributed probe

The Gaussian-distributed probes were superposed in the same condition as used in the dot exposure experiment. The situation of this calculation procedure is shown in Fig.4. The dot spacing is given by p .

III. EXPERIMENT

Some experiments were performed to compare with the calculated results. Electron beam exposure of the FET pattern in Fig.1 was made by using the electron beam exposure system, JBX-5A. The experimental conditions are summarized in Table I.

Table I Experimental conditions

Beam voltage	20kV
Specimen current	10^{-9} A
Probe diameter	0.2 μ m
Dose	1.5, 2.0, 2.4, 3.0 ($\times 10^{-4}$ C/cm ²)
Substrate	Si
Resist	PMMA
Thickness of the resist	0.4 μ m
Prebake	150°C, 30min
Development	MIBK:IPA=1:3, 150sec(22°C)

These doses were determined so that the absorbed energy density around the boundary between the exposed and the unexposed regions may reach the critical value, 1.1×10^{22} eV/cm³

for a successful development, which was proposed previously [7]. After development, the surface profile was observed with the scanning electron microscope. Also cross sectional profiles of the resist in the unexposed region between the source and the drain patterns were observed after cleavage of the sample. For this purpose the rectangular patterns of $50\mu\text{m} \times 3000\mu\text{m}$ were exposed spaced closely together at a distance of $2.0\mu\text{m}$.

Although the probe size was not measured in the present experiment, the result of a previous measurement [8] was utilized to derive the probe size at a working distance of 85mm . Note that we measured the sample current, i_s . Therefore, the beam current i_0 was obtained by the equation $i_0 = i_s(1 - \eta)^{-1}$ using the Monte Carlo data for the back-scattering coefficient η . The value of each dose was calculated using this beam current i_0 .

IV. RESULTS

1. Calculated results

The calculated radial distributions of the absorbed energy density are shown as a smoothed curve in Fig.5 for the Gaussian-distributed probe of $0.2\mu\text{m}$ in diameter. The results are shown at the top and the bottom layers among the 4 layers divided by a 1000\AA length unit. The result shows that the intensity at the bottom layer is about 1.5 times as large as that at the top layer. It is seen in the figure that the relatively large background intensity extends to about $4\mu\text{m}$.

The calculated equi-energy density contours in the area surrounded by a circle in Fig.1 are shown in Figs.6 and 7. The results in Fig.6 are for the interval of $2.0\mu\text{m}$ between the source and the drain patterns both at the top and the bottom layers. Figs.7(a) and (b) are the results for the interval of $2.5\mu\text{m}$. The calculated results are shown in a percentage by arbitrarily labeling the contour of $0.6 \times 10^{26} \text{ eV/c}\cdot\text{cm}$ as 100%. We can see clearly the interproximity effect due to the adjacent pattern in the absorbed energy density contours. From a comparison between the results for $2.0\mu\text{m}$ and $2.5\mu\text{m}$ intervals, we can conclude that the absorbed energy density in the unexposed gap region becomes large and more dense as the gap distance becomes large. Fig.8 shows a variation of the absorbed energy density both at the top and the bottom layers along a line crossing the unexposed region of a $2.0\mu\text{m}$ interval as shown as A-B in the miniature in the figure. As the position of A-B is $3\mu\text{m}$ away from the edge, there is almost

no effect of the edge on the variation of the absorbed energy density. The absorbed energy in the unexposed region reaches about 30% of that in the exposed region.

2. Experimental results

The observed surface patterns for the designed interval l_0 (S-D) of $2.0\mu\text{m}$ are shown in Figs.9(1) to (4) at the doses of $1.5, 2.0, 2.4$ and $3.0(\times 10^{-4}\text{C}/\text{cm}^2)$. It is clearly seen in the figures that the width of a band-shaped undeveloped resist becomes small with an increase in dose. The fine resist band of the unexposed region disappears at the dose of $3.0 \times 10^{-4}\text{C}/\text{cm}^2$ for a $2.0\mu\text{m}$ designed interval. The width of the undeveloped resist band was measured in the SEM pictures. The result is shown in Fig.10 as a function of dose. We can see that it is not easy to obtain a designed interval because of the large slope of the curve and that this slope becomes large with a decrease in the designed interval.

Fig.11 shows a SEM micrograph of a cross sectional profile for a $2.0\mu\text{m}$ designed interval. The result shows an overcut profile.

V. DISCUSSIONS

In Figs.12(a) and (b) the experimental profiles for the case of a $2.0\mu\text{m}$ interval are compared with the calculated contours of the absorbed energy density at the doses of 2.0×10^{-4} and $3.0 \times 10^{-4}\text{C}/\text{cm}^2$. To compare these results quantitatively, the concept of the critical absorbed energy density [14] can be applied as a solvent of MIBK:IPA=1:3 is used in the present experiment. However, the problem occurs at which layer the result should be compared with the experiment. As already seen in the figure, a factor of about 1.5 is found for the energy densities at the top and the bottom layers.

First, we tried to compare the results for the top layer. From a comparison between the calculated contours and the experimental one at a dose of $2.0 \times 10^{-4}\text{C}/\text{cm}^2$, it is found that the contour of about 55% fits the experimental results. From this result, a value of $0.65 \times 10^{22}\text{eV}/\text{cm}^3$ is obtained for the critical absorbed energy density ϵ_c . If we apply this value to the result at a dose of $3 \times 10^{-4}\text{C}/\text{cm}^2$, the contour of 36% corresponds to the experimental profile. This is reasonable result judging from a comparison in the figure. In fact from Fig.8 the lowest level of the absorbed energy density is $0.227 \times 10^{26}\text{eV}/\text{c}\cdot\text{cm}$ and this quantity is sufficient to be developed out for the critical

absorbed energy density of $0.65 \times 10^{22} \text{eV/cm}^3$ at the dose of $3.0 \times 10^{-4} \text{C/cm}^2$. However, this assumption of the value of $0.65 \times 10^{22} \text{eV/cm}^3$ is undesirable for the following two reasons. (1) From Fig.8 at least the undercut shape must be observed at a dose of $2.0 \times 10^{-4} \text{C/cm}^2$ because the sufficient energy is deposited to be developed at the bottom layer. Namely, the energy density of $0.69 \times 10^{22} \text{eV/cm}^3$ ($0.35 \times 10^{26} \times 2.0 \times 10^{-4}$) is brought even at the smallest level. This is greater than a value of ϵ_c , $0.65 \times 10^{22} \text{eV/cm}^3$. However, the observed cross sectional profile in Fig.11 shows the overcut feature. (2) According to the calculated results the exposed region is developed successfully at $1.5 \times 10^{-4} \text{C/cm}^2$. Namely, at largest the resist band width of $2.0 \mu\text{m}$ should be obtained. Whereas a band-shaped resist with the width of more than $3.0 \mu\text{m}$ is observed in the experimental result.

Next, we assumed the value of $0.9 \times 10^{22} \text{eV/cm}^3$ for ϵ_c , which is close to the value of $1.1 \times 10^{22} \text{eV/cm}^3$, proposed previously [5,7]. Then, we obtained a better agreement in the profile between the calculated and experimental results for the bottom layer at doses of $2.0, 2.4$ and $3.0 (\times 10^{-4} \text{C/cm}^2)$. However, we still have the same difficulty as we do previously at the dose of $1.5 \times 10^{-4} \text{C/cm}^2$. The predicted width of the remained resist band is still $2.0 \mu\text{m}$, while the experiment shows the interval of about $3.3 \mu\text{m}$ which is larger than the designed interval, and moreover, the observed SEM micrograph does not show a complete development. The bright contrast in the exposed area is not uniform. We think that this discrepancy is caused from the fact that the Bethe energy loss equation overestimates [15] an energy loss at the very surface by a primary electron. Namely, an absorbed energy density E is possibly around $0.6 \times 10^{26} \text{eV/c.cm}$, which is derived as follows: $E = 0.9 \times 10^{22} \text{eV/cm}^3 / 1.5 \times 10^{-4} \text{C/cm}^2$. In the unexposed region under investigation an energy loss is not overestimated because in this region only back-scattered electrons contribute to the energy loss. In the latter assumption of ϵ_c , one point is not understandable, that the resist surface has to be dissolved even when the stored energy is smaller than the critical absorbed energy density. Therefore, it must be assumed that the resist surface is in an unusual situation that is not explained by the present model for development. This difficulty is not understood at present. Meanwhile, further study is required to determine how accurately the present calculation gives a prediction for an absorbed energy.

VI. CONCLUSION

We investigated the interproximity effect theoretically and experimentally for an example of the FET fabrication

pattern. The experimental results show that the width of the undeveloped resist between the patterns is very sensitive to the dose supplied and an optimum exposure dose exists to obtain the designed size.

We found some problems in the present theory from a comparison between the calculated and the experimental results. Namely, the Bethe law may overestimate an energy loss in the vicinity of the initial penetration. If this is confirmed, we come to the conclusion that the ratio of the absorbed energy density in the exposed area to that in the unexposed area becomes large, which means that the proximity effect becomes more significant.

VII. ACKNOWLEDGMENT

The authors are indebted to Dr. H. Oka of LSI Development Laboratory, Mitsubishi Electric Corporation for his support and encouragement.

REFERENCES

- (1) R. J. Hawryluk and H. I. Smith, Proc. 5th Int. Conf. on Electron and Ion Beam Science and Technology (Electrochem. Soc., Princeton, N. J., 1972), p.51.
- (2) J. S. Greeneich and T. Van Duzer, IEEE Trans. Electron Devices ED-21, 286 (1974).
- (3) M. Hatzakis, C. H. Ting and N. S. Viswanathan, Proc. 6th Int. Conf. on Electron and Ion Beam Science and Technology (Electrochem. Soc., Princeton, N. J., 1974), p.542.
- (4) R. E. Jewett, T. van Duzer and J. S. Greeneich, in Ref. 3, p.49.
- (5) R. J. Hawryluk, A. M. Hawryluk and H. I. Smith, J. Appl. Phys., 45, 2551 (1974).
- (6) N. Saitou, Japan. J. Appl. Phys., 12, 941 (1973).
- (7) D. F. Kyser and K. Murata, in Ref. 3, p.205.
- (8) T. Kato, T. Yahara, H. Nakata, K. Murata and K. Nagami, appears in J. Vac. Sci. Tech., Jan-Feb issue in 1978.
- (9) M. Parikh, Ref (8).
- (10) T. H. P. Chang, J. Vac. Sci. Tech., 12, 1305 (1975).
- (11) D. F. Kyser and N. S. Viswanathan, in Ref. 10, p.1305.
- (12) N. S. Viswanathan, R. Pyle and D. F. Kyser, Proc. 7th Int. Conf. on Electron and Ion Beam Science and Technology (Electrochem. Soc., Princeton, N.J., 1976), p.218.
- (13) J. S. Greeneich, J. Appl. Phys., 45, 5264 (1974).
- (14) J. S. Greeneich and T. Van Duzer, J. Vac. Sci. Tech., 10, 1056 (1973).
- (15) L. V. Spencer and V. Fano, Phys. Rev., 93, 1172 (1974).

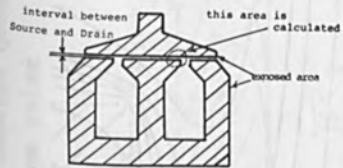


Fig. 1 Source/Drain pattern for FET.

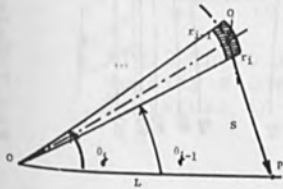


Fig. 3 Geometry on the resist surface to convolve the Gaussian distribution.

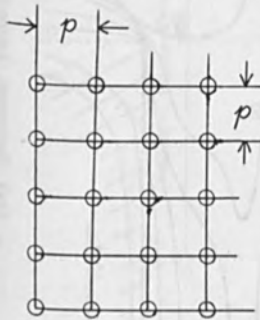


Fig. 4 Superposition of the Gaussian electron probe.

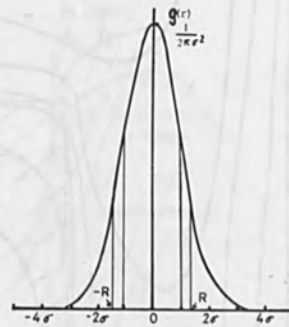


Fig. 2 Gaussian-distributed electron probe, eq. (4).

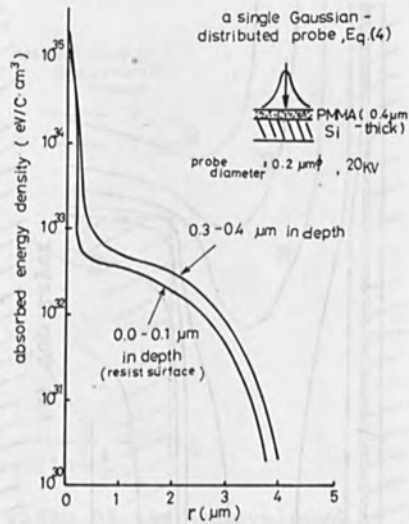


Fig. 5 Radial distribution of the absorbed energy density.

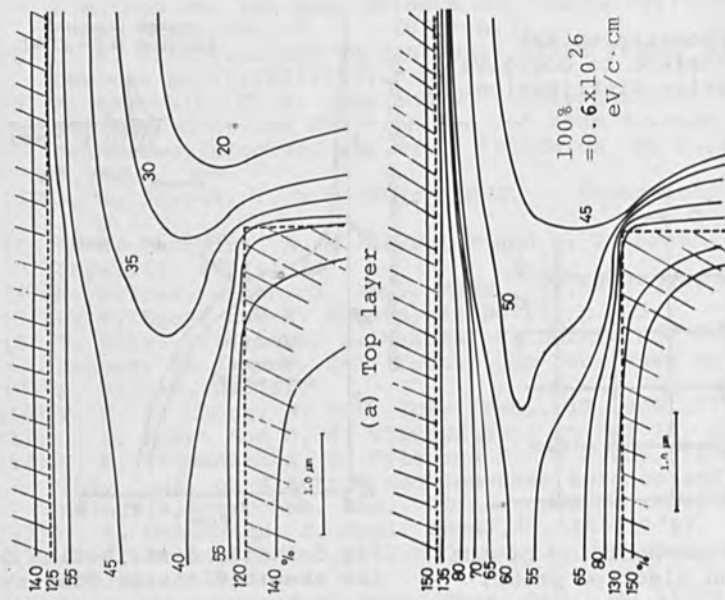


Fig. 6 Calculated equi-energy density contours for an interval of $2\mu\text{m}$

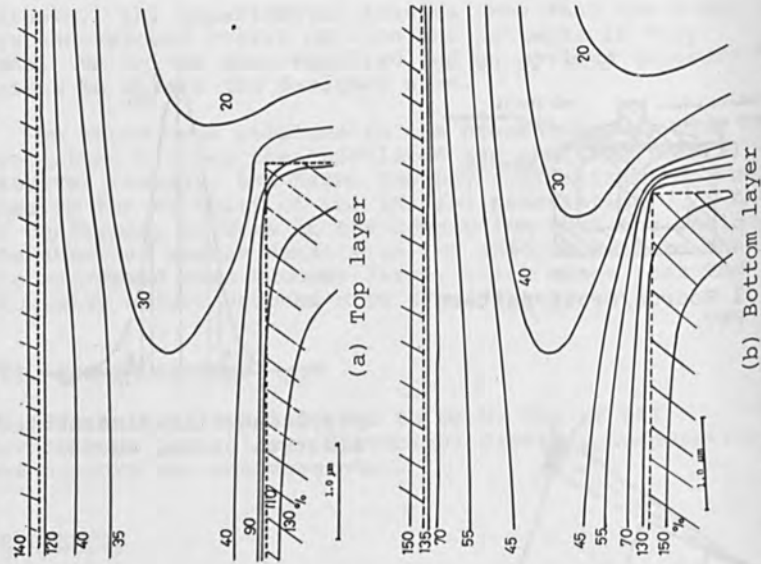


Fig. 7 Calculated equi-energy density contours for an interval of $2.5\mu\text{m}$

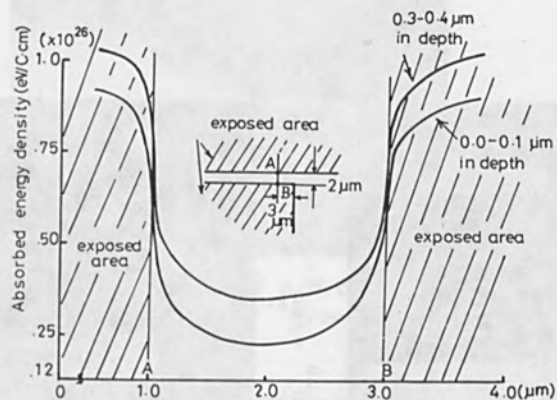


Fig.8 The variation of the absorbed energy density along the A-B line shown in the miniature in the figure.

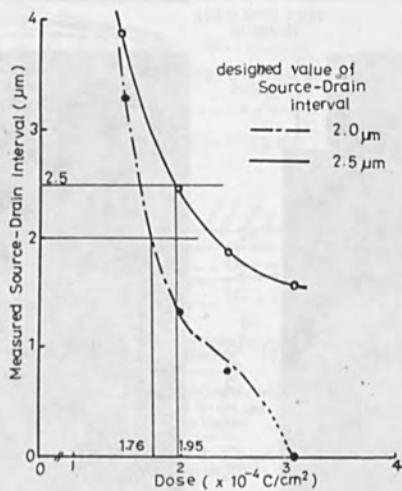
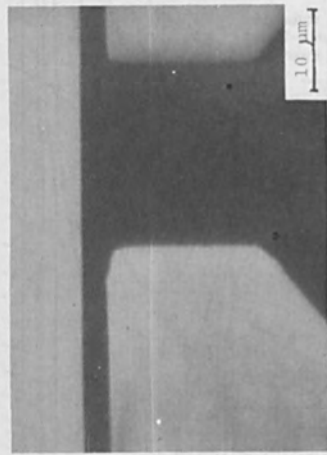
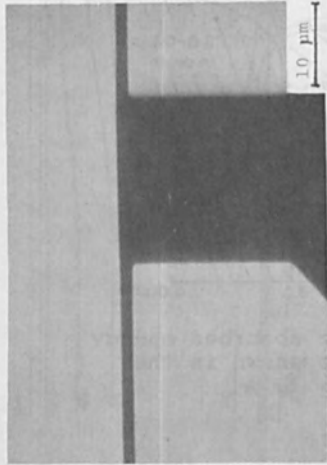


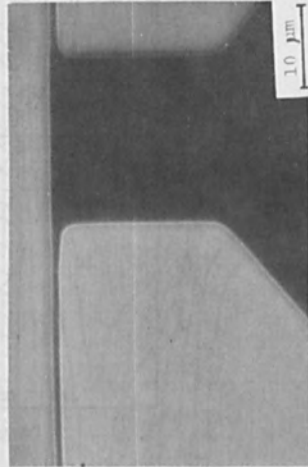
Fig.10 The observed width of the undeveloped resist band between source and drain patterns as a function of dose.



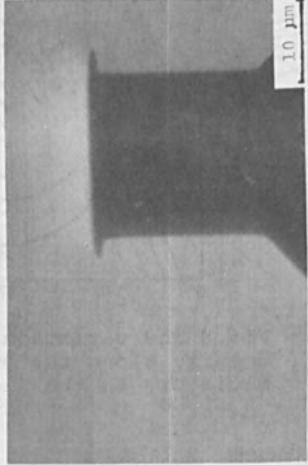
(1) 1.5×10^{-4} c/cm²



(2) 2.0×10^{-4} c/cm²

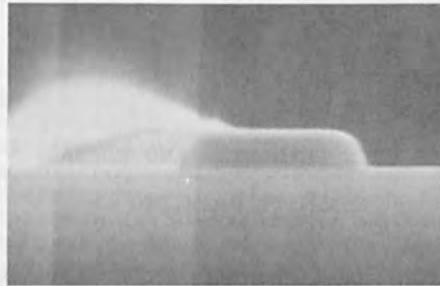


(3) 2.4×10^{-4} c/cm²



(4) 3.0×10^{-4} c/cm²

Fig.9 SEM micrographs of the developed source/drain patterns at various doses



Thickness of
PMMA=4000A

Fig.11 SEM micrograph of a cross sectional Profile
at a dose of $2 \times 10^{-4} \text{C/cm}^2$.

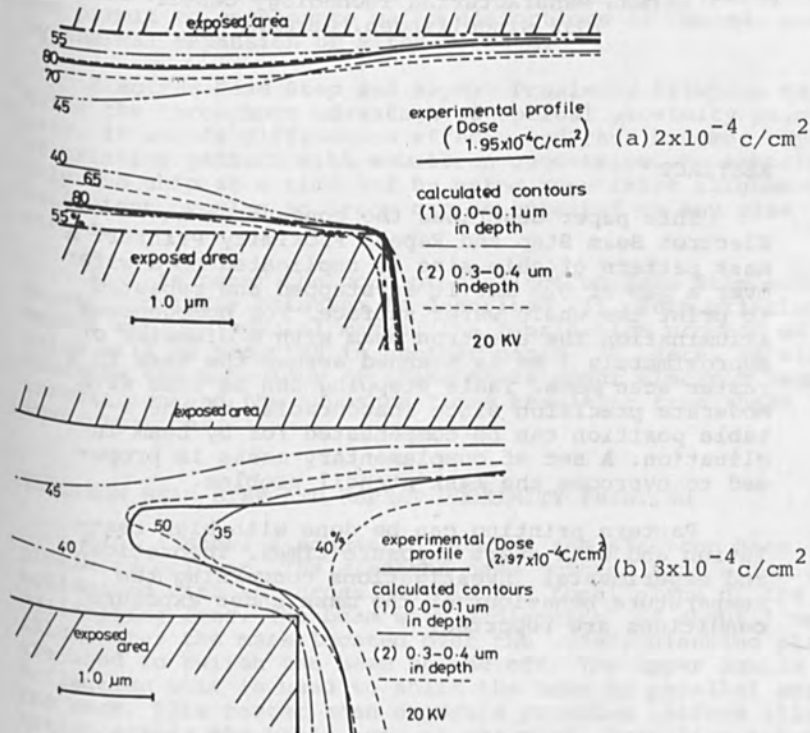


Fig.12 Comparison between the calculated contours
and experimental profiles at two different doses.

ELECTRON BEAM STEP AND REPEAT

PROXIMITY PRINTING

H. Bohlen, J. Greschner, W. Kulcke, and
P. Nehmiz

IBM Deutschland
German Manufacturing Technology Center
7032 Sindelfingen, Germany

ABSTRACT

This paper describes the concept of an Electron Beam Step and Repeat Proximity Printer. A mask pattern of chip size is replicated to a wafer over a gap of 0.5 mm. It is stepped and repeated to print the whole wafer surface. For homogeneous illumination the electron beam with a diameter of approximately 1 mm is scanned across the mask in a raster scan mode. Table stepping can be done with moderate precision since inaccuracies of the x-y table position can be compensated for by beam inclination. A set of complementary masks is proposed to overcome the mask stencil problem.

Pattern printing can be done with high resolution and with short exposure times. Theoretical and experimental investigations concerning the temperature behaviour of the mask under exposure conditions are reported.

INTRODUCTION

Optical proximity (or off-contact) printing is a widely employed photolithographic exposure technique for high throughput fabrication of IC's. Without the need for imaging optics the pattern is shadow projected to the wafer. During exposure the mask is kept in about 20 μm distance from the wafer so that damages of mask and wafer are avoided. The main drawback of this method is diffraction of the light at the mask structures, limiting the pattern resolution to about 3 μm . Another problem arises if pattern overlay to better than 1 μm is required. Exposure of the whole wafer field at a time, as used in optical proximity printing, does not permit to compensate wafer distortions as caused, e.g., by thermal expansion or wafer warpage.

Electron Beam Step and Repeat Proximity Printing maintains the throughput advantage of optical proximity printing, it avoids diffraction effects and thus becomes capable of printing pattern with submicron geometries. By exposing only one chip at a time and by using repetitive alignment sufficient overlay accuracy can be expected on any size wafers.

In this paper the concept of Electron Beam Step and Repeat Proximity Printing is described (1). This printing method employs special masks, the fabrication process of which will be reported in another paper (2). Here, we will describe the behaviour of these masks under electron beam irradiation and the exposure times resulting from these investigations.

ELECTRON BEAM STEP AND REPEAT PROXIMITY PRINTING

Fig. 1 shows a schematic view of the electron beam proximity printer. The electron beam emitted from a gun is collimated with the cross over in the focal plane of the collimating lens. The beam with a diameter of about 1 mm illuminates the mask located over the wafer. Blanking plates are used to switch the beam on and off. The upper double deflection unit is used to shift the beam in parallel across the mask. This raster scan exposure provides uniform illumination across the whole area of the mask. Scan line inhomogeneities of the illumination are avoided by an appropriate overlapping of the scans. The beam itself is properly shaped by the beam forming aperture in the collimating lens.

A second set of deflection coils, the fine correction coils, permits a beam inclination, with the pivot point in the mask plane. As a result of this beam inclination the shadow image of the mask pattern can be slightly shifted on the wafer. This fine shift is limited to a few microns and relieves the requirements on the positioning accuracy of the high speed table. The position of the x-y table is measured by means of a laser interferometer.

The mask contains a repetitive part of the pattern to be printed to the wafer, e.g., the pattern of a chip. That means, the exposure takes place in the step and repeat mode. This mode of exposure with a chip sized mask can take into account in-plane wafer distortions originating from hot processes or thermal expansion of the wafer. Compensation of these distortions may become especially important with increasing wafer diameter. Also, masks of chip size can be fabricated and inspected easier than masks of full wafer size.

Since diffraction effects are negligible when using electron beams, the mask can be arranged in a large distance over the wafer. The mask/wafer gap, however, determines the tolerable beam divergence through the tolerable penumbra of pattern edges (see fig. 2). For a penumbra of $0.1 \mu\text{m}$ and a mask/wafer gap of $500 \mu\text{m}$ the tolerable beam divergence is 10^{-4} radians.

COMPLEMENTARY MASKS, A SOLUTION OF THE MASK STENCIL PROBLEM

Since electrons interact very strongly with matter and would be scattered even in a very thin foil, the mask for an electron beam proximity printer must be self-supporting. The transparent areas of the mask must be physical holes.

With self-supporting masks a special problem occurs: the so-called mask stencil problem. An area opaque for electrons and completely surrounded by an area transparent for electrons is not supported by the remaining mask material and would fall out.

Our solution of this problem is especially suited for 1x masks with micron structures and is explained in fig. 3. The chip pattern is splitted into small elements, mainly rectangles. The two complementary masks share these elements so that each of them contains nearly a half of the original pattern.

Printing chip pattern requires, therefore, the superposition of the two patterns of the complementary mask. This doubles the time required for the exposure of a chip. On the other hand, the complementary masks have a considerably higher mechanical stability. This is of special importance for certain possible patterns as, e.g., long parallel lines or even finger-shaped structures. It is another feature of the complementary mask approach that arbitrarily shaped patterns, e.g. diagonal lines with straight edges, can be printed.

Mask change during the exposure is avoided by arranging the two complementary masks side by side in one mask frame. If the distance of the two complementary masks is the same as the chip distance on the wafer, additional table movements are not required.

BEAM SCANNING VERSUS FLOOD EXPOSURE

The described printing concept uses a scanning beam, small in its diameter with respect to the mask dimensions. The main advantage is that a higher portion of the emitted beam can be used for mask illumination than in the case of a flood exposure. A constant current density across the beam is not necessary since the homogeneous illumination of the mask can be achieved by the scanning technique in combination with an appropriate beam profile.

Also, masks with different chip sizes can be replicated without changing the characteristics of the EB column. Only the scanning area has to be adjusted when the mask dimensions change.

IMAGE FIDELITY

Image fidelity of an exposure method is demonstrated by the transfer of very fine dimensions onto the wafer. The patterns in our masks are fabricated by optical contact printing. Therefore, the finest geometries in the masks are 1 μ m to 2 μ m wide. Submicron dimensions are obtained if, e.g., fine lines are not perfectly etched.

Such a submicron structure in a mask pattern and its image in the resist on a wafer is shown in fig. 4. The ex-

posure is done in an experimental setup of a proximity printer. Fig. 4a shows the TSEM picture of the mask, fig. 4b the SEM picture of the resist pattern. The magnification is 10 000 x. The resist on the wafer is 0.6 μm thick. The resist pattern demonstrates that structures in the submicron range are accurately printed.

MASK TEMPERATURE DURING EXPOSURE

So far investigations concentrated on the mask and on mask related problems. One characteristic of major interest is the maximum beam current tolerable for distortion free pattern replication. This beam current determines the exposure time and, consequently, is of importance for the throughput of an EB proximity printer.

The following experiments were performed in a simple experimental electron beam system.

The electrons of the beam are absorbed in the opaque areas of the mask. Their kinetic energy is transferred to the mask material and warms it up. The temperature of the mask was measured and, also, calculated while an exposure beam was scanned across it. The masks used in these investigations had no physical holes, i.e., unimpaired foils of equal composition and dimension as the real masks, but without patterns (2).

(a) Calculations

In vacuum environment only thermal conduction and radiation can dissipate the heat. Here, the radiation can be neglected since the temperature rise is low. The calculations show that radiation reduces the foil temperature merely by 2 K when the foil temperature is 60 K above room temperature. So, only conduction transports the heat from the thin foil into the outer thick mask section which together with the mask holder acts as a heat sink.

The dynamic behaviour of the foil temperature can be described by a series each term of which contains a so-called heat relaxation time. The longest relaxation time is the essential one since the shorter relaxation times reflect the fast temperature drop. Therefore, in the following,

"relaxation time" shall be understood as the longest heat relaxation time. This is approximately the time during which the temperature difference $\Delta T = T(\text{foil}) - T(\text{room})$ decreases to the value $1/e \cdot \Delta T$. $T(\text{foil})$ is the temperature of the foil at the moment the external heat source is switched off, and $T(\text{room})$ is the ambient temperature.

The relaxation time τ_{mn} depends on the dimensions a, b of the rectangular foil, the density ρ , the specific heat c , and the coefficient of thermal conductivity k of the foil material:

$$\tau_{mn} = \frac{\rho \cdot c}{k \cdot \pi^2 \cdot [(m/a)^2 + (n/b)^2]}$$

where m and n are integers.

For simplicity the calculations were done for an electron beam concentrated in a point on the mask. This gives nearly the same results as in the case the beam diameter is 1 mm. Furthermore, it is assumed that the beam is scanned line after line across the mask. 10 lines make up an entire mask scan, and the mask scans are repeated until the total exposure time is reached.

The calculations yield that the foil temperature is directly proportional to the absorbed electron power converted into heat and is inversely proportional to the foil thickness.

If the beam is scanned across the foil the foil temperature depends on the ratio of the heat relaxation time to the beam scanning time (see figs. 5b, 6b, and 7b): the faster the beam scans, the less oscillates the temperature of the foil center. At fast scanning the beam reappears before the temperature could decrease. The foil is a square with the side length of 5.5 mm. It consists of a 2.0 μm thick supporting silicon layer with a 0.5 μm gold layer deposited on it. The heat relaxation time of the foil is 22 msec. The absorbed beam power is 0.125 W. The times for one line scan and one frame are: in fig. 5b 20 msec and 200 msec, in fig. 6b 2 msec and 20 msec, in fig. 7b 0.2 msec and 2 msec, all respectively. The exposure was finished when the temperature reached its steady state.

Figs. 8 and 9 show the temperature profiles over the entire foil. In fig. 8 the line scan time is in the order

of the relaxation time. The beam scans so slowly across the foil that the "temperature hill" can follow the beam. In fig. 9 the line scan time is much shorter than the relaxation time. This fast scanning acts like a flood illumination, and the temperature distribution is symmetrical over the foil. This flood-like illumination results in the lowest temperature rise of the foil.

(b) Experiments

For measurement of the temperature in the foil center thin film thermocouples of gold - nickel were deposited. The thickness of the nickel layer was 0.25 μm , of the gold layer 0.5 or 1.0 μm . The rise time of the thermocouples was approximately 1 msec.

The measured thermoelectric voltages concur qualitatively well with the calculated temperatures (see figs. 5a, 6a, and 7a). The measured temperature rise is directly proportional to the acceleration voltage and to the absorbed beam current.

A quantitative comparison is done in fig. 10. This illustration shows how the maximum temperature in the foil center depends on the line scan time when the temperature has reached its steady state. The parameter in fig. 10 is the foil composition. The curves show the calculated, the dots and crosses the measured temperatures. The agreement of the calculated and measured values is good. The absorbed beam current is 10 μA , the acceleration voltage is 12.5 kV, the foil dimensions are 5.5 mm x 5.5 mm, and the total exposure time is 350 msec.

The mask temperature investigations can be summarized as follows: for an electron beam of 10 μA and 12.5 kV the temperature rise in the foil center is 20 K if the beam is scanned fast across the foil and if the foil consists of 2.0 μm silicon with 1.0 μm gold on top (see fig. 10). Since the temperature is proportional to the beam current the temperature in the foil center is 100 K with a beam of 50 μA and 12.5 kV.

CONCLUSION

An Electron Beam Step and Repeat Proximity Printer has been described. Using the resolution capabilities of electron beams the method permits printing of submicron geometries. Accurate image positioning on the wafer is achieved by beam inclination to compensate for table inaccuracies. The x-y table movement is controlled by a laser interferometer.

Electron beam proximity printing requires masks with physical holes for transmission of the electrons. The mask stencil problem is solved using two complementary masks. An appropriate beam scanning mode during exposure results in low temperature increase of the mask. Assuming a resist sensitivity of $1 \cdot 10^{-5}$ Coul/cm² and a mask area of 5 mm x 5 mm, a beam of 50 μ A and 12.5 kV yields an exposure time of 50 msec.

ACKNOWLEDGEMENTS

The authors wish to acknowledge the contribution of H. Engelke in calculating the mask temperature. They also would like to thank K. Asch and G. Kraus for their technical contributions in evaporating the thermocouples and in mounting the measuring equipment.

REFERENCES

- (1) B. Lischke, K. Anger, J. Frosien, A. Oelmann, and H. Schuster-Woldan
"Pattern fabrication with electron projection systems. Part 1: Pattern generation by 1:1 shadow printing", International conference on microlithography, Paris, June 21-24, 1977
- (2) H. Bohlen, J. Greschner, and P. Nehmiz
"Silicon supported electron beam proximity masks", this issue

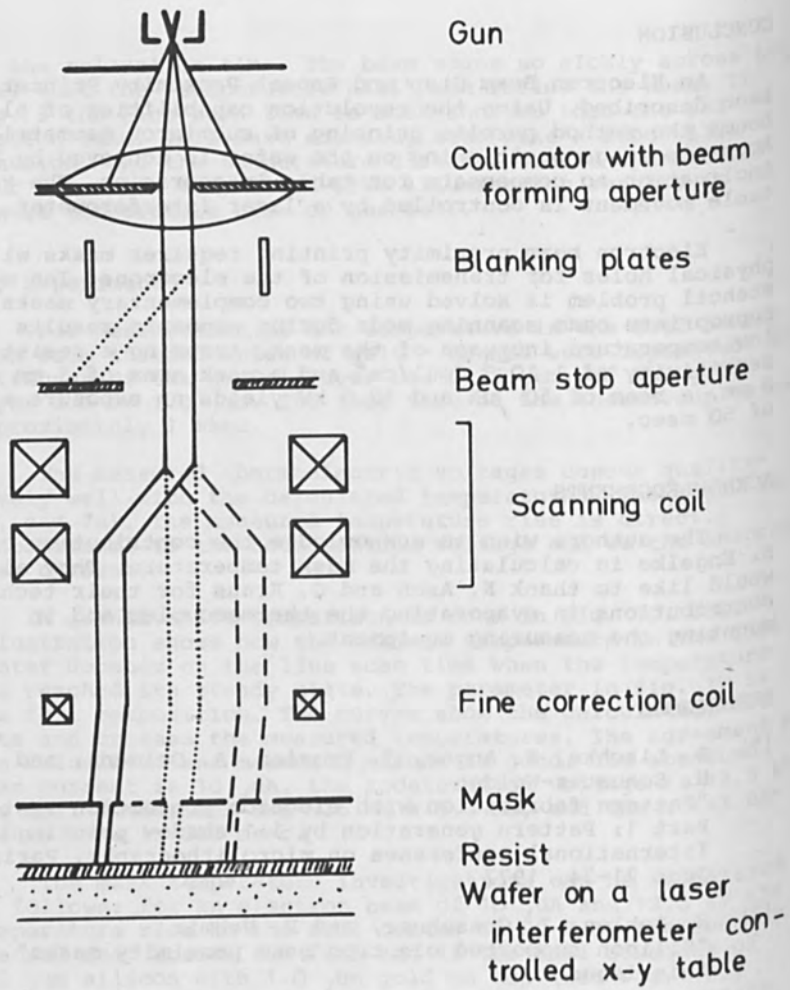


Fig. 1 Schematic view of the Electron Beam Step and Repeat Proximity Printer

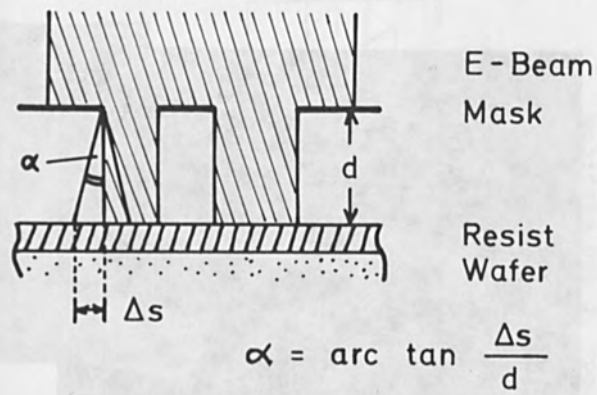


Fig. 2 The tolerable divergence of the collimated beam

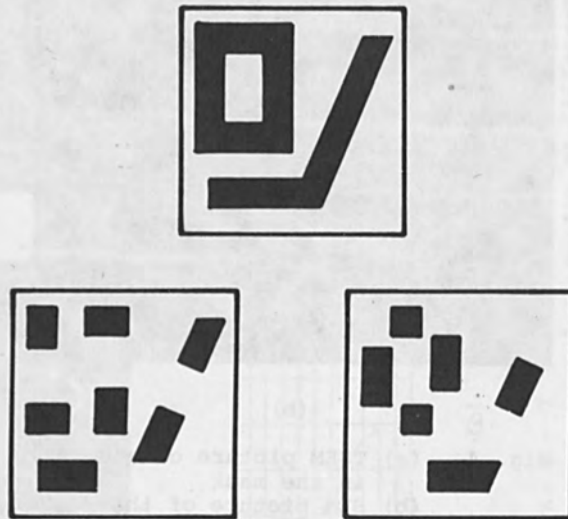
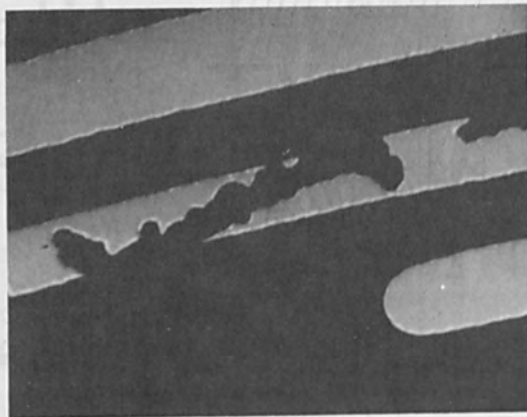
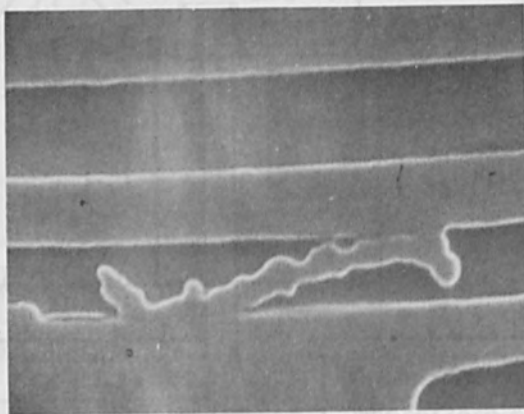


Fig. 3 The complementary mask

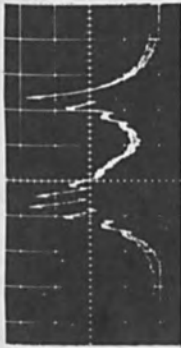


(a)



(b)

Fig. 4 (a) TSEM picture of a detail
in the mask
(b) SEM picture of this detail
shadow projected onto a
resist coated wafer
Magnification is 10 000 x.



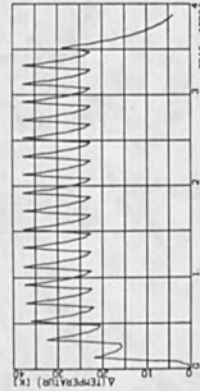
(a)



(b)



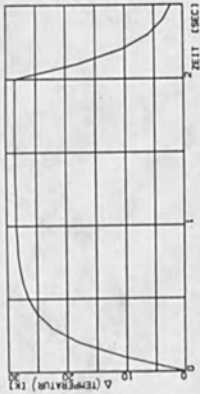
(a)



(b)



(a)



(b)

Figs. 5 - 7 The measured (a) and calculated (b) temperature in the foil center at different scanning speeds of the electron beam

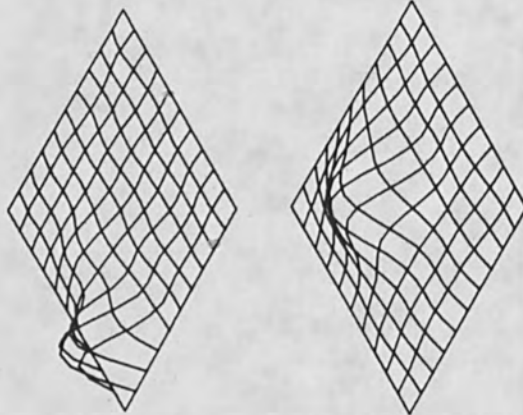


Fig. 8

The temperature distribution across the mask at two different moments for a slowly (fig. 8) and a fast (fig. 9) scanning electron beam

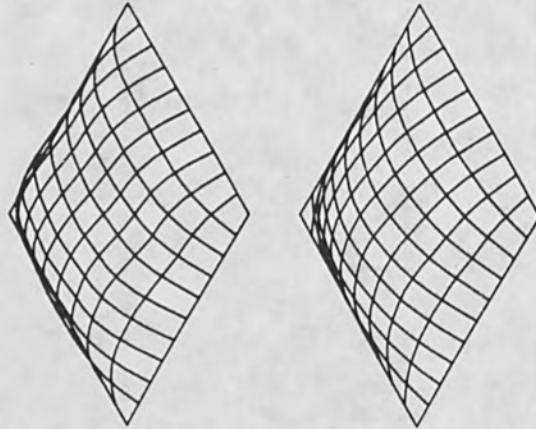


Fig. 9

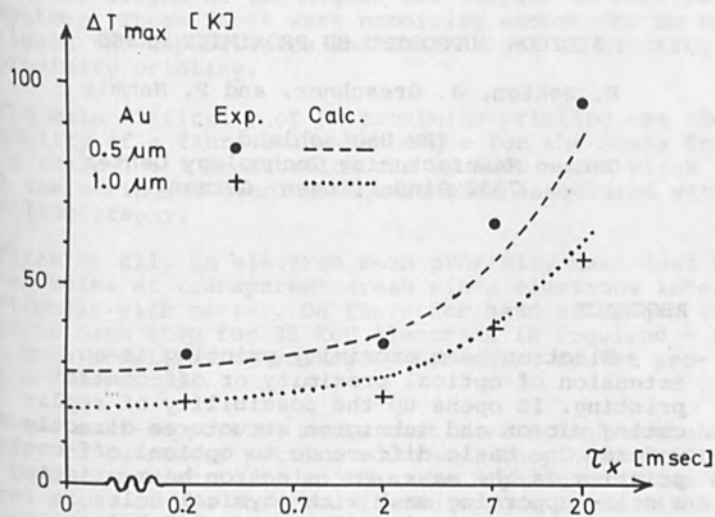


Fig. 10 The maximum temperature in the foil center as a function of the beam line scan time. The supporting silicon membrane is 2.0 μm thick. The experimental and calculated results are given for two different gold layers on the silicon.

SILICON SUPPORTED EB PROXIMITY MASKS

H. Bohlen, J. Greschner, and P. Nehmiz

IBM Deutschland
German Manufacturing Technology Center
7032 Sindelfingen, Germany

ABSTRACT

Electron beam proximity printing is an extension of optical proximity or off-contact printing. It opens up the possibility of replicating micron and submicron structures directly on wafers. One basic difference to optical off-contact printing is the mask. For electron beam printing a self-supporting mask with physical holes is required. This paper describes a mask fabrication process based on silicon thin film technology. The mask consists of a supporting silicon structure of a few microns thickness carrying a gold layer which shapes the illuminating beam at transparent areas and stops it at opaque areas. The mask in chip size contains finest structures of about 1 μm width. The technique is extendable to submicron lithography applications. The thermal properties of the mask permit the use of intense electron beams for short exposure times and yet avoid distortions in the printed patterns.

INTRODUCTION

Optical off-contact or proximity printing is a simple and inexpensive method for high throughput replication of mask patterns on wafers. Substituting the ultraviolet radiation by x-rays (1) or electron beams (2), (3) eliminates diffraction effects and extends the application range of proximity printing to micron or even submicron lithography.

X-ray printers suffer from the low power levels of the exposure source and thus require long exposure times. Electron beams can be much easier produced at high intensities.

Furthermore, alignment techniques are simpler in electron beam systems. These facts were promising enough for us to investigate the capabilities and limitations of electron beam proximity printing.

The main difficulty of EB proximity printing was the availability of a fabrication technique for the masks from which a scale 1 : 1 replication can be made - and which fulfil the stringent overlay requirements associated with micron lithography.

First of all, an electron beam proximity mask must have physical holes at transparent areas since electrons interact very strongly with matter. On the other hand at opaque areas a complete beam stop for 25 keV electrons is required - the common beam accelerating voltage - for which resist processes are developed.

These self-supporting masks must have a high mechanical stability to guarantee pattern accuracy. They need sufficient thermal conductivity so that the high intensities of electron beams can be absorbed in the opaque areas without causing excessive heating. For overlay reasons we restricted the mask dimensions to a chip size. This permits printing of patterns on any sized wafer in a step and repeat mode. Also a set of complementary masks can be arranged side by side on one substrate. Fortunately, mask fabrication and inspection difficulties are reduced when mask sizes are small. We started with a chip size of about $5 \times 5 \text{ mm}^2$, but there are no reasons which prevent the fabrication of larger masks.

MASK FABRICATION PROCESS

Our mask fabrication process is based on the silicon - thin - film technique. It is similar to the known x-ray mask process but incorporates additional process steps to produce the required holes. Fig. 1 shows schematically the fabrication steps. We start with a n-type (1, 0, 0)-oriented silicon wafer. The backside of the wafer is covered with a silicon-dioxide layer. Into the front side a layer of 10^{20} boron atoms/cm³ is doped. This layer later on defines the mask thickness. P-n junctions at 3.8 μm and 6.5 μm have been tried which lead to mask thicknesses of 2.1 μm and 3.5 μm , respectively. A window is then etched into the backside silicon-dioxide layer by means of conventional photolithography steps and HF wet etching. This window is round in shape with a diameter corresponding with the size of a chip pattern.

The front side of the wafer is then covered with the following layers:

- o 0.02 μm thick chromium layer for adhesion purpose
- o 0.3 μm thick gold layer and a
- o 1 μm thick photoresist layer

The desired chip pattern is exposed and developed into the resist. The resist pattern acts as a mask for an ion beam milling process. This step was performed with an argon ion beam of about 4 keV. To achieve a homogeneous etching over the whole pattern area, the beam was scanned by means of an electrostatic deflection unit. The ion beam etching transfers the pattern into the metal layers. The resist mask can then be removed in an oxygen stripper.

In a second etch step the now defined gold pattern serves as a mask for a reactive ion etching process (RIE). This process has a higher etch rate and more selectivity so that the pattern can be etched through the about 3 μm thick boron doped surface of the wafer. A diode configuration system with CF_4 was used for this process step, which, under appropriate conditions, does not affect the gold mask.

The bulk of the wafer is then thinned by a wet preferential etching process (4) driven through the window in the SiO_2 layer on the backside of the wafer. For this etching process an ethylene diamine-pyrocatechol-water mixture (5) (6) is used. It stops at a certain boron concentration in the range of $5 \cdot 10^{19}$ atoms/cm³. The resulting mask consists of a gold-chromium-silicon sandwich structure of about 3 μm thickness surrounded by the thick wafer. The metal layers have the task to shape the illuminating electron beam during exposure. The silicon foil acts as a supporting structure. When electron beams of 25 keV are used, the gold layer has to be strengthened to about 0.8 μm for a complete beam stop at opaque areas. This is achieved by evaporating gold onto the finished mask.

It has been shown that the sequence of the last process steps can be changed: Strengthening of the gold layer before wet etching as well as wet etching before RIE is possible.

EXPERIMENTAL RESULTS

A finished mask fabricated in the described manner is shown in fig. 2. The 400 μm thick silicon frame is shown on the left. On the right part of the SEM-picture is the thinned 2 μm thick silicon foil with a grid structure. The thinned area is about 6 x 6 mm^2 in size. In this case the grid constant is 50 μm with bars of about 10 μm width.

The following figures show mask details of various patterns. All patterns were exposed on the mask substrate using an optical contact printer. Smallest line widths of about 1 μm were achieved.

The mechanical stability of the masks is demonstrated in fig. 3. It shows silicon supported fingers of about 5 μm width and 40 μm length. Even such fingers remain flat in the mask plane. In real applications such complicated structures would never occur. Applying the complementary mask principle (2) such structures are composed of rectangles or similar structures in the two masks of the complementary set.

A micrograph of the silicon side shows that the RIE process resulted in an underetch of the supporting silicon structure, whereas the gold pattern remains unaffected in its dimensions (fig. 4). Latest results showed that this underetch can be avoided by modifying the process parameters. A certain underetch has the advantage that the illuminating electron beam is only shaped by the well defined gold pattern. But in the case of very closely spaced lines this underetch may result in a partially unsupported gold pattern as shown in fig. 5. A cross-section of this part of the mask is shown schematically in fig. 6. Our experiments indicate that even these unsupported gold bars are stable. The flatness of the finished masks was measured by an optical interference method. Areas with small rectangles remain flat within 0.5 μm . At relatively large holes and corners or long fingers a small bending between 1 to 3 μm has been observed. But this is far below the acceptable value which would lead to pattern distortions.

MASK BEHAVIOUR DURING EXPOSURE

A short exposure time is a prerequisite for high throughput, the goal of all exposure systems. To optimize the exposure time we investigated the electron beam doses which can be used for mask pattern replication without introducing distortions.

The electron beam is absorbed in the opaque areas of the mask and heats it up (2). The relatively thick mask frame serves as a heat sink and shows no remarkable temperature increase or thermal expansion.

As a result of mask heating a bending of the foil is expected which takes up the thermal expansion. In a first approximation this mask bending will not lead to a pattern distortion as long as the illuminating beam penetrates the mask in a normal direction. But when the beam is tilted, as proposed in our printing concept, for compensating table inaccuracies (2), this beam tilt introduces a shift Δx of the image of a point P when the mask is bent. The relation between shift Δx and mask bending t is

$$x = t \cdot \tan \alpha$$

where α is the beam inclination. In our concept (2) beam inclination is employed for compensation of positional inaccuracies of the table. The desired shift x is given by:

$$x = d \cdot \tan \alpha$$

where d is the distance between mask and wafer. Elimination of $\tan \alpha$ gives

$$t = d \cdot \frac{\Delta x}{x}$$

the relation for maximum mask bending, when Δx is the permissible pattern inaccuracy and x the possible table positional correction. If Δx should not exceed $0.1 \mu\text{m}$ at a mask wafer gap of 0.5 mm and the required table correction is $1 \mu\text{m}$, the bending height is then limited to $50 \mu\text{m}$.

The temperature increase as a function of beam current and beam energy has been reported in (2). We also investigated the amount of bending as a result of the foil temperature. This effect was studied in an experimental set-up, where the inner part of the foil was heated by an optical light source and the bending height measured in a microscope.

The result is shown in fig 8. It is remarkable that the foil remains flat up to 120 °C above room temperature. Only at higher temperatures the expected bending occurs.

The retarded bending is explained as an effect of the internal stress of the foil due to the high boron concentration. The small boron atom does not perfectly fit into the silicon lattice and thus causes the strain. This effect has been reported elsewhere (7) (8).

To compensate the internal stress by thermal expansion a mean temperature increase of about 80 °C is required. The temperature in the middle of the foil - as measured by the thermocouple (2) - is then 120 °C. The experiments for fig. 8 were performed on foils without hole patterns.

The results of the two measurements - temperature increase as a function of beam power and foil bending versus temperature increase - indicate that beam currents of more than 50 µA can be used for exposure before pattern distortion takes place at maximum beam inclination.

² For a 25 keV beam and a resist sensitivity of 10⁵ coul/cm² this would result in an exposure time of 50 msec of a 5 x 5 mm² area. Twice this time is required if complementary masks are used.

SUMMARY

The investigations reported in this paper are related to electron proximity printing, specifically to the mask fabrication process and the mask behaviour at exposure conditions. It has been shown that masks in chip size with pattern dimensions of 1 µm and smaller can be made using process steps such as ion milling, reactive ion etching and preferential wet etching. The masks are mechanically stable. Distortion free exposure can be expected at beam currents up to 50 µA. The resulting short exposure time of 50 msec per chip field fits into our EB step and repeat proximity printing concept which was reported in the previous paper.

ACKNOWLEDGEMENTS

The authors are indebted to acknowledge the contributions of members from the IBM German Manufacturing Technology Center, Sindelfingen, Development Laboratories Boeblingen, and the Plant in Sindelfingen. Particularly we thank K. Asch, H. Engelke, A. Frosch, G. Kraus, W. Recktenwald, D. Seybold, and H.-J. Trumpp.

REFERENCES

- (1) D. L. Spears and H. I. Smith, *Electronics Letters* 8, 102 (1972)
- (2) H. Bohlen et al, EB Proximity S & R Proximity Printing, this issue
- (3) B. Lischke et al, Intern. Conference on Microlith., 163, Paris (1977)
- (4) R. M. Finne and D. L. Klein, *J. Electrochem. Soc.* 114, 965 (1967)
- (5) A. Bogh, *J. Electrochem. Soc.* 118, 401 (1971)
- (6) H. I. Smith et al, *J. Vac. Sci. Technol.* Vol.10, 913 (1973)
- (7) J. R. Carruthers et al, *J. Appl. Phys.* 34, 3389 (1963)
- (8) J. H. McCoy and P. A. Sullivan, 6. Intern. Conference on Electron and Ion Beam Techn. 3, (1974)

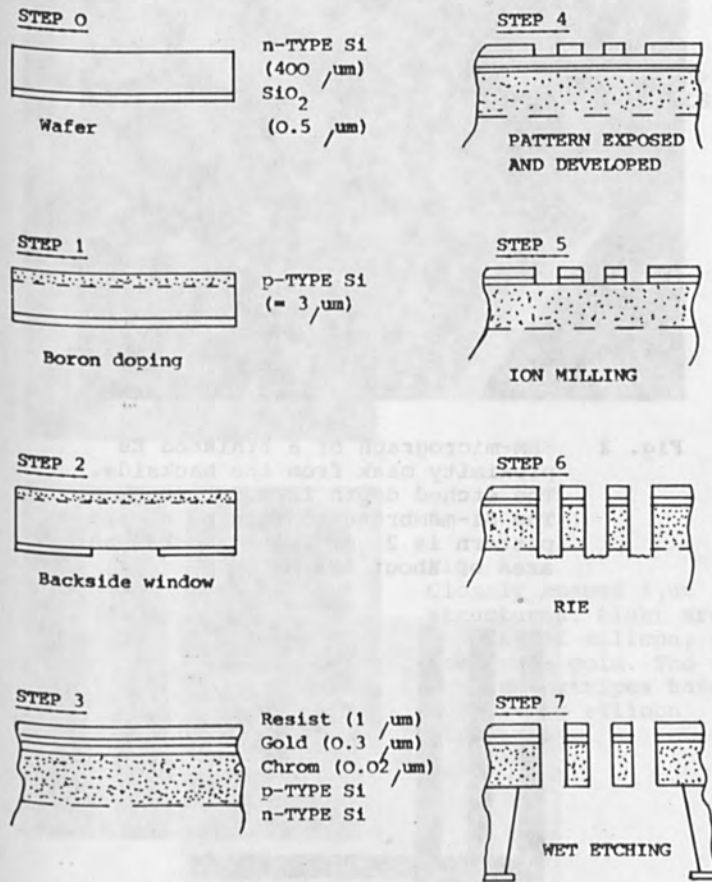


Fig. 1 Mask fabrication scheme

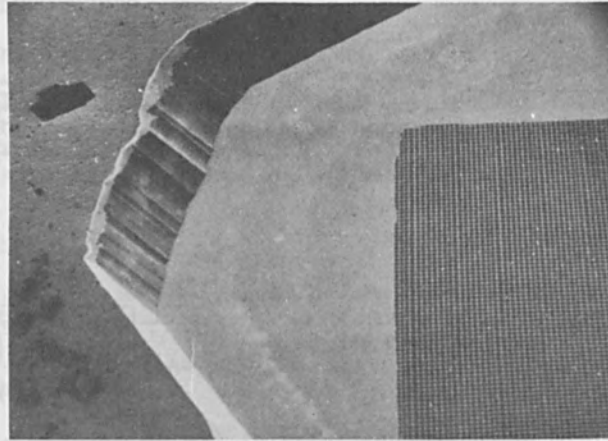


Fig. 2 SEM-micrograph of a finished EB proximity mask from the backside. The etched depth is about $400\ \mu\text{m}$. The Si-membrane containing a grid pattern is $2\ \mu\text{m}$ thick and has an area of about $6 \times 6\ \text{mm}^2$.

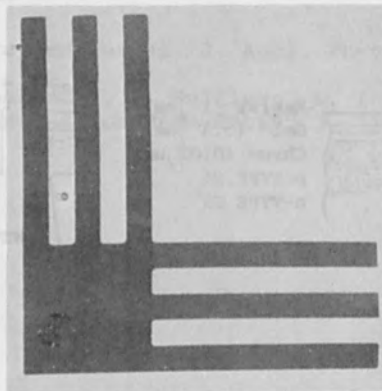


Fig. 3 Mask detail from the gold side

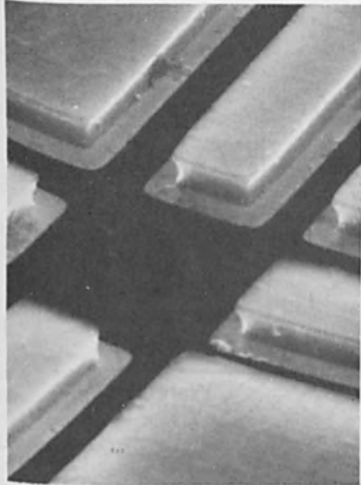


Fig. 4
Mask detail from the silicon side showing RIE underetch

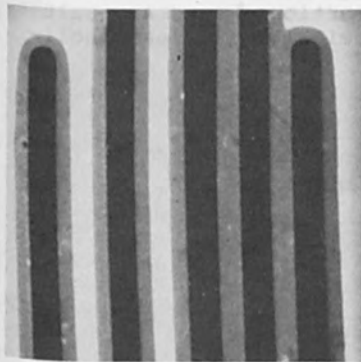


Fig. 5
Closely spaced 1 μ m structures. Light areas consist of silicon, grey areas are gold. The two smallest stripes have no supporting silicon structures.

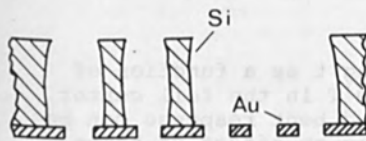


Fig. 6
Schematic cross-section of the mask in fig. 5

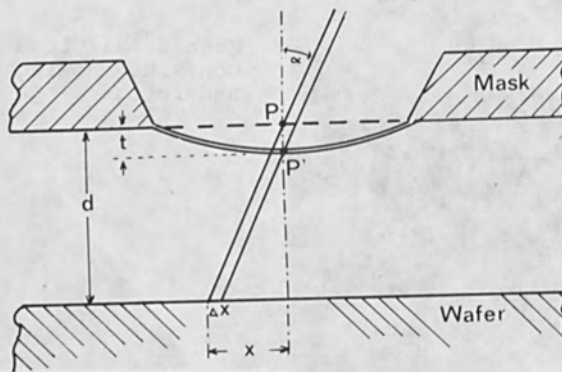


Fig. 7 Pattern distortion Δx as a result of bending height t and beam inclination α .

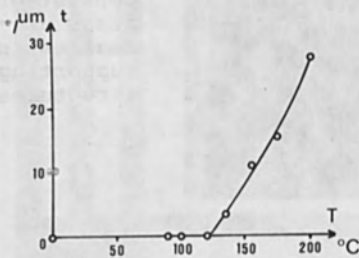


Fig. 8 Mask bending t as a function of temperature T in the foil center. The retarded bent response can be explained as an effect of boron doping.

Faint, illegible text at the top of the page, possibly bleed-through from the reverse side.

Faint, illegible text in the upper middle section of the page.

X-RAY LITHOGRAPHY

Faint, illegible text surrounding the section header.

Section 5

Main body of faint, illegible text in the lower middle section of the page.

HIGH SPEED X-RAY LITHOGRAPHY WITH RADIATION FROM
LASER-PRODUCED PLASMAS

M. C. Peckerar, J. R. Greig, D. J. Nagel
R. E. Pechacek, R. R. Whitlock

Westinghouse Electric Corp. Baltimore, MD 21203
U. S. Naval Research Laboratory, Washington, D.C. 20375

I. INTRODUCTION

X-ray lithography offers the possibility of replication of micron-scale features without the diffraction and multiple reflection effects associated with UV radiation or the scattering effects present in electron-beam exposures. Until recently, electron-impact and synchrotron-radiation sources were the only serious contenders for x-ray lithography exposures. However, a wide variety of pulsed x-ray sources are available.² It was shown recently that short pulses of x-rays from laser-heated, million-degree plasmas could expose an x-ray resist with negligible reciprocity loss and substrate radiation damage.³ That development required attention to both optimization of x-ray intensity from laser plasmas and problems associated with use of the laser plasma source for x-ray lithography. Maximization of x-ray intensity, which depends on laser pulse characteristics (wavelength, pulse-width and energy), focusing conditions, target composition and geometry, was reviewed in a recent paper.⁴ The purpose of this paper is to review the difficulties which may arise in routine use of laser-plasmas for replication and to present methods of overcoming these difficulties. Premature laser-target interaction, debris from the target, mask heating and resist sensitivity are treated in successive sections after the highlights of recent pulsed x-ray lithography measurements are reviewed.

II. SUMMARY OF EARLIER EXPERIMENTS

A Nd:glass laser with a 40ns pulse was used (see Figure 1). The total laser light output possible with the system employed is 100 Joules. However, laser target interaction (to be discussed below) limits the actual power which could be placed on target to 1/3 this value. The laser light incident on target heats the target material (in this case aluminum) to about three million degrees Kelvin. A plasma of free electrons and ions is produced. X-rays are emitted as a result of collisions between different charge species in this hot plasma. The x-ray spectrum contains both line and broad-band continuum. For the aluminum target case, about 90% of the x-ray energy is in an aluminum K-line at 1.6keV. The broad band continuum occurs mostly in the subkilovolt region and is easily filtered with a 25 μ m beryllium foil. The region of intense x-ray emission (as determined by pin-hole pictures) appears to be a circle of about 0.4mm when viewed face-on to the target. The emission region extends 0.6 mm in a direction normal to the surface. The plasma x-rays are emitted in a pulse with a FWHM of 15nsec.

With 30 Joules of laser light incident on target, we have been able to completely expose polybutene-1-sulfone (PBS) behind 25 μ m Be in 60 laser

shots. A relief image (recorded in PBS) of a gold pattern on 25 μ m beryllium is shown as Figure 2. The mask was 5 mils from the wafer and the mask-to-source distance was 5cm. Penumbral blurring due to the asymmetric source spot is evident and will be discussed in the next section. C-V dot radiation monitors run during a resist exposure show little radiation effect (see Figure 3). This is probably due to the absence of high energy continuum. The amount of x-ray energy incident on the mask was determined with a PIN detector placed in the target chamber. Five J/cm³ were needed to obtain exposure of PBS. This compares favorably with the fourteen J/cm³ published value⁵ and indicates no reciprocity loss.

With the present laser system, a fairly long time is required to produce 60 pulses. Five minute rod cooling times are needed between shots. But, by reducing the pulse length to the range between 5 and 10ns, conversion efficiencies of laser light to x-ray energy which are greater than 10% are possible (compared to the 0.3% efficiency of the present system). It should be possible to expose PBS with a single shot if the laser, focusing and target parameters are chosen properly.⁴

III. SOME PROBLEMS WITH LASER-PLASMA X-RAY LITHOGRAPHY

A. Laser-Target Interactions

High-power lasers generally consist of an oscillator in which a pulse is produced, commonly by Q-switching.⁶ The pulse is then sent through one or more amplifiers before being focused on to the target. In normal operation, the oscillator, amplifier(s) and target do not communicate with each other save for single pulse generation, amplification and use. The cause, effects and cures of unwanted interactions between laser components and the target are described in this section.

In the demonstration experiments described above, the target was an aluminum rectangular slab. The slab was tilted so that specular reflection could not send radiation back to the laser. But a "rough" aluminum surface can be a good diffuse reflector. Then as much as 5% of any radiation coming from the laser can be reflected back to it by the aluminum target. If this happens, the laser can be considered as consisting of three interacting cavities - Figure 4. The oscillator cavity contains the reflecting prism, the oscillator rod, a set of polarising plates, a Pockels cell (1) and the sapphire output mirror. What we call the external cavity contains the other side of the sapphire output mirror, a second Pockels cell (2), a set of polarising plates, the two amplifier rods, the focusing lens, and the aluminum target. The third cavity is the combination of these two cavities. While the laser rods are being pumped, the Pockels cells are stressed (electrically) so that they act as $\frac{1}{2}\lambda$ plates. Thus both cavities are prevented from lasing. However, as the population inversion rises, the small signal gain in the amplifier rods (length 82cm) becomes so large that even a few percent reflection from the target is sufficient to over-ride the Pockels cell - polarizing stack combination (rejection ratio $\sim 10^3:1$) and produce net gain in the combined cavities. Such interaction can cause weak "normal mode" pre-lasing to occur as much as 50 μ sec before the desired giant pulse output. The subsequent giant pulse is very small and the x-ray yield negligible. With somewhat less reflection from the target ($\sim 1\%$) such pre-lasing does not occur. But once the

Pockels cells are opened (presently almost simultaneously) the three different cavities all begin to avalanche. Under normal operating conditions and with no reflections from the target, the oscillator cavity takes ~150ns to produce its output pulse. During this time, and because of the large gain in the amplifier rods, pulses also grow both in the external cavity and in the combined cavity. The growth is due to the fact that the single pulse transit time of the combined cavity is ~65ns (i.e., the distance from the retro-prism in the oscillator cavity to the target is ~65 feet). The resultant output pulse from the oscillator is a combination of two or even three pulses coming from the different cavities, which, although amplified non-linearly in the amplifiers (the first peak sees greatest gain), still results in a broadened output pulse with a slower rise and greatly reduced x-ray yield. In both cases the total energy in the laser output pulse remains about the same as in the normal Q-switched output but the power density achieved at the target and the x-ray yield are much lower.

Typical laser output pulses for a normal laser output pulse are shown in Figure 5A and those from a pulse showing small laser-target interaction are shown in Figure 5B. A reduction of about 50% in the laser output is seen to eliminate almost all of the x-ray output (as measured with a PIN diode).

Laser-Target interaction can be controlled by a combination of techniques

- i) If the laser is placed far enough from the target (~200 feet) small interactions cannot affect the laser output.
- ii) Simply delaying the opening of Pockels cell in the external cavity reduces the interaction of the cavities but is not very effective.
- iii) Using optically polished targets eliminates diffuse reflections.
- iv) Using anodized; sand-blasted, aluminum targets removes both specular and diffuse reflections.
- v) Insertion of a Faraday rotator and polarizing plates between the target and the laser (Figure 4) eliminates laser-target interaction by rotating the plane of polarization of the radiation returning through the Faraday rotator so that it is reflected at the polarizing plates.

In our case, not having a Faraday rotator, and before realizing the importance of target surface treatment, laser-target interaction was controlled by limiting the laser energy incident on the target to ~1/3 the laser output energy. This was of course very wasteful but did allow us to demonstrate pulsed x-ray lithography. Now we have found that target surface treatment i.e., sand blasting and anodizing, maintains the characteristic aluminum x-ray emission but eliminates laser-target interaction. With higher powered lasers necessary for single pulse exposures, these surface treatments will probably have to be combined with a Faraday rotation system

B. DEBRIS EJECTED FROM THE TARGET

Target debris can be a serious problem, damaging delicate x-ray

masks if care is not taken. Only a small amount (~a few %) of the material removed from the target is ablated, as vapor, during the laser pulse. The rest leaves the target as liquid material much later as the million-degree plasma dissipates. For thick targets the liquid ejecta is confined to a cone about the normal to the target surface. The setup used to measure the direction of ejected liquid is shown in Figure 6. The distribution obtained with Al target in 10 shots is given in Figure 7. A well-defined cone with a half angle of 55° was found. The obvious way of minimizing debris damage is by keeping the mask away from the main stream of ejected liquid material. The amount of ejected liquid is minimized by the use of high melting point targets. We have also found that by using thin aluminum targets ($\sim 500\mu\text{m}$) the x-ray yield is maintained but most of the liquid debris from the target is ejected through the target, i.e. away from the substrate-mask assembly. This situation is illustrated in Figure 8 using a polyethylene sheet target 0.5mm thick. The small amount of material ablated from the target during the laser pulse, which is inevitably emitted on the mask side of the target, can then be kept from the mask by using a thin film of beryllium or a light plastic sheet in front of the mask. This combination of techniques will, we believe, eliminate the problem of target debris.

C. THERMAL RESPONSE OF MASKS

The heating of masks by x-ray energy absorption is potentially undesirable for long exposures with conventional sources. Heating can cause small dimensional changes and deformation. Thermal cycling may lead to separation of the absorbing material (Au) in a mask from the substrates. Such mask degradation may be serious for pulsed sources in which energy is deposited in a time short compared to thermal-conduction times.

A schematic of an Au-on-Be x-ray mask is given in Figure 9. The maximum deposition and temperature will occur at the surface of each material. The absorbed energy (J) per unit area (A) in a thin surface layer (δ) can be written:

$$\frac{J}{A} = \frac{E}{A} \{1 - \text{Exp}(-\mu\delta)\} \approx \frac{E}{A} \mu\delta \quad (a)$$

where E is the incident energy. From the equation which relates J to specific heat (C) and Temperature rise ΔT , we have $J = MC\Delta T = \rho A\delta\Delta TC$ (b)
 where M is the absorber mass and ρ its density.

Hence,

$$\Delta T = \frac{(E/A) (\mu/\rho)}{C} \quad (c)$$

where (μ/ρ) is the commonly-tabulated x-ray mass absorption coefficient.

To expose PBS, about $20\text{mJ}/\text{cm}^2$ of 1.5 keV radiation incident on the mask is required. Table I gives the numerical values of constants and results of using these values in equation (c). The Be temperature rise will be greater than the x-ray-induced value in Table I due to UV absorption, but this is not expected to be a problem.

Table I: Mask Heating by Pulsed Sources

	Be	Cr	Au
$\frac{\mu}{\rho}$ @ 1.5keV ($\frac{\text{cm}^2}{\text{gm}}$) (a)	181	2720	2300
Density	1.845	7.18	19.29
Transmission	0.43	0.96	0.05
E/A (mJ/cm^2)	20	8.6	8.3
C ($\text{J}/\text{gm deg}$) (b)	1.67	0.46	0.125
ΔT ($^{\circ}\text{C}$)	2.16	50.8	152.7
α (deg^{-1}) $\times 10^6$ (b)	12.3	6.8	14.3
$\Delta L/L = \alpha \Delta T$	2.66×10^{-5}	3.45×10^{-4}	2.18×10^{-3}

(a) W. J. Veigle in "Handbook of Spectroscopy," Vol. I, CRC Press Cleveland, Ohio 1974

(b) CRC Handbook of Chemistry and Physics, CRC Press, Cleveland, Ohio 1977.

The preferential heating of the absorbant Au is clear from the tabulated figures. The resulting expansion, over 6 times that of the Cr layer, could lead to separation at the Au-Cr interface. These calculations indicate the need for experiments to determine the response of x-ray masks to rapid and repeated thermal cycling. However, the heating effect is not strong enough to seriously degrade resolutions of fine line structures. At most, a two micron Au line will swell 50Å when heated the 153°C by the pulse.

D. SHORT PULSE EFFECTS IN THE RESIST

Finally, let us consider the response of the resist to pulsed x-rays. Two problems may arise in this area. First, we may see a change in sensitivity due to the rapid energy deposition (reciprocity failure). This was not true with pulses as short as 40ns. The development curve for the resist under pulsed conditions (see Figure 10) compares favorably with that obtained by steady state sources.⁵ For single shot exposures of PBS, however, 5ns-10ns pulses are required. Reciprocity must still be determined for these pulse lengths. Second, heating of the x-ray resist must be considered. From the above discussion, it was shown that heating is directly proportional to x-ray absorption coefficient (μ) in the film. A similar calculation to that performed above indicates (for PBS) a 5°C temperature rise is possible for single-shot 5ns exposures. This is negligible.

V. CONCLUSION

To conclude, the following potential problems in laser-pulsed x-ray lithography were discussed:

- a) Laser-target interaction
- b) Debris damage
- c) Mask Heating
- d) Short-pulse resist effects

All of these appear to be controllable. Unwanted laser-target interaction can be reduced by a combination of surface treatments and optical isolation. Debris damage can be essentially eliminated by the use of thin targets, proper mask placement and a thin debris shield. Mask heating will not cause resolution degradation and we have observed no reciprocity failure for 40ns pulses.

BIBLIOGRAPHY

1. Spiller, E., Feder, R. "Topics in Applied Physics," H. J. Queisser, ed., Springer-Verlag Berlin, 35 (1977).
2. Nagel, D. J., Dozier, C. M., in Proceedings of the 12th International Conference on High Speed Photography, SPIE, 97, 132 (1977).
3. Nagel, D. J., Peckerar, M. C., Greig, J. R., Pechacek, R. E., Whitlock, R. R. submitted to Appl. Phys. Letters
4. Nagel, D. J., Peckerar, M. C., Greig, J. R., Pechacek, R. E., Whitlock, R. R. to be published, SPIE Proceedings, 135 (1978)
5. Thompson, L. F., Feit, E. D., Bowden, M.J., Lenzo, P.V., Spenser, E. G., J. Electrochem. Soc. 121, 1500 (1974).
6. Lengyel, B.A., "Lasers", Second ed., Wiley-Interscience, New York, (1971).

Figure	Caption
1	Experimental Set-Up of the Laser Plasma X-Ray Exposure System.
2	Relief Image in PBS Showing $1.5\mu\text{m}$ Lines and $0.75\mu\text{m}$ Spaces Exposed with X-Rays From Laser Heated Plasmas.
3	C-V Plots Taken Before and After Exposure to Laser-Plasma Generated X-Rays. Negligible Flatband Shift is Evident.
4	Schematic of Laser Illustrating Various Laser "Cavities". The 25% Sapphire Mirror is Common to Both Cavities.
5	Oscilloscope traces showing laser diagnostics (the fluorescence diode measured the fluorescence radiation from the oscillator rod. The fast diode recorded the laser pulse from the oscillator rod and the visible diode measured the output laser pulse at the target chamber and the x-ray pulse width within the chamber was recorded in the PIN diode). Figure 5a shows normal operation.
5b	Shows reduced laser output and almost no x-ray intensity due to premature laser-target interaction.
6	Schematic of Debris Distribution Experiment.
7	Debris Distribution on the Glass Slide from a Thick Al Target.
8	Shadowgram of Debris Emission From 0.5mm Polyethylene. For Thin Films, the Debris is Shot Out to the Rear, Away From the Wafer, Without Affecting X-Ray Output.
9	Schematic of Au on Be Mask.
10	The Development of Curve for PBS. T_0 is the Post Development Thickness (3500\AA). I_0 is 5 joules/cm^3 .

Plasma
Lines
Rays
X-Ray
ent.
rious
e
e
n
n
se
st
de
e. Sm
ebris
he
t.

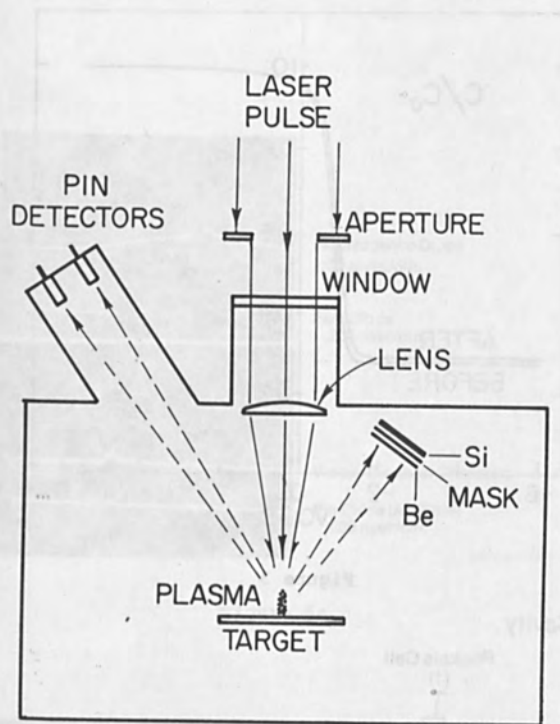


Figure 1

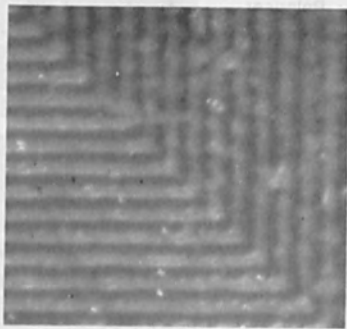


Figure 2

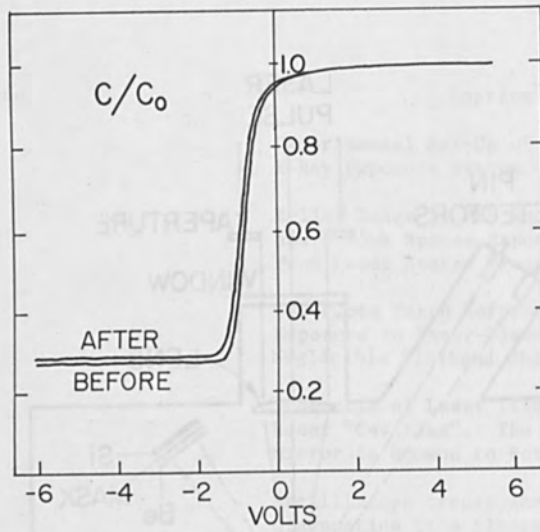
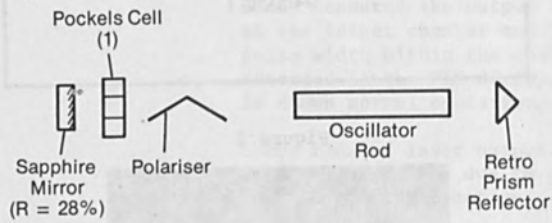


Figure 3

Oscillator Cavity



External Cavity

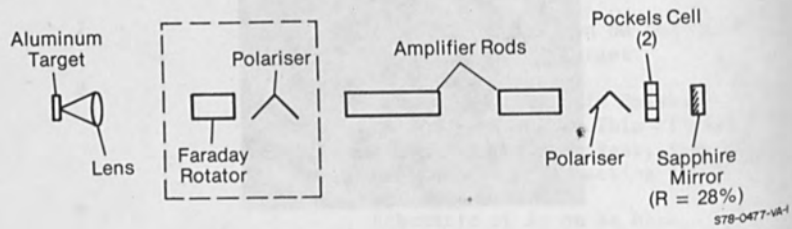


Figure 4

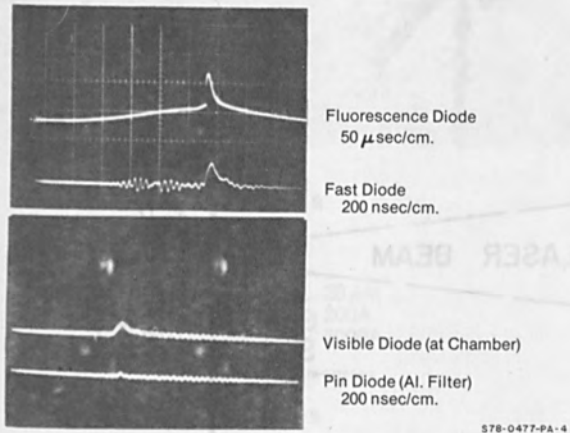


Figure 5a

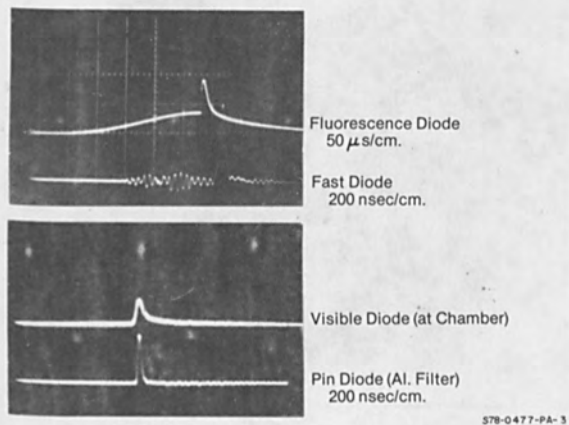


Figure 5b

DEBRIS DISTRIBUTION

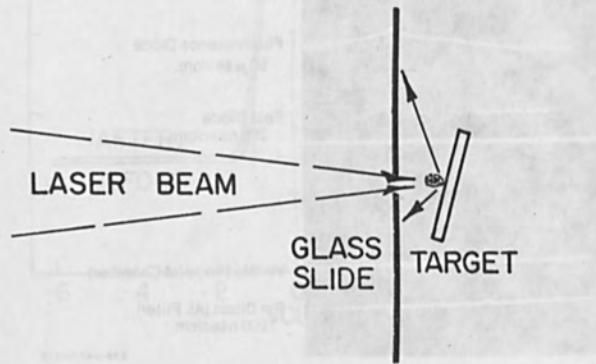


Figure 6

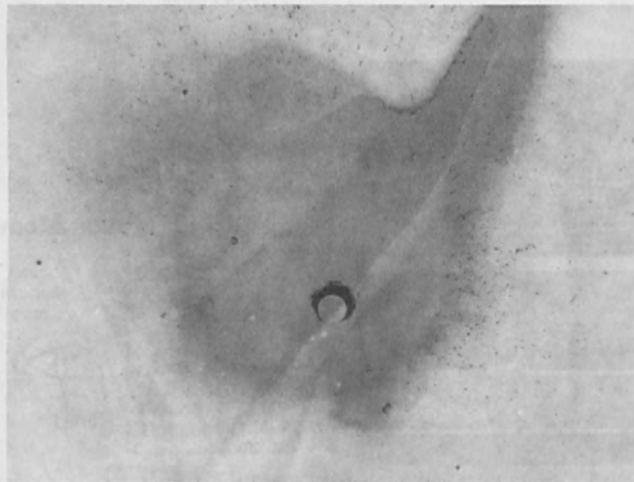


Figure 7

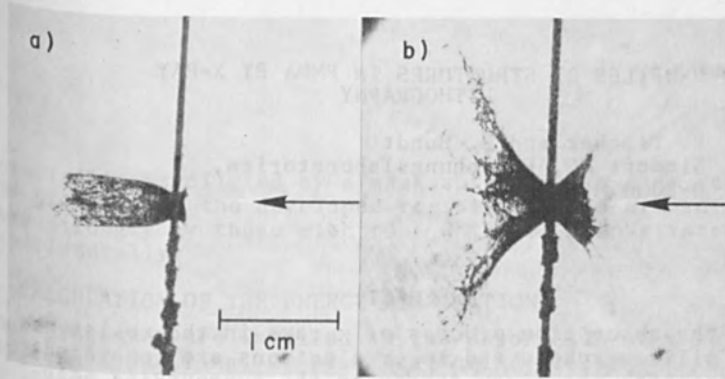


Figure 8

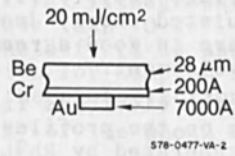


Figure 9

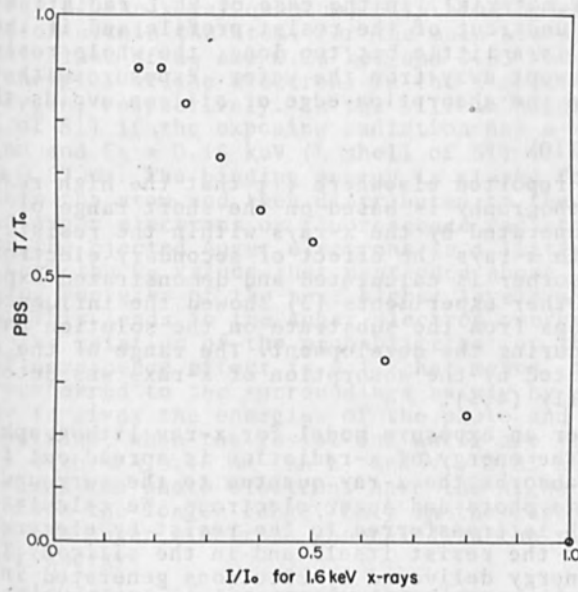


Figure 10

PROFILES OF STRUCTURES IN PMMA BY X-RAY
LITHOGRAPHY

P. Tischer and E. Hundt
Siemens AG, Forschungslaboratorien,
D-8000 München

ABSTRACT

During the absorption process of x-rays in the resist and in the silicon, photo and Auger electrons are generated, which transfer the x-ray energy to the surrounding molecules. From the x-ray absorption and the depth dose function of the electrons, the energy density in the resist is calculated near the interface resist/silicon for various mask contrasts. The calculated energy density curves for Rh L and Al K radiation are in good agreement with the resist profiles after development.

While for Al K radiation the electrons from the silicon have only minor influence on the profiles of the developed patterns, the electrons generated by Rh L in the silicon can give a high contribution to the energy density at the interface resist/silicon even in the areas which are behind the absorber material. In the case of Rh L radiation this leads to an undercut of the resist profile and if the development is a little bit too long, the whole resist pattern is swept away from the wafer. Exposure with a wavelength above the absorption edge of silicon avoids this effect.

1. INTRODUCTION

It has been reported elsewhere (1) that the high resolution of x-ray lithography is based on the short range of the electrons generated by the x-rays within the resist. For exposure with x-rays the effect of secondary electrons from the mask absorber is calculated and demonstrated experimentally (2). Other experiments (3) showed the influence of photoelectrons from the substrate on the solution rate of the resist during the development. The range of the electrons generated by the absorption of x-rays was determined experimentally (4,5).

In this paper an exposure model for x-ray lithography is presented. The energy of x-radiation is spread out from the atom which absorbs the x-ray quantum to the surrounding molecules via photo and Auger electrons. We calculated the energy which is transferred to the resist by electrons generated in the resist itself and in the silicon. The amount of energy delivered by electrons generated in the silicon can be very high even in the areas, where the

x-radiation is diluted by a mask absorber. In some cases the profiles of the developed resist patterns are influenced very strongly by those electrons which is demonstrated also experimentally.

2. CALCULATION OF THE ENERGY DISSIPATION

Four processes are involved in the absorption of x-rays: Rayleigh scattering, Compton scattering, generation of photo electrons and formation of electron positron pairs. In Rayleigh scattering no energy is transferred to the atoms. Pair formation is possible only at x-ray energies above 1.02 MeV. In x-ray lithography the energies of the x-ray quanta are lower than 10 keV. For such energies the cross section for photoeffect is about 100 times larger than the cross section for Compton scattering (6). Therefore only the effect of the photoelectrons has to be considered.

The kinetic energy E_p of the photo electrons is

$$E_p = E_\lambda - E_B$$

E_λ = energy of the x-ray quantum, E_B = binding energy of the electron within the atom. For the main atoms of the PMMA, the values of E_B are 0.28 keV and 0.53 keV, the binding energies of the electrons in the K shells of carbon and of oxygen, respectively. In the silicon holds $E_B=1.8$ keV (K shell of Si) if the exposing radiation has a wavelength $\lambda < 0.67$ nm and $E_B = 0.15$ keV (L shell of Si) if the wavelength $\lambda > 0.67$ nm. The binding energy is stored for a short time within the atom and then distributed to the surroundings via Auger electrons or fluorescence radiation. The energy of the ejected Auger electrons is a little bit smaller than the E_B values just mentioned above, because the binding energies of the next higher levels must be subtracted. This leads to the Auger electron energy values of Fig. 1a. The relation of the probabilities for the Auger and the fluorescence effect is 9:1, that means, the energy E_B is transferred to the surroundings mainly by electrons, too. Fig. 1a gives the energies of the photo and of the Auger electrons, when the resist and wafer are irradiated by x-rays with $\lambda = 0.46$ nm (Rh L) and $\lambda = 0.83$ nm (Al K). In most cases the photo electrons have the higher energies and therefore the longer range. Only in the cases of Rh L radiation the Auger electrons generated in the silicon have the higher energy.

For the calculation of the energy transferred to the resist molecules, the angular distribution of the photo and the Auger electrons is important, too. The Auger electrons have a spherical distribution from their starting point (Fig.1b). The photo electrons generated by x-rays with energies below

10 keV are preferentially emitted perpendicular to the impinging x-rays (7). The photo and the Auger electrons lose their energy by excitation and ionization of the neighboring molecules. In the resist this process leads to chain scission of the organic molecules. The number of chain scissions in the resist is proportional to the number of excitation and ionization processes. Therefore the energy transferred to a volume element is a measure for the number of chain scissions.

The computation is carried out in a similar way as in (8,9) for electron lithography. The area near the interface resist/silicon is divided into a matrix of volume elements (Fig. 2). In each element an x-ray intensity $I(z)$ is absorbed, which is converted into photo and Auger electrons. The electrons dissipate the energy to the surrounding volume elements. Four amounts of energy have to be calculated:

- /1/ the energy in the resist which arises from x-rays absorbed in the resist immediately in those areas where there is no absorber in the mask,
- /2/ same as /1/ but with absorber in the mask,
- /3/ the energy in the resist which arises from the x-rays absorbed in the silicon but transferred back to the resist via the photo and Auger electrons, in areas with no absorber in the mask, and
- /4/ same as /3/ but with absorber in the mask.

For the calculation it is assumed, that an electron with the maximum energy according to Fig. 1a starts at the point, where the x-ray quantum is absorbed. The angular distribution of the photo and the Auger electrons is considered as indicated in Fig. 1b.

The energy density D which is delivered to the volume elements by the absorption of the x-rays is proportional to the absorbed x-ray intensity $I(z)$ and to the specific energy loss of the electrons

$$D \propto \int I(z) \cdot (dE/dr) \cdot dx \cdot dy \cdot dz$$

with x, y, z = coordinates of x-ray absorption, r = distance from the volume where the x-ray quantum is absorbed to the volume element which absorbs a part of the energy of the electron. The energy losses of the electrons are given by $dE/dr = E_p \cdot \Lambda(f)/R_G$

with

$$\begin{aligned} \Lambda(f) &= \text{depth dose function, } R_G = \text{Grün's range,} \\ \Lambda(f) &= 0.74 + 4.7 f - 8.9 f^2 + 3.5 f^3 \text{ for the resist,} \\ \Lambda(f) &= 0.6 + 6.21 f - 12.4 f^2 + 5.69 f^3 \text{ for the silicon,} \\ f &= r/R_G, \end{aligned}$$

$$R_G = 0.046 \text{ (g} \cdot \mu\text{m/cm}^3) \cdot (1/\rho) \cdot (E_p/\text{keV})^{1.75}$$

ρ = density.

For the calculations a point source and a step-like edge of the absorber in the mask are assumed.

3. RESULTS

At first the results at the surface of the resist far away from silicon are presented, where there is no influence of the substrate. The energy density in this area originates only from the absorption of x-rays in the resist (Fig. 3). In the areas behind the absorber it is lower corresponding to the contrast ratio. In the transition region the effect of the energy transfer by photoelectrons is clearly to see. Variation of the contrast values does not change the $D(x)$ -curves appreciably. For all three values of the contrast the transition width of the intensity from the value without absorber to the value behind the absorber is about the same, namely $0.22 \mu\text{m}$ for Rh L radiation and $0.07 \mu\text{m}$ for Al K radiation.

Near the interface resist/silicon the influence of the back-scattered electrons from the silicon is superimposed onto these energy density curves. Fig. 4 shows the equi energy density curves for $D(x,z)/D_0 = 0.5$. There is little influence of the contrast if the exposure is done by Al K. The $D(x,z)/D_0 = 0.5$ curve deviates only $0.02 \mu\text{m}$ from the ideal edge. A variation of the mask contrast from 3:1 to 10:1 makes differences which are hardly to be seen in Fig. 4.

Exposure with Rh L radiation leads to quite different results. Due to the higher energy of the Rh L quanta the range of the electrons is much higher than for Al K radiation. In addition the mask contrast has appreciable influence to the $D(x,z)/D_0 = 0.5$ curves. While for mask contrasts of 10:1 and 6:1 the curves may announce an undercut of $0.05 \mu\text{m}$ and $0.08 \mu\text{m}$, respectively, after the development, a mask contrast of 3:1 can lead to a complete take-off of the whole resist pattern if the development process is not stopped in time.

The effect of the electrons from the substrate can be demonstrated experimentally. For a comparison with experimental resist profiles, the energy density curves must be multiplied with the intensity profiles of a real source. Fig. 5 shows the x-ray intensity profiles behind an absorber edge for a Rh L and an Al K source for the two cases: mask and wafer in contact, and mask and wafer $50 \mu\text{m}$ apart from each other. The multiplication of the x-ray intensity profiles of Fig. 5 with the energy density curves of

Fig. 4 leads to the real energy density curves. The curves for exposure by x-rays from the Al K source with the relatively large focus of 10 mm are shown in Fig. 6. The possible undercut of $0.02 \mu\text{m}$ which might be expected according to Fig. 4 can be neglected. Exposure with mask and wafer in contact leads to a transition region of $0.15 \mu\text{m}$. Exposure with the wafer $50 \mu\text{m}$ apart from the mask leads to a transition region of about $2 \mu\text{m}$. In both cases the width of the transition region is determined by the source, not by the influence of the range of the electrons. The comparison with resist profiles after development (Fig. 6) shows very good agreement of the calculation and the experimentally measured width of the transition region.

In case of Rh L radiation, exposure were carried out only in contact in order to show the influence of the electrons. The penumbral shadow region is only $0.1 \mu\text{m}$ (Fig.5) whereas the transition region due to the electron range is $0.22 \mu\text{m}$ (Fig.3). According to Fig. 4 in this case a strong influence of the backscattered electrons should be visible. Fig. 7 shows the experimental result for a mask with a contrast of 4:1. If the development process is stopped exactly at the moment when the profile is down at the silicon, the profile dimensions are correct (Fig.7a upper SEM image). But if the development time is a little bit longer, the highly irradiated area at the resist/silicon interface will be dissolved. This leads to an undercut of the resist structure, which is shown in the lower part of Fig. 7a and more enlarged in Fig. 7b and 7c. The next step in the development after that in Fig.7b and 7c will be a complete take-off of the whole resist pattern. In Fig.7c the height of the undercut is about twice the value of the calculated results of Fig.4 indicating that in addition to electrons generated by the Rh L radiation the electrons generated by the Bremsstrahlung with the shorter wavelength considerably contribute to the energy density at the interface.

4. CONCLUSION

The effect of the x-ray generated electrons in the silicon on the energy density in the resist is quite different when using Rh L or Al K radiation. There are two reasons for the difference. According to Fig. 1a the maximum energy of the electrons generated in the silicon by Rh L radiation is only 22% higher than that of the electrons generated by the Al K radiation. But this results in a 45% higher range of the electrons which are generated by the Rh L radiation. The second reason is the higher absorption

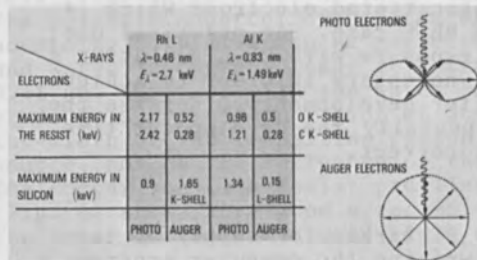
of the Rh L in the silicon compared to Al K. This leads to an intensity of the backscattered electrons which is higher by a factor of 3 in Rh L case. For practical use, this demands that for the exposure with Rh L radiation a mask of higher contrast is necessary in order to achieve correct resist profiles after development. Otherwise the development conditions, especially the development time must be observed extremely correct.

5. ACKNOWLEDGEMENT

We would like to thank Dr. E. Birkle for supplying the resist, Miss B. Jobst for writing the computer program, Miss E. Schöning for the exposure and development work and Mr. H. Treml for technical assistance. This work has been supported by the technological program of the Federal Department of Research and Technology of the Federal Republic of Germany. The authors alone are responsible for the contents.

REFERENCES

- (1) E. Spiller, R. Feder in X-Ray Optics ; edited by H.J. Queisser Springer Verlag Berlin 1977, p. 35-92
- (2) J.R. Maldonado, G.A. Coquin, D. Maydan, S. Somekh J.Vac.Sci-Technol. 12 (1975) 1329
- (3) E. Hundt, P. Tischer, J.Vac.Sci-Technol. 15 (1978)
- (4) P.A. Sullivan, J.H. McCoy, IEEE Trans.ED-23 (1976) 412
- (5) R. Feder, E. Spiller, J. Topalian, Polymer Engineering and Science 17 (1977) 385
- (6) N.A. Dyson, X-Ray in Atomic and Nuclear Physics, Longman Group Ltd., London 1973, p. 203-243
- (7) C.D. Anderson, Phys.Rev. 35 (1930) 1139
- (8) T.E. Everhart, P.H. Hoff, J.Appl.Phys. 42 (1971) 5837
- (9) R.D. Heidenreich, L.F. Thompson, E.D. Feit, C.M. Melliar-Smith, J.Appl.Phys. 44 (1973) 4039



a

b

Fig. 1: (a) Maximum energies of the photo and Auger electrons in the resist and the silicon during exposure with x-rays. $\lambda = 0.46 \text{ nm}$ (Rh L) and $\lambda = 0.83 \text{ nm}$ (Al K). (b) Angular distribution of the photo and of the Auger electrons.

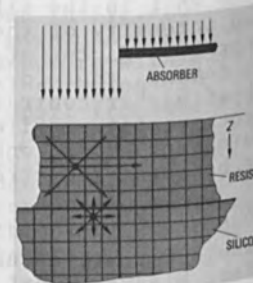


Fig. 2: Matrix of the volume elements near the interface resist/silicon, used for the calculation.

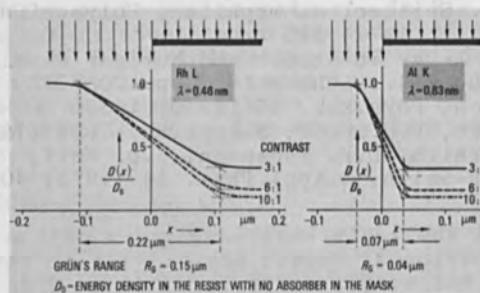


Fig. 3: Energy density curves for various contrast values at the top of the resist layer where there is no influence of the electrons from the substrate. A point source is assumed.

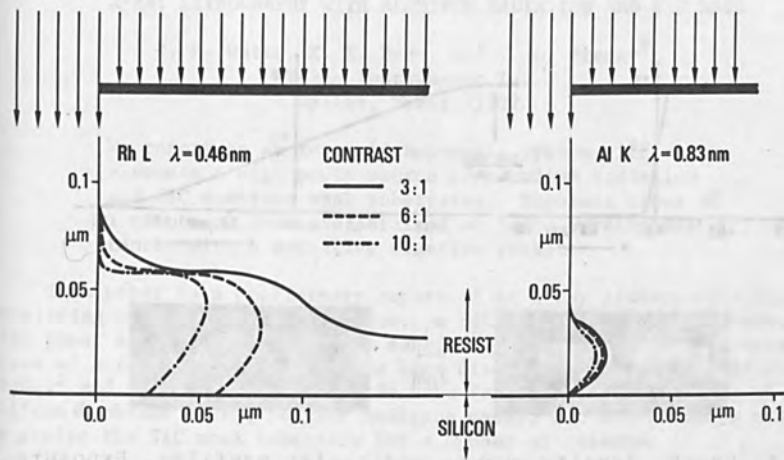


Fig.4: Equi energy density curves ($D(x,z)/D_0 = 0.5$) near the bottom of the resist layer for various contrast values for exposure with Rh L and Al K radiation.

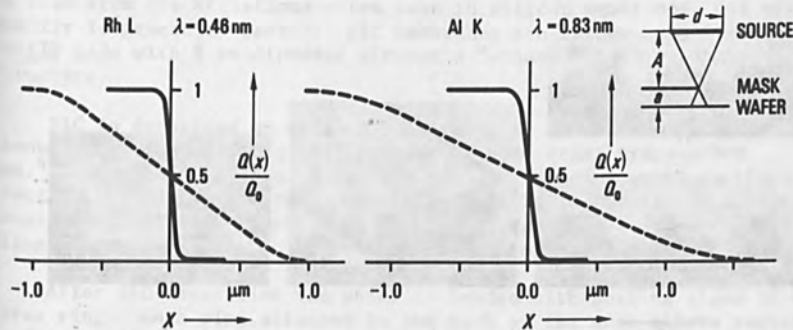


Fig.5: X-ray intensities behind an absorber edge for two real sources.—Mask and wafer in contact ($a = 3 \mu\text{m}$, the resist thickness was $3 \mu\text{m}$),----- mask and wafer in distance ($a = 50 \mu\text{m}$). Q_0 = x-ray intensity without mask absorber.
 (a) Rh L source: $d = 2.5 \text{ mm}$, $A = 75 \text{ mm}$.
 (b) Al K source: $d = 10 \text{ mm}$, $A = 200 \text{ mm}$.

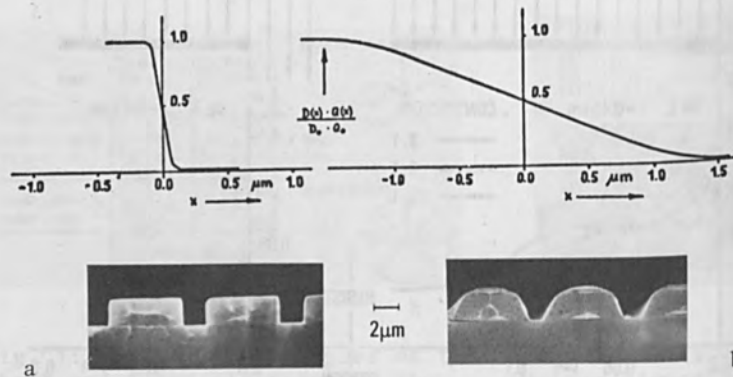


Fig.6: Energy density curves and resist profiles. Exposure with Al K radiation from the source of Fig.5b.
 (a) Mask and wafer in contact
 (b) Mask and wafer 50 μm apart from each other

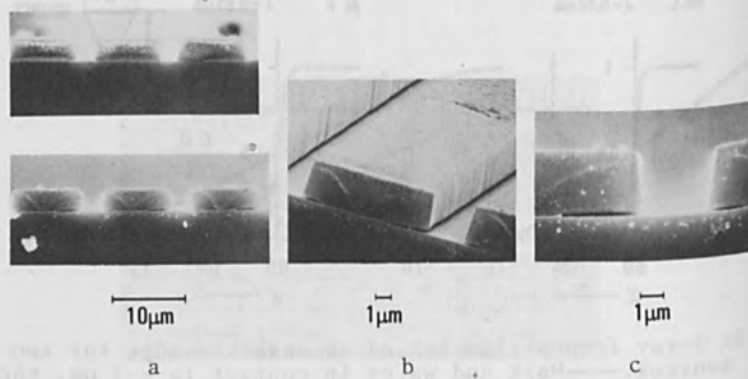


Fig.7: SEM photographs of resist profiles after development. Pattern was replicated by Rh L radiation from a mask with a contrast of 4:1. (a) Two stages of the development process. (b) and (c) Enlarged undercut region demonstrating the effect of the electrons backscattered from the substrate.

X-RAY LITHOGRAPHY WITH ALUMINUM RADIATION AND SiC MASK

R. K. Watts, K. E. Bean, and T. L. Brewer*
Texas Instruments Inc.
Dallas, Texas 75222

We report on an X-ray lithographic system with main elements a high power source of aluminum radiation and SiC membrane mask substrates. Exposure times of 1 minute or less are obtained at large working distances with a sensitive negative resist.

This paper is a preliminary report of an X-ray lithographic system consisting of three main components: a SiC membrane mask substrate, a high power exposure system, and a sensitive negative resist. Several types of X-ray mask substrate have been discussed, including silicon,¹ Si₃N₄,² and polymer³ membranes. We have fabricated and made use of silicon membrane masks, polymer membrane masks, and SiC membrane masks. We prefer the SiC mask substrate for a number of reasons.

Unlike polymer films, SiC is unaffected by humidity changes. It is much stiffer with a Young's modulus two orders of magnitude larger than those of stiff polymers. SiC is an excellent etch stop so that etching away of the silicon substrate to form the membrane is easier than for a silicon membrane where the etch rate is slowed by a change of dopant concentration at the film-substrate interface. The interface is free from the striations often seen in silicon membranes, and optical quality is generally better. SiC membranes are rather rugged and are easily made with 5 cm diameter without a "window frame" support structure.

SiC is deposited on silicon substrates at elevated temperature through reaction of SiCl₄ with propane or some other hydrocarbon gas.⁴ Hydrogen is used as a carrier gas and reducing agent in the reaction. Through adjustment of the Si/C ratio in the gas stream the tension and optical transparency of the membrane can be varied, as illustrated in Figure 1. Optimum conditions are obtained with Si/C \approx 1.

After SiC deposition the wafer is bonded with sealing glass to a pyrex ring. This ring attached to the back of the mask allows easier handling and prevents twisting of the thin 0.76 mm (0.03 in.) wafer. We have reported previously on our techniques for patterning the metal absorber on the mask.⁵ If this patterning is to be by means of ion milling, a thick metal layer is next deposited onto the SiC. The membrane is formed by chemical etching of the silicon substrate in a

* Now with Honeywell Incorporated, Minneapolis, Minnesota

nitric-hydrofluoric-acetic acid mixture. Resist is applied to the membrane and patterned by electron beam. The last step is ion milling of the $0.5 \mu\text{m}$ gold absorber using the resist or an intermediate thin refractory metal layer as milling mask. The order of the process is important. Some flexing of the membrane, leading to small pattern distortions, can occur if the metal absorber layer is patterned before the membrane is formed in the etch step. Measured burst strength of $2.5 \mu\text{m}$ thick membranes is in the range $5\text{-}10 \times 10^9 \text{ dyn/cm}^2$. No membrane has ever been broken in the steps following etching (resist application, patterning, ion milling).

The X-ray exposure system features a high power Rigaku SX-5 X-ray generator and a manual optical mask-wafer registration system. Two electron guns are available for use: a 20 kV, 0.2a. gun which provides a focal spot of diameter 1 mm and a 20 kV, 0.9a. gun which provides a 3 mm focal spot. Exposure is carried out in a helium atmosphere. For exposure a helium filled cannister slides into place over the mask, replacing the registration optics. At distance D from the source maximum flux is about $0.27/D^2 \text{ w/cm}^2$. Figure 3 shows the spectral output of the generator plotted as power absorbed in a hydrocarbon resist per unit volume vs. photon energy. The characteristic AlK α peak is distorted by the low resolution of the spectrometer used to obtain the curve. If the two curves are integrated, the ratio of the integrals is 9.8. The ratio for 15 kV beam voltage is 10.

Typical working distance or separation between X-ray source spot and mask is 43 cm. With gap between mask and wafer fixed at $20 \mu\text{m}$ this gives a value of $0.14 \mu\text{m}$ for the penumbral shadow if the larger 3 mm focal spot is used. At present wafer diameter is 5 cm.

Figure 4 shows exposure curves of two negative X-ray resists, polyglycidyl methacrylate-ethyl acrylate⁶ obtained from Mead Co. of Rolla, Missouri, and our own experimental X-ray resist XR79. Exposure times of one minute or less are obtained with the latter resist even at long working distances D, since it can be exposed properly with a dose of $\sim 2 \text{ mJ/cm}^2$. Patterns with minimum feature size less than $0.5 \mu\text{m}$ have been imaged with this resist. High resolution images are obtained only if the minimum feature size is greater than or equal to the resist thickness, probably because of swelling of the exposed resist in the developer solution.

REFERENCES

1. D. L. Spears and H. I. Smith, "X-ray Lithography - A New High Resolution Replication Process," *Solid State Technology*, July 1972, p. 21.
2. E. Bassous, R. Feder, E. Spiller, and J. Topalian, "High Transmission X-Ray Masks for Lithographic Applications," *Solid State Technology*, Sept. 1976, p. 55.
3. D. Maydan, G. A. Coquin, J. R. Maldonado, S. Somekh, D. Y. Lou, and G. N. Taylor, "High Speed Replication of Submicron Features on Large Areas by X-Ray Lithography," *IEEE Trans. El. Dev.* ED 22, 429 (1975).
4. K. E. Bean and P. S. Gleim, "Some Properties of Vapor Deposited SiC," *J. Electrochem. Soc.* 114, 1158 (1967).
5. R. K. Watts, D. C. Guterman, and H. M. Darley, "Submicron X-Ray Lithography," *Proc. SPIE* 80, 100 (1976).
6. L. F. Thompson, E. D. Feit, and R. D. Heidenreich, "Lithography and Radiation Chemistry of Epoxy Containing Negative Electron Resists," *Polymer Eng. and Sci.* 14, 529 (1974).

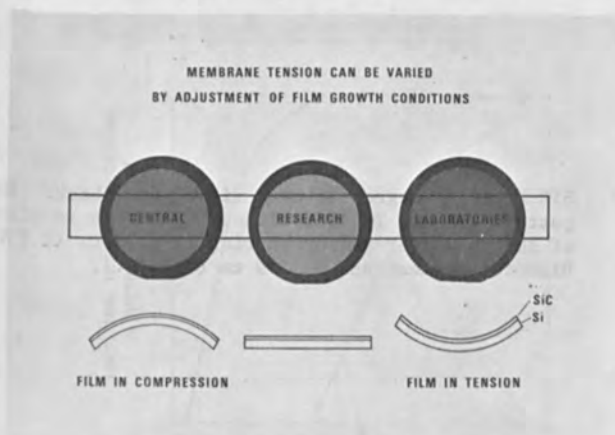
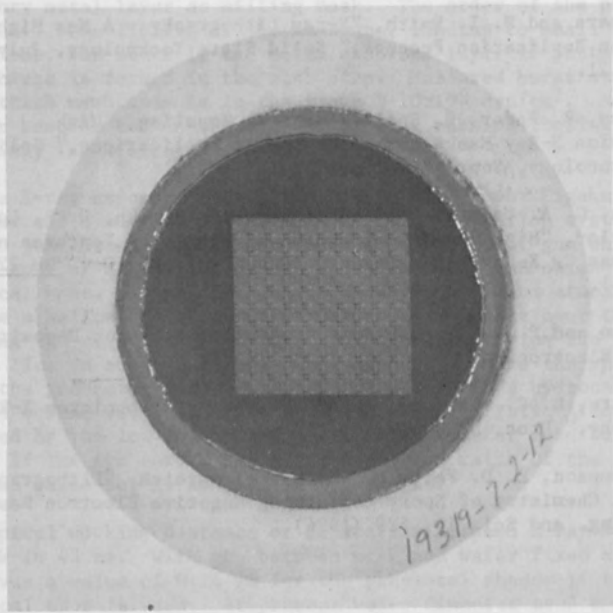


Figure 1. SiC films formed under different deposition conditions. Substrate diameter is 2.5 in. Membrane thickness is 2.5 μm .

nitric-hydrofluoric-acetic acid solution. Resist is applied to the substrate and patterned by electron beam. The final step is etching of the 0.5 μ m gold absorber using the resist as an intermediate thin refractive layer.



The mask is mounted on a silicon wafer and a pyrex ring. The outer diameter of the silicon wafer and pyrex ring is 6.35 cm (2.5 in.). The diameter of the membrane is 3.9 cm (1.5 in.).

Figure 2. SiC X-ray lithographic mask viewed from back. The pattern is seen in transmitted light. Outer diameter of silicon wafer and pyrex ring is 6.35 cm (2.5 in.). Diameter of membrane is 3.9 cm (1.5 in.).

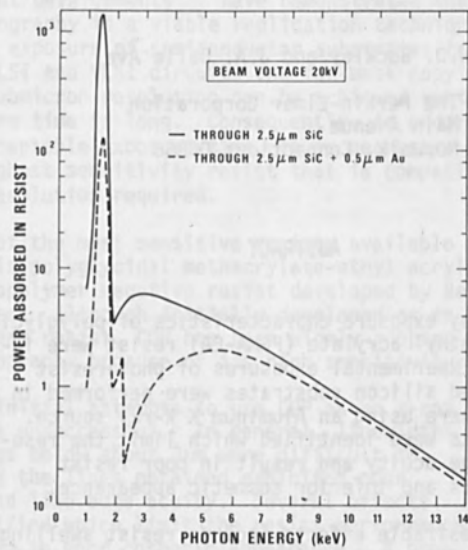


Figure 3. Spectral output of X-ray generator at 20 kV into helium atmosphere. Power density absorbed in resist after passing through the transmissive and absorptive parts of a mask are plotted.

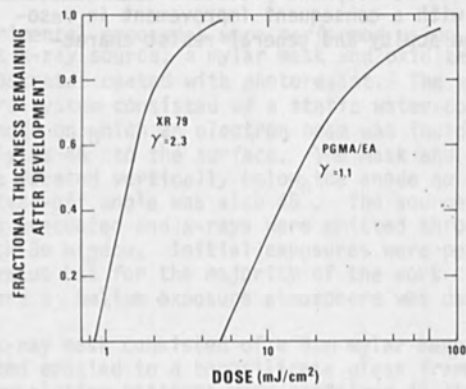


Figure 4. Exposure curves of two negative X-ray resists.

X-RAY EXPOSURE AND DEVELOPMENT CHARACTERISTICS
OF POLYGLYCIDAL METHACRYLATE-ETHYL ACRYLATE

W.D. Buckley and J.A. Dalle Ave

The Perkin-Elmer Corporation
Main Avenue
Norwalk, Connecticut 06856

ABSTRACT

The x-ray exposure characteristics of polyglycidal methacrylate-ethyl acrylate (PGMA-EA) resist were investigated. Experimental exposures of photoresist coated oxidized silicon substrates were performed in a helium atmosphere using an Aluminum K X-ray source. Several effects were identified which limit the resolution and edge acuity and result in poor resist characteristics and inferior cosmetic appearance.

The undesirable effects include resist swelling, low density porous resist with a rough surface which results in a milky appearance, and a surface skin effect. It was shown that these effects are caused by a combination of the exposure conditions and the developer and development procedure. The selection of an appropriate development procedure eliminates these effects with a consequent improvement in resolution and edge acuity and general resist characteristics.

1. Introduction

Recent developments¹⁻⁴ have demonstrated that x-ray lithography is a viable replication technique for direct exposure of semiconductor substrates to fabricate LSI and VLSI circuits and for mask copying. Although submicron resolution can be achieved routinely, the exposure time is long. Consequently, in order to achieve acceptable exposure time, it is necessary to use the highest sensitivity resist that is compatible with the resolution required.

One of the most sensitive resists available commercially is polyglycidal methacrylate-ethyl acrylate (COP), a copolymer negative resist developed by Bell Laboratories. Although initially developed as an electron beam resist, COP has been widely adopted for x-ray lithography because of its high sensitivity.

Our initial attempts to use COP as an x-ray resist were unsuccessful. In general, linewidths and spacings below about $3\mu\text{m}$ were difficult to resolve and the lines obtained exhibited poor fidelity and line edge acuity. Several effects were identified which limit the resist performance and resulted in poor cosmetic appearance. A procedure was established which eliminated these effects and permitted the replication of geometries at least as small as $1\mu\text{m}$.

2. Experimental Method

Experimental exposures were performed using an Al_K soft x-ray source, a mylar mask and oxidized silicon substrates coated with photoresist. The x-ray exposure system consisted of a static water-cooled aluminum anode on which an electron beam was incident horizontally at 45° to the surface. The mask and substrate were located vertically below the anode so that the x-ray take-off angle was also 45° . The source chamber was evacuated and x-rays were emitted through a $25\mu\text{m}$ thick Be window. Initial exposures were performed in vacuo but for the majority of the work reported here a helium exposure atmosphere was used.

The x-ray mask consisted of a $5\mu\text{m}$ mylar membrane stretched and epoxied to a borosilicate glass frame. A series of resolution patterns were contained in the mask

pattern. Each resolution pattern consisted of two groups of equal lines and spaces arranged orthogonal to each other (Figure 8). Linewidths and spaces ranged from a minimum of $1\mu\text{m}$ to a maximum of $5\mu\text{m}$.

The resist was developed initially using a procedure which was recommended by the vendor for developing electron beam exposed resist. Because we obtained poor results on x-ray exposed resist, an alternative procedure was established. This new procedure was based on a solvent, nonsolvent mixture of methyl-ethyl ketone and ethanol as was the recommended procedure.

3. Experimental Results

Initial experimental exposures of COP resist in vacuum were generally unsuccessful. In general, very poor image quality and poor resolution was obtained and the results were non-reproducible. It was determined that thermal effects were partly responsible for the lack of reproducibility.

In Figure 1 the variation of developed resist thickness with exposure is illustrated. The data of Curve B was obtained when the mask and wafer were thermally isolated to enhance thermal effects during exposure. The data points are scattered and the dashed lines mark the approximate boundaries of the shaded area within which highly variable results were obtained. This variability effectively reduces the resist contrast and reduces the resolution. Examination of resist images revealed evidence of radially symmetric relative motion between the mask and wafer during exposure, consistent with differential thermal expansion. Linear features located in radially symmetric positions on the wafer exhibited smooth well-defined edges in the radial direction and sloping edges in the tangential direction. As a result, for small geometries, radial lines were resolved and tangential lines were not. The resolution varied with position on the wafer. At the center no relative motion occurred and the best resolution was obtained. As the radial distance increased, the relative motion increased and therefore the resolution decreased. In general, for resolved geometries, the edge profile was dependent on orientation.

Curve A, Figure 1, illustrates the data obtained when the wafer and mask temperature was controlled by heat sinking to a water-cooled support plate. This

data was reproducible and, in addition, the resist contrast increased as evidenced by the increase in the slope of the exposure characteristic. The resist sensitivity decreased by a factor of two approximately. The variability in the shaded region of Curve B was also eliminated. The resist image exhibited no evidence of differential expansion and the resolution was independent of position and orientation. In order to eliminate thermal effects subsequent exposures were performed in a helium atmosphere.

Although this was effective in removing thermal effects, the resist resolution was still inadequate. In general, lines smaller than $3\mu\text{m}$ approximately were not resolved and resolved geometries tended to have ragged edges. This effect was also observed for contact printing where the resolution was clearly not limited by penumbral effects. Figure 2 is a photograph of an unsuccessful attempt to replicate a $1\mu\text{m}$ line in COP. It is important to note that in addition to the poor resolution the photoresist appears to be collapsing into the unresolved line. This effect will be discussed in more detail below.

Two additional effects were observed. One effect observed in lightly exposed resist is shown in Figure 3. Although an improvement in resolution was obtained, the resist had a milky appearance. On examination in a scanning electron microscope it was apparent that the resist had a porous appearance and a rough surface. In some cases, this effect could be removed by baking the resist. However, high temperatures were required and the resist tended to flow and round off the edges of images.

A second effect appeared to be due to resist swelling during development. For large areas of exposed resist, the surface effect shown in Figure 4 was obtained. For small geometries the swelling originated from two sides and a bicuspid appearance resulted as shown in Figure 5. In general this effect appeared to be only cosmetic and was removed during a post-development bake. This is illustrated by Figure 5 which shows two nominal $1\mu\text{m}$ lines from the same exposure. The scanning electron micrograph on the left is a resist image after exposure and the micrograph on the right is a similar image after a post-development bake.

It was also observed that strong developer solutions appeared to accentuate the porosity effect in some cases and, in addition, in other instances caused exposed resist to dissolve and be redeposited in undesirable areas. This latter effect improved the surface appearance but eliminated the image. Weak developer solutions resulted in improved cosmetic appearance but reduced resolution. Because of these observations, a series of experiments were performed to determine the effect of exposure and development procedures on resolution.

Photoresist coated substrates were exposed so that developed thicknesses between 0% and 80% of the unexposed thickness were obtained. Each substrate was then subdivided and pieces were spray developed in a range of concentrations of a developer which consisted of a mixture of methyl-ethyl ketone and ethanol. The resist thickness was measured by means of a surface profiler. The results obtained are summarized in Figure 6. For developer concentrations of 5:3 MEK to ethanol and stronger the developed thickness is independent of the developer concentration for all exposure conditions. However, weaker solutions result in an increase in thickness in all cases. The curves for different exposures converge at a concentration of approximately 5:6 MEK to ethanol. For weaker developer solutions the resist is essentially undeveloped independent of exposure. It is important to notice that developer concentrations weaker than 5:3 are unable to completely develop unexposed resist as evidenced by the 0% developed thickness data. The concentration 5:3 MEK to ethanol therefore sets the limit for the weakest acceptable developer solution. This is illustrated by the dashed vertical line in Figure 6.

The strong developer concentration limit is determined by the tendency to form porous resist. The dashed diagonal line in Figure 6 indicates the approximate location of this limit. The line marks a transition region rather than a well defined boundary line. In general, to the right of the line the resist is clear, non-porous and has a good cosmetic appearance. To the left of this line the resist has a patchy milky appearance and is porous. The stronger the developer the more pronounced is this effect. However, for a very strong developer, the exposed resist dissolves slowly and is redeposited uniformly over the surface eliminating the porosity and obscuring the desired patterns.

Our initial conclusion was that a developer concentration near to 5:3 should be acceptable for all exposure con-

ditions. However, resist patterns developed in this way exhibited poor resolution when examined in an optical microscope. Closer examination in a scanning electron microscope revealed the cause of this effect. Figure 7 is a micrograph of nominal $1\mu\text{m}$ lines and spaces. It is apparent that what, in an optical microscope, appears to be a residue is in fact a surface skin which is left as a bridge between adjacent resist regions. Below the skin the resist has been removed. Images of this kind are generally resolved during etching.

The surface skin has several effects. On large geometries the skin breaks and falls into the apertures leaving an irregular edge to the pattern. For small geometries the resist may simply sag as shown in Figure 2 and discussed above. For most geometries intermediate effects are observed which affect the line edge profile.

It is apparent from Figure 7 that the skin is under tension. On the right hand line it is clear that wherever a bridge occurs uncompensated by a corresponding bridge on an adjacent line, the resist is distorted during development and a bulge in the line edge occurs. This is particularly evident in the left hand line where a large area bridge remains in position at the top end of the line. Here the entire line is displaced by the skin tension and as a consequence the line edge is perpendicular over approximately half of its length and sloping in the region of bridging. This skin effect may be similar to the effects observed in ultraviolet negative resist caused by atmospheric contaminants.

In order to develop the skin it is necessary to use a developer concentration close to the maximum defined in Figure 6. The preferred sequence is a short exposure to this strong developer followed by longer exposure to the weak developer in order to clean out the apertures and preserve the cosmetic appearance and acceptable resist characteristics. Figure 8 is a scanning electron micrograph of a series of resolution patterns developed by this procedure. The $1\mu\text{m}$ patterns are resolved as indicated by the right hand micrograph. The edge effect on the resist is due to swelling as discussed above (Figure 5). We have successfully etched patterns in silicon oxide using COP resist developed in this way. Although, as expected, the pattern is overetched by the wet chemical technique used, all of the geometries were resolved and pattern integrity was maintained.

REFERENCES

1. D.L. Spears and H.I. Smith, *Electron Letters*, 8, 102, 1972.
2. S.E. Bernacki and H.I. Smith, *IEEE Trans. on Electron Devices*, 22, 421, 1975.
3. D. Maydan, G.A. Coquin, J.R. Maldonado, S. Somekh, D.Y. Lou and G.N. Taylor, *IEEE Trans. Electron Devices*, 22, 429, 1975.
4. H.L. Stover, P.A. Sullivan, J.H. McCoy, F.L. Hause, H. Yuan, E. Harari, 8th Intl. Conferences on Electron and Ion Beam Science & Technology, Seattle, May 21-26, 1978.

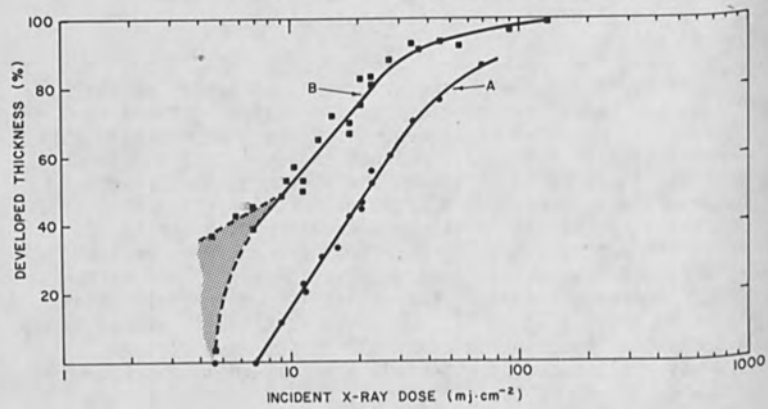


Figure 1. The variation in developed thickness with x-ray dose for COP resist. The data of Curve A was obtained when the wafer temperature was controlled during exposure. The data of Curve B was obtained when the wafer was thermally isolated to enhance thermal effects.

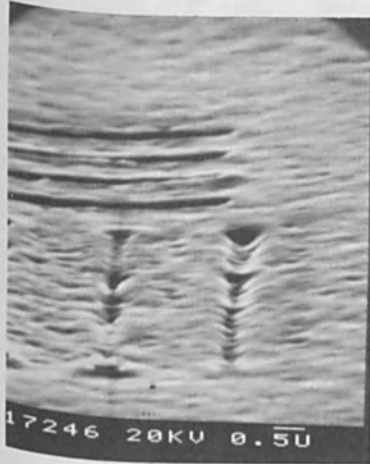


Figure 2. Unresolved $1\mu\text{m}$ lines in COP resist

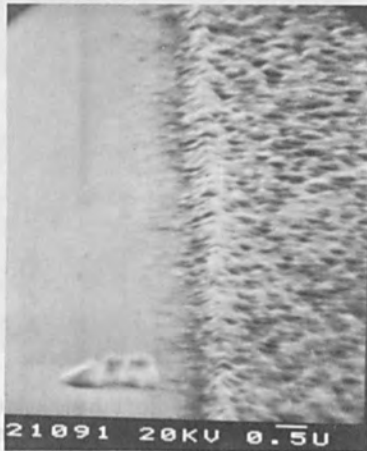


Figure 3. Porous Resist

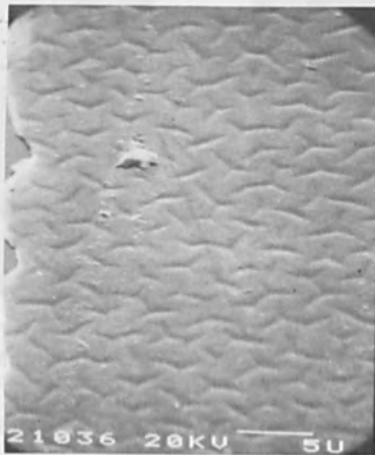


Figure 4. The effect of swelling during development on a large area of resist.

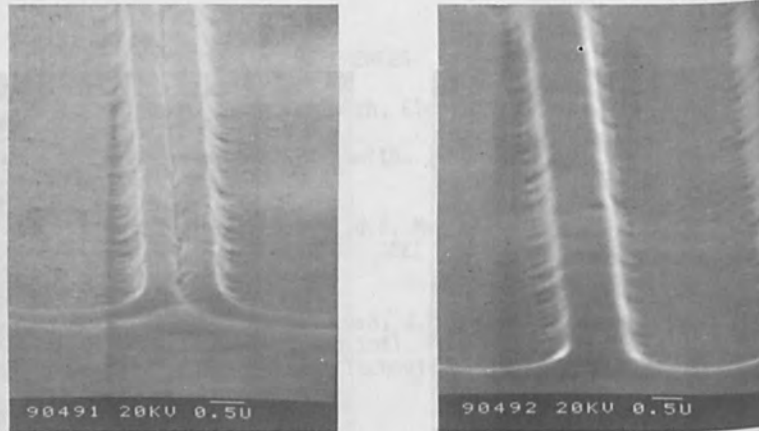


Figure 5. The left hand photograph illustrates the effect of swelling during development on small geometries. As can be seen in the right hand photograph, the swelling is removed by a post-development bake.

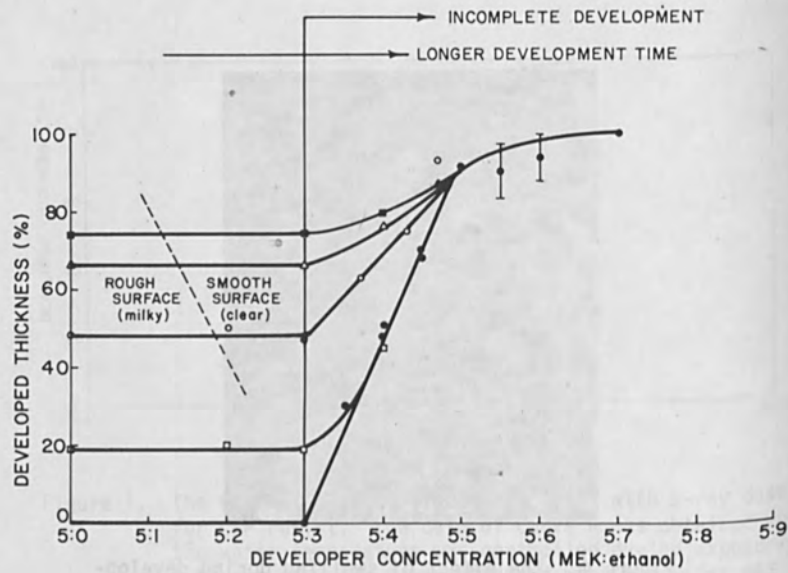


Figure 6. The development characteristics of COP resist.

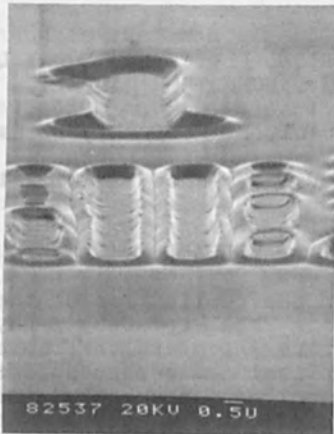


Figure 7. The effect of a surface skin on resolution and pattern fidelity.

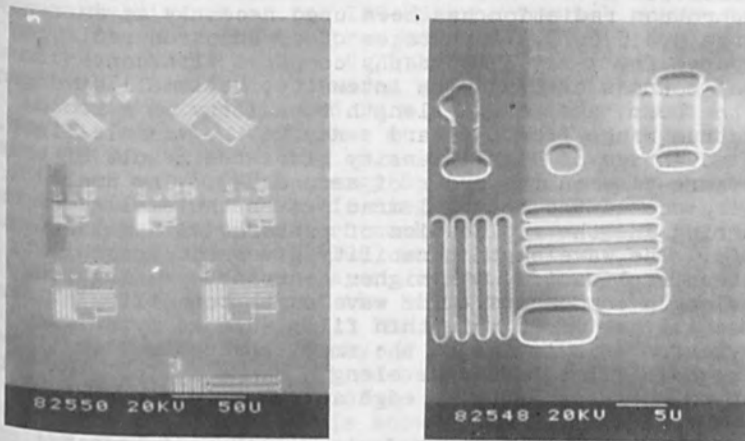


Figure 8. Scanning electron micrograph of successfully developed resolution patterns down to $1\mu\text{m}$ linewidths. The numbers above each pattern represent the nominal line and space width in microns.

FABRICATION OF OPTICAL DEVICES BY X-RAY LITHOGRAPHY
BY USING SYNCHROTRON RADIATION

H. Aritome, S. Matsui, K. Moriwaki, S. Hasegawa, and
S. Namba
Faculty of Engineering Science, Osaka University,
Toyonaka, Osaka 560, JAPAN

ABSTRACT

This paper reports on the replication of the line patterns and grating patterns in PMMA resist by x-ray lithography by synchrotron radiation which are the basic components for the fabrication of optical devices such as integrated optics. Also shown are the results of the pattern replication by using a storage ring of a low electron energy of 0.3 GeV.

INTRODUCTION

The potential of x-ray lithography as a very high resolution replication method has been well demonstrated[1,2]. Synchrotron radiation has been used recently as an x-ray source[3,4,5,6,7]. Advantages of synchrotron radiation as a source for x-ray lithography compared with conventional x-ray sources are (a) high intensity, (b) small divergence of the beam, and (c) wavelength tunability in a broad spectrum range from the hard x-ray to the visible light. The advantage of high intensity gives the result of short exposure-time on the order of seconds[4]. The small divergence of the beam (~1 mrad) gives the small penumbral blurring and the replication of patterns with a large aspect ratio. The wavelength tunability gives the possibility of pattern replication with higher contrast by using long wavelength components. The wavelength tunability allows an effective use of organic thin films such as mylar and parylene. This is due to the small absorption coefficient of organic films in the wavelength range a little more than 45 Å which is a carbon K_α edge as shown in Fig. 1.

For fabrication of optical devices such as integrated optics, line patterns of several μm width are the basic components. In this application a very smooth edge is essential to reduce the scattering loss of the guided light. The vertical walled patterns are desired. This allows the easy design. For fabrication of gratings such as transmission type the similar situation holds although narrower lines less than one μm are required. In this report it is shown that the pattern replication by an x-ray of synchrotron radiation seems to be most desirable from the above points. This

method has advantages that the aspect ratio can be easily controlled compared with the case by an electron-beam lithography and it is possible to obtain the replicated patterns on insulating materials such as SiO_2 , LiNbO_3 and PMMA without any special treatment.

One of the disadvantages of x-ray lithography by synchrotron radiation is that the experimental system becomes large and expensive. It is an interesting problem how low the electron energy of an electron synchrotron can be for the above application.

In this report fine patterns of a large aspect ratio and vertical wall are obtained by using an electron synchrotron of INS-ES at the University of Tokyo. It is also reported that 0.5 μm -wide line-patterns were replicated in smaller exposure time by using a storage ring of an electron energy of 0.3 GeV (SOR-RING) at the University of Tokyo when a 2 μm -thick parylene-N film was used.

EXPERIMENTS BY INS-ES

A schematic diagram of the INS-ES experimental system is shown in Fig. 2. The electron energy of the electron synchrotron INS-ES between 0.75~1.1 GeV was used in this experiment. A mask and a wafer were placed in contact and the assembly was positioned in a vacuum sample-chamber inside the direct-output line at a distance of 10 m from the orbit. Figure 3 shows the calculated power spectrum as a function of an electron energy[8,9] at the sample chamber. Figure 4 shows the schematic diagram of a pattern mask used in this experiment. Pattern masks used were gold layer on silicon-crystal membrane (100) which was 3 μm thick. The thickness of Au absorber-layer was varied between 0.1~0.4 μm . The fabrication process of the Si membrane is similar to that described in Ref. [2]. The Au patterns were made by a conventional photolithography, a holographic method by using 325 nm He-Cd laser or electron-beam lithography. An example of the fabrication process of Au patterns in the case of electron-beam lithography is shown schematically in Fig. 5. A JBX-5B electron exposure system was used for an electron-beam exposure. An electron energy was 20 keV. Samples used were silicon-crystal wafers coated with 1~2 μm -thick PMMA (Elvacite 2041) resist. In Fig. 6 are shown the calculated power spectra through a 3 μm -thick Si wafer and an 1 μm -thick parylene-N film by using the absorption coefficient shown in Fig. 1.

After an exposure by synchrotron radiation, development was done by a solution of methyl-isobutyl-ketone (MiBK) in

isopropanol (1:3) or MIBK for 2 min. After the development the sample was rinsed in isopropanol for one min. For a 3 μm -thick Si mask the exposure time of 20 min was sufficient for removal of 1.5 μm PMMA resist at an electron energy of 1.1 GeV and a beam current of 24 mA when the development was done by MIBK for 2 min. This exposure time was calculated to correspond to the absorbed energy density in PMMA of 2500 J/cm³. The ratio of absorbed energy in PMMA exposed by synchrotron radiation through 3 μm -thick Si with Au and without Au film (i.e. the contrast) was calculated and is shown as a function of an electron energy of INS-ES in Fig. 7. The case of the conventional Al K α source is also shown in the figure. It is clearly seen that the contrast is much improved in those energy range shown in the figure compared with the case of Al K α source.

Experimental results of the developed thickness of PMMA at an electron energy of 0.85 GeV and a beam current of 120 mA is shown in Fig. 8. The thickness of Au is chosen as a parameter. The development was done by MIBK for 2 min. Figure 9 shows the SEM photograph of the replicated line-pattern in 1 μm thick PMMA at an electron energy of 0.75 GeV. From this figure it is seen that a 0.2 μm -thick Au layer gives a good contrast. The calculated contrasts are a) 52, b) 8 and c) 2.7, respectively. The large contrast and the good collimation of the x-ray beam of synchrotron radiation are clearly demonstrated in Fig. 10. The edge of the 0.4 μm -thick Au line-pattern of the mask is smooth but not vertical-walled, but the edge of the replicated pattern is vertical-walled deep into 1.7 μm thickness. Another example of the high collimation of the x-ray beam is demonstrated in Fig. 11 which shows the SEM photograph of a grating pattern of the 0.2 μm width and 0.7 μm period in 2.2 μm -thick PMMA. This mask was made by a holographic method.

In the case of a conventional x-ray lithography, the resolution is mainly limited by penumbral blurring. On the other hand, in the case of x-ray lithography by synchrotron radiation the penumbral blurring can be neglected. When a mask is not closely contacted with a wafer, however, the resolution is limited by the diffraction effect in the energy range used in this experiment. Figure 12 shows the patterns obtained in PMMA with relatively long exposure (~ 15000 J/cm³). The distance between the Si mask and the wafer was 400 μm and the line widths of the pattern were 1, 2 and 4 μm . In the case of an 1 μm -wide line-pattern, grooves are seen on top surfaces and the lateral shrinkage and the side slope of the PMMA wall are more remarkable than those in the cases of wider lines. To interpret those effects, the x-ray intensity distribution at 400 μm from slits was calculated by the

theory of Fresnel diffraction. The slit widths of 1, 2 and 4 μm were used and the power density of the incident beam was assumed to be uniform in the plane of slits and only one single wavelength of 10 A was used. Figure 13 shows the calculated x-ray intensity distribution. In spite of rough assumptions used in the calculation, experimental results can be qualitatively well explained by the Fresnel diffraction. Figure 14 shows the x-ray intensity distribution in a wafer when the slit width is 1 μm . From this figure the gap of 10~20 μm has little effect on the replicated pattern for 1 μm line. This result was experimentally verified.

EXPERIMENTS BY SOR-RING

Figure 15 shows the power spectrum of the storage ring of SOR-RING at an electron energy of 0.3 GeV. The calculated power spectrum through a 5 μm -thick parylene-N film is also shown in the figure. The sample was set in a sample chamber after two-stage differential-pumping system shown in Fig. 16. Figure 17 shows the experimental results of the developed thickness of PMMA as a function of an exposure time when the beam current was 100 mA. The development was done by MIBK for 2 min. Owing to the small absorption coefficient of the parylene-N film around 45~70 A, the resultant exposure time was reduced compared with the case of INS-ES. The value was further reduced to be about one min when a 2 μm -thick parylene-N film was used. Figure 18 shows the SEM photograph of a 0.5 μm -wide line-pattern replicated in PMMA. The 2 μm -thick parylene-N film on Si wafer was used as a mask to support a thin film. The part of Si where patterns are made was etched away. The thickness of Au absorber was about 2000 A. The fabrication process of patterns is similar to that shown in Fig. 5. But Au patterns were made by ion-etching through about 1000 A-thick Cr patterns made by a lift-off technique. Again 0.5 μm -wide line-pattern of 1 μm thick PMMA was obtained. A good collimation of an x-ray beam seems to be held. But the edge is not very sharply vertical-walled. The edge shape will be improved by using a thicker absorber layer of Au or by closer contact between the parylene mask and the sample wafer.

SUMMARY

Line patterns with 1~2 μm -thick vertical-wall were replicated in PMMA by synchrotron radiation of INS-ES. This is due to a large mask contrast and a high collimation of an x-ray beam of synchrotron radiation. A grating pattern of 0.7 μm period, 0.2 μm wide lines and 2.2 μm thickness was obtained in PMMA. This large aspect ratio demonstrates the high collimation of the x-ray beam of synchrotron radiation.

It was shown that x-ray lithography by synchrotron radiation has advantages for the application to fabricate optical devices. It was also shown that it is possible to obtain a thick line-pattern of 0.5 μm width at an electron energy of 0.3 GeV by the SOR-RING. The exposure time was shorter compared with the case of INS-ES when a 2 μm -thick parylene-N film was used as a mask material. This opens the possibility of the more effective use of synchrotron radiation of low electron energy from the point of application for lithography.

ACKNOWLEDGEMENT

The authors thank staffs of the Institute of Nuclear Study and the Synchrotron Orbital Radiation Laboratory of the Institute of Solid State Physics, the University of Tokyo, and staffs of the Electrical Communication Laboratory, Nippon Telegraph and Telephone Public Corporation for their support and valuable discussions during these experiments.

REFERENCES

1. D.L. Spears and H.I. Smith, *Electron. Lett.* **8**, 102 (1972).
2. H.I. Smith, D.L. Spears, and S.E. Bernacki, *J. Vac. Sci. Technol.* **10**, 913 (1973).
3. E. Spiller, R. Feder, J. Topalian, D.E. Eastman, W. Gudat, and D. Sayre, *Science* **1172**, 191 (1976).
4. E. Spiller, D.E. Eastman, R. Feder, W.O. Grobman, W. Gudat, and J. Topalian, *J. Appl. Phys.* **47**, 5450 (1976).
5. B. Fay and J. Trotel, *Appl. Phys. Lett.* **29**, 370 (1976).
6. H. Aritome, T. Nishimura, H. Kotani, S. Matsui, O. Nakagawa, and S. Namba, *J. Vac. Sci. Technol.* **15** (1978, to be pub.).
7. T. Nishimura, H. Kotani, S. Matsui, O. Nakagawa, H. Aritome, and S. Namba, *Japan. J. Appl. Phys.* **17**, Supple. 17-1, 13 (1978).
8. T. Oshio and M. Sasanuma, *J. Japan. Soc. Appl. Phys.* **46**, 43 (1968).
9. T. Oshio, M. Sasanuma, and T. Sasaki, *Butsuri* **22**, 285 (1967).

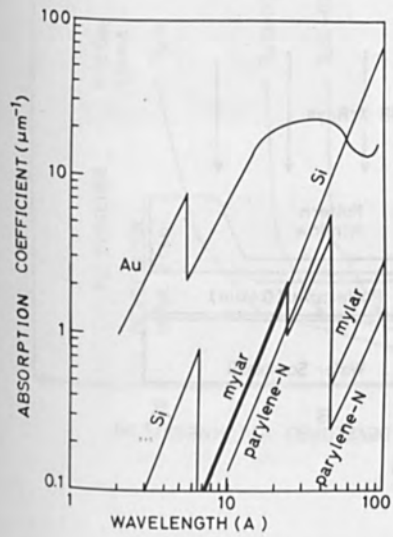


Fig. 1

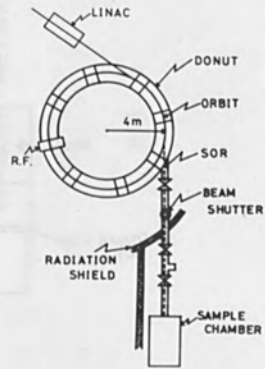


Fig. 2

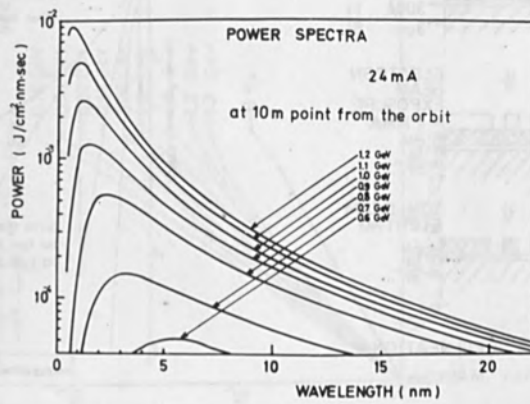


Fig. 3

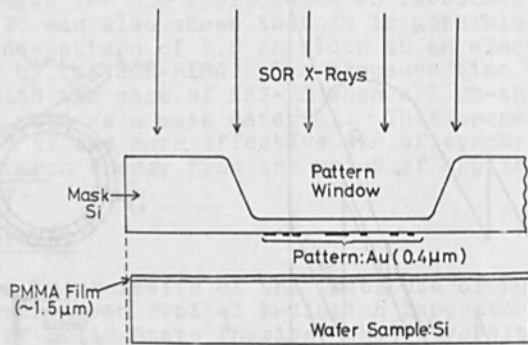


Fig. 4

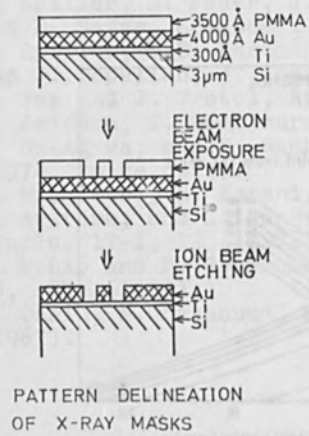


Fig. 5

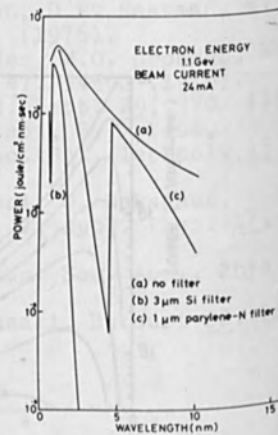


Fig. 6

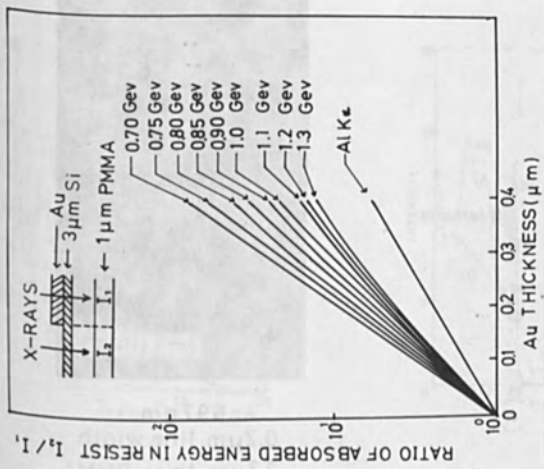


Fig. 7

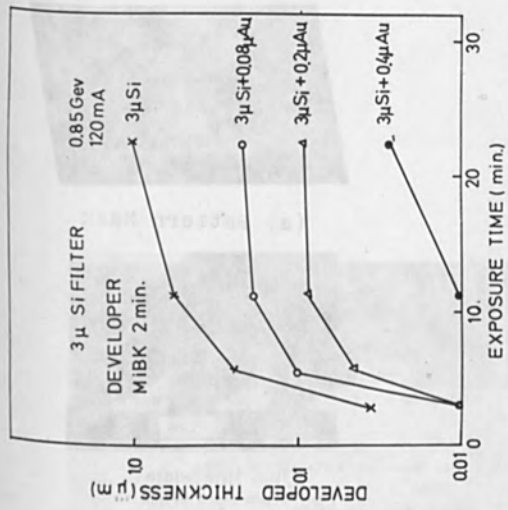
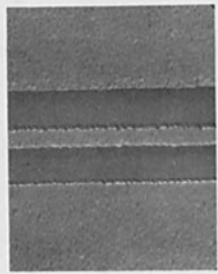
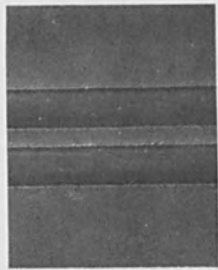


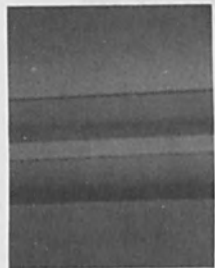
Fig. 8



(c) Au: 0.1 μm

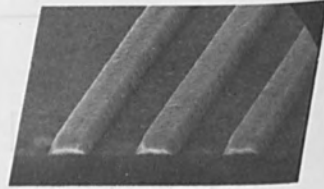


(b) Au: 0.2 μm

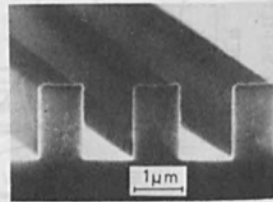


(a) Au: 0.4 μm

FIG. 9

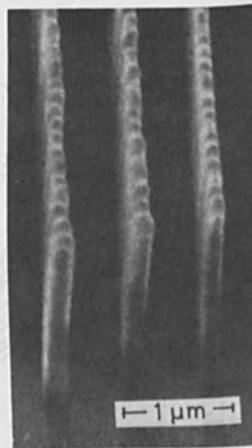


(a) Pattern Mask



1 μm line width
(b) 17 μm thick PMMA
exposure time 20min.

Fig. 10



$\lambda = 692\text{nm}$
0.2 μm line width
2.2 μm thick PMMA

Fig. 11

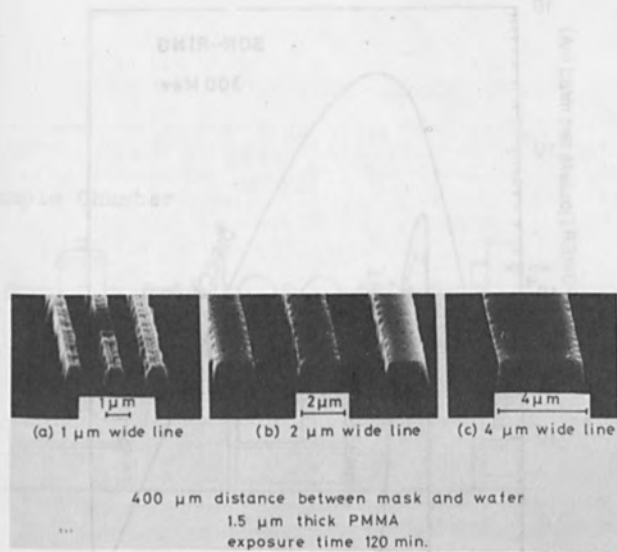


Fig. 12

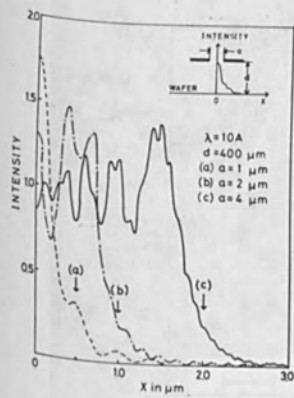


Fig. 13

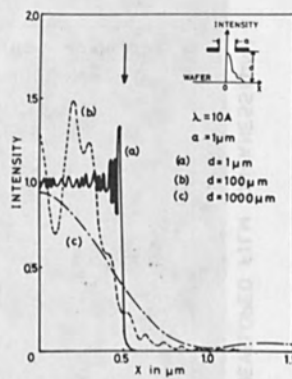


Fig. 14

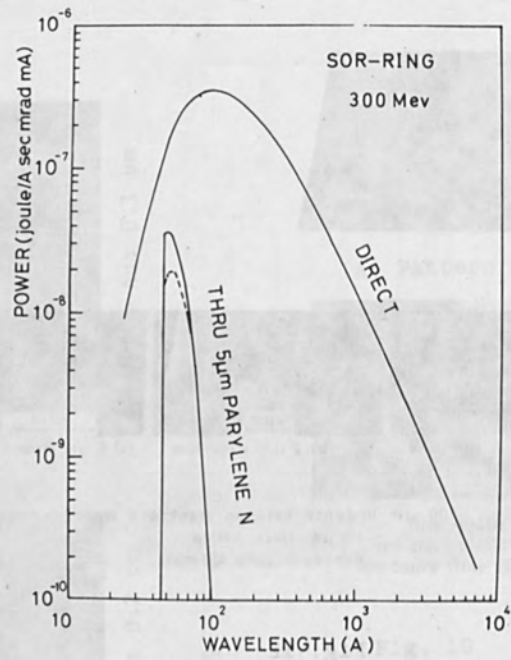


Fig. 15

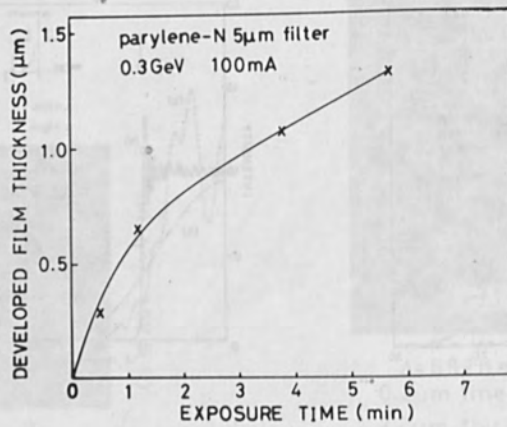


Fig. 16

MAGNETIC BEAMLINE DEVICE FABRICATION USING X-RAY LITHOGRAPHY

Sample Chamber

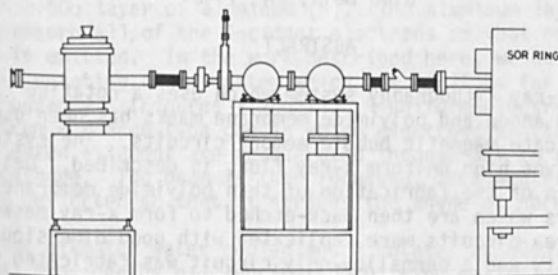


Fig. 17

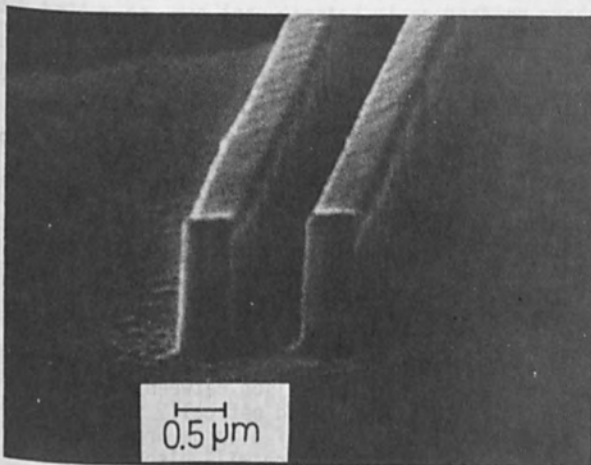


Fig. 18

MAGNETIC BUBBLE DEVICE FABRICATION USING X-RAY LITHOGRAPHY

B. F. Stein and M. J. Casey
Sperry Univac
P.O. Box 500
Blue Bell, PA 19424

ABSTRACT

An x-ray lithography system which uses a rotating aluminum anode and polyimide membrane masks has been used to replicate magnetic bubble memory circuits. The system, which gives high uniform x-ray flux, is described. Details are given of the fabrication of thin polyimide membranes on Si wafers which are then back-etched to form x-ray masks. Large area circuits were replicated with good dimensional uniformity and a permalloy-only circuit was fabricated with a large operating range. Replication of an e-beam resolution pattern demonstrated 0.2μ resolution.

INTRODUCTION

At present, the minimum feature size in magnetic bubble device circuits is limited by optical lithography to approximately 1μ - 2μ . Higher density devices under development require replication of sub-micron features and x-ray lithography (1-4), which offers high resolution over large areas, is an attractive technique.

Soft x-ray systems have evolved from stationary sources such as the modified electron beam evaporator used by Smith (1) and the air cooled anode used by Sullivan and McCoy (2) to rotating anode systems described by Maydan, et al (3) and by Wardley, et al (4).

The x-ray flux obtained in stationary systems, which must be operated so that no material is evaporated, is limited by heat dissipation. A large increase in dissipation, and therefore in flux, is obtained by using a rotating, water cooled anode because of its larger effective surface area. Aluminum ($\lambda=8.34 \text{ \AA}$) is a reasonable choice for a target material because of its large thermal conductivity, high intrinsic resolution (the mean free path of its photoelectrons is only 400 \AA), and high contrast in masks using gold as an absorber.

We shall describe a rotating anode system and a procedure for making thin polyimide masks. A comparison between the quasi-static characteristics of x-ray fabricated and optically fabricated bubble circuits will be given. Replication of a large area bubble circuit and an e-beam written resolution pattern will also be described.

X-RAY SOURCE

The development of soft x-ray rotating anode systems has been slowed by the mechanical limitations associated with the high speed rotation of aluminum and corrosion problems introduced by water cooling. Recently a technique has been developed to coat a copper anode with a 50 μ layer of aluminum (5). The aluminum layer is thick enough to absorb all of the incident electrons so that only Al radiation is emitted. In the work described here, we have used a Rigaku SX-4 rotating anode system which was modified for use in x-ray lithography (Figures 1 and 2). A uniform electron beam is obtained from a Pierce type gun in which electrons emitted from a directly heated filament are accelerated through 3kV to a shaped tantalum cathode. The beam is then focussed, accelerated, and electrostatically deflected so that it strikes the anode at normal incidence.

The 99mm diameter water cooled anode rotates at 6000 rpm with the vacuum seal provided by oil lubricated "O" ring seals. Separate guns are used which provide 2mm and 5mm spot sizes for which the maximum operating parameters are 20kV, 95mA (1.9kW) and 20kV, 350mA (7kW), respectively. In addition to x-rays, both back-scattered and secondary electrons are emitted when the primary beam strikes the target. These would produce undesirable, non-uniform exposures and are absorbed by a 25 μ thick 25mm diameter beryllium window placed between the target and the sample. The beam divergence is limited to 15 $^\circ$ by the size of the beryllium window. With a take-off angle of 30 $^\circ$ the flux uniformity is 10%. The radiation passes through the Be window into a sample chamber which is evacuated. An option to back-fill with helium gas was incorporated since heating produced by absorption of the x-rays may differentially distort the mask and substrate, giving poor resolution. Helium, at a pressure of a few mm, acts as an effective heat transfer medium without significant attenuation of the x-ray flux.

Both mask and substrate are retained in a holder which allows free vertical motion. Before the chamber is evacuated, the substrate and mask are held separated. This prevents a layer of air from being trapped between the mask and the substrate. After the chamber is evacuated, the substrate is translated vertically by means of a screw adjustment until it is either in contact with the mask or is separated from the mask by a shim of suitable thickness. The exposures to be discussed here were made with the chamber evacuated to 10⁻⁶ torr.

The source substrate distance was chosen to be 160mm so that a 38mm diameter wafer could be exposed. With typical operating conditions using the 5mm gun (18kV, 290mA), the exposure time is 60 min in PMMA and 5-7.5min in PBS (6). Mask-substrate separation was kept within 3 μ so that penumbral blurring is expected to be less than 0.1 μ .

MASKS

The thickness of an x-ray mask is a compromise between absorption and mechanical strength. For Al radiation, membranes $< 6\mu$ in thickness are used. This has led to the development of special techniques for forming and patterning thin, strong membranes. The pattern to be copied is usually formed in gold, which is a good absorber of aluminum radiation. X-ray masks were fabricated on silicon (7), mylar (8), kapton, and polyimide membranes. The polyimide membranes which were used in the work described here combine the surface qualities of silicon, the strength of mylar films, and high transmission. Representative values of transmission coefficients are: 2μ polyimide, 0.83; 6μ mylar or kapton, 0.53; 4μ Si, 0.46; and 12μ mylar or kapton, 0.28. The technique to form 2μ thick polyimide membrane masks is shown schematically in Fig. 3. It is similar to that of Flanders and Smith (9) but it eliminates the transfer and bonding of the membrane to a support frame. The membranes are fabricated on silicon wafers $250\text{--}375\mu$ thick and 51mm in diameter with one polished side. The polyimide material is PYRE-ML (RK-692) (duPont) and is supplied as a viscous lacquer. The lacquer (unpolymerized polyamic acid) is applied to the polished side of the silicon wafer by spin coating using a photoresist spinner. At 3500 rpm, a 2.0μ film is produced. The film is dried by baking for 16 hours at 150°C and polymerized by baking for 2 hours at 380°C .

A plating base of 200 \AA chromium and 300 \AA gold is then deposited on the polyimide by vacuum evaporation. The wafer is coated with a resist such as PMMA or AZ1350J and the circuit geometry is produced by the appropriate lithography technique using either electron beam or optical exposure. After development of the resist, the absorber pattern is formed by electroplating gold using a commercial plating solution. A thickness of 5000 \AA is sufficient to absorb 90% of the incident x-ray flux. After plating, the thin plating base is removed by ion milling.

The final step is the etching of the silicon substrate from the back side to form the membrane. The etchant is a 5:3:3 solution of concentrated nitric, acetic and hydrofluoric acids and is used at room temperature. To provide the necessary support ring for the membrane, the silicon is mounted in a specially designed, Teflon etching fixture. An additional function of this fixture is to protect the gold absorber on the front surface and the polyimide-silicon interface from attack during etching. A typical substrate is etched in less than 15 minutes. The polyimide film is not attacked by the etchant so non-uniformity in etching does not damage the film. The finished membrane is under tension, producing a flat, uniformly-taut structure. Figure 4 is a photograph of a typical mask.

RESULTS

Large Area Mask

A mask consisting of a 5x5 array of 6mm square 64K bit bubble circuits, produced optically by a pattern generator, was used to fabricate an x-ray mask. This circuit, whose 1μ features are close to the optical limit, provided a convenient test of the x-ray mask fabrication procedure, of the x-ray exposure parameters for the rotating anode system, and of the pattern uniformity over a wafer.

Portions of the 64K pattern from the original optical mask, the polyimide membrane x-ray mask, and the pattern replicated in PMMA on a 38mm diameter silicon wafer are shown in Fig. 5a,b, and c.

Notice the high surface quality of both the polyimide mask and the PMMA replica. Variations in the circuit dimensions in the PMMA image over the entire wafer were less than 0.25μ , while the gaps are within 0.2μ of those on the original mask.

Half-disk Bubble Circuit

A half-disk bubble circuit was used to compare the performance of a conventionally fabricated device with one made using x-ray lithography. The permalloy-only circuit consists of a closed loop of half-disk elements with a minimum feature size of 2μ .

A garnet wafer, coated with a thin permalloy plating base and PMMA, was exposed through an x-ray mask in the form of a stencil. Permalloy was plated into the stencil pattern using a nickel-iron sulfamate bath. Pattern coverage was complete and the 2μ features were maintained to 0.2μ .

Bubble circuit performance is routinely evaluated by moving a bubble through the circuit. Figure 6 is a comparison of the quasi-static operation of the half-disk circuit replicated optically and with x-rays. H_R is the rotating magnetic field which magnetizes the permalloy half-disk elements and moves the bubble around the circuit. H_B is the bias field, applied perpendicular to the plane of the wafer, which stabilizes the bubble. The operating range at any rotating field is given by the difference in bias field between the upper and lower curves. Thus the area between the curves simply represents the region of satisfactory device operation. The results demonstrate that equivalent performance was obtained for the two circuits.

E-Beam Written Resolution Pattern

A resolution pattern consisting of closely spaced lines was written by e-beam in PMMA on polyimide coated silicon wafers (10). An x-ray mask was fabricated and was used to replicate the pattern onto PMMA/

Au coated silicon wafers.

The x-ray replicated pattern shown in Fig. 7 was delineated in 1000 Å of Au by ion milling. The linewidths within the pattern differ because of uncorrected electron scattering effects during the e-beam writing of the mask. The smallest gap resolved was 0.25 μ . The dimensions of the pattern replicated in gold are within 0.2 μ of the dimensions in PMMA on the mask.

CONCLUSIONS

An x-ray lithography system with a rotating anode source of aluminum radiation and 2 μ thick polyimide membrane masks were used to fabricate magnetic bubble devices. The high flux obtained from the source enabled a large area to be uniformly exposed and significantly reduced exposure times (compared with stationary sources) while retaining high resolution. A simplified technique was developed to form polyimide membrane masks on silicon substrates. The submicron capability of the system was demonstrated by replication of an electron beam written resolution pattern.

ACKNOWLEDGMENTS

The authors wish to thank H. Wetterskog for his help in performing the x-ray exposures, L. Beck for polyimide mask fabrication, and W. Doyle and R. Josephs for valuable discussions and comments on the manuscript. We also thank F. Sewell, Jr., J. Donahue, N. Wittels, and C. Youngman of the Sperry Research Center, Sudbury, MA for helpful discussions and for the e-beam written resolution patterns.

REFERENCES

1. D. L. Spears and Henry I. Smith, *Solid State Technology* **15**, 21 (1972)
2. P. A. Sullivan and J. H. McCoy, *J. Vac. Sci. Technol.* **12**, 1325 (1975)
3. D. Maydan, G. A. Coquin, J. R. Maldondo, J. M. Morgan, S. Somekh, and G. N. Taylor, *Proceedings of the International Conference on Microlithography (Paris, 1977)* p. 195
4. G. A. Wardley, E. Munro, and R. W. Scott, *Proceedings of the International Conference on Microlithography, (Paris, 1977)* p. 217
5. This technique was developed by Rigaku Corporation, Tokyo, Japan. The anode is incorporated into their SX-4 soft x-ray system.
6. PBS is a proprietary resist developed at Bell Telephone Laboratories and available from Mead Chemical, Northweye, Missouri

7. Stephan Bernacki and Henry I. Smith, Proc. of 6th International Conf. on Electron and Ion Beam Science and Technology (Electrochemical Society, 1976) p. 536
8. Dan Maydan, Gerald A. Coquin, Juan R. Maldondo, S. Somekh, David Y. Lou, and Gary N. Taylor, IEEE Trans. on Electron Devices ED-22, 1429 (1975)
9. D. C. Flanders and Henry I. Smith, Proceedings of the 14th Symposium on Electron, Ion, and Photon Beam Technology, J. Vac. Sci. Technol. (to be published)
10. The e-beam patterns were written at the Sperry Research Center, Sudbury, MA, on an ETEC LEBES electron beam system.

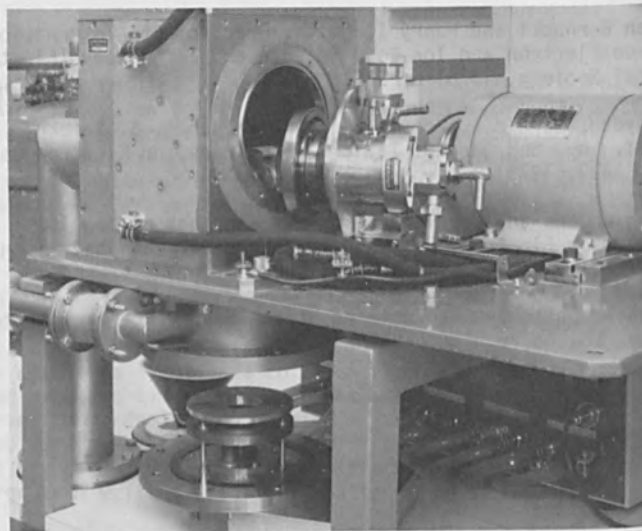


Figure 1. Photograph of rotating anode system

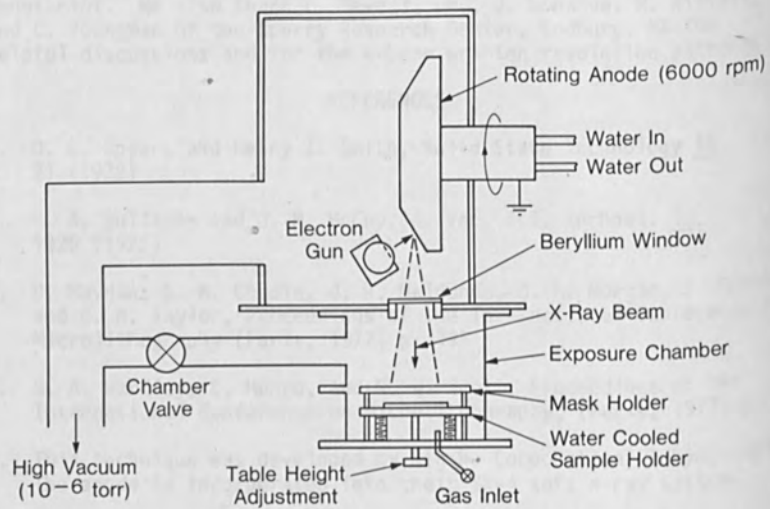


Figure 2. Schematic diagram of rotating anode system.

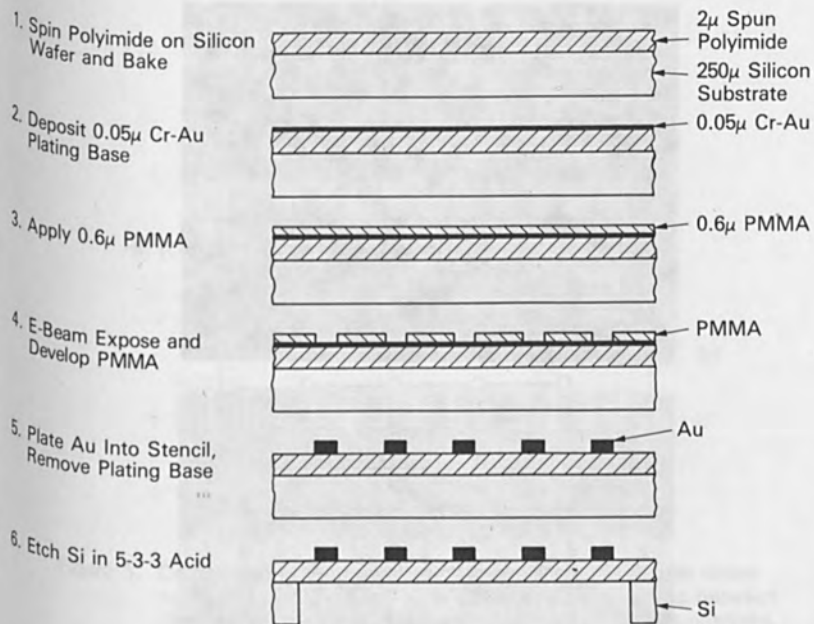


Figure 3. Schematic diagram of the polyimide mask fabrication process.

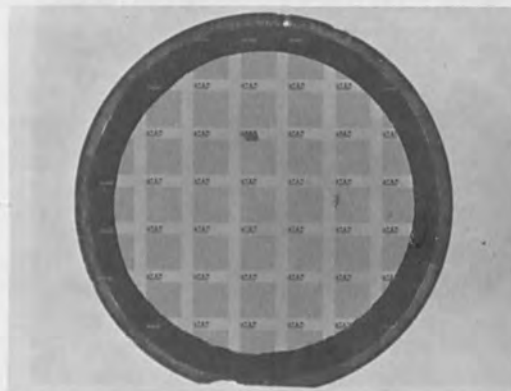


Figure 4. Photograph of a 61 mm diameter polyimide x-ray mask. The mask is patterned with 6 mm square 64K bit bubble circuits.

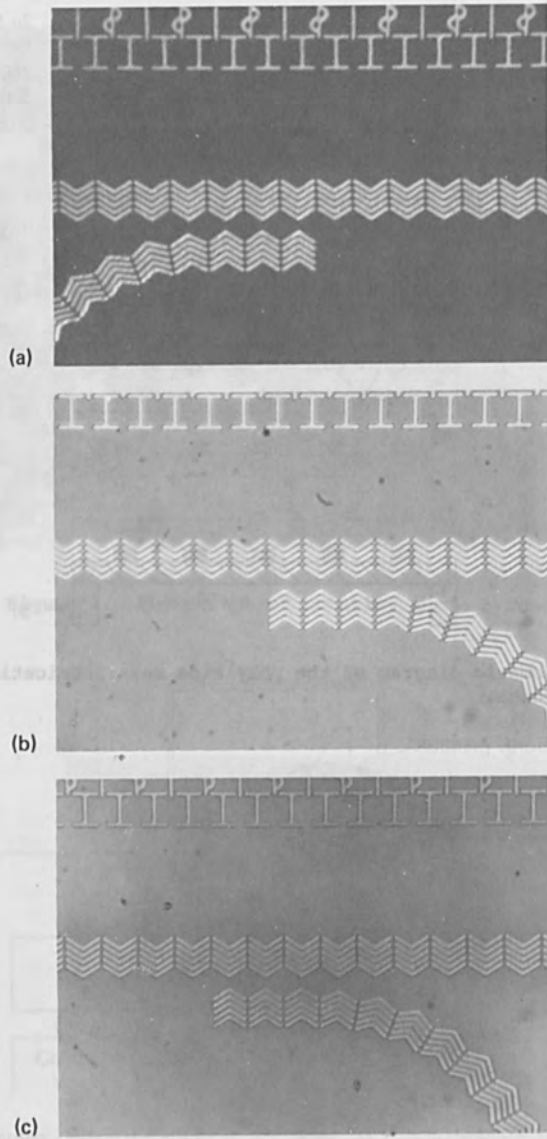


Figure 5. Photographs of (a) a portion of a 64K bit bubble circuit on an optical mask, (b) an equivalent area on a polyimide coated x-ray mask, and (c) the pattern replicated by x-rays in PMMA.

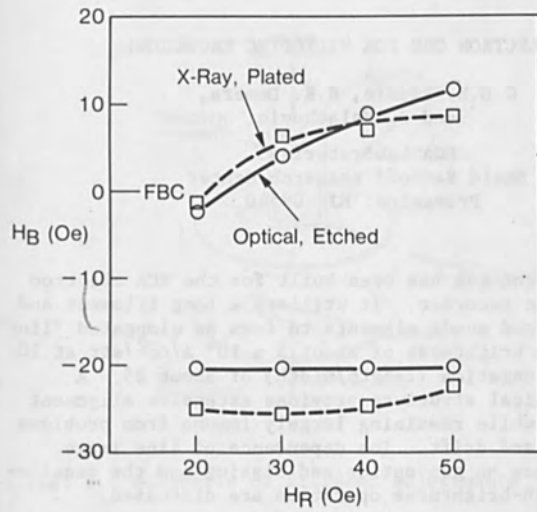


Figure 6. Comparison of the operating characteristics of a bubble circuit replicated by optical and x-ray lithography. In the area between the respective curves, satisfactory device operation is obtained.

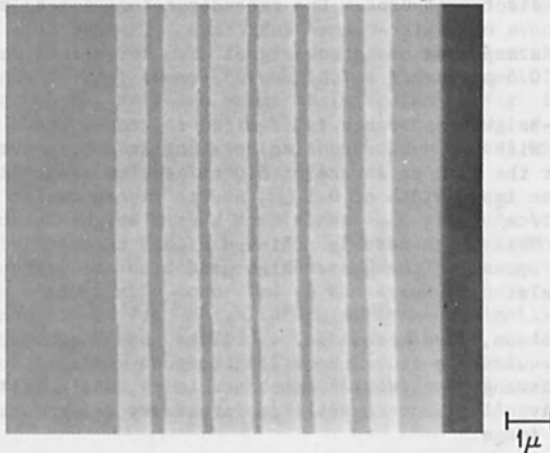


Figure 7. SEM photograph of the e-beam written pattern replicated by x-rays. The texture of the lines is caused by a residue of PMMA.

AN ELECTRON GUN FOR VIDEODISC RECORDING

G.H.N. Riddle, R.R. Demers,
and J. Valachovic

RCA Laboratories
David Sarnoff Research Center
Princeton, NJ 08540

An electron gun has been built for the RCA electron beam VideoDisc recorder. It utilizes a long filament and slotted grid and anode elements to form an elongated "line" source with a brightness of about 5×10^4 A/cm²/str at 10 keV and an elongation (length/width) of about 35. A unique mechanical structure provides extensive alignment capabilities while remaining largely immune from problems of vibration and drift. The dependence of line image characteristics on gun optics and biasing and the requirements for high-brightness operation are discussed.

Introduction

The electron gun used on the RCA electron beam VideoDisc recorder (1,2) is unique in many respects. It utilizes an elongated filament and slotted grid and anode elements to produce an elongated, line-shaped electron source. The recorder column images this source onto the groove of resist-coated substrate. The use of a line-shaped image permits exposure of narrow signal elements with a wavelength as short as 0.5 μ m across a 2.5 μ m wide groove (1).

A high-brightness source is required to record these signals at real time. With the substrate disc rotating at 450 rpm, the groove passes under the beam at a rate of 350 cm/sec. at inner disc radii. To provide an image width of 0.1 μ m, and to expose resist at a 2×10^{-6} cmb/cm² dose, the source must have a brightness of 5×10^{-4} A/cm²/str. This brightness is achieved with a thermionic tungsten filament by operating the gun at high grid bias and high emission current levels.

In addition, good mechanical stability and freedom from thermal drifts is required to record hour-long program material. A unique mechanical arrangement provides such stability, while still permitting extensive alignment capabilities necessary to produce a symmetric line image.

Gun Structure

The gun elements are shown schematically in Fig. 1.

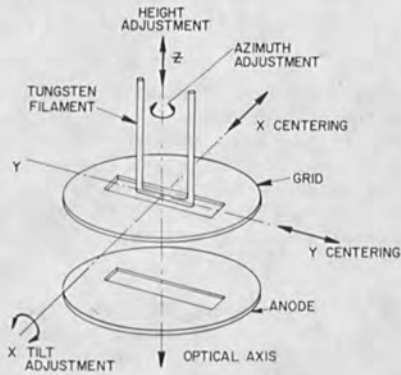


Fig. 1. Schematic of filament adjustments.

The grid and anode are slots 0.375 in. long and, respectively, 0.04 and 0.06 in. wide. They are separated by 0.10 in., and are fixed in position with respect to each other and to the gun body. Small changes to these dimensions do not substantially affect the results presented below, except that increases in the grid width force operation at increased grid bias voltages to achieve equivalent source brightness.

The filament is a 0.005-in. diameter tungsten wire bent to have an emitting length of 0.04 in. The position of the filament is adjustable with respect to the grid and anode as indicated in Fig. 1. In addition to the usual translational motions, proper centering of the line filament requires rotational motion about the vertical axis and tilting motion about an axis across the filament length.

The grid and anode are small, easily replaced elements mounted in a common assembly shown in Fig. 2. In Fig. 2a the grid element and its holder have been removed to expose the anode. The anode is mechanically and electrically connected to the assembly base. The grid is shown in place in Fig. 2b; although it is mechanically rigid with respect to the assembly base and, therefore, to the anode, it is electrically isolated from the anode by a ceramic insulator. Electrical connection to the grid is made through flexible metal contacts, apparent in Fig. 2, which press against a clamp surrounding the filament base.

The filament assembly appears in Fig. 3. The filament is mounted on a ceramic base which is clamped to the end of a high-voltage vacuum feedthru. Electrical connections to the filament and grid are made

via this feedthru. The connection to the grid is completed by the filament clamp and the flexible contacts surrounding the grid as explained above.

The gun housing which positions the filament with respect to the grid and anode is shown in cross-section in Fig. 4. The grid/anode assembly is mounted to the lower part of the gun housing; it can be withdrawn through the bottom of the gun for replacement and cleaning. The filament holder attaches to the upper part of the gun housing on an O-ring seal; it can be rotated about the vertical axis on this seal to achieve proper azimuthal filament alignment with respect to the grid and anode.

A vertical thread surrounding the upper part of the gun housing provides motion along the vertical axis. An axle, whose extension passes through the plane of the grid, permits tilt of the length of the filament in the vertical plane. Dovetail slides and micrometer drives provide translation motion in the horizontal plane.

A bellows completes the vacuum seal between the upper and lower parts of the gun housing. Only rotation about the vertical axis requires motion on an O-ring seal; all other adjustments can be made via the bellows seal, thereby virtually eliminating vacuum leakage problems. All adjustments can be made while the gun is under vacuum and operating. Once proper filament alignment is achieved, the upper housing can be rigidly clamped in place.

The complete gun is shown in Fig. 5. Its structure has been found to be both highly flexible, permitting good alignment of the gun elements, and mechanically stable, free of vibration and thermal drifts. Such stability is important when the gun must be operated without adjustment for extended periods under production conditions. Although, as a precaution, filament centering is routinely checked at the beginning of each recording day, it is seldom necessary to reposition filaments following their initial alignment. Filament drift during gun operation has not been a problem.

Electron-Optical Characteristics

In order to produce a high-brightness source the gun must be operated with a high grid bias potential, up to -2.0 keV, and large emission currents, up to 4.0 mA, must be drawn. Ordinary self-bias gun operation would be unsatisfactory in this application because adjustments or random fluctuations to the emitted current would produce changes in the beam voltage and upset focusing in the column lenses. A special gun controller was therefore built as diagrammed in Fig. 6, to provide proper biasing. This controller is based on an earlier design by R. F. Sanford (unpublished). All components are electrically floated at the -10-keV filament potential, and extensive use is made of fast zener diodes to protect the circuitry

from damage due to electrical arcs. The grid bias potential is provided by a regulated, programmable 0-3 keV dc power supply. This supply is controlled by a comparator which senses the total filament emission and adjusts the bias supply to limit this emission to a preset value independent of filament temperature. The filament heating current is also provided by a programmable dc power supply. The magnitudes of filament heating current, emission current, and grid bias voltage are all indicated on digital panel meters.

Gun operation with this controller is similar to self-bias operation, except that the emission current can be adjusted continuously over a wide range, and the potential drop between the high voltage supply and the filament is negligible.

The gun is operated in a saturated condition. As with pointed filaments, saturation is achieved by increasing the filament heating current until the beam converges to a sharp cross-over with maximum brightness. In the case of the line source, as the filament temperature increases, a "halo", comprised of weak lines parallel to a central emission line and spots beyond the ends of this central line, converges into a strong line image, and the brightness along the length of this image approaches a maximum. At saturation, the current distribution along the length of the line image is symmetric about the image center and remains substantially unaltered with further increases in heating current.

Under saturated conditions the magnitude of the grid bias potential relative to the filament is strongly dependent on the position of the filament with respect to the grid and nearly independent of other variable parameters such as the total emission current. For example, moving the filament from a position about 0.03 in. behind the grid plane to about 0.01 in. behind this plane causes the grid bias potential required to maintain a constant saturated emission current to increase from -500V to -2000V. However, increasing the emission from 0.5 mA to 4.0 mA at a given filament position requires less than 50 V change in bias potential. It is therefore convenient to specify the vertical position of the filament with respect to the grid and anode from the grid bias potential at saturation rather than from measured dimensions within the gun.

The line filament source studies reported below have been carried out with the gun mounted on an electron optical bench. The bench, a modified electron microscope, magnifies the source and projects its image onto a phosphor screen. This image is scanned across a Faraday collector in the center of the phosphor screen, and the current into the collector is measured. Since the collector area and the angle subtended by the beam forming the image are known, the system permits direct measurement of the distribution of brightness across the image. This brightness distribution is displayed by scanning the length of the image slowly along the Faraday collector, at the same time feeding

this scanning signal to the horizontal input of an X-Y oscilloscope. The collected current is amplified and fed to the vertical input. As the image is scanned slowly along its length, it is also rapidly scanned normal to its length across the Faraday collector, producing a sharp peak on the oscilloscope each time the image crosses the collector. The locus of the top of these peaks, some examples of which are shown in Fig. 7, represents the distribution of current, or brightness, along the image, and is referred to as the image "profile."

The current distribution across the width of the image can be displayed in a similar format by scanning the line, generally near its center, across the Faraday collector. The sensitivity of the horizontal display is generally increased by 10X when the width is scanned. Each display in Fig. 7 contains a width scan (the broad peak) superimposed on a length scan (the series of sharp peaks). Each large division in these displays represents about 60 μm along the filament length and about 6 μm across the width. Each large vertical division represents an increment in brightness of $1.3 \times 10^4 \text{ A/cm}^2/\text{str}$.

The profiles in Fig. 7 illustrate the dependence of brightness distribution along the line image on grid bias potential V_g (controlled, as described above, by the filament position along the vertical axis) and emission current, I_c . It is noted that the brightness increases with both increasing V_g and increasing I_c . Typical brightnesses obtained within the ranges of V_g and I_c studied are given in Table I.

Table I. Typical brightness and elongation of line sources at various values of grid bias potential (V_g) and emission Current (I_c).

V_g (keV)	I_c (mA)				I_c (mA)			
	0.5	1.0	2.0	4.0	0.5	1.0	2.0	4.0
	Brightness ($10^4 \text{ A/cm}^2/\text{str}$)				Elongation (length/width)			
-0.5	2.	3.	4.	5.	40	45	50	50
-1.0	3.	4.	5.	6.	30	35	35	35
-2.0	4.	5.	6.	8.	20	25	35	30

The shape of the image profile depends strongly on V_g and I_c . At low bias levels the image is longer than at high bias levels. At $V_g = -500\text{V}$ and $I_c = 4.0 \text{ mA}$, profiles begin to form wings at the ends, probably caused by emission from the filament leads. These wings disappear as the bias is increased, indicating that as the filament is moved toward the anode the emitting region becomes more concentrated near its center. There is also a tendency for the image

length to increase with I_c ; this tendency is most pronounced at high bias levels where end-effects are less pronounced.

The image width varies over a smaller range than the length, tending to decrease with increasing V_g and to increase with I_c . The increase with I_c is most pronounced at high V_g .

For practical purposes, the ratio of the length of the image to its width, referred to as its "elongation", is more important than the absolute value of these dimensions. This is because the column magnification below the gun can be adjusted to provide a final image of arbitrary size, whereas, lens aberrations aside, the image elongation and brightness remain unchanged. Typical elongations measured at various V_g and I_c are given in Table I. With increasing V_g the image length decreases faster than the width, leading to a net decrease in elongation. Both length and width tend to increase with I_c . At $V_g = -2.0$ keV, the net result is a peak in elongation near 2.0 mA. At lower $V_g = -2.0$ keV, the net result is a peak in elongation near 2.0 mA. At lower V_g , the elongation increases slowly with I_c , forming a peak at $I_c > 4$ mA (not shown in Fig. 7).

On a VideoDisc recorder the gun is normally set to operate at $V_g \approx -1.0$ keV and $I_c \approx 2.0$ mA. This provides a source with a brightness of over 5×10^4 A/cm²/str at 10 keV and an elongation in excess of 35. The distribution of brightness along the length of the image is reasonably uniform. Different filaments used on recorders vary as much as $\pm 20\%$ in brightness and elongation from the values quoted here, but given filaments generally retain their characteristics over their lifetime. Filament lifetime is normally sufficient for 25 to 30 hour-long recording sessions.

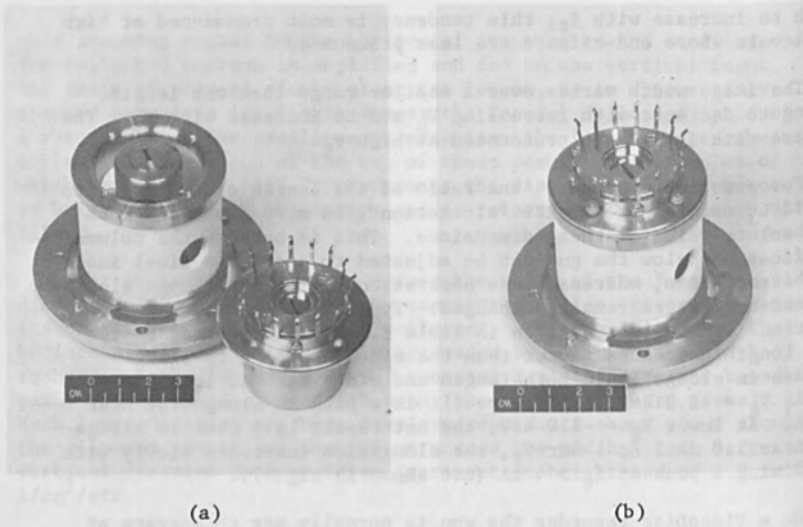
Remarks and Acknowledgements

Several different guns of this design have been built and used routinely over the past four years. Under production conditions, they have proven to be a reliable source of a uniform high-brightness line image, free of thermal drifts and mechanical vibrations.

The authors wish to thank E. G. Ramberg for suggesting the use of a line filament and undertaking an initial theoretical analysis of its operation. We are further indebted to J. H. Reisner for discussions and advice through the course of this work.

References

- (1) J. H. Reisner, G. H. N. Riddle, S. M. Zollers, L. H. Lin, E. D. Simshauser, W. P. Morewood, R. R. Demers, and J. Guarracini, "Electron Beam Recording of Masters for the RCA VideoDisc," this issue.
- (2) E. O. Keizer, "VideoDisc Mastering," RCA Review 39, 60 (1978).



(a)

(b)

Fig. 2. Grid/anode assembly.



Fig. 3. Filament assembly.

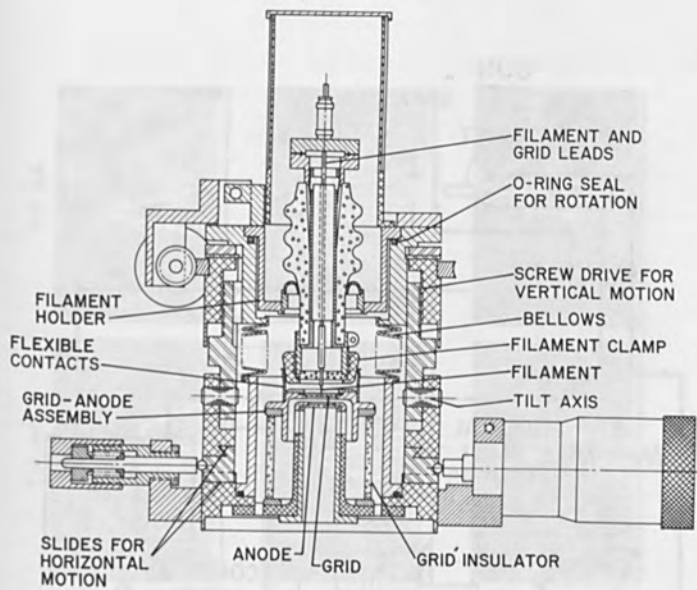


Fig. 4. (above)
Cross-section of gun.



Fig. 5. (right)
Gun exterior.

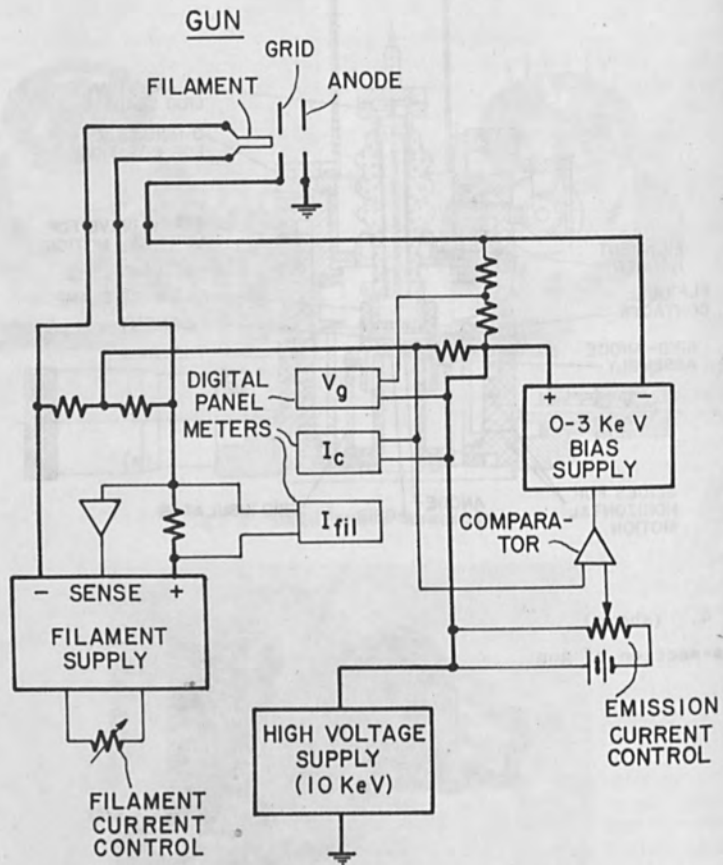


Fig. 6. Controller schematic.

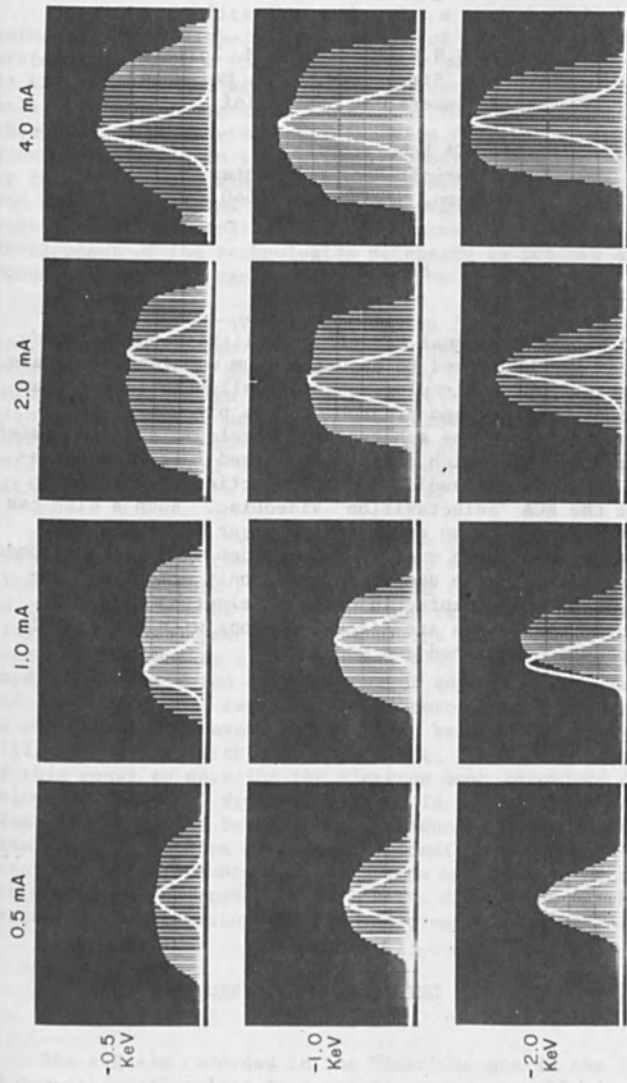


Fig. 7. Image profiles.

ELECTRON BEAM RECORDING OF MASTERS FOR THE VIDEODISC

J. H. Reisner, G.H.N. Riddle, S. M. Zollers,
L. H. Lin, E. D. Simshauser, W. P. Morewood,
R. R. Demers, J. Guarracini

RCA Laboratories
David Sarnoff Research Center
Princeton, New Jersey 08540

ABSTRACT

In a format unusual for electron lithography an electron beam has been used to expose one- μ m wavelength signals on a resist-coated circular substrate slightly larger than a phonograph record and pregrooved at a pitch of 9500 grooves per inch. The substrate is developed and replicated to form a master, which is then processed further by relatively conventional audio record production techniques to produce the RCA "SelectaVision" VideoDisc. Such a disc can be played back with an appropriate player to provide one hour per side of high quality color video with stereo sound. The technique is also useful for read-only memories. The unique problems presented in using an electron beam for "cutting" these discs are discussed along with details of the apparatus developed and used.

INTRODUCTION

Important applications exist for a method of low-cost, permanent, very high-density storage of electronically generated signals in a form that permits quasi-random access to the signals, and with a means of reproducing the signals with a high degree of fidelity. The conventional audio phonograph disc provides this function for electronically-generated signals in the audio-frequency range, typically up to 20 kHz. Its simplicity of operation, the performance and ease of retrieval of the stored signals, and the low cost of multiple replication have spurred interest in the development of the technologies necessary to achieve analogous systems that can handle high density signals.

The RCA "SelectaVision" VideoDisc is just such a system. It stores video and audio information on a disc resembling an audio phonograph record, and plays back that information as a high quality color television image with high quality stereo sound. That portion of the system that initially converts the electronically generated signals into a topographical pattern on a substrate through which ultimately VideoDiscs are fabricated is called the recorder.

Development of recorders has been an integral part of the development of the total VideoDisc system. Initially, electron beam recorders were used, and they were brought to the high states of performance and reliability essential in the developmental phases of the VideoDisc system. Concurrently, but at a slower pace, electromechanical recording was perfected and, because of advantages of cost and simplicity, has replaced the electron beam instruments in production. However, the electron beam recorders are still used in research and development. It is the purpose of this paper to describe the electron beam recorders developed. The total VideoDisc system is sufficiently complex that it cannot be adequately discussed herein except insofar as the system dictates the conditions which determine the performance specifications of the recorder. The reader is referred to a definitive discussion of the system in the literature⁽¹⁾ for additional information.

NATURE OF THE RECORDING

The signals recorded in the VideoDisc are in the form of topographical relief in a spiral groove, roughly analogous to the audio phonograph and at a greatly reduced scale

(Figures 1 and 2). For example, the groove spacing has been reduced from approximately 130 μm on the audio disc to 2.67 μm on the VideoDisc, while the wavelength has been scaled down from approximately 7.5 μm to 0.5 μm . The result is an information density increase in the VideoDisc of the order of 800 times over that of the audio disc. As can be seen from Figure 2, the signal relief is generated in well-defined grooves which have a pitch of about 9500 grooves per inch and are 2.67 μm wide as stated above. The signals--which term is used loosely to refer to the relief corresponding to the electronic signals--are formed radially across the grooves. A wavelength comprises a hollow trench and an adjacent land and ranges from 0.5 μm to 1.5 μm in length depending on the frequency of the corresponding electronic signal and the radius on the substrate at which it is recorded. The depth of the trench below the land, i.e., the signal amplitude, is between 700 and 1000 Angstroms. The trenches extend across more than 75 percent of the groove, and, being half a wavelength wide, are sometimes as narrow as 0.25 μm . In practice, this signal relief is generated by using a narrow line electron beam to expose an electron resist in the grooves; and the exposure of the trenches and the non-exposure of lands are generated by turning the beam on and off in synchronism with the electronic signal to be recorded as the groove moves under the beam. Thus the signal recording is essentially an on and off process from which the recorded signal relief would ideally be rectangular. Actually, in practice, the resulting signals look nearly sinusoidal at the shorter wavelengths.

THE RESIST-SUBSTRATE

A brief description of the electron resist coating, the exposures, and the development of the exposed resist is necessary if one is to understand clearly the conditions for operation of the electron beam recorder. The pre-grooved metal disc which is coated with electron-resist is called the substrate, a term used in audio phonograph record manufacturing. The metal disc is very accurately machined. It is fourteen inches in diameter, flat to ± 7 μm , and pre-grooved from 6 inches radius to 2.7 inches radius. The grooves are V-shaped with a ninety-degree angle between the sides and the pitch of 9524 grooves per inch is rigidly held to maintain uniformity of groove dimensions. The surface of the metal disc is coated with a solution of electron resist which settles, as the solvent evaporates, into the V grooves to provide nearly sinusoidal grooves

about 0.2- μm deep in the resist surface. The coating technique was determined empirically. It involves some art, but is very reproducible. Figure 4 shows diagrammatically the resist covering the grooved metal disc. The depth of the resist at its deepest point is approximately 1 μm .

A positive resist is used. Thus, the development of the exposed areas, such as diagrammed in Figure 4, results in the signal trenches shown in Figure 2. From the standpoint of signal geometry neither the exposure nor the beam voltage is critical as long as the overall system is adjusted to accommodate to their variations. Exposure can range from 1 to 3×10^{-6} coulomb/cm², and beam voltage from 7 to 15 KV. Operation outside of these ranges results in inferior signal profiles ranging from loss of signal depth, to rounding of contours and increase in surface roughness depending on the direction of deviation from the norm. In practice, a somewhat arbitrary exposure specification of $(1.9 \pm 0.06) \times 10^{-6}$ coulomb/cm² at $10,000 \pm 1$ V₀H beam energy is used for routine recording. With such reproducibility of exposure, the important variables in the resist system become the formulation of the resist and its subsequent processing. The parameter most difficult to control is development, which occasioned the work of L. Lin⁽²⁾ in automatic control of development.

THE MECHANICAL SYSTEM

The mechanical equipment involved in exposing the 14" diameter disc can be visualized from Figures 3 and 6. During exposure, the axis of the electron beam is fixed. The disc simultaneously rotates and is traversed radially to maintain the spiral groove under the beam. Figure 3 shows the recorder in operating condition. For loading the master onto the turntable the top plate of the vacuum chamber, which also supports the electron-optical column and its vacuum system, is raised slightly and rolled on a track to the rear of the instrument, Figure 6, thus giving access to the turntable.

The substrate is centered and leveled on the turntable by eye to within ± 5 μm lateral and also vertical run-out. The lateral alignment is made using an optical microscope aligned coincidentally with the recording beam position on a removable alignment fixture (Figure 6). Near its outer circumference the substrate has several circular alignment grooves cut on the same center as the spiral record grooves. These circular alignment grooves are observed with the

microscope to indicate run out of the substrate. The same fixture which supports the microscope also supports a capacitive height gauge used in leveling the substrate and positioning it at a given working distance with respect to the final lens of the column.

The turntable is supported on an oil thrust bearing, and is driven by a hydraulic motor. The turbine of the motor has a smooth periphery which reacts to driving jets of oil to produce a pulse-free rotary motion. Since the oil turbine is in the vacuum, diffusion pump oil is the driving fluid. The oil is automatically stored under vacuum when it is not being used to drive or support the turntable. Since oil droplets are produced by the turbine and are highly mobile in the vacuum, moderately complex mechanical shielding is necessary to prevent oil contamination of the substrate and the tachometer. The turntable must also be grounded through a brush system to prevent electrostatic charging by the oil drive. In turn the substrate is insulated from the turntable so that work current can be measured, and a second brush in the form of a mercury contact is provided for this in the center of the support bearing.

In VideoDisc recording it is important that the rotational speed of the turntable be very stable. In practice, speed stability of three parts per million is regularly maintained in the recorders. This is achieved by using a heavy turntable, i.e. 25 kg., for high inertia and oil bearings with low frictional loss. Also, there is no windage loss during rotation in the vacuum chamber. Additionally, constancy of speed is maintained by a closed loop servo in which the signal from an optical tachometer, attached to the turntable, is compared to the vertical sync frequency generated by the video signal source. The error signal so generated is used to control the rate of oil flow in the turbine driving the turntable.

The turntable, motor and bearing assembly is mounted on the traversing carriage which itself is floated by oil pressure on bearing pads sliding on accurate ways. A very smooth translation is provided by a precision lead screw driven by an externally mounted electric motor through a vacuum seal in the wall of the vacuum chamber.

ELECTRON OPTICAL SYSTEM

The electron optical system is conventional in its general configuration. It is comprised of an electron gun at the top, followed by alignment means, a condenser lens, a

field limiting aperture, a drift tube, a reducing lens, a blanker, a beam limiting aperture, deflection coils, alignment means, stigmators, and a second and final reducing lens (Figures 9 and 10). The electron gun is characterized by its ability to provide a line source with a length to width ratio characteristically 35:1, and with a brightness of 5×10^4 amps/sterad/cm². The electron gun is the basis of a treatise in itself.⁽³⁾ It is not discussed further in this paper, which deals primarily with those aspects of electron lithography peculiar to VideoDisc recording.

The design of the electron optical system used in VideoDisc exposure is unique in several aspects in order to meet the unusual conditions imposed by the disc recording format. These conditions are summarized as follows.

1. The recordings are made at real time, i.e., at the same rpm as playback, typically 450 rpm.
2. The beam is fixed in position and the work moves under it.
3. The beam must remain centered in the groove in the substrate.
4. The linear speed of the work surface under the beam is proportional to its radial distance on the disc.
5. The signal elements must be radial.
6. Vertical run-out of the disc surface normally exceeds the depth of focus of the final lens.
7. Fringing fields from the final lens can induce eddy currents in the rotating metal substrate.

The requirement that recording be done at real time sets a large minimum to the current needed in the line image. The current in the line image can be expressed $i_0 \ell = 1.6 \times 10^{-3} \ell R \eta Q$, where i_0 is the current per μm length of image, ℓ is the length of the image in μm , R is the radius in inches where the beam strikes the substrate, η is the revolutions per second of the turntable, and Q is the exposure in coulomb/cm². The current required in the image is seen to be proportional to the rotational frequency at a given radius. In actual practice for an exposure of 2×10^{-6} coulomb/cm², the current i_0 must be 70×10^{-9} amps at the inside radius of the disc, and 130×10^{-9} amps at the outside. The exposure is not related to the half intensity width of the line image, if that half width is

less than 20% of the wavelength being recorded. However, to make full use of the resolution of signal detail, the width of the line image is held less than $0.12 \mu\text{m}$. In order to reduce to a minimum the brightness required of the gun, thus extending filament life, the angular aperture limiting stop (Figure 10) is made as large as possible commensurate with the above cited image width requirement. In practice, the angular aperture of the final lens is 0.038 radians. The spherical aberration coefficient of the final lens is 1.2 cm, and is not limiting spot size. The major limitation to further reduction in size of the image is higher order astigmatism. However, since the image size is adequately small no attempt has been made to make further lens corrections. In the course of an hour, the rotation of the disc combined with its slow horizontal translation presents to the beam the entire disc area from 5.7 to 2.8 inches radius. For exposure purposes the electron beam is essentially fixed. Consequently, no major beam deflection is required and the working distance of the final lens can be made short (i.e., 6.0 mm). This in turn permits the use of a short focal length final lens with its concomitantly small spherical aberration constant. As stated above, the result is a maximum utilization of beam energy in the final image of the source.

Actually, there is a small deflection applied perpendicular to the groove to keep the beam centered in the groove. A simple feedback system (Figure 5) is used to keep the beam in the groove. If the beam becomes displaced laterally in the groove, the back-scattered electrons increase in an opposite direction. Silicon detectors placed on opposite sides of the groove detect the unbalance in backscatter and cause the beam deflector to return the beam to groove center. A second and much slower correction is used to keep the groove under the mid-position of the beam. To achieve this, the long term unbalance of the signal to the beam deflectors is used to speed up or slow down the turntable traversing motor. This also makes it possible to record in a wide range of groove pitches. The backscatter detectors are shown in Figure 7, on each side of the magnetic lens bore. In operation they are about 1 mm above the resist surface. They are also used to operate the recorder as an SEM on a test object to orient the source, to focus its image, and to measure its dimensions.

The length of the signal elements across the groove is as much as five times greater than the signal wavelength. There is a pickup electrode on the rear surface of the playback stylus which is about the same length as a signal trench and only a fraction of a wavelength thick. In playback, any misalignment of over a degree between signal element and pickup electrode will reduce output. The simplest reference

to assure their alignment is that both are oriented radially with the record. With the use of a line electron source it becomes necessary to provide an independent means for physically orienting the image of the source on the work. Thus after lens magnification and focus adjustments with their concomitant image rotations are completed, it is necessary to rotate the source until it is radially aligned without disturbing the existing optical adjustments. A rotating vacuum-tight joint has been included between the source length limiting aperture and the first reducing lens C_1 . Figure 9 shows the ring gear used to rotate the gun-condenser section with respect to the fixed lower column. For the small amounts of rotation required, resultant minor misalignment between the optical axes of the upper and lower sections can be neglected. One further requirement critical to keeping signal elements radial is that the electron beam must fall on the locus of the center of rotation of the turntable as it is traversed. Since the turntable is referenced to the chamber and the column is fixed to the cover plate, the cover and chamber are aligned with guide pins to provide accurate registry each time the system is closed for recording.

As cited above, the exposure for a given spot size and current is inversely proportional to the radius at which it strikes the disc. In order to maintain the same signal exposures at the inside and outside of a disc, the beam current must be proportional to the radius. This requirement is met very adequately by using a weak lens C_0 (Figure 10) to change the size of the source by changing the location of the virtual image of the source. As the strength of C_0 is varied, the image changes in size much more rapidly than it changes in distance from lens C_1 which forms the first reduced real image of the source. The length of the image seen by lens C_1 is limited by a source length limiting aperture (Figure 9) so that the length remains essentially fixed and only the image width is changed by lens C_0 . Since brightness is constant, the exposure of the resist is changed proportionally to the width. Also, since beam width and wavelength are both proportional to radius, the two are in a fixed ratio, which gives the same fidelity of exposure profile at all radii. In order to prevent rotation of the image of the source by the magnetic lens C_1 , a double gap pole piece is utilized with the field directions opposite in the two identical and closely adjacent gaps. No measurable rotation is evident in the useful range of lens operation. As a matter of convenience, the control of C_0 lens current with radius is automatic through an electronic servo using the BCD output from the turntable radius indicator as the controlling signal.

An interesting complication exists in using a short focal length magnetic lens close to a rapidly moving conductive surface. Any fringing magnetic fields from the C_2 lens will produce eddy currents in the copper substrate which reaches a speed of 680 cm sec^{-1} at the largest radius. The magnetic field thus slows down the speed of rotation. The solution is to use an asymmetric bore size, with the exit bore of the pole piece as small as required to exert no detectable (parts per million) change in speed of the turntable when fully excited. The bore chosen is 6 mm, and the surface of the work is 3 mm from the lower surface of the pole piece. The iron circuit of the pole piece is designed to provide low reluctance to minimize stray fields. These geometrical restrictions on pole piece design limit the minimum spherical aberration of the C_2 lens to approximately 1 cm.

The depth of focus of the image of the source used in recording is approximately $\pm 2 \mu\text{m}$. Deviations greater than this can be detected in SEM examination of the profiles of the developed signals, and in the signal-to-noise ratio of the playback. A deviation of $\pm 5 \mu\text{m}$ will cause marginal performance levels at play-back of the final records and is the specified limit of recorder operation. To maintain focus to better than $\pm 2 \mu\text{m}$ it is necessary to use an automatic focus control, because it is virtually impossible to maintain the distance from the final lens C_2 to the surface of the resist-coated master fixed to this degree of accuracy. The mechanical structure connecting the lens and the work involves the chamber top, walls, bottom, traversing ways, bearing, spindle, turntable, and substrate. Changes in ambient temperature or barometric pressure can frequently change working distance several μm in an hour of recording. Systematic errors, such as tilt of the spindle of more than 0.01° with respect to the traverse direction, use up or swamp the defocus tolerance. Vertical run-out of the substrate above is usually $\pm 2.5 \mu\text{m}$, but many otherwise good substrates may usually run out three times that amount.

The automatic focus control is an open-loop system. A small capacitive height gauge is placed tangentially 16 mm ahead of the beam position, and 0.3 mm above the resist surface (Figure 7). Changes in distance to the work are conveyed as electrical signals which control the current in a small iron-free coil in the gap area. For the relatively small range of focal length changes encountered ($\pm 25 \mu\text{m}$), the effect of the coil is linear, and the system is easily set to keep the source image in focus on the work. Limitations in the system stem from the displacement of the capacitive probe from the beam and are of importance only for irregularities in the surface of the substrate. To improve this situation, a time delay circuit

is used to reduce the effective displacement of the probe from the beam. It is possible to deal with substrate run-outs of $\pm 25 \mu\text{m}$ within distances comparable to the separation of probe and beam. In practice, the system is so stable that once focussed on an initial substrate and set for automatic control, the system will automatically come to focus on subsequent substrates as they are inserted into the recorder.

Stray fields such as from AC lines, or vibrations from mechanical equipment in the building can frequency modulate the carrier but they are of such low frequency compared to the video frequencies that they may be ignored. Because the system is FM, it is important that the signals fall in their correct spacial relationship along the groove. If they are displaced from their correct position, the displacement will cause a spurious signal when it is demodulated. For example, the tracking deflectors must be set to act perpendicular to the groove so that no component of the tracking deflection occurs along the groove. Since tracking correction is a random phenomenon, any component along the groove will look like noise to the record player. To meet this deflection alignment requirement, scan rotation is provided for the scanning/deflection coils in lens C₂.

The blanker is also capable of causing trouble in the signals by extraneous exposures due to finite extinction time of the beam and due to motion of the beam during the blanking process. To minimize this possibility, the electrostatic blanker is operated so as not to cause image deviation, i.e., the real image from lens C₁ is formed at the center of the blanker. However, residual motion of the final image resulting from end-effects and misalignments does occur and is rendered harmless by orienting the blanker to deflect radially, thus minimizing the component tangent to the groove. The extinction time of the blanker is approximately three nanoseconds.

Figure 10 shows diagrammatically the major elements of the electron optical system. The angular aperture of the system is limited by an aperture placed half way between lens C₁ and lens C₂. Fortunately, the position is uncritical as this is the only available space between the lenses. The optically logical space is in the gap of lens C₂, but in that position is subject to contamination from the substrate and the large vacuum chamber. The only field limiting aperture mentioned earlier is located below the C₀ lens. A pair of leaves restrict the length of the line source. The angular aperture of the illumination at this point is sufficiently small to give a usefully sharp termination of the source.

A good quality double deflection scanning system is included above lens C_2 . It provides the means for good operation as an SEM for the conventional procedures of system alignment, lens correction, focus, source orientation, source measurement, and blanker orientation. When the leaves of the source limiting aperture are used to make a point source, lens correction for astigmatism is possible. When the image of the source is elongated, and a test specimen of small platinum particles is observed in the SEM mode, the bright smear of the particles provides an outline of the beam and shows its orientation.

The test specimens used for adjustment of the optical system are set up on a special specimen stage at the edge of the substrate (Figure 8) which traverses with the turntable. It was found essential to keep the set up area several centimeters from the recording area of the resist because stray electrons from the set up procedures will give an excessive general background exposure to the area.

As is characteristic of such instruments, the column has a separate vacuum system. It will be observed from Figure 10 that the valve separating the work chamber and the column is above the angular aperture limiting stop. This was necessitated by the utilization of all space below for high priority operational purposes. In order to protect the several elements in the C_2 lens from rapid contamination in the inferior vacuum of the work chamber, a readily removable glass liner with a thin conducting surface is used in the bore of C_2 . The angular aperture limiting stop actually consists of four quickly available apertures in an easily removable assembly for replacement of apertures. The recorder was frequently run for 20 hours a week, and required cleaning maintenance on a monthly basis. Several recorders identical with that described in this paper have been built. They have performed very reproducibly and very reliably in the hands of a considerable number of operators.

CONCLUSIONS

The high degree of success achieved with the RCA "Selecta-Vision" VideoDisc as a video information storage system strongly suggests other applications for it as a read-only memory. In an hour of recording on one side of a record with an area of 700 cm^2 there are approximately 100,000 video frames comprising 1.8×10^{10} individual signal elements. This is a space utilization of 2.6×10^7 elements/ cm^2 . There is complete random access, although this is slow. As a long term storage medium the disc

has the advantages of small volume, durability, and long life. As a manufactured item, it has the advantages of relatively inexpensive, and high volume production.

There is also the serious possibility that disc exposure has advantages for wide area electron lithography. If rectangular coordinates are converted to polar coordinates and read out as a function of azimuth and radius very large conventional format micro lithographic arrays are possible.

ACKNOWLEDGMENTS

The electron beam disc recorder described in this paper is a second or third generation embodiment of work which was started at the David Sarnoff Research Center ten years ago under the direction of E. O. Keizer. The early recorders were slow, working at 1/200 of real time and slower. The first oil driven turntables, requiring great stability because of the slow speed, were primarily the development of R. W. Jebens and W. H. Morewood. The first exposures on discs were made by L. B. Johnston who devised the groove tracking system. Very many others were also involved in the development of masters, resists, processing, signal generation, and playback. For a survey of the historical background of the RCA "SelectaVision" VideoDisc project and recognition of those who worked on it, the reader is referred to previous publications.⁽¹⁾ In the development of the real time recorder specifically described herein, major design contributions have been made by J. Valachovic, R. Simms, and H. W. Hyde. The extensive electrical circuitry essential to the success of this project, but not described in this paper, was largely the responsibility of C. A. Whybark, C. Corson, and R. F. Sanford. E. R. Campbell, W. P. Marz, and K. B. Bahrs assisted in electrical construction test and operation of the recorders.

REFERENCES

1. The entire issue of the RCA Review, Volume 39, March 1978, is dedicated to the development of the RCA "SelectaVision" VideoDisc System. Of particular relevance to this paper are: Keizer, E.O., VideoDisc Mastering, p. 60; Clemens, J.K., Capacitive Pickup and the Buried Subcarrier Encoding System for the RCA VideoDisc, p. 33.
2. Lin, L. H., Optical Process Control of Video Recordings in Electron Resist Films, in this volume of the Proceedings.
3. Riddle, G.H.N., R. R. Demers, and J. Valachovic, An Electron Gun for VideoDisc Recording, in this volume of the Proceedings.

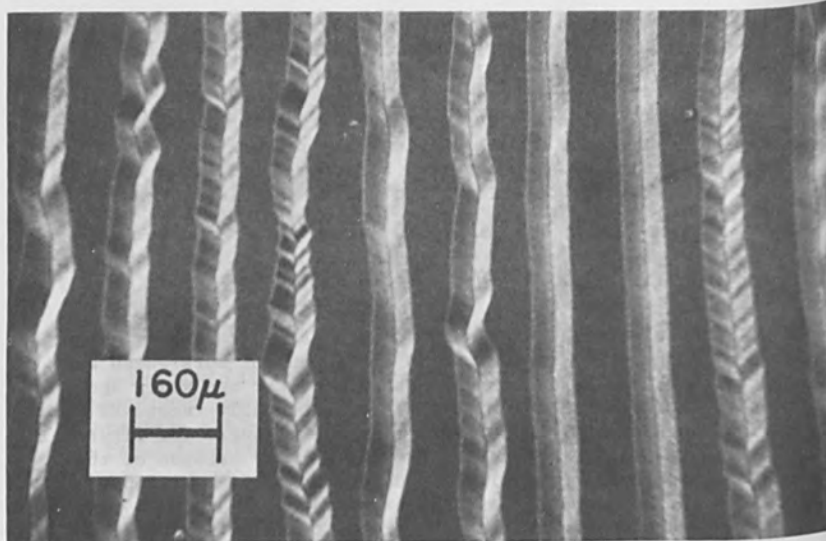


Fig. 1. Grooves in an audio phonograph record (MAG 50X approx.) viewed at 60° to the normal.

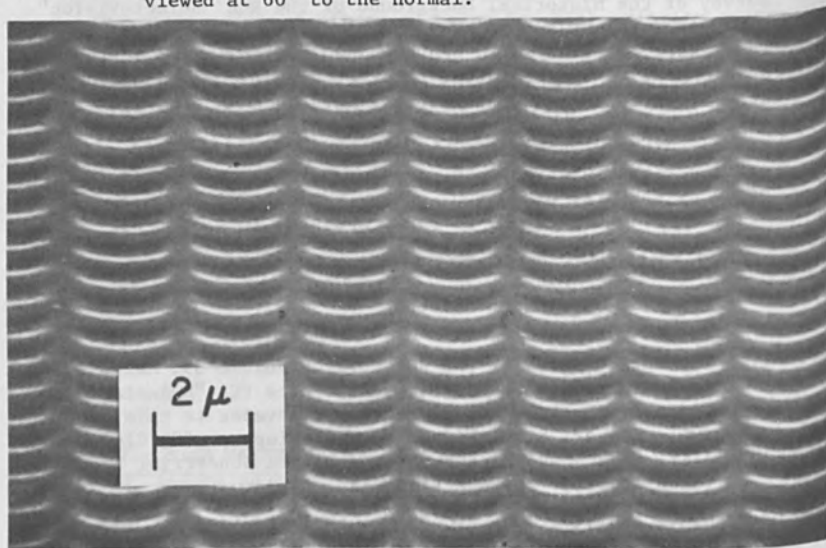


Fig. 2. Grooves in a VideoDisc record at approx. 80 times greater magnification (4000X approx.) viewed at 60° to normal.



Fig. 3. Side view of the recorder with vacuum chamber closed and the column in the recording position.

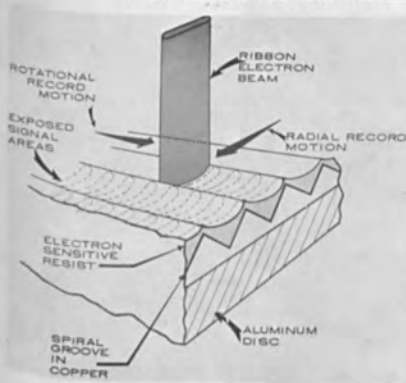


Fig. 4. Diagram of how resist sags into pre-cut grooves and of the exposure profile of the beam.

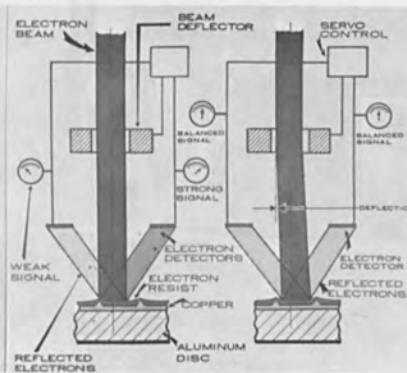


Fig. 5. Diagram of the operation of the groove tracking servo.

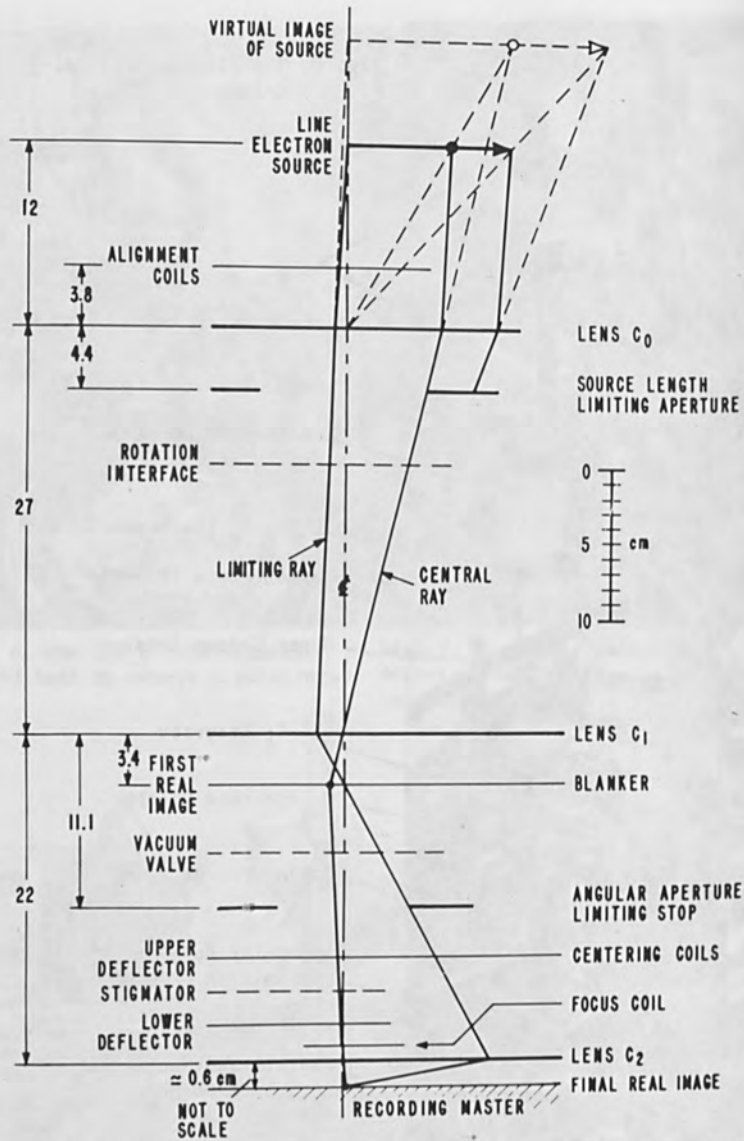


Fig. 10. Diagrammatic representation of the position and function of the major electron optical elements. For size reference, outside diameter of the column is 11.5 cm.

OPTICAL PROCESS CONTROL
OF VIDEO RECORDING IN RESIST FILMS

L. H. Lin

RCA Corporation
David Sarnoff Research Center
Princeton, New Jersey 08540

ABSTRACT

An optical method for the process control of video recording in an electron resist film is described. The method utilizes the diffraction of a laser beam incident on the resist film immersed in the resist developer. The refractive index difference between the developed resist surface and the developer gives rise to a diffraction pattern formed in the back focal-plane of a lens. The light variation in the pattern is shown to correlate closely with both the developed resist topography and the video playback spectrum. Proper optical diffraction measurements can, therefore, be devised to control the resist development for the optimum recording properties. Experimental results of a controlled development for a series of resist films are presented.

INTRODUCTION

Video information recorded on an RCA VideoDisc originates from a master, which can be recorded by a particular means of electron beam lithography.⁽¹⁾ The master begins as a pregrooved metal disc coated with a thin film of electron resist. During the recording an electron beam exposes the resist film along the continuous groove in an on-and-off fashion. Afterwards, the resist film is chemically developed to attain a surface relief pattern, which contains the coded video signal elements. The same relief pattern is finally embossed onto a large number of plastic VideoDiscs after several replication processes starting from the master. The final video playback quality depends very critically on the surface properties of the resist film on the master.

In order to achieve reliably the best possible video signals recorded in the electron resist film, an in situ method for monitoring the resist chemical development is essential. Described in this paper is one such method, which is based on the optical diffraction of a laser beam incident on the resist surface during the development. With this method, optical measurements which are closely related to the geometry of the developed signal elements, as well as the electrical playback signal spectrum, can be monitored continuously. A criterion can be derived from these optical measurements for terminating the resist development process at the optimum moment.

In this paper a semi-quantitative analysis of the diffraction phenomenon involved is first presented. The diffraction arises from the refractive index difference between the developed signal elements and the liquid developer. To the first degree of approximation, a linear relationship exists among the following: (1) the light amplitude diffracted at a given angle, (2) surface relief height at a corresponding spatial frequency, and (3) the electrical playback video amplitude at a corresponding temporal frequency. The analysis is then followed by experimental results correlating optical diffraction measurements with corresponding measurements obtained from scanning electron micrographs of the signal elements and from the electrical playback signal spectrum.

THE OPTICAL ARRANGEMENT

A low power He-Ne laser operating at 6328 Å wavelength is used as the coherent light source for the monitoring system. At this wavelength the photosensitivity of the resist material is essentially not observable. As shown in Figure 1, a slightly converging laser beam illuminates a small area ($< 1 \text{ mm}^2$) on the resist surface immersed in the chemical developer through a thin transparent dome containing also the developer liquid. The incident laser beam is diffracted by the signal elements due to the difference in the refractive indexes of the resist and the developer. The signal elements are perpendicular to the plane of the figure and the illuminated area is approximately at the center of the spherical dome. Under this arrangement, the incident, reflected and diffracted light rays are all nearly normal to the spherical surface and undergo negligible refraction as they enter and leave the dome. The reflected and the diffracted rays are collected by a condenser lens placed at a focal distance from the resist surface. Since the spacings of the signal elements are near the laser wavelength, a very

large numerical aperture of the lens is required to collect the diffracted rays. The use of the dome reduces this requirement by virtually eliminating the refraction mentioned above. The large oblique angle of the incident beam also simplifies the collection of the light diffracted from large angles.

In the back focal-plane of the lens, the far-field diffraction pattern of the light diffracted from the developed signal elements is formed. This light pattern changes continuously during the development and can be monitored with a photo-detection system. Figure 2 shows photographs of the diffraction patterns of some test signals recorded on the developed resist surfaces. It will be shown later that bright lines in the photographs are closely related to the temporal spectrum of the test signal.

THE DIFFRACTION PATTERN

For the purpose of monitoring the resist development, a periodic test signal is recorded on all signal tracks in the small area illuminated by the laser beam. Within this area the spatial wavelengths of the recorded signal elements change very little from one signal track to another, but the relative phases can be quite different. The diffraction angle depends only on the wavelength, not the phase. Therefore, each signal track will produce the same set of bright diffraction lines, superposing on those produced by other signal tracks. The track-to-track phase differences of the recorded signals, however, effect the diffracted light intensity distribution along the resulting diffraction lines.

If the track-to-track phase differences happen to be constant, due to some unusual combinations of the disc rotational rate and the recorded signal frequency, the corresponding diffraction line will be broken up with the same periodicity as the diffraction by the grooves. The latter results in a series of dots in the diffraction line. If the phase differences are completely random, the diffraction line will contain fine speckles which do not change the macroscopic appearance of the continuous diffraction line. In most cases, the diffraction lines will appear in between the above two extremes. If one ignores the speckles and the dots, the diffraction pattern produced by all illuminated tracks is essentially the same pattern produced by a single track, but much more intensified. The total optical power contained in each diffraction line does not depend on the track-to-track phase differences and is directly

proportional to the number and the width of the illuminated signal tracks.

Let's now consider, from the Fourier optics point of view, the diffraction pattern of a single track. The result will only be a semi-quantitative approximation but does provide a useful insight.

In the radial direction of the disc, along the diffraction lines, the diffraction pattern is very broad and is determined by parameters such as the widths and the cross-sectional geometries of the signal track and the groove. However, we shall ignore the light variation in this direction since these parameters are usually kept constant and since we are only interested in the total optical power in each diffraction line. It is the light variation in the direction perpendicular to the diffraction lines that provides us with the desired information characterizing the recorded signal. We shall limit the following discussion, therefore, in this direction only.

Let's approximate the incident laser beam by a plane wave of unit amplitude propagating in the plane normal to the disc radius. If ϕ is the incident angle, measured from the normal to the disc surface, the incident wave front can be written as

$$a_i(X_1) = \exp\left(2\pi i \frac{X_1}{\lambda} n_d \sin \phi\right), \quad (1)$$

where X_1 is the coordinate along the signal track, $\lambda = 6328 \text{ \AA}$ the laser wavelength in air, and $n_d = 1.33$ the refractive index of the developer liquid. Assuming that the resist film is sufficiently thin, we can ignore the dispersive effect of the wave propagation in the film, as well as any interference effect resulting from light reflection at the surface of metal (copper) substrate. Under this assumption, the wave front reflected and diffracted back into the developer is

$$a_d(X_1) = A \exp\left[4\pi i \frac{z(X_1)}{\lambda} \Delta n\right] a_i(X_1), \quad (2)$$

where $z(X_1)$ is the recorded signal depth variation, i.e., surface relief, along the track, $\Delta n \approx 0.27$ the difference in the refractive indexes of the resist and the developer, and A includes all constants not depending on X_1 . If $z(X_1)$ is sufficiently small, we can adopt the following linear approximation:

$$\exp \left[4\pi i \frac{z(X_1)}{\lambda} \right] \Delta n \approx 1 + 4\pi i \frac{z(X_1)}{\lambda} \Delta n. \quad (3)$$

We can further drop the constant 1 in the above, as we are interested only in the variations in X_1 , and substitute the linear term for the exponent in Equation (2). The result, after combining with Equation (1), is

$$a_d(X_1) = A 4\pi i \frac{z(X_1)}{\lambda} \Delta n \exp \left(2\pi i \frac{X_1}{\lambda} n_d \sin \phi \right). \quad (4)$$

As illustrated in Figure 1, the laser illuminated region of the resist surface is small compared to the radius of the transparent dome. We may, therefore, neglect the refraction of the light emerging from the dome to the lens. As a result, we can treat the lens as if it were immersed in the developer. The wave front $a_f(X_2)$ in the back focal-plane of the lens is related to $a_d(X_1)$ in the front focal-plane by the following Fourier transform relation:

$$a_f(X_2) = \frac{i n_d}{\lambda f} \int a_d(X_1) \exp \left(-2\pi i n_d \frac{X_1 X_2}{\lambda f} \right) dX_1,$$

where f is the focal length of the lens, and X_2 -axis in the back focal-plane is parallel to X_1 -axis.⁽²⁾ Substituting Equation (4) into the above, we have

$$a_f(X_2) = B \int z(X_1) \exp \left(-2\pi i n_d \frac{X_1 X_2}{\lambda f} \right) dX_1, \quad (5)$$

where we have lumped all the space-invariant constants into B and let

$$X_2' = X_2 + f \sin \phi.$$

We now compare Equation (5) with the temporal Fourier transform relation between the electrical signal $g(t)$ and its spectrum $G(F)$, where t and F designate the time and the frequency respectively. By definition,

$$G(F) = \int g(t) \exp (-2\pi F t) dt. \quad (6)$$

Comparing Equation (5) with Equation (6), we arrive at the following conclusion: If the recorded signal depth $z(X_1)$ is linearly proportional to the electrical signal amplitude $g(t)$, then the spatial light amplitude distribution $a_f(X_2)$ in the back focal-plane is a linear representation of the temporal spectrum $G(F)$, provided that

$$n_d \frac{X_1 X_2'}{\lambda f} = Ft.$$

Except for an arbitrary starting constant,

$$X_1 = 2\pi r \Omega t,$$

where Ω is the disc rotation rate and r is the mean radius of the signal tracks illuminated by the laser. Consequently we can let

$$F = \left(\frac{n_d X_1}{\lambda f t} \right) X_2' = \left(\frac{2\pi n_d r \Omega}{\lambda f} \right) X_2' = \left(\frac{2\pi n_d r \Omega}{\lambda f} \right) (X_2 + f \sin \phi),$$

or

$$X_2 = \left(\frac{\lambda f}{2\pi n_d r \Omega} \right) F - f \sin \phi. \quad (7)$$

The above relation indicates that the X_2 -axis in the back focal-plane can be calibrated in frequency units (see Figure 2), with a zero-frequency off-set at $X_2 = -f \sin \phi$. (The calibration, however, depends on the disc radius r and rotational rate Ω .)

It should be pointed out again that we arrived at the Fourier transform relation, Equation (5), between $a_f(X_2)$ and $z(X_1)$ by some assumptions whose validities can be quite tenuous in reality. Only for small $z(X_1)$, i.e., shallow signals, such a linear relation holds between $a_f(X_2)$ and $z(X_1)$. For large $z(X_1)$ the assumptions for Equation (2) and Equation (3) are not valid, and hence $a_f(X_2)$ and $z(X_1)$ are no longer linearly related as indicated by Equation (5). (It turns out, however, the frequency calibration in the back focal-plane, given by Equation (7), still holds.) For a given type of test signal, it is necessary therefore to experimentally determine $a_f(X_2)$ at various stages of resist development, using Equation (5) only as a qualitative guide.

OPTICAL DIFFRACTION MEASUREMENTS

As mentioned earlier, the aim for monitoring the diffraction pattern is to provide us with useful information which can be correlated to the properties of the signal recorded in the resist film. The information we wish to have of the developed signals can be separated into two interrelated categories: (1) geometrical configurations of

the signal elements, and (2) electrical playback characteristics of the recorded signal. Scanning electron microscopy techniques are usually employed to measure the geometrical configuration of the signal elements. From these geometrical measurements, one can predict, to a large extent, the characteristics of the electrical playback signal of the finally pressed discs. The quality of the playback signal can be characterized by measuring the spectral response of the signal.

The first step in evaluating the usefulness of the proposed development monitoring method is to correlate optical diffraction measurements with the above mentioned geometrical (by SEM) and spectral measurements. Only for shallow recorded signals we can expect that the correlation can be predicted from the linear Fourier transform relation of Equation (5). To study experimentally this correlation in general, a special tray was constructed. The main feature of the tray was an optical system identical to that illustrated in Figure 1. In addition, a narrow slit was placed in the back focal-plane, along the diffraction lines, and the slit position could be translated in the direction perpendicular to the lines. Behind the slit was another lens which collected all the light passing through the slit onto a silicon photodetector.

Optical diffraction measurements were obtained in the tray under a static condition by the following technique. Instead of the developer, the tray was filled with water. The exposed resist film on the substrate was chemically developed elsewhere for various durations and then placed in the tray for the measurement. Since the developed resist film was completely inert to water, no further development could take place in the tray. Hence, the diffraction pattern in the back focal-plane was static. The refractive indexes of the developer and the water are essentially identical. Therefore, a series of static diffraction patterns obtained in the tray from these developed resist films is a good approximation of a series of "snapshots" of the dynamic pattern at various times of the actual resist development.

In constructing the optical system used for the measurement, the first concern is the very large aperture required of the optical system. From Figure 1 and Equation (7), we see that the (air-equivalent) numerical aperture required of the lens is

$$\frac{\rho}{f} = \frac{\lambda F_m}{2\pi n_d r \Omega} - \sin\phi,$$

where 2ρ is the diameter of the lens, and F_m is the maximum frequency, or the bandwidth, of the electrical signal. Choosing $F_m = 10$ MHz, $\phi = 45^\circ$, the numerical aperture is $\rho/f = 1.24 - .707 = 0.54$ at $r = 3.2''$, $\Omega = 450$ rpm, and for $\lambda = 6328$ Å and $n_d = 1.33$. The actual lens used in the experimental tray had a diameter $2\rho = 6.4$ cm and an effective focal length $f = 5.3$ cm, giving $\rho/f = 0.60$. Using this lens in the optical system, laser powers in the diffraction lines corresponding to major spectral components up to 10 MHz could be measured even at the innermost disc radius.

The test signals used for monitoring the resist development were all periodic and, hence, their temporal spectrums consisted of components only at discrete frequencies. Correspondingly, the diffraction pattern for each test signal recorded on the resist film consisted of all discrete lines at locations given by Equation (7). The diffraction measurements for each test signal were obtained by translating the slit in the back focal-plane to the location of each diffraction line. The total laser power passing the slit was then measured. The slit height (40 mm) and width (1 mm) were kept constant in all cases.

A low power (1-2 mW) He-Ne laser was used as the light source. The polarization of the laser was random for most earlier measurements. It was later changed to a linear polarization with the magnetic vector parallel to the signal elements. For shallow signals the diffracted laser power was found to be insensitive to the direction of polarization. For deep signals, the above linear polarization was preferred, since the diffracted laser power was found to be less critical to slight changes in the angle between the incident laser beam and the signal track.

CORRELATION BETWEEN DIFFRACTION MEASUREMENTS AND SIGNAL GEOMETRY

For this purpose, a special test signal, designated as TDT, was used. This test signal consisted of 3.8 MHz and 6.3 MHz video carriers which were duty-cycle modulated at 620 kHz and 820 kHz audio carrier rates, respectively. The two video carriers were recorded in alternate grooves throughout a test band near 3.2" disc radius.

The optical diffraction pattern (in the back focal-plane) of the TDT signal is shown in Figure 2(c). Laser powers in the diffraction lines corresponding to both the video and the audio carriers were measured after the resist films were chemically developed for various times.

Afterwards the recorded signal elements were transferred to a nickel replica in the usual manner. From the scanning electron micrographs of the replica, the geometry of the signal elements was determined. The geometrical properties of the signal elements, which could be correlated with the diffraction measurements, were (1) the (peak-to-peak) signal amplitudes of the video carrier, (2) the amplitude ratio of the two video carriers, and (3) the signal track drop modulation amplitude at the audio carrier rate. By track drop we mean the height difference between the top surface of the signal track and the original resist surface.

According to the Fourier transform relation of Equation (5), the light amplitude in the diffraction pattern increases linearly with the recorded signal amplitude. Since the measured laser power P_F at the signal frequency F is proportional to the square of the light amplitude in the diffraction line, the square root $P_F^{1/2}$ of the laser power should therefore be linearly proportional to the recorded signal amplitude S_F (determined by SEM technique) at the same frequency F . Plotted in Figure 3 are $P_{3.8}^{1/2}$, $P_{6.3}^{1/2}$, $S_{3.8}$, and $S_{6.3}$, where the subscripts denote the frequency in MHz, as functions of the resist development time. Notice that $S_{6.3}$ or $P_{6.3}^{1/2}$ reaches a peak and then decreases with development time, while $S_{3.8}$ or $P_{3.8}^{1/2}$ is still increasing.

For the purpose of monitoring the developed signal amplitude by optical diffraction, it is more useful to plot $P_F^{1/2}$ as a function of the corresponding S_F . This is shown in Figure 4. Notice that the curves are close to straight lines for signal amplitudes less than $0.1 \mu\text{m}$ and seem to level off after $0.15 \mu\text{m}$. The reason for the leveling off is very likely due to the interference of the two diffracted light amplitudes, one generated as the laser beam enters the resist film and the other as the beam leaves the film after being reflected by the metal substrate. In Figure 4, notice also that the two curves for 3.8 MHz and 6.3 MHz very closely coincide with each other, at least in the region where both curves are close to straight lines. This means that the signal amplitude ratio $S_{6.3}/S_{3.8}$ can be directly obtained by taking the square root of the diffracted laser power ratio $(P_{6.3}/P_{3.8})^{1/2}$.

Another important geometrical property of the recorded signal is the undesirable track-drop modulation at the audio carrier rate. It is commonly believed that the track-drop modulation is a significant cause of the interference of the video signal by the audio during the playback. Under most recording conditions, a great number of scanning electron micrographs of the duty-cycle modulated signal

elements show the following form of the track-drop modulation. The peak-to-peak amplitude of signal elements remains essentially constant, but the average signal depth (ASD) is modulated in-phase with the duty-cycle modulation. Hence, in this case, the ASD modulation is the track-drop modulation. However, the ASD modulation for a properly recorded signal is usually less than 100 Å and becomes very difficult to be measured by SEM techniques. The optical diffraction measurement described in the following can provide a more sensitive means for measuring and monitoring the ASD, or track-drop, modulation.

Let P_V and P_A be the laser powers in the diffraction lines corresponding to the video and the audio carrier frequencies, respectively. Both the duty-cycle modulation and the ASD modulation can contribute to P_A . The component of P_A due to the duty-cycle modulation is fixed by the known modulation index. The modulation index m is defined as the intended audio-to-video amplitude ratio, which is set at -23 dB, or $m \approx .071$. If we assume that the square root of the measured laser power is proportional to the signal amplitude, then the part of $P_A^{1/2}$ due to the duty-cycle modulation is $mP_V^{1/2}$. Consequently, under the same assumption, we should expect the excess, $P_A^{1/2} - mP_V^{1/2}$, to be due to the ASD modulation alone. Plotted in Figure 5 is the excess quantity $P_A^{1/2} - mP_V^{1/2}$ as a function of the ASD modulation amplitude as measured by the SEM technique. Because of the SEM resolution limit, no ASD modulation less than 100 Å was measurable. However, if we extend the curves in Figure 5, they seem to go through the origin. This indicates that the quantity $P_A^{1/2} - mP_V^{1/2}$, which is not difficult to obtain even for ASD modulation of less than 100 Å, may be an indirect measurement of ASD, or track-drop, modulation.

CORRELATION BETWEEN DIFFRACTION MEASUREMENTS AND PLAYBACK SIGNAL SPECTRUM

For this correlation study, two standard test signals BB1 and ST1, normally used for the production quality control, were used. The diffraction patterns of the two signals recorded in the resist films are shown in Figure 2. For this figure the resist films were over-developed in order to bring out the weak diffraction lines in the photographs. For the correlation study, however, the resist films were developed only to such an extent that the signal amplitude for the 5 MHz video carrier was about 800 Å.

The laser powers in the major lines of the diffraction pattern were measured by translating the slit in the back

focal-plane to the locations of the diffraction lines as described previously. Since some of the measured laser powers were sufficiently weak, the background light, or noise, became significant. It was necessary, therefore, to measure the noise level at each slit location in the absence of the recorded signal.

After the diffraction measurements were completed, the resist surface was replicated into a nickel stamper from which the standard discs were pressed. The spectrums of the test signals played back from the disc were measured by the method normally used in evaluating the standard disc. In correlating the playback spectral measurements with the optical diffraction measurements, one must realize that the noise characteristics of the two measuring systems may be different and should be taken into account separately. Consequently, we should compare the signal-to-noise ratios $(S/N)_F$ measured in the two systems at the same frequency F . Furthermore, it is more convenient to compare $(S/N)_F$ relative to $(S/N)_5$ of the 5 MHz carrier component in each system. The result is tabulated in Table 1. Except for the 3 MHz and 7 MHz components of the BBl test signal, the ratios $(S/N)_F/(S/N)_5$ obtained from the optical diffraction measurements agree closely with those obtained from the electrical spectral measurements. The larger discrepancies at 3 MHz and 7 MHz may be due to the very non-linear playback characteristics of the stylus.

IN SITU RESIST DEVELOPMENT CONTROL

Having obtained the correlation between the developed signal amplitude and the diffracted laser power under the described static condition, a more realistic dynamic experiment was carried out. In this experiment, the resist development process was continuously monitored by the optical diffraction method and the process was terminated when the developed signal amplitude reached an expected value. A total of eight video disc master substrates, No. 1112 through No. 1119, were used for the experiment and their resist coatings were all identically prepared in the standard manner. A band of the test signal BBl was exposed on the resist by an electron beam at 3.2 inch disc radius. The exposed resist coating was immersed in the same tray from which the previously described static diffraction measurements were taken, except now the tray was filled with developer instead of water. The same optics and photodetector were employed to continuously monitor the laser power diffracted by the 5 MHz components of the developed signal. When the monitored laser power reached a predetermined value

for 800 Å signal depth at 5 MHz, the development process was stopped by quenching the substrate in a water bath. After the development, the signal amplitude of each test substrate was determined by the usual SEM technique.

Both the signal amplitudes and the required resist development times for all but two substrates are tabulated in Table 2. Even after more than 600 seconds of development time, the monitored laser powers for the substrates No. 1113 and No. 1116 never came close to the predetermined value. The reason for this was later determined to be improper focusing of the electron beam during the recording. As indicated in Table 2, there was a wide variation in the development times to reach the optimum development. The reason for this is not understood. However, despite the large differences in the development times, the signal amplitudes were indeed controlled to be within a range not far from the probable error ± 50 Å of the actual signal-depth measurements.

SUMMARY AND CONCLUDING REMARKS

The experimental results presented above indicate that an optical diffraction method can be devised to monitor the resist development process. A He-Ne laser is used to illuminate the resist surface immersed in the developer. The light diffracted by the signal elements developed on the resist surface forms a diffraction pattern on the back focal plane of a lens. Some measurements of the light distribution of the diffraction pattern have been shown to correlate closely with the geometrical properties (e.g., signal amplitude, track-drop modulation amplitude) and the electrical playback spectrum of the recorded signal. The resist development process can therefore be terminated according to some criterion (based either on the expected geometrical properties or playback spectrum) for the optimum result of the recorded signal. It has been shown, for example, that it is possible to develop the resist films in different substrates with a very narrow spread (about 100 Å) in the 5 MHz carrier signal amplitude. However, developing the resist film for a constant signal amplitude may not be the best criterion for the disc production. A better criterion could be one based on the expected electrical playback spectrum of the disc and deserves more investigation.

Test Signal	Frequency F, (MHz)	(S/N) _F / (S/N) ₅ , (dB)	
		Optical Diffraction	Electrical Playback
ST1	5	0	0
	0.6	-18	-19
BB1	5	0	0
	2	-14	-14
	3	<-30	-28
	7	-24	-19
	8	-17	-19

Table 1. Comparison of signal-to-noise ratio measurements for major spectral components of test signals ST1 and BB1. The S/N for the 5 MHz carrier is taken as the reference and all other ratios are relative to it.

Substrate No.	5 MHz Signal Amplitude (Å)	Development Time Seconds
1112	800	230
1114	900	240
1115	800	180
1117	800	330
1118	900	190
1119	800	180

Table 2. Developed signal amplitudes and the required development times for a series of eight master substrates.

REFERENCES

1. J. H. Reisner, G.H.N. Riddle, S. M. Zollers, L. H. Lin, E. D. Simshauser, W. P. Morewood, R. R. Demers, and J. Guarracini, "Electron Beam Recording of Masters for the RCA VideoDisc," this issue.
2. R. J. Collier, L. B. Burckhardt, and L. H. Lin, "Optical Holography," Chapter 6, Academic Press, New York, 1971.

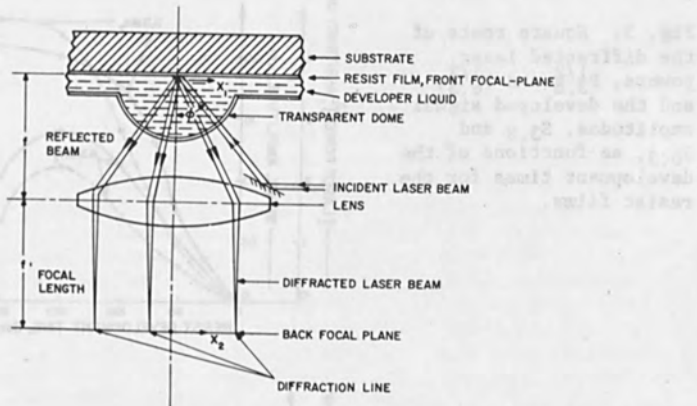


Fig. 1. The optical arrangement for monitoring the far-field diffraction pattern of the signal elements recorded in the resist film.

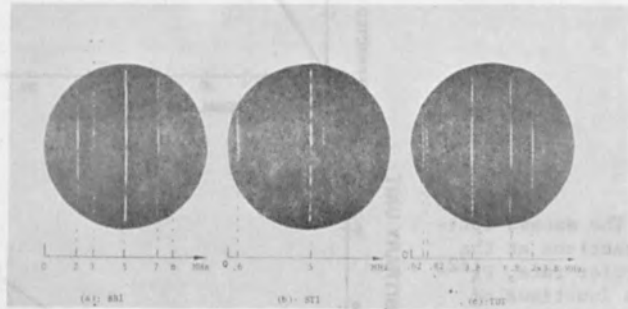


Fig. 2. Photographs of diffraction patterns of test signals (a) BB1, (b) ST1, and (c) TDT, formed in the back focal-plane of the lens shown in Fig. 1.

Fig. 3. Square roots of the diffracted laser powers, $P_{3.8}^{1/2}$ and $P_{6.3}^{1/2}$, and the developed signal amplitudes, $S_{3.8}$ and $S_{6.3}$, as functions of the development times for the resist films.

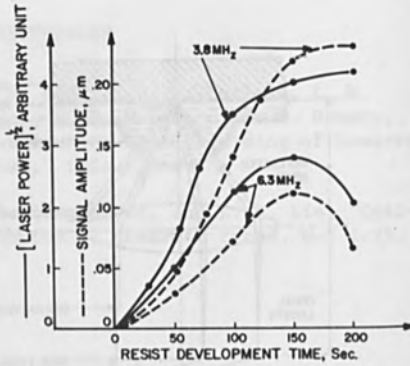


Fig. 4. Square roots of the laser powers $P_{3.8}^{1/2}$ and $P_{6.3}^{1/2}$ as functions of the signal amplitudes $S_{3.8}$ and $S_{6.3}$.

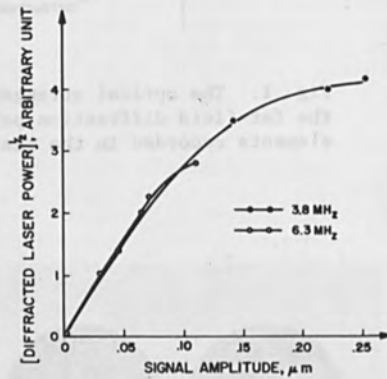
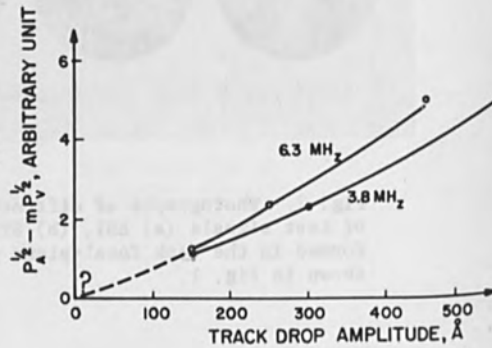


Fig. 5. The excess optical diffractions at the audio carrier rate, $mP_A^{1/2} - mP_V^{1/2}$, as functions of average signal depth (ASD) modulation amplitude.



Faint, illegible text at the top of the page, likely bleed-through from the reverse side.

ION IMPLANTATION

Faint, illegible text in the middle section of the page, likely bleed-through from the reverse side.

Section 6

Faint, illegible text at the bottom of the page, likely bleed-through from the reverse side.

ION IMPLANTATION YESTERDAY, TODAY AND TOMORROW
Peter H. Rose
Nova Associates Incorporated, P. O. Box 457,
Middleton, Massachusetts, 01949

Abstract

1978 is the year in which ion implantation as applied to the semiconductor industry can be said to have come of age. The equipment available for doping semiconductors has reached a standard of performance and reliability suitable for use in a production line. The early history and origin of this doping technology is discussed. From the present state of the art it appears that there will be continued growth in the semiconductor field and the exciting possibility exists that applications in other areas such as metallurgy will rapidly become important. It will be shown how the past has molded the implantation equipment that now exists. The question will be examined as to whether fundamental departures in equipment design are in store for the future.

Introduction

Ion implantation is one of those remarkable techniques in the field of physics that embraces a wide range of physical and engineering problems and has a wide and growing range of applications. Ion beams have been used for many years as a tool for investigation of nuclear reactions, atomic collisions and in other fundamental physical studies. Ion beams are also used for the analytical study of materials for etching or sputtering material by ion bombardment and many other purposes. This paper will restrict itself to a discussion of applications where the ions remain in the target. Implantation differs fundamentally from coating or ion plating. The process of ion implantation is one in which ions are accelerated to a velocity which enables them to penetrate below the surface of the substrate material where after losing their energy they stop changing the properties of the original material both by their presence and the damage they caused during entry. Unlike coating or ion plating there is no boundary between the added material and the target; there is no definable interface or build up of material, and unlike diffusion the process can take place at any temperature. Since the implanted region is shallow the change in properties is confined to the surface and all surface properties are affected. These properties include friction, wear, corrosion, visual appearance, surface energy and resistivity.

Since it is almost universally agreed that the present is an instability in time my discussion will have to be restricted to yesterday and tomorrow. As early as 1949 Shockley filed a patent which explained how nuclear particles could be used for doping semiconductors and

that higher frequency devices could be made in this way, a remarkable look into the future. In the year this first patent on implantation was granted (1954) Shockley filed a second patent (1) which described the apparatus that might be used to provide mono-energetic, variable energy particles using complex arrangements of the type used in nuclear physics. On the basis of this description such apparatus would certainly have employed magnetic analysis to select the ion species of interest so that the target would not be contaminated by other ions. The amount of material that has to be introduced into a semiconductor to change its electrical properties significantly is not large but in the late 1950's many obstacles stood in the way of practical application of the technique. First, nuclear accelerators were really a most unsuitable tool for ion implantation, but all that was available (except for the low energy isotope separators at Harwell). Secondly, radiation damage confused the expected effects. In any case diffusion was already a successful technique for doping semiconductors, a process a lot easier to understand and producing successful devices. It therefore took some time, in spite of a considerable amount of application research, for implantation to be applied on a production scale even in an environment as cost and product performance sensitive as the semiconductor industry. By 1972 a considerable number of specially designed machines were being used by the semiconductor industry and since then the market for this type of equipment has grown rapidly to over 20 million dollars per year.

Surprisingly a similar growth has not occurred for other applications of ion implantation. In spite of the considerable body of applied and basic research of implantation into metals and insulators there has been no commercial application of ion beams in these materials. The reasons are probably not hard to find. The depth of penetration of 100 KeV chromium ions into steel is about 0.1 microns, thinner even than a normal decorative coating and it is easy to be skeptical of the protection afforded to the substrate against scratching and abrasion. Equally important when it comes to application of the technique was the apparent lack of ion sources capable of supplying the large currents necessary to provide a cost effective process.

The physical process

Apart from the selection of the ion species perhaps the most important factor controlling the properties of the implanted layer is the depth of penetration and distribution of the implanted ions. The ions are slowed down and eventually stopped by ion-electron and ion-nuclear collisions and the energy loss may be calculated from the theory of Lindhard, Scharff & Schiott. (2).

The average rate of energy loss of ion can be written as the sum of

$$-\frac{dE}{dx} = N \left[S_n(E) + S_e(E) \right]$$

where E = the energy of the particle

$S_n(E)$ is the nuclear stopping power

and $S_e(E)$ is the electronic stopping power

Gibbons (3) has pointed out that for an amorphous target, S_n is as a crude approximation, constant, and S_e increases with projectile energy so that an energy exists for which $S_n = S_e$. Below this energy, nuclear stopping is the dominant mechanism of energy loss. That is to say in most practical applications energy loss by nuclear collisions is most significant and certainly this is true at the end of the range. Because of the random nature of the energy loss process there will be range straggling and to a first approximation the distribution is Gaussian. If during the process of implantation sputtering occurs, the surface will be eroded and the concentration of implanted ions near the surface will be increased.

Dearnaley and Hartley (4) have discussed how the atomic structure of the target material is changed by the bombardment. Atoms are ejected from their initial sites, creating vacancies and interstitials. The interstitials are likely to migrate rapidly to dislocations or the surface leaving behind more vacancies. The damage created depends upon the strength of the bonds between the atoms of the target. Covalent materials such as silicon have rather weak bonds and damage easily and become amorphous in the implanted zone. In metals the interatomic forces are longer range and are very resistant to ion bombardment so fortunately metals rarely become amorphous. Instead a dislocation network develops in metals which resembles a work hardened surface. The final state of the surface depends not only on the damage but on the concentration of implanted atoms, the implantation rate and temperature. Further if the solubility limit is exceeded, precipitation will occur as agglomerates, or if the impurities are chemically active they will precipitate out as a compound. There are other effects which used to be taken into consideration such as radiation enhanced diffusion (5) which will allow atoms to move into the material to many times their effective range. Apparently other transport mechanisms exist which carry the ions to a thousand times their penetration and are responsible for the durable property changes observed in implanted surfaces.

It is worth emphasizing again the differences between a coating technique such as ion plating and ion implantation. In implantation it is impossible to produce a surface layer which consists only of the implanted material, because of the penetration and sputtering caused by the bombarding ions. The surface will only contain 10-40% of the implanted atomic species. Additionally the process is a "line of sight" process, unlike ion plating which possesses the property called "throw". Under the appropriate conditions because of multiple gas collisions it is possible to coat both the front and back side of a

specimen simultaneously. This difference is an advantage for ion implantation when masking is necessary. Full coverage of a complicated workpiece, such as a turbine blade, can be obtained by manipulation so that all surfaces are covered evenly by the flux of ions.

Applications of Ion Implantation

The title of the paper is very apt with respect to the successful industrial use of ion implantation, because considering yesterday and today the technique has only been successfully applied to semiconductor fabrication. Equally important and larger scale applications lie in the future.

Semiconductors

The trends in semiconductor processing all point to an increased use of ion implantation. This is brought about by several trends many of which result from the reduction in size and increased complexity of the circuits being produced. Implantation fits very well with lower processing temperatures and the requirements of dry processing. A further factor that must be considered in the growth of the industry is the availability of better implantation equipment. In the last five years ion implanters have become a standard production tool. Figure (1) shows one of the first commercial machines built for implantation and Figure (2) illustrates a modern high current machine with more than 100 times the capability.

The equipment becoming available in the future will be automated and microprocessor controlled like most new instruments, but more important the throughput of the equipment will be improved by utilizing the ion beam more effectively and increasing the beam currents to meet the needs of the future. As an example the implanter shown in Figure (3) was designed for solar cell production and will process more than an acre of solar cells a day. (180 m²/hr)

At the other extreme there is the possibility of reducing the masking steps required in device fabrication by writing directly with micro beams. The technique has been demonstrated (6) but so far is only useful as a research tool or laboratory curiosity. In contrast electron beam micro-lithography has been developed in a number of laboratories and commercial equipment is available for mask making. Within a few years E-beam systems fast enough for direct writing on wafers will also exist. With this background technology available, the major and very serious problem preventing the economic use of ion beams for direct writing is the source brightness. (7) However the brightness reported for liquid metal ion sources (8) gives hope that a source with sufficient brightness will be developed for direct writing

Metals

It is surprising that ion implantation has not yet been exploited in metals fabrication technology, the advantages offered are so striking:

- Ions can be selected to suit any requirement without the need to consider solubility, adhesion etc.
- The treated surface region remains integral with the substrate material.
- The quantity of material required is small so that the cost of the material is not a factor.
- The work piece can be masked to select the area to be implanted.
- To achieve a particular property more than one ion can be implanted in controlled quantities.
- The treatment can be carried out at any temperature.
- There is direct electrical measurement of the doping level.
- There are no dimensional changes, so that implantation can be used as a final production step.

The list of surface properties that can be changed is equally impressive; to list only a few

- Wear reduction
- Reduction of friction
- Improvement in fatigue life
- Modification of surface properties to improve bond formation
- Improved corrosion resistance
- New catalytic surfaces
- New super conductors with higher critical temperatures.

These surface properties have dozens of hundreds of applications for example

- Extruder screws and dies
- Cutting tools including drill bits
- Electrical contacts
- Protection of carbon steel from corrosion

These partial lists serve to indicate the enormous possibilities that exist and yet there has been no exploitation so far in any of these areas. The primary reason for this is the lack of suitable equipment capable of implanting heavy doses of ions economically. Figure (5) plots the current required to implant a given area per second at different dose levels. Almost all implantations in the semiconductor industry and research laboratories fall in the shaded area. An exception is the solar cell implanter shown in Figure (3) which lies at the point A. The area of interest for metals implantation would lie above and to the left of this point, clearly indicating the need for currents in the range of 0.1 to 10.0 amperes. A variety of ions is required but for a start beams of nitrogen or chromium ions would find a great deal of application. Figure (4) shows an implanter designed to nitride the surface of extruder screws. These screws must be hardened to reduce the rapid wear caused by the feed material. The available data indicates that ion implantation produces a wear resistant coating at a fraction of the cost of the conventional "Stellite" pro-

cess. A six inch diameter electron bombardment ion source is used in this machine and produces about an ampere of nitrogen ions. Ion sources capable of producing ampere currents of such ions as chromium, have probably not been developed but it is worth noting that the ion sources used during WWII for uranium isotope separation were later run to produce chromium isotopes. The average collector current from these sources was 75 mA. It is not hard to believe that thirty years later an order of magnitude increase in current could be obtained.

Conclusion

A process such as ion implantation will establish itself if it enables products to be produced which have superior properties which cannot be made any other way so that price does not matter, or if the process is competitively cost effective. It is possible to anticipate that an increasing number of applications will be found where these factors apply. It seems clear that if viable processes are developed and the appropriate equipment becomes available, very significant growth will occur in the field of metal fabrication. In the long run the depletion of natural resources will strengthen the trend to ion implantation as the technique uses energy and materials very efficiently.

REFERENCES

- 1) W. Shockley, "Forming Semiconductor Devices by Ion Bombardment" U. S. Patent 2,787,564
- 2) J. Lindhard, M. Scharff, and H. E. Schiott, *Mat. Phys. Medd.*, 33, No. 14, 1963
- 3) J. F. Gibbons, "Ion Implantation in Semiconductors" Part I Range Distribution Theory & Experiments, *Proc IEEE*, 56, 3, 295, 1968
- 4) G. Dearnaley & N. W. Hartley, AERE-R 8562, Harwell, 1976
- 5) G. Dearnaley et al, "Ion Implantation", North Holland Publishing Co., Amsterdam, 1973
- 6) R. L. Seliger and W. P. Fleming, *J. App. Phys.*, 45, 1416, 1974
- 7) A. N. Broers, "Electron and Ion Beam Science and Technology" Ed. R. Bakish, IEEE, 1972
- 8) G. R. Ringo and V. E. Krohn, *Appl. Phys. Lett.* 27, 479, 1975

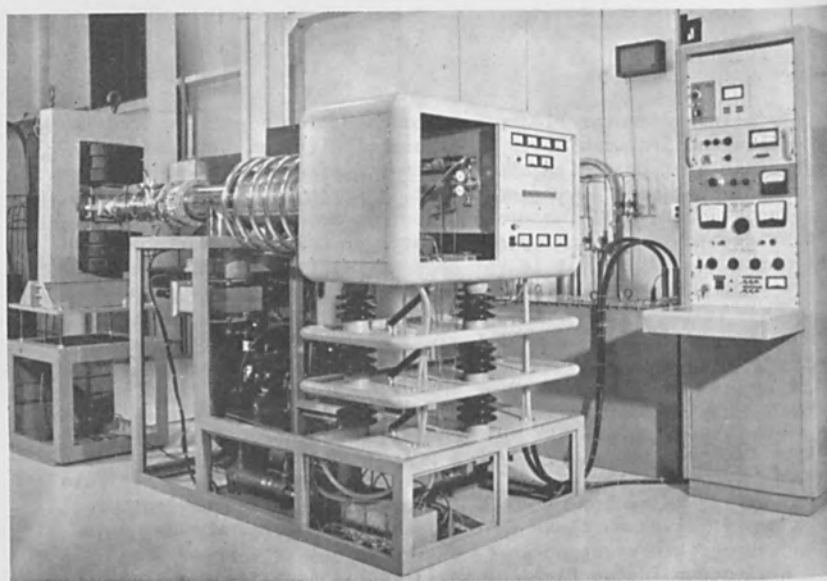


Figure 1. A 1969 ion implanter capable of operating at 150 keV
(Courtesy of High Voltage Engineering Corp.)

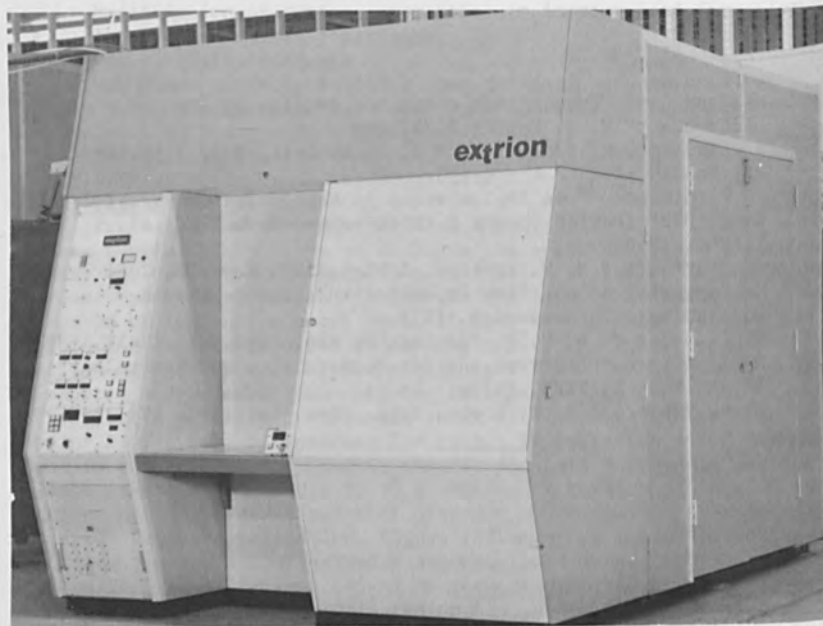


Figure 2. A modern high current 200 keV ion implanter (Courtesy of
Varian/Extrion Corp.)

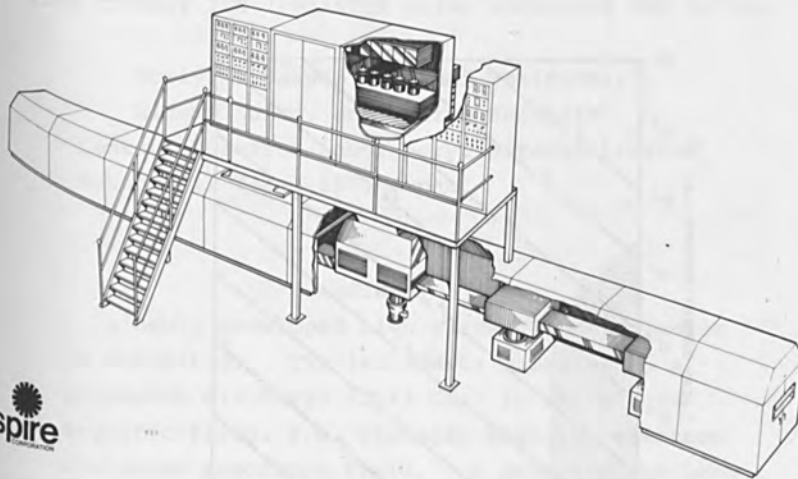


Figure 3 Drawing of an ion implantation system designed for fully automated production of solar cells at a rate of 180 m²/hr (by courtesy of Spire Corporation under contract to JPL)

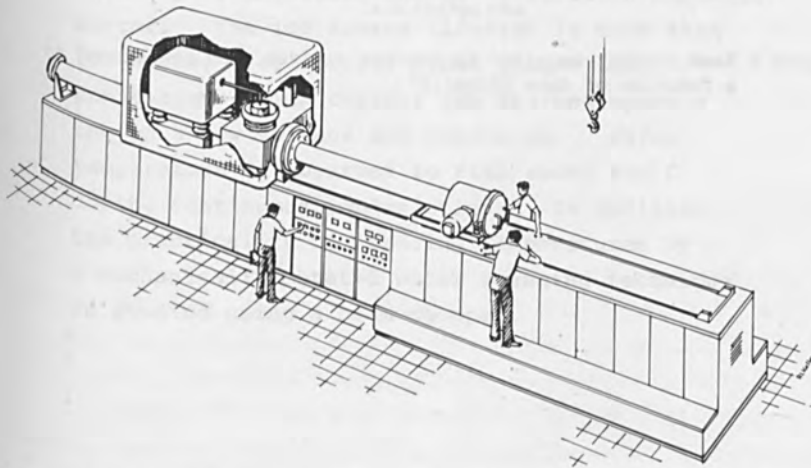


Figure 4 An implantation system for the nitriding of large extruder screws used in the plastics industry.

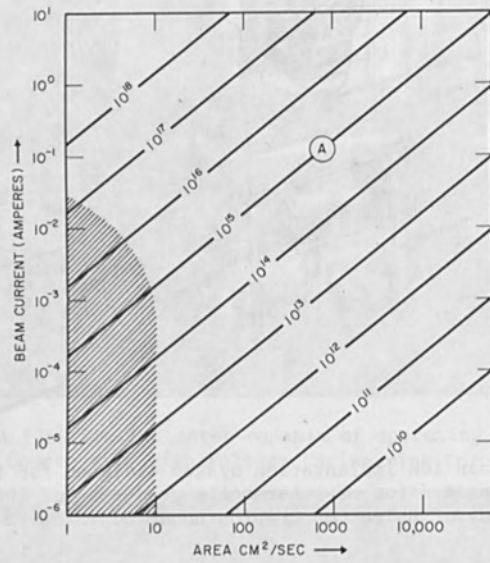


Figure 5 Beam current required to process a given area per second as a function of dose (ions/cm²)

HIGH CURRENT ION IMPLANTER USING MICROWAVE ION SOURCE

Noriyuki Sakudo, Katsumi Tokiguchi,
Hidemi Koike, and Ichiro Kanomata
Central Research Laboratory, Hitachi Limited,
Kokubunji, Tokyo 185, Japan

ABSTRACT

A newly developed high current ion implanter is described. The ion source operates on a microwave discharge (2.45 GHz) in an intense magnetic field, i.e. stronger than the electron cyclotron resonance field. A phosphor ion beam of more than 10 mA can be implanted into Si wafers by combining the ion source with a mass separator having a 40 cm radius and 60° deflection magnetic sector. The ion source lifetime is more than 100 hours, i.e. several times longer than conventional high current ion sources operating on a low voltage arc discharge. Wafer temperature is observed to rise above 850°C during continuous implantation. In addition, the practicality of lowering temperatures by a mechanically rotated wafer scanning technique is studied using a beam chopper.

1. Introduction

Ion implantation has come into wide use in semiconductor manufacture because it facilitates the controllability of the impurity dose. However, most conventional implanters can provide ion beams of only up to several hundreds μA . Thus, industrial applications have been restricted to MOS fabrication, which requires a comparatively lower dose. However, bipolar transistor fabrication requires higher currents.

Some implanters with conventional ion sources which operate on a low voltage arc discharge can provide ion beams of a few mA (1),(2). However, they utilize trouble-prone cathodes which usually limit the source life. This paper describes a newly developed high current ion implanter with an ion source which operates on microwave discharge (2.45 GHz) in an intense magnetic field, i.e. stronger than the electron cyclotron resonance field (3).

2. Ion Implanter

2.1. Microwave ion source

A microwave discharge ion source has been developed which produces a large cross sectional ion beam as the result of the use of a multi-aperture lens (4). This ion source proved that microwave discharge in an intense magnetic field creates a high density plasma. Furthermore, the source works under low pressures ($< 10^{-2}$ Torr) with high power efficiency.

However, since a mass separator for high current ion beam cannot use an electric field as in a Wien filter or a quadrupole mass filter (3), a microwave ion source has been newly developed for combination with a mass separator of the magnetic sector type. In order to obtain the necessary mass resolution, an ion beam is extracted through a slit. At the same time, the discharge chamber and the waveguide were modified as shown in Fig.1. Microwaves are introduced into the discharge chamber through a tapered, ridged waveguide and vacuum sealing dielectric plate. This ion source is placed in a solenoid which produces a magnetic field stronger than the electron cyclotron resonance field (890 gauss).

The discharge chamber is basically a ridged circular waveguide (80 mm inside diameter with 40 mm wide ridges, the gap between which is 8 mm). The electric field between these ridges, i.e. the discharge electrodes, is fairly uniform. The remaining space in the chamber, except for the discharge region, is filled with dielectrics (boron nitride).

In order to effectively utilize the generated ions, the cross section of the discharge region should have a rectangular shape similar to the exit slit. The plasma dimensions are slightly smaller than those of the discharge region because an ion sheath exists between the chamber wall and plasma surface. Since the exit slit is 2 mm x 40 mm to facilitate combination with a practical mass separator (40 cm radius, 60° deflection), the discharge region is determined to be a rectangular area with a cross section of 5 mm x 44 mm between discharge electrodes.

From the microwave circuitry point of view, the waveguide which introduces microwaves into the discharge chamber should have a similar cross section. Consequently a tapered, ridged waveguide is adopted. One end has a cross section similar to that of the discharge chamber, and the other is a 55 mm x 109 mm rectangular waveguide.

The extraction lens is a three-stage Pierce type as shown in Fig.2. The middle element is supplied with a negative potential (-2kV) to prevent low energy electrons, contained in the downstream ion beam, from entering the discharge chamber. The discharge chamber can be supplied with a voltage up to 40 kV.

One merit of this microwave ion source is that the magnetron, microwave source, can be grounded by adopting a choke flange structure which permits the passage of microwaves but is DC insulated. This means that all power supplies for the ion source are grounded.

2.2. Combination with mass separator

The ion source is combined with a mass separator, having a 40 cm radius, 60° deflection magnetic sector, to form an ion implanter as shown in Fig.3. The effective pole gap in the vacuum section is 45 mm. The pole piece edges at the beam entrance and exit positions can be moved to vary the the beam entrance and exit angles. Thus, the focal point of separator optics can be freely changed, i.e. the mass separated ion beam can be either sharply focused on a silicon wafer or defocused.

Furthermore, since an adjustable small amplitude of 50 Hz AC voltage can be superimposed on the ion acceleration voltage, the ion beam can be moved horizontally on a silicon wafer.

A silicon wafer is placed in a Faraday cup composed of a secondary electron suppressor and a grounded shield. A removable beam chopper is located in front of the Faraday cup and was used to test the possibility of lowering temperature through the use of a mechanically rotated wafer scanning technique. Wafer temperature was measured with an infrared detector through a calcium fluoride window located behind the wafer.

3. Experimental

3.1. Ion extraction

PH_3 gas is introduced into the discharge chamber and a microwave power of up to 300 W is applied. The total ion current at the ion source exit and the mass-separated P^+ ion current at the collector are shown in Fig.4. They both increase with incident microwave power. At a microwave power of 300 W, the total and collector currents of P^+ ions are 39.5 mA and 10.5 mA, respectively. In this case, the ion acceleration voltage is 40 kV and mass-separated P^+ ion beam is focused at the entrance of the Faraday cup. The beam chopper was not in place.

The ion current density at the plasma boundary, J , satisfies the Child-Langmuir equation in a first order approximation:

$$J = \frac{4}{9} \epsilon_0 \left(\frac{2e}{M} \right)^{\frac{1}{2}} \frac{V^{\frac{3}{2}}}{d^2}, \quad (1)$$

where ϵ_0 is dielectric constant of vacuum, M ion mass, e electron charge, V potential difference between the plasma and extraction electrode, and d the distance from the extraction electrode to the plasma boundary as shown in Fig.5. d is not a constant in this case. On the other hand, J is expressed according to plasma theory as

$$J = e \cdot n_e \left(\frac{k T_e}{M} \right)^{\frac{1}{2}} \exp\left(-\frac{1}{2}\right), \quad (2)$$

where n_e is electron density, T_e is electron temperature and k is Boltzmann's constant. From Eqs. (1) and (2), d is obtained as follows:

$$d = \frac{2}{3} \left(\frac{2 \epsilon_0^2}{e k T_e} \right)^{\frac{1}{4}} \frac{V^{\frac{3}{4}}}{n_e^{\frac{1}{2}}} \exp\left(\frac{1}{4}\right), \quad (3)$$

d decreases with incident microwave power since both T_e and n_e increase.

The effective area of plasma boundary, S , is proportional to d when S is assumed to be defined by the concave area which is obtained by cutting away a radius d cylinder with an effective angle as shown in Fig.5. Therefore:

$$\Delta S = S \cdot \frac{\Delta d}{d}. \quad (4)$$

S decreases with incident microwave power, although J increases.

Total ion current, I , is expressed as follows:

$$I = S \cdot J \quad (5)$$

Therefore, when only incident microwave power varies:

$$\begin{aligned} \Delta I &= \Delta S \cdot J + S \cdot \Delta J \\ &= I \cdot \left(\frac{1}{2} \cdot \frac{\Delta n_e}{n_e} + \frac{1}{4} \cdot \frac{\Delta T_e}{T_e} \right) \end{aligned} \quad (6)$$

This means that total ion current increases with microwave power.

A mass spectrum of PH_3 is obtained by sweeping the separator coil current and is shown in Fig.6. The P^+ ion current is about 70% of the total ion current. Thus, in conjunction with Fig.4, the dependence of separator transmission on incident microwave power is obtained as shown in Fig.7. In this case, the ratio of P^+ ion current to total ion current is assumed to be a constant value of 0.7 for convenience, although the actual ratio varies slightly with incident microwave power.

The separator transmission decreases as incident microwave power is reduced as shown in Fig.7. The reason for this is assumed to be that, at lower microwave power levels, plasma parameters n_e and T_e are so small that the plasma boundary moves backward. Therefore, an extracted ion beam diverges because of the deterioration of extraction lens optics. This works to reduce the mass separator transmission level.

3.2. Observation of wafer temperature rise

Wafer temperature is measured through a calcium

fluoride window located behind the wafer. Infrared rays in the 4.8 to 5.6 μm wavelength region are measured using an infrared detector. The detector is calibrated with a platinum thermocouple using a silicon wafer in an oven.

When a 35 kV, 2 mA/cm^2 density ion beam is focused on a silicon wafer, the temperature rapidly rises to above 1000°C. After 5 minute implantation, the wafer surface shows slip lines which are assumed to be due to heat distortion.

The dependence of beam density on wafer temperature is obtained using a 12 mm x 42 mm wafer placed in the Faraday cup. Then an ion beam is swiftly moved horizontally by superimposing the small amplitude 50 Hz AC voltage on the ion accelerating voltage so as to uniformly implant the wafer. The results are shown in Fig.8. The ion accelerating voltage is 27 kV and the parameter is current density.

An example of mechanically rotated wafer scanning techniques for lowering wafer temperature is shown in Fig.9. Silicon wafers are attached to a cylinder which is rotated as well as axially moved. The implantation duty cycle is given by the ratio of beam width to cylinder circle length.

In order to simulate this method a beam chopper is placed in front of the Faraday cup. It is rotated at 15 rpm. The results with a beam chopper for a 3/40 duty cycle are indicated in Fig.10. If the beam diameter in a mechanically rotated wafer scanning technique is assumed to be 75 mm or the same size as a 3 inch wafer, this

simu
The
in F
resp

cycl
out
cyl

4. 2

Tam
Hit
ion

(1)

(2)

(3)

(4)

simulates implantation with a 320 mm diameter cylinder. The results with current densities of 480 and 200 $\mu\text{A}/\text{cm}^2$ in Fig.10 correspond to 20, 16 and 8.5 mA implantations, respectively.

From experiments with a beam chopper with a 1/40 duty cycle, it is shown that 8.5 mA implantation can be carried out keeping the wafer temperature below 100°C using a cylinder of 800 mm diameter.

4. Acknowledgement

The authors are grateful to Dr. K. Yagi, Dr. M. Tamura and T. Tokuyama of the Central Research Laboratory, Hitachi Ltd. for participating in very valuable discussions on wafer temperature measurement.

REFERENCES

- (1) J.H. Freeman, Nucl. Instr. and Meth., 22 (1963) 306-316
- (2) N. Williams, "High Current Ion Source for Use on the PR-30 Implanter", 14th Symp. on Electron, Ion and Photon Beam Tech., (1977)
- (3) N. Sakudo, K. Tokiguchi, H. Koike, and I. Kanomata, " Microwave Ion Source for High Current Implanter", to be published in Rev. Sci. Instr., 49, July (1978)
- (4) N. Sakudo, K. Tokiguchi, H. Koike, and I. Kanomata, Rev. Sci. Instr., 48 (1977) 762-766

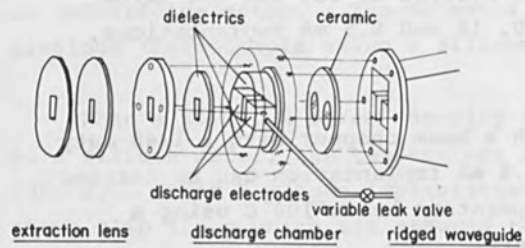


Fig.1
Microwave ion
source

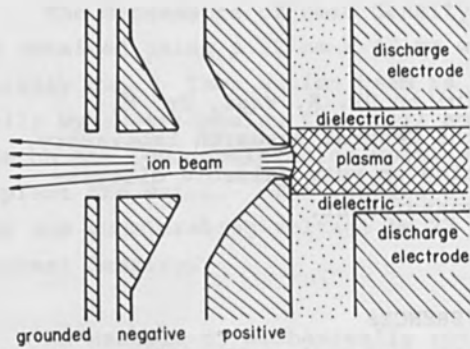


Fig.2
Ion extraction lens

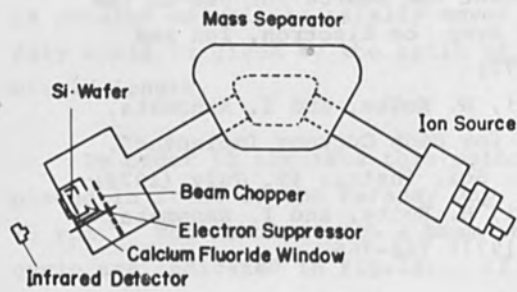


Fig.3
Combination of the
ion source with a
mass separator

ion currents

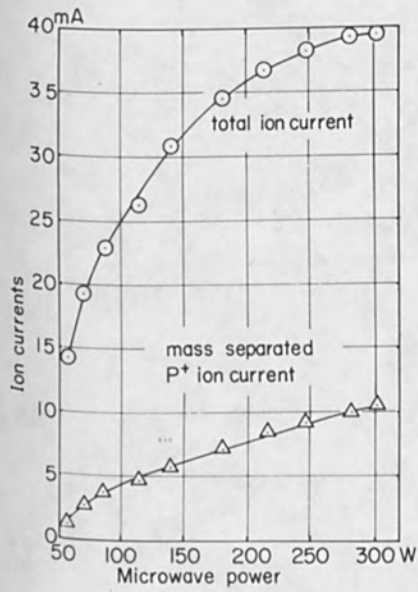


Fig.4 Dependence of ion currents on incident microwave power

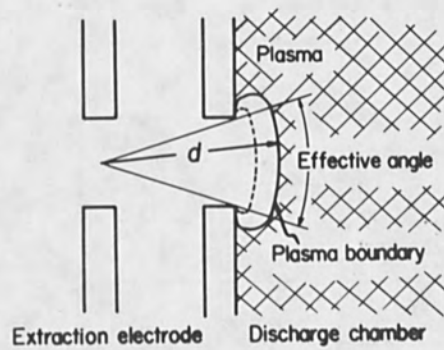


Fig.5 Schematic diagram of ion extraction

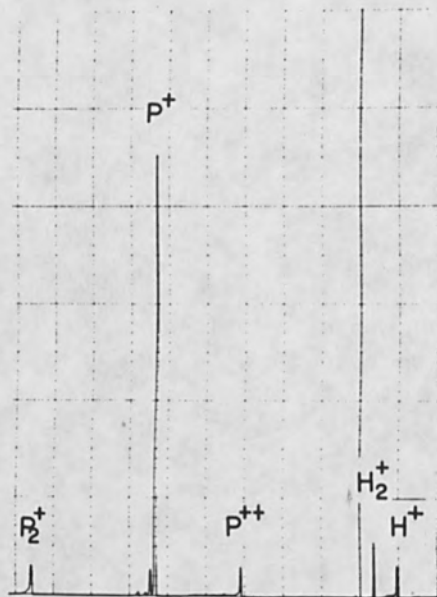


Fig.6 PH₃ mass spectrum

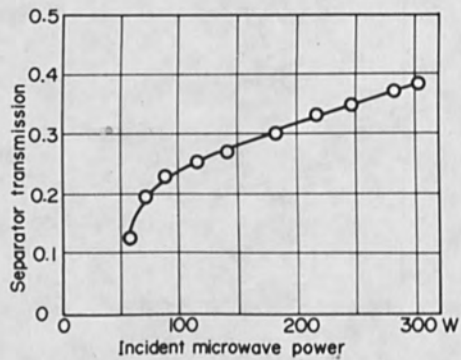


Fig.7 Dependence of separator transmission on incident microwave power

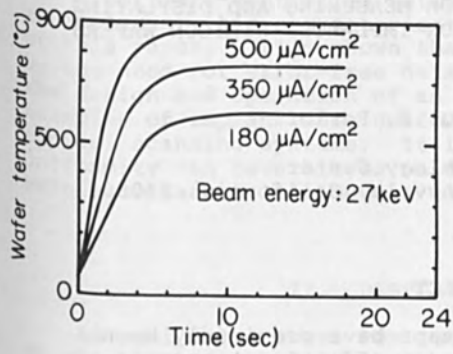


Fig.8
Wafer temperature rise during continuous implantation

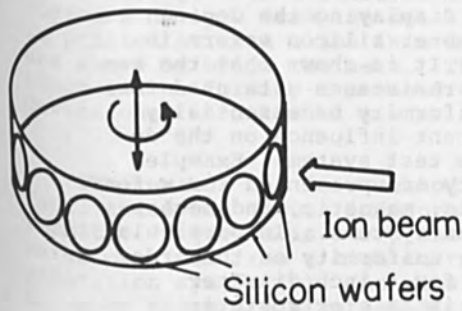


Fig.9
A mechanically rotated wafer scanning technique

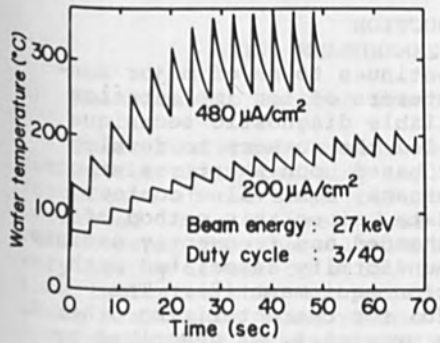


Fig.10
Temperature lowering effect of a 3/40 duty cycle beam chopper

AN AUTOMATED TEST SYSTEM FOR MEASURING AND DISPLAYING
THE DOPING UNIFORMITY OF ION-IMPLANTED SILICON WAFERS

F. E. Wahl and D. S. Perloff

Advanced Technology Center
Signetics Corporation, Sunnyvale, California 94086

ABSTRACT

Sheet resistance contour maps have previously been shown by the authors to be an effective means of displaying the doping uniformity provided by ion implantation equipment. An automated test system capable of measuring and displaying the doping uniformity of 5 inch diameter silicon wafers is described in this paper. It is shown that the requirement that the sheet resistance data used for characterizing doping uniformity be essentially error-free has a significant influence on the design and operation of the test system. Examples of implant dose uniformity are presented for wafers implanted on electrostatic, magnetic, and mechanical scanning implantation systems. In particular, it is shown that a doping uniformity on the order of $\pm 0.5\%$ may be obtained for 4 inch diameter silicon wafers implanted in an electrostatic scanning system.

I. INTRODUCTION

Implant dose uniformity continues to be of major concern to both users and manufacturers of ion implantation equipment. The need for a reliable diagnostic technique for evaluating uniformity has led the authors to develop a characterization methodology based upon sheet resistance measurements (1). In this approach, equi-value contour maps are used to display the data, since this method of presentation is readily comprehended and frequently assists in identifying sources of non-uniformity associated with the design or use of implantation equipment (2). The technique has also proved useful for characterizing other integrated circuit fabrication processes, as described by Perloff, Wahl and Reimer (3).

A software-controlled automatic test system designed to implement this characterization technique is the subject of this paper. It is shown that the requirements imposed by the need for error-free data significantly influence the design and operation of an automated test system. Examples of implant dose uniformity are presented for some typical scanning systems. It is found that exceptional uniformity can be achieved on 4 inch diameter silicon wafers implanted in a modern electrostatic scanning system.

II. DISPLAY TECHNIQUES

An equi-value sheet resistance contour map (1) obtained by the test system described below is shown in Figure 1. The heavy contours represent the wafer mean sheet resistance derived from a total of 118 data points. The lighter contours deviate from the mean in steps of 1%. A + or a - is printed at test sites in order to identify regions which are above or below the mean. The wafer mean sheet resistance and uniformity expressed as two relative standard deviations, in percent, are printed beneath the map.

The contour map is a method of presenting data which facilitates the visual interpretation of wafer doping uniformity. Figure 1 is a representative boron-implanted wafer obtained from a high current, magnetic scanning implantation system (4). An annular-shaped doping pattern, in which there are alternating regions of light and heavy doping, can be easily identified using this method of data presentation.

III. MEASUREMENT CONSIDERATIONS

A) Relationship Between Sheet Resistance and Dose

Sheet resistance measurements continue to be the prime method for characterizing implant dose uniformity. The dependence of the sheet resistance of a junction-isolated implanted layer on boron dose is shown in Figure 2. The relationship for these implant and anneal conditions is very nearly linear on a log-log scale. The slope of this line indicates that the uniformity values obtained from sheet resistance measurements will underestimate the actual dose uniformity by about one third. This fact should be kept in mind when interpreting the uniformity data presented in this paper.

B) Measurement Vehicles

Various methods have been used to measure the sheet resistance of junction-isolated implanted layers including microelectronic resistors (1,5) the four-point probe (1, 6-8), and the spreading resistance probe (9). In each of these methods, a measured resistance value (ohms) can be converted to sheet resistance (ohms/sq.) by multiplying by an appropriate geometrical correction factor. This factor, however, depends on a particular set of geometric variables which must be taken into account in order to obtain accurate and repeatable data.

Van der Pauw (10) has supplied the measurement and analysis technique needed to correct for the geometrical variations associated with the fabrication of microelectronic resistor structures. As shown in Figure 3, two current-voltage configurations are used to analytically remove the dimensional variability associated with photolithographic and etching steps.

In a similar fashion, Rymaszewski (11) has provided the technique for removing the effect of random variations in the pin spacings of collinear probe arrays as long as the four pins are aligned along the radius of the wafer. This source of error, which may be different for every probe array contact with the wafer, can be corrected in situ by performing the two-configuration measurement sequence shown in Figure 4.

In addition to pin spacing variations, wafer boundary effects can also lead to error in specifying the correction factor for four-point probe arrays. Perloff (6) has shown that the factor k_a' (Figure 4) may be computed as a function of probe orientation and distance from the edge of a circular wafer for probe arrays for which the probe spacings are approximately equal. It appears sufficient, however, to utilize the configuration switching technique described above as long as the probe array does not approach the edge of the wafer by a distance less than about 10 probe spacings.

C) Example of the Removal of Geometric Effects

Shown in Figure 5 are contour maps of the same electrostatically scanned boron-implanted wafer (12). The four-point probe data shown in Figure 5a are free from the effects of pin-spacing variations and the influence of the non-conducting wafer boundary. It thus exhibits the true underlying pattern of non-uniformity, i.e., a linear gradient from the top of the wafer to the flat.

In contrast, the four-point probe data used for the map of Figure 5b were not corrected for pin-spacing variations, although the effect of the wafer boundary was taken into account. This map appears chaotic, and the underlying gradient is consequently not recognizable.

It is clear from these examples that in order to fairly characterize implanted wafers, careful attention must be paid to removing all sources of measurement error. The automatic test system which will be described in the next section has been designed to provide the electronic switching and wafer positioning capability necessary to eliminate all significant sources of error.

IV. TEST SYSTEM

A) Requirements

Test system requirements are compared in Table I for the case of the van der Pauw resistor structure and the four-point probe. It should be noted that although the van der Pauw resistor requires masking and processing steps, it is capable of sampling a much smaller area and is useful over a larger range of sheet resistance than the four-point probe. In contrast, it is generally necessary to account for geometric effects associated with the non-conductive wafer boundary when employing a four-point probe array.

A number of requirements which must be met by the test system are common to both the van der Pauw resistor and four-point probe. The test wafer must be shielded from light and its temperature must remain stable during the measurement procedure. The current source should be stable and electronic noise minimized. The output voltage from the four terminal device must be large enough to achieve adequate resolution but small enough to prevent device heating or junction leakage effects. The four contacts must be ohmic over a suitable range of voltage. Contact voltage offsets must be eliminated by averaging the two voltage values which result from a reversal of the current source polarity (13). Finally, configuration switching, as discussed in Section III, must be utilized when the natural geometric variations of the test device become large in comparison with its characteristic dimension.

B) Equipment Design

A test system constructed with commercially available instruments which may be programmed to satisfy the various requirements described above is shown schematically in Figure 6 and in the photograph of Figure 7. Sheet resistance data are obtained from a number of predetermined locations on the wafer by employing various calculator-controlled instruments. An Electroglas Model 1034X x-y wafer prober equipped with Option C interface and Fairchild Instruments 4883 Data Coupler, capable of accommodating 5 inch diameter wafers, is used for positioning the test wafers. A Hewlett-Packard Model 3495A Scanner with four thermal options is wired as a 4 x 10 matrix switch and is used to select appropriate current and voltage leads. A Hewlett-Packard Model 3455A digital multimeter is employed for measuring voltages with a resolution of μV . The current source consists of two complementary instruments: an Electronic Development Corporation Model 501J voltage standard and Model PCS-1 current standard. When characterizing van der Pauw resistor structures, a fixed probe card is employed. An A. and M. Fell precision four-point probe with 0.025 inch probe spacing may be readily substituted for the probe card by using a convenient fixture which is permanently mounted upon the probe card insertion frame.

System control, data analysis, and display functions are provided by a BASIC language Tektronix Model 4051 Calculator equipped with 32 kilobytes of memory, a 300 kilobyte magnetic cartridge for program storage, an RS232-C communications port, and an IEEE-488 General Purpose Interface Bus (GPIB) port. The calculator sends digital commands over the GPIB (Figure 6) to the instruments described above in order to execute the required measurement functions. A Tektronix Model 4361 Copier is used for obtaining permanent records of the information displayed on the Calculator memory phosphor CRT screen (Figure 7).

After collecting the data from the test wafer, the calculator sends reduced data over the RS232-C channel (Figure 6) to a REMEX Model RJA 2321 interface and in turn to the REMEX Model RAB6075 paper tape punch/reader. This paper tape is then processed by a Digital Equipment Corporation Model PDP11/40 Minicomputer in order to obtain a high resolution equi-value sheet resistance contour map (1).

C) Operation

The test system described above has been designed for ease of use by a trained operator. The test wafer is first loaded on the vacuum chuck of the x-y prober and program control information is entered. Next the wafer is aligned and positioned manually with respect to the probe in the case of van der Pauw resistor structures, or automatically, in the case of the four-point probe. A current-voltage trace display is then used by the operator to examine device contact quality and to adjust the probe-to-wafer clearance. At the same time, a measurement current of sufficient magnitude to obtain an output voltage of approximately 30mV is established.

During the test, 118 individual test sites are probed and the resulting data converted to sheet resistance using the techniques discussed in Section III. A real-time numeric deviation map (1) is used by the operator to monitor the progress of the test. The data are sorted and the wafer mean and standard deviation are computed and displayed.

Once the test has been completed the operator may choose to have the calculator create a simplified contour map in order to assess the doping variability. Otherwise, the reduced data are punched on paper tape for transfer to the minicomputer system, as described above.

The time required to probe a wafer, review the data, and punch a paper tape is approximately 10 minutes. If selected, the simplified contour map requires an additional 3 minutes. The final contour map, generated by the minicomputer system, takes an average of 7 minutes to draw using a high resolution thermal plotter. The actual time required to produce either contour map depends upon the number of contours drawn.

V. RESULTS

The authors have previously presented examples of implant dose non-uniformity occurring on 2 and 3 inch diameter wafers (2). Both electrostatic scanning and mechanical scanning implantation systems were examined. The map of Figure 1, which was discussed in Section II, was obtained from a magnetic scanning system designed for high throughput of wafers used for solar cell applications (4). Figures 8a and 8b represent data obtained from a 2

inch diameter silicon wafer implanted in a mechanical scanning system (13). In this case doping oscillations occur across the surface of the wafer as a consequence of insufficient overlap of adjacent doping tracks. Figure 8b is a high spatial resolution linear scan obtained by carrying out four-point probe voltage measurements at 40 mil increments along the line labelled 1 + 2 in Figure 8a. (This behavior can be minimized by adhering to operational guidelines provided by the manufacturer (15).)

Examples of the doping uniformity obtained for the case of representative 4 inch diameter wafers implanted in two different electrostatic scanning implantation systems are shown in Figure 9. The contour map of Figure 9a (12) shows a linear resistivity gradient associated with tilting the wafer 7° relative to the incident ion beam. The contour map of Figure 9b (16) shows only a residual doping gradient, the overall uniformity being $\pm 0.53\%$. In this case, the wafer was maintained normal to the incident beam, so that the only source of variability is that due to the beam deflection required to scan a $4 \times 4 \text{ in}^2$ area.

VI. CONCLUSION

A sophisticated test system which utilizes sheet resistance measurements of implanted wafers to create contour maps for the purpose of characterizing dose uniformity has been described. The requirements of the measurement and display method have been shown to influence the design of the test system.

New examples of characteristic doping patterns have been presented for electrostatic, magnetic and mechanical scanning systems. Contour maps for 4 inch diameter implanted silicon wafers demonstrate that present day production ion implantation equipment is capable of delivering excellent uniformity.

ACKNOWLEDGEMENT

The authors wish to thank L. Amon and J. Reimer of the Signetics Corporate Process Control Department and L. Kerner of the Signetics Process Control Laboratory for funding the development of the test system and encouraging its use within Signetics and N.V. Philips' Corporation; K. Dettenrieder for her technical support; and Varian/

Extrion, Accelerators, Inc., and Spires, Inc. for their assistance in providing data for this presentation.

REFERENCES

- 1) D. S. Perloff, F. E. Wahl and J. Conragan, J. Electrochem. Soc., 124, 582 (1977).
- 2) D. S. Perloff, F. E. Wahl and J. T. Kerr, in Proceedings of 7th International Conference on Electron and Ion Beam Science and Technology, Washington, D.C. 1976.
- 3) D. S. Perloff, F. E. Wahl and J. D. Reimer, Solid State Technology, 20, 31 (Feb. 1977).
- 4) Spires Corp. Implantation System, Bedford, Mass.
- 5) M. G. Buehler and W. R. Thurber, J. Electrochem. Soc., 125, 645 (1978).
- 6) D. S. Perloff, J. Electrochem. Soc., 123, 1745 (1976).
- 7) D. S. Perloff, Solid State Elec., 20, 681 (1977).
- 8) B. J. Smith and J. Stephen, Rev. Phys. Appl. (FR), 12, 493 (1977).
- 9) Proc. NBS Spreading Resistance Symp., NBS Spec. Publ. 400-10, 1974.
- 10) L. J. van der Pauw, Philips Res. Rep., 13, 1 (1958).
- 11) R. Rymaszewski, J. Sci. Instr., 2, 170 (1969).
- 12) Implanter Model 200-20 A2F, Varian/Extrion, Gloucester, Mass.
- 13) ASTM Designation F84, "Annual Book of ASTM Standards", Part 43, Nov. 1977.
- 14) Implanter Model 1000-200, Varian/Extrion, Gloucester, Mass.
- 15) D. Downey and G. Ryding, Varian/Extrion T.R. 2007D, April, 1977.
- 16) Implanter Model AIM210, Accelerators, Inc., Austin, Tex.

Thin diameter silicon wafer impaled in a mechanical...
 mounting with...
 Figure 10...
 This behavior can be...
 (10)

The...
 of the...
 The...
 The...

TABLE I. Comparison of system requirements for the case of the four-point probe and van der Pauw resistor structure.

SYSTEM REQUIREMENTS	FOUR POINT PROBE	VAN DER PAUW
Masking steps	none	1 to 4
Minimum sample size	100 ² mil ²	10 ² μm ²
Sheet resistance range	<3000 Ω/□	<20,000 Ω/□
Junction depth range	>.1 μm	>.01 μm
Wafer probing temperature	25+/- 2° C, .1° C/min	
Wafer shielded from light	>100 Ω/□	
Current source stability	.03% of reading	
Device output voltage	V _A ~ 30mv	
Voltmeter resolution	10 μv	
Minimum ohmic contact range	+/- 300mv	
Polarity reversal and averaging	Always	
Wafer position correction	$\frac{a}{R} < .5$ & $\frac{s}{R} > .05$	never
Configuration switching	s < 40 mils	b < 20 μm

The authors wish to thank...
 significant...
 support of the...
 primary...
 to the...
 A. Department...



111.17 OHM/SQ. \pm 4.79 %

Figure 1 A sheet resistance contour map of a boron-implanted wafer obtained from a magnetic scanning implantation system.

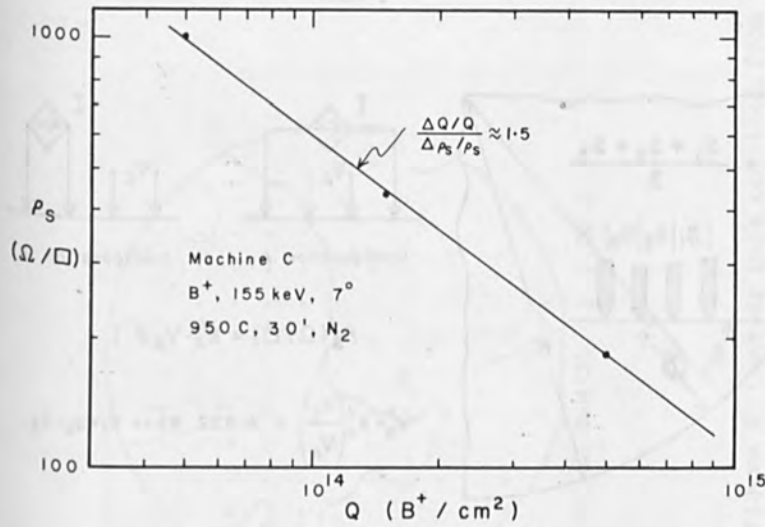


Figure 2 Empirical relationship between implanted boron dose and measured sheet resistance for the conditions indicated. Each data point represents the average of 118 readings.

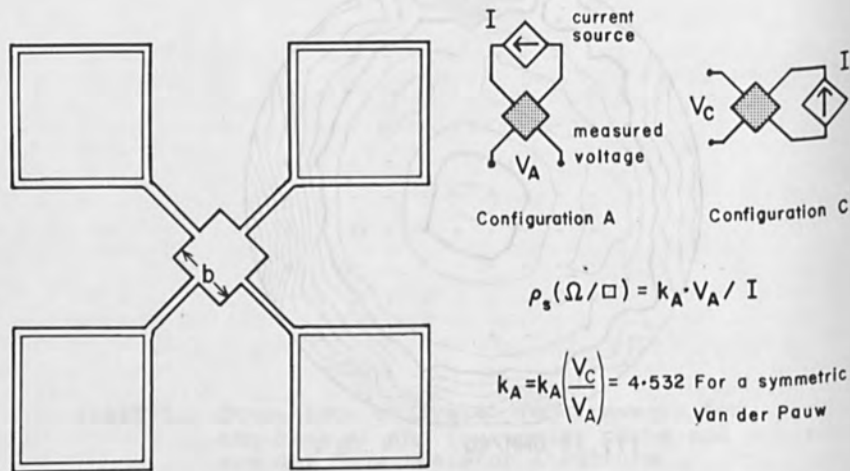


Figure 3 Van der Pauw structure and the current-voltage configurations used to eliminate geometric sources of error.

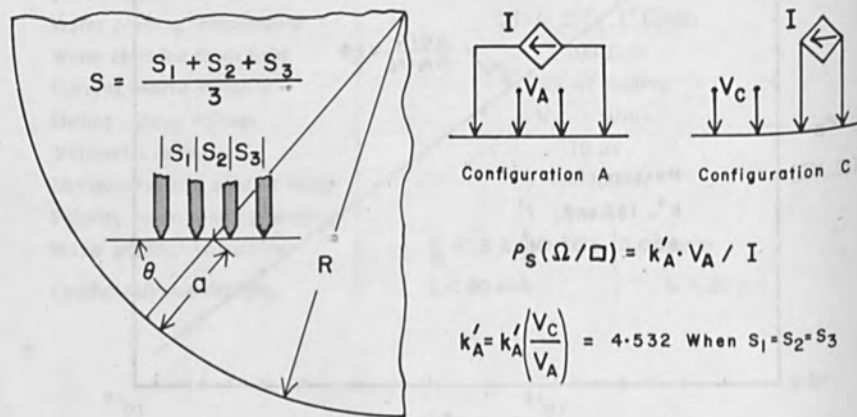


Figure 4 Four-point probe and the current-voltage configurations used to eliminate the effect of probe spacing variations.



242.82 OHM/SQ. \pm 1.30 %

a



239.41 OHM/SQ. \pm 2.05 %

b

Figure 5 Contour maps obtained from the same boron-implanted wafer: (a) corrected for measurement error associated with probe spacing variations; (b) uncorrected data.

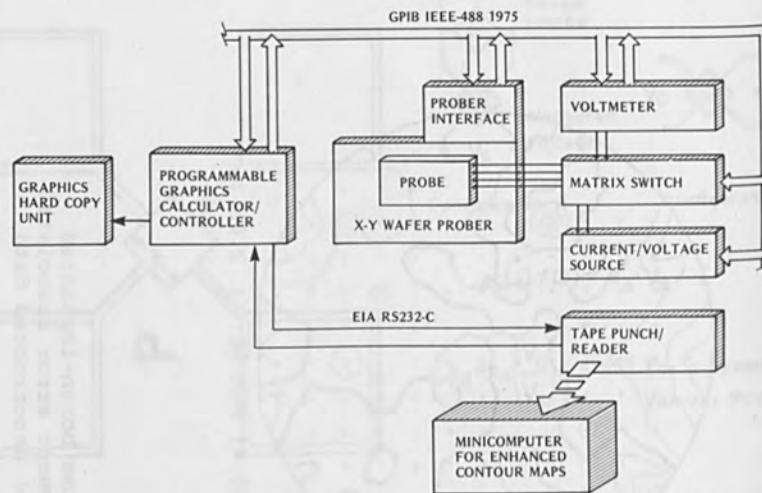
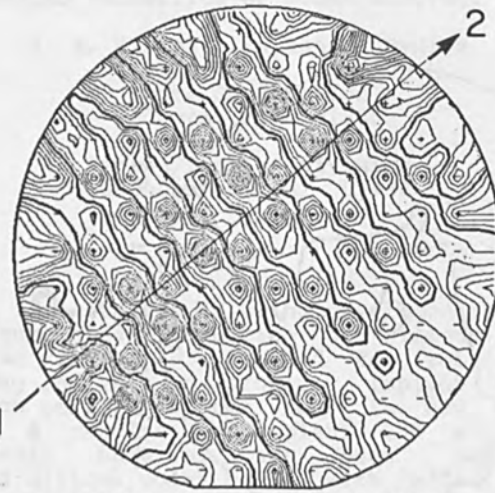


Figure 6 Test system schematic.

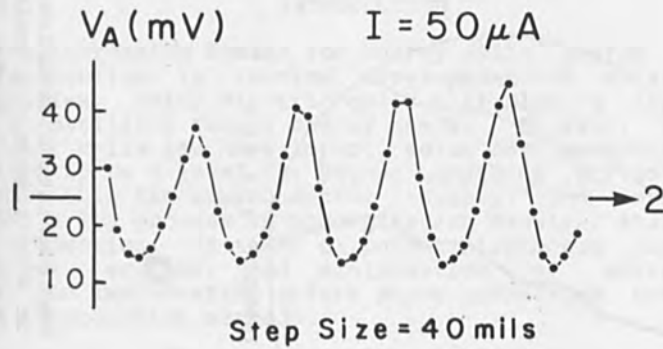


Figure 7 Photograph of the test system being operated by Ms. K. Dettenrieder.



2932.24 OHM/SQ. \pm 48.79 %

a



b

Figure 8 Doping oscillations occurring in a mechanical scanning implantation system: (a) contour map; (b) high resolution linear scan.

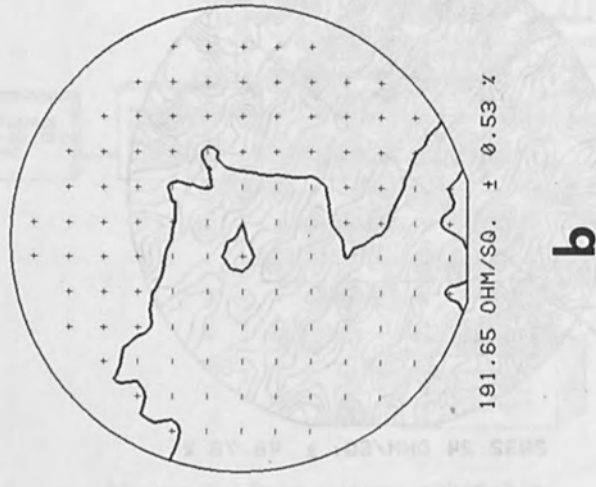
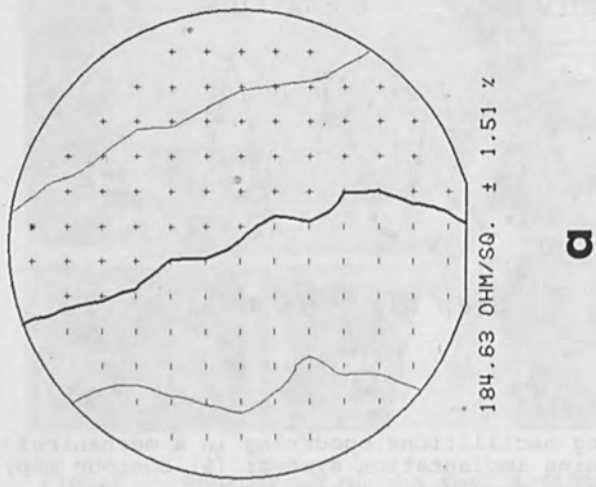


Figure 9 Representative examples of 4 inch diameter wafers implanted on electrostatic scanning implantation systems: (a) 7° tilt resulting in a linear doping gradient; (b) 0° tilt exhibiting excellent doping uniformity.

ION IMPLANTATION FOR LARGE SCALE
AUTOMATED PRODUCTION OF SOLAR ELECTRIC CELLS

A. R. Kirkpatrick and G. Ryding

Spire Corporation
Bedford, MA 01730

Varian/Extrion Division
Gloucester, MA 01930

ABSTRACT

Ion implantation is being developed for high volume automated production of silicon solar cells. An implanter designed for solar cell processing and able to properly implant up to 300 4-inch cell wafers per hour is now operational. A machine to implant 180 m²/hr of solar cell material has been designed. Implanted silicon solar cells with efficiencies exceeding 16% AM1 are now being produced and higher efficiencies are expected. Ion implantation and transient processing by pulsed electron beams are being integrated into a simple method for large scale, high speed, low cost production of solar cell arrays.

INTRODUCTION

The increasing demand for energy while energy resource reserves decline is forcing development of solar energy technologies. Solar electric cells will play a significant role in fulfilling future energy needs. However, in order that solar cells can have impact, solar cell production must be scaled up to a level far beyond anything previously attempted within the semiconductor industry. Ion implantation is to be a key process in accomplishing massive scale automated production. In terms of potential process simplicity, throughput, economy, and minimization of environmental threat, ion implantation offers major advantages over other dopant introduction methods.

Production of solar cells using ion implantation has been considered for more than a decade⁽¹⁾. The modest production levels necessary to provide power for space vehicles have been satisfied by other methods. But the advantages of implantation for meeting future needs are easily recognized. Among these advantages are process control and reproducibility, reduction of associated processing requirements and ease of total process automation.

Among considerations remaining relative to the use of ion implantation for solar cell production have been questions regarding:

- (i) Limitations of ion implantation equipment
- (ii) Efficiency of ion implanted solar cells
- (iii) Integration of implantation into a cost effective total process.

These are now being addressed.

ION IMPLANTATION EQUIPMENT FOR SOLAR CELL PRODUCTION

Standard ion implantation equipment used by the semiconductor industry is not adequate for solar cell production purposes. High performance solar cells are best produced using ion energies lower than can be delivered by most machines. Ion fluences required for solar cells are sufficiently high that existing machines have limited, impractical throughput capabilities. However, implant uniformity and reproducibility requirements for solar cells are not as critical as for many devices and can probably be relaxed to + 10% allowable variation over all material processed. A typical solar cell is a single device utilizing all of the area of the material from which it is produced. Wafer holding methods which cause local shadowing during implant are not acceptable. The surfaces of solar cell materials are not necessarily of high quality and may be intentionally featured or texturized to improve cell performance by reducing reflection losses. A standard implantation process in which ions are introduced from a fixed direction relative to the wafer is not satisfactory for these surfaces.

A first high throughput dedicated solar cell process implanter has been developed. This machine, which is shown in Figure 1, was designed and constructed by Varian/Extrion Division and is now operational at Spire Corporation to support the Low Cost Solar Array Project of the Jet Propulsion Laboratory. Features of the dedicated solar cell process implanter which distinguish it from previously existing machines include:

- (i) Low ion energies
- (ii) High currents of mass analyzed ion beam efficiently utilized on target
- (iii) Wafer holding without beam shadowing
- (iv) Wafer rotation in the ion beam during implant.

Performance specifications for the machine are summarized in Table I. The system combines components developed previously for other implanters⁽²⁾ together with new components for the solar cell process application. Figure 2 illustrates major subsystems which are described below.

a) Ion Source

The ion source is a modified "Freeman"⁽³⁾ source fed from a manifold providing three independent gas supplies to allow dopant ion selection. Ions are extracted from the source using a conventional two-electrode acceleration-deceleration system by means of a 35 kV, 20 mA regulated power supply. The emerging beam diverges in the horizontal plane with an angle of $\pm 1.5^\circ$ and is essentially parallel in the vertical plane.

b) Analyzing Magnet

A 90° double focusing analyzing magnet is used both as mass-filter and to refocus the diverging beam. The magnet poles have been designed to produce both vertical and horizontal focusing so that a stigmatic circular image of the slit is formed and the beam converges to the cross-over in an essentially symmetric cone.

c) Magnetic x-y Scanner

After analysis the beam passes through a magnetic scanning system which provides horizontal and vertical scan fields up to ± 400 Gauss. Power amplifiers driven by triangular waveform generators can be controlled independently in the frequency range 0-10 Hz in order to produce the required beam scan uniformity at the wafer plane. Since extreme uniformity is not required to produce efficient solar cells, the scan waveforms and amplitudes have been optimized so that the resulting beam scan, when combined with a mechanical motion of the wafer gives minimum overscan loss of beam and the maximum wafer throughput.

d) High voltage Terminal

The machine features a "pre-analysis" configuration in which the beam is decelerated to the final on-target energy after analysis of the beam. In order to accomplish this, the entire ion source, analyzer and associated vacuum systems are self-contained in a compact high voltage terminal. Power to the terminal is supplied by a 15 kVA generator driven through an insulating shaft. A novel power supply configuration is used to implement the deceleration. If a negative power supply is connected to the high voltage terminal in a conventional manner, then the supply

experiences a "negative load" from the beam and the final energy is determined as the difference between two power supply voltages. Instead a second positive power supply has been connected between ground and the ion source. In this way the ion beam load on the supply is "normal" and the final energy of the beam is controlled uniquely by this supply.

e) Retardation Lens

After scanning, the beam enters a 3-electrode retarding lens system which reduces the beam energy from 35 keV to the final required implant energy (typically 5-10 keV) and at the same time focuses the beam on target. The potential of the center electrode can be adjusted to optimize focus and transmission as a function of space charge effects and ion source conditions. Typically a beam size of 3-4 cm is produced but since this is not critical a fixed value of -18 kV with respect to the terminal has been selected.

f) Wafer Processing Station

The beam finally enters a WayflowTM processing station⁽²⁾ which is compatible with standard industrial wafer carriers and can process up to 300 four-inch wafers per hour using 5 second implants. For this application the platen which supports the wafer in the implant position has been modified so that the wafer rotates about an axis perpendicular to the centre of the wafer at a speed of approximately 60 r.p.m. during implant. This extra scanning motion enhances uniformity, and ensures that beam shadows from wafer retaining clips are avoided and total front surface area implantation is achieved.

The solar cell process implanter shown in Figure 1 can perform junction implants into as many as 300 4-inch wafers per hour. If utilized to full capacity the machine could support a production line manufacturing up to one megawatt of solar cell product per year, the approximate equivalent of total us production of solar cells in 1977. However, automated production lines which are to become operational in the 1980's will require implanters with much higher throughput capabilities.

Spire has designed an ion implanter to perform junction implants into 180 m² of solar cell silicon per hour⁽⁴⁾. Solar cell product throughput of this machine is to exceed 100 megawatts per year. Design specifications for the machine are listed in Table II, a conceptual drawing is given in Figure 3. It is planned that such implanters will be incorporated into totally automated production lines, perhaps by as early as 1982.

ION IMPLANTED SILICON SOLAR CELLS

In recent years relatively little development has been performed on ion implanted silicon solar cells. Work is now in progress to optimize implanted junctions and back layers in an N^+/PP^+ cell. High performance cells are being achieved. Implantation is being used for single crystal silicon with planar or texture etched surfaces and for cast polycrystalline sheet silicon. Good junction performance is being accomplished by implantation into polycrystalline thin film silicon.

The process description listed in Table III can be employed to fabricate single crystal silicon 7.6cm diameter cells of efficiency better than 16% AM1. Figure 4 shows the I-V characteristic of a representative cell. The complex implant anneal cycle indicated in Table III produces effective removal of crystal damage in the implanted layers, causes satisfactory electrical activation of both the phosphorus junction implant and the heavy boron implant used to produce back surface field effect, and delivers good minority carrier lifetime in the cell base region. However the 850°C component of this particular anneal causes significant dopant diffusion and results in a rather deep 0.3 micrometer junction. Higher cell efficiencies are to be accomplished using modified implant conditions, improved anneal parameters plus a texture etched front surface on the silicon.

ADVANCED PROCESSING TECHNOLOGY FOR AUTOMATED PRODUCTION

The processing listed in Table III represents technology which can be employed today for production of ion implanted solar cells. Much simpler, lower cost procedures should be used in high volume automated production lines for the 1980's. Spire is developing an advanced approach to simplified, high speed production.

Directly or indirectly, elevated temperature steps are responsible for most of the energy consumption, waste generation, processing complexity and time required to produce a silicon solar cell from adequate starting material. Each thermal step has the purpose of performing some treatment, annealing, sintering, etc., in the vicinity of the device surfaces. A very short duration pulse of energy from an electron beam or laser, deposited directly into the region to be processed, can cause equivalent effects to occur. When ion implantation and pulsed energy techniques are combined, major process simplifications and a very effective automated production approach can result.

The basis for producing transient processing effects is the ability to achieve, then quickly quench, a high temperature in the localized region being treated. Because of considerations related to obtaining sufficient energy deposition, uniformity and reproducibility over large areas with ability to build energy efficient high repetition rate production machines, the pulsed electron beam has advantages over lasers for solar cell production applications. Development is being conducted using a pulsed electron beam of duration 10^{-7} second, uniform beam diameter 6 cm, and mean electron energy approximately 10 keV. Figure 5 shows transient temperature conditions produced in the region of a silicon wafer surface when a 0.2 cal/cm^2 pulse is used for implant damage annealing. Annealed layers are found to be single crystalline and free of dislocations with excellent activation of implanted dopant.

(1)

(2)

(3)

(4)

Using ion implantation and pulsed electron beam processing, silicon solar cells have been fabricated at high speed, without conventional thermal operations and without the use of any wet chemistry or gas phase operations⁽⁵⁾. The concept now under development is suggested in Figure 6. A sheet of texture etched silicon will have both surfaces implanted and pulse annealed. A thin contact interface, perhaps only a few hundred Angstroms thick, will be deposited by one of several candidate methods. Then cells will be loaded into glass sheet arrays with wire screens positioned to provide the bulk of the cell contacts and also the interconnections between cells. Electrostatic bonding will be employed to hermetically seal the cells and wire contact/interconnections within the glass array structure. This concept has been successfully demonstrated on single cells and small test modules.

(5)

ACKNOWLEDGEMENT

This work has been supported by Jet Propulsion Laboratory, California Institute of Technology, under the Low Cost Solar Array Project sponsored by the US Department of Energy.

REFERENCES

- (1) Burrill, J., King, W., Harrison, S. and McNally, P., IEEE Trans. Electron Devices, ED-14, No. 1, 10 (1967).
- (2) Ryding, G., Wittkower, A. B. and Rose, P. H., J. Vac. Sci. Technol., 13, 1030 (1976).
- (3) Freeman, J. H., Nuclear Instruments and Methods, 22, May 1978. 306 (1963).
- (4) Rose, P. H., "Ion Implantation - Yesterday, Today, and Tomorrow" Electrochemical Society Meeting, Seattle, 22, May 1978.
- (5) Kirkpatrick, A. R., Minnucci, J. A. and Greenwald, A. C., IEEE Trans. Electron Devices, ED-14, No. 4, 429 (1977).

TABLE I
 PERFORMANCE SPECIFICATION
 SOLAR CELL PROCESS IMPLANTER

Energy Range:	5-50 keV
Beam Current on Wafer:	p31+ > 2mA B11+ 1 mA
Wafer Size:	Up to 4 inch
Doping Uniformity:	$\pm 10\%$ or better
Implant Angle:	Adjustable 0-10°
Wafer Handling	Compatible with standard carriers
Beam Scan:	Magnetic x-y 0-10Hz
Wafer Scan:	60 r.p.m. spin

TABLE II
 DESIGN SPECIFICATION
 SOLAR CELL PRODUCTION IMPLANTER

Ion Species:	p31+, As ⁷⁵⁺ or B11+
Ion Energy:	Fixed in range 10-30 keV
Beam Current:	Minimum 100 mA p31+
Uniformity/Reproducibility	Not worse than $\pm 10\%$
Substrate Throughput:	500 cm ² /sec at 10 ¹⁵ ions/cm ²
Materials/Handling	Any material/cassettes

TABLE III
 PROCESS SPECIFICATION
 HIGH EFFICIENCY IMPLANTED 7.6cm DIAMETER CELLS

<u>Silicon Material</u>	10 ohm-cm 100 CZ p-type Surfaces: Front - Polished Back - Bright Etched
<u>Process Sequence</u>	
Implant:	Front - 2 x 10 ¹⁵ 31p ⁺ /cm ² , 5 keV Back - 5 x 10 ¹⁵ 11B ⁺ /cm ² , 25 keV
Anneal:	Simultaneous phosphorus and boron anneal in nitrogen 550°C - 2 hours 850°C - 15 minutes 550°C - 2 hours
Clean:	Buffered HF DI rinse
Front Contact:	Evaporate 400 Å Cr + 400 Å Au Define Spire Starburst pattern with Kodak KTRF process Electroplate 12 μm Ag
Clean:	Buffered HF DI rinse
Back Contact:	Evaporate 400 Å Al + 1 μm Ag
AR Coat :	Evaporate 700 Å TiO ₂
Sinter:	400°C - 10 minutes in nitrogen

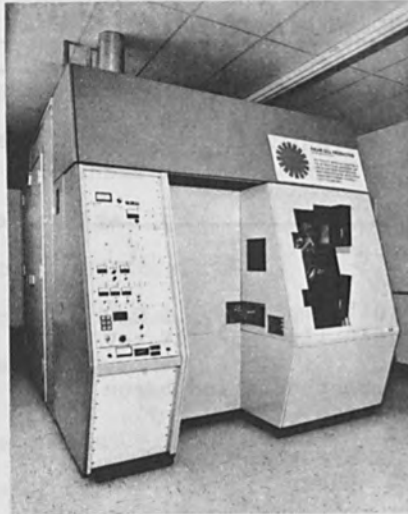


Figure 1. Solar Cell Process Ion Implanter

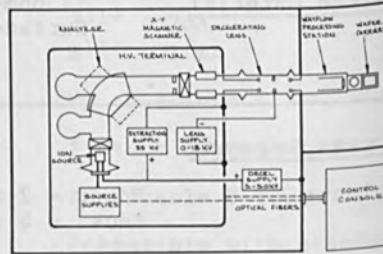


Figure 2. Solar Cell Process Implanter Schematic

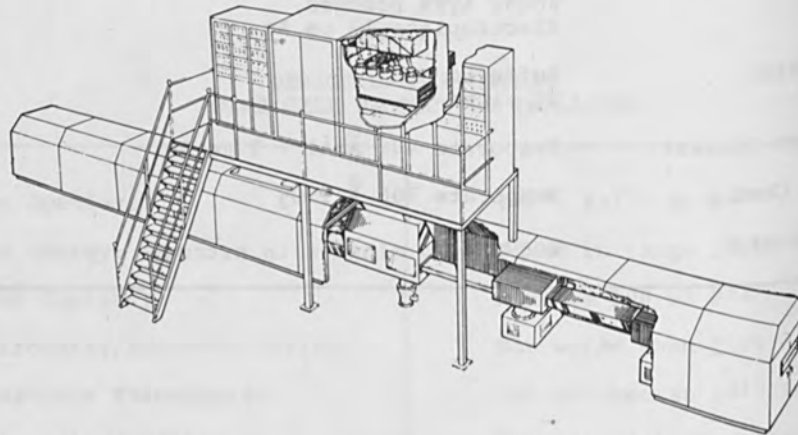


Figure 3. Conceptual Design of Solar Cell Production Implanter

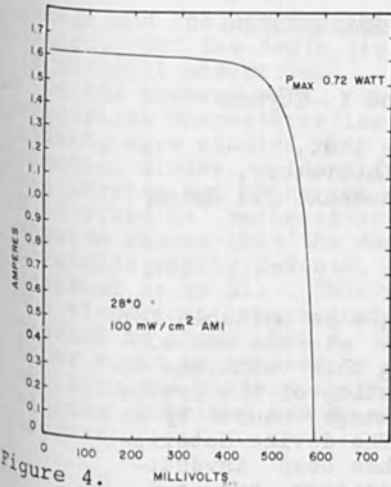


Figure 4. I-V Characteristic of Ion Implanted 7.6 cm Diameter Silicon Solar Cell

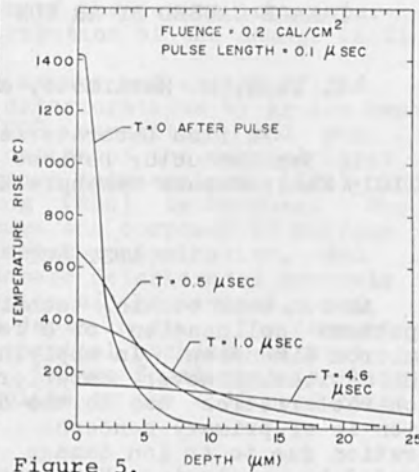


Figure 5. Temperature Profiles in Silicon Following Electron Beam Pulse

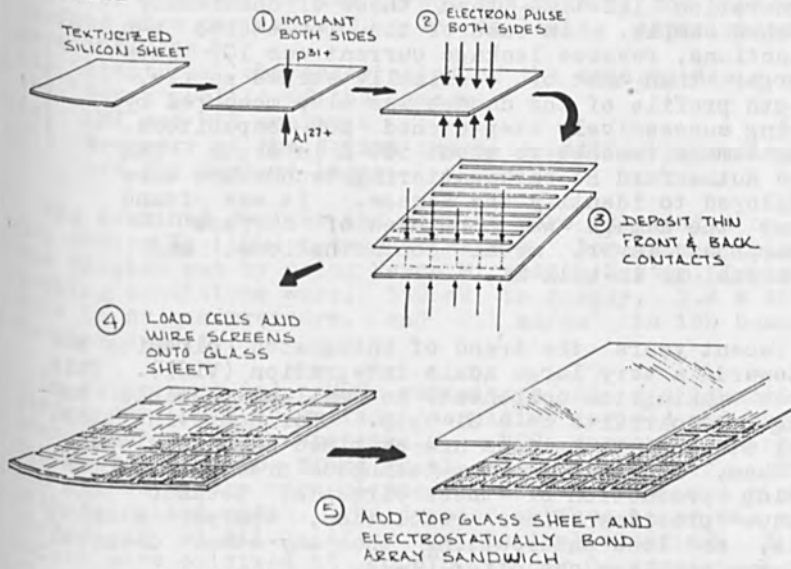


Figure 6. Automated Production Concept for Solar Cell Arrays

DAMAGE CAUSED BY AR ION BEAM ETCHING

H. Yano, H. Hashimoto, and Y. Toyama

Fujitsu Laboratories Ltd.,
Semiconductor Devices Laboratory,
1015 Kamikodanaka Nakahara Kawasaki 211 Japan

ABSTRACT

Ar ion beam etching technique is suitable for pattern delineation of a few microns and sub-micron dimension. In applying this technique to Si devices, however, deterioration of the device characteristics due to the damage caused by Ar ion is of primary concern. The device deterioration due to Ar ion damage has been investigated by analyzing MOS capacitors and p-n junction diodes characteristics. The ion-etched MOS capacitors showed $10^2 - 10^3$ times larger surface-state density and 10^{-2} time smaller generation lifetime than those of chemically etched sample. In case of the ion-etched p-n junctions, reverse leakage current was 10^5 times larger than that of chemically etched sample. Depth profile of the damage was also measured by using successively step-etched MOS capacitors. The damage reached to about 500 Å in depth. IMA and Rutherford He backscattering techniques were employed to identify the damage. It was found that the damage was composed of surface amorphous layer, metal contaminations, and residual Ar in bulk Si.

In recent years the trend of integrated circuits has been towards a very large scale integration (VLSI). This requires making the components as small as possible and packing more circuits on a Si chip. For achieving them, several etching techniques are examined and developed. Among them, ion beam etching technique presents the most promising production of these circuits, because this technique provides finer resolution, sharper etching profile, and less undercutting than any other chemical and plasma etchings can offer (1-3).

However, surface crystallographic perfection is damaged by Ar bombardment (4,5). H. R. Deppe et al. examined the

damage and the deterioration of the device characteristics. But the depth distribution of the damage in Si is not well understood.

In the present work, the manner and extent of the electrical characteristics deteriorations by Ar ion beam etching were studied with MOS capacitors and p-n junction diodes. Identification of the damaged layer was carried out using ion micro mass analyzer (IMA) and Rutherford He⁺ backscattering (RBS) techniques. The results showed that the damage was composed of surface crystallographic defects, metal contamination, and residual Ar in Si. This damage deteriorated severely the electrical characteristics of the devices, and reached to about 500 Å in depth in Si. The damaged layer could be removed by chemical etchant without spoiling the pattern shape. It was found that ion beam etching technique can be applied to the VLSI production process.

Experimental

For identification of the damage and investigation of the extent of damaged layer in Si, electrical measurements of the devices and direct analysis of the damaged surface were carried out. The following experiments were included.

- (a) Electrical characteristics of the damaged devices
- (b) Depth profile of the damage
- (c) IMA and RBS analysis
- (d) Recovery of the device characteristics by etching off the damaged layer.

The examined devices and samples were fabricated on 3-5 ohm-cm Si (100) p-type CZ wafers. Ion beam etching was carried out by using Veeco Microetch System. Typical etching conditions were, 550 eV in energy, 2.8×10^{-4} Torr in Ar gas pressure, and 0.5 mA/cm^2 in ion beam current density.

In experiment (a), MOS capacitors and p-n junction diodes were used as surface sensitive devices and bulk sensitive devices respectively. MOS capacitors were fabricated by using standard Al-gate MOS process. The ion etched wafers were cleaned by HNO₃ boiling and rinsed with deionized water. The damaged surface layer was not etched off at all. After the chemical cleaning, Si wafers were oxidized at 1000°C in dry O₂ atmosphere for 30 min. and 320 Å thick SiO₂ films were grown as shown in Fig. 1 - (a). The surface-state densities of the MOS

capacitors were measured by using the quasi-static C-V method (6-9). The breakdown voltage of gate oxide was measured with negative bias voltage on the 400 microns square Al electrode. In the examined p-n junctions, 0.6 micron thick SiO₂ was grown by steam oxidation at 1100°C and the diffusion regions were etched off by ion beam with Ti mask as shown in Fig. 1 - (b). Arsenic was diffused into Si from arsenosilicate glasses at 1100°C. Junction depth was 0.15 micron. Al electrodes were evaporated and patterned by the photolithography techniques. Reverse leakage currents were measured on the wire-bonded chips in a shield box, at room temperature. Carrier lifetime was measured from the switching time and calculated by Kingston's method (10).

In experiment (b), the damaged wafers were successively step-etched and MOS capacitors were formed on their surfaces as shown in Fig. 2. Fabrication process and sample dimensions were the same as shown in Fig. 1 - (a). NH₄OH-H₂O₂ solution was used to remove the damaged layers. The thickness of removed damage layer was measured by Taly-Step. Surface-state density N_{ss} and generation lifetime T_g were calculated from MOS C-V and C-t measurements (11).

In experiment (c), identification of the damage was carried out by IMA and RBS analysis. The damaged layers, which were ion etched without mask material, were examined and compared with the initial surface. IMA was used to analyze the contaminated impurity of the damaged surfaces. In the IMA measurements, as Ar sputtering was used, information about Ar⁺ in Si was not obtained. Therefore, RBS spectra were used in order to measure Ar and crystallographic defects at the ion-etched surface, with using 1.5 MeV He⁺ ions. RBS analysis was carried out in both random and channeling directions.

In experiment (d), recovery of the damaged device characteristics was examined by using MOS FET's. The samples were fabricated with standard Si-gate process. The thickness of the gate oxide was 320 Å and n⁺ source-drain layer was 0.5 micron deep. After the gate oxidation, 0.3 micron thick phosphorus doped polysilicon was deposited at 600°C and annealed. And the dimension of the gate was 10 microns in length and 500 microns in width. Phosphorus was diffused into Si from phosphosilicate glasses at 1100°C. Ion beam etching was applied for etching off SiO₂ layer in the gate and source-drain regions. And additional chemical etching after the ion etching was

employed to remove the damaged layer. I_D-V_D characteristics were measured.

Results and discussion

(a) Characteristics of the damaged devices

The obtained data are listed in Table 1. Typical high frequency C-V and quasi-static C-V curves of MOS capacitors are shown in Fig. 3. Ion-etched samples showed severe distortion in both curves due to the damage. Surface-state density N_{ss} was calculated from the obtained quasi-static C-V curves, and typical N_{ss} distribution in band gap is also shown in Fig. 4. N_{ss} values shown in Table 1 are the values at near the mid gap. A large amount of fixed charges were detected. This large and broad distributed N_{ss} may be caused by contamination metals and crystallographic defects in Si. The damage without metal contaminations was also investigated to study the origin of damage more clear, with using Ar ion implantation. The implanted energy was 40 KeV, and the dose was $1 \times 10^{16} \text{ cm}^{-2}$. The implanted layer was chemically etched off about 400 Å, in order to avoid the surface contaminations caused by ion implantation and to obtain the maximum concentration at the surface. MOS capacitors were fabricated on this Ar implanted surface in the same way as shown in Fig. 1 - (a). The measured high frequency and quasi-static C-V curves were similar to the curves (b), (d) in Fig. 3. The calculated N_{ss} values in the mid gap was about $10^{12} \text{ cm}^{-2} \cdot \text{eV}^{-1}$. Although in this case the surface was free from metal contamination, large N_{ss} was observed.

Reduction of the electrical breakdown field is shown in Table 1. The damage also affects the gate oxide and decreases the dielectric strength.

In case of p-n junction diodes, large reverse leakage current and reduction of the carrier lifetime were measured. This deterioration may result from a number of generation-recombination centers in bulk Si. Therefore two types of the damage can be considered, one is the surface contaminations and amorphous layer as seen in MOS capacitors, and the other is the bulk type damage as seen in p-n junction diodes.

(b) Depth profiles of the damage

For removal of the damage, depth profile of the damage was measured. Results are shown in Fig. 5. Recovery of the surface-state density N_{ss} and the generation lifetime T_g are studied. N_{ss} recovered when the damaged layer was chemically etched off about 150 Å, but T_g did not recover

till the surface was etched off about 500 Å. N_{ss} is influenced mainly with the Si-SiO₂ interface characteristics, while T_g is influenced with the recombination centers existing deeper region in Si. Decrease of T_g coincides with increase of leakage current of p-n junction diodes. It is found that removal of 500 Å thickness of the damaged layer by chemical etching after ion beam etching is necessary to recover the damaged device characteristics.

(c) IMA and RBS analysis

The metal contamination and crystallographic imperfection of ion-etched Si surface were investigated by IMA and RBS techniques. IMA data showed the existence of a large amount of Cr⁺ ions at the damaged surface layer. Cr⁺ ions may result from the redeposition from the parts of etching apparatus. The He⁺ ion backscattering spectra are shown in Fig. 6. From the Si spectra of both random and channeling directions, the existence of the amorphous layer of about 200 Å at the surface region is estimated. Cr ions were detected and its concentration was about 10²⁰ cm⁻³. A large amount of Ar also existed. Remaining Ar had been verified in another RBS experiments, which had been carried out with Ar implantation and annealing in dry O₂ atmosphere. So, the residual Ar in Si after the gate oxidation may also form generation-recombination centers and deteriorate the device characteristics.

(d) Recovery of the device characteristics

The recovery of the device characteristics was examined on MOS FET's using additional chemical etching. The I_D-V_D characteristics of MOS FET's, produced by the various etching manner, are shown in Fig. 7. In Photographs (a) and (c), threshold voltages were well agree with theoretical value. Ion-etched sample showed large shifts of the threshold voltage due to the large N_{ss} value. Ion-etched and 500 Å chemically etched FET showed almost normal characteristics. This additional chemical etching of the damaged layer, about 500 Å in depth, does not spoil the pattern accuracy for 1 micron patterning process. The ion beam etching technique can be applied to the high density VLSI.

Conclusion

The damage caused by Ar ion beam etching deteriorates the device characteristics. The damage exists as deep as 500 Å. The origins of the damage are considered as

follows.

- (1) surface amorphous layer caused by low energy Ar bombardment
- (2) metal contaminations at the surface
- (3) residual Ar in bulk Si

The additional chemical etching of about 500 Å depth after ion beam etching can remove the damaged layer without spoiling the pattern shape in case of the 1 micron pattern process. It is found that ion beam etching is applicable to high density LSI process.

Acknowledgements

The authors wish to express their thanks to Dr. T. Sakurai for the RBS analysis and to T. Hisatsugu, Dr. M. Shinoda, Dr. Y. Fukukawa, and Dr. T. Misugi for useful discussion and encouragement.

REFERENCES

1. C. M. Melliar-Smith, J. Vac. Sci. Technol., Vol. 13, No. 5, 1008 (1976)
2. L. Mader and J. Hoepfner, J. Electrochem. Soc., Vol. 123, No. 12, 1893 (1976)
3. L. D. Bollinger, Solid State Technol., November, 66 (1977)
4. H. R. Deppe, B. Hasler, and J. Hopfner, Solid State Electron., Vol. 20, 51 (1977)
5. G. W. Sachse, W. E. Miller, and C. Gross, Solid State Electron., Vol. 18, 431 (1975)
6. M. Kuhn, Solid State Electro., Vol. 13, 873 (1976)
7. A. Goetzberger, Bell Syst. Tech. J., Vol. 45, 1097 (1966)
8. R. Van. Overstraeten, G. Declerck, and G. Broux, J. Electrochem. Soc., Vol. 120, 1785 (1973)
9. W. Fahrner and A. Goetzberger, Appl. Phys. Lett., Vol. 21, 329 (1972)
10. R. H. Kingston, Proc. IRE, Vol. 42, 829 (1954)
11. D. K. Schroder and J. Guldberg, Solid State Electron. Vol. 14, 1285 (1971)

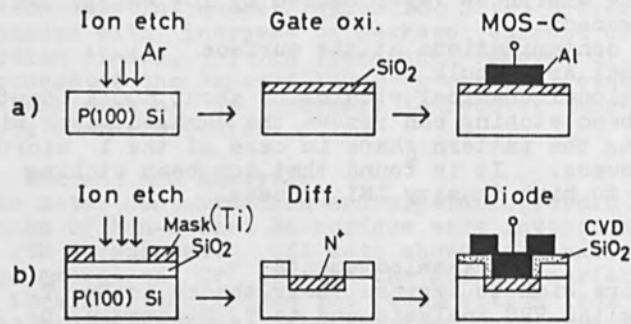


Fig. 1. Flow charts of the sample fabrication
(a) MOS-capacitors, (b) P-N junction diodes

Table 1. Effects on the device characteristics

MOS-C		Ion etch	Wet etch
Surface-state density			
N_{ss}	cm^{-2}/eV	3×10^{12}	3×10^{10}
Breakdown field			
E_B	V/cm	6.2×10^6	9.4×10^6
P-N diode			
Reverse leakage current			
I_R	A/cm^2	3.0×10^{-1}	9.3×10^{-7}
Carrier lifetime			
T	n. sec.	300	1600

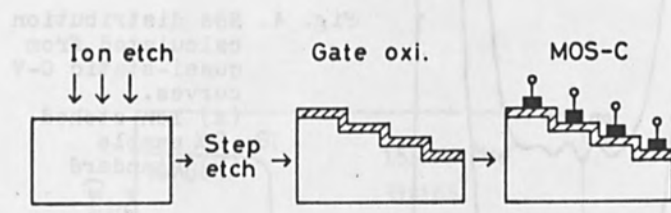


Fig. 2. Fabrication process for measurements of the depth profile of the damage.

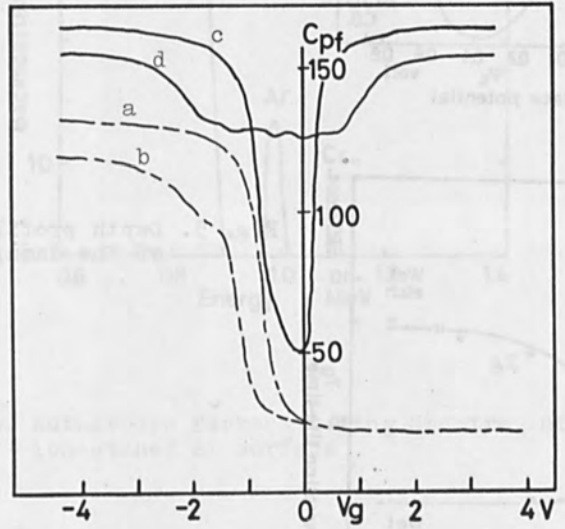


Fig. 3. Typical high frequency and quasi-static C-V curves.
 (a), (c) - standard, (b), (d) - ion-etched
 (a), (b) - 1MHz high frequency C-V
 (c), (d) - quasi-static C-V

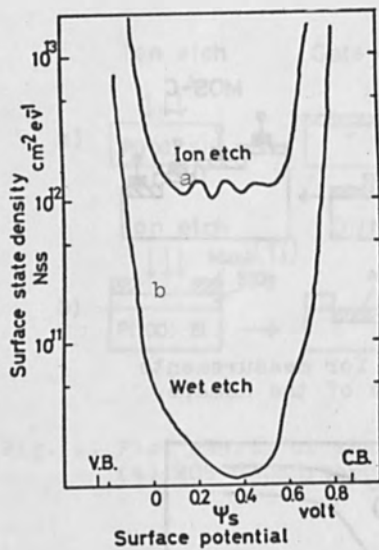


Fig. 4. Nss distribution calculated from quasi-static C-V curves.
 (a) Ion-etched sample
 (b) standard

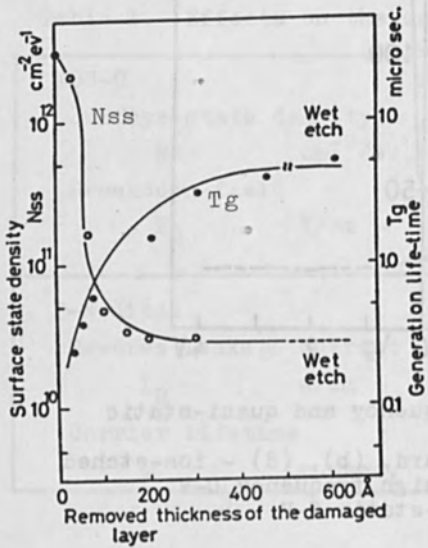


Fig. 5. Depth profile of the damage.

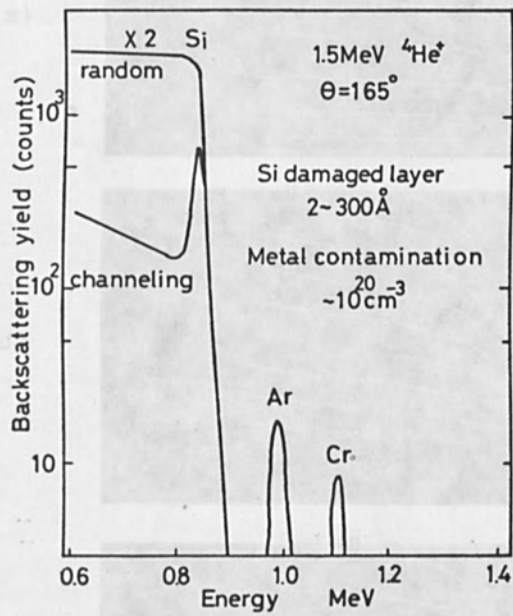
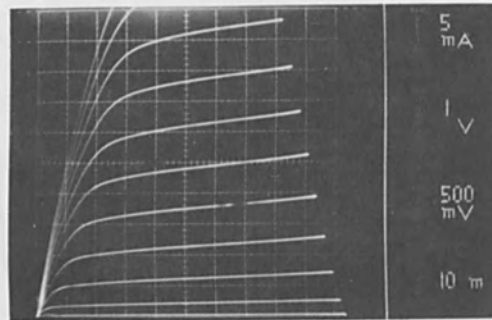
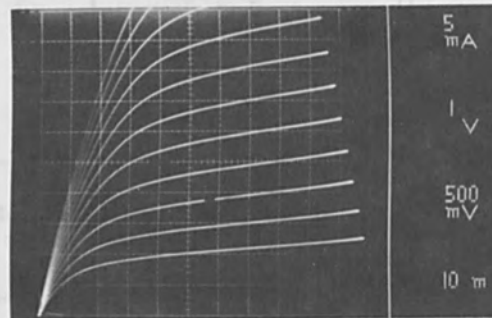


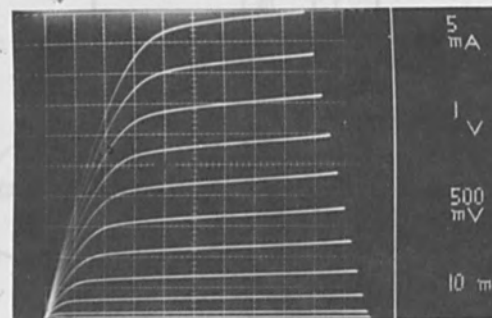
Fig. 6. Rutherford Backscattering Spectra of the ion-etched Si surface



(a)



(b)



(c)

Fig. 7. Photographs of the examined I_D-V_D characteristics
 (a) chemical etch (b) ion etch
 (c) ion etch + 500Å chemical etch

History, Present Status and Future

details of the history of electron beams are given in the Appendix. It is pointed out that the first electron beam was produced in 1897 by J. J. Thomson in Cambridge, England. The first electron beam was produced in 1897 by J. J. Thomson in Cambridge, England. The first electron beam was produced in 1897 by J. J. Thomson in Cambridge, England.

In this report, the history of electron beams is reviewed in detail. It is pointed out that the first electron beam was produced in 1897 by J. J. Thomson in Cambridge, England. The first electron beam was produced in 1897 by J. J. Thomson in Cambridge, England. The first electron beam was produced in 1897 by J. J. Thomson in Cambridge, England.

HIGH POWER BEAMS

This section discusses the development of high power electron beams. It is pointed out that the first high power electron beam was produced in 1937 by R. W. Good in Cambridge, England. The first high power electron beam was produced in 1937 by R. W. Good in Cambridge, England. The first high power electron beam was produced in 1937 by R. W. Good in Cambridge, England.

Section 7

This section discusses the development of high power electron beams. It is pointed out that the first high power electron beam was produced in 1937 by R. W. Good in Cambridge, England. The first high power electron beam was produced in 1937 by R. W. Good in Cambridge, England. The first high power electron beam was produced in 1937 by R. W. Good in Cambridge, England.

History, Present State and Future
of the Use of Electron Beams as
Thermic Tool

H. K. Steigerwald
Steigerwald Strahltechnik GmbH
Munche-Puchheim, Germany

In July 1978, it will be 20 years since the first EB-machine for welding, built by C. Zeiss in Oberkochen, West Germany, was introduced into the United States. At this time, the today well known capability of producing EB-deep welds was discovered just a few months earlier. The ability to produce deepwelds was the fact that a machine for general use of electron beams as a thermic tool, i.e. for drilling, engraving, welding, and general heat treatment, has been designed.

Westinghouse's request to produce very slim welding zones was successfully met by combining the drilling capability with movement of workpiece. Fig. 1 shows a number of EB-drilled holes (Nimonic 90, 0.4 mm thick, 0.12 mm hole diameter). Fig. 2 shows a historic picture out of 1958 which demonstrates how the first deepwelds were produced. Two plates of zircalloy 2, 4 mm thick, were tacked together by spot welds. Blind EB-welds, normal to the attaching sides of both the plates, were then produced. We could then break the plates apart and observe the molten area, i.e. the fusion zone. We increased the current and, therefore, the power from right to left and one can clearly see how the penetration and the total depth is increased.

The discovery of the deepwelding effect gave the decisive impact on the development of EB-welding applications. Not only was this the reason for the first order of an EB-welding machine to be delivered to the United States but also, from there on, numerous applications emerged. Fig. 3 shows a picture of one of the first EB-deepwelds in stainless steel, 15 mm thick, produced with a welding speed of 33 cm/Min, power 2.5 kW.

The first practical application for EB-welding was demonstrated by Dr. Stohr in Paris. He decided that it would be advantageous to weld the highly reactive zircalloy for nuclear fuel elements in vacuum and applied an EB as heat source for the production of shallow welds. This work, as well as virtually simultaneous but independent work by Weyman of G. E. Hanford, preceded the deepwelding effect. The development of the EB-equipment of the STEIGERWALD-group started in the years 1948/49 and stemmed from the EB-technology of electron microscopes and electron-oscillographs. The application of the high speed oscillograph

applying focused electron beams on photosensitive plates was only a short way distant from the thermic EB-tool. Fig. 4 shows the schematic of the first EB-apparatus derived from this technology. The process can be observed through a binocular microscope.

In contrast to this relatively simple first equipment, Fig. 5 shows a schematic diagram of a modern EB-gun.

The important features of the electron beam as a thermic tool are not only the high power and high power density which can be produced but also the power density distribution in the beam and the possible short time control of the beam. Its practically instant energy transfer into the material of the workpiece is also most important. It turned out that by proper selection of beam parameters and control, it would be possible to generate quite different effects on the workpiece. Fig. 6 shows a diagram which compares the power density of the electron beam and the average time of impingement on the workpiece. In this field are arranged different EB-processes, beginning from engraving, leading to drilling, welding, and heat treatment. Several other processes are also shown.

The fact that EB-processes take place at relatively high speeds and the necessity of very fast time controls, made it obvious that the combination of EB-gun and workpiece handling with CNC would be very advantageous. Therefore, the electron gun, shown in Fig. 5, is developed with the option to be computer controlled. The workpiece handling is also integrated in this system. Fig. 7 shows a block diagram of this system.

This combination of an inertialess EB-tool with the fast computer control opens outstanding possibilities for the applications of electron beams. Figures 8 to 10 show a number of practical examples. Fig. 11 shows a workpiece manipulator for EB-drilling. In most cases, the workpiece is moved by the manipulator under the electron beam without stopping the movement for the drilling operation. The drilling is done in a flying mode triggering the electron beam when the workpiece is in proper position and deflecting the electron beam in the direction of the movement. Fig. 12 gives an impression of the working speed possible with an electron beam. There are no limitations in principle, but only limitations of a special EB-drilling machine.

Another practical application of EB is heat treatment of metals. Fig. 13 shows an example of surface structure which is fusion heat treated by melting the surface of grey cast

iron in local areas, cooling them down sharply into the body of the workpiece by switching off the EB. Such structures can be produced in an economic manner by scanning the surface of a workpiece. Also transition hardening is possible.

The many advantages of EB-deepwelding are well known and it is not necessary to explain them here. In recent years, the interest of welding very heavy cross section workpieces is growing more and more. This development led to the realization that the penetration of the vertical beam, applied for instance on steel, was limited by the hydrostatic pressure of the molten metal building up in the deepweld. Therefore, it was found that it would be advantageous to apply the EB-gun and the EB in a horizontal direction, thus preventing this phenomenon. Fig. 14 shows a diagram which demonstrates beam power, welding speed and penetration depth both for vertical and horizontal EB-gun geometry.

Fig. 15 shows an example of a deepweld in Ck 15 steel, penetrating through 150 mm of steel, using 52 kW beam power at a welding speed of 1.5 mm/s. Observe the relatively wide fusion zone which is practically parallel. This makes it possible to outgas the fusion area to both sides of the workpiece, thus producing a good porosityfree weld. There was no supporting bar applied at either the front or the back bead. Today, in the STEIGERWALD-group EB-powers up to 120 kW are available, using an accelerating voltage of 150 kV.

Heavy sections of workpieces make it unavoidable that the dimensions of workpieces are also growing. It is, therefore, necessary to find ways for EB-welding which are not using vacuum chambers to apply the EB-process. Numerous developments are presently taking place applying a localized vacuum along the area to be welded. The STEIGERWALD-group has developed its own concept of a mobile vacuum. This is a system which produces the vacuum only around the welding spot, being capable to migrate along the welding seam by relative movement between workpiece and the mobile vacuum system. Fig. 16 shows schematically the difference between local vacuum (a) and mobile vacuum (b). Fig. 17 gives an explanation for the principal operation of the mobile vacuum system. Two groups of pressure step systems are arranged around the welding area. One system is the internal system of the EB-gun which is divided into two pressure steps, beginning with 10^{-5} mbar and 10^{-3} mbar where the welding takes place. This area is surrounded by an outer ring system and pressure step, leading from 10^{-3} mbar over 10^{-1} mbar to 10^1 mbar and from there to atmospheric pressure. The workpiece to be welded is shown. On the

other side of the workpiece a similar pressure step system is necessary. Fig. 18 shows the practical arrangement which is applied to two vertical standing steel plates, each of them 16 mm thick, 1 m wide and 5 m long. Fig. 19 gives an impression how to apply the mobile vacuum to cylindrical workpieces for producing longitudinal and circumferential welds.

The expansion of EB-applications, especially in welding, is still going on. Large workpieces and large steel constructions will in the near future be a field of application for EB-welding and their design and material selection will be influenced considerably by the EB-welding process. Generally, the history of the development of the electron beam as a thermic tool is now going into its 30th year. Fig. 20 shows one of the very first experimental apparatus, vintage 1950, for EB-drilling and -welding. The diagram of this equipment is shown in Fig. 4. Fig. 21 demonstrates the arrangement of a modern CNC-controlled machine for EB-perforation. Fig. 22 shows an automatic EB-welding machine with horizontal 15 kW-EB-gun for welding of heavy valve bodies.

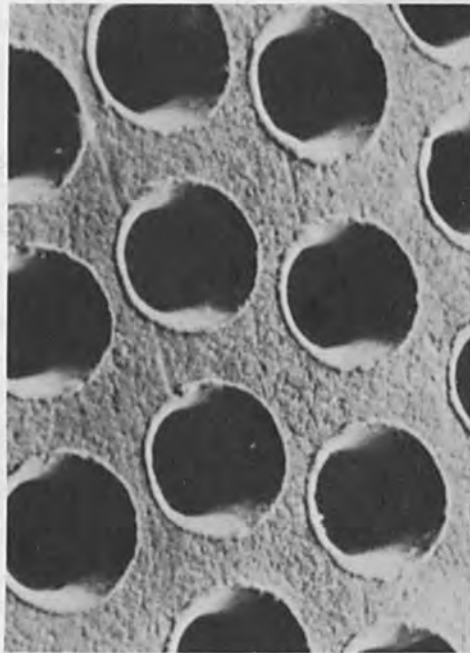
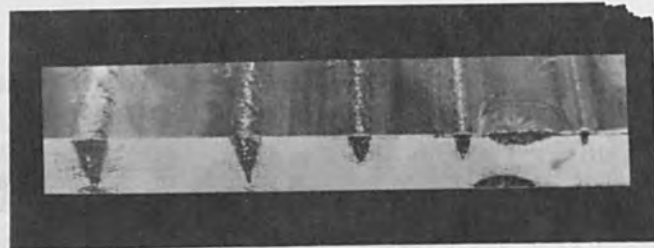


Fig. 1



70 kV

10 mA	8 mA	6 mA	4 mA	2 mA
700 W	560 W	420 W	280 W	140 W

Fig. 2

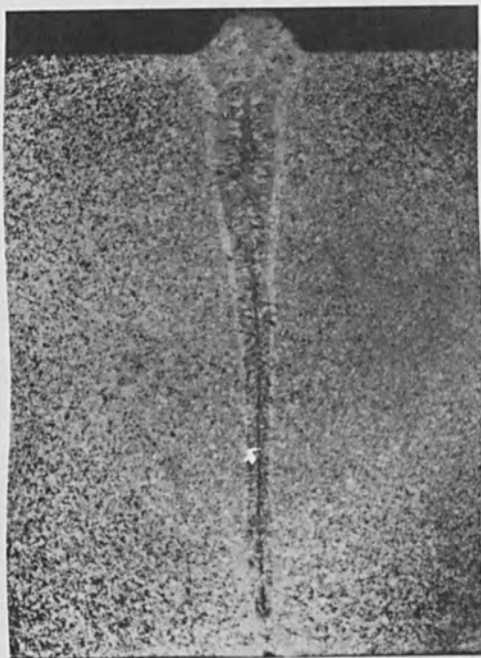


Fig. 3

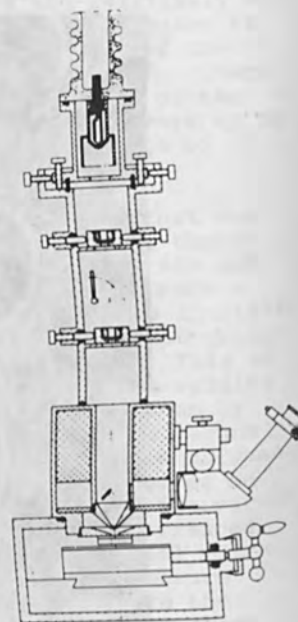


Fig. 4

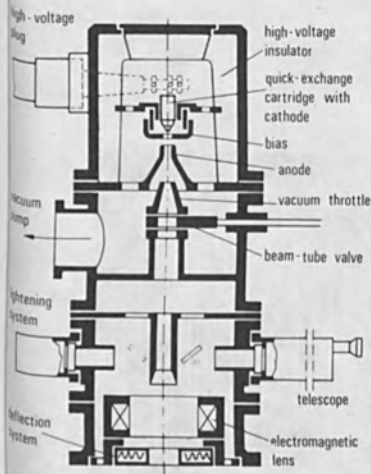


Figure 5

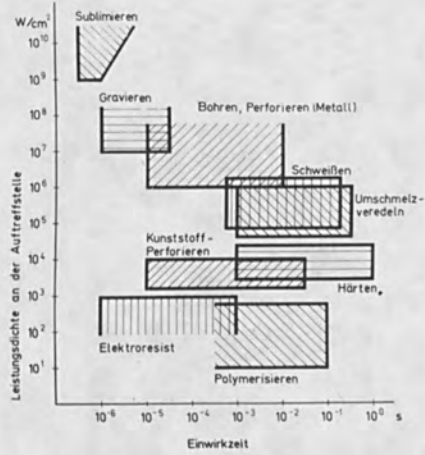


Figure 6



Figure 7

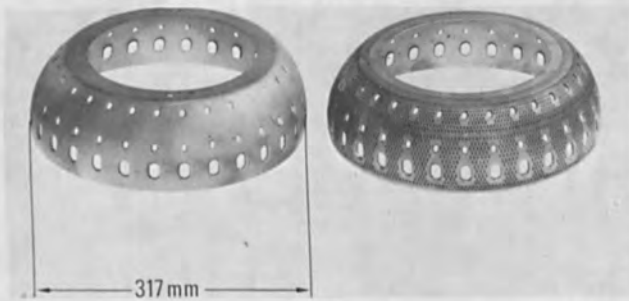


Figure 8

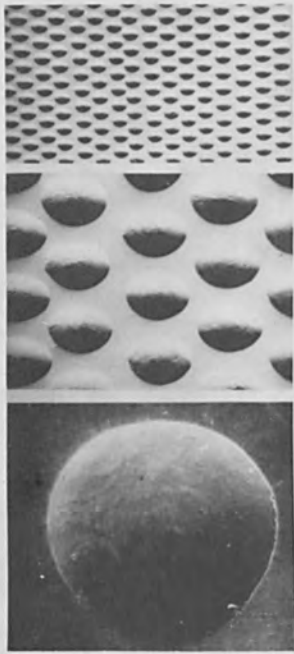


Figure 9

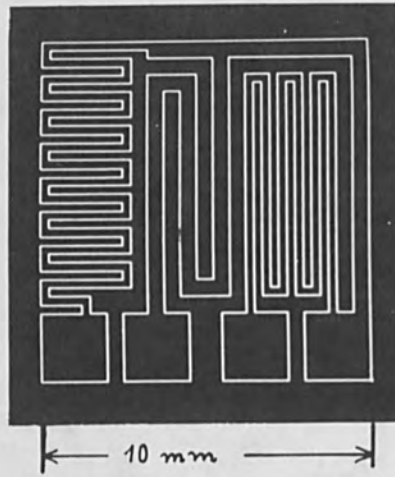


Figure 10



Figure 11

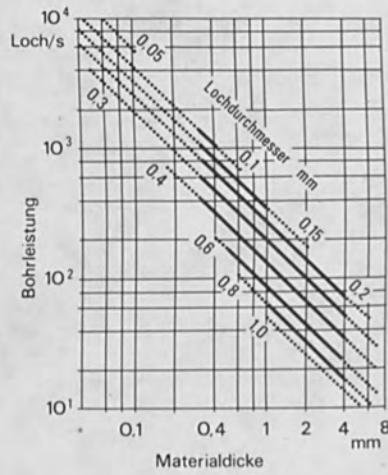


Figure 12

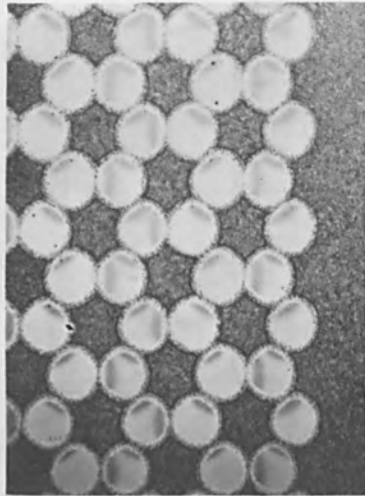


Figure 13a



Figure 13b

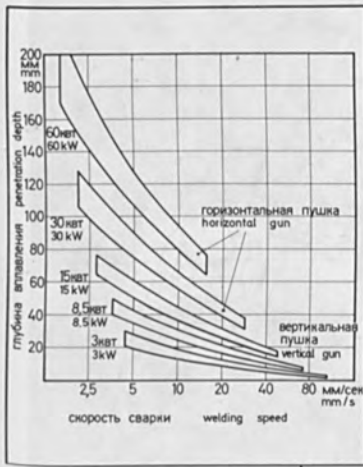


Figure 14

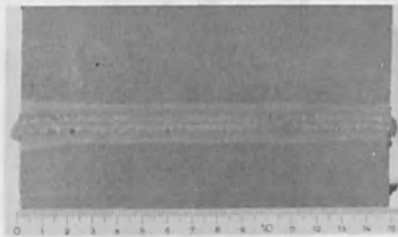


Figure 15

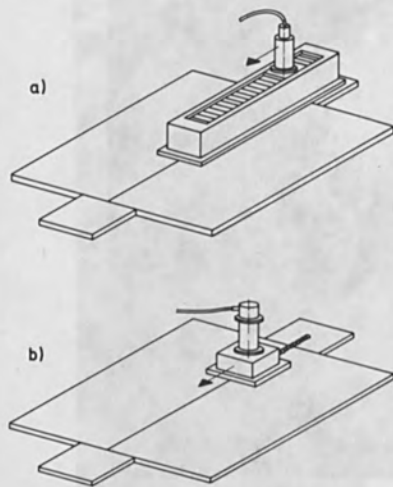


Figure 16

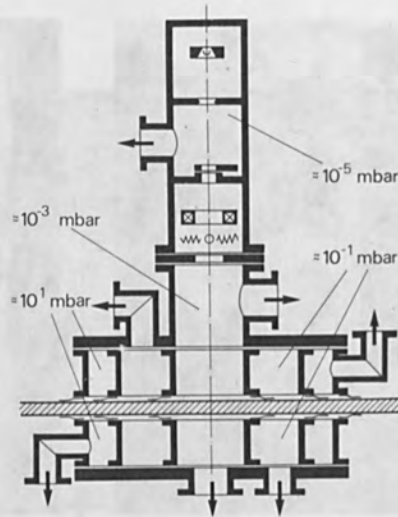


Figure 17

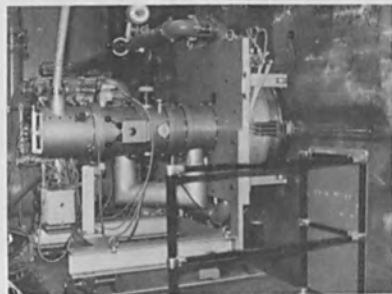


Figure 18

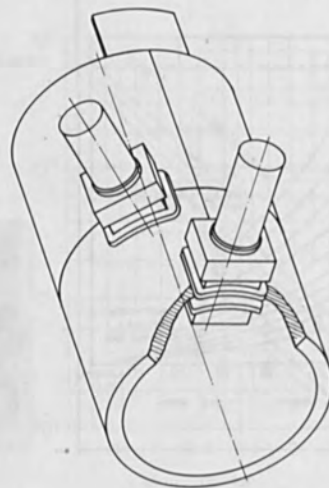


Figure 19



Figure 20

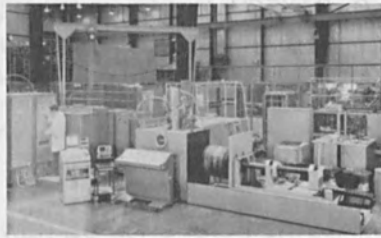


Figure 21

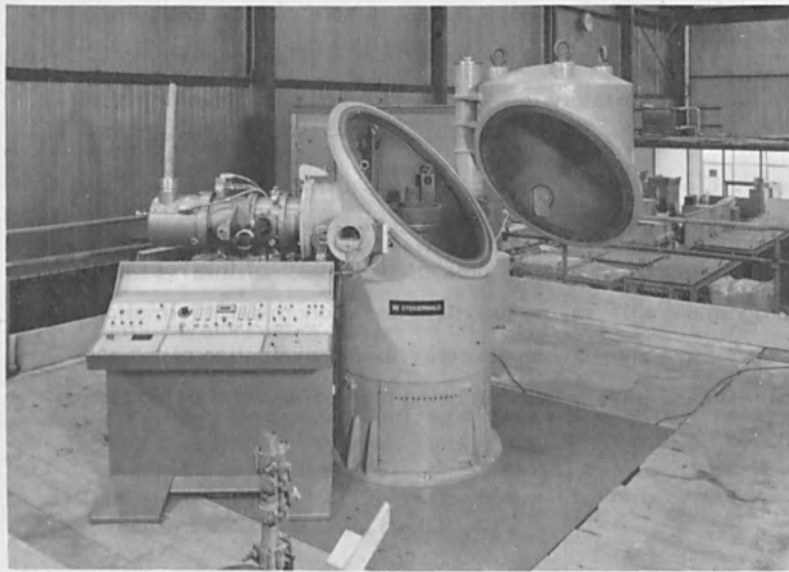


Figure 22

POSSIBILITIES AND FUTURE OF HIGH POWER EBW
IN THE HEAVY INDUSTRIES

G. SAYEGH and R. ROUDIER
SCIACY S.A - 119, QUAI JULES GUESDE
94400 VITRY/SEINE-FRANCE

.....

SUMMARY

High power EBW guns of 100kW and more are now available on the market for welding very heavy sections of steels exceeding 200mm. Interesting laboratory results have been obtained in welding different steels : SS 304 L, 533 grade B, 387 grade 22....

An experimental programme for butt-welding shells of 3m diameter and up to 150mm thick is presented. Results of this research programme will provide technical and economical information to heavy industries which will permit better evaluation of the possibilities and the interest in using high power EBW in production.

- INTRODUCTION -

Two reasons can explain why the heavy industries remained reluctant to accept EBW process in their joining techniques : one is psychological due to the difficulty to introduce a sophisticated , new technique into a traditional conventional field ; the other is technological because the equipment available on the market do not respond to the specific needs of heavy industries .

Since the energy crisis of 1973, EBW equipment manufacturers have developed equipment to satisfy the specific needs of the heavy industries /1⁺/, /2/. This paper will deal with the possibilities and future of high power EBW guns in the heavy industries to weld very heavy sections.

1 - EVOLUTION OF HIGH POWER EB GUNS AND PERFORMANCES -

Until 1972, the power of EBW guns available on the market was limited to 25-30kW. This could achieve welds up to 60 to 75mm, in steel. In 1973, several high power EB guns were developed in G.B., Japan, USSR, France... for welding heavier sections : 200-250mm of steel. These guns operate at 100kV to 150kV and can produce 100 to 120kW /3/.

We have developed a 100kV - 1A electron gun (figure 1). The main components of the gun were optimized by using computer programmes which solve the various equations which define the characteristics of the EB /4/.

From laboratory tests conducted on melt runs in the flat and horizontal positions the following conclusions are drawn :

- Welding in the flat position is not favourable for deep penetration : in a given material, there is a penetration limit beyond which the beam does not reach. For steel this limit seems to be around 130 to 150mm for the optimal welding conditions (power, focus, welding speed) /5/.

.. + see references

If the power is increased, or the welding speed decreased, no gain in beam penetration is obtained, only the molten zone increases in width. It seems that beyond a given penetration (which depends on the material and the thermal characteristics of the material) the bottom of the capillary under the beam impact cannot stand the weight of the molten metal located above, which flows down filling the capillary and limiting the penetration.

- One of the greatest difficulties in heavy section welding is obtaining sound welds, free of large porosity. Because of the importance of the molten liquid which is displaced during welding, any instability in welding conditions, stemming from beam characteristics, or the composition of the material can result in flow of the molten zone out of the workpiece.
- High stability in welding parameters is required ; this can be achieved industrially by a careful choice of gun components.
- The shape of the beam, and more specifically its divergence at the workpiece, can affect the quality of the bead : the thicker the section to be welded the smaller should be the beam divergence. A semi divergence angle of 0,025 radians is sufficient to weld up to 150mm of steel.
- With suitable choice of welding parameters it is possible to obtain sound welds with different bead shapes. Figure 2 shows examples of several welds obtained in different materials with beads of various geometries.
- It seems that the most stable beads are those which are V-shaped rather than parallel-side.
- When comparing the bead shape in heavy section, i.e. 200mm, to the natural shape of the beam the shape of the beam is larger than the molten zone and a fortiori larger than the capillary hole created under the beam. This means that, during welding, the plasma contained in the capillary, which can be under pressure, completely modifies the characteristics and the shape of the beam which passes through it.

The effect of the plasma on the beam is to pinch it in the cavity through out its path in the capillary. An important investigation to be undertaken is the better understanding and explanation of this interaction quantitatively.

2 - INDUSTRIAL POSSIBILITIES OF HIGH POWER EBW -

To explore the possibilities of the 100kV, 1A, EB gun under actual industrial conditions, a research programme (internationally supported with the participation of French, German, Italian and Japanese companies) was set up. This programme consists of studying and resolving the industrial problems which are raised in butt welding thick shells (up to 150mm) of 3m diameter in SS 304 L and 533 grade B steels.

Preliminary tests were conducted in the laboratory to define the best welding parameters with respect to the influence of joint geometry (gap, mismatch). Also fading zones and defects repairs were investigated and limiting values defined.

The particular feature of this research programme is that the working chamber is composed from shells themselves. Figure 3 shows the schematic of the equipment which is now entirely manufactured. It comprises the following main components :

- mobile mechanical part on the top of the shell which can be adapted to several different diameters. The gun is fixed to this part and can rotate around the shell's axis.. At the bottom of the shell another mechanical part is fixed through which the inner volume is pumped down.
- A counter chamber placed around the joint to be welded and pumped to the desired vacuum (primary vacuum).
- Auxiliary elements : pumps, power supply, seam tracking, controls... During welding the main parameters are recorded and a picture of the weld is taken on a tape. It is thus easy to refer the different records to know exactly the welding conditions of the shells. The different parameters can be preprogrammed.

The research programme should provide technical and economic information to heavy industry which will permit better evaluation of the possibilities and the interest in using this high power EB in production.

Figure 4 shows the equipment used to achieve the programmes. This equipment has the following characteristics :

- . EB gun of 100kV - 1A pumped by turbomolecular pumps.
- . Diameter of shells to be welded : 150 to 600cm by changing the adaptive part of the top plate.
- . Welding speed from 0,005 to 0,15 tours/mn.
- . Weight of the top plate with gun : 2500 daN.
- . Pumping system adapted to the volume to be pumped.

Figure 5 and 6 show some details of the equipment. All components are sturdy and robust to stand the industrial environment in which they will be placed.

3 - PROBLEMS TO BE RESOLVED AND FUTURE OF EBW -

One can classify the problems to be resolved into several categories :

- Metallurgical problems.

Generally, the qualities of steels used in heavy industry (composition and gas content) are not the best suited for EBW. Particularly, cracking and toughness of the weld are the major weaknesses of the seam. Steel manufacturers are now ready to make an effort to improve the composition of their products in order to render them more acceptable for EBW.

Nuclear steels are usually of very high quality, nevertheless, toughness of thick steels exceeding 100mm should be still improved by appropriate heat treatment cycles.

- Problems encountered in industrial operating conditions.

EBW necessitates machining of the workpiece because a flame cut edge is not appropriate to produce good mechanical joint qualities, potential users do not consider machining of the workpieces as an unsurmountable obstacle, because in many cases they do machine them.

Concerning the variation of the gap which can be tolerated without using a filler, one can say that a fluctuation of the gap corresponding to 1% of the thickness of the workpiece is acceptable. The other manufacturing parameters such as mismatch, can be produced by a normal manufacturing cycle.

A particular problem met in welding heavy alloy steel sections is the permissible level of residual magnetic field to avoid missing the seam by unwanted deflection of the beam. A maximum level of 2 to 3 gauss should not be exceeded in 150mm thick sections. As a matter of fact it can be shown that deflection of the beam in a ferretic steel sample of 150mm thickness, where a residual magnetic field of 3 gauss is present, will reach at the root of the weld 3,6mm from the gun axis for a beam acceleration voltage of 100kV and 3,15mm from the gun axis for a beam acceleration voltage of 150kV. Let us point out that this deflection due to residual magnetism does not exist in the austenitic stainless steels and aluminium alloys.

- Inspection and standard.

Because of the shape of the welds in heavy sections, radiographic testing does not seem to be entirely capable to detect the various types of defects which might be present in the weld. Probably other NDT methods, such like focussed US beams, can efficiently complement radiographic techniques, for a better weld inspection.

During the coming years, one can expect the following development of high power EBW in the heavy industries :

- . Developments in welding the internal parts of reactors made of stainless steel attaining 80 to 100mm, and welding of aluminium alloys of more than 100mm used in LNG tanks.
- . Additional R & D will be necessary to improve welding performances of low alloy steels used in pressure vessel. Particularly, improvement of the steel composition and heat treatment cycles which will help acceptable toughness of the EBW joints.

- CONCLUSIONS -

EBW manufacturers have developed during the past few years high power EBW guns capable of welding very heavy sections of steel or light alloys material to satisfy the needs of the heavy industries.

Industrial equipment for welding shells of heavy sections and up to 3m in diameter are now available and can operate in an industrial environment.

The first foreseeable applications of EBW will concern welding of SS, some selected low alloy steels and aluminium alloys.

REFERENCES

- /1/ G. SAYEGH,
R.ROUDIER, H.HELM Electron beam welding equipment for the
nuclear industry
3^d int. conf. on welding in nuclear
Engineering HAMBURG - Nov. 1978
(to be published)
- /2/ Ph. Dard,
R.ROUDIER, G.SAYEGH New realisations of EBW equipment to
join tubes to tubsheet
Advances in welding processes
Harrogate 9-11 May 1978
- /3/ K. TERAI and
H. NAGAI General view of appl ication of EBW
in pressure vessel technology
IIW - Doc. IV - 217- 1977
- /4/ G. SAYEGH and
R. ROUDIER 100 kW EBW gun for heavy industries
7th Int. conf. on Elec. and ion beam
Science and technology
WASHINGTON May, 1976
- /5/ R. CAZES and
G. SAYEGH The design and realisation of 100kV
1A EB gun
Advances in welding processes
Harrogate 9-11 May 1978.

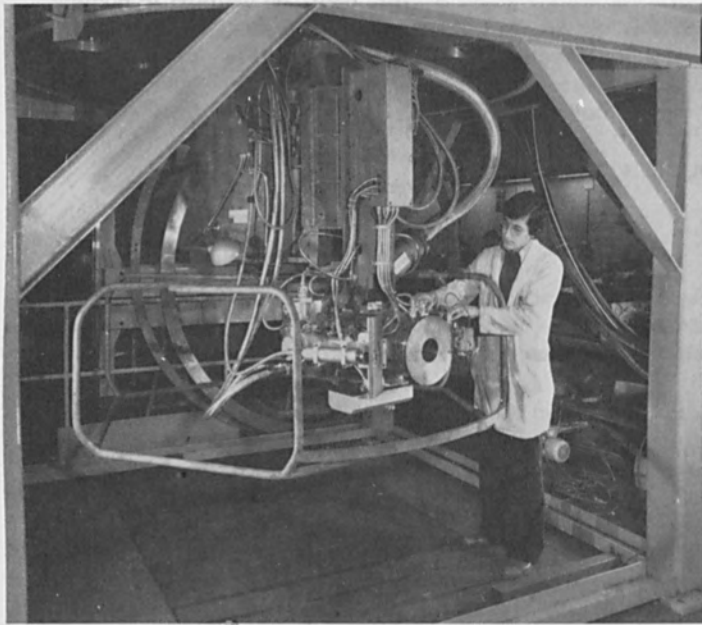
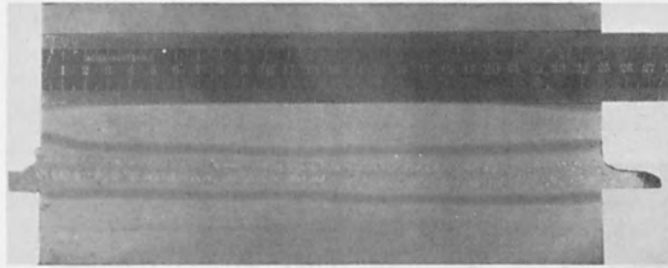
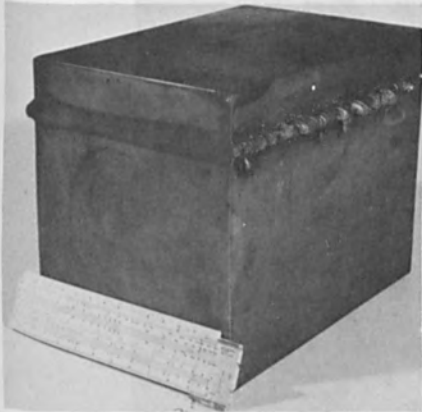


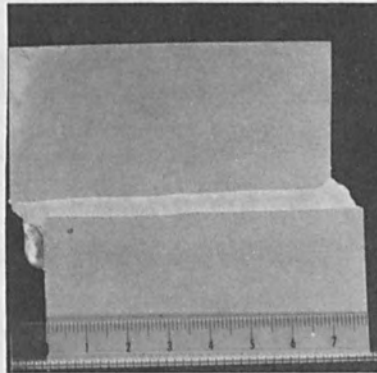
Figure 1 : View of the 100 kV - 1 Amp. gun



A



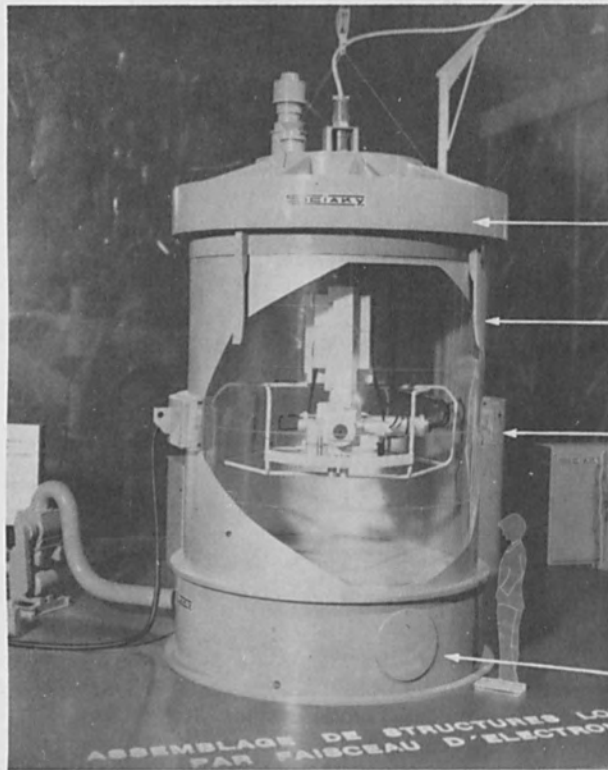
B



C

Figure 2 : macrographs in some welds.

- A : weld in 250 mm of 533 grade B steel.
V = 100 kV - I = 850 mA - v = 8 cm/min.
- B : weld in 150 mm of steel 387 grade 22.
V = 80 kV - I = 500 mA - v = 12 cm/min.
- C : weld in 80 mm of SS 304 L .
V = 75 kV - I = 450 mA - v = 15 cm/min.



top plate

shells to be
welded

counterchamber

base plate

ASSEMBLAGE DE STRUCTURES LOU
PAR FAISCEAU D'ELECTRON

Figure 3 : Schema of the equipment

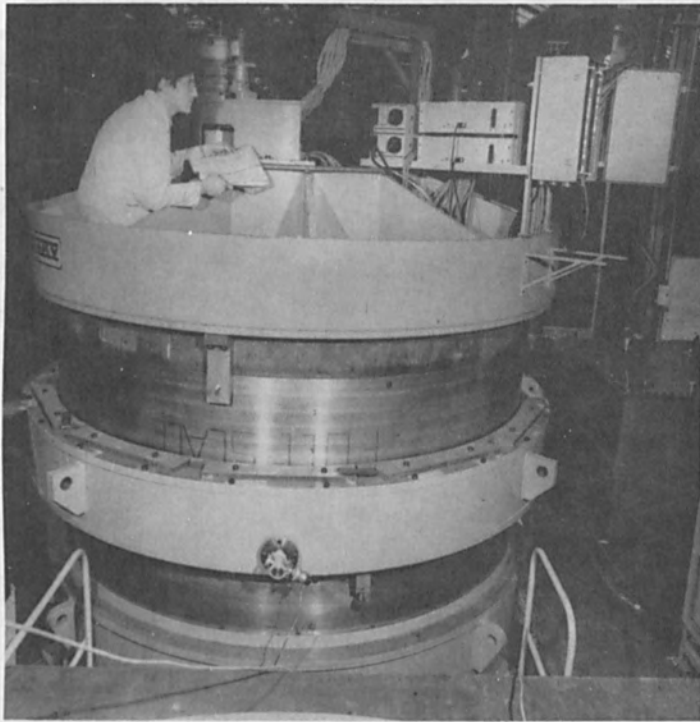


Figure 4 : View of the equipment for butt welding of shells

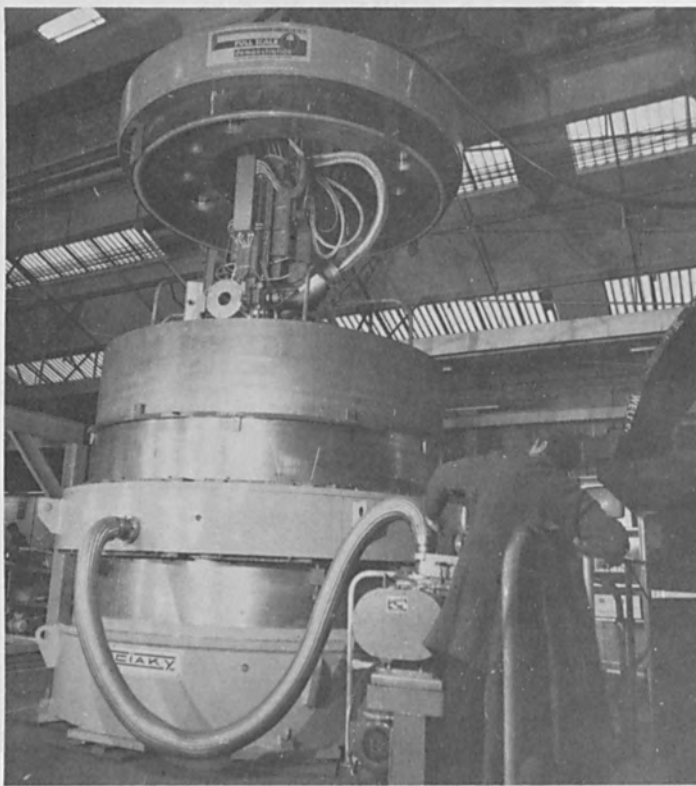


Figure 5 : Details of the top plate with gun.



Figure 6 : View of the control panel of the equipment.

TEMPERATURE DISTRIBUTION IN SOLIDS
DURING ELECTRON BEAM WELDING

G. BASILE and A. MOISAN
Laboratoire de Mécanique Industrielle
Ecole Nationale Supérieure d'Arts et Métiers
75640 PARIS cedex 13 (FRANCE)

ABSTRACT

This article reports on the study of temperature distribution in an electron beam welded workpiece. After presenting those models capable of representing the distribution limited to the two - dimensional state, an experimental study on the welding TA6V is described, and a discussion follows as to whether the results obtained permit judgment on the validity of the models. The proposed numerical model is the most representative, notably during the cooling phase.

INTRODUCTION

Knowledge of temperature distribution equations is necessary for the determination and prediction of the mechanical behaviour of a joint during and after welding. This behaviour is essentially due to the appearance of thermal stresses during the welding operation.

Analytical models have been developed, and among them, reference must be made to the models of ROSENTHAL (1) and GROSH et al (2). Their agreement with the facts is however unsatisfactory, particularly during the cooling phase. This justifies an attempt to develop a numerical model capable of considering the thermal variations within the material. Experimental results validate this attempt.

For the welding of flat plates of homogeneous and isotropic materials, the system can be considered bidimensional. The retained physical system is the one shown in figure 1. L , l , h , are respectively the length, the width, and the thickness of each plate. The thermal conductivity, the specific heat and the density of the material being k , c , ρ .

The heat source representing the action of the E.B. gun is considered as linear, and constant according to the thickness of the plate. It is characterized by the quantity of heat produced per unit of time and per unit of thickness, Q . It moves at the welding velocity, v .

The latent heats of phase change and the energy loss to the outside are not taken into consideration.

The temperature T in any part of the heat-affected zone and at a time t , obeys to the heat conduction equation :

$$\frac{\partial}{\partial x} \left[k(T) \frac{\partial T}{\partial x} \right] + \frac{\partial}{\partial y} \left[k(T) \frac{\partial T}{\partial y} \right] = \rho(T) c(T) \frac{\partial T}{\partial t} \quad (1)$$

REPRESENTATION AND MODELISATION

Analytical models

The analytical models consider the non-finite medium, and the stationary state established. The rate of heating, Q , is supposed constant throughout the thickness. ROSENTHAL's model assumes the heat characteristics of the material to be independant of temperature ; GROSH et al allow for their variation, but take the thermal diffusivity as constant :

$$\lambda = \rho c / 2k.$$

- ROSENTHAL's model : the temperature at any point (ξ, y) located at a distance r ($r^2 = \xi^2 + y^2$) from the source is given by (see figure 1) :

$$T = T_0 + \frac{Q}{2\pi k} K_0(\lambda v r) e^{-\lambda v \xi} \quad (2)$$

where : K_0 is a modified BESSEL function of second type and 0 order,
 T_0 is the initial temperature of the plates and also the temperature at $r \infty$.

- GROSH et al model : the variation of k is put in the following form :

$$k(T) = k(T_0) \frac{\partial \theta}{\partial T}, \quad \text{with} \quad \theta = \theta(T).$$

$$\text{Then, } \rho c(T) = \rho c(T_0) \frac{\partial \theta}{\partial T}$$

and the solution of (1) is :

$$\theta(T) = \theta(T_0) + \frac{Q}{2\pi k} K_0(\lambda v r) e^{-\lambda v \xi} \quad (3)$$

If, in addition, the variation of $k(T)$ and of $(\rho c)(T)$ are linear,

$$\frac{\partial \theta}{\partial T} = 1 + M T$$

and equation (3) becomes :

$$(T - T_0) + \frac{M}{2} (T^2 - T_0^2) = \frac{Q}{2\pi k} K_0(\lambda v r) e^{-\lambda v \xi} \quad (4)$$

Further to the assumption of the non - variation of the thermal characteristics of the material regardless of its temperature, the above models take the medium as non - finite, and consequently, the heat source has no effect at infinity : hence, the temperature at infinity is the same before and after the welding operation. But, the medium is finite, and tests show that the temperature of equilibrium after welding is distinctly different from the temperature before welding, as is shown in the table below.

: Epaisseur (mm)	: 5	: 10	: 15	: 20	: 25	:
: Température d'équilibre:	127	200	275	302	320	:
: (°C)	:	:	:	:	:	:

These observations force us to distinguish the cooling phase from the heating phase. The latter can be assumed to obey the existing models. However, the temperature reached at $r = \infty$ during the cooling phase must be taken as $T_E \neq T_0$, T_E being the equilibrium temperature after welding :

$$T_E = T_0 + \frac{Q}{\rho c v T}$$

To respect the continuity and the temperature - gradient around the maximum temperature reached T_M (see figure 2), the existing models must be modified in order to represent the cooling phase ($t > t_M$) :

- ROSENTHAL's model modified gives :

$$T = T_E + \frac{T_M - T_E}{T_M - T_0} \frac{Q}{2\pi k} K_0(\lambda v r) e^{-\lambda v \xi} \quad (5)$$

- GROSH et al's model modified gives :

$$\theta(T) = \theta(T_E) + \frac{\theta(T_M) - \theta(T_E)}{\theta(T_M) - \theta(T_0)} \frac{Q}{2\pi k} K_0(\lambda \sqrt{r}) e^{-\lambda \sqrt{v} \xi} \quad (6)$$

None the less, these analytical models remain imperfect because they cannot take into consideration the variations in the heat characteristics of the material as functions of temperature. Furthermore, they remain limited in the case of stationary established state. Here, a numerical model is proposed which frees us from such assumptions.

Presentation of a numerical model

The application of a finite difference method is proposed, using adimensional quantities determined from a dimensional analysis :

$$x^* = \frac{x}{L}, \quad y^* = \frac{y}{L}, \quad \alpha^* = \frac{1}{L}, \quad t^* = \frac{vt}{L}$$

$$T^* = \frac{T \cdot k(T_0)}{Q}, \quad k^* = \frac{k(T)}{k(T_0)}, \quad (\rho \cdot c)^* = \frac{(\rho \cdot c)(T)}{(\rho \cdot c)(T_0)}, \quad \beta^* = \frac{(\rho \cdot c)(T_0)VL}{k(T_0)}$$

The heat conduction equation (1) becomes :

$$\frac{\partial}{\partial x^*} \left[k^* \frac{\partial T^*}{\partial x^*} \right] + \frac{\partial}{\partial y^*} \left[k^* \frac{\partial T^*}{\partial y^*} \right] = (\rho \cdot c)^* \beta^* \frac{\partial T^*}{\partial t^*} \quad (7)$$

The mesh chosen is shown in figure 3 : this mesh is related to the workpiece, and varied by zone according to y ; it becomes fine in the neighbourhood of the heat source. The calculation of the temperature very near to heat source is impossible as k , ρ , c , are unknown at temperatures above the melting point.

Δx^* , Δy^* , Δt^* , are the grids of the mesh according to x , y , t , respectively. The application of TAYLOR expansion to the derivation with respect to x (or y) and to t leads to the following expressions in which the upper index corresponds to the time mesh and the lower index refers to the space mesh

$$\left(\frac{\partial}{\partial x^*} \left(k^* \frac{\partial T^*}{\partial x^*} \right) \right)_{(I,J)}^{(m)} = \frac{\left(k_{(I+1,J)}^{*(m)} + k_{(I,J)}^{*(m)} \right) \left(T_{(I+1,J)}^{*(m)} - T_{(I,J)}^{*(m)} \right) - \left(k_{(I,J)}^{*(m)} + k_{(I-1,J)}^{*(m)} \right) \left(T_{(I,J)}^{*(m)} - T_{(I-1,J)}^{*(m)} \right)}{2(\Delta x^{*2})} + O(\Delta x^{*2})$$

$$\left(\frac{\partial T^*}{\partial t^*} \right)_{(I,J)}^{(m)} = \frac{3T_{(I,J)}^{*(m)} - 4T_{(I,J)}^{*(m-1)} + T_{(I,J)}^{*(m-2)}}{2\Delta t^*} + O(\Delta t^{*2})$$

The limiting conditions are :

(i) there is no heat exchange with the outside at the edges of the plate : $\partial T^*/\partial v^* = 0$, v^* being normal to the edge at the point considered ;

(ii) the heat is transmitted by a source moving by steps on the points of the mesh along the x-axis.

The determination of the temperatures at points close to the source will be made by a heat balance on elements of volume at constant temperature around these points (figure 4). Figure 5 shows the balance for a particular volume : the various energies transmitted through the different sides of the volume are :

$$Q_s = Q \cdot \Delta T \cdot \frac{\theta}{2\pi}$$

$$Q_1 = \frac{1}{2\Delta x} \left(k_{(I+1,J)}^{(n)} + k_{(I,J)}^{(n)} \right) \Delta y \cdot \Delta t \left(T_{(I+1,J)}^{(n)} - T_{(I,J)}^{(n)} \right)$$

$$Q_1 = k_1 S_1 \Delta t \quad \partial T / \partial v_1$$

The heat balance is represented by :

$$Q_1 + Q_2 + Q_3 + Q_s = \rho \cdot c \cdot \Delta x \cdot \Delta y \cdot \Delta T$$

From where

$$\Delta T_{(I,J)}^{(n)} = \left(\sum_i k_i^* S_i^* \frac{\partial T^*}{\partial v^*} + \frac{\theta}{2\pi} \right) \frac{\Delta t^*}{(\rho \cdot c)^* \beta^x \Delta x^* \Delta y^*}$$

This leads to a linear system which will be solved by a method of successive over - relaxation.

THE EXPERIMENT

Figure 6 shows the two plates in position, the temperature measurement points (1 - 5), the fire - screen which is placed under the joint, and the insulating elements.

The conduction heat flow is determined by subtracting the various heat losses from the available energy : the heat crossing the

weld, Q_T , is received by the fire - screen, and then is measured by calorimetry, reading the equilibrium temperature of the screen ; the other forms of heat loss are estimated at 10 %. From where,

$$h \cdot Q = 0.9 (U I - Q_T)$$

The temperature is taken at various points in time and at different positions along the workpiece, using thermocouples (0,5 mm \emptyset) inserted into the depth of the workpiece, perpendicular to the welds, at distances ranging from 0.1 to 5 mm from the edge of the molten region. The experimental analysis was carried out on TA6V sheet metal of thickness varying from 5 to 25 mm, 5 measurements by thickness.

The experimental results obtained during the welding of two 10 mm plates ($v = 55$ mm/s, $Q = 203$ cal/s.mm) are shown in figure 7 : each curves plots the values measured by each thermocouple, characterized by its distance from the axis of the weld. This set of curves is highly representative of all the results obtained.

Figure 8 shows the curves obtained both experimentally and those theoretically determined by using the different models mentioned above, at a point 1.65 mm from the axis of the joint.

CONCLUSION

(i) The maximum temperature reached at the end of the heating phase is superior to the measured value regardless of the model. The lack of precision in measuring the temperature comes essentially from the inaccuracy in positioning the thermocouple. The numerical model remains incontestably the most representative of the heating phase, as it takes into account the true variation in the physical characteristics of the material.

(ii) As far as the cooling phase is concerned, the modification made to the analytical models are fruitful in as much as it is useful to understand the thermal behaviour during long periods of time. However, the numerical model is practically in complete agreement with the physical model considered. Such a conclusion is true for the domain investigated.

ACKNOWLEDGEMENTS

The authors wish to express their sincere appreciation to Mrs. BRUSSON, BOIRE and ZOLOTOVSKY (AEROSPATIALE - SURESNES) for their constant help throughout this investigation.

REFERENCES

- (1) ROSENTHAL D., Mathematical theory of heat distribution during welding and cutting. Welding JI, May 1941.
- (2) GROSH R. J. and al, Temperature distribution in solids of variable thermal properties heated by moving heat source. 1955, 13, 16, CNAS, Code 03092.

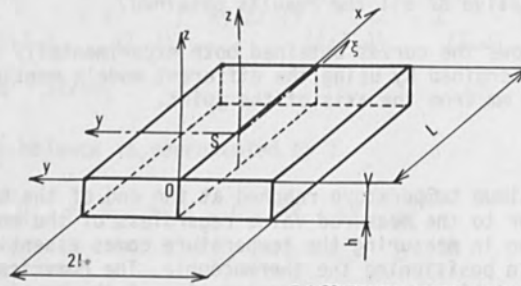


Fig1: SCHEMATIC REPRESENTATION OF WORKPIECE

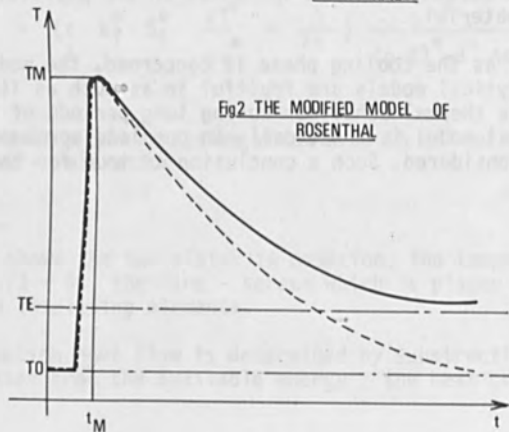


Fig2 THE MODIFIED MODEL OF ROSENTHAL

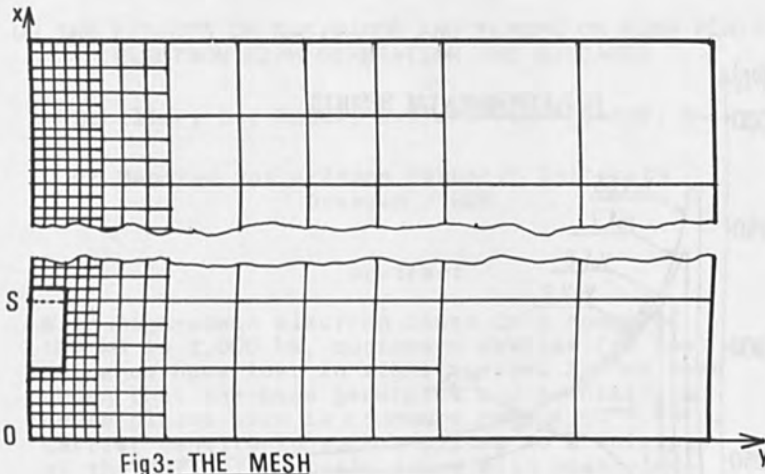


Fig 3: THE MESH



Fig 4: THE HEAT SOURCE

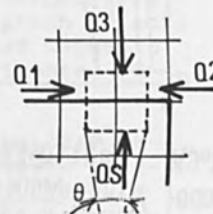


Fig 5: HEAT BALANCE OF THE VOLUME 1

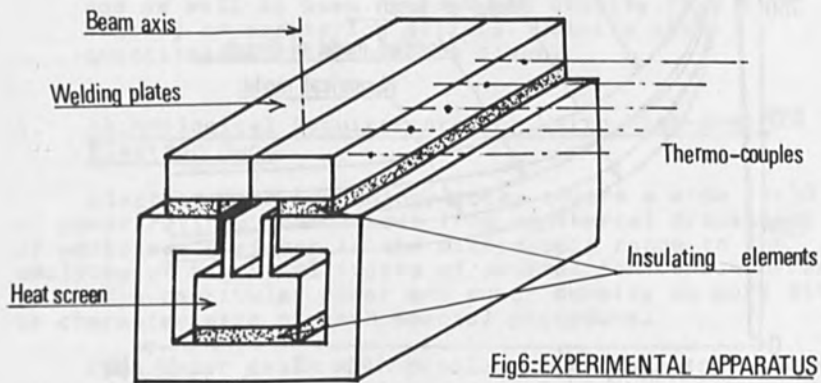
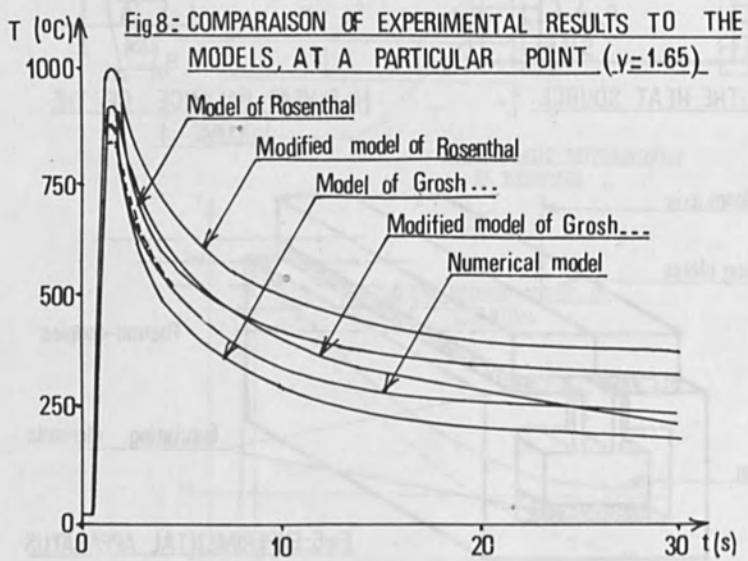
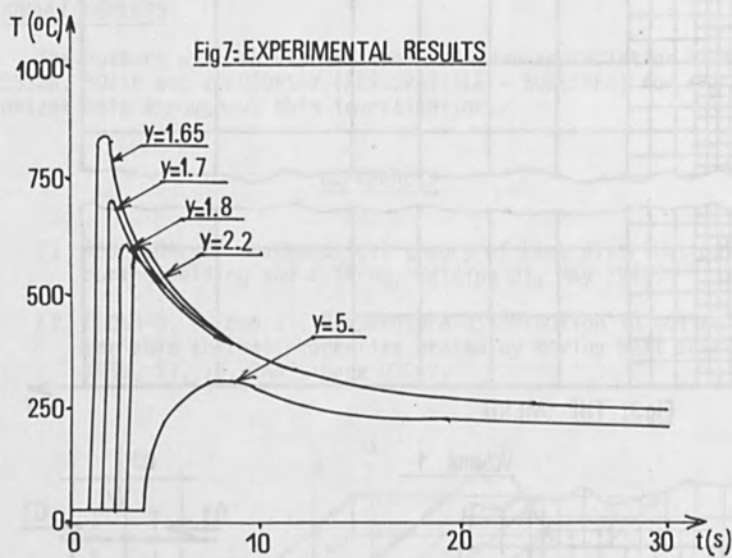


Fig 6: EXPERIMENTAL APPARATUS



ON THE EFFECTS OF GAS/VAPOR AND PLASMA ON HIGH POWER
ELECTRON BEAM GENERATION AND GUIDANCE

Schiller, S., Jäsch, G., and von Ardenne, A.

Manfred von Ardenne Research Institute
Dresden / GDR

Abstract

With high-power electron beams in a range of 100 kW to 1,000 kW, customary devices for beam guidance have lost in significance. It has been shown that the beam generates and maintains a dense plasma even in a pressure range of 10^{-4} Torr. Carrier density in such a plasma is a multiple of the particle density found with beam electrons which creates all physical prerequisites to self-focusing due to a magnetic pinch effect. In our work this phenomenon is termed magnetic gas focusing. Theoretical and experimental results of the latter are given.

In the processing chamber - where the beam becomes active - the residual gas pressure is about 10^{-2} to 10^{-5} Torr and the vapor pressure ranges from 10^{-2} to 1 Torr. Under these conditions the beam must pass a distance of several metres. Contrary to the classical theory of scattering it was found that accelerating voltage as well as beam current and density have a bearing on scattering actions. Details about quantitative relations are given.

1. Technological Requirements for Using High-power Electron Guns

Electron beam technology today covers a wide field of power ratings and methods from nonthermal processing of workpiece surfaces in the microscopic range to the smelting of big steel ingots of several ten tons. The action of a particular power and power density on work site is characteristic of each special procedure.

This paper deals with problems that have to be considered in the development and use of high-power guns used in the field of, say, metallurgy for melting, high-rate

evaporation and heat treatment (1, 2, 3). With ratings of 15 kW to 1,200 kW, they are exclusively used to release at the point of action thermal energy at a power density of 10^3 to some 10^4 W/cm². Explained in Figure 1 are the technological conditions for using high-power guns in practice where the beam must cover a working distance and field width of up to some metres. The residual gas or vapor pressures are in a span of 10^{-3} Pa to some 10^2 Pa (10^{-5} Torr up to the Torr range). All three previously mentioned applications call for a programmed beam deflection over the working area with respect to time and location at frequencies of 0 to about 10^3 Hz.

In our opinion, axial guns with separate evacuation of the beam generating chamber are best suited for technological processes in the high-power range since they are well matched to prevailing requirements. As a consequence, the following considerations have been restricted to this gun type (4, 5).

2. Physical Aspects of Beam Generation and Guidance in High-power Guns

While the residual gas pressure in the working chamber reaches a level of up to 1 Pa (10^{-2} Torr), operating reliability requires to maintain a pressure in the beam generating chamber that must be less than 10^{-2} Pa (10^{-4} Torr). Apart from satisfying the previously mentioned technological requirements in the working chamber, high-power guns have to ensure proper pressure decoupling also.

Application of high-power guns in practice has shown time and again that - with all general dimensioning rules for electron guns duly considered - their operating reliability depends on the attained degree of pressure decoupling between beam generating system and working chamber. Adequate pressure decoupling can only be achieved when an electron beam of high power density and narrow aperture is injected into the beam guidance system and then passed on to the point of action in the form of a slender beam of parallel rays.

In the design and dimensioning of these systems it was soon found that classical geometric electron optics turned out to be inadequate. Requirements with respect to boundary conditions (such as paraxiality of the beam, no space charge effects and interactions, as well as straight-lined trajectories between electron-optical elements in the so-called zero-field space) cannot be met any longer as far as high-power guns are concerned (6).

The particularities of beam generation and guidance in high-power guns (7) shall be discussed in the subsequent chapters.

2.1. Beam Generation

In effect, the beam generating system comprises a two-electrode emitter with solid cathode, anode and a focusing electrode put on cathode potential. Two-electrode arrays of this type are based on the theory of Pierce (8).

Owing to the back-flow of ions in the beam generating chamber (subsequently termed BF ions) and all related sequential phenomena, however, it is impossible to calculate the geometric parameters of the gun according to Pierce any longer because other contributory effects must be taken into account that cannot be adequately described by Pierce's theory; i.e.: -

- (a) Strong deformation of the emitting surface within the service life of the cathode due to sputtering by BF ions;
- (b) Pronounced drop in electric field strength in front of the emitting surface towards the cathode center caused by the penetration of the accelerating field through the anode and the deformation of the emitting surface by BF ions;
- (c) Decrease of beam power density owing to the dispersing lens action of the anode and the space-charge effect of beam electrons with its trend towards divergence.

To (a): BF ions of two different kinds are in existence in the electron gun. Although the pressure in the beam generating chamber is kept at a constant pressure of less than 10^{-2} Pa (10^{-4} Torr), ions are produced by electron collisions also there. Since the differential probability of ionization reaches its maximum at an electron energy of about 100 eV, most of the ions are produced immediately in front of the cathode and, owing to this voltage gradient, accelerated towards the cathode.

Another ion flow is extracted from the beam guidance tube in the anode region by the accelerating field which penetrates the anode bore. These ions are passing the whole accelerating field and impinge on the cathode with a corresponding energy. Due to the low density of the BF ions,

however, their contribution to the space charge in the beam generating system remains rather low.

It was possible to prove that both partial ion currents produce about the same sputter rate at the emitting surface. The sputtering action of ion current (I) at the emitting surface is regular whereas the partial current (II) will be formed in the accelerating field and thus reaches its lowest cross-section in the cathode region.

Figure 2 shows some typical BF ion trajectories of both partial currents found with a 1,200-kW gun after 150 service hours of the cathode. The gun must be designed in such a way that operational reliability is ensured despite the changes in the cathode surface.

With respect to beam electrons, irregular sputtering at the emitting surface causes that the center range becomes ineffective as emitting surface, that the electrical field strength reduces in the border zone of the ion hole - which lowers the emission current density - and that the trajectories of the electrons emerging at the border zone of this ion hole are passing the anode bore at a comparatively wide angle of inclination to the optical axis.

To (b): The emitting surface - deformed by BF ion bombardment - results in electron trajectories of different inclination to the optical axis. Because it is only a very low proportion of electrons that can be faded out from the beam in high-power guns, the diameter of the anode bore must be practically the same as that of the cathode. Owing to the penetration of the accelerating field through the anode bore - and owing to the deformation of the emitting surface by BF ions - the electrical field strength at this surface, and thus the current density, will drop from the boundary towards the center. Thus the outer zone of the cathode must compensate the emission loss in the cathode center by an increased current density. But such an increase in current density is limited by both vapor pressure and mechanical strength of the cathode material.

To (c): In order to reduce the radial drop in field strength at the emitting surface to the absolutely necessary minimum level, the anode bore must be kept as small as possible. Whereas electron trajectories in the region of the optical axis remain rather unaffected by such a measure, the marginal rays receive a radial velocity component by the accelerating field which penetrates the an-

ode bore. Generally, this phenomenon is termed dispersing lens action of the anode bore. Based on membrane model tests, Figure 3 illustrates this effect of the anode bore. Added to this action is an additional radial velocity component caused by the electrostatic repulsive force of the self-charge of the electrons which is determined by the current density of the beam. Figure 3 shows the calculated trajectory of boundary electrons passing the anode bore in parallel which - because of their self-charge - now show to have an increasing radial velocity component.

2.2. Beam Guidance

2.2.1. On the Task of Beam Guidance Lens Systems

Arranged next to the beam generating system is a beam guidance lens which serves to pass the beam through the guidance tube in the form of parallel rays having a configuration that is as slender as possible.

To obtain a deeper insight into this mechanism, Figure 4 shows some typical electron trajectories derived from membrane model tests without consideration of self-charges. Owing to the discussed effects in the gun, the electrons are entering the beam guidance tube at different angles of inclination, viz: -

- (i) Some rays with a cross-over in the anode region;
- (ii) Some rays with a cross-over in the cathode region;
- (iii) Some rays with a virtual cross-over behind the cathode;
- (iv) Some rays with a virtual cross-over in the infinity.

Such a heterocentric beam of rays cannot be converted into a slender beam of parallel rays by way of electron-optical lens system alone. Whereas conversion with a short-focus lens results in a beam with localized small cross-section and large aperture, a long-focus lens gives a beam with large cross-section but narrow aperture. For this reason, ionizable gases are used in our guns in a directed manner together with a comparatively short-focus beam guidance lens so as to pass the beam through the guidance tube in the form of a slender beam of parallel rays.

2.2.2. On the Principle of Gas Focusing

Gas focusing in high-power electron guns is based on a complex mechanism and cannot be explained in detail within the scope of this paper although its use for beam guidance is decisive for the overall design of the gun.

This process is based on electrostatic, magnetic and mechanical forces. In pertinent literature, the known effect of ionizable gases in the beam region has been termed narrow beam formation, electrostatic gas focusing, magnetic pinch effect etc. (9, 10, 11, 12). In electron guns, however, effects of this type can be observed only in part.

We have defined three different steps of gas focusing in high-power electron guns, i.e.: -

Step 1 - Compensation of beam electron self-charges

Step 2 - Magnetic gas focusing

Step 3 - Generation of a highly ionized plasma; creation of an ion barrier in the anode region.

Step 1: In the beam region, neutral atoms are ionized by collision with the electrons. The number of the thus ionized gas atoms per unit of time depends on gas pressure, kind of gas and beam electron velocity. Whilst the ions are kept in a potential well caused by the self-charge of the beam electrons, the secondary electrons will first be forced out of this well until the radial potential gradient vanishes. The first step is attained as soon as the negative potential well is filled up by the positive charge of the ions.

Step 2: Each of the beam electrons is subjected to a force evoked by the magnetic field which is produced by charge carriers that show to have a relative motion with respect to the said beam electrons. These charge carriers are ions and secondary electrons created by collision ionization. Plotted in Figure 5 is the effect on beam electrons caused by the surrounding magnetic field. This presentation is based on the assumption that the space charge of the beam electrons is compensated in full. Corresponding to the amount of space charge compensation, an electron beam with a current density $j(r)$ is surrounded by a magnetic field of an induction $B(r)$. Each beam electron outside of the optical axis is influenced by the magnetic field such that its trajectory becomes curved towards the

optical axis. According to the Lorentz force \vec{F} with

$$\vec{F} = -e (\vec{v} \times \vec{B})$$

the magnetic force then depends on the velocity \vec{v} of the electrons as well as on beam current and current density $j(r)$. When the angles of inclination of the electron trajectories towards the optical axis are narrow enough, the beam electrons will oscillate about the latter with constant amplitude.

So it is only a rather wide angle of inclination towards the optical axis which allows the beam electrons to escape from the region of the magnetic field. In practice, however, the proportion of beam electrons being lost will be greater. But since the pressure-decoupling flow resistances closely embrace the beam, even those electrons will be absorbed by the latter that oscillate about the optical axis at amplitudes which are very high.

Step 3: From measurements on the carrier balance in the beam region - performed with the aid of rotating Langmuir probes - it is concluded that in the beam region of high-power guns and at a residual gas pressure of, say, 10^{-1} Pa (10^{-3} Torr) the ion density exceeds the density of beam electrons by more than 10^3 times. As a consequence, there will be the formation of a regular plasma.

In effect, the relatively high degree of ionization is determined by the magnetic field which surrounds the beam. It not only acts on the beam electrons but also on secondary electrons. Because of their low velocity, the latter are unable to leave the beam region in radial direction. All this results in a kind of magnetic trap. Practically independent of their initial (starting) direction, the secondary electrons therefore drift away on oscillating orbits along the flight path of the beam electrons. Shown in Figure 6 are orbits in the magnetic field of the beam for various energy levels of the secondary electrons; assuming that they originate in the optical axis and that their initial direction runs normal to the latter.

As compared to the representation of a gas-focused beam, a different picture will be obtained in the anode region. Owing to the high carrier density in the beam, the number of secondary electrons and ions suffices for magnetic gas focusing also deep into the anode region. Penetrating through the anode bore, the existing field extracts a space charge limited ion flow from this region.

On the other hand, however, secondary electrons produced in this region (as indicated in Figure 6) are drifting in beam direction so that the anode region becomes deprived of secondary electrons. This yields a potential gradient in axial direction which prevents a possible ingress of ions from the beam guidance system into the beam generating system. Thus the axial potential gradient forms an ion barrier. Because the latter is fixed by space charges of the secondary charge carriers, its potential - referred to the usual potential of the beam axis - amounts to a few Volts only.

It should be pointed out here that the use of magnetic gas focusing in high-power guns prevents "electrostatic gas focusing" (13); an effect which is due to a carrier drift in radial direction. As a consequence of the beam-surrounding magnetic field, however, such a process cannot take place here any longer.

The formation of a highly ionized plasma is used in our guns also to improve pressure decoupling. Its existence increases the viscosity of the flowing gas and, as subsequently shown, the high temperature causes a reduction of particle density. Both effects support the various facilities provided to maintain the pressure difference between working chamber and gun.

3. Electron Beams in the Working Chamber

In the foregoing, scattering actions at the beam caused by interactions of the latter with either gas, vapor or plasma have not been taken into account. This is fully justified insofar that, in high-power guns with sequential pressure grading and utilization of gas focusing, actions of this type must not necessarily play a role within the gun.

Analogous to the effects of ionizable gases in the beam region within the gun, similar effects must be present also on the path of the beam from the gun to the point of action (14). Magnetic gas focusing is by no means restricted to the gun region but also becomes effective outside of the latter. Its action can only be reduced to the very degree external effects are likely to diminish the current density of the beam.

For obtaining quantitative data about scattering actions of residual gas or vapor at a beam guided by means of magnetic gas focusing we have carried out directed

studies with the test setup schematically illustrated in Figure 7. Here a special calorimeter made up of concentric rings with different diameters was employed to determine the beam power density at the simulated point of action. The beam was guided over a path length of 100 cm either unscattered, scattered at the residual gas or scattered at a localized vapor source.

Based on the Rutherford scattering formula it can now be derived that the integral

$$\gamma = \int p \, ds$$

is a characteristic feature for creating a particular scattering action at the beam. Here p is the pressure of the residual gas or vapor and s the path length of the beam in this gas or vapor. In our studies, the above integral is termed $p \times s$ coefficient. The vapor source was arranged in such a way that - with the same γ in the residual gas - scattering at the vapor practically is the same. Plotted in Figure 8 are characteristic results (one each) obtained with comparable parameters used in the scattering tests at vapor and residual gas. It can be shown that, compared to a passage through residual gas, the same beam scattering action is obtained in vapor only with a much greater $p \times s$ coefficient. Similar results were also found after variation of performance parameters such as accelerating voltage, beam power and power density. With equal $p \times s$ coefficients, similar beam scattering actions may only be attained when the number of scattering centers is the same. Interactions between beam and scattering media also transfer a particular amount of energy to the latter. With constant total pressure, however, the particle density n in the beam region must drop proportional to the rise of the temperature T in this region. Hence:

$$n \sim \frac{1}{T} \quad \text{with} \quad p = \text{constant}$$

The smaller the volume within which the energy is converted the higher the temperature and the lower the density of the scattering centers.

From this it follows that it is not only the $p \times s$ coefficient alone but also the energy per volume unit of the beam absorbed over this path length which has a bearing on the beam scattering action. Apart from the mechanical and geometrical quantities of the scattering medium, this energy density further depends on beam current and current density. Therefore, attention must be paid to the

generation of a maximum current density in the beam when using high-power guns for processes where a great $p \times s$ coefficient has to be taken into account.

4. Realization of High-power Electron Guns

As mentioned at the beginning (and then verified by the various statements) the guiding principles used for dimensioning in the field of classical geometric electron optics cannot be applied to high-power guns. Because there is a permanent action of electrostatic, magnetic and mechanical forces on the whole beam path in high-power guns, it is not possible to exactly speak of a zero-field space any longer. To theoretically predict the effects of a particular power and power density on the point of action - brought about by certain means under various conditions - it would be necessary to determine the fate of each individual electron on its way from the cathode to the point of action. At the present state of the art, a closed computation of high-power guns still proves to be impossible. It therefore seems to be indicated to use step-by-step procedures by separating the individual effects. So we have used various methods ranging from experimental investigation and application of membrane models to numerical calculation of subsystems. With the aid of trial and error methods the boundary conditions needed for the theoretical treatment of the subsystems were then quantified by experimental means, using the theoretical model for further improving the experimental setup in an iterative procedure. In this way it is ensured that latest theoretical knowledge and experience gained in industrial application will reap rewards in the further development of high-power guns. Given in Figure 9 is a compilation of high-power guns which may serve to come to an assessment on the degree to which physical particularities can be mastered in guns of this type based on a far-reaching utilization of the discussed effects.

The accelerating voltages, U_b , of the mentioned gun types cover a span of up to 50 kV^b and are still low enough so that additional protective measures (e.g., X-ray shields at the working chamber) can be dispensed with. By combining high current densities in the beam with gas focusing it is now possible to cover large working distances of up to 3 m and to obtain $p \times s$ coefficients that are as high as 100 Torr/cm, max.

Being well matched to the beam, the guidance tube in the high-power gun permits pressure decoupling such that

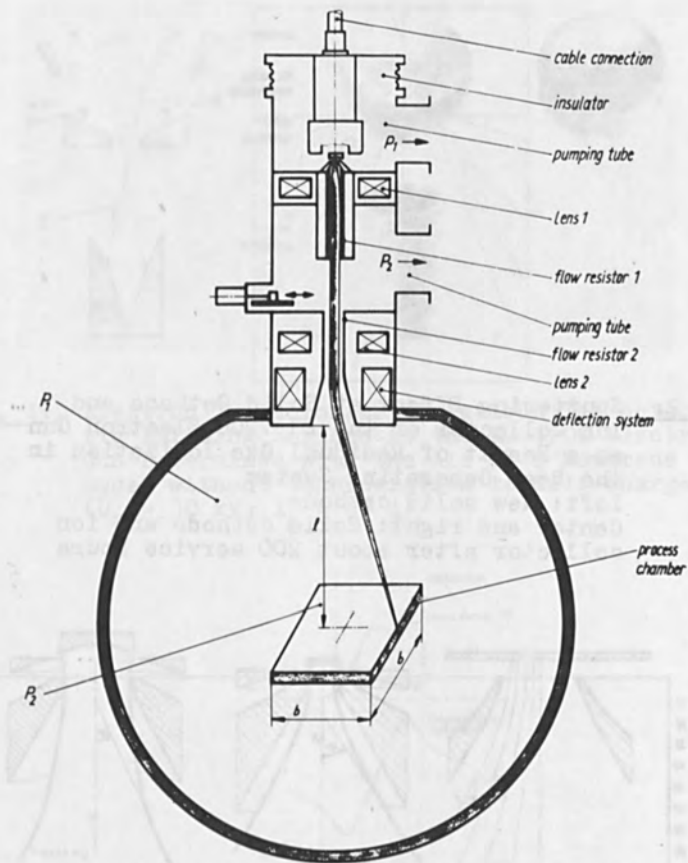
the operating pressure in the working chamber substantially depends on the technological task to be performed rather than on the pressure stability of the gun. Shown in Figure 10 is the actual design of a EH 80/30 High-power Gun with a beam power of 80 kW. Stable operation of this type is ensured even in case that the pressure in the working chamber exceeds 5 Pa ($3 \cdot 10^{-2}$ Torr).

The actual design of a Model EH 1200/50 High-power Electron Gun with a beam power of 1,200 kW is illustrated in Figure 11. This gun obviously is the largest all over the world and serves for smelting very big ingots. Its reliability in service is obtained by stable geometric parameters of the beam generating system and the use of optimized pressure decoupling. To maintain the latter, the gun has been fitted with three diffusion pumps having a nominal bore of 250 mm, each.

References

1. Gruber, H.: Das Schmelzen von Metallen im Elektronenstrahlöfen. *Z. f. Metallkunde*, 52 (1961), p 291
2. Schiller, S.; Förster, H.; Jäsch, G.: Possibilities and Limitations of Large-scale electron beam evaporation. *J. Vac. Sci. Technol.*, 12 (1975), p 800
3. Schiller, S.; Förster, H.; Jäsch, G.; Schroller, R.; Wenzel, B.: Leistungsfähige Elektronenstrahltechnik im Industrieofenbau. *Elektrowärme Int.*, 35 (1977) vol 4, p 219
4. N. N.: Elektronenstrahl in der Aufdampftechnik. Business Publication, Leybold Haereus GmbH, Hanau, FRG, 1975
5. N. N.: Elektronenkanonen von 200 W bis 1200000 W. Business Publication, VEB LEW "Hans Beimler", Hennigsdorf, GDR, 1977
6. Brüche, E.; Scherzer, O.: Geometrische Elektronenoptik, Springer, Berlin 1934
7. v. Ardenne, A.: Dissertation at Technische Hochschule Karl-Marx-Stadt
8. Pierce, J.R.: Theory and design of electron beams D. van Nostrand Company, Inc., 1949

9. Rogowski, W.; Graupner, H.: Zur Erklärung des gas-konzentrierten Elektronenstrahles. Arch. Elektrotech., 26 (1932), p 807
10. Rollwagen, W.: Potentialmessungen an Fadenstrahlen. Z. f. Physik, 89 (1934), p 395
11. Bennett, W.H.: Self focusing streams. Phys. Review, 98 (1955), 6, p 1584
12. Halsted, A.S.; Dunn, D.A.: Electrostatic and magnetic pinch effects in beam generated plasma. J. appl. Phys., 37 (1966), 4, p 1810
13. McCorkle, R.A.; Bennett, W.H.: Electrostatic self-focusing of electron streams. J. Phys. A: gen. phys. 5 (1972), p 524
14. Jäsch, G.: Dissertation at Technische Hochschule Karl-Marx-Stadt



		Melting	Evaporation	Heat Treatment
Working Distance	l	$\leq 3\text{m}$	$\leq 1\text{m}$	$\leq 3\text{m}$
Working Width	b	$\leq 2\text{m}$	$\leq 1\text{m}$	$\leq 1\text{m}$
Pressure of Gas	P_2	$\leq 10^{-2}\text{Torr}$	$\leq 10^{-1}\text{Torr}$	$< 10^{-2}\text{Torr}$
Pressure of Vapor	P_2	$\leq 10^{-1}\text{Torr}$	$> 1\text{Torr}$	

Fig. 1: High-power Electron Gun Mounted to the Working Chamber - Specifications of Characteristic Performance Parameters

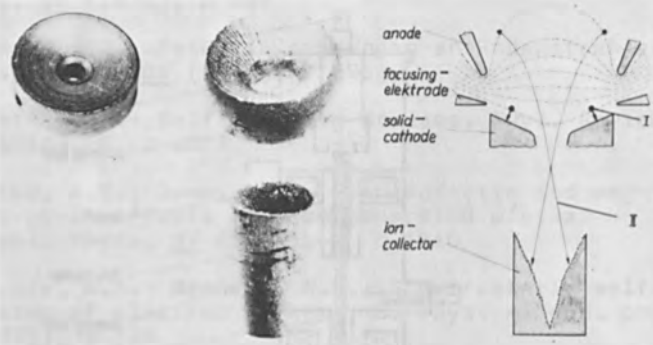


Fig. 2: Sputtering Effect at Solid Cathode and Ion Collector of the EH 1200 Electron Gun as a Result of Residual Gas Ionization in the Beam Generating System
 Left: New solid cathode
 Center and right: Solid cathode and ion collector after about 200 service hours

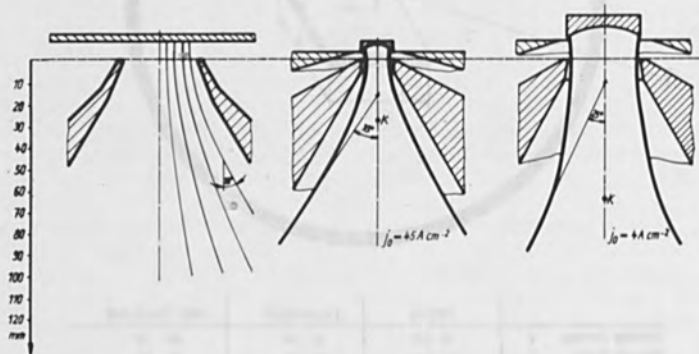


Fig. 3: Effect of Anode Bore Dispersing Lens Action (Left) and Electron Self-charge (Middle, Right) on Beam Formation in the EH 1200 Electron Gun (j_0 = Initial Current Density)
 ($U_b = 30$ kV; $I_b = 35$ A)

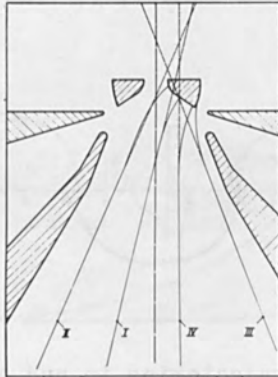


Fig. 4: Electron Trajectories at Various Characteristic Emitting Regions in the EH 1200 Electron Gun Determined with the Aid of a Membrane Model without Consideration to Self-charges ($U_b = 30$ kV; $I_b = 35$ A)

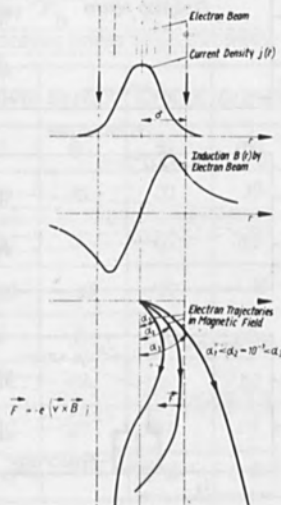


Fig. 5: Schematic Trajectories of Beam Electrons in the Magnetic Proper Field for a 1,200 kW Electron Beam ($U_b = 35$ kV; $\bar{j} = 3$ A/cm²)

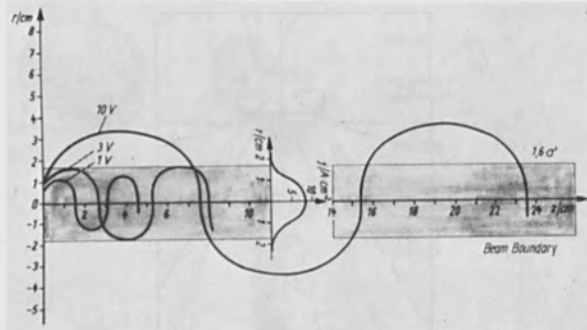


Fig. 6: Electron Trajectories in and Around the Beam Resulting from the Magnetic Proper Field of the Beam with Radial Ejection and Different Volt Velocity of the Electrons

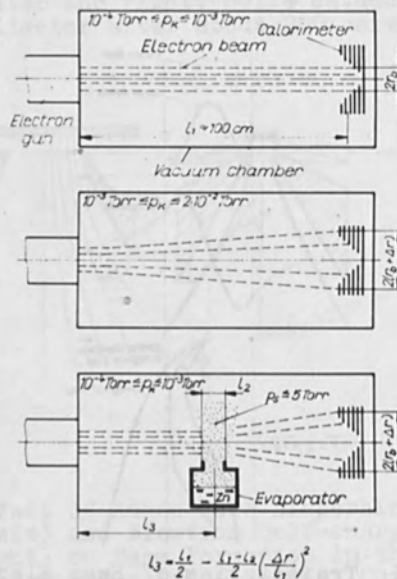


Fig. 7: Test Setup for Determining Beam Scattering at Residual Gas and Vapor

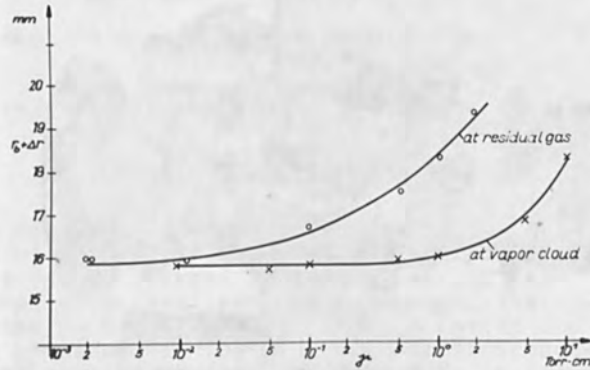


Fig. 8: Increase in Beam Diameter ($r_b + \Delta r$) Due to Scattering at Residual Gas and Vapor vs $p \times s$ Coefficient τ ($U_b = 15$ kV; $P_b = 5$ kW)

Parameters / Type	EH 15/10	EH 30/20	EH 60/20	EH 80/30	EH 250/30	EH 1200/50	Dim.
Rated power	15	30	60	80	250	1200	kW
Max. accelerating voltage	10	20	20	30	30	50	kV
Max. beam current	1.5	1.5	3	2.7	8.5	27	A
Max. beam deflection angle	$> \pm 60$	$> \pm 60$	± 20	± 22	± 35	± 35	degr.
Max. coverage in high vacuum ($p \approx 10^{-4}$ Torr)	0.2	0.6	1	2	2	3	m
Max. $p \times s$ coefficient in the vapor cloud	5	15	20	50	50	> 100	Torr cm
Power density at max. coverage	7	10	30	50	50	50	kW cm ²
Max. pressure in working chamber	$5 \cdot 10^{-3}$	$5 \cdot 10^{-3}$	10^{-2}	$5 \cdot 10^{-2}$	$2 \cdot 10^{-2}$	$\leq 10^{-2}$	Torr

Fig. 9: Comparison of Characteristic Parameters for Some High-power Axial Guns

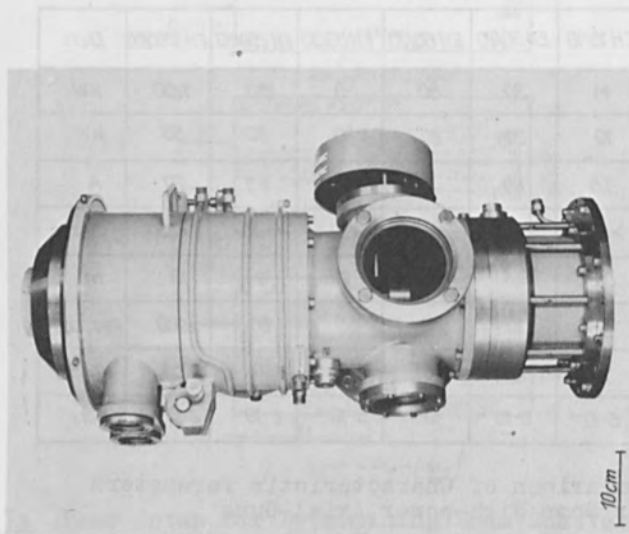


Fig. 10: EH 80/30
High-power Electron Gun
($U_b = 30$ kV; $P_b = 80$ kW)

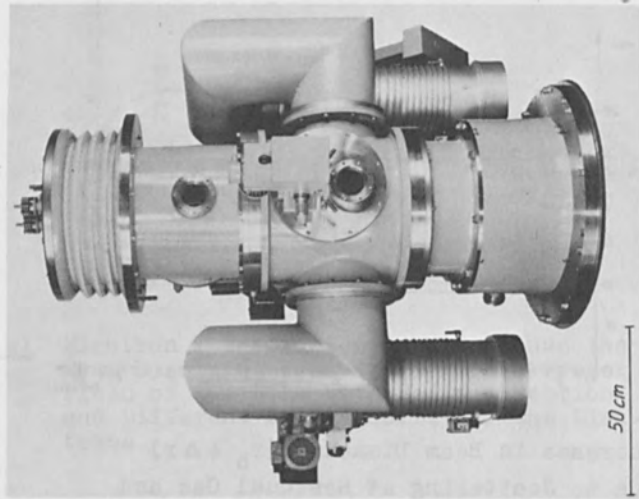


Fig. 11: EH 1200/50
High-power Electron Gun
($U_b = 50$ kV; $P_b = 1,200$ kW)

ELECTRON BEAM MACHINING IN THE FIELD OF
HYBRID TECHNIQUE

Schiller, S., Panzer, S.,
and Henneberger, J.

Manfred von Ardenne Research Institute
Dresden / GDR
and
Kombinat VEB Keramische Werke Hermsdorf

Abstract

Electron beam and laser beam fabrication techniques are of significance in modern electronics. In recent years, thermal electron beam (EB) machining has been developed to maturity and therefore became the dominating pattern generating and trimming procedure in the GDR. With the introduction of EB trimming for screen-printed thick film resistors and fusion scratching of ceramic substrates, EB machining at the present time still increases in importance although thermal effects on the edge zones of the tracks and thus on the attainable degree of integration have to be duly considered.

1. Beam Machining Techniques in Microelectronics

Microelectronic circuits are to be made by two complementary variants either as solid state circuits or hybrid circuits. In the fabrication of microelectronic circuits, pattern generation plays a significant role. Apart from creating the circuit topology this requires micromachining for trimming and fusion scratching of the substrates to obtain the individual circuits. In part, conventional techniques are unable to meet the present requirements for increasing degree of integration, further reduction of pattern dimensions as well as the high demands with respect to productivity and performance parameters (Figure 1).

From Figure 1 it is seen that electron beam and laser beam fabrication techniques are of greatest significance in modern microelectronics. Depending on the task to be performed, either nonthermal or thermal effects will be utilized. The former are used to produce latent patterns in resists and the latter serve for the direct removal

of materials.

Since electron beams and laser beams can readily be focused and deflected, various fabrication techniques may be put into being by way of both beam tools. The three basic versions are illustrated in Figure 2, viz:

- Programmed pointlike or line-shaped machining;
- Programmed machining of substructures and
- Image fabrication.

These processes are characterized by countermoving trends with respect to productivity and flexibility. In solid state technology it is nonthermal EB machining which plays a particular role. Being easily programmed, it streamlines mask making for X-ray and photolithography and allows the fabrication of submicron patterns. Whilst the electron probe technique proves to be suitable only for making masks and, if the occasion arises, for sample circuits, the image method permits direct series fabrication of circuits. When high demands have to be placed on both flexibility and productivity, composed substructure technique (by image probe) often turns out to be the most practicable solution. All three methods operate on the EB principle and are now being introduced into practice.

Above all, it is thermal or nonthermal EB and laser beam machining with the aid of a probe having a programmed deflection which is to be used in the field of hybrid technique. Nonthermal machining with programmed tools noticeably reduces the expenditure for making photomasks or sample circuits and thus substantially improves the flexibility of processes required in hybrid technique. At present times, pattern dimensions beyond the scope of photolithography still are no object in this field.

Thermal EB and laser beam machining are procedures used in hybrid technique for direct pattern generation of active electronic layers such as resistive films, individual trimming of components and cutting of substrates into single circuits. Both techniques have been developed to maturity and are now being used on an industrial scale. The comprehensive use of thermal EB machining in hybrid technique shall now be explained in the subsequent chapters.

2. Tasks to be Performed in Hybrid Technique

Hybrid circuits are put into being by using thin film and thick film techniques. In either case it is resistive, conductive or contacting films as well as dielectric deposits which are to be applied to an electrically insulating substrate made of low-alkali hard glass or ceramics. Whereas film geometry in thick film technique is fixed by screen-printing, continuous resistive films are to be vacuum deposited in thin film technique. Because of the rather coarse configuration, conductive tracks or contact patterns as well as pattern generation of dielectric films still takes place by masked coating in many cases. With thick film technique, precise alignment of resistance values is by trimming without causing noticeable changes in the lateral geometry of the resistance pattern. The production of thin film resistor networks, on the other hand, calls for comprehensive pattern generation of the resistive film.

The previously mentioned layers are deposited on large-area substrates that must then be cut to obtain the individual circuits.

As indicated in Figure 3 the tasks of pattern generation in hybrid technique therefore include:

- Pattern generation of thin resistive films to create resistor networks;
- Trimming of thick film resistors;
- Fusion scratching of ceramic substrates (glass substrates are to be subdivided by scratch breaking).

3. Procedure of EB Machining

Fabrication takes place on an automatic EB machining plant with accelerating voltages of 40 kV and a maximum beam power of 100 W (Figure 4) (1). Equipment of this type operates with an electron probe produced by a two-stage reducing image of the beam cross-over. The second image stage is of a long-focal-length design and permits to sweep the probe over a working field of up to 60 mm x 40 mm. Depending on the size of this field, focal spot diameters range from 20 μm to 40 μm . From magazine to magazine, substrates with dimensions of 100 mm x 60 mm are passed through the working chamber via pressure stage locks. In the working chamber the substrates are accommo-

dated on a pneumatically actuated compound table, contacted and processed in step-and-repeat mode. Beam control with respect to time and space is by a special digital program control unit (2, 3, 4, 5). Automatic beam positioning on the workpiece takes place with the aid of backscattered electron control (6).

The tasks listed in Figure 3 range from the removal of 10-nm NiCr films on glass substrates to the melting of Al_2O_3 ceramic in a depth of some tenth of a millimeter. All this results in different requirements with respect to the EB tool that have to be met by an adequate selection of beam current, machining rate and timed regime of electron probe scanning; i.e., either steady or pulsed operation. However, the accelerating voltage remains constant irrespective of the fabrication technique employed.

Trimming of resistor networks not only calls for an adequate choice of trimming pattern and regime but also requires proper matching of machining rates to the operating speed of the resistance measuring facility used. With the short trimming paths usually found in thick film technique this necessitates the use of a rather low machining rate. Because the focal spot diameter of the electron probe increases with rising beam current, a higher current also results in a larger milling width of the pattern.

When using an adequately selected beam current for film machining on Al_2O_3 substrates and fusion scratching of the latter, both processes can be performed in a single procedure.

A review of performance parameters adapted to the respective tasks and of the resulting milling width is given in Figure 5. For EB machining, the performance parameters not only depend on the film to be removed but equally on the substrate and its thermal conductivity. The relatively low machining rate used for trimming thick film resistors is not caused by the milling process as such but solely by the limited operating speed of the resistance measuring facility used to control the trimming procedure.

The different energetic requirements of the individual tasks become manifest in the needed energy per unit length.

The specified beam current ranges and pulsing parameters are necessary to match the performance parameters

to the size of the working field and, in the case of thick film machining, also to the type and thickness of the layers to be handled.

As far as thin films and thick films on Al_2O_3 substrates are concerned, well-chosen pulsing parameters permit substrate scratching and film machining with the same beam current in a single procedure.

With EB fusion scratching of ceramic substrates, a wedge-shaped zone of the substrate is fused to a depth of some tenth of a millimeter. Under the subsequent action of force the substrate will then break along the scratched line.

Owing to the low-inertia controllability of the electron probe the discussed mode of EB machining is of high precision and productivity; in particular as far as the fabrication of thin film resistor networks with comprehensive pattern generation is concerned. Shown in Figure 6 is a typical example of thin film machining. An EB machined thin film hybrid circuit is illustrated in Figure 7.

Whilst thin film EB machining is widely used for more than 5 years, thick film EB machining has entered the industrial scene only recently.

4. EB Machining and its Effect on Component Properties

Even with optimized performance parameters the "tails" of the Gaussian power density distribution in the focal spot of the electron probe (which do not participate in actual machining) and heat dissipation from the produced track will heat up the adjacent resistive layer as indicated in Figure 8. For a fraction of a millisecond the zones in the immediate vicinity of the track will therefore reach a temperature that comes close to the melting temperature of the film. As a consequence, some (partly reversible) changes in sheet resistivity, temperature coefficient and stability of film properties at the edge zones of the track have to be taken into account. The effects on the components increase with the "scribing density" (i.e., length of machined track per unit area of the resistive film) and depend on both performance parameters and film properties (7).

In part, the effect on sheet resistivity is compensated by the trimming procedure and it is the remaining portion which determines the process-dependent tolerance

limit. If necessary, changes in the temperature coefficient can be eliminated when machining takes place with a uniform scribing density. According to given requirements the effects on the stability restrict the attainable degree of pattern generation.

Plotted in Figure 9 are changes with respect to temperature coefficient and stability caused by the affected edge zones in comparison to the corresponding values of untreated resistive films together with data on the scribing density and thus on the width of the cut track. With thick film resistive layers the chosen degree of pattern generation exceeds the scribing density actually used in practice by a factor of 3 to 5.

Experience has shown that the temperature coefficient, T_c , of the resistance always shifts toward positive values when thin NiCr films are to be machined. With the relatively high positive T_c value of thick film resistors, however, machining reduces the T_c value as compared to that of the untreated film. With NiCr layers, the effects on the stability of the resistive film can generally be ignored. In the case of thick film resistors, however, such an effect is likely to be doubled because it approaches nearly the same order of magnitude as originally found in untreated films.

It must be pointed out here that the resistance pastes listed in Figure 9 were especially developed for laser trimming. With EB trimming of other pastes (i.e., pastes preferably used for trimming by micro-sandblasting) stable resistors will only be obtained when EB trimming is immediately followed by heat treatment.

5. Summary

To sum up, it can be stated that thermal EB machining allows to perform all micromachining procedures found in hybrid technique with high precision and productivity. Back effects of machining on component properties are kept within close limits. EB machining is a fully adequate alternative to thermal laser machining and even turned out to be superior with respect to productivity as far as thin film hybrid technique with its inherent high degree of pattern generation is concerned.

References

1. Schiller, S.; Heisig, U.; Panzer, S.; Henneberger, J.: Zur Weiterentwicklung der thermischen Elektronenstrahlbearbeitung dünner Schichten. Nachrichtentechnik 22 (1972) No. 11, pp 398-401
2. Panzer, S.: Zur Elektronenstrahlbearbeitung dünner Ni-Cr-Schichten auf Hartglassubstrat und zur Anwendung des Verfahrens für die Strukturierung und den Abgleich von Dünnschichtwiderständen. Diss. TH Karl-Marx-Stadt 1968
3. Schiller, S.; Panzer, S.; Heisig, U.: The physical fundamentals of thin film machining. In: Bakish, R.: Electron Beam Science and Technology. 6th Int. Conf. San Francisco, Calif. 1974. New York: Electrochem. Soc. Inc. 1974, pp 412-430
4. Schiller, S.; Panzer, S.; Heisig, U.: Electron beam machining of thin films. In: Silva, R.M.: 3rd Electron Beam Processing Seminar Stratford-upon-Avon, England 1974
5. Schiller, S.; Heisig, U.; Panzer, S.: Elektronenstrahltechnologie. Berlin: VEB Verlag Technik 1977, pp 286-317
6. Panzer, S. et al.: Verfahren und Einrichtung zur automatischen Positionierung und Kontrolle einer Elektronenstrahlsonde auf statistisch positionierten strukturierten Objekten. Economic Patent 87 874 (GDR, 1971)
7. Dänhardt, J.: Vergleichende Untersuchungen zum Einsatz verschiedener Strukturierungsverfahren zur Herstellung von Dünn- und Dickschichtbauelementen. Grad. paper, TU Dresden, 1977

Task to be Performed	Conventional Techniques	Deficiencies	Recent Techniques
Pattern generation of active or passivating layers	Photolithography	Expensive mask making: smallest pattern > 1 μm	EB or laser beam machining X-ray lithography
Trimming	Spark eroding Micro-sandblasting	Low productivity Large track width Dirty work	Thermal laser beam or EB machining
Cutting of substrates into individual circuits	Scratching Abrasive cutting	Low productivity Dirty work Expensive tools	Thermal laser beam or EB machining

Fig. 1
Fabrication Techniques in Microelectronics





Beam Tool	Machining Element	Pattern	Application
Probe	Point		Trimming in thick film hybrid technique Fusion scratching (thermal laser beam or EB machining)
	Line		Pattern generation and trimming in thin film hybrid technique (thermal laser beam or EB machining) Photomasks for solid state technology (nonthermal EB or laser beam machining)
Image Probe	Substructure (e.g., rectangles)		Mask making and direct exposure in solid state technology (nonthermal EB machining)
Image	Complete Structure		Direct exposure in solid state technology (nonthermal EB machining)

Fig. 2
Beam Machining Techniques in Microelectronics




Task	Machined Pattern	Working Conditions
Thin film pattern generation and trimming of resistor networks		Removal of thin NiCr films from hard glass or Al ₂ O ₃ substrates
Trimming of thick film resistor networks		Removal of thick screen-printed glass/metal/metal-oxide layers from Al ₂ O ₃ substrates
Scratching of Al ₂ O ₃ substrates		Fusing of Al ₂ O ₃ substrates over a fraction of their thickness

Fig. 3
Tasks to be Performed in Hybrid Technique



Fig. 4 Automatic EB Machining Plant

Parameter	NiCr Thin Film Machining		Thick Film Machining	Al ₂ O ₃ Fusion Scratching
	On Glass Substrates	On Al ₂ O ₃ Substrates		
Accelerating voltage	kV	40	40	40
Beam current	μA	130 to 180	350 to 450	650 to 700
Pulse duration	μs	—	25 to 30	800 to 1500
Pulse interval	μs	—	250 to 1000	60
Pulse spacing	μm	—	2.5 to 12.5	125
Machining rate	m/s	2	2	0.05 to 0.001
Energy per unit length	Ws/m	2.6 to 3.6	7 to 9	65 to 100
Milling width	μm	25 to 30	35 to 45	45 to 55

Fig. 5 Performance Parameters for Various EB Machining Tasks in Hybrid Technique

Substrate	100 mm × 60 mm, hard glass, Al ₂ O ₃
Resistor networks per substrate	24 (25 mm × 10 mm)
Range of resistance values	< 10 Ohms to > 1 M-ohm
No. of resistors per network	10
Length of machining lines per resistor network	approx. 1 m
Milling width	20 μm to 30 μm
Trimming accuracy	< 0.1% to 1% (depending on requirements and resistance value)
Cycle time	30 s to 60 s

Fig. 6 Characteristic of Thin Film Pattern Generation for the Fabrication of Resistor Networks by Thermal EB Machining

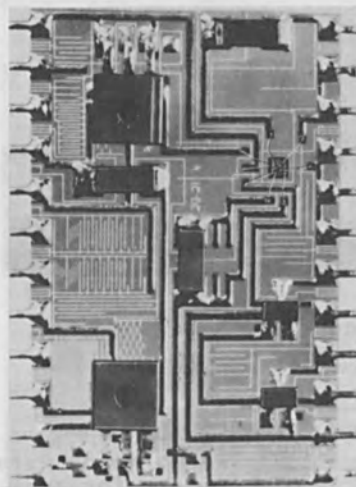


Fig. 7
EB Machined Thin Film Hybrid Circuit with Insertion

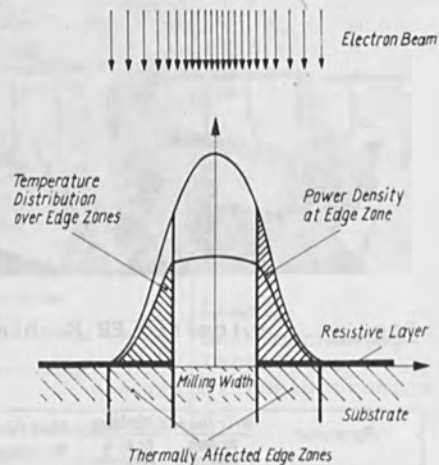


Fig. 8
Thermally Affected Edge Zones Along the Machining Lines

Resistive Film	ρ Ω/\square	T_c $10^{-6} K^{-1}$	$\frac{\Delta R}{R}$ %	LD mm^{-1}	σ' μm	δT_c $10^{-6} K^{-1}$	$\delta(\frac{\Delta R}{R})$ %	
Ni Cr on hard glass	200	12 ± 3	0.5^1	6.6	25	5^1	0.04^1	
Thick film on Al_2O_3 ceramic	Paste 1	10^2	205^{+13}_{-25}	0.1^2	1	50	0	0.3^2
	Paste 2	10^4	210^{+20}_{-12}	0.05^2	1	50	-10	0.2^2
	Paste 3	10^6	55^{+15}_{-10}	0.1^2	1	50	-60	0.1^2

LEGEND: ρ = sheet resistivity
 T_c = temperature coefficient of untreated resistive film
 $\Delta R/R$ = change in resistivity of untreated film
 LD = line density
 σ' = milling width
 δT_c and $\delta(\Delta R/R)$ = change in temperature coefficient and resistance as a consequence of machining
¹⁾ Stored at 200 °C for 6 hours
²⁾ Stored in normal ambient for 1 month

Fig. 9 Effect of EB Machining on Component Properties

TESTS OF FOURTH-ORDER DIFFERENCE EQUATIONS FOR LAPLACE'S EQUATION
IN CYLINDRICAL COORDINATES

C. E. Kuyatt and A. Galejs
National Bureau of Standards, Washington, DC 20234

We wish to test the accuracy of several difference equations which have been derived to represent the Laplace equation

$$\frac{\partial^2 \phi(z,r)}{\partial z^2} + \frac{1}{r} \frac{\partial \phi(z,r)}{\partial r} + \frac{\partial^2 \phi(z,r)}{\partial r^2} = 0 \quad (1)$$

in cylindrical coordinates, where the z-axis is the axis of symmetry. While most digital computer solutions of Laplace's equation have employed five-point difference equations,[1,2] a few calculations have been made using nine-point difference equations.[3-5] Because of the higher accuracy possible with nine-point equations (or gain in speed by using fewer mesh points) it would be useful to know which of the various equations are the most accurate. Although a few assessments of the accuracy of the solutions to Eq. (1) obtained from nine-point difference equations have been made,[4,6,7] no tests of the accuracy of the difference equations themselves appears to have been made. Such tests are important, because they can show the accuracy of the general difference equations as compared to special equations used on the axis and near boundary points, as well as to locate regions which produce the largest errors. As shown by Skölleremo,[7] the overall error of a solution to Eq. (1) is significantly affected by the largest errors which exist in the region.

Our approach is to test the various difference equations on the analytic potential distribution between two spheres. We introduce a square mesh with dimension h in the (z,r) plane and define $\phi_{i,j} = \phi(ih,jh)$ for integer values of i and j. Then, for example, the standard five-point equation for an off-axis mesh point is

$$\phi_{i,j}^* = \frac{1}{4}(\phi_{i-1,j} + \phi_{i+1,j} + \phi_{i,j+1} + \phi_{i,j-1}) + \frac{1}{8j}(\phi_{i,j+1} - \phi_{i,j-1}), \quad (2)$$

where $\phi_{i,j}^*$ is the approximation to $\phi_{i,j}$ calculated from the values of ϕ on the neighboring mesh points. The potential distribution is generated by two concentric spheres, with center at (0,0), radii of 1 and 11 units, and potentials of 0 and 1, respectively:

$$\phi(r,z) = 1.1 \left[1 - \frac{1}{(z^2+r^2)^{1/2}} \right]. \quad (3)$$

For a mesh with $h = 1$, $\phi_{i,j}^*$ was calculated at various mesh points between the spheres using exact ϕ 's from Eq. (3) and the equations from refs. 1-5, (analogous to Eq. (2)). Tables I-IV give a selection of results in the form of differences $\phi_{i,j}^* - \phi_{i,j}$ between the approximate potentials and the exact potentials from Eq. (3). The last number of

each pair in the tables gives the power of 10. In all cases the error is largest close to the small sphere, as one would expect from the large potential gradients which exist there, and decreases rapidly with distance from the small sphere.

On the axis of rotation ($r = 0$, Table I) the Durand formula [5] is clearly better than the formulas of Natali et al [3] or of Vaughan and Buneman,[4] even though there is one point, $z = 4$, where the formula of Vaughan and Buneman gives a smaller error. For off-axis points (Tables II-IV) the formula of Vaughan and Buneman [4] is clearly superior. This is surprising, because the method used to derive Durand's formula appears capable of giving the best possible nine-point formula, and this is borne out by the superiority of Durand's formula for the axis. It is possible that Vaughan and Buneman's formula may be especially good for the spherical potential distribution, while Durand's formula may be better for less well-behaved potential distribution. Further investigation is clearly needed.

[1] The usual five-point difference equations for cylindrical coordinates can be found, for example, in P. T. Kirstein and J. S. Hornsby, IEEE Trans. on Electron Devices 11, 196 (1964).

[2] Another form of five-point difference equations for cylindrical coordinates has been given by P. H. Rose, A. Galejs and L. Peck, Nucl. Instr. and Methods 31, 262 (1964).

[3] S. Natali, D. DiChio and C. E. Kuyatt, J. Research National Bureau of Standards 76A, 27 (1972).

[4] J. R. M. Vaughan and O. Buneman, 'Electron Ray-Tracing Program for Image Intensifiers', Final Report, Contract #DAAK02-67-C-0182 to Night Vision Laboratory, Fort Belvoir, Va. 22060, Sept. 1970.

[5] E. Durand, 'Electrostatique', Vol. II, (Masson, Paris, 1966), p. 34.

[6] E. Durand, 'Electrostatique', Vol. III, (Masson, Paris, 1966) pp 58-59.

[7] A. Skölleremo, J. Comp. Phys., in press.

Table I

Errors for $r = 0$

z	Ref. 3	Ref. 4	Ref. 5
2		-7.0 -3	-6.7 -4
3	8.7 -4	-3.0 -4	6.3 -5
4	6.7 -5	-1.4 -6	1.4 -5
5	1.1 -5	1.2 -5	3.3 -6
6	2.5 -6	7.9 -6	1.0 -6
7	7.7 -7	4.6 -6	3.6 -7
8	2.8 -7	2.7 -6	1.4 -7
9	1.2 -7	1.6 -6	6.4 -8

Table II

Errors for $r = 1$

z	Ref. 3	Ref. 4	Ref. 5
2	-4.2 -3	1.3 -3	2.4 -4
3	-2.0 -4	2.1 -5	-7.5 -5
4	-5.8 -6	-2.7 -6	-1.8 -5
5	-5.0 -7	-9.1 -7	-4.3 -6
6	-2.6 -7	-2.6 -7	-1.3 -6
7	-1.5 -7	-8.3 -8	-4.3 -7
8	-8.3 -8	-2.9 -8	-1.7 -7
9	-4.5 -8	-1.1 -8	-7.2 -8

Table III

Errors for $r = 2$

z	Ref. 3	Ref. 4	Ref. 5
2	2.9 -4	-1.4 -4	-2.5 -4
3	-5.1 -5	5.8 -6	-1.8 -5
4	-1.7 -5	2.2 -6	-3.8 -6
5	-3.8 -6	3.0 -7	-1.4 -6
6	-9.7 -7	1.4 -8	-5.7 -7
7	-3.1 -7	-1.3 -8	-2.4 -7
8	-1.2 -7	-9.2 -9	-1.0 -7
9	-5.5 -8	-5.1 -9	-4.9 -8

Table IV

Errors for $z = 0$

r	Ref. 3	Ref. 4	Ref. 5
2		-2.2 -3	-2.6 -3
3	6.5 -4	-6.6 -5	-8.6 -5
4	5.0 -5	-5.4 -6	-8.0 -6
5	8.0 -6	-7.9 -7	-1.3 -6
6	1.9 -6	-1.7 -7	-3.2 -7
7	5.8 -7	-4.6 -8	-9.7 -8
8	2.1 -7	-1.6 -8	-3.5 -8
9	8.7 -8	-6.0 -9	-1.5 -8

Ref. 3 - Natali, DiChio and Kuyatt.

Ref. 4 - Vaughan and Buneman.

Ref. 5 - Durand.

Table 1.01 shows the error in Target: a one to the wall error, as one would expect from the error in the target. The error in the target is proportional to the error in the target with distance from the wall sphere.

Distance from Wall (m)	Target Error (m)	Target Error (m)	Target Error (m)	Target Error (m)	Target Error (m)	Target Error (m)
0.5	0.05	0.05	0.05	0.05	0.05	0.05
1.0	0.10	0.10	0.10	0.10	0.10	0.10
1.5	0.15	0.15	0.15	0.15	0.15	0.15
2.0	0.20	0.20	0.20	0.20	0.20	0.20
2.5	0.25	0.25	0.25	0.25	0.25	0.25
3.0	0.30	0.30	0.30	0.30	0.30	0.30
3.5	0.35	0.35	0.35	0.35	0.35	0.35
4.0	0.40	0.40	0.40	0.40	0.40	0.40
4.5	0.45	0.45	0.45	0.45	0.45	0.45
5.0	0.50	0.50	0.50	0.50	0.50	0.50
5.5	0.55	0.55	0.55	0.55	0.55	0.55
6.0	0.60	0.60	0.60	0.60	0.60	0.60
6.5	0.65	0.65	0.65	0.65	0.65	0.65
7.0	0.70	0.70	0.70	0.70	0.70	0.70
7.5	0.75	0.75	0.75	0.75	0.75	0.75
8.0	0.80	0.80	0.80	0.80	0.80	0.80
8.5	0.85	0.85	0.85	0.85	0.85	0.85
9.0	0.90	0.90	0.90	0.90	0.90	0.90

[1] The usual five-point difference approximation for cylindrical coordinates can be used for the error in the target.

[2] Another form of the error in the target is given by J. J. Durand, *Journal of Applied Physics*, 42, 2, 1971, p. 1044.

Distance from Wall (m)	Target Error (m)	Target Error (m)	Target Error (m)	Target Error (m)	Target Error (m)	Target Error (m)
0.5	0.05	0.05	0.05	0.05	0.05	0.05
1.0	0.10	0.10	0.10	0.10	0.10	0.10
1.5	0.15	0.15	0.15	0.15	0.15	0.15
2.0	0.20	0.20	0.20	0.20	0.20	0.20
2.5	0.25	0.25	0.25	0.25	0.25	0.25
3.0	0.30	0.30	0.30	0.30	0.30	0.30
3.5	0.35	0.35	0.35	0.35	0.35	0.35
4.0	0.40	0.40	0.40	0.40	0.40	0.40
4.5	0.45	0.45	0.45	0.45	0.45	0.45
5.0	0.50	0.50	0.50	0.50	0.50	0.50
5.5	0.55	0.55	0.55	0.55	0.55	0.55
6.0	0.60	0.60	0.60	0.60	0.60	0.60
6.5	0.65	0.65	0.65	0.65	0.65	0.65
7.0	0.70	0.70	0.70	0.70	0.70	0.70
7.5	0.75	0.75	0.75	0.75	0.75	0.75
8.0	0.80	0.80	0.80	0.80	0.80	0.80
8.5	0.85	0.85	0.85	0.85	0.85	0.85
9.0	0.90	0.90	0.90	0.90	0.90	0.90

Ref. 1 - Hataki, Kato and Koyama
 Ref. 2 - Yaguchi and Hataki
 Ref. 3 - Durand

A

Abel Integral Equation: 71, 79
Abel Matrix: 73, 74, 75
Aberrations, -
- Polar Piece: 25
- Chromatic: 38
- Coulomb: 38
- Fefflection: 36
- Spherical: 35
Absorbed Energy Distribution: 396
Achromatic Imaging System: 171
Achromatic Zoom Lens: 162
Advanced Production Concept: 576
Alignment: 173
- Mark: 66
Aligning: 88
Al K Radiation: 447
Aluminum Radiation: 453
Amdes: 184
Amorphous Layer: 587
Analytical Models: 618
Angular Divergence: 5
Arylodiazonium Salts: 310
Auto Registration: 63, 66
AZ 1350 J: 321
AZ 2400: 320, 321, 323
Auger Electrons: 445

B

Backscatter: 506
Backscatter Contribution: 259
Backscattered Electrons: 256, 374, 399
Baking Conditions: 334
Beam -
- Chopper: 548, 551
- Generation: 628, 630
- Guidance: 628, 631, 641, 644
- Pattern Generation: 135, 142
- Profile: 71, 77
- Quality: 267, 269
- Synthesis: 266

Bethe Law: 395
Bipolar Transistor: 544
Blanker: 509
Bremsstrahlung: 448
Bubble Circuit: 483

C

Chromium: 539
Coating: 537
Compensation of Positional Inaccuracies: 424
Complementary Mask: 406, 421
Computer Control: 354
Computer Program: 351
Computer Simulation: 265, 354
Computing Techniques: 190
Contamination: 510
Contour Fitting: 365
Correction Hardware: 45
Correction Procedure: 46
Correction Wave Form: 46
Corrosion: 535
Critical Absorbed Energy Density: 398
Critical Dose: 208, 362
Critical Energy Density: 246
Critical Gen Dose: 246*
Crosslinking: 304
Cross Sectional Profile: 397
Cu and Au Substrates: 375

D

DAC: 87
Damage: 582
Deep UV Resist: 321, 324
Deflection: 24, 518
- Aberrations: 5
- Diaphragm: 26
- System: 138
- Yoke Inside Lens: 32, 33
Depth Dose Function: 446
Depth of Focus: 210

Depth Profile: 582, 585
 Developer: 518
 Development -
 - Algorithm: 207, 266
 - Characteristics: 458
 - Isocontour: 365
 - Rate Measurement: 257
 Diazanium Salts: 305
 Diazo Type Photo Resist System: 285
 Diaphragm: 26
 Diffraction: 531
 Differential Probe: 71
 Digital Switching Circuit: 219
 Dimethylantracene: 344
 Distortion: 172
 - Characteristics: 44
 - Correction: 44
 - Proximity, Newton-Raphson: 185
 Dose: 362
 Dose Compensation: 269
 Dose Sensitivity: 210
 Double-Wire Probe: 71
 Dynamic Distortion: 161

E

EBES: 199
 Eddy-Currents: 508
 Effects off Gass Vapor: 528
 Effects off Plasma: 528
 Effective Backscattering Coefficient: 245
 Effective Brightness: 3
 Effective Source Size: 2, 3
 Electrodeposition: 232, 234
 Electron Beam: 232
 - Amdes: 184
 - Deflection/Projection: 150, 152
 - Exposure Systems: 150, 152, 285
 - Lithographic System: 179, 180
 - Lithography: 32, 117, 149, 222, 224, 276, 354, 362, 382
 - Lithography Writing Strategies: 13
 - Microfabrication: 216
 - Microfabrication System: 179, 180
 - Microlithography: 23

Electron Beam Micromachining: 645

- Effect on Components: 645
- In Hybrid Technique: 646
- Non Thermal: 646
- Of Ceramics: 646
- Of Thick Films: 646
- Of Thin Films: 646
- Parameters: 647
- Plant: 647
- Principles: 645
- Thermal: 645

Electron Beam -

- Profiles: 150
- Proximity Printing: 420
- Resist Interactions: 242
- Shaping Techniques: 150
- Step and Repeat Proximity Printing: 406
- Welding: 604, 618

Electron -

- Density: 548
- Detector: 63, 64, 65
- Gun: 507, 517
- Image Projector: 108, 109
- Optical: 504, 516
- Optics: 137, 118
- Optics, Spherical Aberration, Correction of: 152
- Projection Lithography: 108
- Projection Mask: 162
- Projection System: 160
- Projector: 170
- Resist: 345
- Scattering: 265, 361, 363, 371
- Temperature: 548

Electroplating Through a Mask: 233

Energy: 539

- Deposition Function: 372
- Stragging, Landau Distribution: 243

Equal Average Dose: 355

Equienergy Density Curves: 447

Experimental Data: 376

Exposure: 362, 515

- Characteristics: 333
- Intensity MIBK: 187
- Profile: 355
- Speed: 160
- Wedge: 276

F

Faraday Cup: 547
FBM: 89
FET: 217, 218, 393
Fermi's Solution: 244
Field Emitter: 1
Field Emission: 4
Field Emission Optics: 12
Filament: 495
Final Spot Size: 3, 6
Fine Pattern Fabrication: 335
Fizeau Interferometer: 323
Fly's Eye Optics: 141
Focus: 508
Forsythe Procedure: 77
Forward Beam Spreading, Fermi's Solution: 244
Forward Scattered Electrons: 374
Four Point Probe: 571
Four Step Exposure Technique: 164
FPM: 90
Friction: 535

G

Ga As Integrated Circuits: 216
Gas Focussing: 632
Gaussian -
- Approximations: 373
- Probe: 395
- Type Beam Profile: 71, 77
Grounding: 504
Gruñ's Range: 446
G-Values for P (MMA-AN) and PMMA: 333

H

Heavy Industries: 604
High Current Beams: 12
High Current Bipolar Transistor: 544
Higher Power Electron Guns: 627
Highly Sensitive Positive EB Resist: 332
High Power Electron Beam Welding: 604, 605, 618
High Speed X-Ray Lithography: 432
Hybrid (Additive/Subtractive) Process: 232, 233
Hybrid Lens: 17

I

Illumination Stability: 173
Image Fidelity: 410
Image Rotation: 507
Impedance Matching: 208
Implanted Dose: 557
Implanter: 543
Implantation Equipment: 572
Implant Uniformity: 557
Information Storage: 501
Infrared Detector: 547
Infrared Rays: 550
Interference: 509
Internal Foil Stress: 425
Ion Beam Etching: 582
Ion Extraction: 549
Ion Implanter: 543, 544
Ion Implantation: 534, 550, 571, 584
Ion Source: 543
Ion Sheath: 545

K

Kodak: 286

L

LaB: 61
Landau Distribution: 243
Laplace's Equation: 655
Laser: 432
- Interferometer: 100, 198
- Interferometer Service System: 198, 199, 200, 201
- Plasma X-Ray Lithography: 433
- Produced Plasma: 432
Lens Aberrations: 18
Lens Field Variation: 18
Light Propagation Efficiency: 65
Line: 495
- Edge Profiles: 265
- Image: 495, 505
- Pattern: 409
Lithography Optics: 11
Long Parallel: 409
Long Working Distance Lens: 179
LSI: 117

M

Machine Alignment: 109
Magnetic Bubble Devices: 232, 480
Magnetic Bubble Memory: 154
Magnetic Interaction Effects: 201
Magnetic Lens: 24
Magnetic Lens Shift: 163
Magnetic Pre-Accelerator Lens: 1
Magnetic Sector: 546
Mask -
- Contrast: 447, 448
- Flatness: 423
- Heating: 436
- Irradiation: 19
- Making and Direct Writing: 99
- Pattern Reproduction: 424
- Self Supporting: 408
- Stencil Problem: 408
- Temperature: 401
- Writing: 268
Mass Separator: 545
Maximum Beam Current: 4
Mechanically Rotated Water Scanning Technique: 547, 550
Membrane: 89
Merged Charge Memory Cells: 22, 225, 226
MIBK: 187
Microlithography: 23
Microprojection: 17
Microprojector: 17
Microwave: 543, 544
Microwave Discharge: 545
Microwave Ion Source: 544
Modified Models: 620
Modulation Transfer Function: 207
Monte Carlo Calculation: 242, 394
Monte Carlo Range: 375
Monte Carlo Simulation: 372
Multi Beam Mask: 164
Multiple Exposure Elimination: 188

N

Narrow-Slit Probe: 71
 Negative: 189
 - Resists: 341
 - X-Ray Resist: 454
 Newton-Raphson: 185
 Non-Fractional Development: 334
 Numerical Model: 621

O

Optical Devices: 490
 Optical Thickness: 209
 Optics: 32
 Optimization Theory For Optics: 13
 Orthogonal Polynomials: 72, 76, 77
 Overlapping: 188
 Oxide Layer: 209

P

Partial Coherence: 211
 Patching Scanfields: 100
 Pattern -
 - Drawing: 101
 - Format: 120
 - Generator and Scanfields: 98
 - Registration: 110
 - Stitching: 198
 Penumbral Blur: 88
 PH₃: 549
 Photo Electrons: 444, 445
 Photolysis: 303, 343, 344
 Photolysis Kinetics: 306
 Photoresists: 303, 343, 344
 Photoresist System: 285
 Pierce: 546
 Plasma: 544, 545
 Plasma Boundary: 548
 Plastic Scintillator: 64
 PMMA: 89, 201, 256, 257, 260, 277, 279, 287,
 288, 321, 325, 396, 478, 480, 482
 Pockels Cell: 422, 436
 Point Probe: 71
 Polar Piece: 25

Poly (Vinylbenzyl Azide): 341, 342, 344, 345
Poly (Vinyl Benzene Sulfonyl Azide): 345
Poly (Vinyl Benzene Sulfonyl Aziolo): 346
Polychrome PC: 129, 286
Polyglycidal Methacrylate-Ethyl Acrylate (PGMA-EA): 458
Polyimide X-Ray Mask: 482
Positive: 189
Post Lens Deflection: 179
Practical Resist: 335
Pre-Accelerator Lens: 1
Preferential Wet Etching: 422
P(MMA-AN) Copolymer: 332
Primary Electron: 399
Probing of Energy Dissipation Profile: 247
Processed < 100 > Field Emitter: 2, 3
Production Implanter: 574
Profile Sensitivity: 268
Projection Printing: 206
Proximity: 185
Proximity and Size Effects: 354
Proximity Effect: 87, 267, 371, 361, 393
Proximity Effect Correction: 382
Proximity Effect Parameters: 276, 278
Proximity Function: 383
Proximity Parameter: 259

R

Radiation Damage: 536
RAM Cells: 222
Random Access Memory (RAM): 222, 223, 227
Raster Scan: 86
Raster Scan Exposure: 407
Reactive Ion Etching: 422
Rectangular Waveguide: 546
Registration by Adsorbed Electrons: 400
Relaxation Time, Heat: 411
Resist: 502
Resist Contrast: 270
Resist Development: 276, 277
Resist Exposure: 257
Resist Model: 266
Resist Parameters: 207
Resist Performance: 459
Resist, PMMA: 444

Resist Profile: 208, 448
RESPECT: 386
Retarded Foil Bending: 425
RhL Radiation: 447
Ridged Circular Waveguide: 545
Rotary Target: 88
Rotating Anode: 481
Rotation, Working Distance: 27
Round Beam: 86

S

Sample Points: 384
Scanning: 510
Scanning Electron Beam System: 44
Self-Supporting Mask: 420
Semiconductor Process: 556
Semiconductors: 537
SEM: 398
- Optics: 11
SEM Profile Measurements: 267
Sensitization: 9, 10, 344
Separator Transmission: 549
SERVO Control: 198
Shaped Beam: 86
Shape Dimension Adjustment: 384
Sheet Resistance: 556
Shipley AZ 1350-J: 286
Shipley AZ 2400: 286
SIC Mask: 453
Silicon Foil: 423
Silicon Thin-Film-Technology: 421
Simulation: 206
Single Level Masking: 232
Si O₂ Pedestal: 232, 233
Soft X-Ray Source: 481
Solar Cell Performance: 575
Solar Cell Production: 572
Solar Cells: 538
Source/Drian Pattern: 394
Spectral Photo Sensitivity: 322
Spectral Transmission: 323
SPECTRE: 385
Spectrum: 521
Sputter Etching: 234

Standing Wave: 207
Stitching Accuracy: 200
Straightedge Probe: 71, 72, 73
Submicron Structure: 410
Substrate: 502
Subtractive Patterning: 232
Substrate Effects: 269
Superimposition Principle: 186
Surface Relief: 520
Synchrotron Radiation: 478, 482
Synthesis: 342
System Tolerance of: 170

T

Temperature Distribution: 618
Test System: 556
Thermal Damage: 435
Thermal Stability of Poly (Vinylbenzyl Azide): 346
Thermionic Emitter: 4
Thermoelectronic Voltage: 412
Thiirane Copolymers: 308
Thiirane Polymers: 303, 304, 309
Thin Film Thermocouple: 412
T & I Bar, -E-Beam Lithography of: 154
Transfer Function: 171
Trapezoid: 189

U

UHV: 57, 59, 61
Ultraviolet: 304

V

Van Der Pauw Resistor: 558
Variable Shaped Beam: 117, 122
- Column: 32
- System: 135, 136
Vector Scan: 362
Video: 501
- Disc Recorder: 490, 495, 507
- Disc Resist: 517
- Playback: 517
- Recording: 517

W

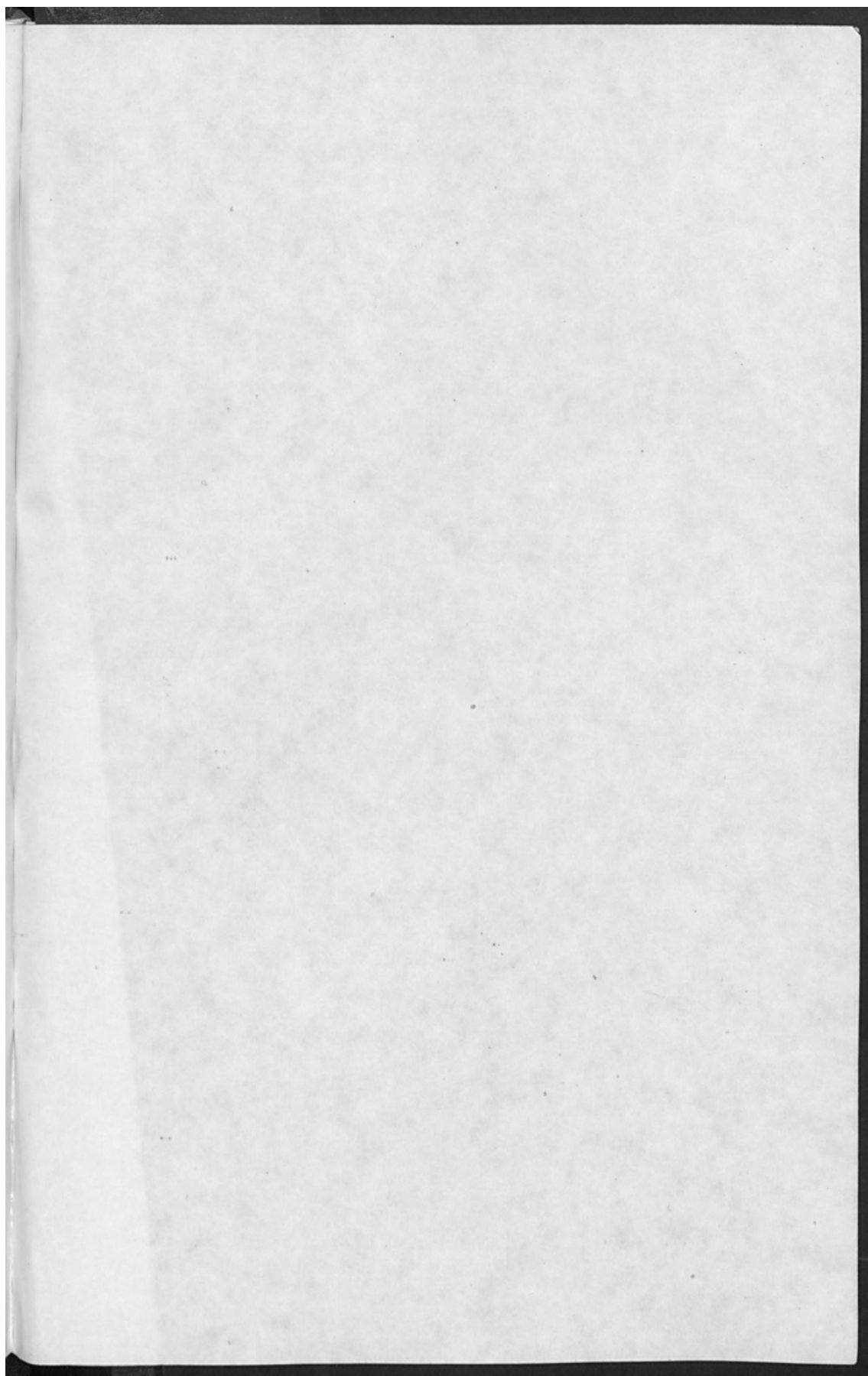
Water Temperature Rise: 549
Wire Probe: 71, 72
Working Distance: 27

X

X-Ray Absorption: 445
X-Ray Exposure: 458
- System: 454
X-Ray Lithography: 232, 432, 434, 447, 453, 480
X-Ray Lithographic System: 85
X-Ray Micro Focus and Anode: 57
X-Ray Resolution: 484

Z

Zoom Lens: 19



Water Temperature Rise: 347

Wire Probe: 71, 72

Working Distance: 27, A

X

X-Ray Absorption: 455

X-Ray Exposure: 455

- Systems: 454

X-Ray Lithography: 432, 433, 434, 447, 448, 486

X-Ray Lithographic Systems: 55

X-Ray Micro-Focus and Anodes: 57

X-Ray Resolution: 457

Z

Zoom Lens: 19

